U.S. DEPARTMENT OF INTERIOR

GEOLOGICAL SURVEY

North Atlantic Slope and Canyon Study

Volume 2

Edited by

Bradford Butman[1]

Open-File Report 88-27B

Prepared in cooperation with
U.S. Minerals Management Service
IA14-12-001-30180

This report is preliminary and has not been reviewed for conformity with U.S. Geological Survey or Minerals Management Service editorial standards.

[1]Woods Hole, MA 02543

1988

50272-101

REPORT DOCUMENTATION PAGE	1. REPORT NO. MMS 86-0086	2.	3. Recipient's Accession No.
4. Title and Subtitle: North Atlantic Slope and Canyon Study			5. Report Date: December, 1986
			6.
7. Author(s): Edited by B. Butman. Authors: B. Butman, M.H. Bothner, V.D. Lyne, J.A. Moody, M.A. Noble, C.M. Parmenter, R.R. Rendigs and M. Rubin			8. Performing Organization Rept. No.
9. Performing Organization Name and Address: U.S. Geological Survey, Branch of Atlantic Marine Geology, Quissett Campus, Woods Hole, MA 02543			10. Project/Task/Work Unit No.
			11. Contract(C) or Grant(G) No. (C) Interagency Agreement IA 14-12-0001-30180 (G)
12. Sponsoring Organization Name and Address: U.S. Dept. of Interior, Minerals Management Service, Atlantic OCS, 1951 Kidwell Drive, Vienna, VA 22180			13. Type of Report & Period Covered: Final Report 1984-1986
			14.

15. Supplementary Notes

A two volume set: Vol. 1 Executive Summary, Vol. 2 Final Report

16. Abstract (Limit: 200 words)

A field program to investigate the currents and sediment transport along the outer-shelf and upper slope along the southern flank of Georges Bank was conducted between 1980 and 1984. A major part of the field experiment was conducted in Lydonia Canyon, a large submarine canyon which cuts northward about 20 km into the continental shelf from the shelfbreak. A smaller experiment was conducted in Oceanographer Canyon to compare the currents in these two major canyons. Long-term current observations were made at 20 locations in or adjacent to Lydonia Canyon, and at 9 stations on the continental slope. Detailed semi-synoptic hydrographic observations were made on 9 cruises. The long-term current observations made in Lydonia and Oceanographer Canyons show that the current regime in these topographic features differs from the adjacent slope, and between canyons. Based on the sediments, geochemistry, and currents observed in Lydonia Canyon, fine-grained sediments, some derived from the shelf, are accumulating in the head of the canyon. The canyons are not tranquil depositional environments however; sediments near the head (depths shallower than about 600 m) in both Lydonia and Oceanographer are frequently resuspended. This frequent resuspension may allow the sediments to strip pollutants from the water column. Currents in Oceanographer Canyon are stronger and the sediments coarser than in Lydonia at comparable depths. The currents associated with Gulf Stream warm core rings (WCR's) strongly affect the flow along the outer shelf and upper slope; eastward currents in excess of 75cm/s were associated with WCR's.

17. Document Analysis a. Descriptors

Lydonia Canyon, continental slope, Oceanographer Canyon, Georges Bank, North Atlantic, sediment transport, Gulf Stream warm core rings.

b. Identifiers/Open-Ended Terms

c. COSATI Field/Group

18. Availability Statement: Availability unlimited	19. Security Class (This Report): unclassified	21. No. of Pages: V1 65; V2 563
	20. Security Class (This Page): unclassified	22. Price

(ANSI-Z39.18) See Instructions on Reverse OPTIONAL FORM 272 (4-77) (Formerly NTIS-35) Department of Commerce

II

VOLUME 1

TABLE OF CONTENTS

EXECUTIVE SUMMARY

	Page
Introduction	1
Field Program	4
Lydonia Canyon Experiment	4
Slope Experiment	15
Results	15
Canyon geometry and sediment texture	15
Currents	22
Suspended particle distribution	26
Sediment transport	32
Canyon comparisons	33
Currents over the slope	34
Instrument calibrations	34
Major Findings	35
Acknowledgements	37
References	38

VOLUME 2

TABLE OF CONTENTS

CHAPTER 1: INTRODUCTION

CHAPTER 2: AN OVERVIEW OF THE LYDONIA CANYON EXPERIMENT: SEDIMENTS, HYDROGRAPHY, AND CURRENTS, by B. Butman

Page

Abstract....2-1
Introduction....2-3
Field Program....2-6
    Instrumentation....2-6
    Moored array....2-8
        Deployment 1....2-9
        Deployments 2-5....2-13
        Data Recovery....2-13
        Mooring Position....2-24
    Hydrography....2-25
    Sediments....2-25
Results....2-28
    Canyon topography....2-28
    Surficial sediment texture....2-32
    Hydrography....2-42
        January 1981....2-43
        May 1981....2-50
        September 1981....2-50
        February 1982....2-58
        Summary of hydrography and suspended sediments....2-65
    Currents....2-66
        Spectra....2-66
        Internal wave characteristics....2-87
        Coherence structure in internal wave band....2-92
        M_2 tidal currents....2-94
        Time variability of semidiurnal fluctuations....2-98
        Mean flow....2-104
            Deployment 1....2-105
            Deployment 2-5....2-113
            Relationship of mean flow to high-frequency fluctuations....2-116
            Summary and discussion of mean flow....2-118
        Gulf Stream Warm Core Rings....2-122
            Frequency....2-122
            Effects on shelf and canyon....2-124
            Effect on near-bottom speeds....2-128
    Currents near the bottom and sediment transport....2-132
    Effect of storms....2-142
    Oceanographer Canyon....2-145
Discussion....2-146
Acknowledgements....2-155
References....2-156

CHAPTER 3: SAND TRANSPORT AND FINE PARTICLE SUSPENSION WITHIN AND AROUND LYDONIA CANYON, by V. D. Lyne and B. Butman

Page

Abstract....3-1
Introduction....3-2
Field data....3-4
Mooring information....3-4
Bottom roughness observations....3-6
Wave and current measurements....3-14
Beam transmissometer fouling....3-15
Sediment transport model....3-17
Model application....3-23
Comparisons of measured and model attenuation....3-25
Predicted sand transport rates....3-31
Fine sediment transport....3-41
Relation to hydrography....3-43
Attenuation time-series interpretation....3-46
Vertical and horizontal interrelationships....3-46
Internal wave packets and sediment suspension....3-53
Discussion on internal wave effects....3-62
Conclusions....3-66
Acknowledgements....3-68
References....3-69

CHAPTER 4: MIXING OF WATER IN SUBMARINE CANYONS INDICATED BY CHANGES IN TEMPERATURE-SALINITY CURVES, by J. A. Moody and B. Butman

Page

Abstract....4-1
Introduction....4-1
Water masses....4-3
Georges Bank water....4-4
Scotian Shelf water....4-4
Winter water....4-6
Western North Atlantic water....4-6
Methods....4-8
Field measurements....4-8
Reference TS curve....4-8
Mixing types....4-10
Results....4-21
January 1981 (OCEANUS Cruise 91)....4-21
April 1981 (OCEANUS Cruise 95)....4-23
October 1981 (OCEANUS Cruise 104)....4-23
January 1982 (OCEANUS Cruise 113)....4-26
November 1982 (OCEANUS Cruise 130)....4-26
Mixing time scales....4-26
Other canyons (OCEANUS Cruise 130)....4-30
Summary....4-32
References....4-35

CHAPTER 5: THE REGIONAL STRUCTURE OF SUBTIDAL CURRENTS WITHIN AND AROUND LYDONIA CANYON, by M. A. Noble

Page

Abstract....5-1
Introduction....5-2
Data Set....5-4
Results....5-12
The regional structure in the subtidal current field....5-12
Subtidal currents over the shelf....5-12
Subtidal currents over the slope....5-19
Subtidal currents in Lydonia Canyon....5-28
Coupling among the regional current fields....5-36
Wind-driven currents....5-40
Discussion....5-46
Summary....5-53
Acknowledgments....5-55
References....5-56

CHAPTER 6: THE FLUX AND COMPOSITION OF RESUSPENDED SEDIMENT IN SUBMARINE CANYONS OFF THE NORTHEASTERN UNITED STATES: IMPLICATIONS FOR POLLUTANT SCAVANGING, by M. H. Bothner, C. M. Parmenter, R. R. Rendigs, and M. Rubin

Page

Abstract....6-1
Introduction....6-2
Equipment and methods....6-3
Sediment traps....6-3
Poison dispensers....6-6
Deployment and recovery....6-8
Laboratory methods....6-8
Results and Discussion....6-10
Comparison of different size traps....6-10
Sediment flux in different physiographic areas....6-11
Depth profile of resuspended sediment flux....6-19
Time variability in flux....6-19
Trace-metal concentrations in sediment-trap samples....6-30
Sediment sources....6-42
Potential of pollutant adsorption by resuspended sediments....6-48
Conclusions....6-55
References....6-57

CHAPTER 7: DOWNSLOPE FLOW ASSOCIATED WITH HIGH-FREQUENCY CURRENT FLUCTUATIONS OBSERVED ON THE OUTER CONTINENTAL SHELF AND UPPER-SLOPE ALONG THE NORTHEASTERN U.S. CONTINENTAL MARGIN: IMPLICATIONS FOR SEDIMENT TRANSPORT, by B. Butman

Page

Abstract....7-1
Introduction....7-1
Field Program....7-3
Results....7-9
    Hydrographic Setting....7-9
    Mean Flow....7-16
    Currents at Station SF....7-21
    Near-bottom flow at other stations....7-37
Discussion and Conclusions....7-47
Acknowledgements....7-50
References....7-51

APPENDIX 1: A FIELD COMPARISON OF FOUR SEDIMENT TRAPS: CHANGES IN COLLECTION WITH TRAP GEOMETRY AND SIZE, by M. H. Bothner, B. Butman, and C. M. Parmenter

Page

Abstract....A1-1
Introduction....A1-1
Equipment and Methods....A1-3
    Traps....A1-3
    Poison Dispensers....A1-5
    Baffles....A1-6
    Deployment and Recovery....A1-7
    Current Measurements....A1-10
    Laboratory Methods....A1-10
Results and Discussion....A1-11
    Changes in collection rate with trap type....A1-11
    Influence of mooring tilt....A1-17
    Influence of poison....A1-18
Conclusions....A1-19
Acknowledgements....A1-20
References....A1-21

APPENDIX 2: NEAR-BOTTOM SUSPENDED MATTER CONCENTRATION ON THE CONTINENTAL SHELF DURING STORMS: ESTIMATES BASED ON IN-SITU OBSERVATIONS OF LIGHT TRANSMISSION AND A PARTICLE SIZE DEPENDENT TRANSMISSOMETER CALIBRATION, by J. A. Moody and B. Butman

Page

Abstract....A2-1
Introduction....A2-1
Theory....A2-4
Calibration Methods and Results....A2-5
    Single particle classes....A2-5

Page
Mixture of particle sizes.....A2-11
Field Measurements.....A2-14
Size distribution of trapped sediments.....A2-22
Estimates of B and suspended-matter concentration.....A2-25
Discussion.....A2-30
Summary.....A2-35
Acknowledgements.....A2-36
References.....A2-37

APPENDIX 3: LYDONIA CANYON EXPERIMENT: MOORING LOCATIONS AND DATA QUALITY.....

APPENDIX 4: SLOPE EXPERIMENT: MOORING LOCATIONS AND DATA QUALITY.....

Volume 1

List of Illustrations

Figure		Page
1	Base map showing location of Lydonia Canyon.....	2
2a	Location of all moorings deployed as part of the Lydonia Canyon Experiment.....	6
2b	Location of moorings in and around Lydonia canyon.....	7
3	Base map and cross-section of Lydonia Canyon.....	8
4	Cruise track for OCEANUS 91.....	10
5a	Schematic of typical moorings deployed on the shelf as part of the Lydonia Canyon Experiment.....	11
5b	Schematic of typical moorings deployed in Lydonia Canyon and on the continental slope.....	12
6	Bottom tripod system.....	13
7	Deep instrument package.....	14
8	Location of moorings deployed as part of the Slope Array Experiment.....	16
9	Cruise track for OCEANUS 140.....	17
10	Bathymetric map of Lydonia Canyon.....	18
11	Percent silt plus clay in the surficial sediments on the southern flank of Georges Bank near Lydonia and Oceanographer Canyons.....	20
12	Surficial sediment texture along the axis of Lydonia Canyon.....	21
13a	Schematic of the Eulerian mean flow on the shelf and slope adjacent to Lydonia Canyon.....	23
13b	Schematic of the upcanyon-downcanyon Eulerian mean flow along the axis of Lydonia Canyon.....	25
14	Histogram of near-bottom currents along the axis of Lydonia and Oceanographer Canyons.....	27
15	Hydrographic section along the axis of Lydonia canyon made in January 1981.....	28

Figure Page

16 Histogram of the current of sediment caught in traps of different heights above the bottom..... 29

17 Time series of currents at LCB..... 30

18 Bottom photograph at LCB..... 31

Volume 1

List of Tables

Table Page

1 Dates of moored array and hydrographic cruises conducted as part of the Lydonia Canyon and Slope Experiment..... 5

Volume 2

List of Illustrations

Figure		Page
2-1	Base map showing location of Lydonia Canyon on the southern flank of Georges Bank.....	2-4
2-2	Map of Lydonia Canyon and section along the canyon axis showing location of instruments in Dl.....	2-10
2-3	Map of Lydonia Canyon and section along the canyon axis showing locaton of instruments in D2.....	2-14
2-4	Map of Lydonia Canyon and section along the canyon axis showing location of instruments in D3.....	2-16
2-5	Map of Lydonia Canyon and section along the canyon axis showing location of instruments in D4.....	2-18
2-6	Map of Lydonia Canyon and section along the canyon axis showing location of instruments in D5.....	2-20
2-7	Time line of all current measurements made as part of the Lydonia Canyon Experiment.....	2-23
2-8a	Location of hydrographic sections for OCEANUS 91 and 95. Circled numbers indicate the section number.....	2-26
2-8b	Location of hydrographic sections for OCEANUS 104 and 117. Circled numbers indicate the section number.....	2-27
2-9	Detailed bathymetric map of Lydonia Canyon.....	2-29
2-10	Bottom slope along the axis of Lydonia Canyon.....	2-31
2-11	Bathymetric sections across the axis of Lydonia Canyon....	2-33
2-12a	Surface sediment texture on the southern flank of Georges Bank adjacent to Lydonia and Oceanographer Canyons. Mean phi.....	2-35
2-12b	Surface sediment texture on the southern flank of Georges Bank adjacent to Lydonia and Oceanographer Canyons. Percent silt plus clay.....	2-36
2-12c	Surface sediment texture on the southern flank of Georges Bank adjacent to Lydonia and Oceanographer Canyons. Percent very fine sand.....	2-37

Figure		Page
2-13a	Surface sediment texture across the southern flank of Georges Bank and along the thalweg of Lydonia Canyon to 1,600 m. Mean Φ.....	2-39
2-13b	Surface sediment texture across the southern flank of Georges Bank and along the thalweg of Lydonia Canyon to 1,600 m.Percent silt plus clay, sand, and gravel.....	2-40
2-13c	Surface sediment texture across the southern flank of Georges Bank and along the thalweg of Lydonia Canyon to 1,600 m. Percent coarse sand (0.5-1.0 mm), medium sand (0.250-0.500 mm), fine sand (0.125-0.250 mm), and very fine sand (0.063-0.125 mm).....	2-41
2-14a	Section 4 made on OCEANUS 91 showing temperature, salinity, sigma-t, and beam attenuation across the shelf and slope east of Lydonia Canyon.....	2-44
2-14b	Section 3 made on OCEANUS 91 showing temperature, salinity, sigma-t, and beam attenuation along the axis of Lydonia Canyon.....	2-45
2-14c	Section 2 made on OCEANUS 91 showing temperature and salinity across the mouth of Lydonia Canyon.....	2-47
2-14d	Section 2 made on OCEANUS 91, showing sigma-t and beam attenuation across the mouth of Lydonia Canyon.....	2-48
2-14e	Vertical distribution of suspended matter at selected stations.....	2-49
2-15a	Section 6 made on OCEANUS 95 showing temperature, salinity, and sigma-t, across the shelf and slope east of Lydonia Canyon.....	2-51
2-15b	Section 5 made on OCEANUS 95 showing temperature, salinity, and sigma-t along the axis of Lydonia Canyon....	2-52
2-16a	Section 5 made on OCEANUS 104 showing temperature, salinity, sigma-t, and beam attenuation across the shelf and slope east of Lydonia Canyon.....	2-54
2-16b	Section 7 made on OCEANUS 104 showing temperature, salinity, sigma-t, and beam attenuation and along the axis of Lydonia Canyon.....	2-55
2-16c	Vertical distribution of suspended matter at selected stations.....	2-56
2-16d	Vertical distribution of suspended matter at selected stations.....	2-57

Figure		Page
2-16e	Vertical distribution of suspended matter at selected stations.....	2-59
2-17a	Section 2 made on OCEANUS 113 showing temperature, salinity, sigma-t, and beam attenuation across the shelf and slope to the east of Lydonia Canyon.....	2-60
2-17b	Section 5 made on OCEANUS 113 showing temperature, salinity, sigma-t, and beam attenuation along the axis of Lydonia Canyon.	2-61
2-17c	Section 3 made on OCEANUS 113 showing temperature and salinity across the mouth of Lydonia Canyon.....	2-62
2-17d	Section 3 made on OCEANUS 113 showing sigma-t and beam attenuation across the mouth of Lydonia Canyon.	2-63
2-17e	Vertical distribution of suspended matter at selected stations.....	2-64
2-18	Variance conserving spectra of currents at LCA, LCI, LCB, LCE and LCH on the shelf, slope and in Lydonia Canyon.	2-74
2-19	Current ellipses in the low-frequency (LF), diurnal (D), inertial (I), semidiurnal (SD) and high-frequency (HF) band at LCB and LCI.....	2-80
2-20	Near-bottom current ellipses along the axis of Lydonia Canyon showing current ellipse orientaton, amplitude, and stability in five frequency bands.....	2-81
2-21a,b	Section along the axis of Lydonia Canyon showing the amplitude of the current fluctuations in the high-frequency, and semidiurnal band.....	2-83
2-21c,d	Section along the axis of Lydonia Canyon showing the amplitude of the current fluctuations in the inertial and low-frequency band.....	2-84
2-22	Brunt-Vaisaila frequency (in cycles/hour) along the axis of Lydonia Canyon.....	2-88
2-23	Amplitude of energy near the bottom along the axis of Lydonia Canyon by frequency band.....	2-91
2-24	Percent of energy in the M_2 tidal band (periods 12.21 to 12.52 hours) which is coherent with the tide on the shelf.....	2-96

Figure Page

2-25 Amplitude of the major axis of the tidal ellipse and phase of the coherent M_2 (periods 12.31 to 12.52 hours) current..... 2-97

2-26 Amplitude of the current at the M_2 tidal period determined in 128 hour segments for the long-term observations at LCB (100 m) and LCB (5 mab)..... 2-99

2-27a Time-series plot of hour-averaged up-canyon current at LCE at 6 mab and 106 mab, beam attenuation at 6 mab, and bottom pressure at LCA during D3..... 2-101

2-27b Time-series plot of hour-averaged upcanyon current at LCB(248) and LCB(294), beam attenuation at LCB(294), current at LCS(5 mab) and bottom pressure at LCL during D4..... 2-102

2-27c Time-series plot of hour-averaged current at LCU(7 mab), beam attenuation at LCU(7 mab), current at LCB(5 mab) and bottom pressure at LCA during D5..... 2-103

2-28 Weekly Ocean Frontal Analysis charts for November 1980 to February 1981. The locations of the moorings are shown as small dots..... 2-106

2-29a Monthly mean Eulerian currents during D1 (November and December, 1980)..... 2-107

2-29b Monthly mean Eulerian currents during D1 (January and February, 1981)..... 2-108

2-29c Monthly mean Eulerian currents during D1 (March and April, 1981)..... 2-109

2-30a Mean Eulerian current for D1 and D2..... 2-111

2-30b Mean Eulerian current for D3 and D4..... 2-114

2-30c Mean Eulerian current for D5..... 2-117

2-31a Preliminary schematic of the Eulerian mean flow on the and slope adjacent to Lydonia Canyon and along the walls of the canyon..... 2-119

2-31b Preliminary schematic of Lydonia Canyon showing upcanyon-downcanyon component the mean Eulerian current at LCB, LCS, and LCE along the canyon axis..... 2-121

2-32 Low-passed along-slope component of flow at LCI(55) and LCI(5 mab) for D1 through D4..... 2-123

2-33 Vector stickplot of low-passed current at LCB(92), LCL(65), LCE(116), LCI(55) and LCJ(103) during D1..... 2-125

Figure		Page
2-34	Vector stickplot of low-passed current at LCB, LCQ, LCR, LCT and LCI during D4	2-127
2-35	Low-passed temperature at selected stations during D4	2-129
2-36	Schematic of flow induced by WCRs around the mouth of Lydonia Canyon at about 200 m based on observations made during WCR 82-A	2-130
2-37	Histogram of current speeds 5 mab at LCI during ring and non-ring periods	2-131
2-38	Cumulative speed distribution curve for stations along the canyon axis showing percent occurrence in excess of given speed	2-133
2-39a	Time series of temperature, beam attenuation, speed and upcanyon current at LCB1 (5 mab)	2-135
2-39b	Time series of temperature, beam attenuation, speed and upcanyon current at LCB4 (5 mab)	2-136
2-39c	Time series of temperature, beam attenuation, speed and upcanyon current at LCE1 (5 mab)	2-137
2-39d	Time series of temperature, beam attenuation, speed and upcanyon current at LCU (5 mab)	2-138
2-40	Scatterplot of hour-averaged currents at LCU, LCB, LCS, and LCE	2-140
2-41	Histogram of near-bottom currents greater than 30 cm/s and between 20 and 30 cm/s as a function of direction for stations along the axis of Lydonia Canyon	2-141
2-42	Standard deviation of bottom pressure at shelf stations during D1 through D5 indicating periods of major wave activity near the bottom	2-143
2-43	Histogram of near-bottom currents greater than 40 cm/s and between 30 and 40 cm/s at stations OCB and OCC in the axis of Oceanographer Canyon	2-147
2-44	Net Eulerian near-bottom flow in Oceanographer Canyon at OCB and OCC	2-148
2-45	Time series of observations made 6 mab at station OCC	2-149
3-1	Bottom photograph at station LCA	3-7
3-2	Bottom photograph at station LCM	3-8
3-3	Bottom photograph at station LCB	3-9

Figure		Page
3-4	Bottom photograph at station LCE.....	3-10
3-5	Bottom photograph near station LCS.....	3-11
3-6	Bottom photograph at station LCH.....	3-12
3-7	Bottom photograph at station LCI.....	3-13
3-8	Output from constrained digital filter.....	3-16
3-9	Measured and predicted attenuation at LCA.....	3-27
3-10	Measured and predicted attenuation at LCB.....	3-28
3-11	Measured and predicted attenuation at LCE.....	3-29
3-12	Measured and prdeicted attenuation at LCM.....	3-30
3-13a	Predicted sand transport roses for stations surrounding Lydonia Canyon.....	3-33
3-13b	Predicted sand transport roses for Lydonia Canyon axis stations.....	3-34
3-13c	Predicted percentage of time of sand transport for stations surrounding Lydonia Canyon.....	3-36
3-13d	Predicted percentage of time of sand transport for canyon axis stations.....	3-37
3-14	Vertical cross-section of salinity and beam attenuation coefficient.....	3-44
3-15a	Time-series of beam attenuation at LCA, LCB and LCE for measurements 20 mab or more.....	3-47
3-15b	Time-series of beam attenuation at LCB and LCE for measurements 5 mab.....	3-48
3-16	Measured and predicted attenuation at LCB.....	3-50
3-17	Measured and predicted attenuation at LCE.....	3-51
3-18a	Time-series of measurements at LCB during energetic internal wave activity.....	3-54
3-18b	Time-series of attenuation, speed shear and vertical temperature difference during energetic internal wave activity.....	3-55
3-19	Measured and predicted attenuation at LCB.....	3-59

Figure		Page
3-20	Comparison of hourly and 450 second current speed at LCB	3-20
3-21	Predicted attenuation at LCB using 450 second data	3-21
3-22	Semidiurnal packets of upcanyon speed and attenuation at LCB	3-22
4-1	Location of submarine canyons	4-2
4-2	Water mass characteristics	4-5
4-3	Standard Western North Atlantic TS curve	4-7
4-4	Hydrographic stations	4-9
4-5a	Western North Atlantic salinity anomaly versus depth	4-11
4-5b	Western North Atlantic salinity anomaly versus density	4-12
4-5c	Western North Atlantic salinity anomaly for OCEANUS 95	4-13
4-6	Hypothetical TS curves for internal mixing	4-15
4-7a	Vertical mixing of a local salinity minimum	4-16
4-7b	Vertical mixing of a local salinity maximum	4-17
4-7c	Vertical mixing resulting in a salinity increase and decrease at different depths	4-18
4-8a	External mixing with less saline water	4-19
4-8b	External mixing with a second water mass	4-20
4-9	January 1981 canyon salinity anomaly	4-22
4-10	April-May 1981 canyon salinity anomaly	4-24
4-11	September-October 1981 canyon salinity anomaly	4-25
4-12	January-February 1982 canyon salinity anomaly	4-27
4-13	November 1982 canyon salinity anomaly	4-28
4-14	Time series of Western North Atlantic salinity anomaly near Lydonia Canyon	4-29
4-15a	TS curves for Oceanographer Canyon	4-31
4-15b	TS curves for Welker Canyon	4-32

Figure		Page
5-1	Location of Lydonia Canyon and the Nantucket wind measurement site	5-3
5-2	Locations of the current-meter moorings deployed in and around Lydonia Canyon	5-7
5-3	Locations of the current meters within and above Lydonia Canyon showing the mooring name and current-meter category	5-8
5-4	Wind stress and typical current-meter records illustrating the flow on the shelf, slope and in the canyon	5-13
5-5	The first mode for alongshelf currents over the shelf	5-18
5-6	Coherence between mid-depth currents at shelf site LCL(70) and the first mode, Shelf EOF, currents	5-20
5-7	Variance-conserving spectra of alongshelf currents and wind stress and cross-shelf currents and wind stress	5-21
5-8	The first mode along-slope currents for Slope(200) EOF and Slope(500) EOF	5-24
5-9	Variance-conserving spectra of along-slope currents at Slope(200) and Slope(500) sites	5-25
5-10	Cross-slope current amplitudes at sites in the second Slope(200) EOF mode	5-27
5-11	Subtidal along-canyon current amplitudes at all canyon sites	5-31
5-12	Mean along-canyon current amplitudes at canyon sites	5-32
5-13	Variance-conserving spectra of along and cross-canyon currents	5-33
5-14	The amplitude of Mode 1 along-canyon currents	5-37
6-1	Map showing locations of moorings in and around Lydonia and Oceanographer Canyons	6-4
6-2	Diagram showing physical dimensions of sediment traps	6-5
6-3	Histograms showing the flux of resuspended sediments at different locations and depths in Lydonia Canyon	6-15
6-4	Comparison of sediment flux at different locations in the study area	6-17

Figure		Page
6-5	Comparison of sediment flux in Lydonia and Oceanographer Canyons	6-18
6-6	Flux of sediments in axis of Lydonia Canyon during 5 deployment periods	6-20
6-7	Sediment flux in the axis of Lydonia Canyon, station LCB	6-22
6-8	Record of pressure standard deviation measured near the rim of Lydonia Canyon for each deployment period	6-23
6-9	Comparison of sediment flux in Lydonia Canyon axis and on the Continental Shelf at 5 meters above bottom	6-24
6-10	Diagram showing texture, structure, and x-radiograph of a sediment trap sample from station LCA. Calculated stress and predicted flux also shown	6-25
6-11	Diagram showing texture, structure, and x-radiograph of a sediment trap sample from station LCP. Calculated stress and predicted flux also shown	6-28
6-12	X-radiographs of trap samples from station LCB	6-31
6-13	Histograms showing the average metal to aluminum ratio in sediment trap samples from different geographical areas	6-38
6-14	Concentrations of barium in the fine fraction of sediment collected at station LCB during 5 deployments	6-44
6-15	^{14}C age of organic carbon in sediment cores from the head of Lydonia Canyon	6-47
7-1a	Bathymetric map showing location of current measurements made along the outer shelf and upper slope south of New England	7-4
7-1b	Detailed map showing location of moorings near 70°W	7-5
7-2	Hydrographic sections of temperature, salinity, sigma-t, Brunt-Vaisaila frequency, and beam attenuation made across the outer shelf and upper slope near 70°W	7-11
7-3	Near-bottom mean flow observed at selected stations during slope array II, slope array III, and the Lydonia Canyon experiment	7-18
7-4	Time series of temperature, speed, beam attenuation, and hour hour-averaged and low-passed along-slope and cross-slope current at station SF for record 2751 (126 m, 76 mab) and record 2752 (195 m, 7 mab)	7-23

Figure		Page
7-5	Time series of beam attenuation, salinity, temperature, speed, and cross-slope current at 7 mab at station SF.....	7-26
7-6	Histogram of near-bottom current speed, and histogram of current direction for various speed intervals for currents measured at station SF at 7 and 76 mab.....	7-29
7-7	Variance conserving kinetic energy spectra for currents observed at station SF at 7 and 76 mab.....	7-30
7-8	Current ellipses at 7 and 76 mab at station SF for energy in the low frequency, diurnal, inertial, semidiurnal, and high frequency bands.....	7-31
7-9	Coherence between the along-slope and cross-slope currents at station SF at 7 and 76 mab.....	7-33
7-10	Coherence between the cross-slope current and sigma-t at 7 mab and 76 mab at station SF.....	7-36
7-11	Scatter plot of low-passed cross-slope Reynolds flux of density (sigma-t) vs low-passed cross-slope current at station SF.....	7-38
7-12	Time series plot of a portion of record 2752 at station SF illustrating the procedure used to estimate the envelope of the high frequency current fluctuations...	7-39
7-13	Scatter-plot of low-passed cross-slope flow vs amplitude of high-frequency fluctuations for currents at 7 and 76 mab at station SF.....	7-40
7-14	Speed exceeded 5% of the time, downslope flow exceeded 1% of the time, and ratio of down-slope flow exceeded 1% of the time to upslope flow exceeded 1% of the time for measurements at 7 and 50-200 mab as a function of water depth.....	7-41
7-15	Scatter plot of low-passed cross-slope flow vs amplitude of high frequency fluctuations for currents at 7 and 50-200 mab at LCI, SE, and SG in water depths of 250, 500, and 1150 m respectively.....	7-44
7-16	Net cross-slope flow vs standard deviation of cross-slope flow for current observations 5-7 mab at stations SF, LCI, SA, SE, and SG at nominal water depths of 200, 250, 500,and 1150 m.....	7-45
A1-1	Physical dimensions of the sediment traps used in this experiment.....	A1-4
A1-2	Configuration of the poison dispenser.....	A1-4

Figure		Page
A1-3	Map showing the station locations and a schematic showing trap spacing on the mooring wire.....	A1-9
A1-4	Variation in the flux of sediment for traps of different diameter.....	A1-12
A1-5	Variation in the flux of trapped sediment as a function of traps aspect ratio.....	A1-15
A2-1	Transmissometer calibration slope B_1 as function of particle diameter.....	A2-8
A2-2	Size distribution of tested sediment mixtures.....	A2-12
A2-3	Station locations.....	A2-14
A2-4	Bottom photographs.....	A2-15
A2-5	Time series for station K.....	A2-19
A2-6	Time series for station B.....	A2-20
A2-7	Graphic representation of an x-ray photograph of material collected in a sediment trap.....	A2-23

Volume 2

List of Tables

Table		Page
2-1	Dates of moored array deployments and hydrographic cruises	2-7
2-2	Mooring information for Deployment 1 of the moored array	2-11
2-3	Mooring information for Deployment 2 of the moored array	2-15
2-4	Mooring information for Deployment 3 of the moored array	2-17
2-5	Mooring information for Deployment 4 of the moored array	2-19
2-6	Mooring information for Deployment 5 of the moored array	2-21
2-7	Mooring information for moorings in Oceanographer Canyon	2-22
2-8a	Statistics of hour-averaged current observations	2-67
2-8b	Statistics of low-passed current observations	2-70
2-8c	Statistics of hour-averaged and low-passed current observations made in Oceanographer Canyon	2-73
2-9	Total energy and ellipse statistics by frequency band	2-76
2-10	Confidence limits for current amplitude	2-85
2-11	Bottom slope, range of Brunt-Vaisaila frequencies, and critical period for segments of the axis of Lydonia Canyon	2-90
2-12	Coherence and phase between selected current observations at the inertial, semi-diurnal and high-frequency periods	2-93
2-13	A comparison of current statistics in Lydonia, Oceanographer and Baltimore Canyons	2-153

Table		Page
3-1	Location and deployment information.....	3-5
3-2	Model parameters for bottom roughness and surficial sediment.....	3-24
3-3	Components of predicted net sand transport.....	3-32
5-1	Locations of current meters in and around Lydonia Canyon in Deployment 1.....	5-5
5-2	Ellipse statistics of the subtidal flow field.....	5-10
5-3	Mean and variance of the subtidal currents at each site.....	5-15
5-4	The first mode in the along and cross-shelf currents.....	5-17
5-5	The first mode in the along and cross-slope currents over the slope.....	5-22
5-6	Coherences among the slope(200) and slope(500) alongslope currents.....	5-29
5-7a	Correlations and coherences among the alongcanyon currents.....	5-34
5-7b	First mode for alongcanyon currents.....	5-35
5-8	Coherences among the regional currents.....	5-38
5-9	Correlation of the alongisobath shelf and slope modal currents with the alongcanyon currents.....	5-41
5-10a	Coherences between the alongshelf wind stress and alongisobath currents.....	5-43
5-10b	Coherences between cross-shelf wind stress and alongisobath currents.....	5-44
5-10c	Coherences between 110^{o} wind stress and alongisobath currents.....	5-45
5-11	Angle between the wind stress and alongisobath current that represents the maximum coherent current forcing.....	5-47
5-12	The coherence between alongisobath wind stress and cross-slope currents.....	5-48

Table		Page
6-1	Sediment-trap deployments and flux data	6-12
6-2A	Chemical analyses of sediment-trap samples before drilling	6-32
6-2B	Chemical analyses of sediment-trap samples-continued	6-33
6-2C	Chemical analyses of sediment-trap samples-continued	6-34
6-2D	Sediment-trap deployments-continued	6-35
6-2E	Sediment-trap locations and deployment dates-continued	6-36
6-3	^{14}C ages determined on total organic carbon in sediment	6-46
6-4	Sediment radionuclide distributions	6-50
6-5	Textural analyses of box cores	6-53
7-1	Station identifier, water-depth, and location of stations where current observations were made	7-7
7-2	Statistics of the alongisobath and crossisobath currents	7-8
7-3	Total energy and ellipse statistics for currents in low-frequency, diurnal, inertial, semi-diurnal and high-frequency bands	7-32
A1-1	Deployment data and results of two sediment trap comparison experiments	A1-8
A1-2	Statistics of currents measured at station LCS and LCB	A1-14
A2-1	Calibration slopes B_i	A2-7
A2-2	Comparison of predicted and measured calibration slopes B	A2-11
A2-3	Estimates of suspended-matter concentration during six winter storms	A2-28
A2-4	Field measurements of the calibration slope $\bar{B}$	A2-31
A3-1	Lydonia Canyon Experiment; mooring locations and data quality	A3-2
A4-1	Slope Experiment; mooring locations and data quality	A4-2

CHAPTER 1

INTRODUCTION

This final report presents the results of research conducted in the vicinity of Lydonia Canyon and on the outer shelf and upper slope along the western North Atlantic continental margin by the U.S. Geological Survey (USGS) in cooperation with the Bureau of Land Management (BLM) and the Minerals Management Service (MMS) in accordance with Interagency Agreements AA851-IA1-17, AA851-IA2-26, and IA 14-12-0001-30180. The program is called the North Atlantic Slope and Canyon Study (NASACS). Field measurements in and around Lydonia Canyon were made between October 1980 and November 1982 and on the outer shelf and upper slope between November 1982 and November 1984. More than 60 current meter moorings were deployed on 11 research cruises; extensive hydrographic observations were made on 10 of these. To our knowledge, this field program is the largest and most detailed ever conducted in a submarine canyon.

The major objective of the research was to describe and understand the physical oceanography and sediment transport of Lydonia Canyon, a major submarine canyon located on the southern flank of Georges Bank. Of particular interest was the transport of water and sediment from the shelf into the canyon and across the shelfbreak to the continental slope. Canyons and gullies dissect a substantial part of the continental margin south of Georges Bank. They are important sites biologically and may be sites for accumulation of pollutants introduced onto the margin by OCS activity.

This report contains 6 interpretive chapters and 2 appendices which describe the major results of the field program. Chapter 2 presents an overview of the canyon experiment and a description of the sediments, hydrography and currents. Chapter 3 describes the transport of sand and fine particles in Lydonia Canyon and chapter 4 presents evidence for mixing within the canyon based on analysis of temperature-salinity characteristics.

Chapter 5 describes the low-frequency currents which fluctuate at periods longer than about 40 hours, and the coupling of these currents on the shelf, slope and in Lydonia Canyon. Chapter 6 is an analysis of sediment resuspension and pollutant scavenging by fine-grained sediments, based on material collected by sediment traps and on material collected in sediment cores. This geochemical analysis provides independent support for conclusions based on the physical oceanographic observations. Chapter 7 presents observations made on the outer shelf and upper slope and implications for the transport of sediment. Appendix 1 describes a field comparison of the collection rate of different sediment traps and Appendix 2 the calibration of beam transmissometers. Both transmissometers and traps were used extensively in the field experiments and these studies are essential to the interpretation of the results. Appendices 3 and 4 contain tabulations of the mooring locations and data quality for the Lydonia Canyon and Slope Experiments respectively.

Three other field experiments compliment this study. Measurements were made in Baltimore Canyon as part of the Canyon and Slope Process Study (LDGO, 1983). The MASARS (Middle Atlantic Slope and Rise Study), conducted by Science Applications International, and SEEP (Shelf Edge Exchange Processes), a Department of Energy study, both measured currents along the outer shelf, slope, and rise to understand the transport of sediments from the shelf to the slope and the ultimate sink for this material. Preliminary results from MASAR, SEEP and NASAC are presented in Csanady and others (submitted).

Both components of the NASAC study, the Lydonia Canyon Experiment and the Slope Experiment, provide an extensive new data set where few long-term observations existed previously. The interpretive chapters in this report present analysis of the most important aspects of these data sets. However,

the data are a rich source for additional analysis of processes within submarine canyons and on the continental slope.

REFERENCES

Csanady, G. T., Churchill, J. H., and Butman, B., Near-bottom currents over the continental slope in the Mid-Atlantic Bight: Continental Shelf Research. (Submitted).

LDGO, 1983, Canyon and Slope Processes Study, 3 vols., Final report prepared for U.S. Minerals Management Service, Contract 14-12-0001-29178. Lamont Doherty Geological Observatory, Palisades, N.Y.

CHAPTER 2

AN OVERVIEW OF THE LYDONIA CANYON EXPERIMENT: SEDIMENTS, HYDROGRAPHY AND CURRENTS

By

Bradford Butman

CHAPTER 2

Table of Contents

Page

Abstract.....2-1

Introduction.....2-3

Field Program.....2-6

Instrumentation.....2-6

Moored array.....2-8

Deployment 1.....2-9

Deployments 2-5.....2-13

Data Recovery.....2-13

Mooring Position.....2-24

Hydrography.....2-25

Sediments.....2-25

Results.....2-28

Canyon topography.....2-28

Surficial sediment texture.....2-32

Hydrography.....2-42

January 1981.....2-43

May 1981.....2-50

September 1981.....2-50

February 1982.....2-58

Summary of hydrography and suspended sediments.....2-65

Currents.....2-66

Spectra.....2-66

Internal wave characteristics.....2-87

Coherence structure in internal wave band.....2-92

Page

M_2 tidal currents.....2-94
Time variability of semidiurnal fluctuations.....2-98
Mean flow.....2-104
Deployment 1.....2-105
Deployment 2-5.....2-113
Relationship of mean flow to high-frequency fluctuations.....2-116
Summary and discussion of mean flow.....2-118
Gulf Stream Warm Core Rings.....2-122
Frequency.....2-122
Effects on shelf and canyon.....2-124
Effect on near-bottom speeds.....2-128
Currents near the bottom and sediment transport.....2-132
Effect of storms.....2-142
Oceanographer Canyon.....2-145
Discussion.....2-146
Acknowledgements.....2-155
References.....2-156

ABSTRACT

A field program was conducted to study the circulation and sediment dynamics in Lydonia canyon, located on the southern flank of Georges Bank, and on the adjacent shelf and slope. The program included: (1) measurements by an array of moored current meters, bottom tripods, and sediment traps maintained between November 1980 and November 1982; (2) synoptic observations of the hydrography and suspended sediments; (3) sidescan and high-resolution profiles; (4) samples of the surficial sediments; and (5) direct observations of the sea floor from the submersible ALVIN. An overview of the surficial sediment, hydrography and moored observations is presented here.

The surficial sediment distribution and the high-resolution profiles (Twichell, 1983) suggest that very fine sand and silts and clays accumulate in the head of the canyon, and on an area of the adjacent shelf. However, the moored current measurements show that the surficial sediments are reworked and resuspended along the canyon axis to a depth of at least 600 m. Thus, although fine sediments may be accumulating, the axis is not tranquil. Maximum hour-averaged current speeds 5 meters above bottom (mab) were greater than 60 cm/s at about 300 and 600 m in the canyon axis. No evidence of sediment movement was observed at 1,380 m. The current observations suggest down-canyon transport of sediment along the axis near the head and up-canyon transport at about 600 m implying a convergence in the transport of sand as bedload toward the head. Qualitatively, the sediment distribution along the axis mirrors the strength of the near-bottom currents.

The mean Eulerian current on the shelf adjacent to Lydonia Canyon and above the level of the canyon rim was southwestward, consistent with previous studies of the mean circulation on Georges Bank. On the Continental Slope, the mean flow was strongly influenced by Gulf Stream warm core rings. Several

rings passed to the south of Lydonia Canyon during the observation period; the strong clockwise flow around them caused eastward flow along the edge of the shelf as strong as 80 cm/s. On the slope the influence of the rings in the water column extended to at least 250 m, but not to 500 m. The influence of the rings did not extend onto the Continental Shelf to water depths of 125 m. There was a persistent off-shelf and downslope component of flow near the bottom of a few cm/s. There is some evidence that the warm core rings affect flow in the canyon by generating packets of high-frequency current fluctuations.

Within the canyon, the mean Eulerian flow near the bottom was complex. Near the head of the canyon, net Eulerian flow 5 mab was down-canyon at about 3 cm/s and weak 50 mab. At 550 m the near-bottom flow was up-canyon. At 600 m the near-bottom flow was weak, and the flow 100 mab was up-canyon. These observations suggest a convergence of the mean Eulerian flow between 300 and 600 m, and possibly several cells of recirculation along the canyon axis. However, because of the energetic non-linear high-frequency motion observed in the canyon and the small spatial scales, the mean Eulerian current may not indicate the actual Lagrangian water particle motion. Further analysis is required to determine the Lagrangian circulation pattern. Measurements made on the eastern rim of the canyon at about 200 m show westward flow directly across the canyon axis. Measurements on the eastern wall of the canyon just a few km away at comparable depths show northward inflow along the eastern wall. Measurements on the western wall show southward outflow. The mean Eulerian currents in the canyon thus suggest a complex vertical Eulerian circulation along the axis, and horizontal exchange along the canyon walls.

The current fluctuations within the canyon are aligned with the canyon axis. The strength of the high-frequency fluctuations increase toward the

bottom and the head of the canyon. The low-frequency currents were strongest over the slope and weakest in the canyon. The fluctuations at semidiurnal period dominate the current spectra; near the canyon head their strength changes substantially with time, indicating random generation of internal wave packets.

Currents in Oceanographer were dominated by the tidal currents and were stronger than in Lydonia. Net Eulerian down-canyon flow was observed at both 200 and 600 m.

INTRODUCTION

The continental slope south of Georges Bank and the New England continental shelf is incised by numerous submarine canyons (fig. 2-1). Lydonia Canyon is the easternmost of four major canyons located along the southern flank of Georges Bank east of Great South Channel. The canyon, as defined by the 200 m isobath, cuts northward approximately 20 km onto the continental shelf.

Canyons have long been of interest to marine geologists for their role in the transport of sediments from the shelf to the deep ocean (Shepard and Dill, 1966; Shepard et al., 1979; Stanley and Kelling, 1978), and the canyons provide a variety of habitats and substrates for organisms (Hecker and others, 1983). However, it is only recently that long-term current observations have been made in some of these canyons (Hotchkiss and Wunsch, 1982; Gardner, 1983; Hunkins, 1983; Carson and others, 1986; Hickey and others, 1986) to document the current dynamics and exchange in these topographic features.

In 1980 the U.S. Geological Survey, in cooperation with the U.S. Bureau of Land Management (now Minerals Management Service), began a field study of

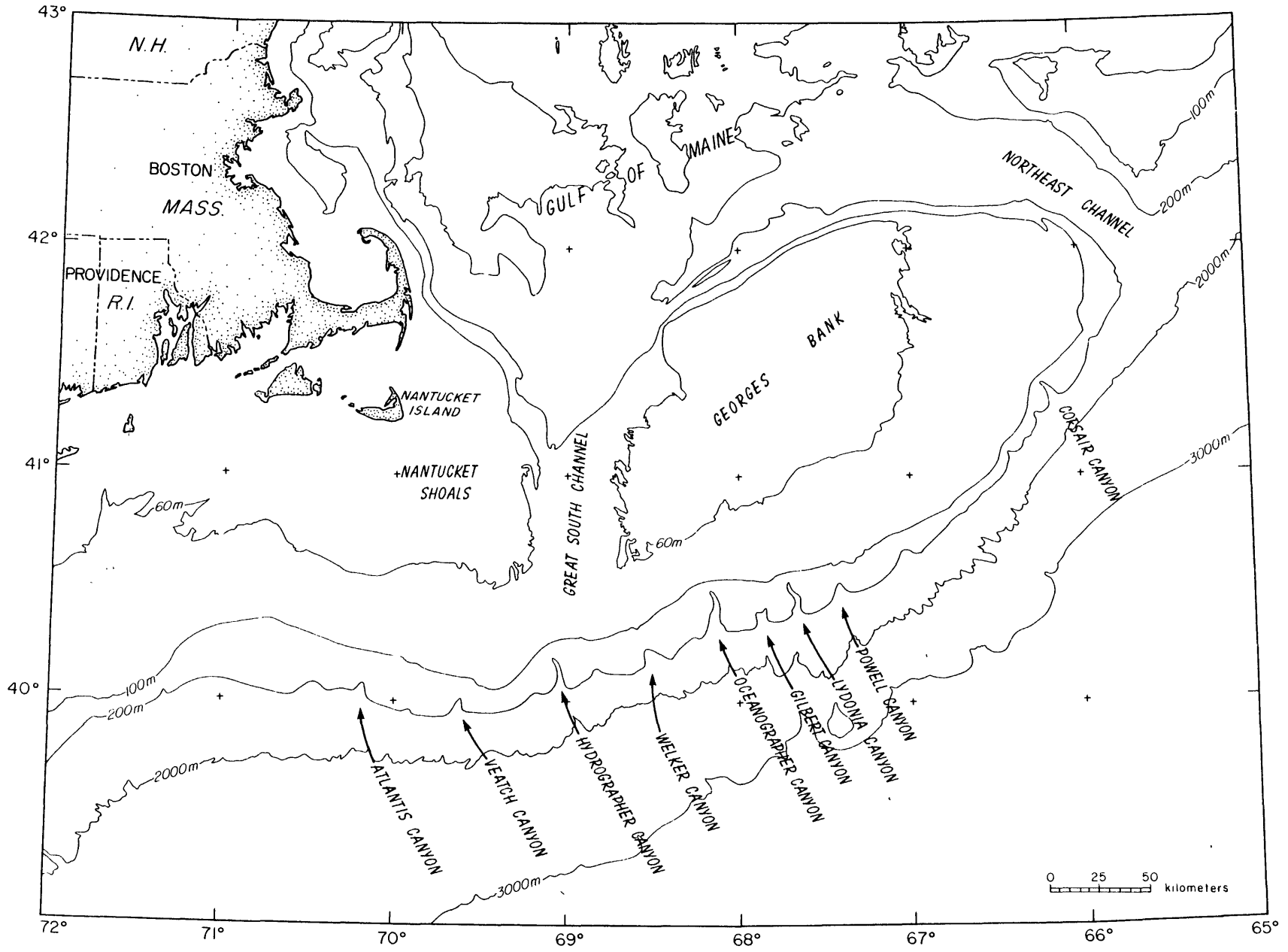

Figure 2-1. Base map showing location of Lydonia Canyon on the southern flank of Georges Bank.

the physical oceanography and geology of Lydonia Canyon and the adjacent shelf and slope. The major objectives of the field program were to:

1. Describe the currents, hydrography, and suspended sediments in Lydonia Canyon and on the adjacent shelf and slope;
2. Map the surficial geology of the region, particularly regions of sediment deposition or erosion;
3. Determine the role of canyons in transporting sediment on or off the Continental Shelf, and to assess whether canyons enhance cross-shelf transport as compared to the adjacent slope;
4. Determine if Lydonia Canyon is a sink for fine sediment and thus a potential sink for drill muds or cuttings discharged onto the Outer Continental Shelf by petroleum exploration; and
5. Compare the currents in Lydonia and Oceanographer Canyons to assess whether the currents and sediment dynamics in the two canyons are similar.

The study was designed to primarily investigate flow in the canyons landward of the shelfbreak (depths in the axis shallower than about 800 m). Major components of the field program, conducted between 1980 and 1982, included detailed bathymetric surveys of the canyon and adjacent shelf and slope; surveys of the surficial sediment texture; longterm measurements by an array of moored current meters, bottom tripods and sediment traps; synoptic hydrographic observations; bottom surveys utilizing sidescan sonographs and high-resolution acoustic profiles; and surveys of the canyon utilizing a research submersible.

The moored array experiments were the largest component of the field program. This chapter presents a description of these experiments, and an overview of the current structure and variability in Lydonia Canyon obtained

from them. The results of the bathymetric and high-resolution surveys have been published previously (Butman and Moody, 1984; Twichell, 1983). Additional chapters in this volume describe other components of the canyon experiment.

FIELD PROGRAM

Five deployments of moored instruments were made as part of the Lydonia Canyon experiment; Deployment 1 from October 1980 to May 1981, Deployment 2 from May 1981 to September 1981, Deployment 3 from September 1981 to January 1982, Deployment 4 from January to July 1982, and Deployment 5 from July to November 1982 (hereafter D1-D5). Hydrographic observations were made on all deployment and recovery cruises and on one additional cruise conducted midway through D1 (table 2-1).

Instrumentation

Several types of current meters and instrument packages were used in the experiment to measure currents, temperature, pressure, light transmission, and to document sediment movement. Current and temperature were measured by means of EG&G vector averaging current meters (VACM). Some VACMs were modified to measure and record additional variables. VACMs modified to record pressure were used to determine mooring depth at selected stations, primarily in areas of rough topography. VACMs modified to measure light transmission were used to qualitatively document the level and variability of suspended sediment in the water column or near the sea floor. VACMs modified for conductivity were used to determine water salinity (Strahle and Butman, 1984).

A bottom tripod instrument system which measured near-bottom current, temperature, pressure, and light transmission, and photographed the sea floor

Table 2-1. Dates of moored array deployments and hydrographic cruises conducted as part of the Lydonia Canyon Experiment.

Deployment		Date	Cruise
Start	Stop		
I		November 1980	OCEANUS 88
I		December 1980	OCEANUS 90
		January 1981	OCEANUS 91
II	I	April 1981	OCEANUS 95
III	II	September 1981	OCEANUS 104
IV	III	January 1982	OCEANUS 113
V	IV	July 1982	OCEANUS 122
	V	November 1982	OCEANUS 130

was deployed on the shelf around the head of Lydonia Canyon to document near-bottom currents and sediment movement. This instrument system was developed for long-term studies of sediment movement on the Continental Shelf (Butman and Folger, 1979). The instrument sampled pressure in 48 s bursts every 7.5 min (12 samples at a rate of 4 s). The standard deviation of the high-frequency burst pressure measurements is a measure of the bottom-pressure fluctuations caused by surface waves and, with the current measurements, can be used to determine bottom stress using the model of Grant and Madsen (1979).

A second instrument package was constructed to measure currents and light transmission and to obtain time-lapse photographs of the sea floor (see Butman and Conley, 1984). These packages were used in the canyon axis, where the bottom tripod system was unsuitable because of rough topography, and in water depths deeper than 125 m, where the tripod deployment and recovery system is unworkable. The instrument package was deployed as a component of a subsurface mooring. The instrument package consisted of a VACM modified to measure light transmission or light transmission and conductivity, a 35-mm camera and strobe, a sediment trap, and an acoustic release mounted on a triangular stainless-steel frame. The current sensor in the instrument package was approximately 5 m above the sea floor. All instruments in the moored array experiment were set to sample every 3.75 or 7.5 minutes to adequately resolve rapid fluctuations of the current.

Moored array

The mean flow in this region of the Outer Continental Shelf is generally westward although Gulf Stream eddies may reverse the flow for 1-2 month periods near the shelf break (Butman and others, 1982; Beardsley and others, 1985; Butman, in press). The shelf-water/slope-water front intersects the

bottom near the 100-m isobath. The moored array was designed to document currents upstream and downstream of Lydonia Canyon on both the shelf and upper slope and on either side of the shelf-water/slope-water front. The array was designed primarily to describe the near-bottom currents and sediment movement on the continental shelf, the currents and sediment movement in the canyon, and transport from the shelf into the canyon. Long-term measurements were made at a few stations throughout the entire experiment to provide continuity between deployments, and to assess seasonal and long-term variability. Data obtained in D1 of the moored array is reported in Butman and Conley (1984). A data report covering D2-D5 is in preparation.

Deployment 1

D1 was the largest array deployed as part of the canyon experiment. Instruments were deployed at 15 locations in Lydonia Canyon and on the adjacent shelf and slope (fig. 2-2, table 2-2). Throughout the array, instruments were deployed at common depths from the surface of approximately 10, 50, 100, 200, 400, and 800 m. Bottom tripods and VACMs 15-20 meters above bottom (mab) were placed at stations LCA, LCL, and LCM around the head of the canyon on the Continental Shelf. At LCA and LCL, the VACMs 20 mab measured light transmission and conductivity to monitor the variability in the position of the shelf-water/slope-water front and to determine the height of any near-bottom sediment resuspension. Instruments were also deployed at 10 and 50 m at LCL.

Currents were measured at four stations along the canyon axis (stations LCB, LCE, LCN, and LCH) from approximately 300 to 1,500 m. At LCB and LCE, in the shallower parts of the axis where the canyon cuts northward into the continental shelf, instruments were placed at depths above and below the depth

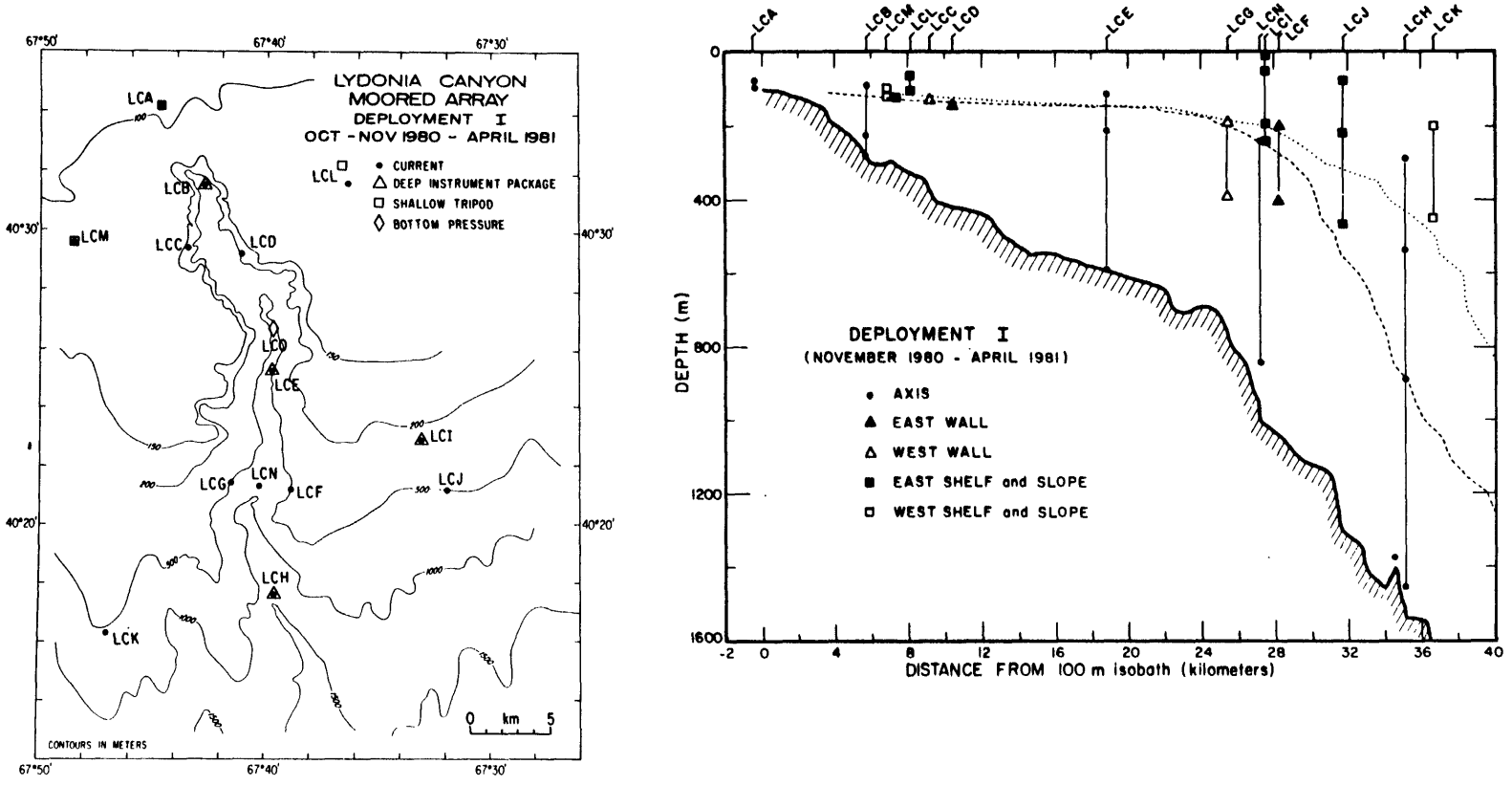

Figure 2-2. Map of Lydonia Canyon and section along the canyon axis showing location of instruments in Dl. Dotted and dashed lines show the slope to the west and east respectively.

Table 2-2. Mooring information for Deployment 1 of the moored array. The mooring type code is: S, surface mooring; SS, subsurface mooring; T, tripod. The instrument code is: DIP, deep instrument package; V, vector averaging current meter (VACM); VP, VACM with pressure; VT, VACM with transmission; VTC, VACM with transmission and pressure.

Station	Moor. no.	Water depth (m)	Latitude (N.)	Longitude (W.)	Moor. type	Inst. type	Inst. depth (m)	Deployed (YrMoDy)	Recovered (YrMoDy)
LCA	204	100	40°34.20'	67°44.81'	T		99	801024	810424
	207	100	40°34.21'	67°44.55'	SS	VCT	80	801130	810424
LCB	2081	282	40°31.55'	67°42.82'	SS	VTC	92	801128	810428
	2082					VP	227		
	2083					DIP	277		
LCC	209	184	40°29.43'	67°43.50'	SS	V	134	801024	810425
		135	40°29.08'	67°44.50'				(Dragged	3/25/81)
LCD	210	193	40°29.25'	67°41.25'	SS	V	143	801027	810425
		240	40°29.24'	67°41.79'				(Dragged	3/10/81)
LCE	2111	600	40°25.38'	67°39.88'	SS	VT	116	801201	810501
	2112					VT	216		
	2113					VP	441		Lost
	2114					DIP	595		810701
LCF	2121	505	40°21.18'	67°39.01'	SS	VP	205	801027	810427
	2122					V	405		
LCG	2131	495	40°21.44'	67°41.63'	SS	V	195	801027	810427
	2132					V	395		
LCH	2141	1,554	40°17.59'	67°39.54'	SS	VP	290	801201	810427
	2142					V	540		
	2143					V	890		
	2144					V	1,454		
	2211	1,380	40°17.93'	69°39.52'	SS	DIP	1,375	810120	810428
LCI	2151	250	40°22.84'	67°33.14'	S	V	10	801127	810430
	2152		40°22.95'	67°32.94'	SS	VT	55	801202	810429
	2153					V	195		
	2154					DIP	245		
LCJ	2161	571	40°21.18'	67°31.98'	SS	VP	83	801127	810429
	2162					V	223		
	2163					V	471		
LCK	2171	554	40°16.27'	67°46.99'	SS	V	204	801127	810427
	2172					V	454		
LCL	205	125	40°32.30'	67°36.83'	T		124	801125	810502
	2181	125	40°32.31'	67°36.40'	S	V	10	801024	Lost
	2182	125	40°31.68'	67°36.50'	SS	V	65	801130	810425
	2183					VTC	105		
LCM	203	120	40°29.57'	67°48.55'	T		119	801024	810426
	2191	123	40°29.47'	67°48.24'	SS	V	103	801202	810425
LCN	2201	1,041	40°21.32'	67°40.38'	SS	VP	243	801129	810427
	2202					V	841		

of the adjacent shelf to investigate the coupling between shelf and canyon currents, and particularly the transport of resuspended material from the shelf into the canyon. The uppermost instrument (100 m) at LCB measured transmission and conductivity, and the upper two instruments at station LCE measured transmission. At LCH, instruments were deployed above the depth of the adjacent slope at 200, 400, and 800 m, and below the adjacent slope at approximately 1,400 m.

At two locations along the canyon axis, instruments were placed on the canyon walls to document the horizontal variability of the currents in the canyon. Moorings were placed on the canyon walls at LCC and LCD slightly below the depth of the adjacent shelf. At LCF and LCG, instruments were placed at approximately 200 m, just above the depth of the adjacent shelf. The instruments at LCB, LCC, and LCD formed a small cross-canyon array near the canyon head, and the instruments at LCF, LCG, and LCN formed a cross-canyon array near the shelf break. All instruments on moorings on the canyon walls were placed 50 to 100 mab because near-vertical cliffs were observed in some areas during submersible dives. Although near-bottom currents on the walls are of interest, interpreting any observations would be difficult without knowing the location of the instruments with respect to the rugged topography.

To the east of Lydonia Canyon, instruments were deployed across the shelf and slope at LCL, LCI, and LCJ at depths of 10 m (LCL and LCI), 50 m (LCL, LCI, LCJ), 100 m (LCL), and 200 m (LCI, LCJ), and near the bottom (LCL and LCI). To the west of the canyon, near-bottom instruments were deployed at LCL on the shelf and at LCK on the slope at approximately 200 and 450 m. The instruments at LCJ, LCH, and LCK form an along-slope array at a water depth of approximately 500 m with instruments at common depths of approximately 200 and 400 m.

To monitor near-bottom current, sediment resuspension, and sediment movement, deep instrument packages were deployed at LCB, LCE, and LCH in the canyon axis and LCI on the slope. Similar near-bottom observations were made at LCA, LCL, and LCM by means of bottom-tripod systems. Bottom pressure was measured at LCA, LCL, and LCM on the shelf and at LCO in the canyon axis to estimate alongshelf and cross-shelf pressure gradients near the canyon head.

Deployments D2-D5

D2 through D5 of the moored array were modest in size in comparison to D1 (figs. 2-3 to 2-6, tables 2-3 to 2-7). To provide long-term observations typical of the shelf, canyon head, mid-canyon, and slope, moorings were continued at LCA and LCB throughout the experiment, at LCI for D2 through D4, and at LCE through D3. Observations of the near-bottom flow were made on the canyon rim near the head at LCP during D3, and near the mouth at LCQ in D4. A small cross-canyon array was deployed in D4 to supplement the cross-canyon observations made near the mouth at LCF and LCG and near the head at LCC and LCD in D1. Additional near-bottom observations in the axis at LCS and LCU were made in D4 and D5 respectively. Two moorings were deployed in the axis of Oceanographer Canyon in D3, one at 227 m and one at 560 m (table 2-7).

Data recovery and naming convention

A time line of all current observations obtained as part of the Lydonia Canyon experiment is shown in figure 2-7. In general, data return was excellent, except at LCA where there were tripod failures in D3 and D4. The long-term observations at LCB and LCI were continuous, except at 50 mab, and provide an extremely important time series used throughout this chapter to illustrate various aspects of canyon and slope flow. Only two instruments

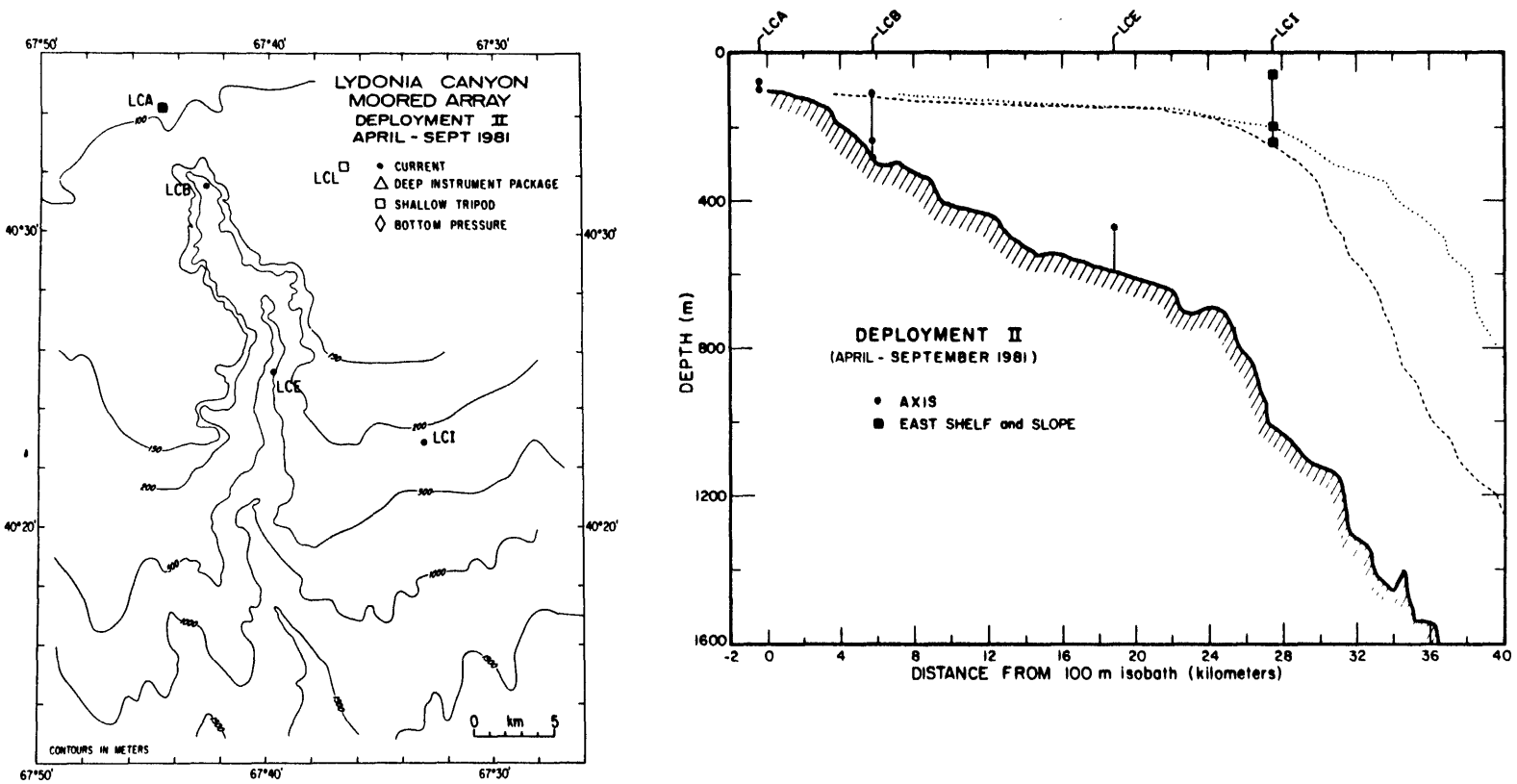

Figure 2-3. Map of Lydonia Canyon and section along the canyon axis showing location of instruments in D2. Dotted and dashed lines show the slope to the west and east respectively.

Table 2-3. Mooring information for Deployment 2 of the moored array. (see table 2-2 for explanation).

Station	Moor. no.	Water depth (m)	Latitude (N.)	Longitude (W.)	Moor. type	Inst. type	Inst. depth (m)	Deployed (YrMoDy)	Recovered (YrMoDy)
LCA	223	100	40°34.25	67°44.76	T	T	100	810505	810926
	225		40°34.38	67°44.63	SS	V	80	810504	810926
LCB	226	288	40°31.56	67°42.83	SS	V	108	810429	810926
						V	238		
						V	282		
LCE	228	580	40°25.61	67°39.60	SS	V	475	810505	810926
LCI	227	250	40°22.96	67°33.01	SS	V	59	810503	810927
						V	199		
						V	243		
LCL	224	125	40°32.37	67°36.26	T	T	125	810426	810926

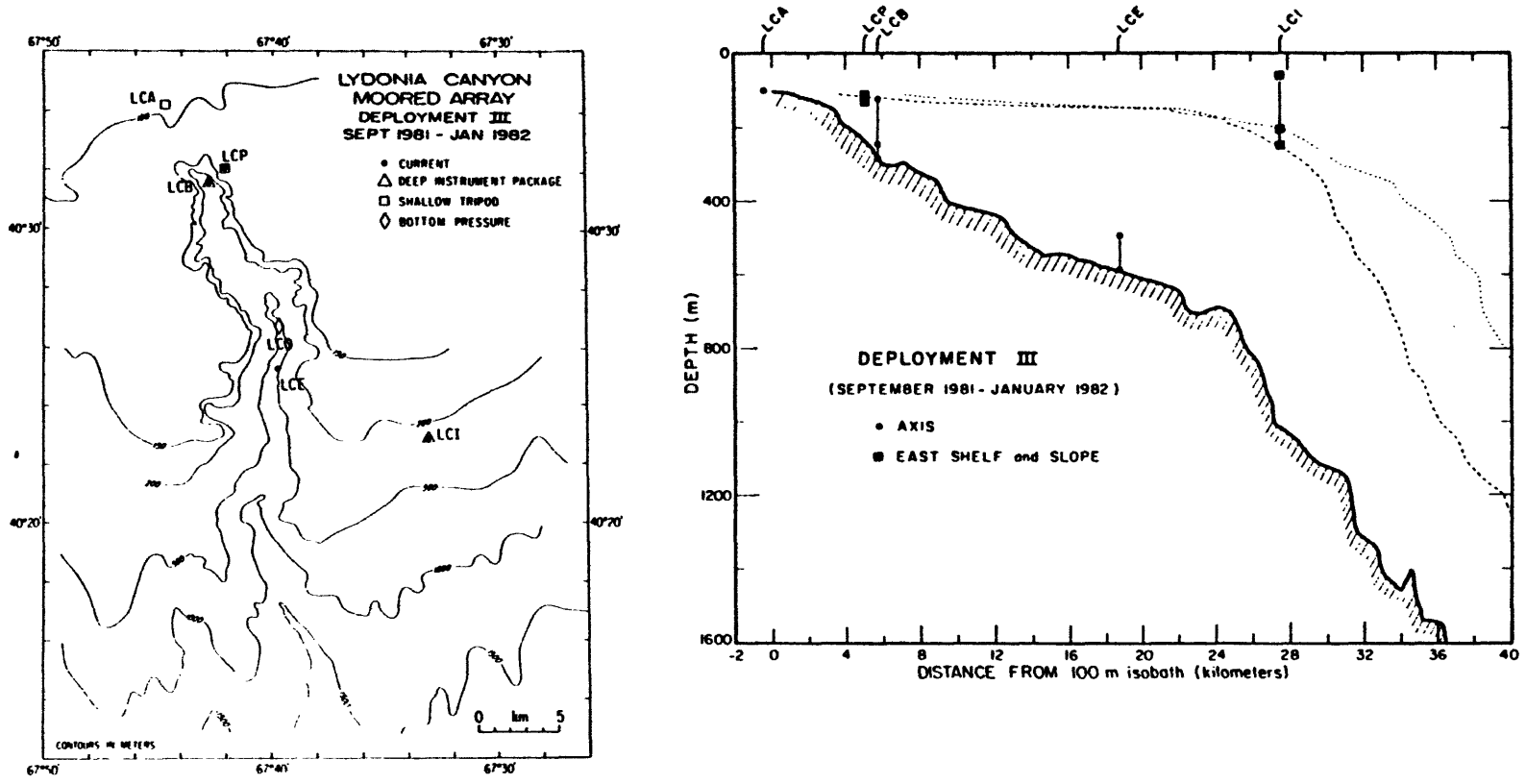

Figure 2-4. Map of Lydonia Canyon and section along the canyon axis showing location of instruments in D3. Dotted and dashed lines show the slope to the west and east respectively.

Table 2-4. Mooring information for Deployment 3 of the moored array (see table 2-2 for explanation).

Station	Moor. no.	Water depth (m)	Latitude (N.)	Longitude (W.)	Moor. type	Inst. type	Inst. depth (m)	Deployed (YrMoDy)	Recovered (YrMoDy)
LCA	229	100	40°34.35'	67°44.03'	T	T	100	810926	820128
	238	101	40°34.37'	67°43.50'	T	T	101	810926	811001
LCB	231	290	40°31.54'	67°42.79'	SS	DIP	285	810927	820127
	230	295	40°31.50'	67°42.74'	SS	VTC	125	810927	820130
						V	245		
LCE	232	590	40°25.40'	67°39.84'	SS	V	493	810928	820130
						VT	584		
LCI	234	247	40°23.11'	67°32.60'	SS	DIP	242	810927	820131
	233	251	40°22.95'	67°32.97'	SS	V	55	810927	820131
						V	201		
LCP	237	131	40°32.02'	67°42.07'	T	T	131	810926	820128
	236	132	40°31.95'	67°42.07'	SS	V	113	810928	820128
LCO	235	555	40°26.74'	67°39.75'	P	P	555	811001	820129

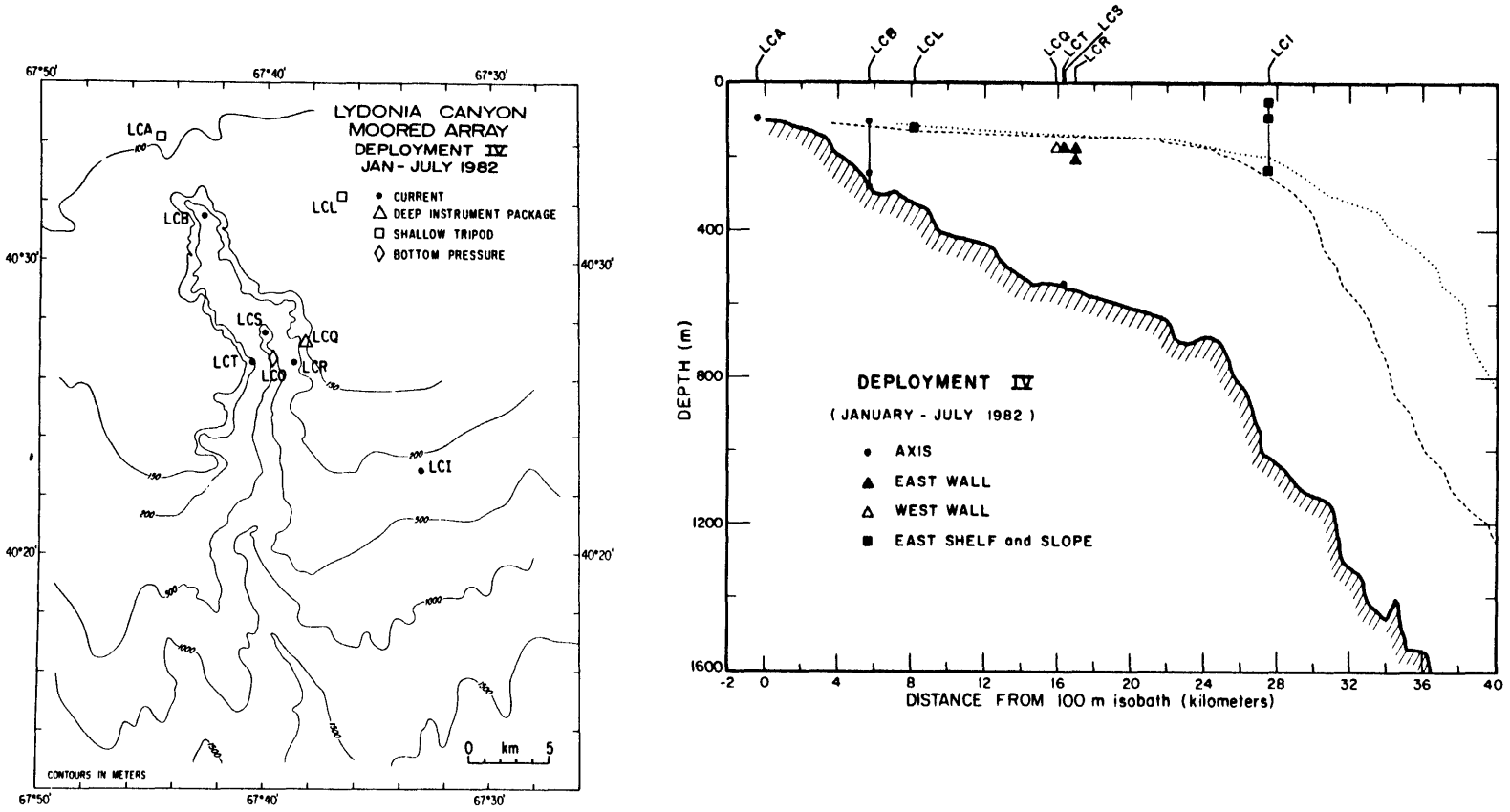

Figure 2-5. Map of Lydonia Canyon and section along the canyon axis showing location of instruments in D4. Dotted and dashed lines show the slope to the west and east respectively.

Table 2-5. Mooring information for Deployment 4 of the moored array (see table 2-2 for explanation).

Station	Moor. no.	Water depth (m)	Latitude (N.)	Longitude (W.)	Moor. type	Inst. type	Inst. depth (m)	Deployed (YrMoDy)	Recovered (YrMoDy)
LCA	240	100	40°33.78'	67°44.76'	T	T	100	820128	820707
LCB	241	300	40°31.52'	67°42.83'	SS	VTC V	108 248	820131	820707
LCI	242	249	40°23.05'	67°32.96'	SS	V V VT	59 199 243	820131	820708
LCQ	243	185	40°27.25'	67°38.27'	SS	DIP	180	820130	820707
LCR	244	240	40°26.62'	67°38.80'	SS	V V	183 215	820130	820707
LCS	245	560	40°27.61'	67°40.03'	SS	V	554	820129	820707
LCT	246	203	40°26.62'	67°40.61'	SS	V	178	820102	820707
LCO	247	552	40°26.77'	67°39.72'	P	P	552	820202	820707
LCL	251	127	40°32.40'	67°36.52'	T	T	127	820131	820709

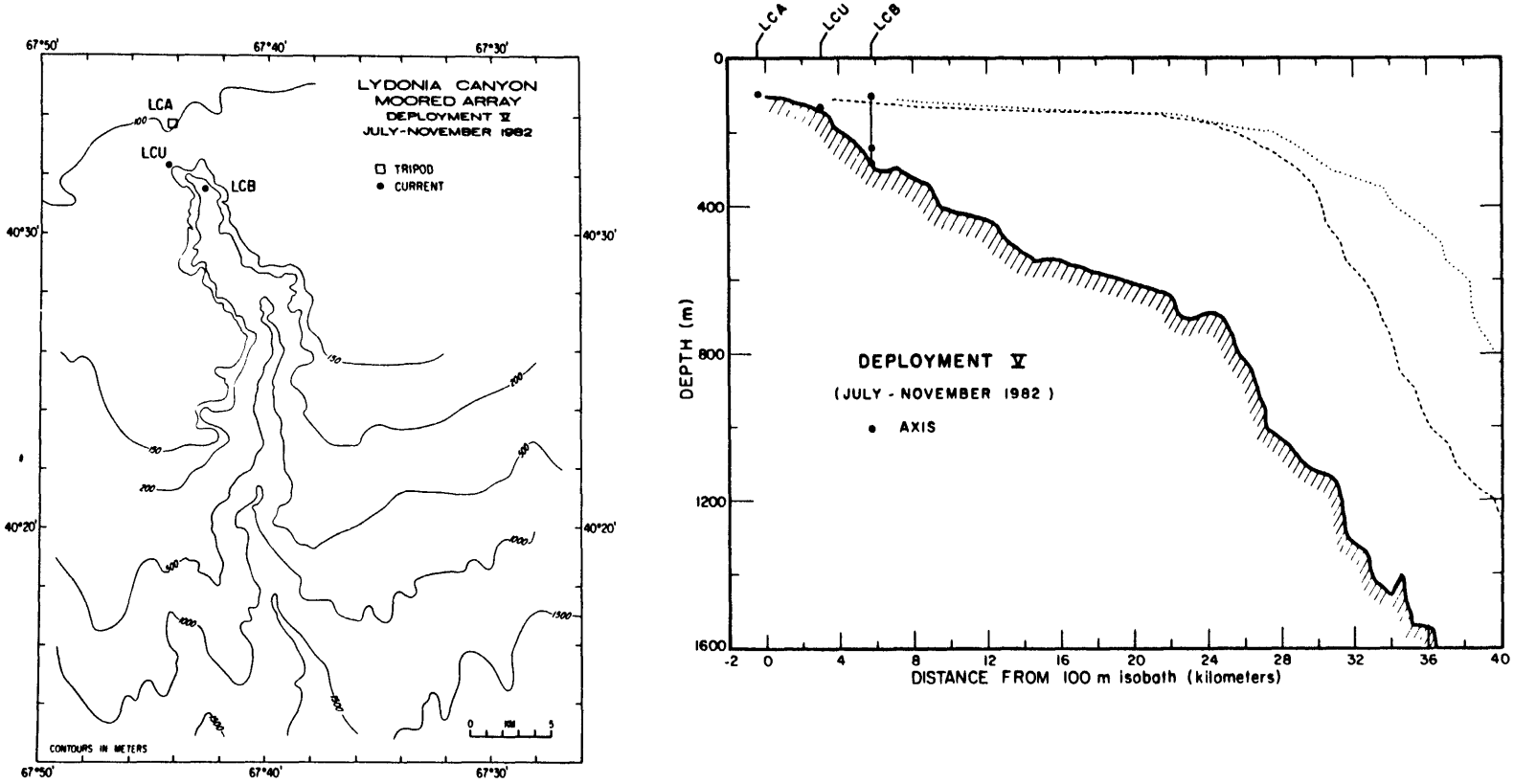

Figure 2-6. Map of Lydonia Canyon and section along the canyon axis showing location of instruments in D5. Dotted and dashed lines show the slope to the west and east respectively.

Table 2-6. Mooring information for Deployment 5 of the moored array (see table 2-2 for explanation).

Station	Moor. no.	Water depth (m)	Latitude (N.)	Longitude (W.)	Moor. type	Inst. type	Inst. depth (m)	Deployed (YrMoDy)	Recovered (YrMoDy)
LCA	257	104	40°33.83'	67°44.21'	T	T	103	820708	820812
	264		40°33.76'	67°44.58'	T	T		820812	821111
LCB	258	295	40°31.49'	67°42.29'	SS	V	104	820708	821111
					Ψ	VTC	244		
						VT	290		
LCU	259	141	40°32.37'	67°44.37'	SS	VTC	134	820708	821111

Table 2-7. Mooring information for moorings in Oceanographer Canyon (see table 2-2 for explanation).

Station	Moor. no.	Water depth (m)	Latitude (N.)	Longitude (W.)	Moor. type	Inst. type	Inst. depth (m)	Deployed (YrMoDy)	Recovered (YrMoDy)
OCA	248	104	40°30.76'	68°14.83'	T	T	104	820127 (Dragged)	820709
OCB	249	227	40°29.44'	68°11.06'	SS	V DIP	177 223	820128	820709
OCC	250	560	40°24.93'	68°07.83'	SS	VTC	554	820127	820709

LYDONIA CANYON

CURRENT

STA.	DEPTH (m)	INST. DEPTH (m)	MAB (m)
LCA	101	80	20
		100	1
LCB	300*	92-125	190
		227-248	55
		277-294	5
LCC	184†	134†	50
LCD	193†	143†	50
LCE	600*	116	484
		216	384
		475-493	105
		584-595	5
LCF	505	205	300
		405	100
LCG	495	195	300
		395	100
LCH	1554	290	1264
		540	1014
		890	664
		1454	100
	1380	1375	5
LCI	250	10	240
		55-59	195
		195-201	50
		242-245	5
LCJ	571	83	488
		223	348
		471	100
LCK	554	204	350
		454	100
LCL	125	70	55
		110	15
		124	1
LCM	123	103	20
	120	119	1
LCN	1041	243	798
		841	200
LCO	555	555	0
LCP	132	112	20
	131	130	1
LCQ	185	180	5
LCR	240	183	57
		215	25
LCS	560	554	6
LCT	203	178	25
LCU	141	134	7

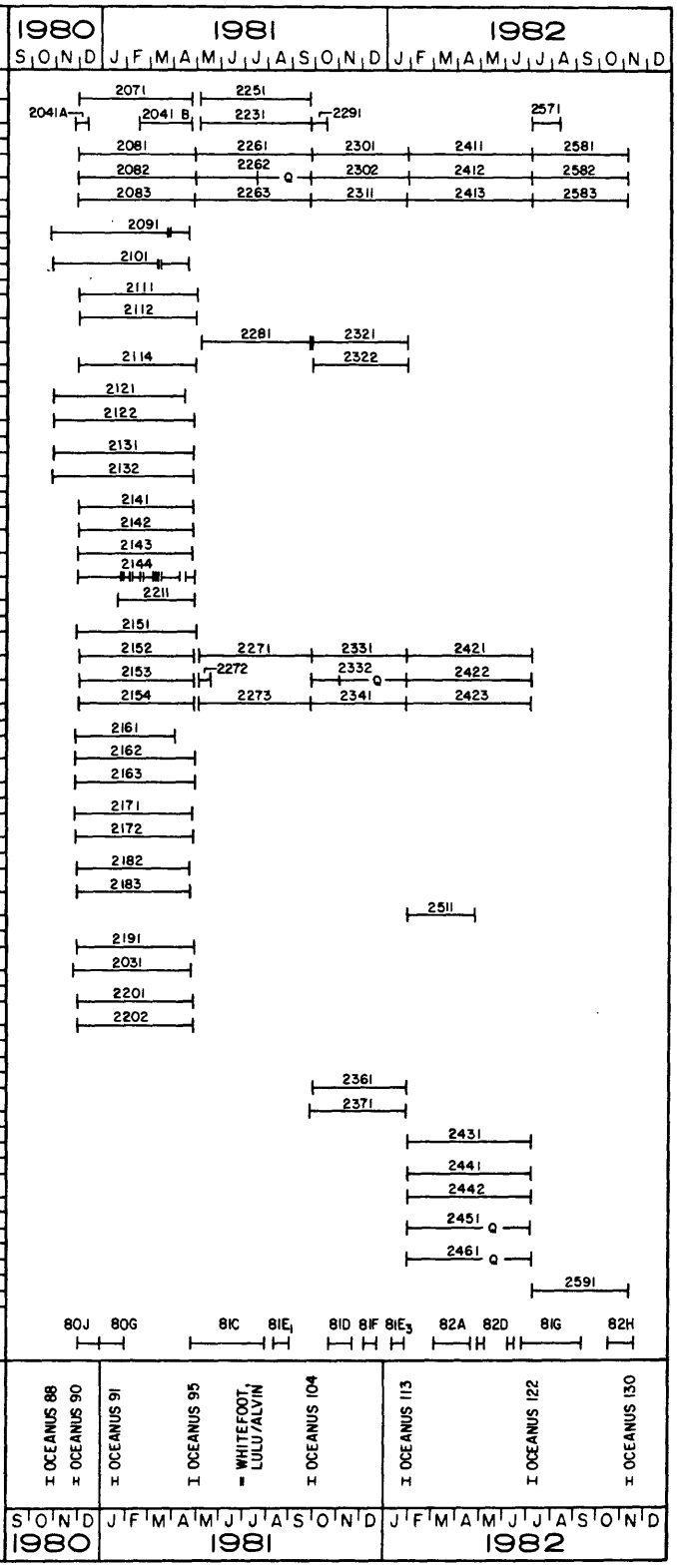

† Initial depth - mooring dragged
* Maximum depth

CRUISES

Q Questionable data

Figure 2-7. Time line of all current measurements made as part of the Lydonia Canyon Experiment. The four digit number is the record identification (see tables 2-2 to 2-6).

were lost during the experiment, a surface-moored VACM at LCL and a VACM at 100 mab at LCE in D1.

All USGS moorings are assigned a three-digit identification number (tables 2-2 to 2-7, fig. 2-7). Data are referenced by four digits; the first three are the mooring number and the last indicates the vertical position of the instrument from the top. Thus 2114 is the fourth instrument from the top on mooring 211. In this chapter however, data are primarily referenced as LCB1(277) which indicates the station (LCB), deployment number (1), and depth of the instrument below the surface (277). Where the deployment number is unambiguous, it is omitted, and if the height above bottom is more appropriate than the depth, it is listed as mab (LCB(5 mab)).

Mooring Positions

Positioning the moorings in the canyon axis and on the walls of the canyon was critical and required considerable care. The detailed bathymetric map of Lydonia Canyon (Butman and Moody, 1984) was used to locate all moorings. A bathymetric transect was run across the canyon axis prior to deployment of a mooring. The moorings were deployed from OCEANUS anchor last; components were strung astern and the mooring was slowly towed across the canyon axis toward the launch point. The depth was monitored continuously and the anchor released in the center of the axis as determined by the maximum depth and/or at the desired launch point (or a judicious decision). The bathymetric transect across the axis was continued after the mooring was let go to confirm the position of the mooring in the axis. The mooring position after deployment and before recovery was determined to about ±100 m by ranging to the acoustic release. The placement of moorings near the center of the canyon axis near the head was excellent. At the deeper stations LCN and LCH,

where side echoes from the canyon walls and the narrow axis made the bathymetry extremely difficult to interpret, the moorings may not have been exactly in the center of the axis. Loran C was used for all navigation.

Hydrography

Hydrographic observations were made on all mooring deployment and recovery cruises (table 2-1). In general, sections were run along the canyon axis, and across the adjacent shelf and slope to the east and west. On some cruises, sections were also run across the canyon axis. Because the mooring work was always first priority during cruises, the number and location of hydrographic sections varied from cruise to cruise depending on the weather and the time available. Cruise tracks for OCEANUS 91, 95, 104, and 113 are shown in figure 2-8 .

Profiles of temperature, salinity, oxygen, and light transmission were made by means of a Neil Brown Instrument Systems, Inc. conductivity-temperature-depth (CTD) profiler. Additional temperature profiles were obtained using expendable bathythermographs (XBT's). Details of the hydrography may be found in a series of data reports (Moody and others, 1986a; Moody and others, 1986b; Moody and others, 1986c; Butman and others, 1986a, Butman and others, 1986b).

Sediment texture

Samples of the surface sediment were obtained on the shelf and slope adjacent to Lydonia and Oceanographer Canyons by means of a modified Van Veen grab. The upper 2 cm of sediment were skimmed from the surface of the grab. Samples were obtained on several cruises at different times of the year. Samples of the surficial sediment were obtained from the axis of Lydonia

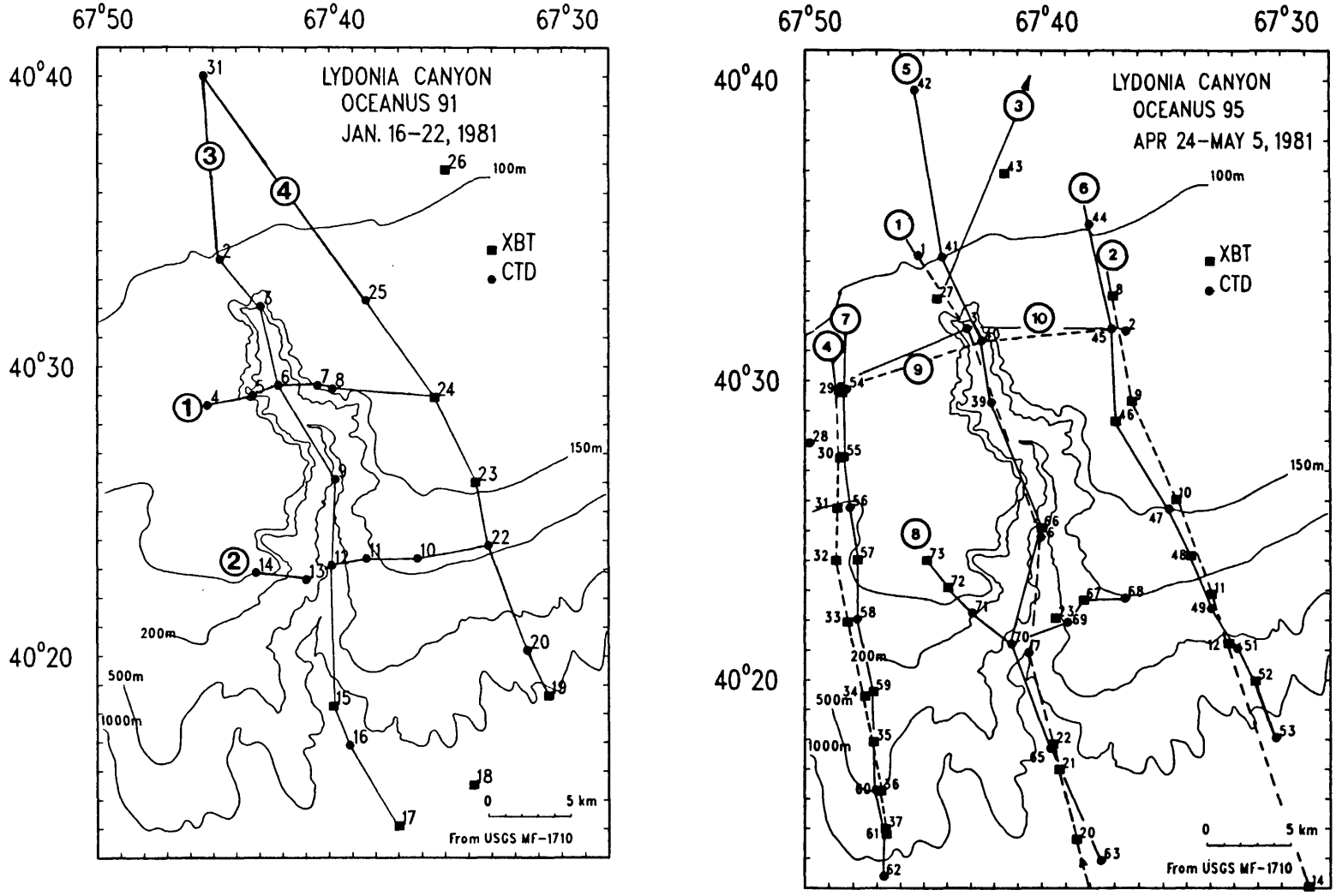

Figure 2-8a. Location of hydrographic sections for OCEANUS 91 and 95. Circled numbers indicate the section number.

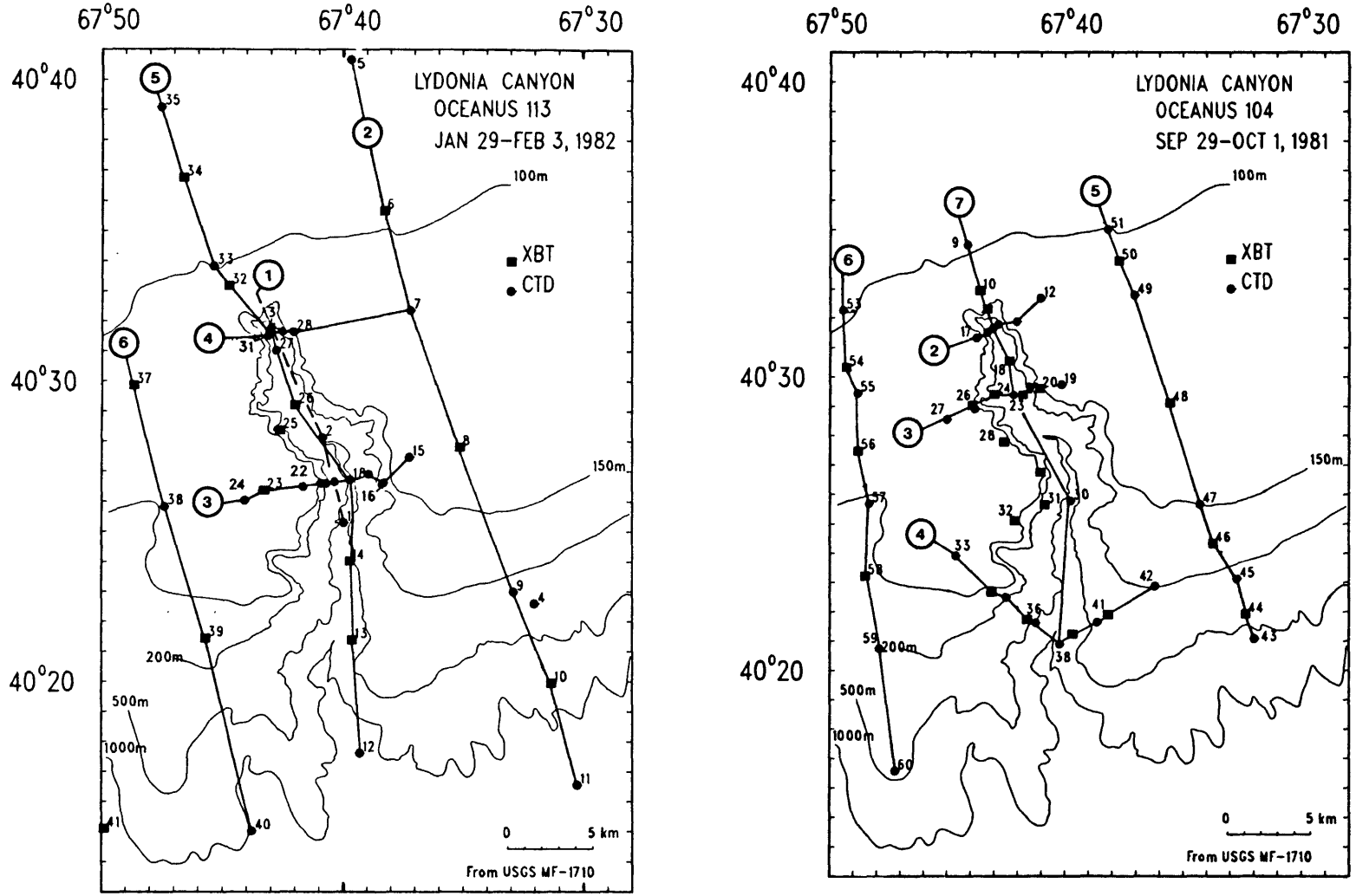

Figure 2-8b. Location of hydrographic sections for OCEANUS 104 and 113. Circled numbers indicate the section number.

Canyon on nine ALVIN dives in September 1980. Samples were scooped from the surface with a heavy canvas bag attached to a rigid stainless-steel frame held in the manipulator of the submersible. Sediment grain size was determined by wet seiving the samples to gravel, sand, and fine (silt and clay) fraction. A Rapid Sediment Analyser was used to determine the size distribution in the sand fraction and a Coulter Counter for the silt and clay. Additional surface sediment texture observations were obtained from the U.S. Geological Survey Continental Margin Program (Hathaway, 1971) and from samples obtained as part of the Georges Bank Biological Task Force Monitoring Program (Bothner and others, 1982). The observations were used to map the surface sediment texture on the southern flank of Georges Bank adjacent to Lydonia and Oceanographer Canyons and within Lydonia Canyon.

RESULTS

Canyon topography

Lydonia Canyon, as defined by the 200-m isobath, cuts northward into the northwestern Atlantic continental shelf approximately 20 km from the shelf edge (fig. 2-9). Throughout this chapter, the region between 120 m and 300 m in the canyon axis will be referred to as the head of the canyon. The region where an extension of the 200-m isobath on the outer shelf crosses the canyon axis (canyon axis water depth of about 800 m) will be referred to as the mouth of the canyon.

Although oriented approximately north-south, the axis of the canyon is sinuous. On the continental shelf, Lydonia Canyon is first indicated by the 120-m isobath. At the head of the canyon, the axis bifurcates; the east channel trends approximately north-south and the west channel trends approximately northwest-southeast. At a depth of 500 m, the canyon axis jogs

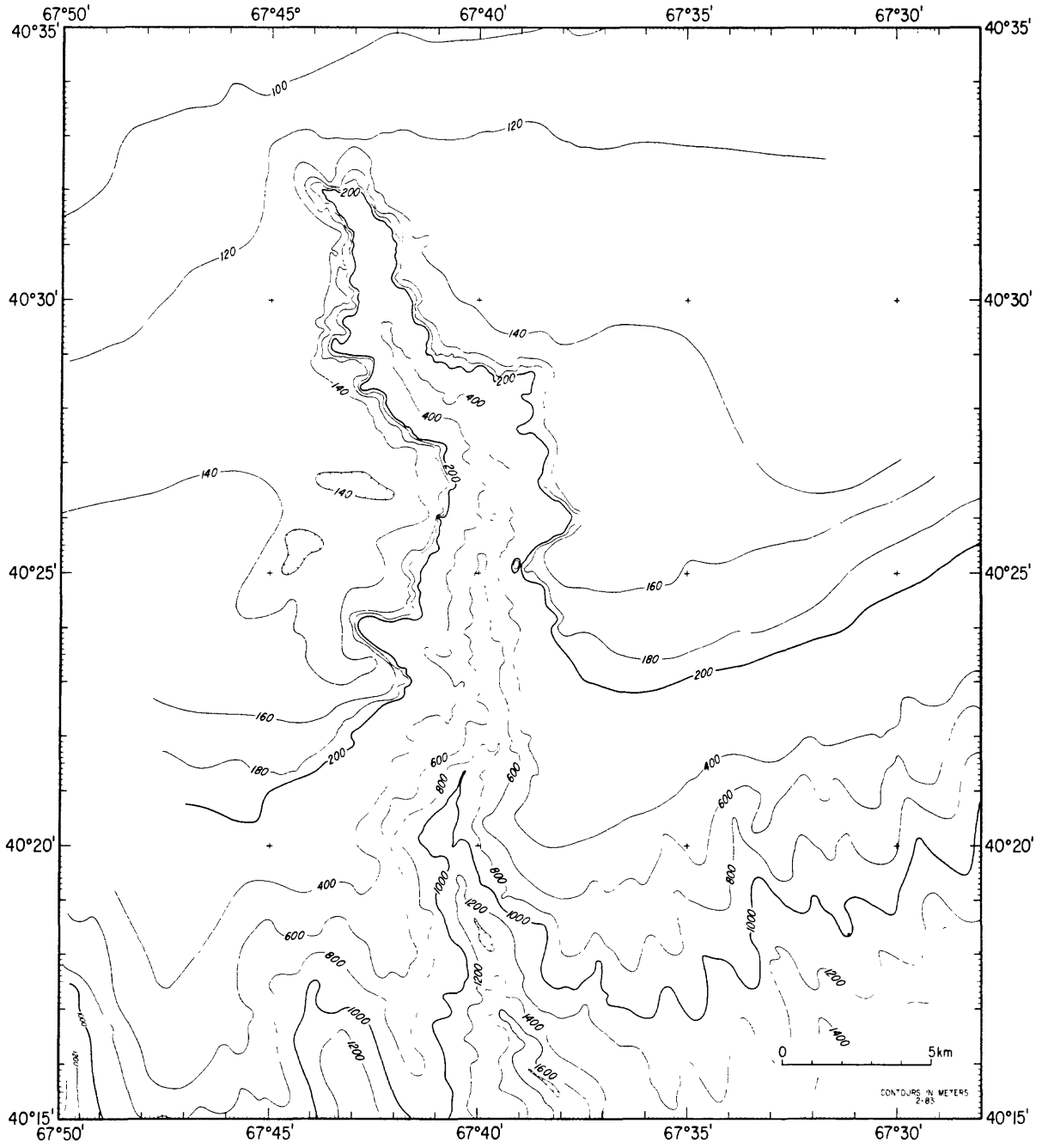

Figure 2-9. Detailed bathymetric map of Lydonia Canyon (redrawn from Butman and Moody, 1984).

to the east about 1.5 km. There are many gullies and spurs along the walls of the canyon. The canyon is 1 to 2 km wide near the head and about 5 km wide near the mouth. The width of the canyon floor ranges from 200 to 1,000 m landward of the shelf break (Twichell, 1983). The width of the thalwag at depths greater than about 800 m cannot be determined with the wide-beam echosounder data because of numerous side echoes from the canyon walls.

In making near-bottom current measurements in such rough topography, there is concern over the representativeness of the observations caused by small scale obstructions in the axis. ALVIN transects along the axis showed that the central axis floor was generally free from large boulders and other obstructions. Near 600 m (LCE), some large sand waves 1-2 m in height were observed, and in some parts of the axis there are depth changes of as much as 50 m within several kilometers. The similarity of measurements obtained at the same stations during repeated deployments, where the moorings are not located in exactly the same spot, suggest that the observations are representative of moderate lengths of the canyon.

The bottom slope along the axis varies substantially along its length (fig. 2-10). The axis slope was estimated by fitting a straight line by eye to the bathymetry (as shown in Butman and Moody, 1984) over segments of the axis several kilometers in length, ignoring changes in the bottom slope over spatial scales of a few kilometers. Near the head of the canyon between 140 and 300 m (following the western branch of the axis), the axis slope is about 3.3^{o}. The slope is steeper, about 6^{o}, ascending between the two branches. Between 300 and 540 m the axis slope is about 1.6^{o}; there are several distinct steps in the bottom in this segment and local slopes range from 0.7^{o} to 3.9^{o}. Between 540 and 700 m the slope of the axis is about 0.9^{o}. Below 700 m, the average bottom slope is about 4.2^{o}, but there are steeper and

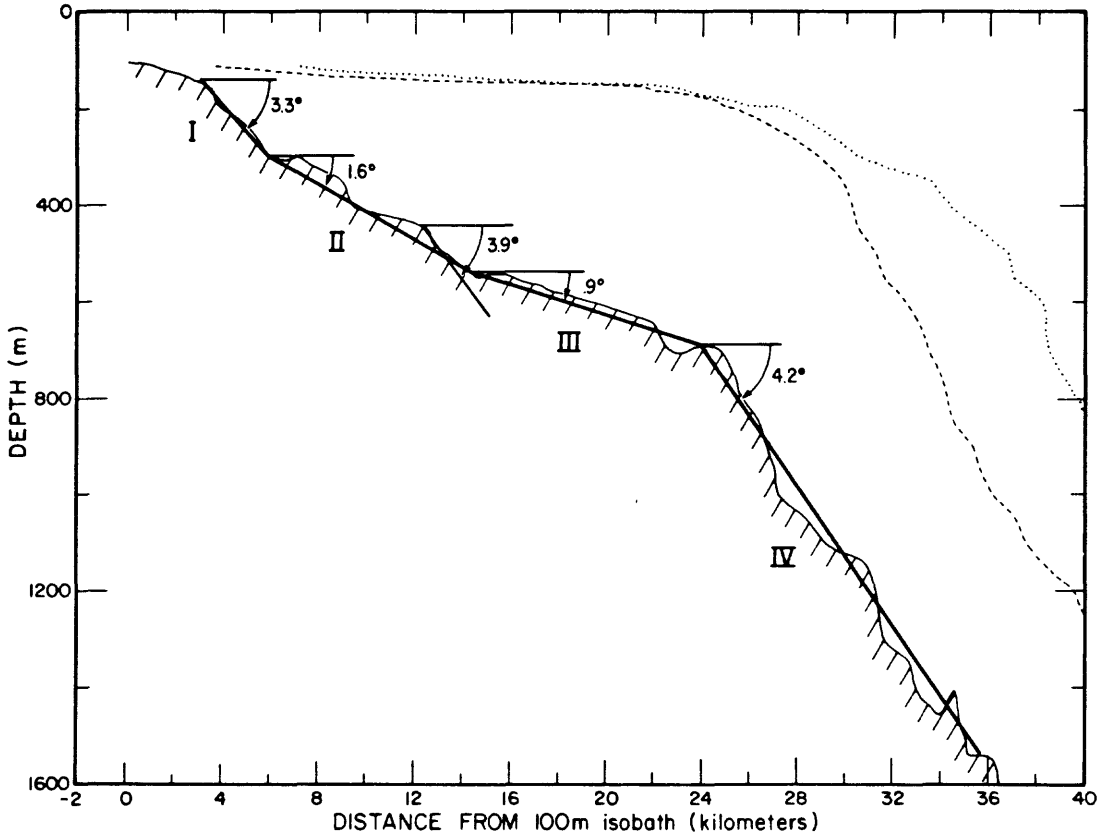

Figure 2-10. Bottom slope along the axis of Lydonia Canyon. Segments I-IV indicate regions of approximately constant slope.

flatter sections. For comparison, the slope on the adjacent continental shelf is less than 1^{o} for depths shallower than about 200 m, and about 5^{o} between 200 and 500 m.

Lydonia Canyon is approximately V-shaped along its length (fig. 2-11). The slope of the walls are about 20^{o} near the mouth and about 10^{o} near the head. The walls were observed to be almost vertical in places along several ALVIN transects starting at about 500, 600 and 1,500 m in the axis and ascending from the canyon floor to the rim. Based on an ALVIN transect ascending from about 300 m in the axis, the walls are much smoother near the canyon head.

There are numerous valleys on the slope to the east of Lydonia, mainly in water depths greater than 500 m. Jigger Submarine Canyon, located between Lydonia and Gilbert Canyons, is not shown on the National Ocean Survey Charts. The head of Jigger Canyon begins at about 400 m and does not incise the continental shelf. Scanlon (1982) has shown that Lydonia Canyon joins Jigger Canyon at a depth of about 2,000 m.

Surface sediment texture

The present distribution of sediments in the Georges Bank region reflects their glacial source and reworking by currents and waves during and since the last rise in sea level (Schlee, 1973; Bothner and others, 1981; Twichell and others, 1981; Twichell, 1983). The surficial sediments on the crest of Georges Bank are primarily coarse sand where the tidal currents have winnowed all fine material from the surface sediments. Surficial sediments become finer across the southern flank of the bank as the water depth increases and the tidal currents and wave influence decrease. The sediments on the Continental Slope are mostly silt and clay. Along the southern flank of

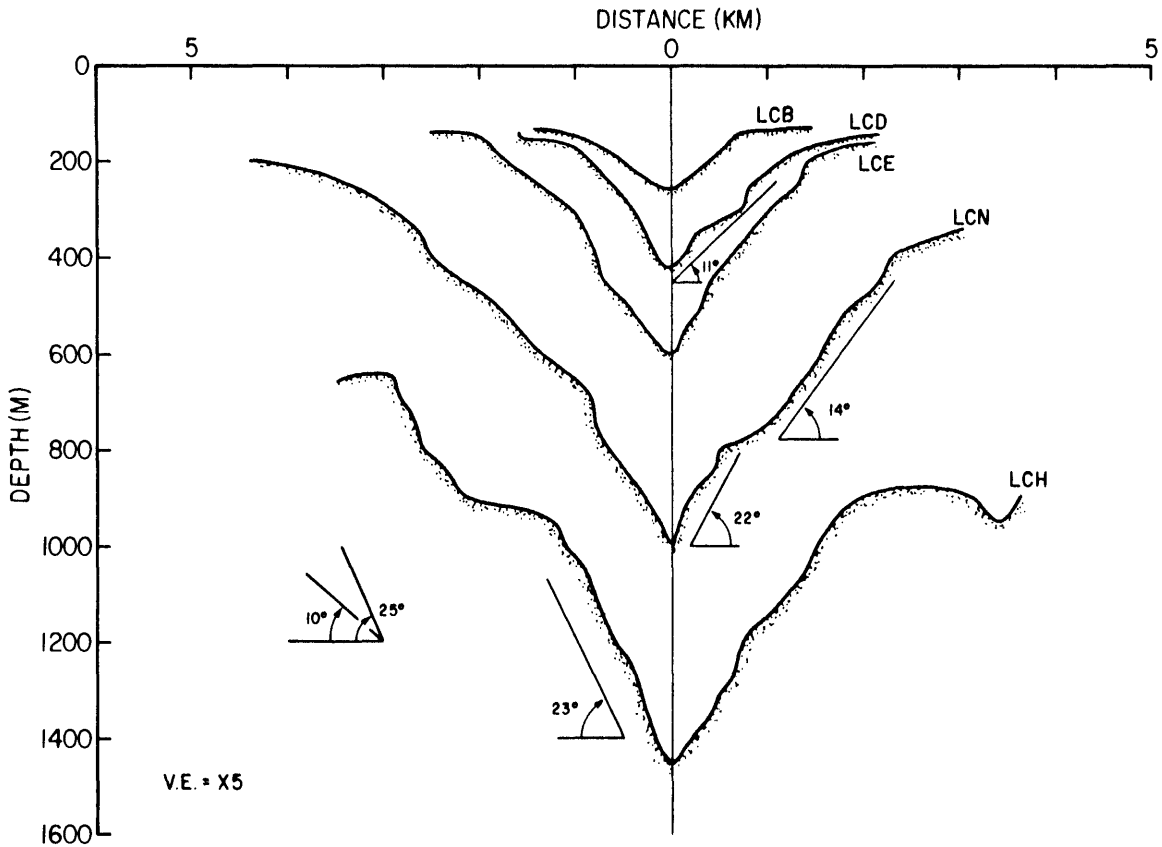

Figure 2-11. Bathymetric sections across the axis of Lydonia Canyon through selected mooring locations (station name on right side). Vertical exaggeration is 5 to 1 (drawn from Butman and Moody, 1984).

Georges Bank, between the water depths of about 60 to 100 m, the surface sediments become finer from east to west. The fine sediments found on the Continental Shelf south of Cape Cod are a modern deposit and are thought to be fine-grained sediments winnowed from the crest of Georges Bank by the strong tidal currents and surface waves and carried westward into the Middle Atlantic Bight by the mean current (Bothner and others, 1981; Twichell and others, 1981; Butman, in press).

Around Lydonia and Oceanographer Canyons in depths shallower than 100 m, the mean sediment grain size decreased toward deeper water snd toward the west (fig. 2-12a), which is consistent with the regional pattern observed on the shelf (Schlee, 1973). The samples between the 100 and 200-m isobath, however, show that the surface sediments have a complex distribution apparently associated with Lydonia and Oceanographer Canyons. On the shelf adjacent to Lydonia Canyon, a band of fine sediment about 8-10 km wide extended about 10 km to the east and west along the shelf. The sediments were slightly finer and more extensive to the east of Lydonia Canyon than to the west. These sediments contained 5-10% silt plus clay and 25-50% very fine sand (fig. 2-12b,c). On the eastern side of the canyon, the fine sediment (as defined by the 2.50 mean grain diameter) extended southward from the 100-m isobath to about 135-140 m water depth; on the western side of the canyon, the finer sediments covered the shelf between 100 and 125 m depths. The sediments were coarser south of the band of fine sediments, especially near the rim of the canyon where sediments contained 15-30% gravel. Although the samples on the upper slope were sparse, they generally indicate a decrease in grain size as the water depth increases.

Fine-grained sediments were also found on the shelf adjacent to Oceanographer Canyon. The finest sediments occurred in the lobes to the east

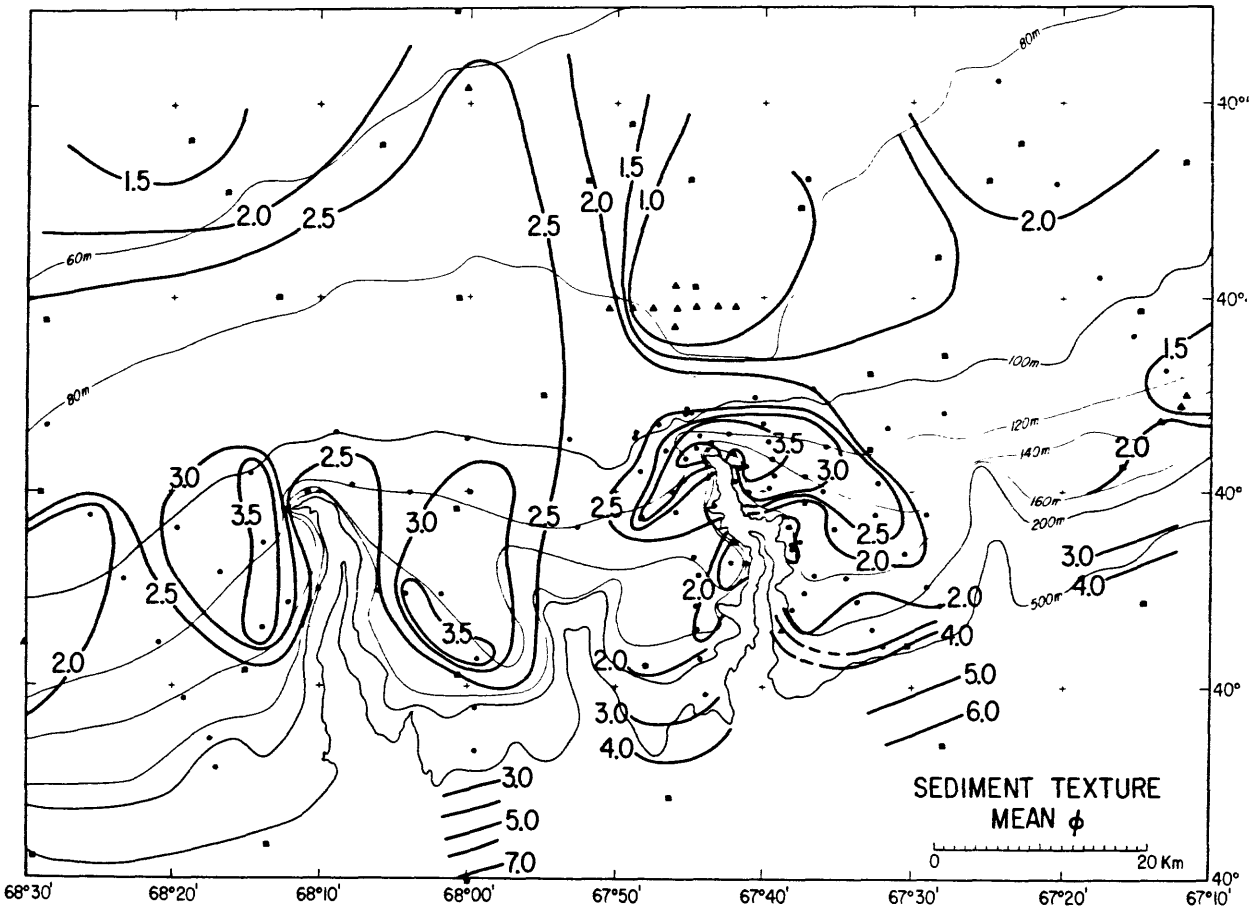

Figure 2-12a. Surface sediment texture on the southern flank of Georges Bank adjacent to Lydonia and Oceanographer Canyons. The surface texture in the canyons at depths greater than 200 m is not shown. Triangles indicate samples from Bothner and others (1982) and squares from Hathaway (1971). Circles are data from this study. Mean Φ (computed by method of moments).

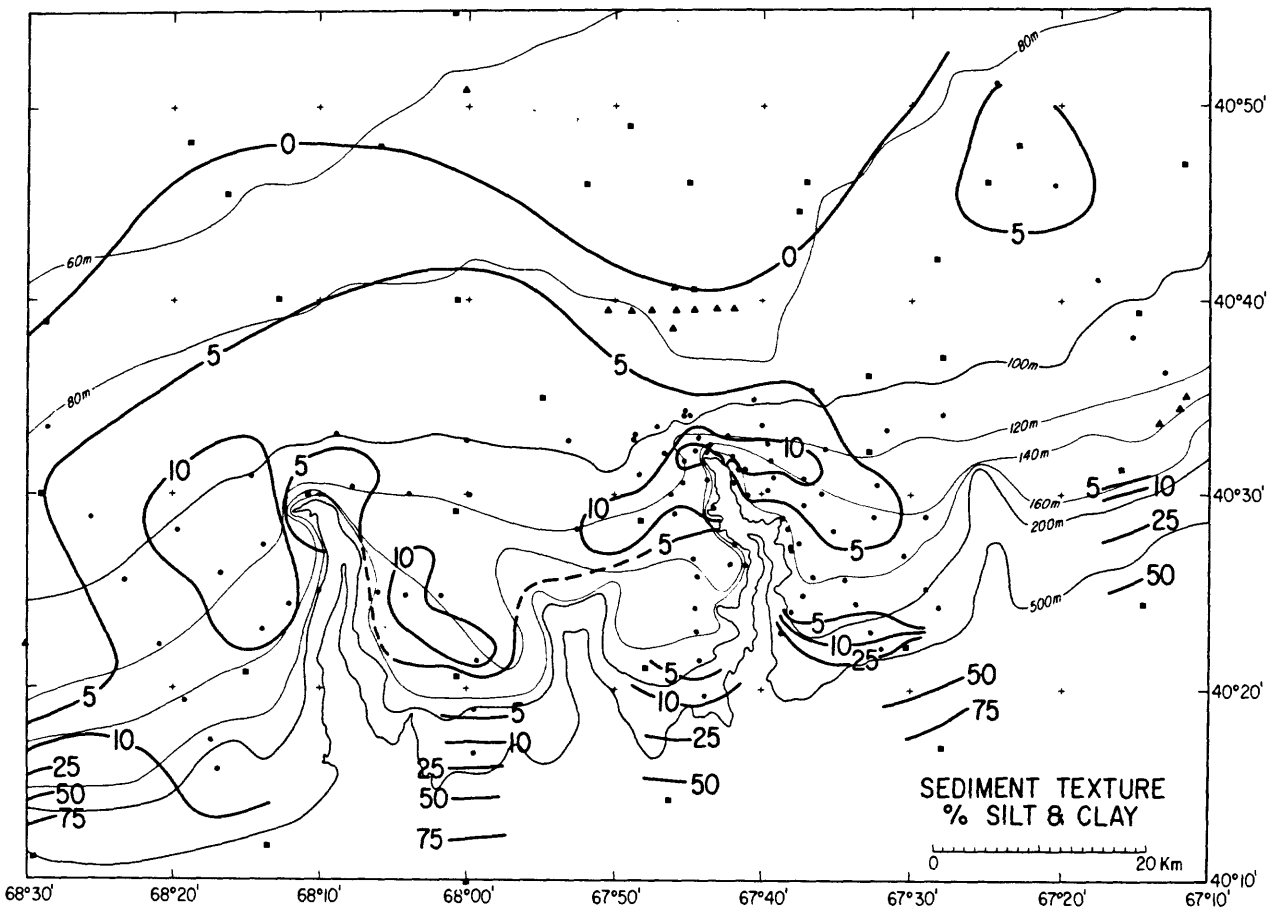

Figure 2-12b. Surface sediment texture on the southern flank of Georges Bank adjacent to Lydonia and Oceanographer Canyons. The surface texture in the canyons at depths greater than 200 m is not shown. Triangles indicate samples from Bothner and others (1982) and squares from Hathaway (1971). Circles are data from this study. Percent silt plus clay.

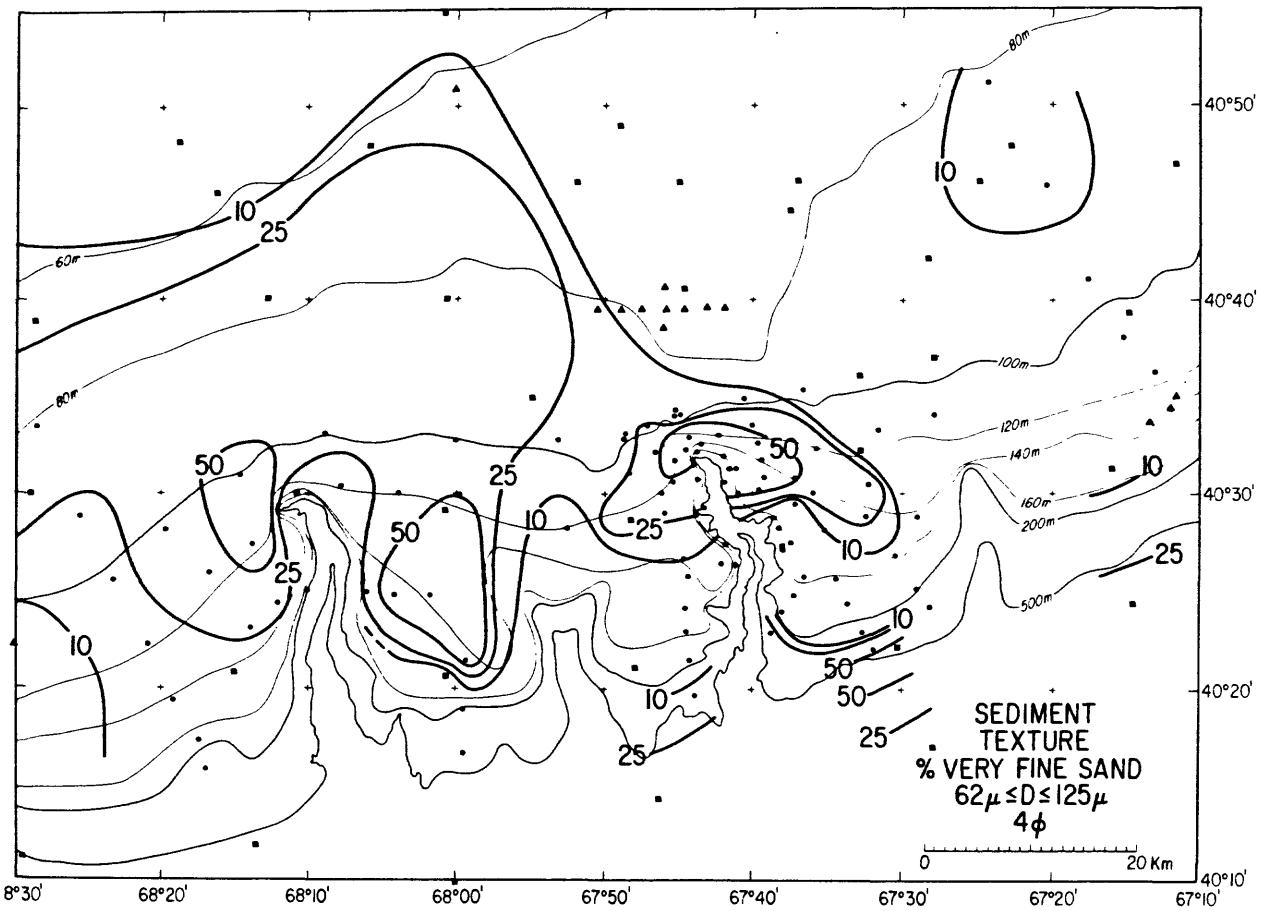

Figure 2-12c. Surface sediment texture on the southern flank of Georges Bank adjacent to Lydonia and Oceanographer Canyons. The surface texture in the canyons at depths greater than 200 m is not shown. Triangles indicate samples from Bothner and others (1982) and squares from Hathaway (1971). Circles are data from this study. Percent very fine sand (62.5μ < D<125.0μ).

and west of the canyon between 100-m and the 150-m isobath. In contrast to the fine sediments around the head of Lydonia Canyon which extended almost to the canyon rim, the fine sediments around Oceanographer Canyon apparently were separated from the canyon by a broader region of coarse material. The sediment in the two lobes was composed of 5-10% silt plus clay and 25-50% very fine sand.

Samples of the surficial sediment were obtained in the thalweg of Lydonia Canyon from about 200 to 1,600 m using the submersible ALVIN. Although these samples are limited in number and indicate some small-scale spatial variability, they do show consistent trends in the surface sediment texture along the canyon axis (fig.2-13). Although the sediments at 1,600 m were finer than the sediments in the head of the canyon, the sediment texture did not decrease uniformly with depth. The surficial sediment texture of the canyon thalweg can be described in four segments. In segment 1, between 100 m on the canyon shelf and 250 m in the canyon head, the surficial sediments become rapidly finer. In this segment the silt plus clay and the very fine sand content increased from less than 10% to greater than 20% and 60%, respectively, while the fine, medium, and coarse sand content decreased. In segment 2, between about 250 and 450 m, the surficial sediments became slightly coarser; the fine sand content gradually increased while the silt plus clay and the very fine sand content decreased. In segment 3, between 450 and 650 m, there was an abrupt change to coarser sediments between 450 and 500 m and a return to fine sediments between 600 and 650 m. In the center of segment 3 between about 500 and 600 m, there was less than 10% silt plus clay and very fine sand, and medium and coarse sand comprised greater than 30% and 20% of the surficial sediments, respectively. This section of coarse-grained sediments is located just south of the major western shift in the canyon axis

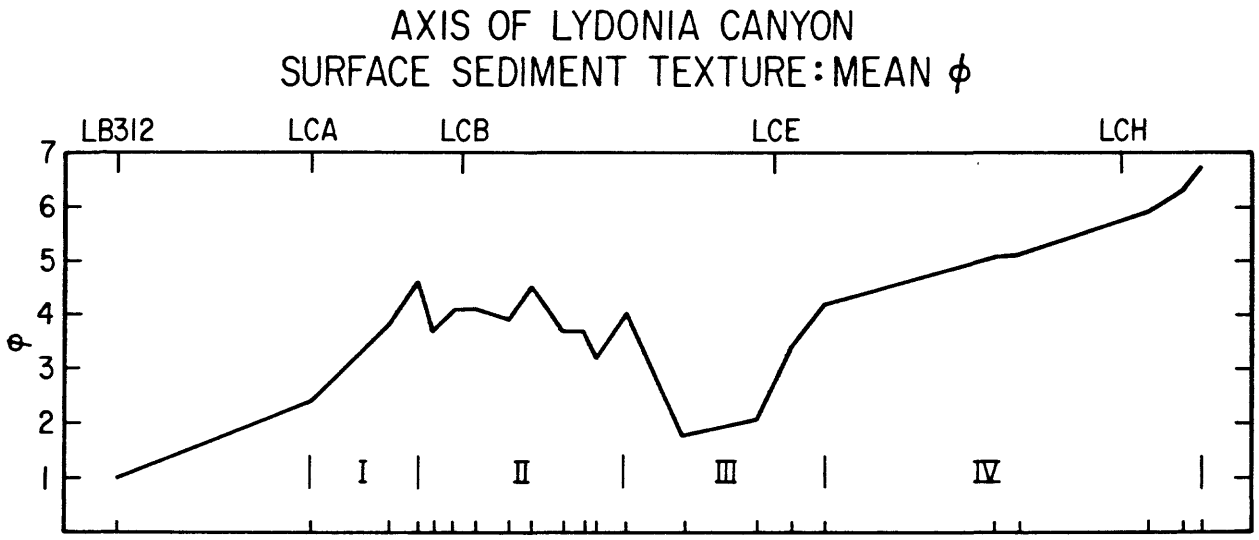

Figure 2-13a. Surface sediment texture across the southern flank of Georges Bank and along the thalweg of Lydonia Canyon to 1,600 m. I-IV indicate textural regions (see text). LB312 is Mobil Lease Block 312, and LCA, LCB, LCE, and LCH indicate the location of mooring stations in the canyon axis. Samples in the axis were obtained from the submersible ALVIN. Mean Φ of sediments computed by method of moments.

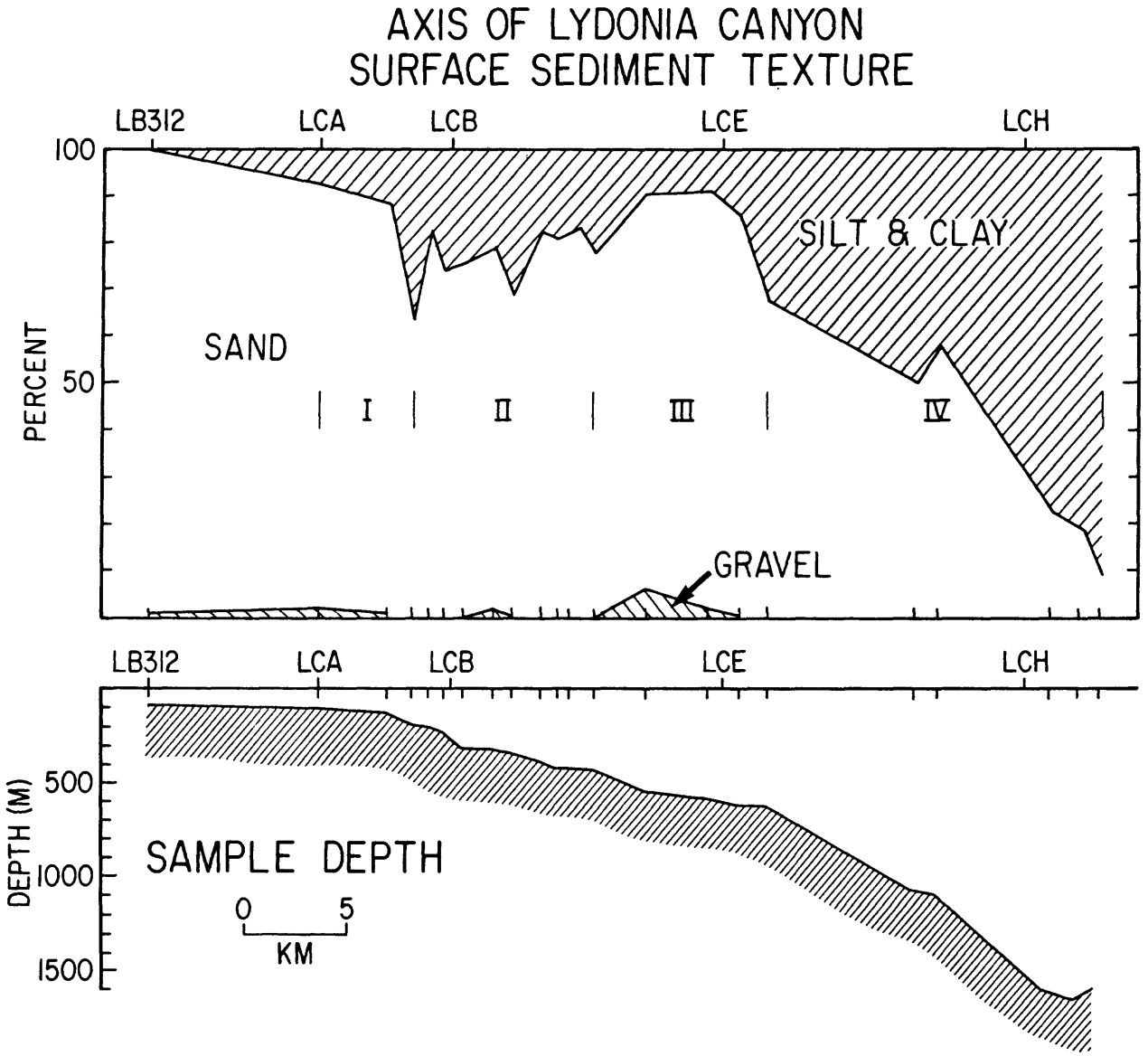

Figure 2-13b. Surface sediment texture across the southern flank of Georges Bank and along the thalweg of Lydonia Canyon to 1,600 m. I-IV indicate textural regions (see text). LB312 is Mobil Lease Block 312, and LCA, LCB, LCE, and LCH indicate the location of mooring stations in the canyon axis. Samples in the axis were obtained from the submersible ALVIN. Percent silt plus clay, sand, and gravel. Depth of samples is shown in lower panel.

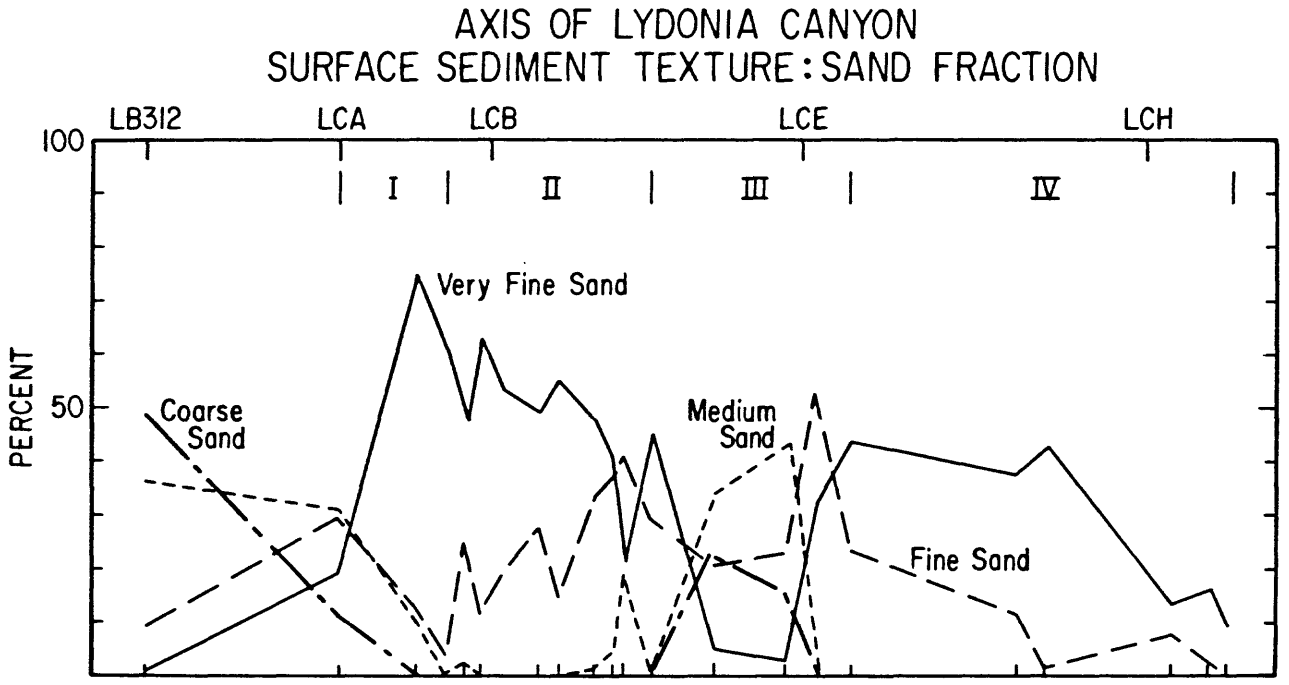

Figure 2-13c. Surface sediment texture across the southern flank of Georges Bank and along the thalweg of Lydonia Canyon to 1,600 m. I-IV indicate textural regions (see text). LB 312 is Mobil Lease Block 312, and LCA, LCB, LCE, and LCH indicate the location of mooring stations in the canyon axis. Samples in the axis were obtained from the submersible ALVIN. Percent coarse sand (0.5-1.0 mm), medium sand (0.250-0.500 mm), fine sand (0.125-0.250 mm), and very fine sand (0.063-0.125 mm).

near LCS (fig. 2-9). In segment 4, down-canyon of 650 m to 1,600 m, the surface sediments became gradually finer. The silt plus clay content gradually increased while the very fine sand and fine sand decreased.

Hydrography

The synoptic hydrographic sections provide an overview of the fields of temperature, salinity, density, and suspended sediment on the shelf and slope and within the canyon. Several questions are of interest: Is there hydrographic evidence for mixing or exchange within the canyon? How do Gulf Stream warm core rings (WCRs) affect the canyon fields? Does the canyon affect the position of the shelf-water/slope-water front? What is the typical Brunt-Vaisaila field that determines the propagation and reflection characteristics of internal waves? Sections from four cruises, which span the first year of the moored array, are presented here to illustrate the major hydrographic features and to locate the various current meters with respect to these features. In addition, selected vertical profiles of beam attenuation are presented to illustrate the distribution of suspended sediments on the shelf and slope, and in the canyons.

The hydrographic sections are smoothed over 10-20 m, and were all contoured using a computer routine (see the data reports for a detailed description of the processing techniques). The contouring near the bottom should be interpreted with care because of the vertically exaggerated sections and because of the large depth changes between stations. The sections are also snapshots of the hydrographic fields typically obtained in one day or less. Internal waves may cause vertical excursions of 50-100 m in amplitude (see section on vertical water-particle excursions) and thus fluctuations of this size may not reflect significant changes of the mean fields. Note also

that the bottom topography used in these sections is defined only by the hydrographic stations.

January 1981 (OCEANUS 91)

The observations on OCEANUS 91 were made between January 19 and 21, 1981, midway through D1. At this time, a large Gulf Stream warm core ring, 80-G, was located to the south of the canyon (see fig. 2-28 for maps of the surface temperature field, and the discussion on mean currents). Section 4, across the shelf and slope to the east of Lydonia Canyon, shows a sharp surface-to-bottom front in both temperature and salinity (fig. 2-14a). Inshore of the front, the water on the shelf is vertically well mixed; offshore of station 20, the water is well mixed between about 50 m and 200 m with temperature and salinity in excess of 12°C and 35.4 o/oo, respectively. This warm salty water is presumably associated with WCR 80-G, although the section does not extend far enough offshore to show much of the ring itself. The total density change across the front is about 0.4 sigma-t units; based on the 26.4 sigma-t contour, the slope of the front is about 4.8×10^{-3}. The beam attenuation at station 31 indicates near-bottom sediment resuspension on the shelf. Mooring LCI was located just offshore of station 22; the upper instruments on the mooring (at 10 and 55 m) were above and inshore of the front, while the lower instruments at 195 and 245 m were below and offshore of the front. The near-bottom instruments on the mooring at station LCL (near station 25) were also below the strongest section of the front, while the upper instruments were in the well mixed shelf water.

Section 3 (fig. 2-14b) along the axis of the canyon extended slightly further into the WCR than section 4; temperature and salinity exceeded 14°C and 35.6 o/oo respectively in the vertically well mixed water above about 220

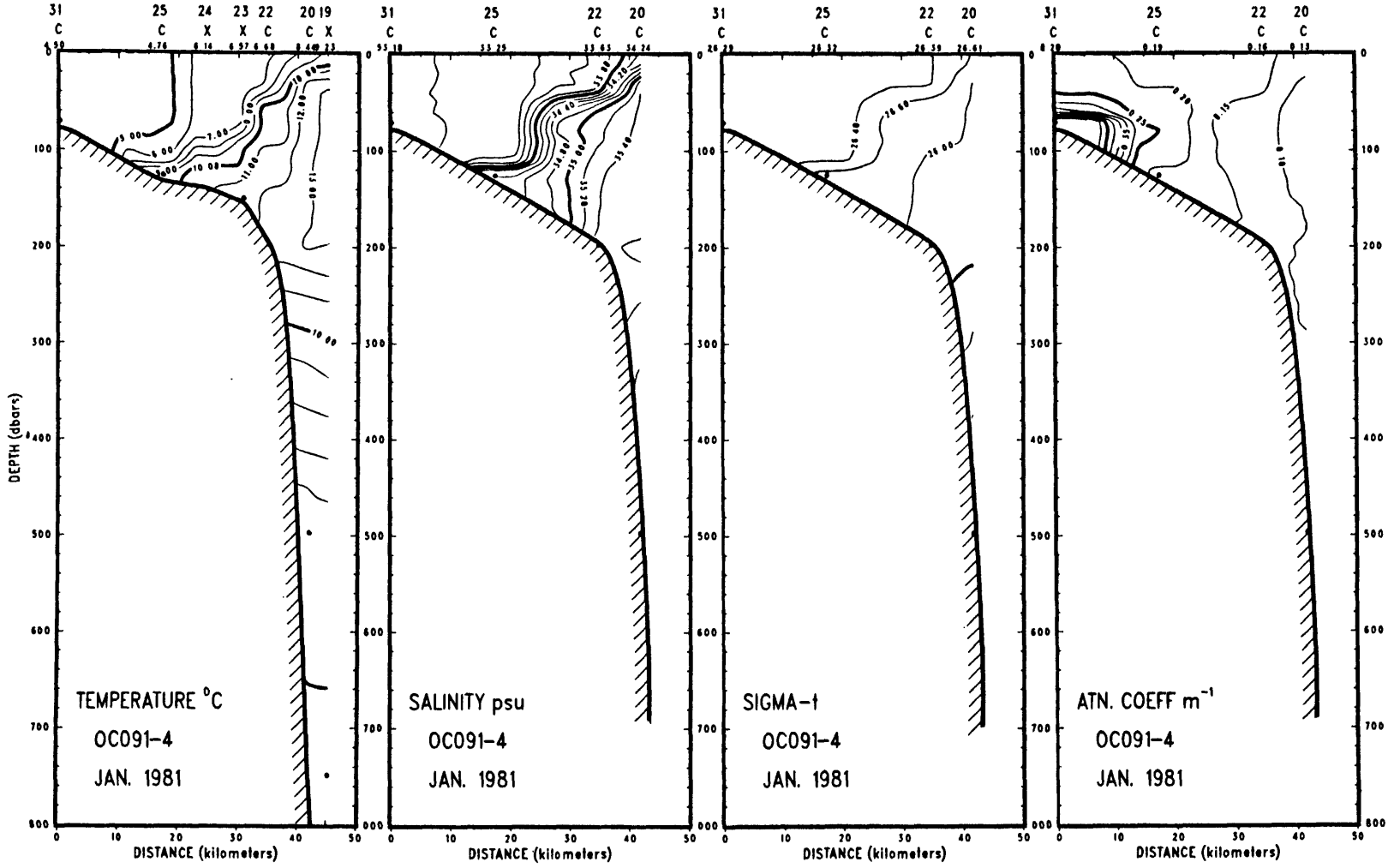

Figure 2-14a. Section 4 made on OCEANUS 91 showing temperature, salinity, sigma-t, and beam attenuation across the shelf and slope east of Lydonia Canyon. See figure 2-8a for location.

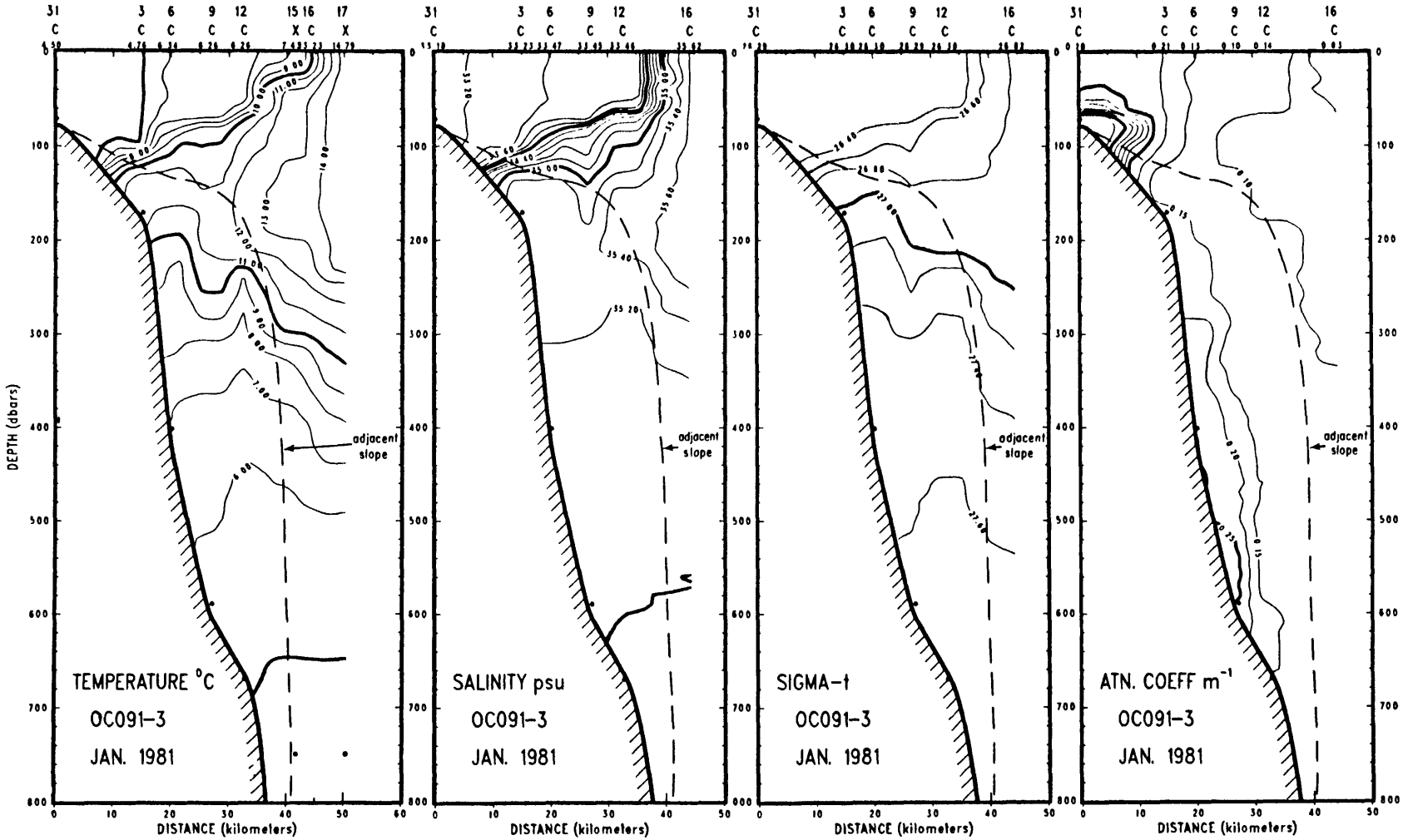

Figure 2-14b. Section 3 made on OCEANUS 91 showing temperature, salinity, sigma-t, and beam attenuation along the axis of Lydonia Canyon. See figure 2-8a for location.

m seaward of station 16. The downward-sloping isopycnals suggest that the ring influenced the flow as deep as 400-500 m. The shelf-water/slope-water front is similar in shape and slope to the front observed on section 4. In the canyon, there is a salinity maximum (salinity in excess of 35.2 o/oo) centered at about 200 m that extends to the head of the canyon. The slight widening of the sigma-t surfaces between stations 12 and 6 suggest some vertical mixing. The section of beam attenuation shows two separate areas of near-bottom increases in suspended sediment concentration, one on the shelf and the other along the canyon axis.

Section 2 (fig.2-14c,d) across the canyon near the mouth shows slightly warmer and saltier water on the eastern side of the canyon, and sigma-t surfaces rising to the east.

The vertical distribution of suspended matter, as indicated by beam attenuation, at selected stations on the shelf, slope and in the canyon is shown in figure 2-14e. At 400 and 600 m in the canyon axis, the beam attenuation increeased nearly linearly toward the bottom over a distance of 200-300 m (sta. 6 and 9). The increase was not observed at station 12 at about 675 m water depth. Although it is difficult to determine the increase in suspended sediment concentration from the beam attenuation measurements alone (see Appendix 2), the proportionality constant between beam attenuation and suspended sediments, using grain size information from the sediment traps (see Chapter 6), is on the order of 5 $(mg/l)/(m^{-1})$. Thus the observed increase in beam attenuation in the canyon axis of 0.10-0.20 m^{-1} probably reflects an increase in suspended sediment concentration of order 0.5 to 1.0 mg/l. At the stations (20 and 22) on the continental slope, the beam attenuation did not increase markedly toward the bottom. The beam attenuation was highest on the shelf near the bottom, as already illustrated in the vertical sections.

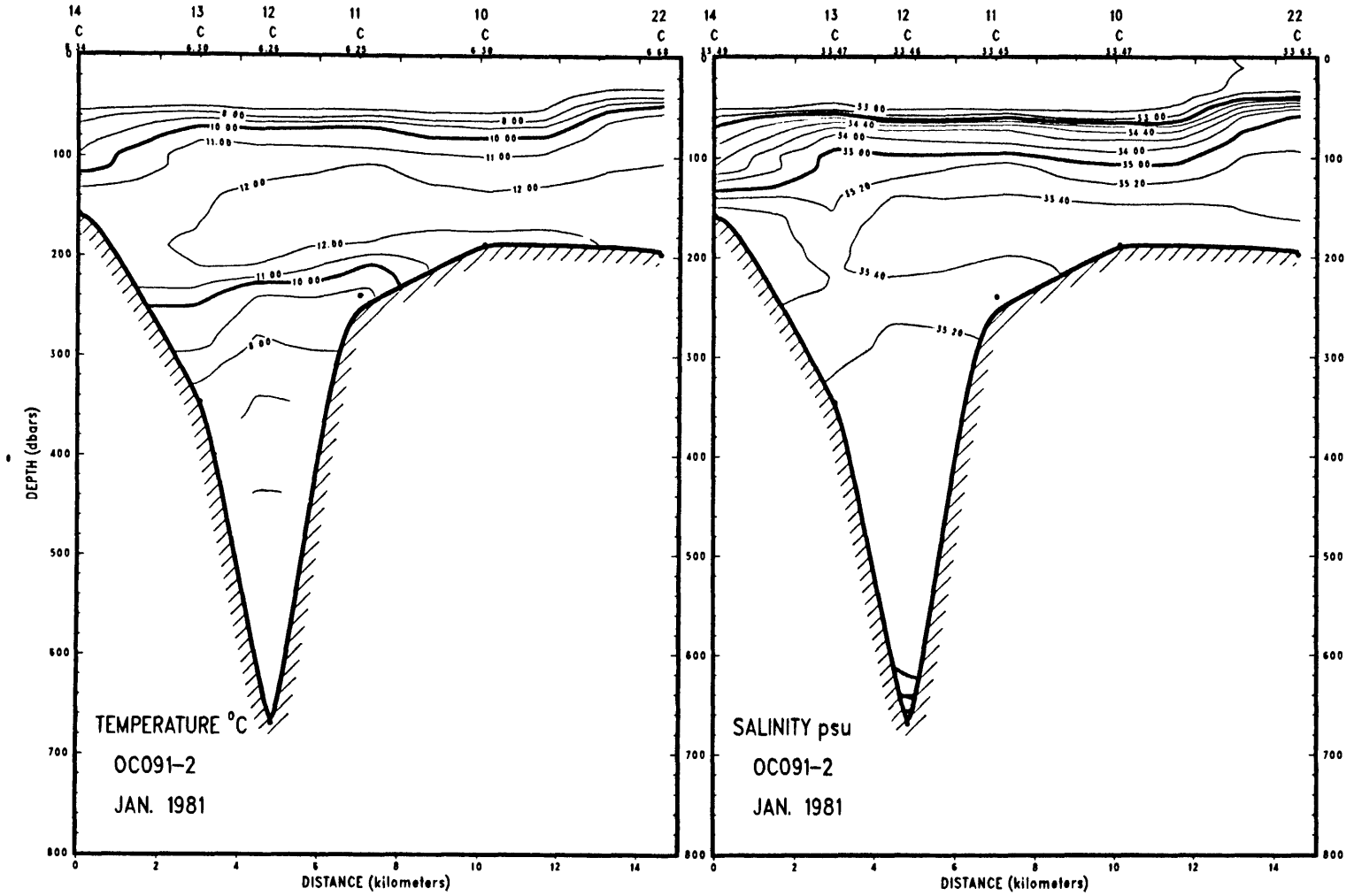

Figure 2-14c. Section 2 made on OCEANUS 91 showing temperature and salinity across the mouth of Lydonia Canyon. See figure 2-8a for location.

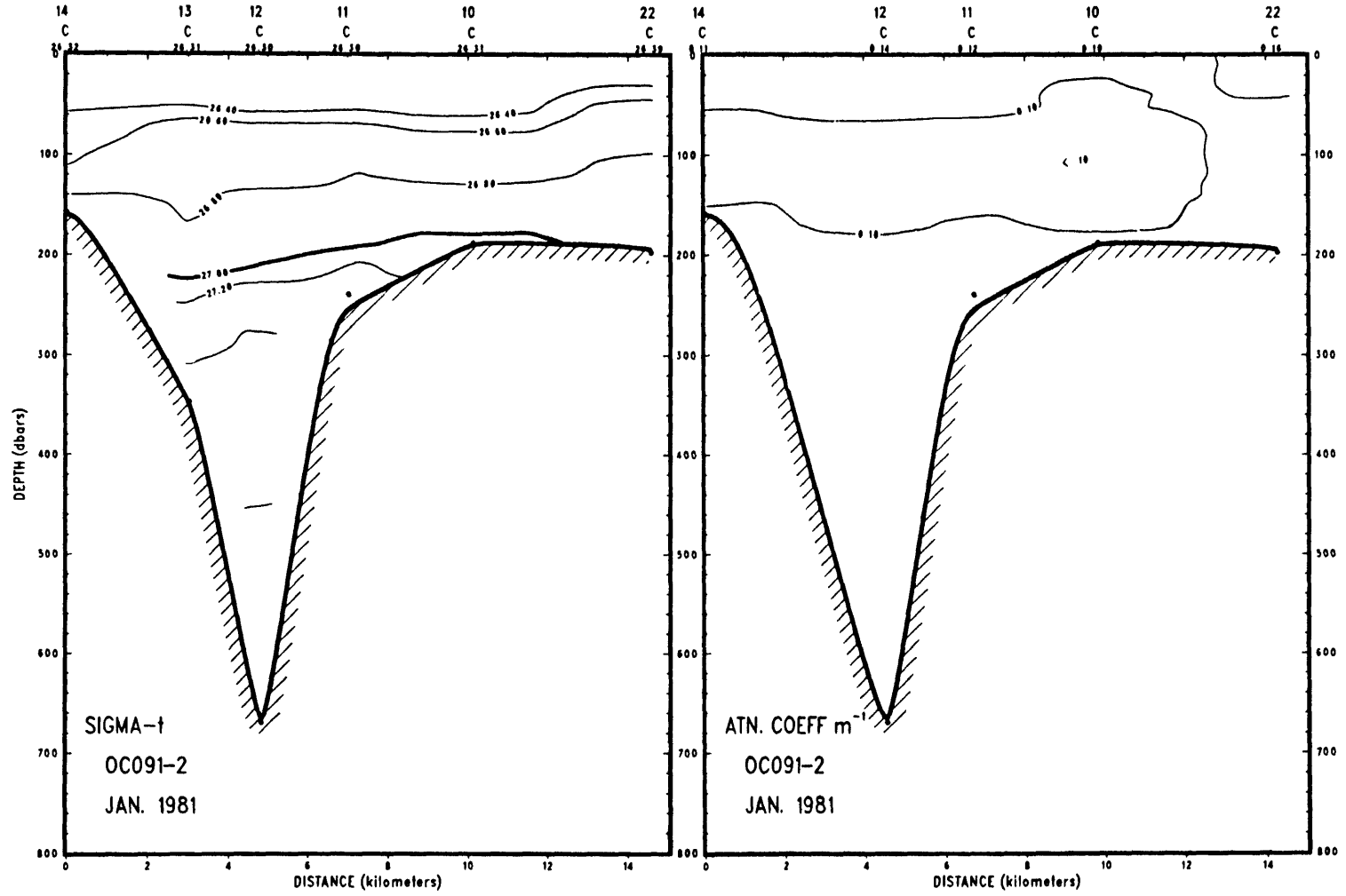

Figure 2-14d. Section 2 made on OCEANUS 91, showing sigma-t and beam attenuation across the mouth of Lydonia Canyon. See figure 2-8a for location.

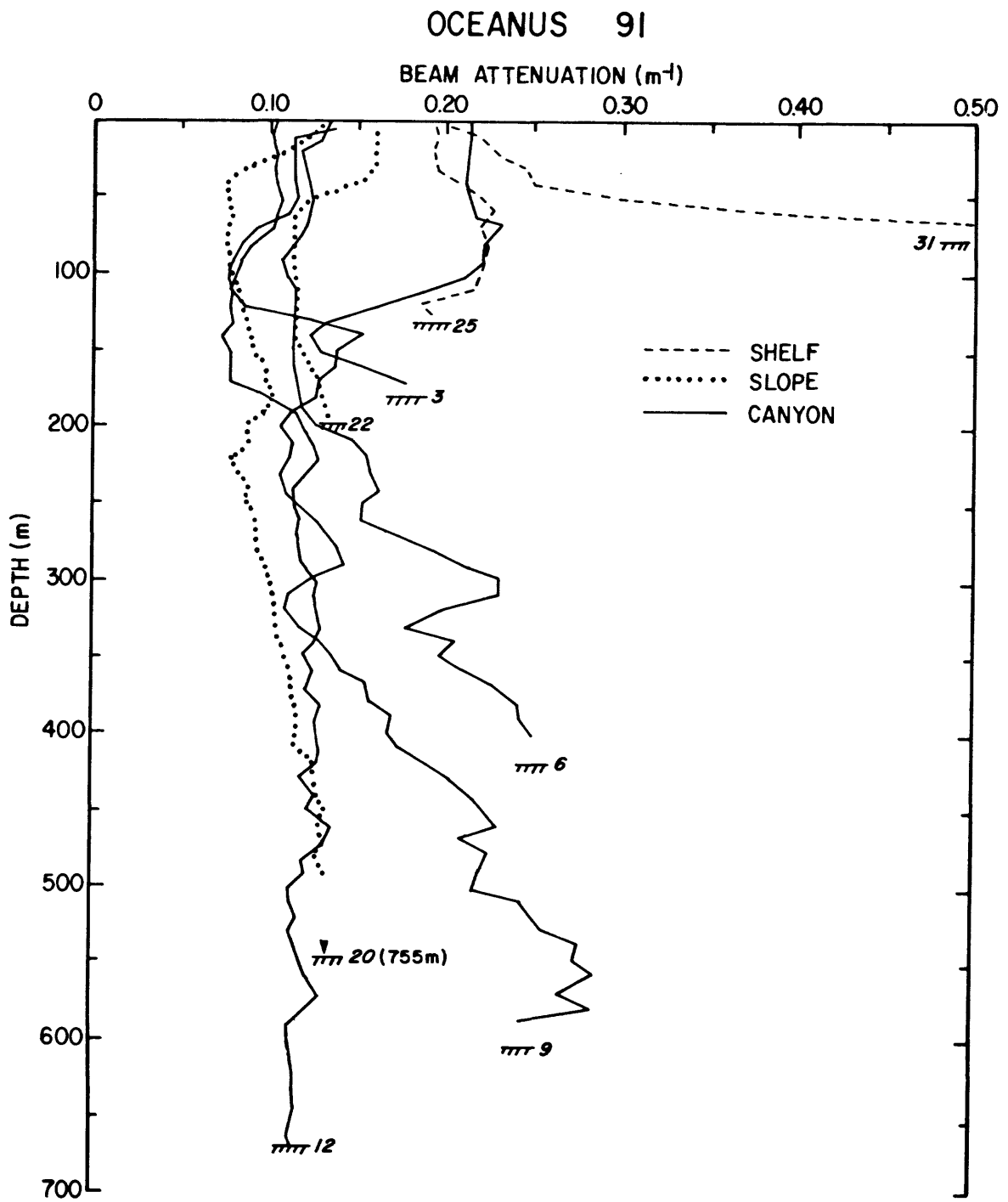

Figure 2-14e. Vertical profiles of beam attenuation at selected stations on the shelf, slope and in Lydonia Canyon. See figure 2-8a for station locations. Where the observations did not extend to the bottom, the bottom depth in parenthesis follows the station number.

May 1981 (OCEANUS 95)

The hydrographic observations on OC95 were made between D1 and D2. The Oceanographic Analysis Charts shows WCR 81-C located south of Lydonia Canyon during this period. The surface expression of the ring was not apparent north of 40°N however. There were no measurements of beam attenuation made on this cruise.

The shelf-water/slope-water front shown in section 6 (fig. 2-15a) across the shelf and slope was somewhat stronger than in January, and there was some vertical stratification above the front, primarily due to low salinity water (<34 o/oo) at depths less than 50 m. A warm (>10°C) and salty (>35.4 o/oo) lens of water was observed off-shelf just below the front, possibly a subsurface expression of WCR 81-C. Current observations at LCI, located just onshore of station 4, showed weak easterly flow at 60 m when this section was made. The flow was sharply eastward about 15 days after the section, indicating WCR 81C (see section on WCR). Based on the 26.4 isopycnal, the slope of the front on the shelf below 50 m was about 5.8×10^{-3}.

The section made along the canyon axis shows the front above the canyon rim and the warm salinity maximum centered at about 170 m at the seaward end of the section (fig. 2-15b). At the head of the canyon, the salinity reaches only about 34.8 o/oo at 200 m , at least 0.4 o/oo fresher than in January. Isotherms and isopycnals slope downward beneath the salinity maximum seaward of station 70. Toward the canyon head (landward of station 70), the isopycnals diverge, especially between 200 and 400 m.

September 1981 (OCEANUS 104)

The hydrographic observations on OC104 were made between September 29 and October 1, 1981, between D2 and D3. The Ocean Frontal Analysis charts show no

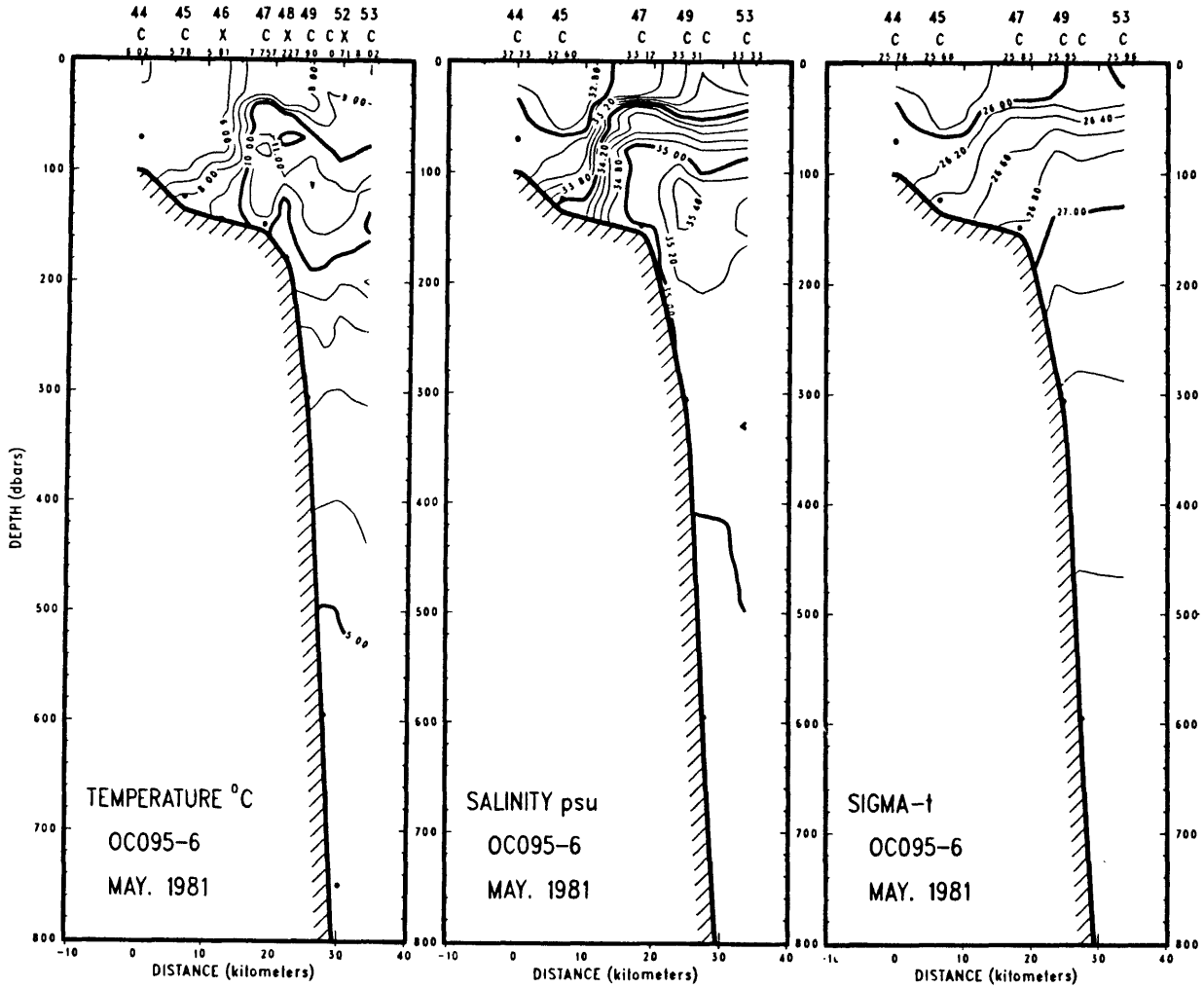

Figure 2-15a. Section 6 made on OCEANUS 95 showing temperature, salinity, and sigma-t, across the shelf and slope east of Lydonia Canyon. See figure 2-8a for location.

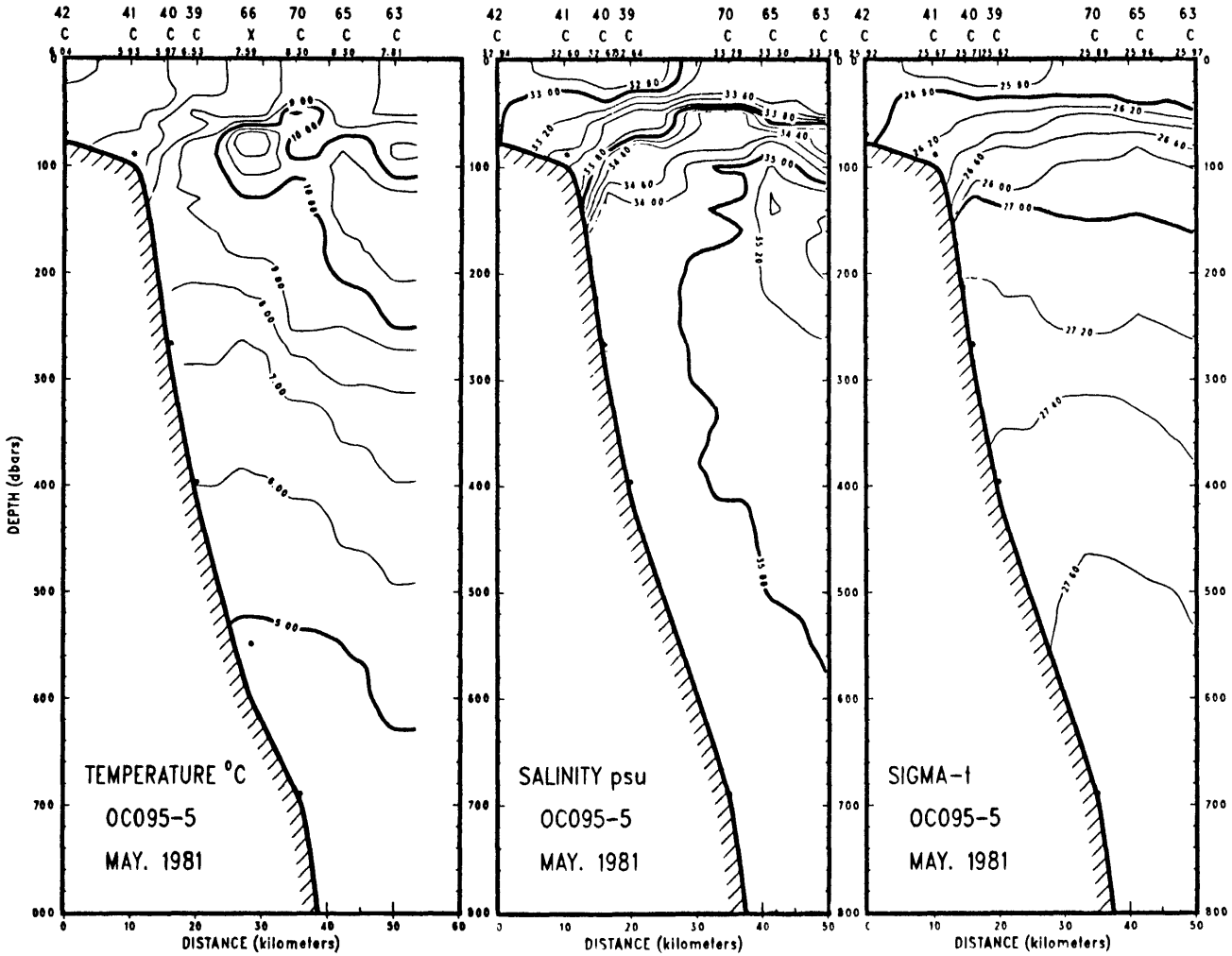

Figure 2-15b. Section 5 made on OCEANUS 95 showing temperature, salinity, and sigma-t along the axis of Lydonia Canyon. See figure 2-8a for location.

WCRs near Lydonia Canyon at this time. The section to the west of Lydonia Canyon shows strong vertical stratification caused by both temperature and salt (fig. 2-16a). Based on the 26.0 sigma-t isopycnal, the slope of the front is about 1.4×10^{-3}. The section of beam attenuation suggests a near-bottom increase in suspended matter over the shelf. The attenuation was also relatively large near the surface at the seaward end of the section, possibly caused by a phytoplankton bloom.

Along the canyon axis, the salinity maximum between about 180 and 360 m at the head of the canyon exceeds 35.0 o/oo (fig. 2-16b). The isopycnals (27.2 and 27.4) diverge toward the canyon head (upcanyon of station 30) but, in contrast to their shape in January and May, they are almost flat seaward of station 30. The section of beam attenuation shows an increase near the bottom in a layer 50-100 m thick along the axis of about 0.05 to 0.10 m^{-1}.

The vertical distribution of suspended matter as indicated by beam attenuation at selected stations on the shelf, slope and in the canyon is shown in figure 2-16 c-e. The beam attenuation increased toward the bottom in the canyon axis at stations 15, 23, and 38 (note station 30 did not extend to the bottom and only the upper 600 m of station 38 is shown in fig. 2-16c). The hydrographic observations on OCEANUS 104 were made during a period of strong winds from the northwest (see section on effect of storms and fig. 2-42), which caused near-bottom sediment resuspension over the shelf. The well-defined mid-water increase in beam attenuation at about 125 m at stations 15 and 23 (fig. 2-16c) is material suspended on the shelf and carried over the canyon rim. Section 3 across the canyon axis (see fig. 2-8b for location) shows the plume originating on the west side of the canyon and extending over the axis (fig. 2-16d). Net flow during the time of this section, based on the current observations at 125 m at station LCB, was to the east. The lack of

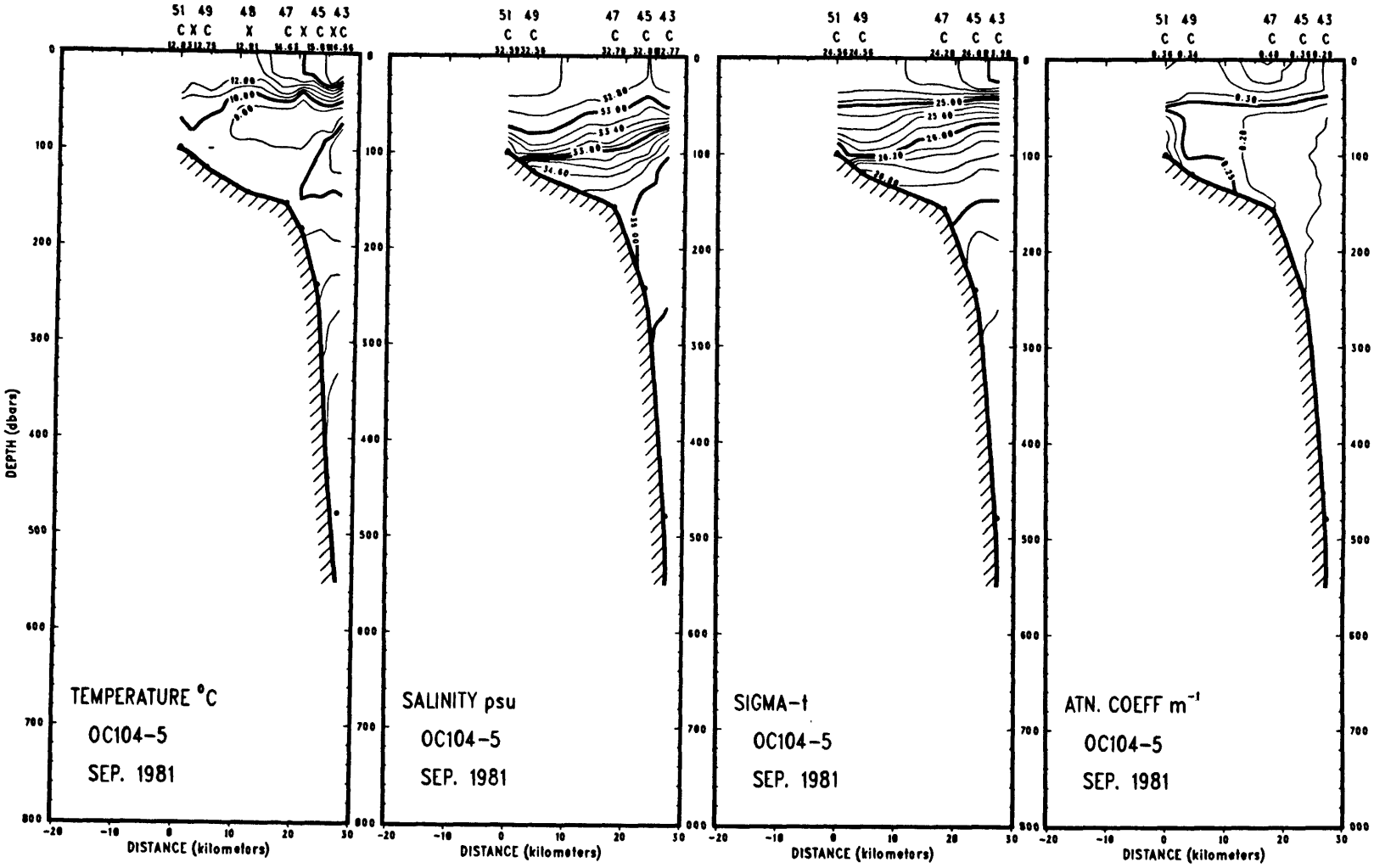

Figure 2-16a. Section 5 made on OCEANUS 104 showing temperature, salinity, sigma-t, and beam attenuation across the shelf and slope east of Lydonia Canyon. See figure 2-8a for location.

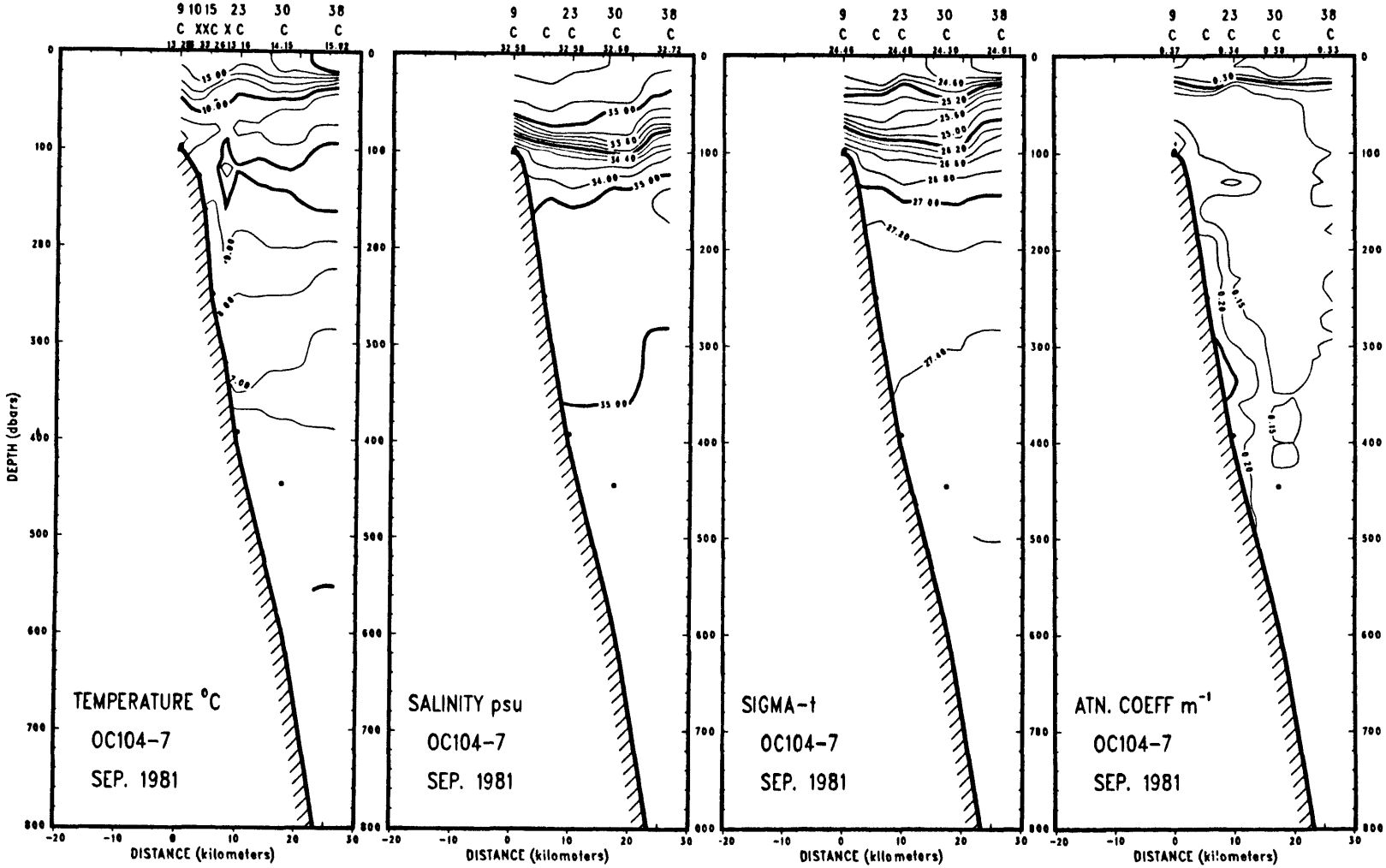

Figure 2-16b. Section 7 made on OCEANUS 104 showing temperature, salinity, sigma-t, and beam attenuation and along the axis of Lydonia Canyon. See figure 2-8b for location.

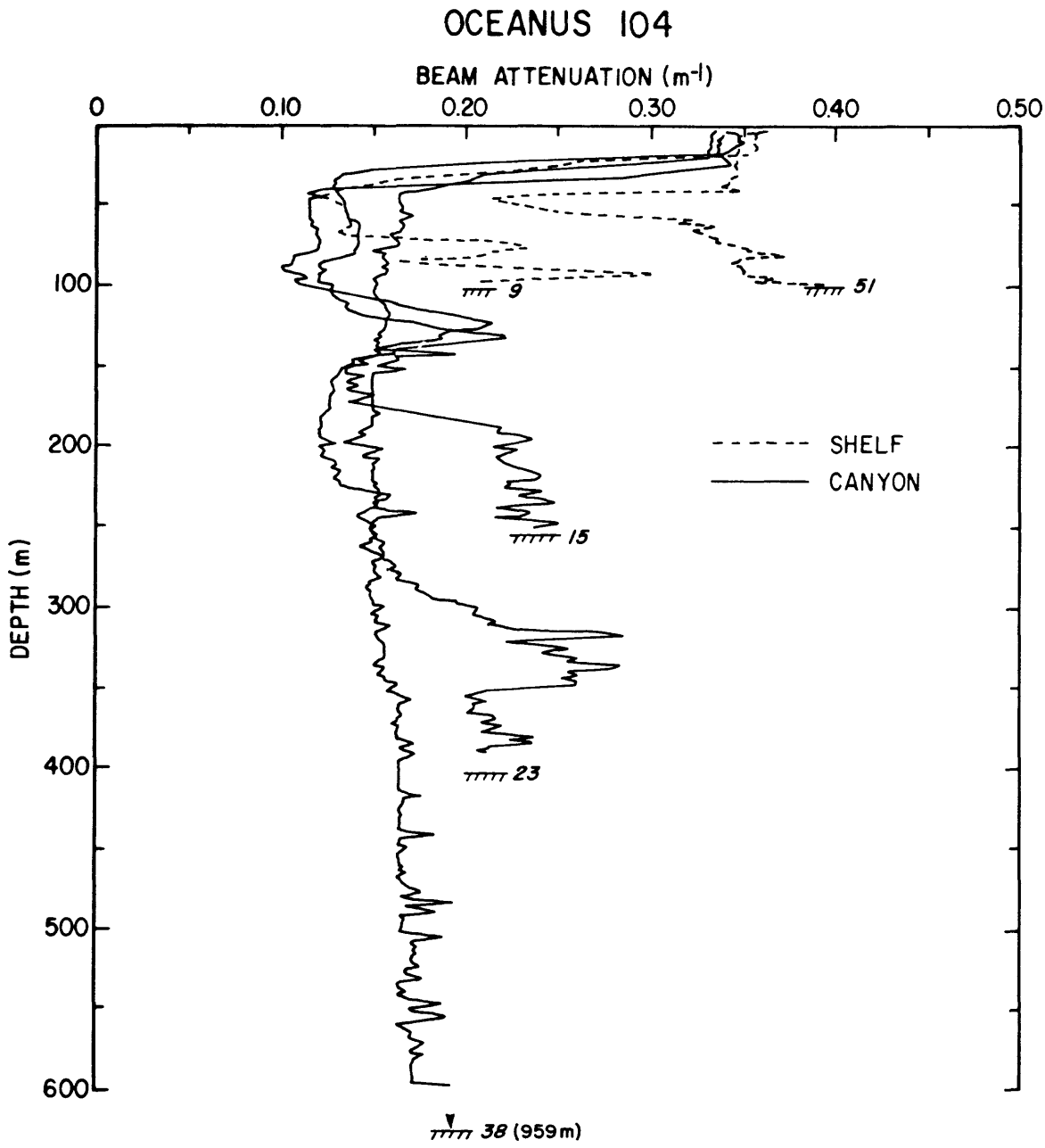

Figure 2-16c. Vertical profiles of beam attenuation at selected stations on the shelf, slope and in Lydonia Canyon. See 2-8b for station locations. Where the observations did not extend to the bottom, the bottom depth in parenthesis follows the station number.

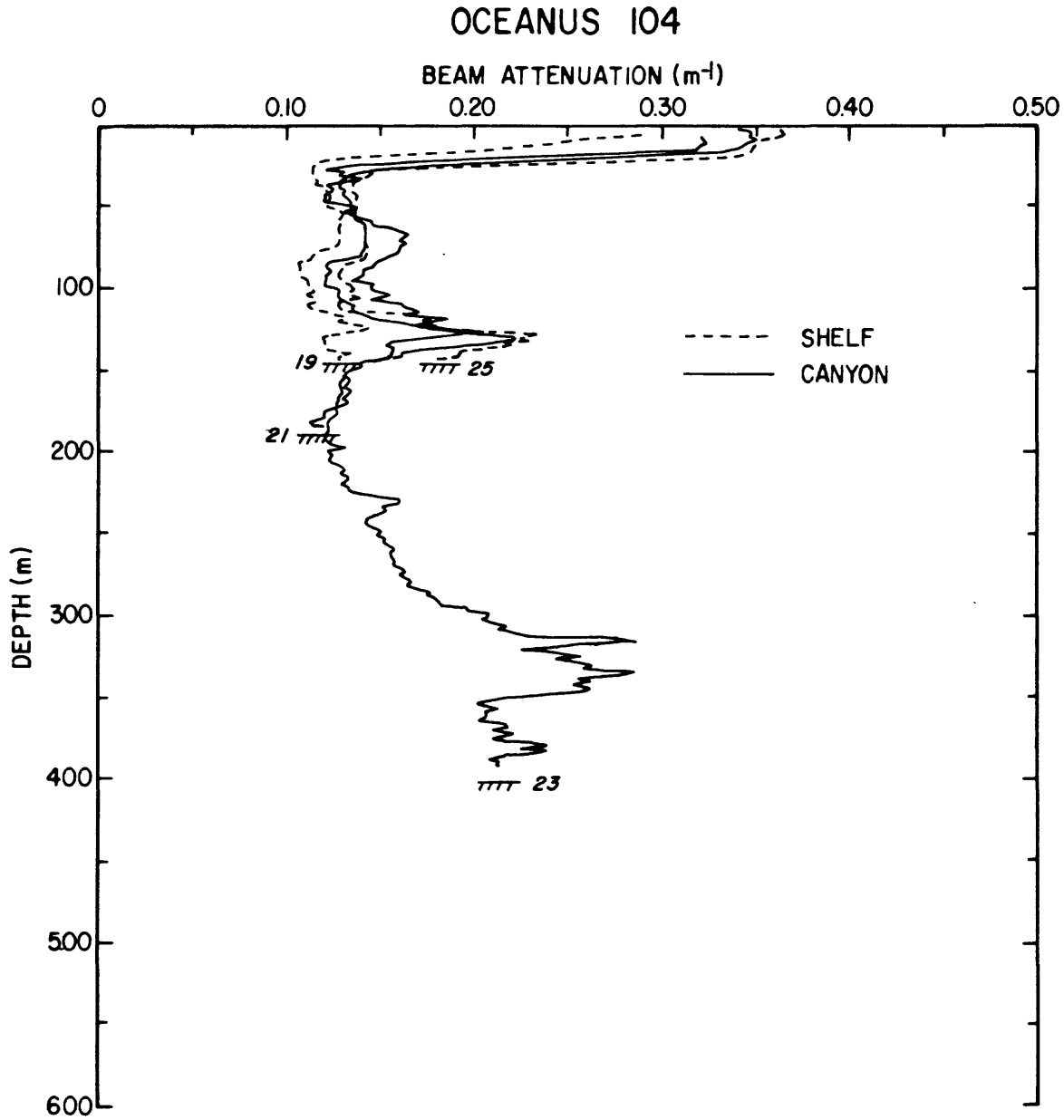

Figure 2-16d. Vertical profiles of beam attenuation at selected stations on the shelf and in Lydonia Canyon. See figure 2-8b for station locations.

suspended material at station 19 on the east side of the canyon suggests that the sediment may have been trapped by the canyon. Stations 47, 45 and 43 form a section across the slope, and show progressively increased beam attenuation toward the shelf break, and some increase toward the bottom on the outer shelf (fig. 2-16e).

February 1982 (OCEANUS 113)

The sections on OC113 were made between January 29 and February 3, 1982 between D3 and D4. The center of WCR 82-A was centered to the east of Lydonia Canyon at about 64°30'W. The section across the shelf and slope to the west shows the shelf-water/slope-water front with a slope of about 2×10^{-3} (fig. 2-17a). Water with a salinity of 35.6 o/oo and temperature greater than 13°C was observed beneath the front, centered at about 160 m. The beam attenuation section indicates almost no increase near the bottom over the shelf.

Along the axis of the canyon, the salinity maximum is centered at about 200 m at the canyon head, and salinity is in excess of 35 o/oo (fig. 2-17b). The isopycnals are nearly horizontal seaward of station 15 below 200 m.

The vertical distribution of suspended matter at selected stations, as indicated by beam attenuation, is shown in figure 2-17e. The observations again show near-bottom resuspension in the canyon axis. Stations 3 and 30, in almost the same location in the canyon head but occupied about 4 days apart, show markedly different beam attenuation profiles, although both increase toward the bottom. The beam attenuation profiles at stations 9 and 11 on the slope suggest lower suspended concentrations than in the canyon, and less near-bottom resuspension.

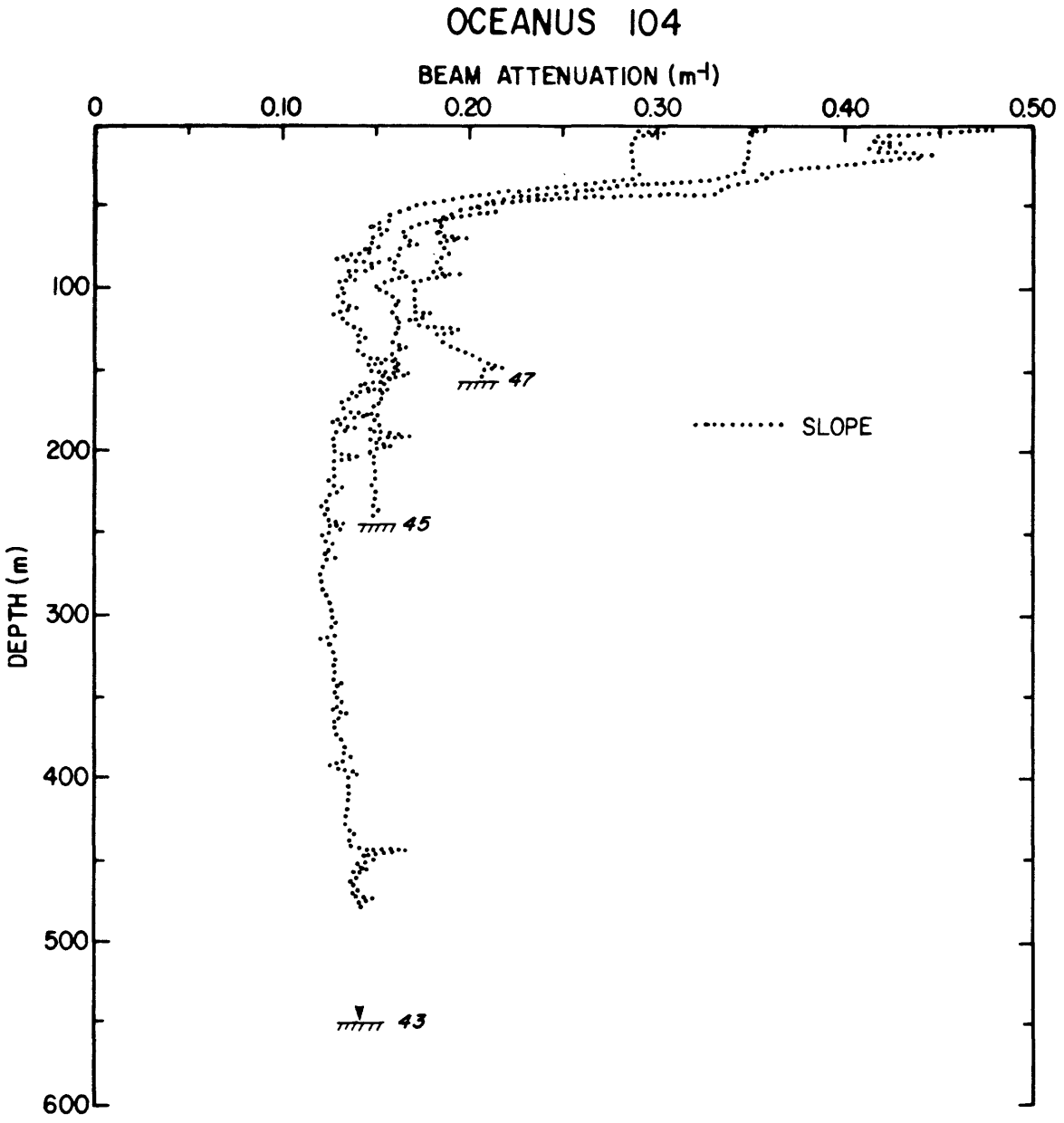

Figure 2-16e. Vertical profiles of beam attenuation at selected stations on the slope adjacent to Lydonia Canyon. See figure 2-8b for station locations.

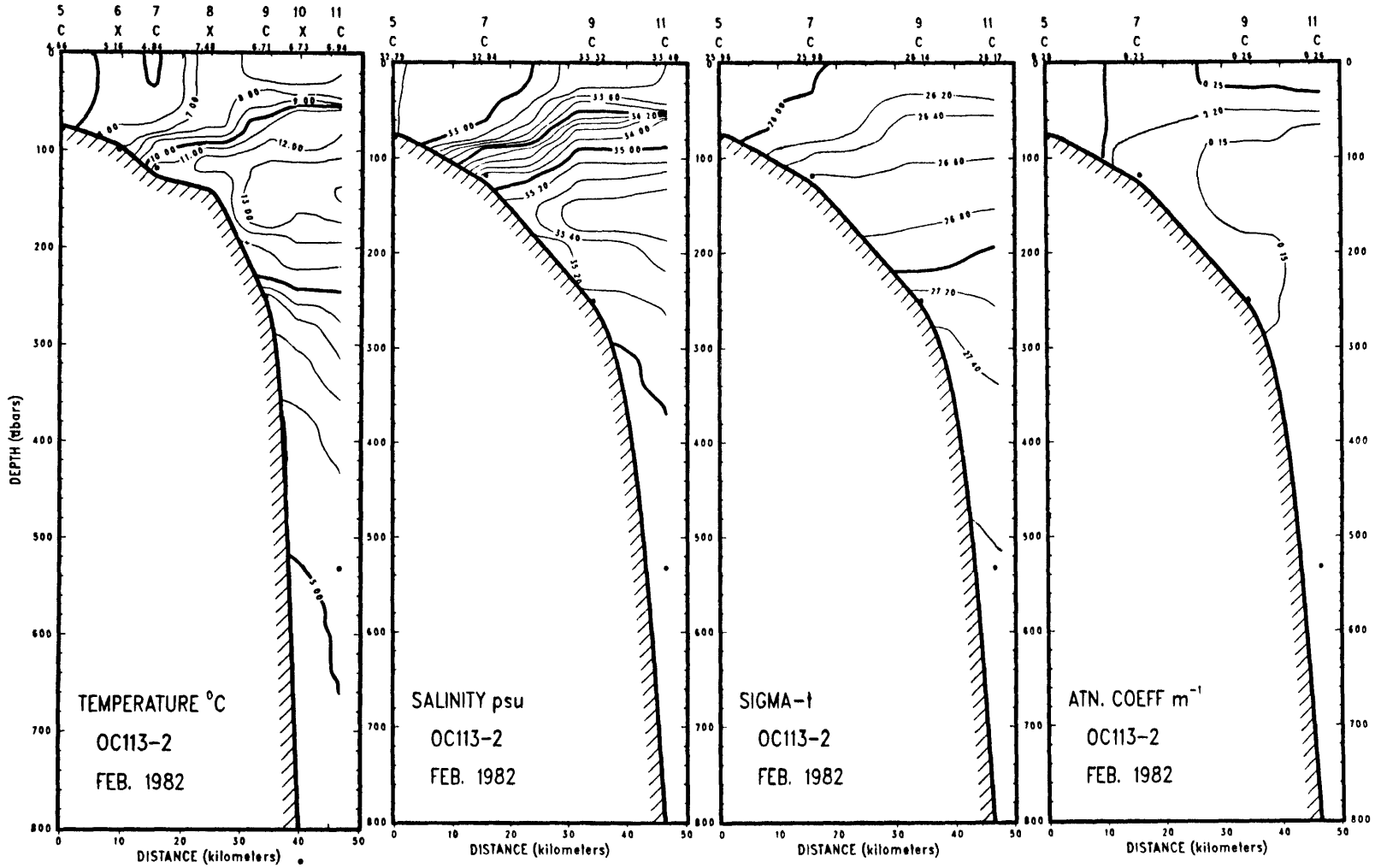

Figure 2-17a. Section 2 made on OCEANUS 113 showing temperature, salinity, sigma-t, and beam attenuation across the shelf and slope to the east of Lydonia Canyon. See figure 2-8b for location.

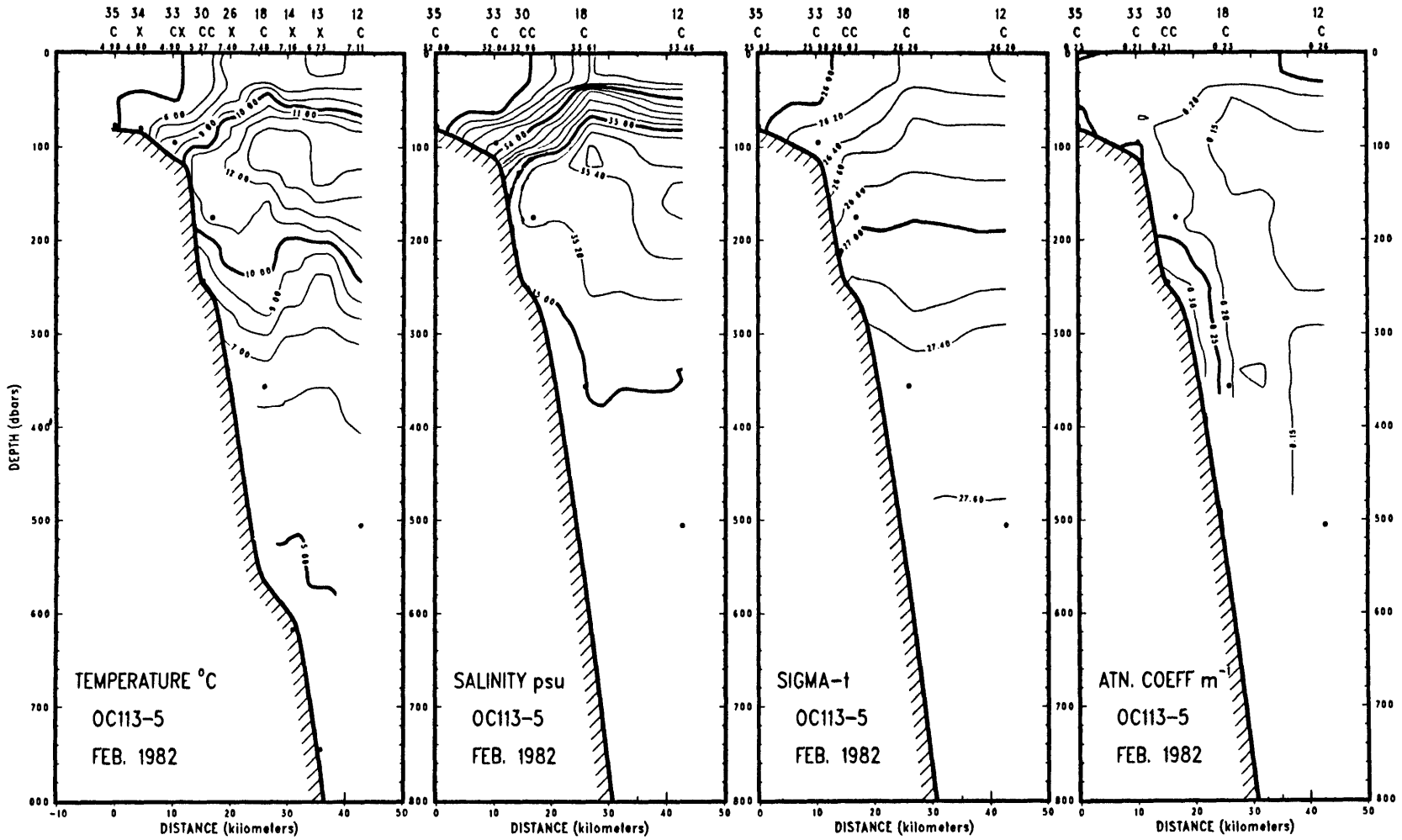

Figure 2-17b. Section 5 made on OCEANUS 113 showing temperature, salinity, sigma-t, and beam attenuation along the axis of Lydonia Canyon. See figure 2-8b for location.

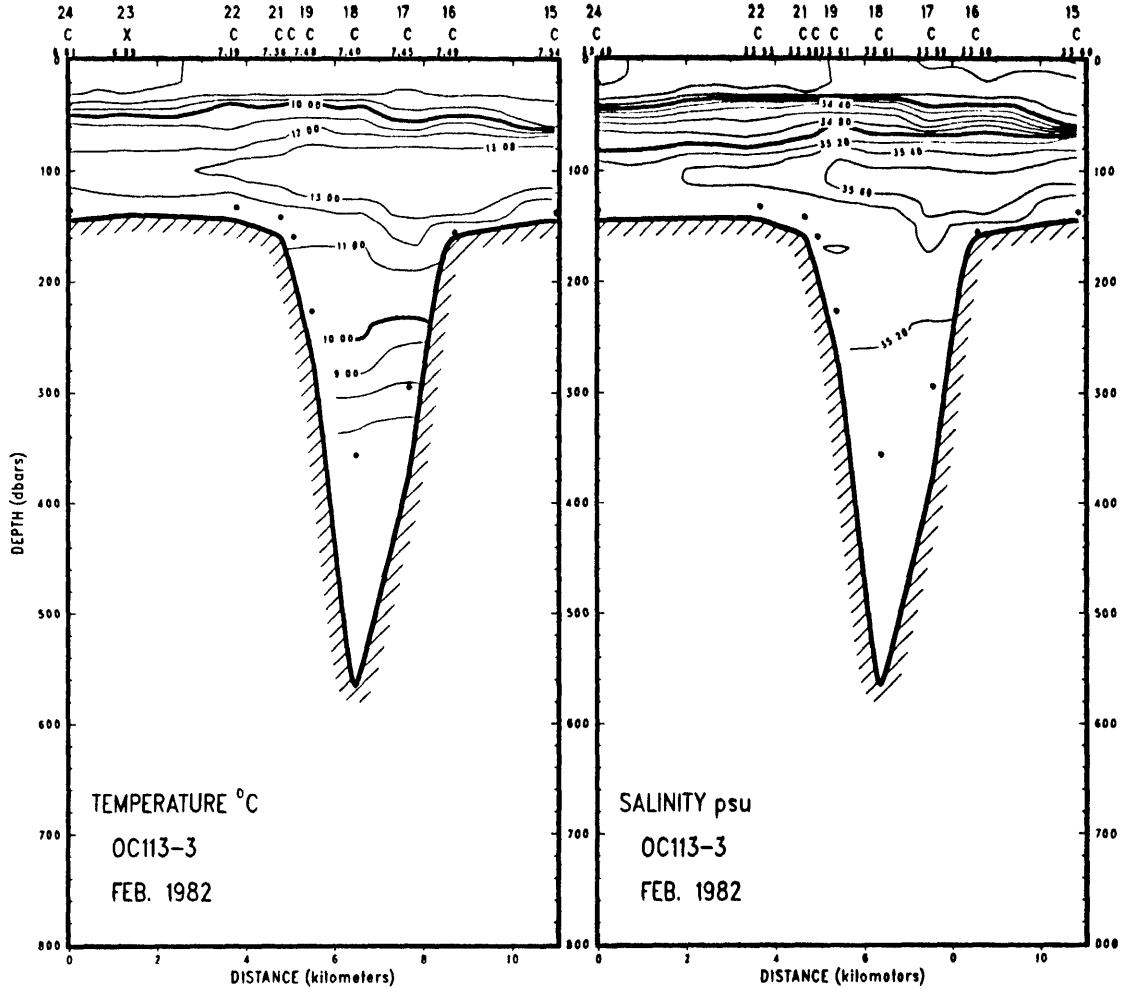

Figure 2-17c. Section 3 made on OCEANUS 113 showing temperature and salinity across the mouth of Lydonia Canyon. See figure 2-8b for location.

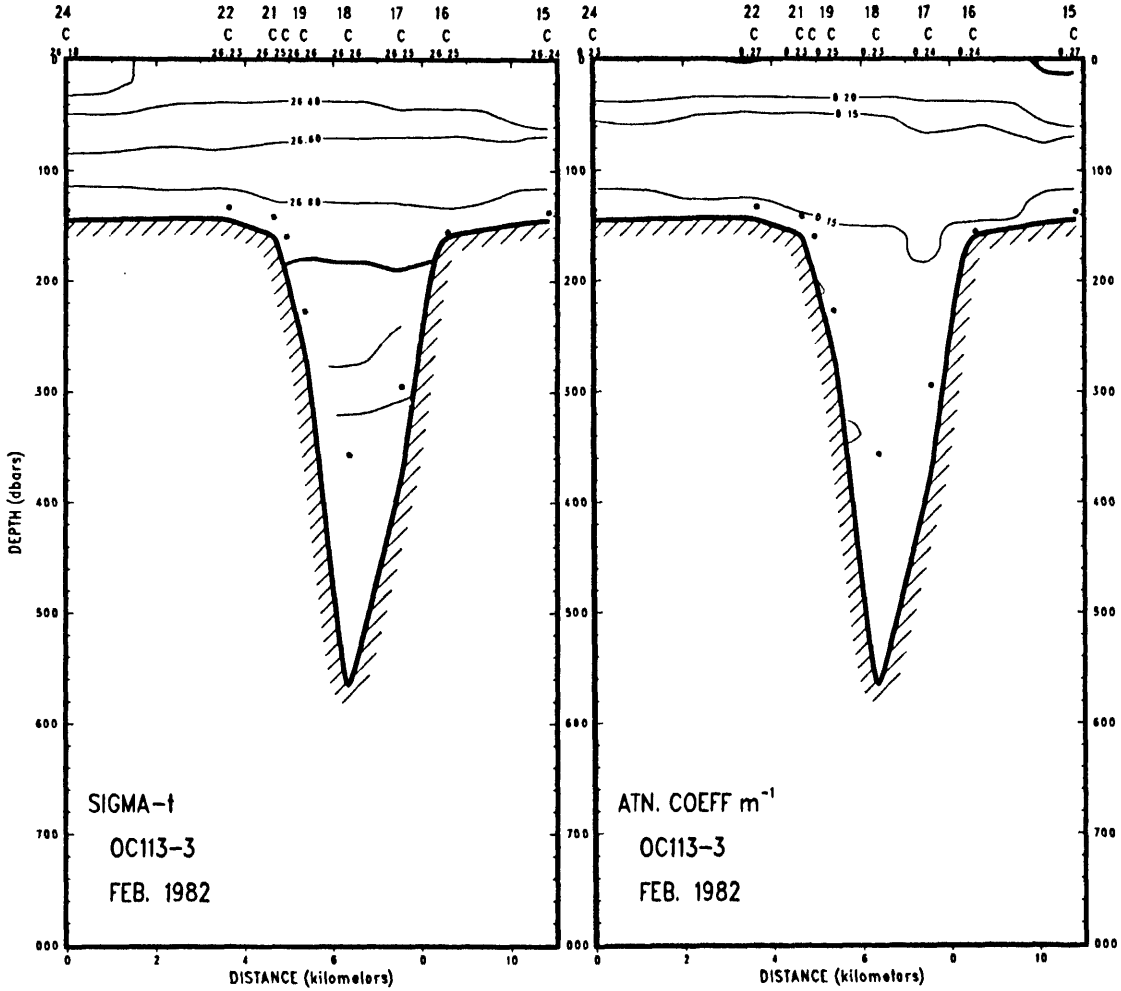

Figure 2-17d. Section 3 made on OCEANUS 113 showing sigma-t and beam attenuation across the mouth of Lydonia Canyon. See figure 2-8b for location.

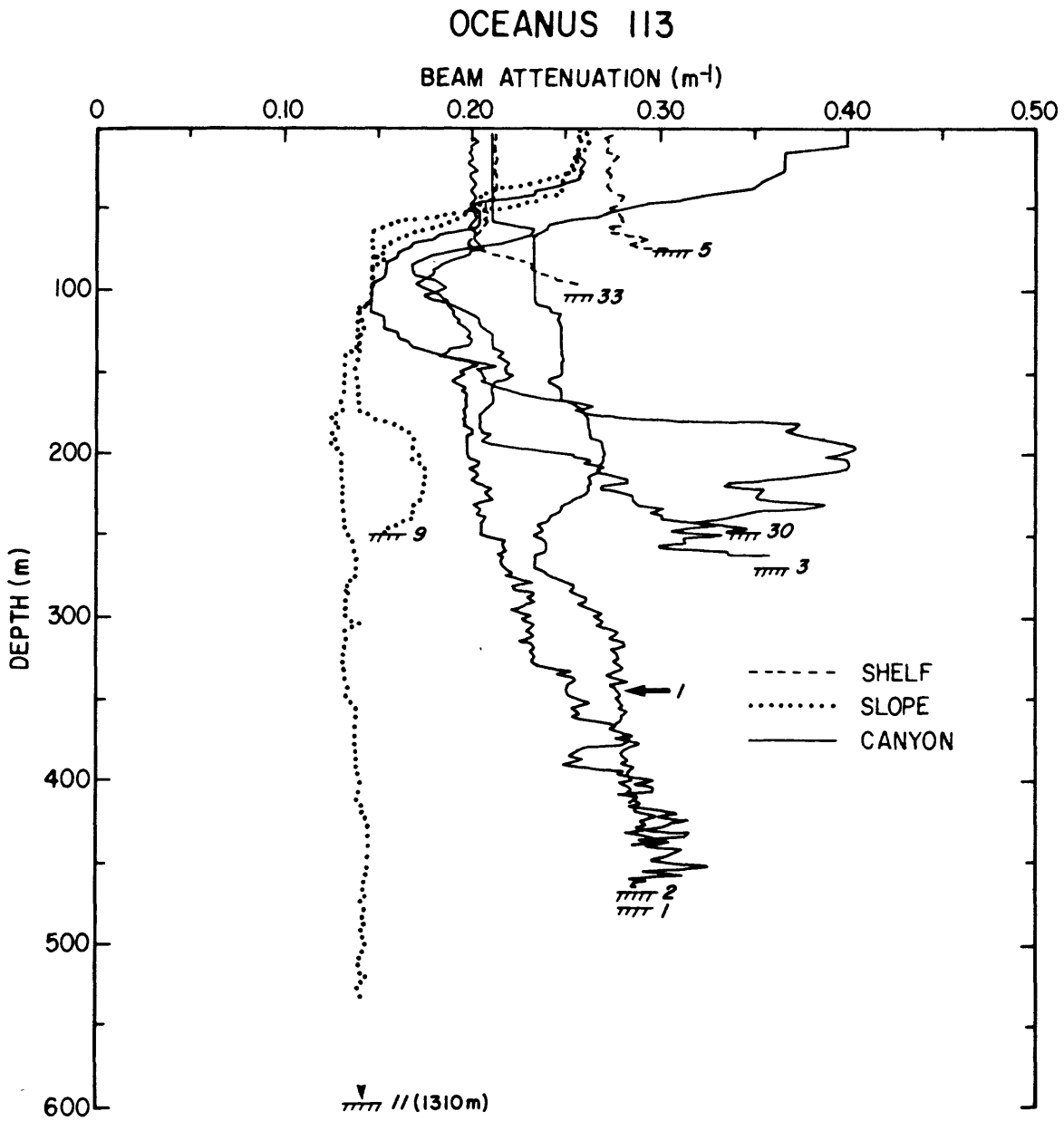

Figure 2-17e. Vertical profiles of beam attenuation at selected stations on the shelf, slope and in Lydonia Canyon. See figure 2-8b for station locations. Where the observations did not extend to the bottom, the bottom depth in parenthesis follows the station number.

Summary of hydrography and suspended sediments

The hydrographic observations made in and around Lydonia Canyon show the following major features:

1. The shelf-water/slope-water front extends above the canyon axis and, based on the position of the 34 o/oo isohaline, intersects the bottom between the 100 and 125 m isobath near the canyon head.
2. Below the front is a mid-depth temperature maximum, centered at about 150 m, where water temperature generally exceeds 10°C. Also below the front is a mid-depth salinity maximum, typically centered between 200 and 300 m near the canyon head, where salinities exceed 35 o/oo.
3. On cruises where there was good data coverage for determining the slope of the contours near the bottom in the canyon axis, the sigma-t surfaces diverged slightly toward the canyon head (see section OC95-5 and OC104-7).
4. When warm core rings are present south of the mouth of the canyon, warmer and saltier water extends deeper in the canyon head. Based on the OC91 observations, sigma-t surfaces below about 150 m slope downward toward the canyon mouth with the steepest gradient off-shore of the adjacent slope. The strength of this off-shore gradient probably depends on the location of the ring with respect to the canyon and the size of the ring.
5. Increased suspended sediment concentrations of order 0.5 to 1.0 mg/l occur along the bottom in a layer 50-200 m thick along the canyon axis at least between water depths of about 300 and 600 m. The near-bottom sediment concentrations are larger in the canyon than on the slope at comparable depths.

Currents

The current observations made in Lydonia Canyon and on the adjacent shelf and slope show a rich diversity in the strength, orientation, and frequency of current fluctuations. The basic statistics of the hour-averaged and low-passed currents are tabulated in table 2-8a and 2-8b , respectively. The statistics for the observations made in Oceanographer Canyon are in table 2-8c. The along-axis current speeds in the canyon are of order 10-20 cm/s, and thus water particle displacements are 2-4 km in 6 hours. Because the displacements are a substantial fraction of the canyon length, one immediate conclusion from the basic statistics is that the flow field will be strongly channeled by the canyon geometry.

Spectra

Kinetic energy spectra show major differences in the current strength and frequency structure on the shelf, slope, and in the canyon (fig. 2-18). On the shelf and slope, the flow is characterized by low-frequency fluctuations (periods longer than 50 hours) essentially parallel to the local isobaths, and by higher frequency fluctuations at the diurnal, inertial, and semidiurnal periods, primarily in the cross-isobath direction. The semidiurnal peak dominates the spectrum. In contrast in the canyon, the energy at low frequencies is much weaker than on the shelf and slope, with no increase in the synoptic band, and there is a large concentration of energy over a wide range of periods shorter than M_2. This band of high-frequency energy is often centered at M_4 (6.21 hours), the semidiurnal harmonic.

To investigate the spatial variability of the amplitude and principal orientation of the current fluctuations as a function of frequency, the spectrum was divided into 5 frequency bands: low frequency (periods of 720 to

Table 2-8a. Statistics of hour-averaged current observations made in D1 through D5 of the Lydonia Canyon moored array. Coordinate system gives the positive along-axis and cross-axis direction.

	Water Depth	Inst Depth	Dep #	Moor Id	Start YrMoDy	Stop YrMoDy	# day	Coord System	ALONG AXIS cm/sec Mean	S.D.	Min	Max	CROSS AXIS cm/sec Mean	S.D.	Min	Max	SPEED cm/sec Mean	S.D.	Min	Max	TEMPERATURE degrees C Mean	S.D.	Min	Max
A	100	80	1	2071	801130	810424	144	75/345	-8.26	19.28	-65.71	44.59	-0.20	26.09	-59.26	52.11	31.70	10.75	0.72	69.48	7.30	1.95	4.19	12.76
	100	80	2	2251	810504	810926	144		-9.77	19.97	-74.52	42.18	-0.00	27.15	-62.53	55.45	33.35	10.91	1.53	77.87	8.21	1.57	5.68	16.02
	100	99	1	204A	801024	801212	48	75/345	-0.50	8.97	-56.84	18.13	-2.31	14.93	-45.99	34.31	15.69	7.92	0.18	62.41	12.31	0.71	10.13	13.65
	100	99	1	204B	810216	810424	66		-4.15	10.79	-47.62	17.82	-2.57	14.41	-43.90	34.63	16.67	8.35	0.98	53.32	7.40	1.73	4.66	11.56
	100	100	2	2231	810505	810926	144		-0.31	7.93	-37.85	18.84	-1.85	13.95	-43.35	32.24	14.70	6.68	0.13	44.39	9.15	1.39	5.93	14.35
	100	100	3	2291	810926	811014	17		-1.38	8.52	-23.81	23.04	-5.62	14.69	-40.74	29.18	15.19	9.53	0.06	41.38	9.20	1.15	4.19	15.46
	104	103	5	2571	820708	820812	34		-1.50	7.69	-27.33	18.41	-2.77	13.20	-41.59	29.93	13.81	7.23	0.09	42.48	11.81	0.80	9.13	13.39
B	282	92	1	2081	801128	810428	150	75/345	-7.72	17.26	-58.69	44.14	2.30	20.65	-45.22	52.55	26.19	10.14	1.32	64.60	8.20	2.20	4.36	14.45
	288	108	2	2261	810429	810926	150		-4.28	16.93	-51.77	38.60	1.27	21.86	-47.07	51.40	26.29	9.63	0.32	53.96	9.57	1.78	5.72	15.84
	295	125	3	2301	810927	820130	124		-2.43	15.77	-61.87	44.40	2.64	20.09	-50.31	49.64	23.49	10.65	0.12	62.43	9.59	0.91	6.11	16.40
	300	108	4	2411	820131	820707	156		-4.31	16.85	-57.70	41.68	1.99	21.21	-49.63	52.23	25.64	9.92	0.22	58.09	10.56	2.00	4.10	14.55
	295	104	5	2581	820708	821111	125		-5.72	16.58	-58.71	37.42	2.42	20.96	-49.12	54.66	25.49	10.15	1.98	59.57	11.60	1.36	7.65	15.85
	282	227	1	2082	801128	810428	150	326/56	2.07	11.24	-27.42	48.23	0.09	4.14	-27.87	15.71	10.37	6.34	0.22	50.12	9.66	1.33	5.95	12.90
	288	238	2	2262	810429	810718	79		0.68	9.43	-28.47	34.28	-0.48	3.31	-13.31	10.94	8.61	5.14	0.16	34.63	9.02	0.79	6.51	11.53
	295	245	3	2302	810927	820130	124		0.61	12.47	-43.69	61.09	-0.13	3.68	-14.07	13.81	10.59	7.57	0.09	61.12	8.05	0.88	5.46	10.29
	300	248	4	2412	820131	820707	156		-0.55	11.80	-40.67	54.12	-0.54	3.43	-15.06	15.27	10.27	6.80	0.15	54.20	9.22	1.17	6.12	12.80
	295	244	5	2582	820708	821111	125		0.63	9.99	-37.62	41.92	-0.78	3.66	-14.79	14.95	9.13	5.54	0.19	42.10	9.25	0.91	6.70	11.52
	282	277	1	2083	801128	810428	150	315/45	-2.91	13.67	-48.05	46.90	-2.02	6.00	-26.05	18.99	12.39	9.05	0.02	48.63	8.54	1.18	5.50	12.17
	288	282	2	2263	810429	810926	150		-5.44	13.94	-46.13	58.44	1.46	5.57	-17.33	30.40	13.10	9.23	0.12	59.32	8.18	0.82	5.84	11.35
	290	285	3	2311	810927	820128	122		-3.22	14.65	-63.30	49.16	-1.15	5.66	-30.38	22.59	12.63	9.94	0.16	63.31	7.14	0.75	5.28	9.31
	300	294	4	2413	820131	820707	156		-4.50	15.41	-58.69	56.82	1.20	6.00	-20.77	31.20	13.15	11.06	0.13	64.93	8.23	1.10	5.75	11.39
	295	290	5	2583	820708	821111	125		-5.02	15.17	-57.86	45.12	1.43	5.37	-15.99	30.97	13.56	10.11	0.28	59.94	8.36	0.92	6.15	11.28
C	184	134	1	2091	801024	810325	151	75/345	-3.92	11.43	-54.70	35.35	-2.17	15.01	-48.95	33.73	17.15	9.03	0.15	61.84	11.43	1.27	7.09	14.09
D	193	143	1	2101	801027	810310	133	75/345	-2.45	11.28	-48.86	23.70	3.03	19.11	-43.80	48.45	20.23	9.92	0.75	54.15	11.84	1.00	7.29	14.24
E	600	116	1	2111	801201	810501	150	75/345	3.35	15.29	-41.49	54.10	0.06	16.81	-52.95	55.12	20.54	10.29	0.33	59.71	11.29	2.29	5.17	16.58
	600	216	1	2112	801201	810501	150	75/345	-1.51	8.39	-40.95	22.52	3.53	11.12	-45.21	48.03	12.74	6.81	0.13	49.20	10.34	1.33	7.27	13.57
	580	475	2	2281	810505	810926	144	20/110	-1.25	16.77	-49.07	43.52	1.02	3.93	-13.02	15.64	14.46	9.50	0.23	50.78	5.61	0.39	4.60	7.36
	590	493	3	2321	810928	820130	123		-2.29	19.55	-69.26	49.07	-0.56	3.56	-14.39	12.56	16.27	11.65	0.26	69.29	5.33	0.35	4.63	6.73
	600	595	1	2114	801201	810501	150	20/110	0.02	16.56	-47.33	47.82	1.42	5.17	-23.13	18.81	15.09	8.69	0.10	49.03	5.08	0.34	4.33	7.06
	590	584	3	2322	810928	820130	123		1.14	18.35	-60.75	53.45	0.52	5.84	-17.95	22.24	16.14	10.57	0.08	60.81	5.05	0.24	4.55	6.49

Table 2-8a (continued)

	Water Depth	Inst Depth	Dep #	Moor Id	Start YrMoDy	Stop YrMoDy	# day	Coord System	ALONG AXIS cm/sec Mean	S.D.	Min	Max	CROSS AXIS cm/sec Mean	S.D.	Min	Max	SPEED cm/sec Mean	S.D.	Min	Max	TEMPERATURE degrees C Mean	S.D.	Min	Max
F	505	205	1	2121	801027	810416	170	75/145	14.86	24.91	-67.90	79.77	1.66	9.97	-29.02	35.79	26.75	15.09	0.43	79.94	11.70	1.49	7.43	15.89
	505	405	1	2122	801027	810427	181	49/139	-2.12	7.71	-28.80	25.30	0.01	3.27	-12.84	12.41	7.45	4.38	0.08	29.09	6.37	0.60	4.84	9.40
G	495	195	1	2131	801027	810427	181	75/345	3.42	15.32	-46.66	62.46	0.42	7.92	-28.19	26.25	14.70	9.66	0.26	64.08	10.02	1.39	6.57	14.93
	495	395	1	2132	801027	810427	181	49/139	-0.47	5.44	-24.70	19.68	-0.67	3.24	-16.78	9.66	5.55	3.16	0.11	25.12	6.03	0.48	4.86	8.31
H	1,554	290	1	2141	801201	810427	146	75/345	11.98	23.01	-42.64	68.52	2.16	9.32	-33.98	33.94	23.54	14.49	0.44	68.80	9.18	1.26	6.22	12.23
	1,554	540	1	2142	801201	810427	146	75/345	-2.31	9.15	-32.60	29.75	0.75	5.26	-16.70	17.38	9.54	5.12	0.68	32.68	5.21	0.28	4.53	6.34
	1,554	890	1	2143	801201	810427	146	0/90	0.16	4.50	-16.12	16.76	-0.31	3.61	-16.07	10.73	5.15	2.63	0.11	18.34	4.42	0.13	4.01	4.73
	1,380	1,375	1	2211	810120	810428	97	0/90	0.23	6.94	-22.29	22.04	-2.84	3.47	-16.01	11.34	7.41	3.65	0.05	22.35	3.99	0.11	3.62	4.24
	1,554	1,454	1	2144	801201	810427	146	0/90	-0.05	6.37	-26.40	22.02	0.74	2.55	-10.06	9.69	5.76	3.81	0.12	26.53	3.99	0.12	3.60	4.25
I	250	10	1	2151	801127	810430	154	75/345	-8.11	24.18	-70.67	68.01	-3.87	17.56	-64.06	55.80	27.72	14.33	0.65	78.74	8.02	2.48	3.82	17.69
	250	55	1	2152	801202	810429	148	75/345	7.78	25.59	-62.47	80.04	0.45	12.10	-44.67	45.22	25.14	15.15	0.44	80.04	10.29	3.41	4.39	17.35
	250	59	2	2271	810503	810927	146		0.82	22.78	-59.36	113.81	1.30	13.65	-45.63	42.13	22.85	13.61	0.25	114.18	12.14	3.49	5.70	22.15
	251	55	3	2331	810927	820131	125		-9.50	16.86	-69.47	40.61	0.22	13.99	-59.52	40.25	21.08	11.23	0.50	69.49	11.12	3.54	5.48	19.63
	249	59	4	2421	820201	820708	157		0.16	20.75	-63.42	85.34	0.35	13.07	-44.48	58.42	21.68	11.48	0.34	85.38	12.07	2.97	4.49	18.60
	250	195	1	2153	801202	810429	148	75/345	12.24	26.60	-55.67	75.26	-0.41	9.46	-31.72	27.49	26.50	15.64	0.21	75.55	11.37	1.74	7.31	15.54
	250	199	2	2272	810503	810514	11		28.89	21.86	-20.59	80.54	-6.49	10.12	-32.31	18.06	32.83	19.47	2.68	81.69	10.61	1.06	7.78	15.58
	251	201	3	2332A	810927	811019	22		-8.52	8.52	-34.24	11.79	2.53	8.36	-20.05	18.98	13.46	6.33	0.80	35.56	8.81	0.92	5.67	10.75
	251	201	3	2332B	810927	811029	32		-5.15	10.27	-34.02	23.45	2.14	9.02	-22.09	24.19	13.38	6.23	0.19	35.81				
	249	199	4	2422	820201	820708	157		3.15	17.15	-39.16	81.38	-0.22	8.97	-32.45	26.21	16.46	10.64	0.47	81.44	11.33	0.95	8.54	14.31
	250	245	1	2154	801202	810429	148	75/345	6.83	15.26	-40.52	43.61	-5.08	9.81	-42.72	21.19	17.83	9.15	0.28	44.84	9.59	1.47	6.11	14.19
	250	245	2	2273	810503	810927	146		4.57	14.45	-30.04	52.26	-2.77	8.86	-39.02	21.30	15.53	8.64	0.26	54.00	9.23	1.09	6.48	12.99
	247	242	3	2341	810927	820131	125		0.39	10.87	-37.83	33.50	-3.89	9.93	-47.96	26.17	13.17	7.64	0.12	50.02	8.31	1.09	5.29	10.98
	249	243	4	2423	820201	820708	157		3.75	13.96	-38.36	58.88	-5.33	11.95	-66.22	22.80	16.29	10.70	0.06	68.72	10.10	1.16	6.65	13.25
J	571	83	1	2161	801127	810402	125	75/345	18.20	30.82	-61.30	98.66	-0.33	11.04	-35.59	42.46	32.20	19.13	0.26	98.67	12.69	2.93	4.61	17.98
	571	223	1	2162	801127	810429	152		18.06	28.05	-58.74	77.08	0.51	9.06	-35.64	30.70	29.87	17.40	0.34	77.20	10.90	1.39	7.18	14.20
	571	471	1	2163	801127	810429	152		-0.30	6.78	-33.65	18.33	0.44	4.78	-17.90	17.40	7.10	4.32	0.16	34.72	5.57	0.41	4.60	7.44

Table 2-8a (continued)

	Water Depth	Inst Depth	Dep #	Moor Id	Start YrMoDy	Stop YrMoDy	# day	Coord System	ALONG AXIS cm/sec Mean	S.D.	Min	Max	CROSS AXIS cm/sec Mean	S.D.	Min	Max	SPEED cm/sec Mean	S.D.	Min	Max	TEMPERATURE degrees C Mean	S.D.	Min	Max
K	554	204	1	2171	801128	810427	150	75/345	11.18	22.69	-49.52	71.88	1.08	9.34	-43.82	47.90	23.43	13.39	0.46	72.14	11.31	1.35	7.61	15.06
	554	454	1	2172	801128	810427	150		-1.40	12.95	-38.31	40.18	-1.21	6.38	-27.59	21.37	12.79	6.95	0.23	40.76	5.82	0.47	4.68	7.73
L	125	65	1	2182	801130	810425	145	84/354	-10.79	18.47	-79.42	50.81	-0.05	18.99	-48.74	57.78	26.06	11.77	1.65	80.89	7.59	2.02	4.37	13.83
	125	105	1	2183	801130	810425	145		-3.68	19.01	-59.73	56.08	-0.43	18.81	-48.01	47.17	24.88	10.49	0.38	61.66	9.51	2.12	4.65	13.93
	127	127	4	2511	820131	820426	84		-0.63	9.51	-35.75	29.57	-1.92	10.64	-46.73	23.54	12.59	7.02	0.01	46.77	11.12	1.48	4.40	13.64
M	123	103	1	2191	801128	810427	150	81/351	-4.37	18.75	-58.97	60.84	-2.58	20.89	-74.07	42.69	25.94	11.86	0.04	74.48	9.67	3.01	4.82	24.38
	120	119	1	2031	801024	810426	183		1.33	12.44	-47.57	42.62	-3.95	14.78	-50.85	39.11	17.27	9.61	0.01	61.66	10.46	2.23	5.00	14.57
N	1,041	243	1	2201	801129	810427	148	75/345	10.62	20.96	-43.94	76.29	2.17	9.27	-30.42	30.28	21.27	13.80	0.42	78.19	10.26	1.54	6.84	14.72
	1,041	841	1	2202	801129	810427	148	49/139	-0.88	8.08	-29.93	25.28	-1.07	3.49	-13.45	11.34	7.70	4.48	0.22	30.09	4.59	0.19	4.15	5.31
P	132	113	3	2361	810928	820128	122	75/345	-2.63	18.76	-65.13	39.28	0.48	19.71	-52.97	47.63	25.08	10.89	0.38	70.71	9.52	0.92	6.41	14.47
	131	131	3	2371	810926	820128	124		-2.34	8.72	-36.63	20.65	-1.34	8.71	-32.94	26.30	11.18	5.84	0.24	37.74	9.22	0.69	5.96	11.45
Q	185	180	4	2431	820130	820707	157	75/345	-10.12	15.13	-73.20	20.49	2.61	8.35	-26.08	36.23	15.26	13.23	0.11	73.86	10.95	0.93	7.40	13.45
R	240	183	4	2441	820130	820707	157	10/100	4.89	15.04	-41.00	54.53	-1.43	8.07	-28.37	27.07	15.55	8.69	0.09	55.01	11.19	0.94	8.17	13.48
	240	215	4	2442	820130	820707	157		3.42	11.95	-35.71	36.45	-3.43	4.52	-27.18	11.61	11.91	6.68	0.28	42.07	10.57	1.04	7.28	13.52
S	560	554	4	2451	820129	820707	158	355/85	6.52	19.03	-55.02	66.13	-0.61	6.71	-32.41	36.28	16.79	12.96	0.12	66.38	5.37	0.33	4.72	6.56
T	203	178	4	2461	820129	820707	158	0/90	-2.49	16.48	-52.85	38.88	1.86	5.37	-17.07	40.85	14.82	9.53	0.16	65.45	10.60	0.86	7.35	12.89
U	141	134	5	2591	820708	821111	125	75/345	-3.12	5.39	-24.23	21.79	-2.71	14.68	-60.46	37.65	13.13	9.44	0.37	64.27	11.27	0.71	7.95	13.25

Table 2-8b. Statistics of lowpassed current observations made in D1 through D5 of the Lydonia Canyon moored array. Coordinate system gives the positive along-axis and cross-axis direction.

	Water Depth	Inst Depth	Dep #	Moor Id	Start YrMoDy	Stop YrMoDy	# day	Coord System	ALONG AXIS cm/sec Mean	S.D.	Min	Max	CROSS AXIS cm/sec Mean	S.D.	Min	Max	SPEED cm/sec Mean	S.D.	Min	Max	TEMPERATURE degrees C Mean	S.D.	Min	Max
A	100	80	1	2071	801202	810423	141	75/345	-8.36	9.56	-50.94	17.10	-0.13	3.64	-13.04	10.43	10.89	7.48	0.19	51.08	7.28	1.82	4.31	11.64
	100	80	2	2251	810506	810925	141		-9.70	6.99	-38.41	9.96	0.06	3.63	-12.91	10.72	10.91	6.08	0.12	39.54	8.23	1.48	5.73	14.46
	100	99	1	204A	801026	801211	46	75/345	-0.39	5.07	-22.91	9.07	-2.21	3.65	-10.83	10.58	5.40	3.87	0.14	23.73	12.34	0.67	10.71	13.27
	100	99	1	204B	810217	810422	64		-4.34	6.74	-36.17	6.50	-2.56	4.03	-16.55	7.40	6.95	6.22	0.09	37.89	7.42	1.65	4.89	11.00
	100	100	2	2231	810506	810925	141		-0.24	3.66	-15.60	8.18	-1.77	2.16	-10.22	4.37	3.87	2.49	0.03	15.98	9.17	1.22	6.06	14.03
	100	100	3	2291	810927	811012	15		-1.10	1.73	-6.32	1.11	-6.10	4.42	-15.13	1.01	6.54	4.26	0.54	15.14	9.25	1.03	5.71	12.39
	104	103	5	2571	820709	820810	32		-1.67	2.81	-9.66	3.64	-2.69	2.17	-10.00	2.78	4.30	2.03	0.20	10.54	11.80	0.57	10.85	13.13
B	282	92	1	2081	801130	810426	147	75/345	-7.68	8.62	-40.53	24.02	2.35	3.95	-7.96	14.85	10.69	6.33	0.40	42.85	8.18	2.04	4.69	12.65
	288	108	2	2261	810430	810925	147		-4.10	6.78	-24.64	12.08	1.26	3.43	-9.16	11.03	7.66	4.19	0.12	24.81	9.60	1.56	6.45	15.17
	295	125	3	2301	810929	820128	121		-2.36	8.45	-30.86	18.70	2.63	4.14	-9.43	19.83	8.49	5.37	0.15	30.92	9.60	0.82	7.31	12.93
	300	108	4	2411	820202	820706	154		-4.28	7.85	-25.52	16.70	2.01	3.72	-13.07	14.16	8.72	4.66	0.26	26.77	10.54	1.80	3.94	13.15
	295	104	5	2581	820709	821109	123		-5.79	6.83	-29.95	15.76	2.44	3.32	-7.02	12.50	8.51	4.96	0.20	31.46	11.57	1.11	8.34	14.12
	282	227	1	2082	801130	810426	147	326/56	2.09	2.48	-5.06	12.06	-0.09	1.19	-4.81	3.83	2.93	1.84	0.03	12.30	9.67	1.14	7.32	12.34
	288	238	2	2262	810430	810717	77		0.70	1.26	-3.06	4.88	-0.49	0.88	-2.83	1.98	1.56	0.82	0.04	4.89	9.04	0.55	7.74	10.77
	295	245	3	2302	810929	820128	121		0.63	1.89	-5.20	6.17	-0.11	1.12	-3.63	3.47	1.97	1.16	0.03	6.32	8.05	0.68	6.15	9.43
	300	248	4	2412	820202	820706	154		-0.56	2.07	-11.76	8.92	-0.56	1.11	-3.88	3.84	2.07	1.37	0.05	12.38	9.24	0.76	7.41	11.15
	295	244	5	2582	820709	821109	123		0.65	1.40	-3.25	5.34	-0.80	1.00	-3.59	2.46	1.81	0.88	0.02	5.35	9.25	0.59	7.91	10.51
	282	277	1	2083	801130	810426	147	315/45	-2.95	3.35	-15.75	3.91	-2.03	1.44	-7.70	2.72	4.33	2.70	0.18	16.18	8.55	0.84	6.46	10.99
	288	282	2	2263	810430	810925	147		-5.42	3.02	-13.69	0.30	1.44	2.42	-3.86	9.88	5.95	3.31	0.21	15.43	8.20	0.54	6.51	9.60
	290	285	3	2311	810929	820127	120		-3.22	3.06	-15.40	5.77	-1.14	1.78	-5.18	6.04	4.27	2.43	0.08	16.30	7.14	0.60	5.48	8.45
	300	294	4	2413	820202	820706	154		-4.53	4.05	-17.54	3.38	1.21	2.47	-4.35	10.43	5.31	4.04	0.03	19.36	8.25	0.77	6.38	10.47
	295	290	5	2583	820709	821109	123		-5.07	2.99	-15.61	1.86	1.48	2.31	-3.53	10.03	5.65	3.19	0.17	16.54	8.36	0.64	7.01	10.01
C	184	134	1	2091	801026	810324	149	75/345	-3.81	6.19	-24.74	12.46	-2.16	3.60	-12.22	7.49	7.13	4.41	0.05	26.43	11.45	1.15	7.93	13.41
D	193	143	1	2101	801029	810308	130	75/345	-2.32	4.80	-21.43	8.65	3.01	3.81	-9.84	19.25	6.13	3.80	0.27	24.72	11.86	0.84	8.33	13.56
E	600	116	1	2111	801203	810429	147	75/345	3.27	10.56	-22.34	33.02	0.04	4.39	-13.45	16.48	9.77	6.78	0.09	33.49	11.29	2.25	6.28	15.64
	600	216	1	2112	801203	810429	147	75/345	-1.50	3.33	-11.99	8.59	3.46	5.67	-18.89	33.84	6.31	4.20	0.07	33.94	10.34	1.24	7.91	12.82
	580	475	2	2281	810506	810925	141	20/110	-1.21	2.50	-10.37	6.43	1.01	0.75	-1.25	3.04	2.56	1.65	0.03	10.55	5.61	0.34	4.88	6.88
	590	493	3	2321	810929	820128	121		-2.27	4.04	-17.56	15.95	-0.56	0.90	-4.69	1.57	3.69	2.99	0.03	17.70	5.33	0.30	4.71	6.37
	600	595	1	2114	801203	810429	147	20/110	0.03	3.42	-15.64	8.18	1.42	1.50	-4.44	6.25	3.49	1.94	0.09	15.82	5.08	0.28	4.52	5.75
	590	584	3	2322	810929	820128	121		1.12	3.36	-12.07	10.66	0.51	1.16	-2.60	4.00	3.18	2.02	0.04	12.33	5.05	0.19	4.68	5.76

Table 2-8b (continued)

	Water Depth	Inst Depth	Dep #	Moor Id	Start YrMoDy	Stop YrMoDy	# day	Coord System	ALONG AXIS cm/sec Mean	S.D.	Min	Max	CROSS AXIS cm/sec Mean	S.D.	Min	Max	SPEED cm/sec Mean	S.D.	Min	Max	TEMPERATURE degrees C Mean	S.D.	Min	Max
F	505	205	1	2121	801029	810414	167	75/145	14.91	23.85	-49.13	59.30	1.67	4.03	-10.21	13.08	24.08	15.17	0.33	59.39	11.70	1.43	8.23	15.28
	505	405	1	2122	801029	810425	178	49/139	-2.12	2.65	-9.28	3.93	0.01	1.07	-3.08	3.32	2.96	1.98	0.04	9.30	6.38	0.53	5.22	8.33
G	495	195	1	2131	801028	810425	178	75/345	3.42	12.85	-32.63	43.67	0.45	3.00	-14.79	12.63	10.77	8.37	0.06	45.25	10.04	1.27	7.23	13.77
	495	395	1	2132	801028	810425	178	49/139	-0.48	1.84	-5.78	7.08	-0.67	0.82	-4.42	2.07	1.87	1.11	0.03	7.47	6.03	0.44	4.98	7.48
H	1,554	290	1	2141	801202	810425	144	75/345	12.04	22.48	-27.65	59.22	2.11	4.29	-19.42	21.78	20.99	15.23	0.35	59.38	9.18	1.20	6.45	11.91
	1,554	540	1	2142	801202	810425	144	75/345	-2.34	8.53	-25.85	19.76	0.74	2.27	-5.94	8.23	7.86	4.71	0.02	25.85	5.21	0.26	4.67	6.05
	1,554	890	1	2143	801202	810425	144	0/90	0.15	2.04	-7.45	5.55	-0.33	2.70	-12.66	6.40	2.85	1.86	0.03	12.67	4.42	0.13	4.16	4.67
	1,380	1,375	1	2211	810122	810427	95	0/90	0.20	2.57	-8.56	6.41	-2.86	1.05	-6.31	0.07	3.78	1.30	0.43	8.72	3.99	0.10	3.65	4.17
	1,554	1,454	1	2144	801202	810425	144	0/90	-0.07	2.98	-12.06	14.29	0.74	1.08	-5.51	5.88	2.71	1.81	0.07	14.35	3.99	0.12	3.65	4.22
I	250	10	1	2151	801129	810429	151	75/345	-8.35	19.34	-50.22	51.45	-3.86	9.89	-36.70	36.27	20.59	11.51	0.32	52.71	7.97	2.35	3.73	14.34
	250	55	1	2152	801203	810428	145	75/345	7.59	23.62	-40.16	58.65	0.40	5.92	-25.71	22.25	21.15	14.26	0.48	58.76	10.24	3.30	4.64	17.37
	250	59	2	2271	810504	810925	144		0.89	19.98	-46.96	79.68	1.39	6.46	-15.30	23.61	16.93	12.54	0.06	79.70	12.21	3.37	6.39	19.21
	251	55	3	2331	810928	820129	123		-9.71	12.55	-44.70	13.49	0.05	7.40	-17.91	23.77	14.58	9.68	0.31	44.93	11.19	3.43	5.72	19.38
	249	59	4	2421	820202	820707	155		-0.08	17.58	-31.98	47.83	0.17	6.35	-23.15	18.20	16.60	8.59	0.90	48.28	12.05	2.80	4.55	17.51
	250	195	1	2153	801203	810428	145	75/345	12.04	24.75	-43.65	57.64	-0.42	2.74	-9.20	7.22	23.46	14.65	0.36	57.68	11.36	1.69	7.61	15.04
	250	199	2	2272	810504	810513	8		30.86	12.84	3.77	57.32	-6.72	3.33	-10.64	-0.31	31.62	13.17	4.01	58.30	10.64	0.95	8.19	14.11
	251	201	3	2332A	810928	811018	19		-8.13	5.48	-22.96	1.27	2.50	2.08	-4.23	6.43	9.01	5.04	0.18	23.02	8.83	0.83	6.75	10.31
	251	201	3	2332B	810928	811028	29		-4.91	7.30	-22.90	13.68	2.35	2.23	-3.72	6.96	8.10	4.72	0.06	23.07				
	249	199	4	2422	820202	820707	155		2.95	14.96	-29.94	57.31	-0.26	2.63	-10.69	6.71	11.84	9.97	0.07	57.44	11.33	0.81	9.46	13.68
	250	245	1	2154	801203	810428	145	75/345	6.61	14.17	-29.31	36.51	-5.06	2.89	-15.92	0.61	14.45	8.33	0.16	36.63	9.59	1.25	7.14	11.90
	250	245	2	2273	810504	810925	144		4.65	13.64	-20.80	37.35	-2.81	2.53	-15.25	6.69	12.26	8.46	0.16	37.37	9.26	0.93	7.03	12.70
	247	242	3	2341	810928	820129	123		0.66	9.05	-30.61	25.82	-3.93	3.23	-15.18	1.51	8.80	5.55	0.05	30.92	8.31	0.94	6.03	10.17
	249	243	4	2423	820202	820707	155		3.57	11.93	-27.57	40.85	-5.29	4.68	-23.58	1.25	11.63	8.35	0.15	41.32	10.11	0.93	7.74	12.51
J	571	83	1	2161	801129	810401	123	75/345	18.27	30.07	-40.83	74.15	0.30	5.97	-15.22	18.63	30.43	18.64	0.57	74.62	12.66	2.90	4.90	18.03
	571	223	1	2162	801129	810428	149		17.94	27.57	-46.96	71.62	0.46	3.76	-18.21	11.05	27.47	18.48	0.02	71.62	10.89	1.28	7.52	13.25
	571	471	1	2163	801129	810428	149		-0.39	5.90	-28.39	12.49	0.44	1.45	-3.63	5.75	4.73	3.86	0.03	28.54	5.57	0.37	4.82	6.67

Table 2-8b (continued)

	Water Depth	Inst Depth	Dep #	Moor Id	Start YrMoDy	Stop YrMoDy	# day	Coord System	ALONG AXIS cm/sec Mean	S.D.	Min	Max	CROSS AXIS cm/sec Mean	S.D.	Min	Max	SPEED cm/sec Mean	S.D.	Min	Max	TEMPERATURE degrees C Mean	S.D.	Min	Max
K	554	204	1	2171	801129	810426	148	75/345	11.32	22.10	-39.20	55.95	1.03	5.42	-19.62	28.49	21.83	13.05	0.39	56.00	11.32	1.29	7.93	14.22
	554	454	1	2172	801129	810426	148		-1.36	12.07	-31.37	27.97	-1.25	2.00	-8.06	3.94	10.40	6.71	0.14	32.18	5.82	0.41	4.96	7.19
L	125	65	1	2182	801201	810423	143	84/354	-10.79	10.61	-47.33	24.06	-0.07	3.90	-11.12	11.09	13.43	7.99	0.60	47.42	7.57	1.88	4.38	11.83
	125	105	1	2183	801201	810423	143		-3.65	9.93	-35.59	26.88	-0.40	4.05	-14.88	11.82	9.59	6.05	0.20	35.61	9.50	2.01	5.23	13.14
	127	127	4	2511	820201	820424	82		-0.45	6.14	-21.28	14.81	-2.00	3.50	-11.90	7.74	6.33	3.74	0.06	22.04	11.10	1.43	4.78	13.42
M	123	103	1	2191	801129	810426	147	81/351	-4.45	10.25	-45.92	23.64	-2.63	4.17	-16.26	8.55	9.87	7.20	0.03	47.48	9.46	2.52	5.21	21.01
	120	119	1	2031	801026	810424	180		1.25	7.49	-31.73	20.72	-3.96	3.97	-19.15	6.72	7.95	5.09	0.04	31.80	10.46	2.18	5.42	14.02
N	1,041	243	1	2201	801201	810425	145	75/345	10.35	19.28	-30.06	58.94	2.11	4.29	-12.74	20.14	17.77	13.64	0.05	60.11	10.27	1.42	7.16	13.74
	1,041	841	1	2202	801201	810425	145	49/139	-0.92	2.46	-8.64	6.15	-1.09	0.92	-3.49	1.59	2.53	1.58	0.04	8.87	4.60	0.17	4.26	5.03
P	132	113	3	2361	810930	820127	119	75/345	-2.66	10.07	-37.29	18.21	0.58	4.51	-11.43	18.03	9.52	6.21	0.06	38.81	9.54	0.80	7.13	11.86
	131	131	3	2371	810928	820127	121		-2.30	3.21	-15.60	6.32	-1.30	2.45	-8.52	5.60	4.20	2.36	0.11	16.33	9.24	0.60	7.26	10.86
Q	185	180	4	2431	820201	820706	154	75/345	-10.17	4.60	-20.51	5.87	2.61	3.42	-5.43	14.78	11.21	4.18	0.12	20.63	10.95	0.80	8.90	12.80
R	240	183	4	2441	820201	820706	154	10/100	4.93	6.26	-10.28	27.63	-1.39	2.45	-8.09	7.42	6.79	5.03	0.04	27.70	11.19	0.82	9.66	13.10
	240	215	4	2442	820201	820706	154		3.43	4.51	-12.55	20.78	-3.46	1.62	-8.95	1.65	6.00	3.27	0.06	21.03	10.58	0.85	8.91	12.74
S	560	554	4	2451	820131	820706	156	355/85	6.51	4.18	-6.59	18.55	-0.62	1.63	-5.39	6.09	7.05	3.63	0.07	18.56	5.37	0.24	4.82	6.29
T	203	178	4	2461	820131	820706	156	0/90	-2.53	4.43	-15.92	10.32	1.90	2.53	-3.32	15.45	5.16	3.06	0.03	15.93	10.61	0.77	9.12	12.63
U	141	134	5	2591	820710	821109	122	75/345	-3.15	2.30	-10.38	2.88	-2.67	4.17	-17.99	5.17	5.36	3.32	0.06	18.07	11.25	0.54	9.07	12.74

TABLE 2-8C. Statistics of hour-averaged and lowpassed current observations made in Oceanographer Canyon. Coordinate system gives the positive along-axis and cross-axis direction.

	Water Depth	Inst Depth	Dep #	Moor Id	Start YrMoDy	Stop YrMoDy	# day	Coord System	ALONG AXIS cm/sec Mean	S.D.	Min	Max	CROSS AXIS cm/sec Mean	S.D.	Min	Max	SPEED cm/sec Mean	S.D.	Min	Max	TEMPERATURE degrees C Mean	S.D.	Min	Max
A	104	104	1	2481	820127	820319	51	70/340	-3.56	7.50	-34.12	21.00	1.66	13.00	-35.56	32.20	13.63	7.41	0.12	39.65	7.78	1.95	3.94	11.86
B	227	223	1	2492	820128	820709	161	92/2	6.34	20.94	-53.71	64.00	-1.28	5.81	-34.86	20.18	19.09	12.24	0.17	64.58	9.08	1.23	5.89	12.22
C	560	554	1	2501	820127	820709	162	5/95	-4.05	30.28	-90.89	57.85	-2.75	7.41	-31.85	24.80	27.23	15.95	0.19	92.21	5.32	0.48	4.49	7.57
Lowpassed data																								
A	104	104	1	2481	820129	820318	48	70/340	-3.49	4.56	-16.56	7.56	1.79	4.09	-11.35	10.56	6.50	3.27	0.14	19.29	7.73	1.79	4.10	11.11
B	227	223	1	2492	820129	820707	159	92/2	6.26	3.51	-2.28	17.88	-1.29	1.86	-6.89	4.13	6.84	3.15	0.10	17.92	9.08	0.73	7.01	10.73
C	560	554	1	2501	820129	820707	159	5/95	-4.13	6.83	-26.83	12.11	-2.78	2.59	-11.15	3.68	7.17	5.17	0.11	27.08	5.32	0.23	4.78	6.39

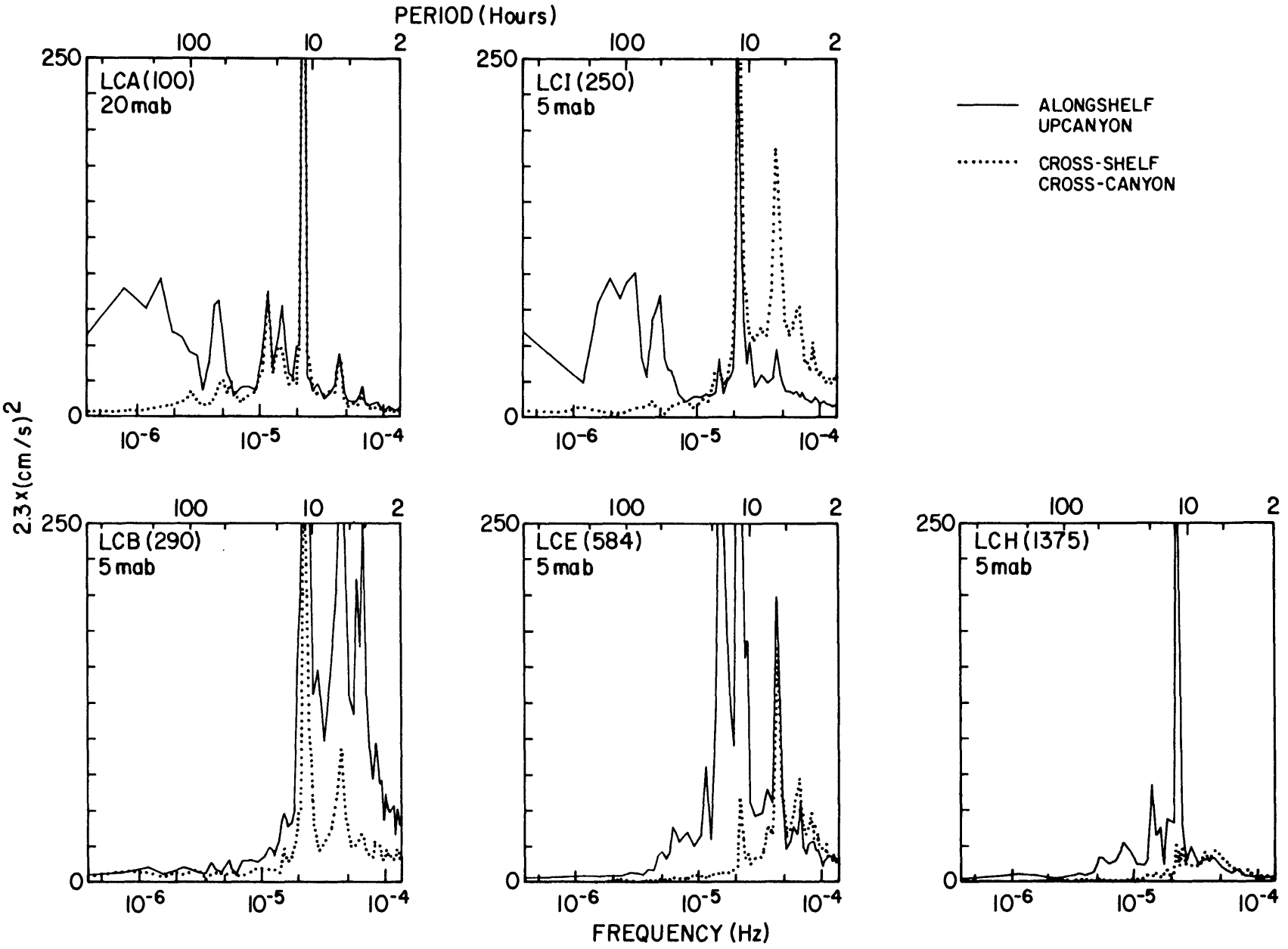

Figure 2-18. Variance conserving spectra of currents at LCA, LCI, LCB, LCE and LCH on the shelf, slope and in Lydonia Canyon (see text for description).

60 hours), diurnal (periods of 26.7 to 22.5), inertial (21.8 to 13.3 hours), semidiurnal (13.1 to 11.6 hours), and high frequency (11.4 to 2.0 hours). The total energy and the ellipse parameters (major and minor axis, orientation, and stability) were computed for each current record in each of these five frequency bands (table 2-9).

The current ellipses at LCB show the dramatic effect of the canyon on the orientation and amplitude of the currents (fig. 2-19). Above the canyon rim, only the low-frequency and semidiurnal fluctuations have a stable orientation; the low-frequency fluctuations are strongly polarized and oriented alongshelf, while the semidiurnal fluctuations are oriented across-shelf, consistent with the large-scale regional tidal flow. Below the canyon rim, the current ellipses in all frequency bands are stable, aligned with the orientation of the canyon axis, and within a few degrees of each other. At LCB(227) and LCB(277), the largest fluctuations are in the high-frequency band and they are strongest near the bottom.

On the outer slope at LCI, the currents are dominated by large amplitude fluctuations at low-frequencies oriented parallel to the isobaths which decrease with depth (fig. 2-19). The inertial and semidiurnal fluctuations are moderate, but the orientation is not very stable except near the bottom for fluctuations that have periods in the semidiurnal band. The fluctuations at high frequencies are most stable and largest near the bottom, where they are oriented across isobaths (see chapter 7 for more discussion of the high-frequency currents on the slope).

Along the canyon axis, the near-bottom currents have the same characteristics as observed at LCB (fig.2-20). The fluctuations in all bands are aligned approximately parallel to the canyon axis, and the orientation of the current ellipses are typically quite stable. A local maximum in the

Table 2-9a. Total energy T (in cm^2/sec^2), major and minor axis of ellipse (in cm/s), ratio of major to minor axis (R), ellipse orientation Θ (measured clockwise from the up-canyon or cross-slope direction, see table 2-8), and ellipse stability S (underlined if significant) for observations made in the canyon experiment in five frequency bands; low frequency, periods from 720 to 60 hours; diurnal, periods from 26.7 to 22.5 hours; inertial, periods from 21.8 to 13.3 hours; semidiurnal, periods from 13.1 to 11.6 hours; and high-frequency, periods from 11.4 to 2.0 hours. A negative U minor indicates the current rotates counter-clockwise. Spectra computed for data pieces 720 hours long (DOF).

Sta	Depth	Record ID	DOF	Low Frequency					Diurnal					Inertial				
				T	U_{major}	U_{minor}	R	Θ(s)	T	U_{major}	U_{minor}	R	Θ(s)	T	U_{major}	U_{minor}	R	Θ(s)
LCA	80	2071	8	96.82	13.86	1.28	0.09	90(0.84)	11.44	4.05	2.55	0.63	89(0.13)	18.44	5.65	2.23	0.39	72(0.26)
	80	2251	8	66.69	11.50	1.03	0.09	102(0.74)	15.58	4.75	2.93	0.62	60(0.45)	21.41	6.06	2.46	0.41	47(0.20)
	100	2231	8	18.34	6.02	0.62	0.10	91(0.69)	3.48	2.44	1.01	0.41	154(0.17)	9.98	4.24	1.39	0.33	177(0.19)
LCB	92	2081	9	70.4	11.84	0.75	0.06	103(0.76)	10.01	3.98	2.04	0.51	132(0.25)	28.76	6.86	3.23	0.47	11(0.11)
	227	2082	9	5.6	3.35	-0.04	0.01	5(0.68)	1.41	1.68	0.06	0.04	15(0.55)	20.12	6.32	-0.49	0.08	9(0.84)
	277	2083	9	9.62	4.38	0.26	0.06	172(0.74)	2.38	2.18	0.02	0.01	3(0.74)	19.86	6.30	0.01	0.00	5(0.79)
LCC	134	2091	9	36.69	8.53	0.77	0.09	79(0.56)	5.57	3.21	0.92	0.29	2(0.06)	21.35	6.09	2.36	0.39	129(0.03)
LCD	143	2101	7	24.08	6.89	0.81	0.12	114(0.33)	4.76	2.92	0.98	0.34	162(0.18)	26.16	6.95	2.00	0.29	170(0.41)
LCE	116	2111	9	84.70	13.01	-0.29	0.02	86(0.61)	7.65	3.66	1.16	0.37	9(0.22)	38.40	7.90	3.81	0.48	17(0.42)
	216	2112	9	32.05	8.01	0.54	0.01	20(0.55)	2.89	2.41	0.03	0.01	19(0.66)	13.91	5.27	-0.13	0.02	21(0.54)
	595	2114	9	9.48	4.35	-0.27	0.06	0(0.64)	4.89	3.12	-0.09	0.03	2(0.84)	42.96	9.27	0.01	0.00	4(0.93)
	475	2281	8	4.73	3.08	0.05	0.02	170(0.90)	5.40	3.29	-0.02	0.01	172(0.97)	16.49	5.74	0.06	0.01	171(0.94)
	493	2321	7	11.47	4.78	0.25	0.05	2(0.91)	5.08	3.19	-0.01	0.00	1(0.96)	49.60	9.96	0.12	0.01	2(0.98)
	584	2322	7	6.99	3.74	-0.07	0.02	4(0.71)	5.16	3.21	0.07	0.02	2(0.84)	48.51	3.11	0.09	0.03	179(0.94)
LCF	205	2121	10	358.8	26.75	1.36	0.05	92(0.93)	3.34	2.53	0.50	0.20	76(0.32)	26.86	6.74	2.87	0.43	46(0.16)
	405	2122	11	6.56	3.62	-0.09	-0.02	178(0.74)	1.54	1.75	-0.12	-0.07	11(0.67)	6.69	3.66	0.13	0.04	5(0.67)
LCG	195	2131	11	122.8	15.63	1.05	0.07	83(0.92)	2.84	2.38	0.17	0.07	72(0.61)	18.92	6.05	1.10	0.18	71(0.40)
	395	2132	11	2.79	2.36	0.06	0.02	4(0.73)	1.02	1.42	0.16	0.11	177(0.66)	3.64	2.67	0.35	0.13	170(0.62)
LCH	290	2141	8	199.1	19.95	0.55	0.03	87(0.89)	2.88	2.33	0.58	0.75	153(0.23)	28.49	6.56	3.75	0.57	164(0.36)
	540	2142	8	71.3	11.94	-0.20	-0.02	89(0.90)	1.83	1.78	0.69	0.39	119(0.25)	11.20	4.32	1.94	0.45	168(0.22)
	890	2143	8	9.67	4.39	0.29	0.07	76(0.50)	0.76	1.22	0.24	0.20	177(0.38)	4.17	2.82	0.62	0.22	169(0.38)
	1375	2211		5.42	3.29	-0.23	-0.07	1(0.67)	1.23	1.56	0.15	0.09	177(0.69)	9.76	4.41	0.19	0.04	0(0.74)
LCI	10	2151	9	476.6	30.86	-0.75	-0.02	86(0.67)	31.89	7.32	3.20	0.44	90(0.18)	135.8	14.32	8.15	0.57	95(0.11)
	55	2152	8	292.6	24.19	-0.12	-0.00	91(0.82)	8.27	3.96	0.92	0.23	40(0.29)	39.49	8.05	3.77	0.47	14(0.04)
	195	2153	8	237.2	21.78	0.08	0.00	91(0.96)	3.55	2.61	0.52	0.20	88(0.40)	26.20	6.79	2.51	0.37	80(0.21)
	245	2154	8	86.8	13.18	-0.02	-0.00	93(0.85)	2.45	2.21	-0.13	-0.06	62(0.21)	14.62	5.39	0.49	0.09	159(0.15)
LCJ	83	2161	7	411.3	28.68	-0.24	-0.01	96(0.90)	5.94	3.43	0.35	0.10	38(0.08)	26.50	6.82	2.56	0.38	6(0.08)
	223	2162	9	330.0	25.67	1.01	0.04	88(0.93)	2.99	2.33	0.72	0.31	110(0.09)	24.50	6.21	3.23	0.52	175(0.20)
	471	2163	9	32.23	8.01	-0.48	-0.06	97(0.93)	1.58	1.77	0.12	0.07	131(0.52)	6.27	3.53	0.30	0.09	137(0.46)
LCK	204	2171	9	351.0	26.39	2.33	0.89	95(0.85)	3.24	2.41	0.83	0.34	32(0.23)	26.90	6.32	3.72	0.59	166(0.23)
	454	2172	9	115.4	15.19	0.23	0.02	89(0.96)	2.41	2.14	0.47	0.22	78(0.46)	12.38	4.64	1.81	0.39	111(0.23)

Table 2-9a (continued).

Sta	Depth	Record ID	DOF	Low Frequency					Diurnal					Inertial				
				T	U_{major}	U_{minor}	R	Θ(s)	T	U_{major}	U_{minor}	R	Θ(s)	T	U_{major}	U_{minor}	R	Θ(s)
LCL	65	2182	8	131.8	16.22	0.84	0.05	91(0.81)	11.43	4.18	2.32	0.55	48(0.16)	29.99	6.77	3.77	0.56	98(0.10)
	105	2183	8	108.2	14.67	1.12	0.08	93(0.77)	8.31	3.70	1.70	0.46	78(0.32)	44.25	8.35	4.33	0.52	77(0.14)
	127	2511	4	40.67	9.00	0.53	0.06	112(0.71)	1.93	1.91	0.48	0.25	63(0.19)	17.44	5.55	2.02	0.36	69(0.19)
LCM	103	2191	9	102.6	10.63	4.90	0.46	92(0.76)	9.58	3.98	1.83	0.46	87(0.24)	37.14	7.96	3.31	0.42	62(0.13)
	119	2031	11	52.89	10.26	0.75	0.07	97(0.63)	4.86	2.93	1.07	0.36	162(0.13)	22.40	6.25	2.38	0.38	161(0.26)
LCN	243	2201	8	169.7	18.42	0.35	0.02	85(0.86)	3.47	2.63	0.03	0.01	68(0.30)	24.74	6.83	1.69	0.25	73(0.40)
	841	2202	8	4.45	2.97	0.31	0.10	0(0.78)	1.31	1.61	0.13	0.08	171(0.79)	8.95	4.18	0.68	0.16	168(0.84)
LCP	113	2361	7	108.3	14.72	-0.13	-0.01	75(0.75)	5.94	3.33	0.88	0.26	56(0.11)	44.14	8.80	3.30	0.38	73(0.27)
	131	2371	7	12.97	5.09	0.11	0.02	81(0.25)	2.20	2.09	0.17	0.08	48(0.17)	16.57	5.57	1.44	0.26	59(0.23)
LCQ	180	2431	9	26.57	7.27	-0.52	-0.07	90(0.39)	5.247	3.21	0.46	0.14	98(0.67)	17.34	5.85	0.64	0.11	105(0.51)
LCR	183	2441	9	38.96	8.81	0.48	0.05	6(0.78)	2.91	2.40	0.18	0.08	5(0.55)	13.14	5.09	0.62	0.12	6(0.44)
	215	2442	9	19.54	6.25	0.25	0.04	173(0.83)	1.91	1.95	-0.09	-0.05	8(0.69)	8.31	4.07	0.27	0.07	179(0.65)
LCS	554	2451	9	13.23	5.14	-0.18	0.03	178(0.72)	6.56	3.62	-0.19	0.05	178(0.78)	45.44	9.53	0.31	0.03	174(0.86)
LCT	178	2461	9	22.02	6.64	0.01	0.00	16(0.48)	4.06	2.84	0.26	0.09	171(0.69)	14.78	5.44	0.07	0.01	178(0.69)
LCU	134	2591	7	8.73	6.12	0.17	0.03	20(0.67)	2.09	2.04	0.06	0.03	169(0.30)	16.55	5.67	0.95	0.17	179(0.65)

Table 2- 9b.

Sta	depth	Record ID	DOF	Semidiurnal					High-frequency				
				T	U_{major}	U_{minor}	R	Θ(s)	T	U_{major}	U_{minor}	R	Θ(s)
LCA	80	2071	8	874.9	35.46	22.18	0.63	2(0.98)	20.37	6.34	0.72	0.11	79(0.08)
	80	2251	8	1019.	37.51	25.10	0.67	1(0.96)	29.36	7.75	1.28	0.17	27(0.08)
	100	2231	8	198.0	18.19	8.06	0.44	179(0.96)	26.71	7.11	1.69	0.24	18(0.36)
LCB	92	2081	9	552.0	27.51	18.63	0.68	178(0.89)	36.62	8.28	2.15	0.26	171(0.11)
	227	2082	9	49.04	9.87	-0.82	-0.08	11(0.94)	65.61	11.45	-0.12	-0.01	11(0.94)
	277	2083	9	63.18	11.24	-0.16	-0.01	10(0.95)	124.2	15.76	0.18	0.01	7(0.80)
LCC	134	2091	9	233.8	19.11	10.12	0.53	179(0.89)	38.11	8.47	2.11	0.25	103(0.03)
LCD	143	2101	7	353.8	24.55	10.25	0.42	10(0.94)	44.46	9.32	1.46	0.16	159(0.30)
LCE	116	2111	9	288.80	20.72	12.18	0.59	5(0.90)	31.41	7.75	1.65	0.21	175(0.04)
	216	2112	9	101.0	14.21	0.31	0.02	37(0.90)	31.86	7.83	1.55	0.20	5(0.07)
	595	2114	9	187.3	19.36	0.06	0.00	3(0.98)	56.89	10.66	0.34	0.03	173(0.29)
	475	2281	8	259.1	22.77	0.36	0.02	171(1.00)	29.76	7.69	0.64	0.08	166(0.47)
	493	2321	7	305.8	24.71	0.91	0.04	1(1.00)	40.93	9.00	0.86	0.10	178(0.51)
	584	2322	7	262.8	22.90	1.10	0.05	177(0.99)	65.92	11.46	0.65	0.06	3(0.11)
LCF	205	2121	10	88.23	11.23	7.10	0.63	9(0.57)	30.90	7.61	1.96	0.26	0(0.08)
	405	2122	11	34.39	8.29	-0.19	-0.02	3(0.95)	18.78	6.10	0.63	0.10	14(0.29)
LCG	195	2131	11	71.72	11.21	4.22	0.38	60(0.41)	32.99	8.00	1.44	0.18	77(0.14)
	395	2132	11	17.40	5.78	1.18	0.20	166(0.91)	13.99	5.27	0.46	0.09	28(0.11)
LCH	290	2141	8	49.49	8.75	4.74	0.54	0(0.83)	20.49	6.18	1.66	0.27	171(0.29)
	540	2142	8	13.10	4.80	1.76	0.37	15(0.58)	9.71	4.30	0.95	0.22	3(0.24)
	890	2143	8	9.53	4.37	0.01	0.00	160(0.90)	5.46	3.25	0.62	0.19	154(0.28)
	1375	2211		23.34	6.79	0.76	0.11	174(0.95)	16.06	5.65	0.46	0.08	119(0.08)
LCI	10	2151	9	192.7	16.24	11.04	0.68	177(0.08)	54.63	10.07	2.81	0.28	106(0.05)
	55	2152	8	148.0	14.17	9.76	0.69	35(0.30)	28.87	7.44	1.55	0.21	96(0.12)
	195	2153	8	130.6	13.75	8.49	0.62	84(0.39)	34.05	8.10	1.58	0.20	46(0.09)
	245	2154	8	43.16	8.65	3.39	0.39	4(0.63)	61.95	11.07	1.16	0.11	180(0.52)
LCJ	83	2161	7	88.18	11.27	7.03	0.62	17(0.63)	21.60	6.47	1.18	0.18	152(0.07)
	223	2162	9	58.15	9.24	5.56	0.60	3(0.69)	23.00	6.61	1.51	0.23	174(0.25)
	471	2163	9	7.08	3.67	0.82	0.22	145(0.43)	18.74	6.07	0.78	0.13	170(0.45)
LCK	204	2171	9	45.40	8.41	4.48	0.53	6(0.67)	22.73	6.53	1.67	0.26	1(0.12)
	454	2172	9	30.16	7.41	2.34	0.32	154(0.65)	16.27	5.63	0.90	0.16	2(0.16)

Table 2-9b (continued).

Sta	Depth	Record ID	DOF	Semidiurnal T	Semidiurnal U_{major}	Semidiurnal U_{minor}	Semidiurnal R	Semidiurnal Θ(s)	High-frequency T	High-frequency U_{major}	High-frequency U_{minor}	High-frequency R	High-frequency Θ(s)
LCL	65	2182	8	490.5	25.23	18.56	0.74	165(0.88)	22.24	6.59	1.04	0.16	116(0.05)
	105	2183	8	505.2	25.78	18.59	0.72	156(0.71)	39.01	8.60	2.03	0.24	118(0.05)
	127	2511	4	107.5	12.85	7.06	0.55	173(0.73)	37.10	8.24	2.51	0.30	25(0.37)
LCM	103	2191	9	626.1	28.86	20.48	0.71	5(0.88)	39.53	8.61	2.21	0.26	173(0.08)
	119	2031	11	245.9	19.02	11.40	0.60	176(0.85)	43.87	9.08	2.30	0.25	158(0.34)
LCN	243	2201	8	66.98	10.84	4.04	0.37	44(0.22)	36.46	8.43	1.38	0.16	69(0.17)
	841	2202	8	42.52	9.11	1.45	0.16	165(0.98)	13.98	5.25	0.66	0.13	178(0.19)
LCP	113	2361	7	554.6	27.51	18.78	0.68	13(0.76)	61.67	10.94	1.90	0.17	71(0.22)
	131	2371	7	85.11	11.41	6.33	0.56	34(0.65)	33.12	8.06	1.13	0.14	57(0.37)
LCQ	180	2431	9	152.7	16.34	6.20	0.38	100(0.89)	79.25	12.44	1.94	0.16	107(0.54)
LCR	183	2441	9	189.0	17.81	7.79	0.44	177(0.92)	38.69	8.74	1.02	0.12	179(0.12)
	215	2442	9	96.83	13.77	2.04	0.15	1(0.96)	30.56	7.80	0.57	0.07	178(0.33)
LCS	554	2451	9	164.5	18.10	1.11	0.06	176(0.97)	108.2	14.71	0.20	0.01	9(0.41)
LCT	178	2461	9	208.3	20.39	0.82	0.04	1(0.98)	37.46	8.59	1.05	0.12	161(0.24)
LCU	134	2591	7	121.2	15.56	-0.02	0.00	178(0.93)	83.55	12.73	2.27	0.18	174(0.73)

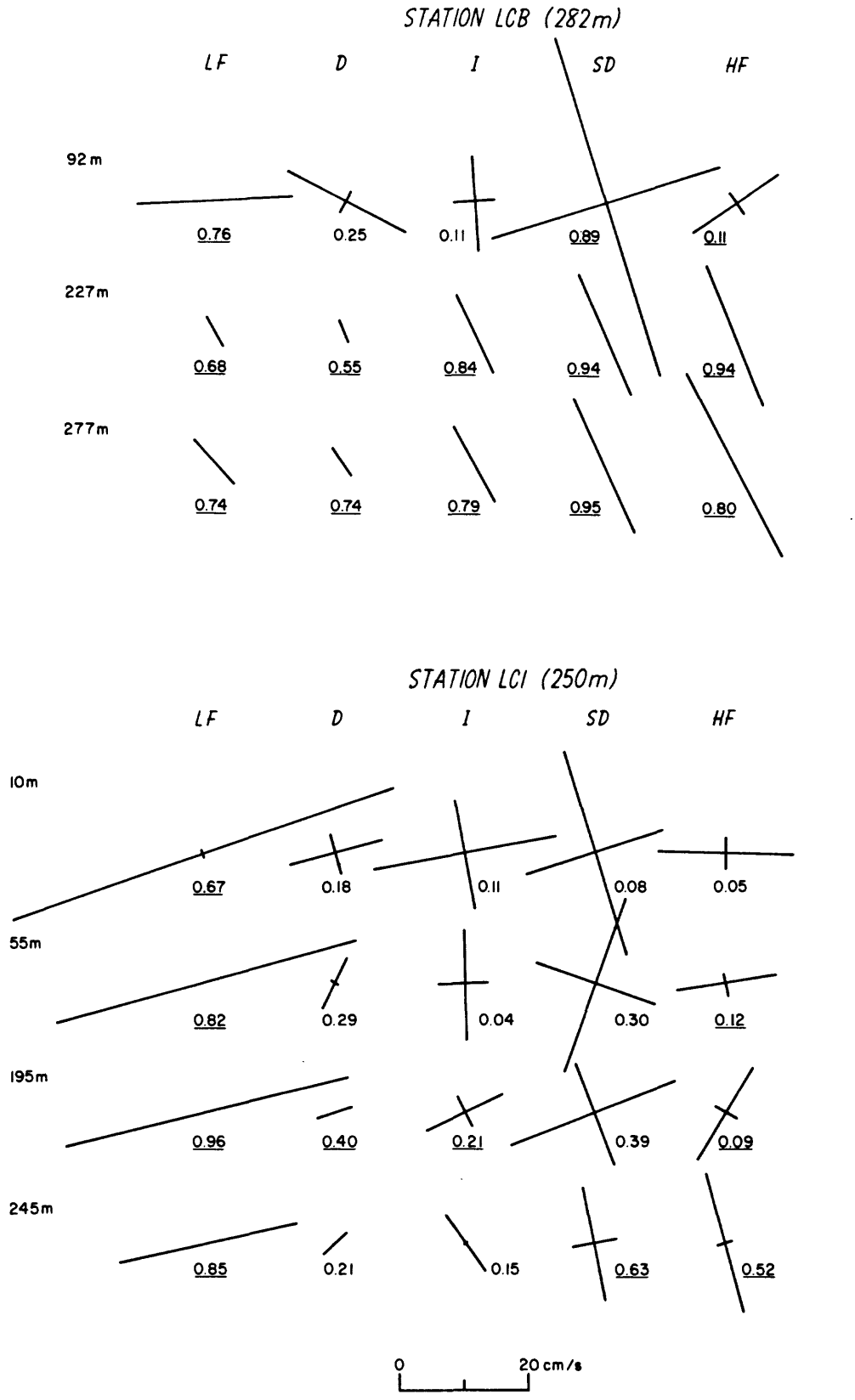

Figure 2-19. Current ellipses in the low-frequency (LF), diurnal (D), inertial (I), semidiurnal (SD) and high-frequency (HF) band at LCB and LCI. The number associated with each ellipse is the stability and is underlined if significant. The number at the left is the depth in m. North is toward the top of the page.

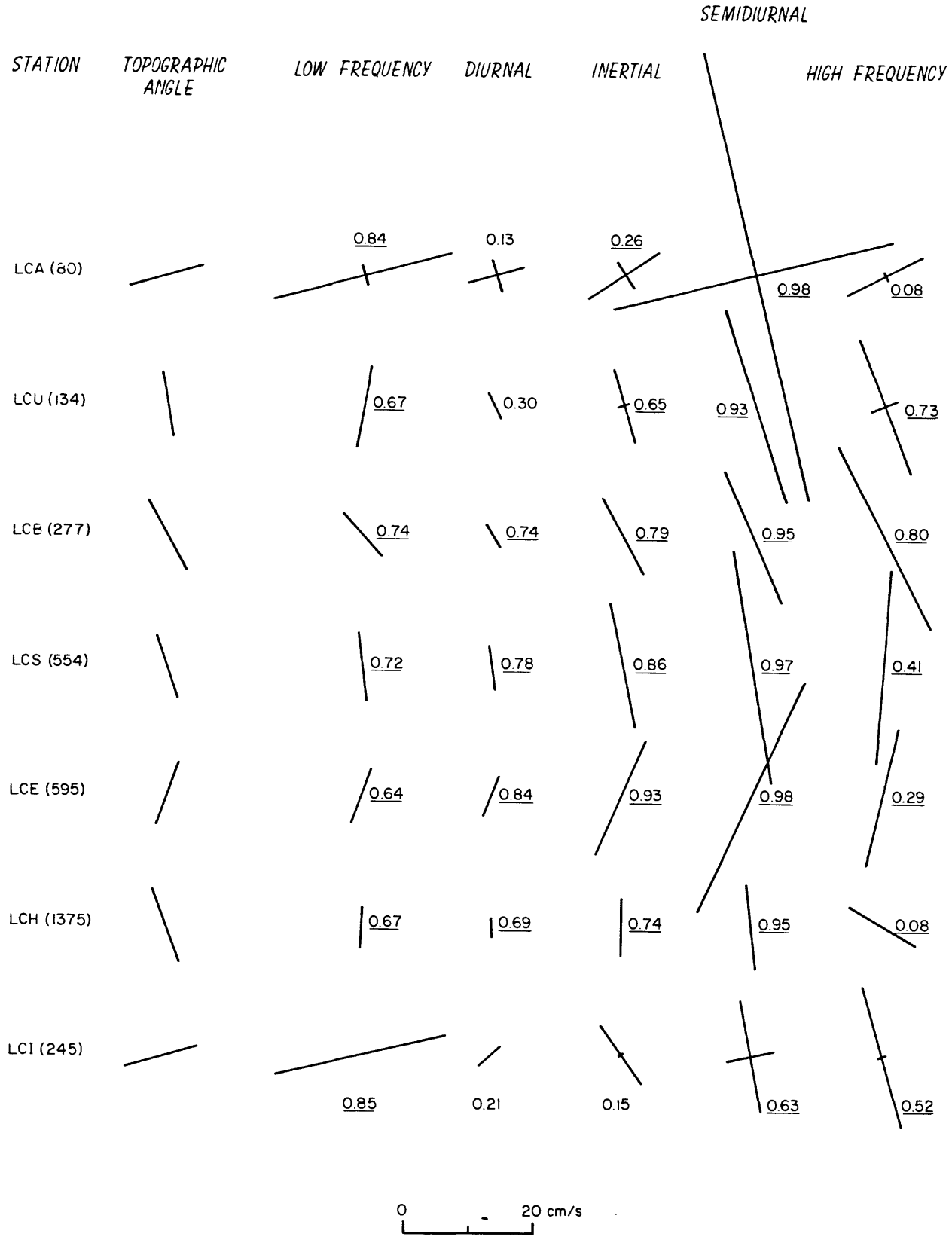

Figure 2-20. Near-bottom current ellipses along the axis of Lydonia Canyon showing current ellipse orientation, amplitude, and stability (underlined if significant) in five frequency bands. North is toward the top of the page.

strength of the inertial and semidiurnal currents occur around LCS and LCE, and a local maximum in the high-frequency fluctuations at LCB. The low-frequency fluctuations near the bottom in the canyon are smaller than on the shelf and slope, while the high frequency fluctuations are stronger, especially near the canyon head.

The spatial distribution of current amplitude by frequency band along the canyon axis, wall, and rim is shown in figure 2-21a-d. Data from all deployments are included in these composite figures, and thus are not computed over the same time periods. However, the only component expected to have a strong variation between deployments might be the low-frequency energy, which is on the shelf associated with seasonal changes in windstress and on the slope, with the passage of WCRs. Confidence limits for the current in each band are tabulated in table 2-10, and vary according to the record length (DOF in table 2-9) and the number of individual frequency estimates in each band. The current amplitude in each band was computed as $(2A)^{1/2}$, where A is the total energy.

The confidence limits on the estimates of current in the high-frequency band are only a few percent of its value (table 2-10). In the outer canyon at LCH, LCE, LCG and LCN at depths below 200 m, the amplitude is 6 cm/s or less (fig. 2-21a). Along the canyon axis, away from the bottom between 100 and 300 m, the amplitude ranges from 6 to 9 cm/s. Toward the head of the canyon (LCE, LCS, LCB, and LCU), the high-frequency currents are intensified toward the bottom (11-17 cm/s), and reach a maximum of 17 cm/s at LCB. The high-frequency currents are also large near the bottom on the eastern rim of the canyon at LCP and LCQ.

In the semidiurnal band, the estimates are typically good to 20-30 percent (table 2-10). The semidiurnal energy is strongest above the canyon

a.

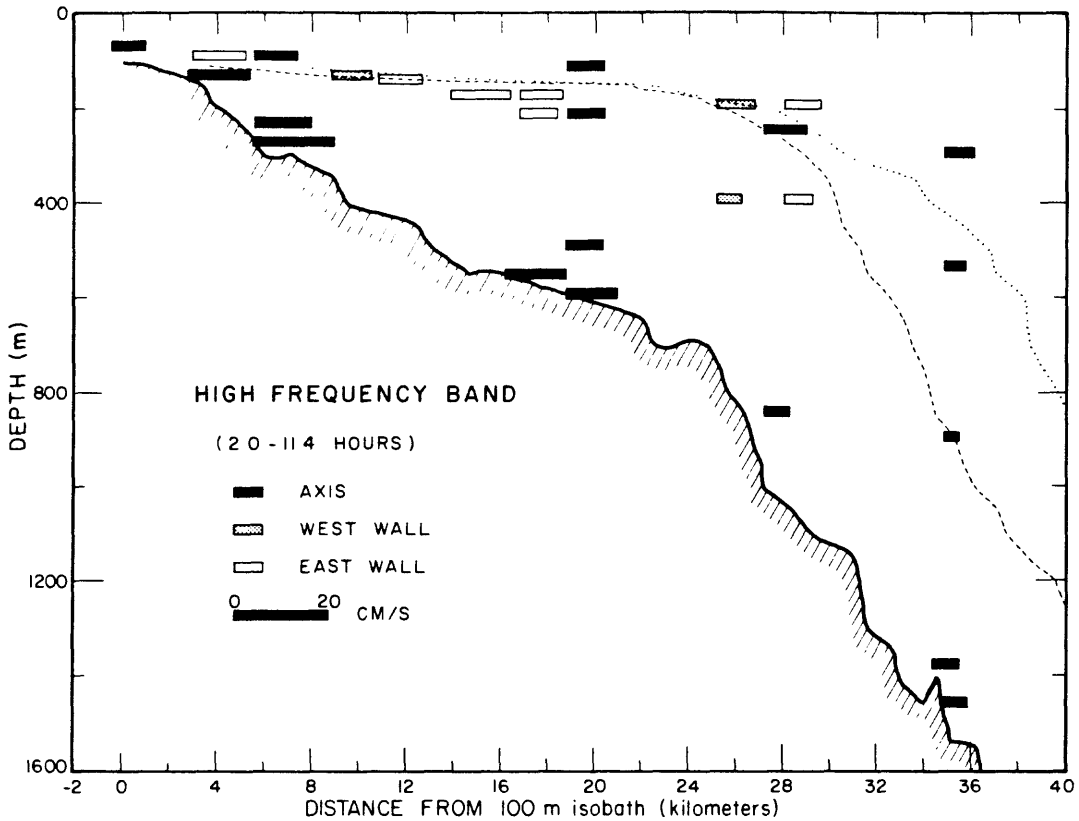

b.

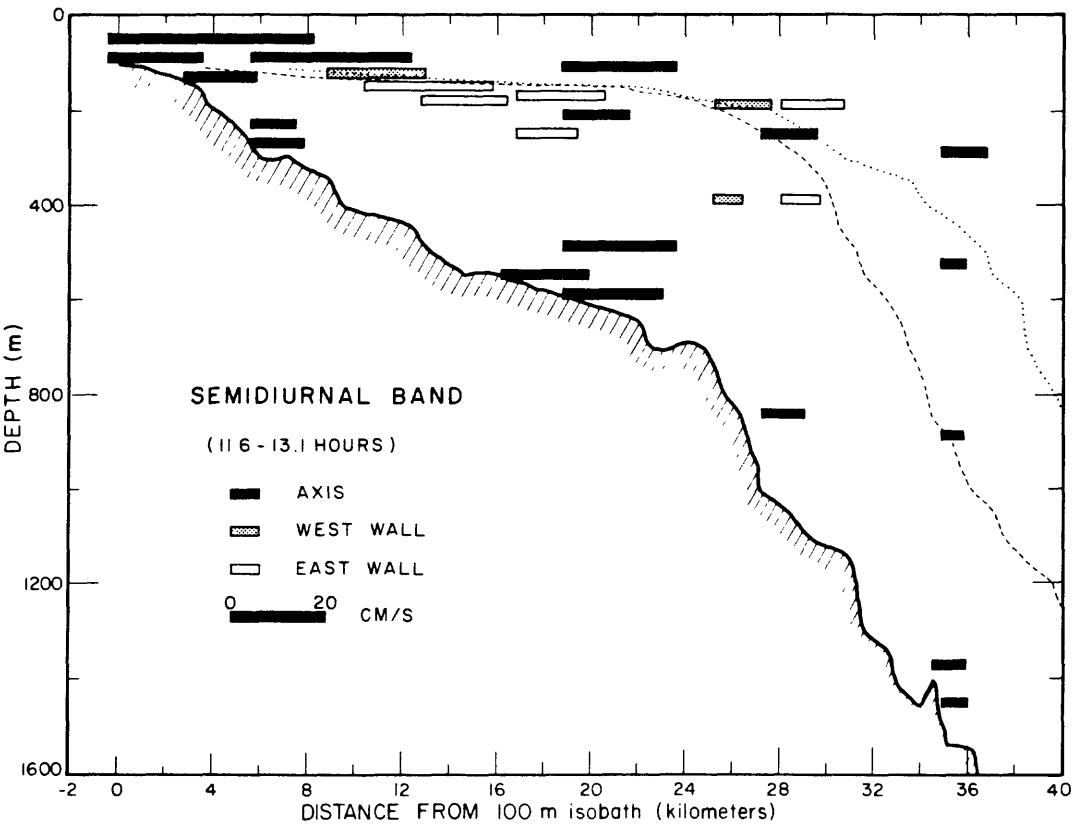

Figure 2-21a,b. Section along the axis of Lydonia Canyon showing the amplitude of the current fluctuations in the high-frequency (a, top), and semidiurnal (b, bottom) band. See text for discussion.

c.

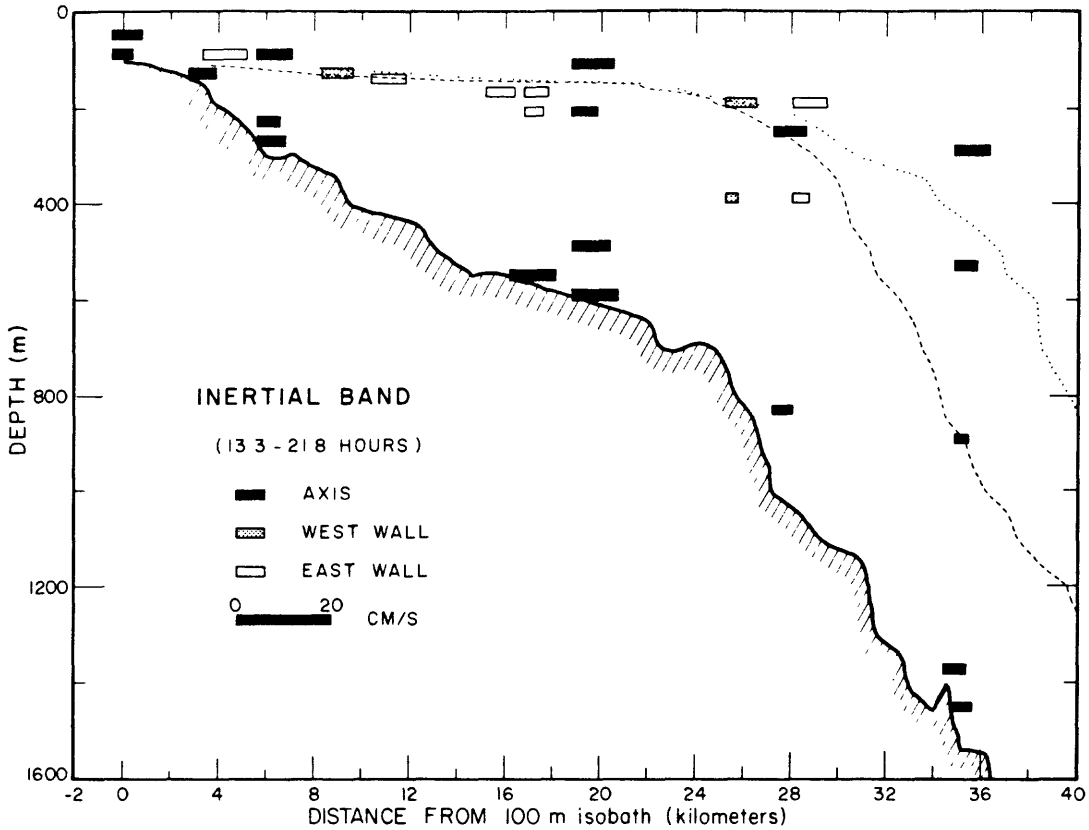

d.

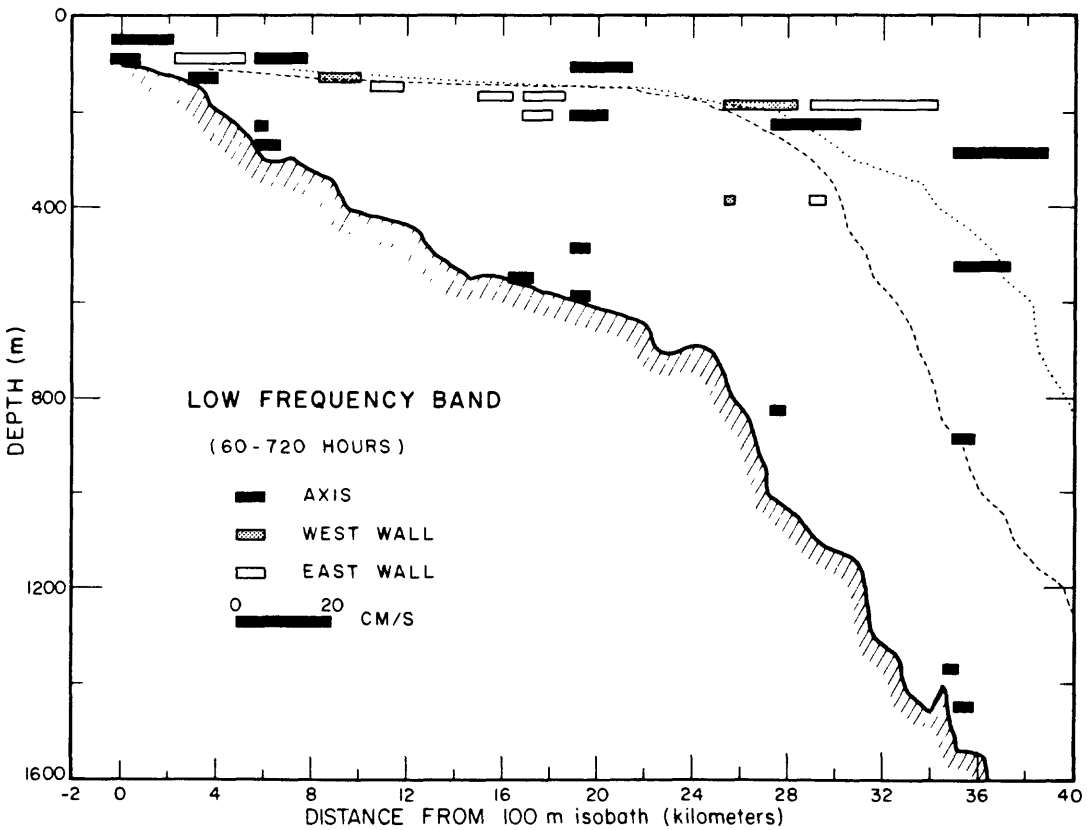

Figure 2-21c,d. Section along the axis of Lydonia Canyon showing the amplitude of the current fluctuations in the inertial (c, top) and low-frequency (d, bottom) band. See text for discussion.

Table 2-10. Confidence limits for current amplitude in each frequency band as function of the number of 720-hour data pieces. See table 2- for the number of pieces for each data record. L•A and U•A give the lower and upper bands on the current amplitude A. LF, D, I, SD, and HF are the low-frequency, diurnal, inertial, semidiurnal and high-frequency bands respectively.

Pieces	LF		D		I		SD		HF	
#	L	U	L	U	L	U	L	U	L	U
4	0.83	1.25	0.78	1.39	0.87	1.17	0.81	1.32	0.96	1.04
8	0.88	1.17	0.84	1.25	0.91	1.12	0.85	1.21	0.97	1.03
16	0.91	1.11	0.88	1.17	0.93	1.08	0.89	1.14	0.98	1.02
46	0.94	1.06	0.92	1.09	0.96	1.04	0.93	1.08	0.99	1.01

rim, where it increases toward the shelf, and is a maximum at LCA (fig. 2-21b). In the canyon the semidiurnal energy is also intensified toward the bottom at LCB, LCS, and LCE, and is a maximum (21 cm/s) at LCE(5 mab). In the outer part of the canyon at LCH below 300 m, the currents in the semidiurnal band are less than 5 cm/s.

The currents in the inertial band are weakest in the outer canyon (less than 5 cm/s), and are slightly stronger toward the canyon head (fig. 2-21c). The observations at LCE and LCS suggest near-bottom intensification in the mid-canyon where the inertial fluctuations are about 9 cm/s. The currents in the diurnal band are weak throughout the canyon, generally less than 2-3 cm/s.

The low-frequency currents are strongest above 300 m in the outer canyon where the current fluctuations were 15-25 cm/s (fig. 2-21d). The low-frequency currents were weaker above the canyon rim and weakest deep in the canyon (3-5 cm/s). There is a slight increase of the low-frequency currents near the bottom at LCB and LCS, where they are about 5 cm/s (see chapter 5 for a detailed description of the low-frequency currents measured during D1).

In summary, the currents in the high-frequency, semidiurnal, and inertial bands increase into the canyon, are intensified toward the bottom, and reach local maxima at LCB (high frequency fluctuations) or near LCS and LCE (semidiurnal and inertial fluctuations). In contrast, the low-frequency currents are maximum over the upper slope in water less than 200 m and are minimum in the canyon. Within the canyon, fluctuations at all frequencies are oriented primarily parallel to the canyon axis. On the shelf and slope and over the canyon above the rim, the low-frequency fluctuations are oriented parallel to the shelf isobaths, while the fluctuations at the semidiurnal period and at high frequencies are oriented primarily across-isobath.

Internal wave characteristics

Internal wave energy propagates at an angle c to the horizontal given by

$$c^2 = \frac{\sigma^2 - f^2}{N^2 - \sigma^2}$$

where σ is the wave frequency, f is the local inertial frequency, and N is the Brunt-Vaisaila frequency ($N^2 = (g/\rho o)(\partial\rho/\partial z)$, where g is acceleration due to gravity, ρ is average fluid density, and $\partial\rho/\partial z$ is the vertical density gradient). For internal waves to exist, the frequency σ must be greater than N but less than f. Waves near the inertial period propagate nearly horizontally, and waves near the buoyancy frequency propagate nearly vertically.

The reflection properties of internal waves over a sloping bottom are well known (Ericksen 1982), and Wunsch (1969) has developed a theoretical description of the propagation of waves into a wedge which has been examined in the laboratory (Cacchione and Wunsch, 1974). The important parameter governing wave propagation is the ratio of bottom slope γ to the angle of wave propagation c. For $\gamma/c<1$ (transmissive case), internal waves are reflected shoreward into the wedge; linear theory and lab results show an intensification of wave orbital velocities near the bottom and toward the apex. For $\gamma/c = 1$ (critical case), reflected waves travel parallel to the bottom and wave energy is trapped along the bottom. The frequency at which $\gamma = c$ is called the critical frequency. For $\gamma/c>1$ (reflective case), the wave energy propagating into the wedge is reflected seaward.

Sections along the axis of Lydonia Canyon show that near the bottom, the Brunt-Vaisaila frequency increases from about 0.5 cph (cycles per hour) near the mouth of the canyon (800 m) to greater than 5 cph near the head (fig. 2-22). The observed Brunt Vaisaila frequencies and bottom slopes can be used to

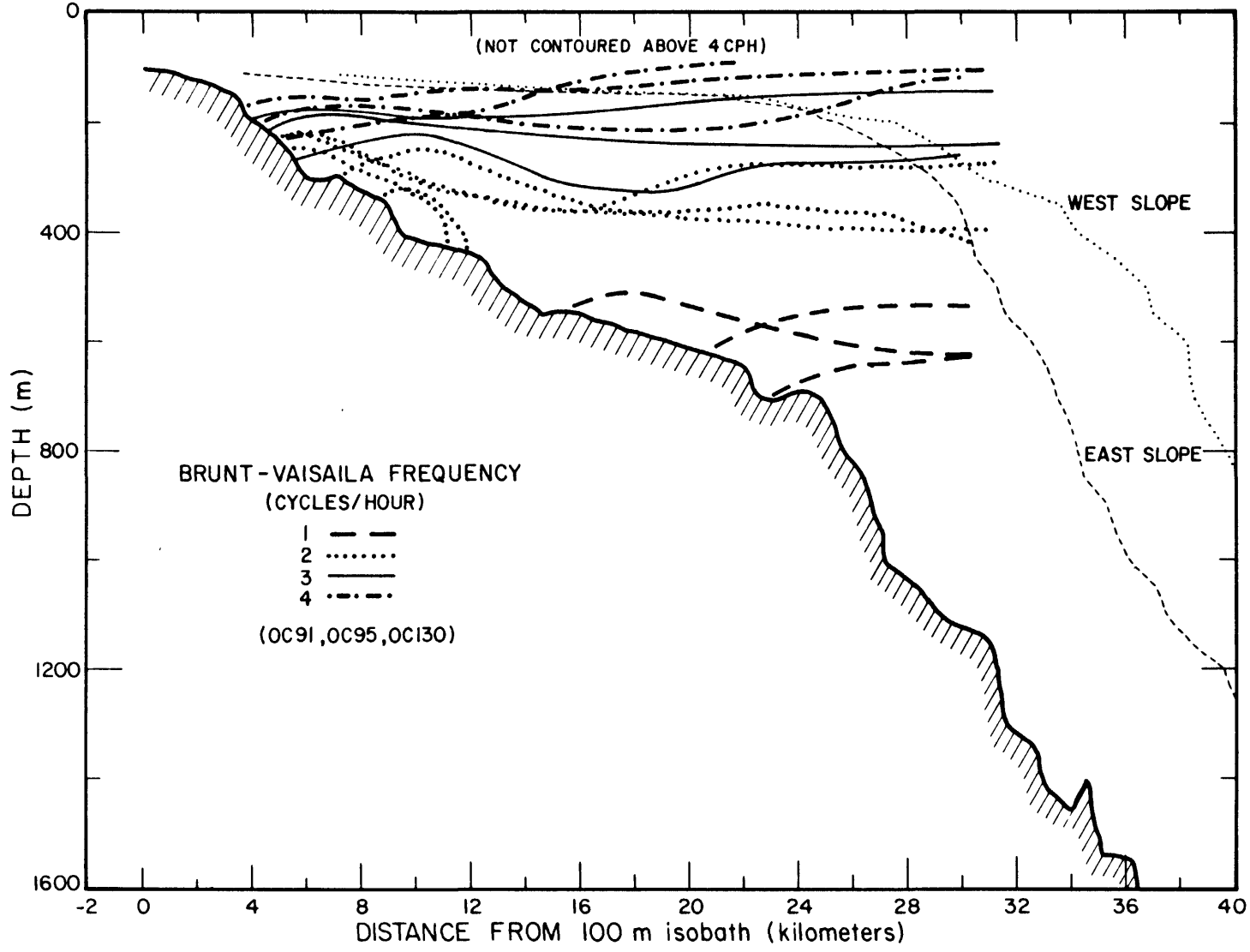

Figure 2-22. Brunt-Vaisala frequency (in cycles/hour) along the axis of Lydonia Canyon based on hydrographic observations made on OCEANUS 91, 95, and 130.

estimate what frequencies of motion will be transmitted [reflected] into [out of] the canyon as function of position in the axis (table 2-11).

The distribution of energy near the bottom in the axis (fig. 2-23) can be explained to some extent by the local Brunt-Vaisaila frequency and the bottom slope of the axis (table 2-11). Based on the observed Brunt Vaisaila periods, the bottom slope is near critical for both the semidiurnal and inertial periods near LCS and LCE; the observed local maxima of inertial and semidiurnal energy reflects energy trapped in this section of the axis. The energy at higher frequencies can propagate up-canyon to LCB, and the steep slope just up-canyon of LCB is a generation region for these fluctuations. The local maximum at LCB in high-frequency energy may reflect nearby generation as well as possible accumulation of energy generated elsewhere.

Most of the tidal and high-frequency current fluctuations are probably associated with internal waves. An estimate of the vertical water-particle excursions associated with these motions at LCB, LCE and LCI can be made using the moored temperature observations and assuming that changes in temperature are caused by vertical displacement of the mean temperature field past the instruments. The record-averaged temperatures give estimates of the mean vertical temperature gradient, and the amplitude of the temperature fluctuations (A) at periods faster than about 30 hours is given by $(2\ \sigma^2_T - \sigma^2_{LP})^{1/2}$ where σ^2_T is the total variance of the record computed from the hour-averaged temperature time series and σ^2_{LP} is the variance of the low-passed time series (table 2-8). The amplitude of the vertical excursions is (A/dT/dz). This simple model was applied only at LCB, LCE, and LCI near the bottom where horizontal advection of the shelf-water/slope-water front does not complicate the analysis. At LCB, based on observations 5 mab and 50 mab during D1, D3, and D4, the peak-to-trough amplitude of water particle

Table 2-11. Bottom slope, range of Brunt-Vaisaila frequencies (based on hydrographic sections), and critical period for segments of the axis of Lydonia Canyon (see fig. 2-22). The critical period T_c is defined by $1/\sigma_c$ where $\sigma_c = [(f^2 + N^2\gamma^2)/(\gamma^2 + 1)]^{1/2}$. Given N, the local Brunt-Vaisaila frequency, γ, the local bottom slope, and f the coriolis parameter, σ_c is the frequency of an internal wave that travels at slope γ and thus is trapped along the bottom. Waves with longer [shorter] periods than T_c are reflected [transmitted].

Region	Bottom Slope (°)	N (cph)	Depth (m)	Critical Period (hrs)	Comments
I	3.3°	4.0	140	4.2	Periods > 4.2 hours reflected near shallow end of section. All M_2 reflected at junction between I and II.
		2.0	300	7.9	
II	1.6°	2.0	300	12.9	Close to critical for M_2 (N = 2.1 cph). Most inertial energy reflected at junction between II and III.
		1.5	540	14.7	
III	0.9°	1.5	540	17.0	Near critical for inertial. M_2 transmitted.
		1.0	700	17.9	
IV	4.2°	<1.0	700	11.0	M_2 and inertial reflected near shallow end of section.
		(0.5)	1600	15.4	

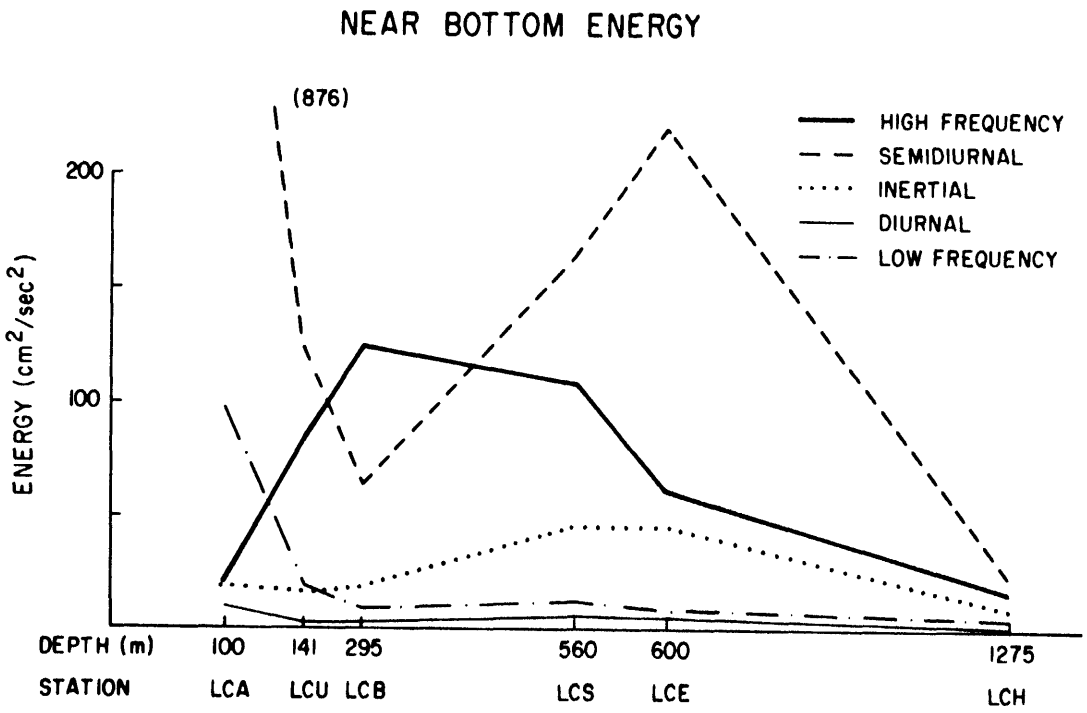

Figure 2-23. Amplitude of energy near the bottom along the axis of Lydonia Canyon by frequency band. All measurements at 5 mab except at LCA where they are at 1 mab.

excursions was on the order of 60 m. Excursions at LCE, based on measurements 5 mab and 100 mab made during D3, were about 100 m; excursions at LCI, based on observations 5 mab and 50 mab during D1 and D3, were 40-50 m. These excursions are 10-20 percent of the water depth.

Measurements that are more closely spaced in the horizontal than those obtained in this experiment are needed to resolve the amplitude and propagation characteristics of the internal wave field. However, it is clear from these rough estimates that there are large-amplitude internal waves in the canyon. There must be considerable mixing caused by these waves as they propagate throughout the canyon and break on the sidewalls or near the head (see chapter 4 for a description of the mixing based on the hydrographic measurements).

Coherence structure in the internal wave band

The current fluctuations in the internal wave band (periods faster than inertial) account for most of the energy in the canyon. The coherence and phase between currents at selected locations in relatively narrow frequency bands centered at the inertial, semidiurnal, and M_4 period illustrate the vertical and horizontal structure of these fluctuations (table 2-12). Analysis is confined to flow within the canyon.

Fluctuations of LCB (5 mab) and LCB (50 mab) were coherent in all three bands. The coherence in the inertial band was higher in D1 and D3 than in D4 and D5, and vica-versa for the semidiurnal band. Fluctuations 5 mab consistently lagged those 50 mab in the semidiurnal and high-frequency band. Fluctuations at LCE (5 mab) and LCE (100 mab) were also coherent in all three bands, and the flow 5 mab consistently leads. At LCH (at 5 and 100 mab) and LCN (243 and 841) only the fluctuations at the semidiurnal period were

Table 2-12. Coherence (coh) and phase between selected current observations at inertial (I), semidiurnal (SD), and high-frequency (HF) periods. Coherence was determined over data pieces 360 hours long and averaged in bands with periods from 18.5 to 19.5 hours, from 12.2 to 12.6 hours, and 6.0 to 6.4 hours. A positive phase indicates that the second variable leads the first. If no phase is listed, the coherence is not significant. The coherence is between the up-canyon components of flow at all stations.

A1		A2		I		SD		HF	
Sta.	Depth	Sta.	Depth	Coh.	Phase	Coh.	Phase	Coh.	Phase
Vertical Coherences									
LCB1	5 mab	LCB1	92	0.53	115(33)	0.68	162(22)	0.25	
LCB2	6 mab	LCB2	108	0.23		0.75	-175(17)	0.12	
LCB3	5 mab	LCB3	125	0.42		0.53	68(38)	0.14	
LCB4	6 mab	LCB4	108	0.25		0.56	-166(30)	0.23	
LCB1	5 mab	LCB1	50 mab	0.72	12(19)	0.66	-25(23)	0.77	-22(10)
LCB3	5 mab	LCB3	50 mab	0.81	13(17)	0.66	-7(25)	0.76	-16(12)
LCB4	5 mab	LCB4	50 mab	0.59	23(27)	0.95	-4(6)	0.82	-23(8)
LCB5	5 mab	LCB5	50 mab	0.39		0.92	-33(9)	0.87	-18(8)
LCB5	5 mab	LCB5	104	0.11		0.86	173(13)	0.43	173(29)
LCE1	5 mab	LCE1	216	0.63	-21(24)	0.90	(9)	0.32	144(38)
LCE3	5 mab	LCE3	100 mab	0.92	-14(9)	0.99	-9(2)	0.82	-10(9)
LCN1	841	LCN1	243	0.22		0.78	-59(16)	0.24	
LCH1	5 mab	LCH1	100 mab	0.32		0.96	-18(7)	0.16	
Near Bottom Horizontal Coherences									
LCU5	5 mab	LCB5	5 mab	0.36		0.73	138(21)	0.50	66(24)
LCB4	5 mab	LCS4	5 mab	0.58	34(28)	0.54	99(32)	0.39	156(29)
LCB1	5 mab	LCE1	5 mab	0.72	53(19)	0.67	122(23)	0.44	-98(26)
LCB3	5 mab	LCE3	5 mab	0.43		0.50	117(42)	0.32	-106(44)
LCE1	5 mab	LCH1	5 mab	0.39		0.89	65(13)	0.27	
OCB	5 mab	OCC	5 mab	0.65	14(23)	0.91	1(8)	0.67	200(13)
Horizontal Coherences									
LCU5	134	LCB5	104	0.33		0.88	-44(12)	0.19	
LCB1	227	LCE1	216	0.29		0.39		0.33	-52(38)
LCB4	248	LCR4	215	0.52	-7(34)	0.58	-153(28)		
LCR4	183	LCT4	178	0.80	-10(15)	0.99	-10(3)	0.56	25(18)
LCR4	183	LCQ4	180	0.54	-41(31)	0.98	-42(3)	0.73	-23(11)
LCF	405	LCG	395	0.72	-15(17)	0.96	-11(5)	0.17	
LCC	134	LCD	143	0.58	14(31)	0.90	73(10)	0.28	-46(51)
LCB	227	LCN	243	0.37		0.37		0.13	

vertically coherent.

The flow 5 mab was coherent along the entire upper axis (LCU, LCB, LCS, LCE and LCH) at the semidiurnal period and the flow at the deeper stations consistently leads. In the high-frequency band, the flow was moderately coherent along the axis from LCU to LCE, but was not coherent between LCE and LCH. In the inertial band, the flow 5 mab was only coherent between LCB and LCS (D4) and between LCB and LCE (D2, but not D3). The inertial fluctuations 5 mab were not coherent between LCU and LCB or between LCE and LCH.

Selected coherence between instruments separated horizontally at about the same depth show decreasing coherence for increasing separation. Along the axis at about 200 m water depth only the fluctuations at LCB and LCU at the semidiurnal period were strongly coherent. Fluctuations at further separations (LCB x LCE, LCB x LCN) were not coherent. Fluctuations at stations located across the canyon from each other were strongly coherent in the semidiurnal band (LCC x LCB, LCR x LCT, LCR x LCQ, LCF x LCG), less so in the inertial and high frequency band.

M_2 Tidal Currents

The large current fluctuations in the semidiurnal band were investigated in more detail at the M_2 period (12.42 hours). The amplitude and phase of the fluctuations at M_2 (here defined as fluctuations with periods between 12.31 and 12.52 hours) were determined from the transfer function between the observed current and a standard unit reference M_2 signal (see Noble and others, 1985). This method gives nearly identical estimates of amplitude and phase as the standard tidal analysis (Moody and others, 1984) but has the advantage that the coherent part of the total energy at M_2 can be determined. The data were analyzed in 720-hour segments; the incoherent

energy reflects changes in phase between 720 hour segments.

The amount of the energy at M_2 that is coherent is generally greater than 95 percent over the inner shelf and near the mouth of the canyon (fig. 2-24). Over the outer shelf and upper slope about 80 percent of the energy at M_2 is coherent. Toward the head of the canyon especially near the bottom at LCB, the coherent energy in the M_2 band is less than 60 percent. This indicates that the phase of about 40 percent of the energy fluctuates randomly with respect to the tide on the shelf.

The amplitude of the coherent part of the M_2 tidal current is well behaved over the shelf (fig. 2-25). The amplitude of the major axis of the tidal ellipse increases from about 10 cm/s at 250 m (LCI) to about 30 cm/s at 100 m (LCA). The phase difference across the shelf from LCI to LCA is a few degrees. These tidal observations are in good agreement with the smooth large scale M_2 tidal current and elevation along the southern flank of Georges Bank (Moody and others, 1984).

Within the canyon, the coherent tide reaches a maximum of about 20 cm/s near LCE and LCS (fig. 2-25). The coherent tidal current decreases to about 5 cm/s near the bottom at LCB where the current is nearly 180^{o} out of phase with the flow on the shelf. Thus the predictable M_2 tidal currents in the canyon are not in phase with the flow on the shelf, and about 40 percent of the energy at M_2 near the head has random phase with respect to the shelf flow. The observations thus suggest a substantial phase locked internal tide in the canyon, as well as a large random fluctuations at M_2. Further modelling of the complex flow field is required.

The short-term variability of the M_2 tidal current at about 5-day intervals at LCB(5 mab) and at LCB(100) was estimated using the fourrier coefficients at 12.8 hours from spectra computed for data segments 128 hours

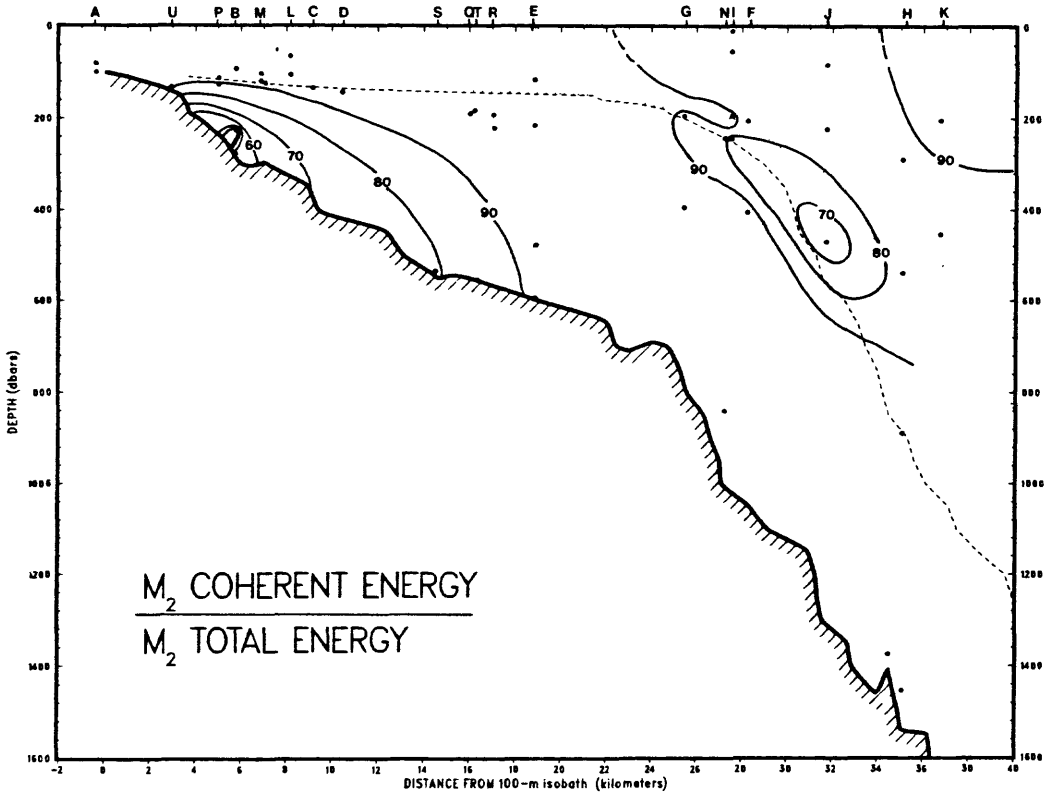

Figure 2-24. Percent of energy in the M_2 tidal band (periods 12.31 to 12.52 hours) which is coherent with the tide on the shelf.

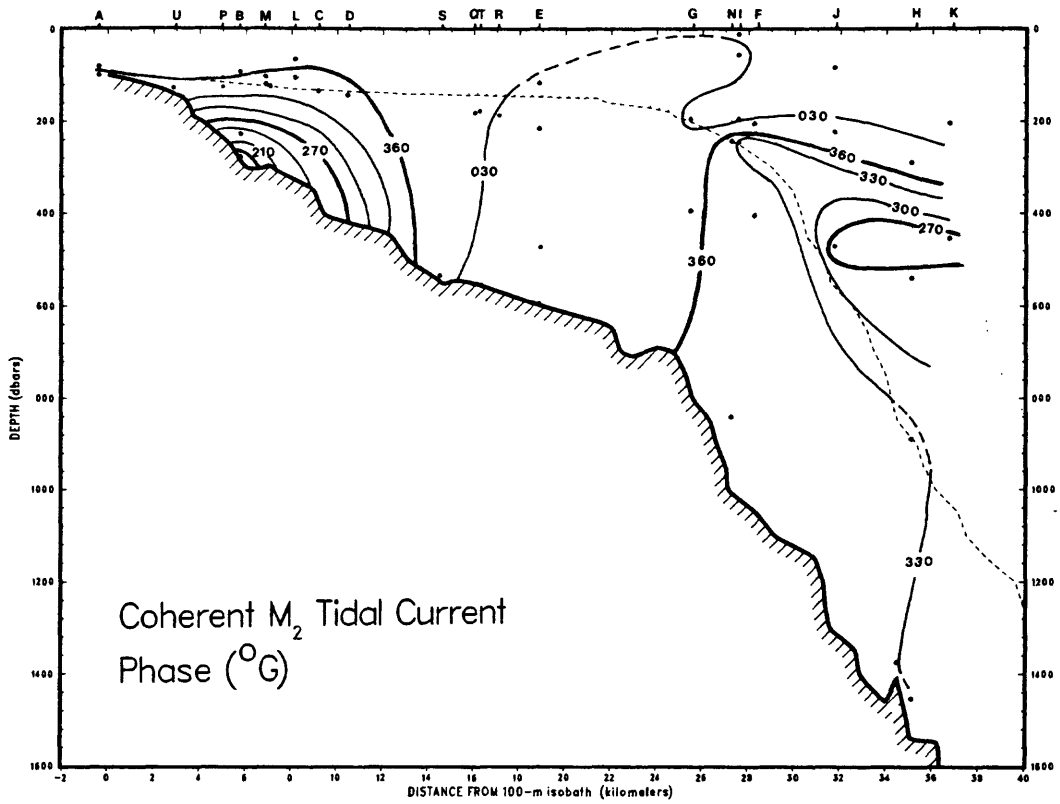

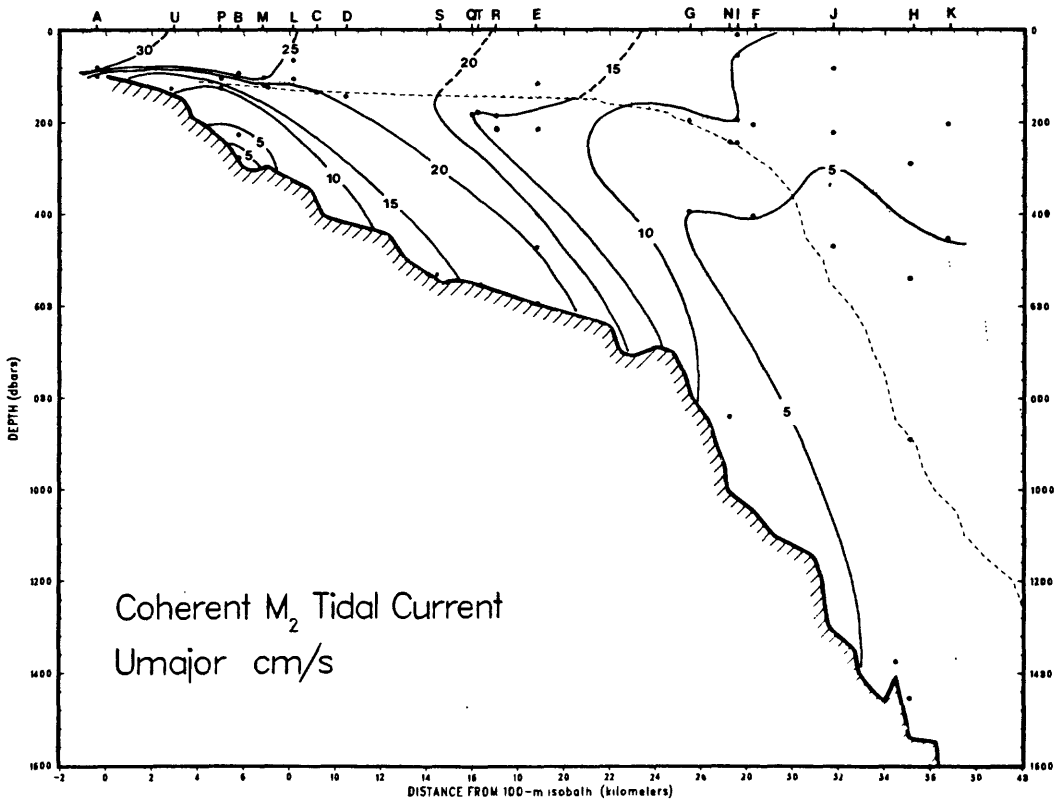

Figure 2-25. Amplitude of the major axis of the tidal ellipse and phase of the coherent M_2 (periods 12.31 to 12.52 hours) current.

long (fig. 2-26). This coefficient includes energy at periods from 12.19 to 13.47 hours, thus including both M_2 and N_2 components. A time series of the phase-locked M_2 and N_2 fluctuations was generated using the constituents determined from tidal analysis of the entire 2 year data record. An estimate of the amplitude of the randomly fluctuating component of the tide was computed by subtracting the 5-day estimates determined from this generated series from the 5-day estimates determined from the original time series (fig. 2-26).

At LCB(5 mab), the amplitude of the randomly fluctuating component ranged from about -5 cm/s (out of phase with the coherent tide) to greater than 15 cm/s. The amplitude of the fluctuations at M_2 period can thus change by about 20 cm/s over a few days. The fluctuating tide generally adds in phase to the coherent tide because the amplitude in the fluctuations is generally positive (fig. 2-26). An interpretation of the fluctuations is that they change in amplitude over time scales of a few days, but are phase-locked to the shelf tide. The amplitude of the variable M_2 fluctuations are 1 to 2 times the amplitude of the phase-locked fluctuations. At LCB(100) the incoherent tidal amplitude ranges from -10 to 10 cm/s, and the phase of the fluctautions is more random with respect to the shelf tide. Because the phase-locked tide is of order 25 cm/s, the fluctuations are much smaller percentage of the tidal signal (order 10-20 percent). Thus above the rim of the canyon, the M_2 tidal currents are much more predictable.

Time variability of fluctuations

One of the most intriguing aspects of the flow in Lydonia Canyon is the time variability of current fluctuations of semidiurnal and inertial period. This variability is illustrated in time-series plots of the up-canyon

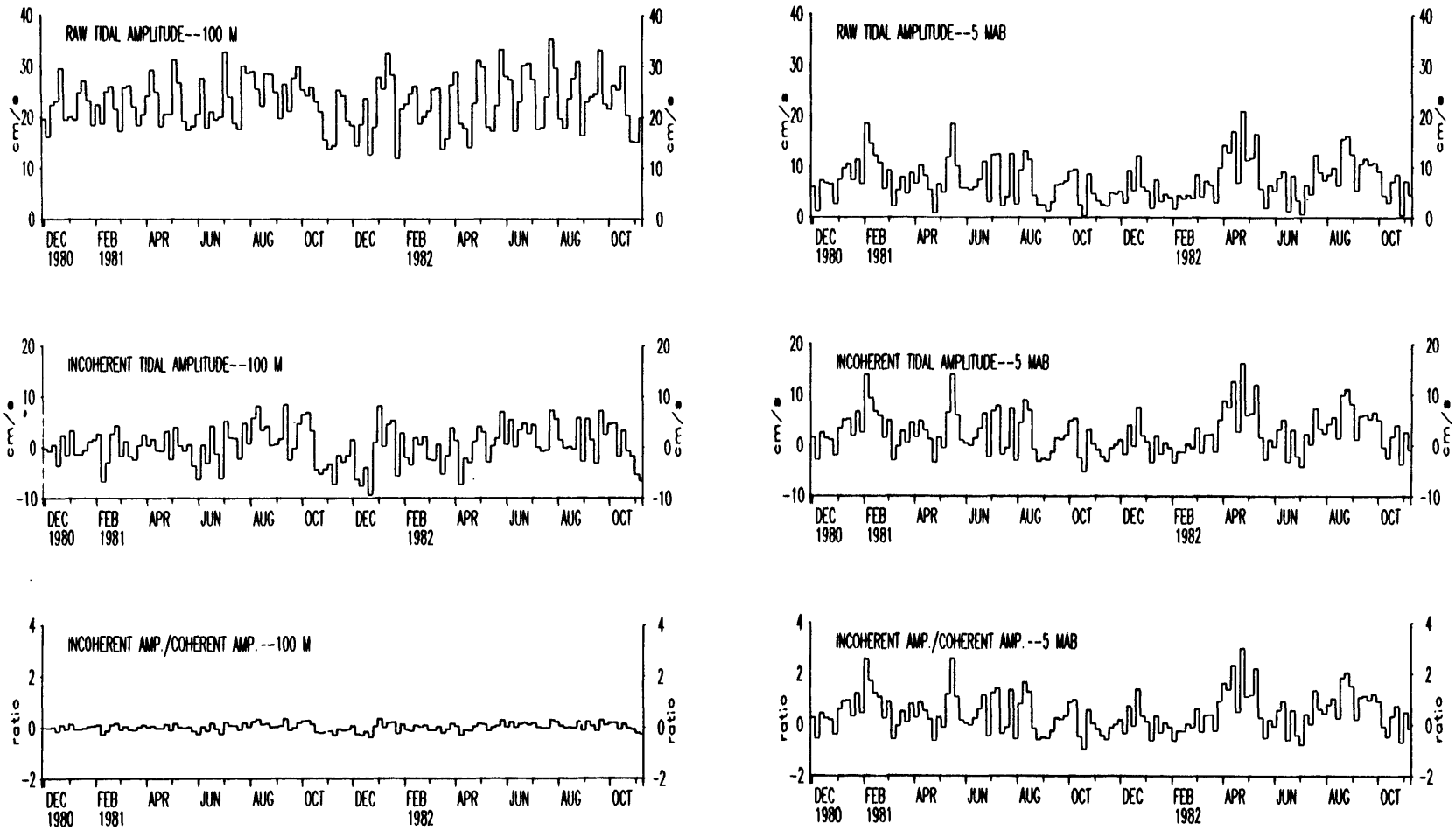

Figure 2-26. Amplitude of the current at the M_2 tidal period determined in 128 hour segments for the long-term observations at LCB(100) and LCB(5mab). The raw tidal amplitude (top panel) is the amplitude of the tidal current determined by the spectral estimate at 12.8 hours (12.19 to 13.47 hours). The incoherent tidal amplitude (second panel) is the raw amplitude minus the amplitude of the coherent tidal signal (determined from a generated series composed of M_2 and N_2). The bottom panel shows the ratio of the incoherent to coherent amplitude.

component of flow at stations along the canyon axis (fig. 2-27a-c). At these stations there were oscillations at approximately the semidiurnal period for several days, while during other periods the fluctuations were small. The amplitude of the semidiurnal fluctuations ranges from < 5 cm/s to > 40 cm/s. The fluctuations dominate the near-bottom current speeds along the canyon axis from LCU to LCE and during some periods of large amplitude fluctuations, there are increased fluctuations in beam attenuation. In addition, the net down-canyon flow at LCB is correlated with the strength of the high-frequency fluctuations. Thus both the Eulerian residual circulation and the resuspension of bottom sediment are intimately coupled to the strength of these packets of high-frequency currents.

The fluctuations are sometimes well correlated vertically. For example, at LCE during D3, the occurrence of fluctuations at 5 mab and 100 mab was almost identical (fig. 2-27a). The fluctuations are not well correlated horizontally, however. For example, between LCB and LCS during D4 (fig. 2-27b) and between LCU and LCB during D5 (fig. 2-27c), packets observed at some stations were not observed at others. Thus the packets appear to have small horizontal extent and to be largest near the bottom.

The cause of these intermittent fluctuations or packets is uncertain. One hypothesis is that they are internal tides, generated in some way by interaction of the barotropic tide with the canyon walls, shelf edge, or canyon floor. If so, the amplitude of the packets should be correlated with the amplitude of the tide on the shelf. Although some of the packets do occur during spring tides (see shelf pressure records in fig. 2-27), some do not, and during many spring tides on the shelf there is no evidence of increased activity in the canyon. The correlation is difficult because the packets may take some time to propagate from the generation region and may be modified

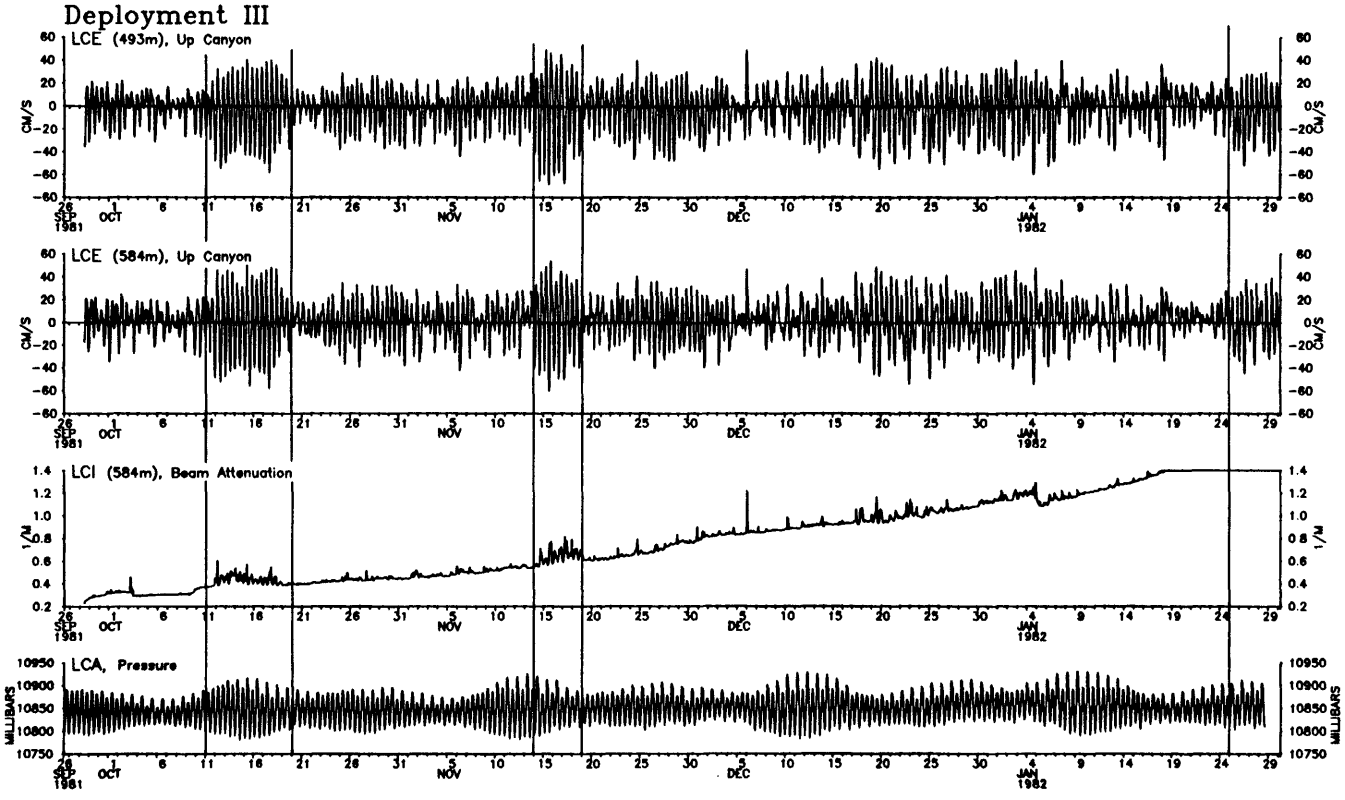

Figure 2-27a. Time-series of hour-averaged up-canyon current at LCE at 6 mab and 106 mab, beam attenuation at 6 mab, and bottom pressure at LCA during D3. Periods of large amplitude current fluctuations are indicated by vertical lines.

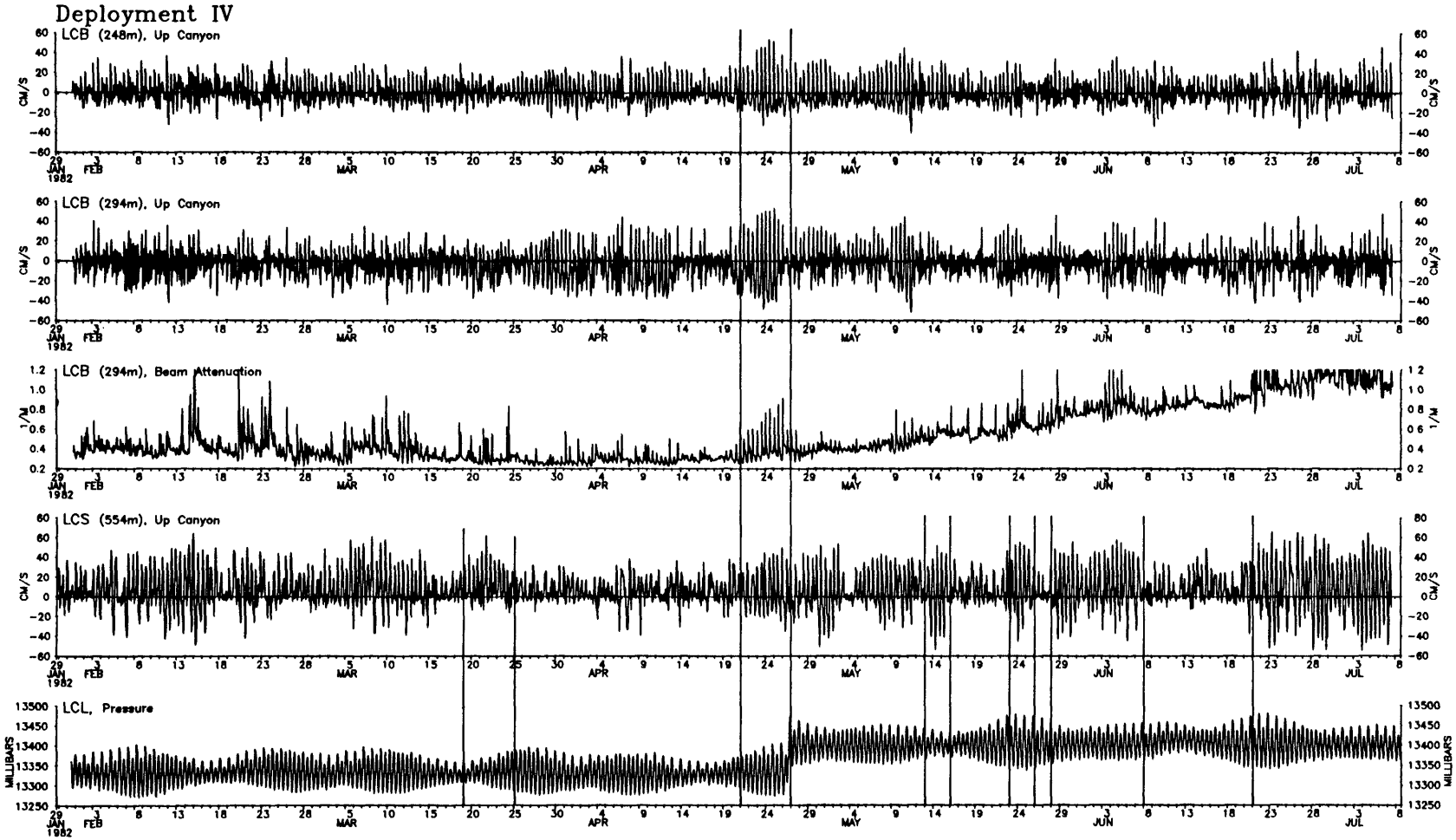

Figure 2-27b. Time-series of hour-averaged up-canyon current at LCB(248) and LCB(294), beam attenuation at LCB(294), current at LCS(5 mab) and bottom pressure at LCL during D4. Periods of large amplitude fluctuations are indicated by the vertical lines.

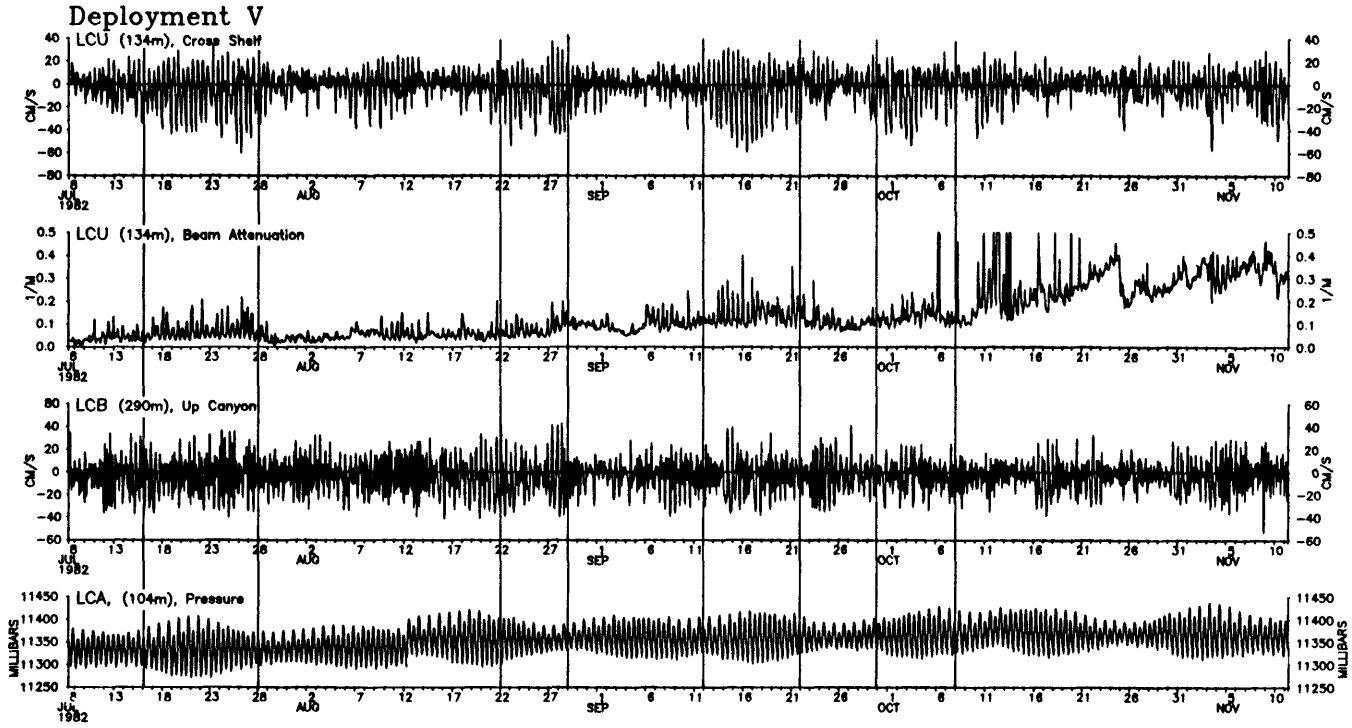

Figure 2-27c. Time-series plot of hour-averaged current at LCU(7 mab), beam attenuation at LCU(7 mab), current at LCB(5 mab) and bottom pressure at LCA during D5. Periods of large amplitude fluctuations are indicated by the vertical lines.

substantially as they interact with the canyon topography and density field.

A second hypothesis for the formation of the packets is that they are generated in some way by WCRs near the canyon mouth. There is a weak correlation between the along-slope flow at LCI and the envelope of the semidiurnal fluctuations at LCB at periods of 50 days and longer. The phase is such that the low-frequency along-slope flow at LCI leads the wave packets at LCB by about 5 days. Only the observations at LCB and LCI are of sufficient duration to determine the coherence at these long periods. However, the results do suggest that the low-frequency flow on the upper slope affects the flow in the canyon by generating packets of the semidiurnal fluctuations.

Mean Flow

The mean flow during each deployment of the moored array is tabulated in table 2-8. The mean flow was on the order of 5 cm/sec at all locations except those on the outer edge of the shelf when Gulf Stream warm core rings influenced the flow. In many shelf situations, the mean current measured at one location is representative of the flow over large spatial scales, and thus the Eulerian mean is approximately equivalent to the Lagrangian mean (the flow of water particles). However, in a region as topographically complex as submarine canyons, strong horizontal and vertical shears in the current field are anticipated, especially where the current oscillations are strong. Thus the mean flow as measured by the fixed instruments in this experiment may not indicate the net flow of water or particles. More detailed field measurements and theory are required to fully resolve this issue and to understand transport within the canyon. With this caution, the mean flow during each deployment is discussed briefly below.

Deployment 1 (November 1980 to April 1981)

Three Gulf Stream rings, based on analysis of the National Weather Service charts (as modified by the Atlantic Environmental Group), passed to the south of Lydonia Canyon during D1 (fig. 2-28). Eddies 80-H, 80-J, and 80-G were located south of Lydonia Canyon in November 1980, December 1980, and January 1981, respectively. The clockwise circulation around these eddies causes a strong eastward current along the outer shelf. The mean flow was examined by month to illustrate the circulation pattern around Lydonia Canyon during ring and non-ring periods (fig. 2-29). The monthly mean flow is influenced both by the seasonal hydrography and the low-frequency variability associated with rings; the variability associated with wind stress, shelf waves, and with small meanders of the shelf-water/slope-water front, which have time scales less than one month, are averaged out. Aspects of the monthly mean flow which were steady over the entire deployment period will be presented following the discussion of the monthly mean flow.

Only a portion of the moored array was in place during November (instruments at LCA, LCC, LCD, LCF, LCG, and LCM, fig. 2-29a). The monthly mean flow 1 mab on the shelf at LCA and LCM was to the south and southwest at about 5 cm/s. Flow on the east wall of the canyon at LCD was westward, and flow on the west wall at LCC was southerly. Flow at LCF(205) was to the east, while flow at LCG was weak (less than 1 cm/s). During November, WCR 80-H was located to the southwest of Lydonia Canyon. The southerly flow observed on the shelf suggests a significant offshelf near-bottom flow, possibly caused by entrainment of shelf water by WCR 80-H.

WCR 80-J and WCR 80-G were located to the south of Lydonia Canyon in December 1980 and January 1981, respectively (fig. 2-28). The clockwise circulation around these eddies caused strong eastward flow along the

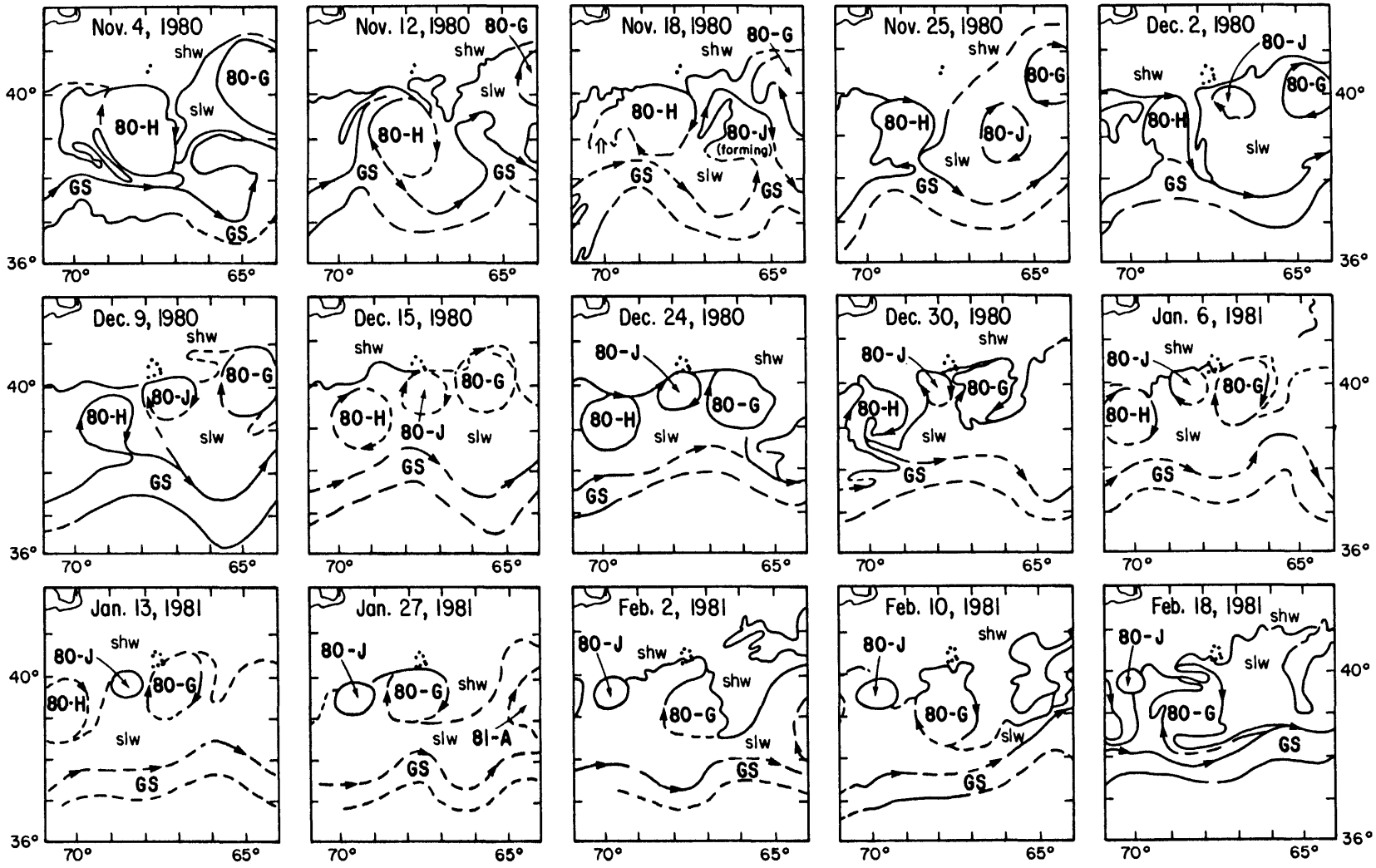

Figure 2-28. Weekly Ocean Frontal Analysis charts for November 1980 to February 1981. The Gulf Stream warm core rings are numbered sequentially in the year they were formed (80-A is the first eddy formed in 1980 for example). shw indicates shelf water; slw, slope water; and GS indicates the position of the Gulf Stream. The locations of the moorings are shown as small dots.

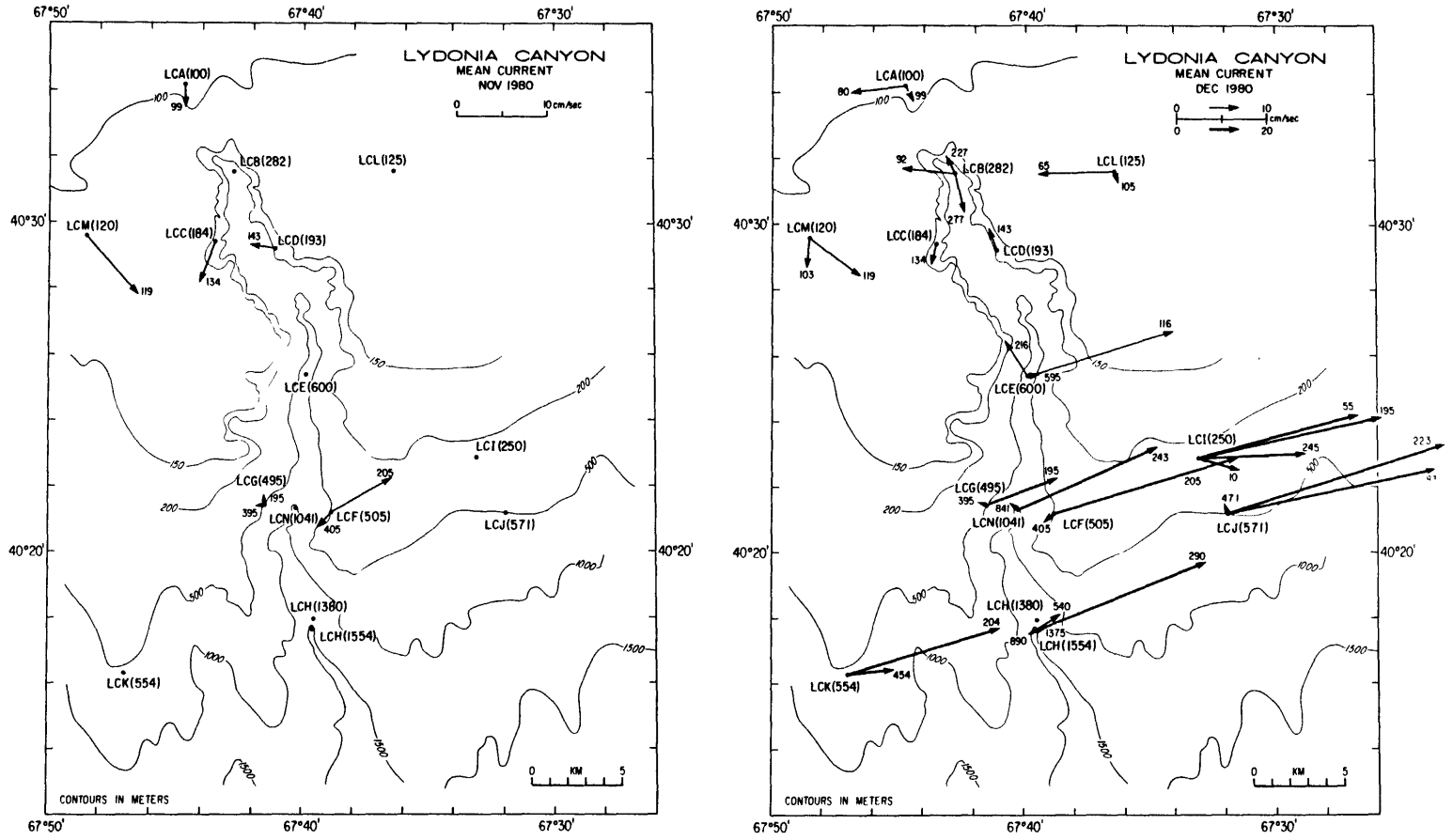

Figure 2-29a. Monthly mean Eulerian currents during D1 (November and December, 1980). The arrow points in the direction of the mean flow and the length of the arrow is proportional to the current amplitude. Two speed scales are used for December (heavy and light lines). The water depth of each station is shown in parenthesis after the station identifier. The number of the tip of the arrow indicates the depth of the measurement in meters. Dashed lines indicate less than a full month of sata.

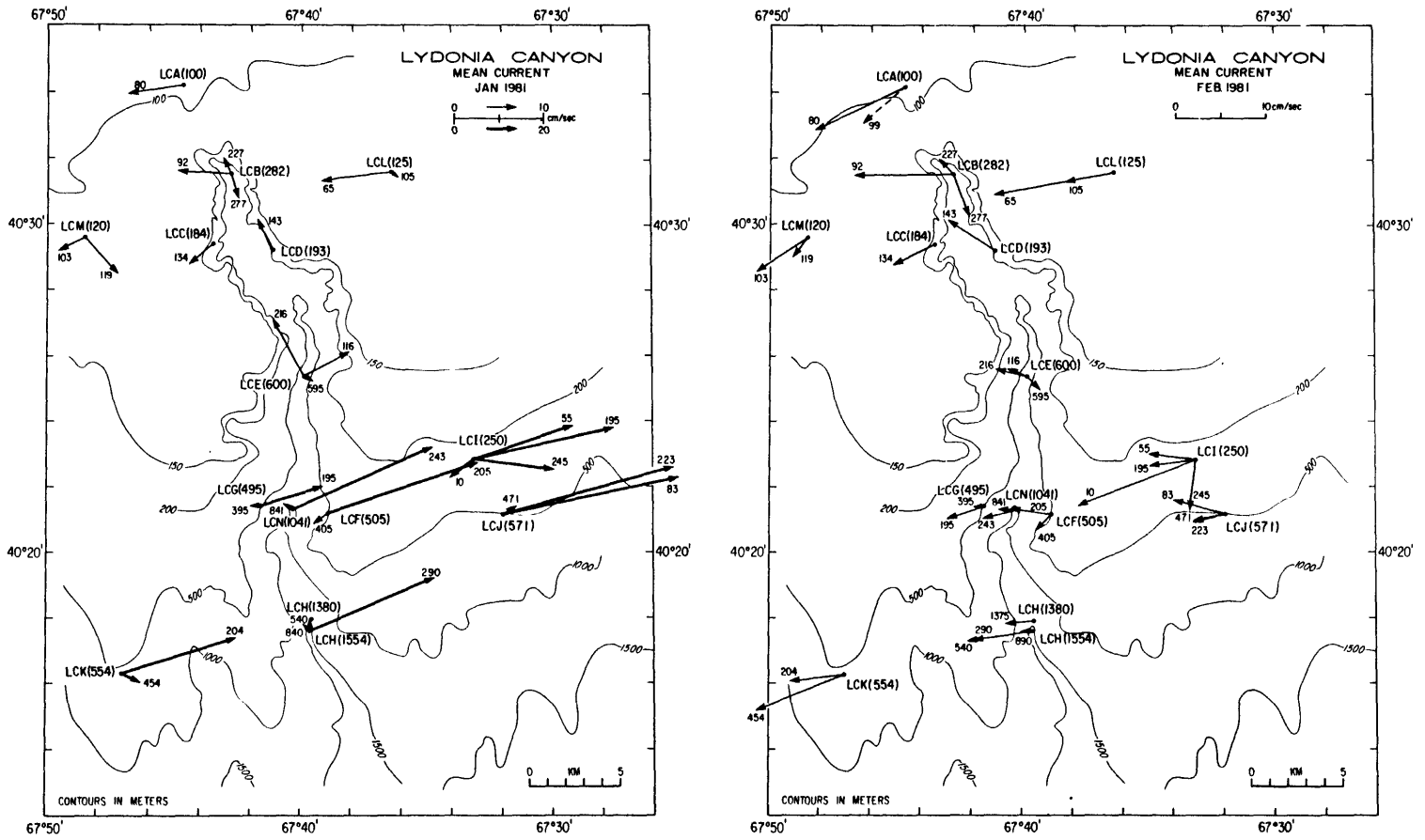

Figure 2-29b. Monthly mean Eulerian currents during D1 (January and February, 1981). The arrow points in the direction of the mean flow and the length of the arrow is proportional to the current amplitude. Two speed scales are used for January (heavy and light lines). See figure 2-29a for explanations of symbols.

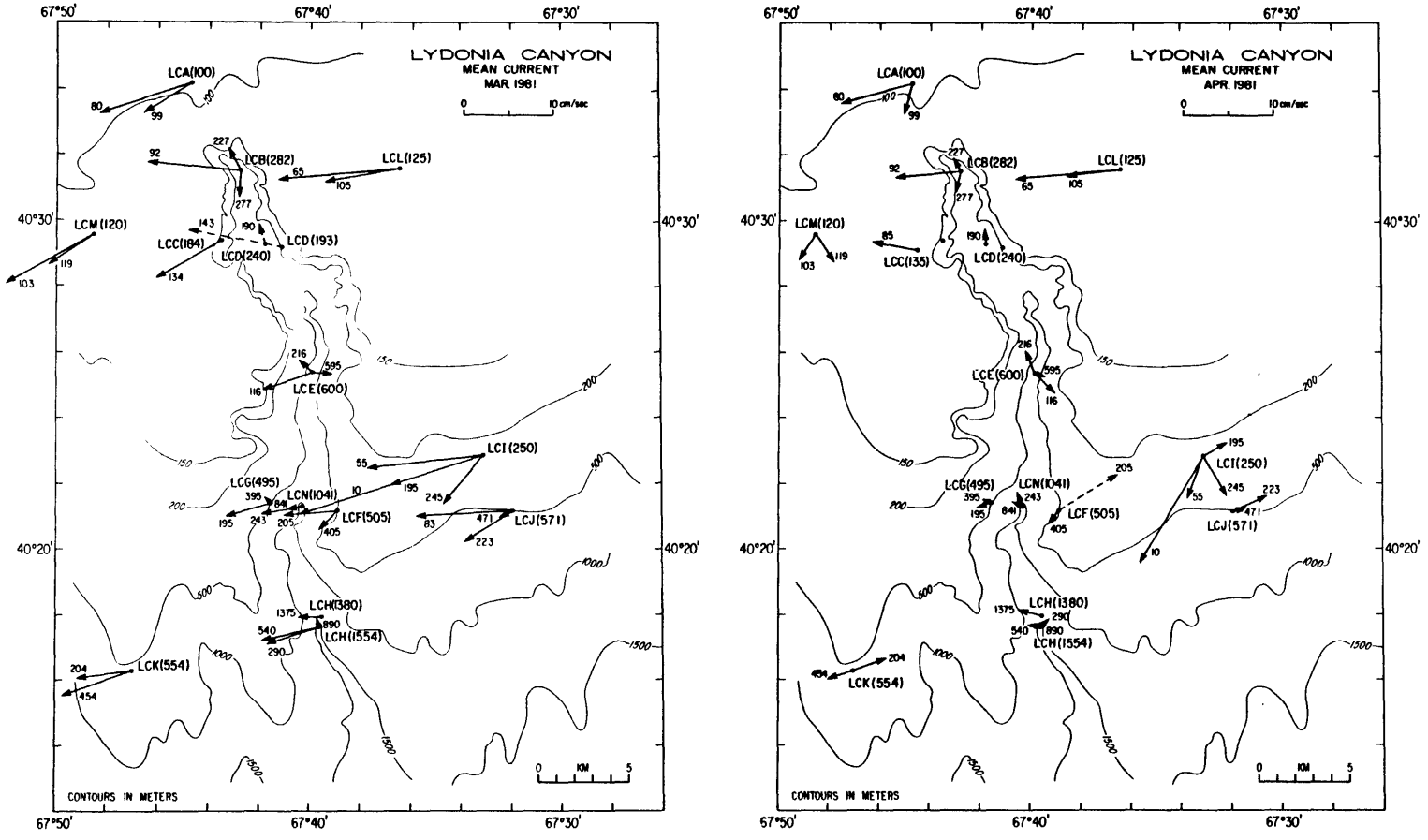

Figure 2-29c. Monthly mean Eulerian currents during D1 (March and April, 1981). See figure 2-29a for explanation of symbols.

continental slope. The mean flow was eastward at all depths shallower than about 250 m at stations along the upper slope (LCF, LCG, LCH, LCI, LCJ, LCK, and LCN) in December 1980 and January 1981 (fig. 2-29a,b). The monthly mean current exceeded 40 cm/s at LCF, LCJ, and LCH and 30 cm/s at LCI, LCK, and LCN. The influence of the strong easterly flow associated with the ring extended as far north as LCE, where the mean current at 116 m (above the canyon rim) was also to the east. On the shelf, the current observations at LCA, LCL, and LCM suggested westward alongshelf flow at mid-depths and an offshelf southerly flow near the bottom. The near-bottom mean flow was southerly at LCA(1 mab), at LCM(1 and 20 mab), and at LCL(20 mab). The mean flow was westward alongshelf at LCA(20 mab), at LCB(92), and at LCL(65).

In February and March no Gulf Stream rings were located near Lydonia Canyon. The monthly mean flow was generally westward at all stations on the shelf and slope at speeds typically less than 10 cm/s (fig. 2-29b,c). At LCB and LCE, flow at depths above the level of the adjacent shelf was also westward. At stations LCC and LCD on the canyon walls, the mean current was primarily across the canyon axis toward the west. However, there was a slight upcanyon flow at LCD on the east wall, and a slight downcanyon flow at LCC on the west wall. At LCA, LCL, and LCM on the shelf and LCI, LCJ, and LCK on the slope, the near-bottom currents were consistently to the left (offshelf or downslope) from the currents at mid-depth. The current at LCI(5 mab) was almost directly downslope in February.

The monthly mean flow in April at LCA and LCL, at LCB(92), and at LCC (now moved westward to a new position) was generally westward (fig. 2-29c). In contrast, the mean flow at LCM was southerly. On the slope, the mean flow was weak and variable. At LCI, the near-surface flow was westward, the flow at 195 m was eastward, and the near-bottom flow was directly downslope. At

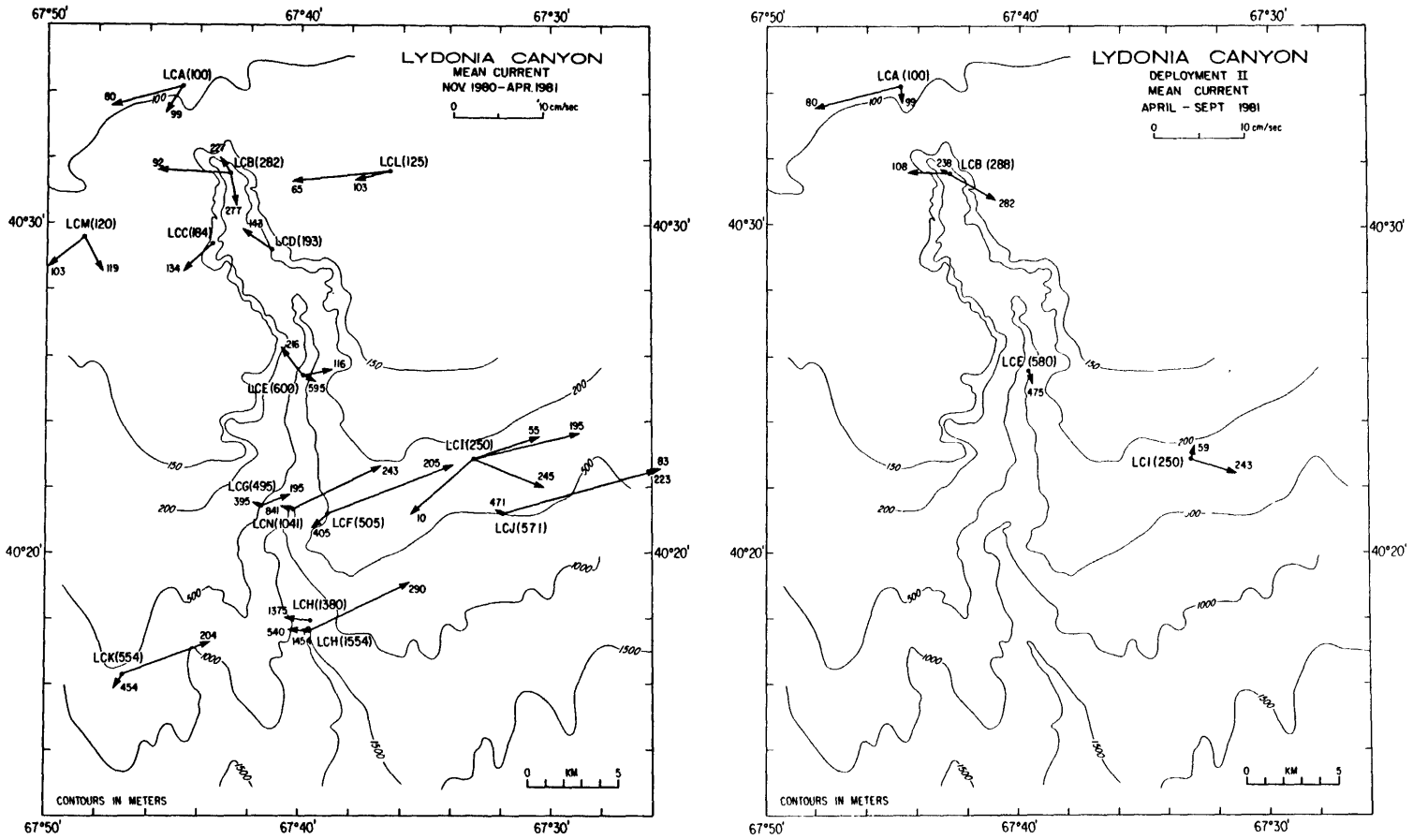

Figure 2-30a. Mean Eulerian current for D1 and D2 (see figure 2-29a for explanation of symbols).

LCF, LCH, LCJ, and LCK, there was a suggestion of a weak eastward flow at depths above 200 m. No obvious Gulf Stream rings were located near Lydonia Canyon in April, although WCR 81-D was about 200 km to the east.

Several features of the monthly mean circulation within the canyon were quite steady over the five-month deployment (fig. 2-30a). At LCB(92) the mean flow above the level of the canyon walls was westward across the canyon axis. At LCB(50 mab), the mean flow was consistently up-canyon at about 2 cm/s and at LCB(5 mab), the mean flow was consistently down-canyon at about 3 cm/s. The mean current at LCD and LCC suggested westward flow across the canyon axis, but with northward (up-canyon) flow on the east side and southward (downcanyon) flow on the west side. At LCE(116) the mean flow above the level of the canyon rim followed the direction of flow on the adjacent slope; eastward in December and January and westward in February and March. The mean current at LCE(216), just below the level of the adjacent shelf, was toward the northwest, primarily across the canyon and slightly upcanyon. The mean near-bottom flow at LCE(5 mab) was weak (less than 1.5 cm/s) and was generally oriented across the canyon axis to the west. At LCH(5 mab), the mean flow was westerly across the canyon axis.

In summary, the current observations made during D1 show that the monthly mean flow at the outer edge of the shelf was strongly influenced by the circulation around Gulf Stream WCRs; the strongest monthly mean flows were caused by the rings and were eastward at greater than 35 cm/s. Maximum lowpassed currents associated with the rings exceeded 80 cm/s. The effect of the rings extended northward onto the shelf at least to station LCE. On the shelf, inshore of the shelf-water/slope-water front, the mean flow was westward, as expected. However, there was a persistent off-shelf near-bottom flow that may occur when Gulf Stream rings are present. In Lydonia Canyon the

mean flow was generally weak. At LCB, a persistent near-bottom down-canyon flow was observed. At LCE and LCH, however, the mean flow was weak, marginally significant, and oriented across the canyon axis.

Deployments 2-5 (April 1981 to November 1982)

The additional current observations obtained in D2-D5 were designed to determine the long-term current variability at selected stations on the shelf and slope and in the canyon, to further define the mean current pattern determined during the first deployment, and to determine the frequency of sediment movement in regions of the canyon not explored during D1. Stations LCA, LCB, LCE, and LCI were maintained as long-term stations.

In D2 (April-September 1981), instruments were deployed at stations LCA, LCB, LCE, and LCI (fig. 2-30a). The mean current was similar to the mean flow observed during D1, especially at LCA and LCB. At LCA, flow 10 mab was alongshelf at about 9 cm/s and was off-shelf 1 mab at about 2 cm/s. At LCB, flow was cross-canyon above the level of the adjacent shelf, up-canyon 50 mab, and down-canyon 5 mab. At LCE about 125 mab, the mean flow was down-canyon at about 2 cm/s, and on the slope at LCI(59) flow was slightly onshelf, and flow 5 mab was eastward and off-shelf at about 5 cm/s.

In D3 (September 1981 to January 1982), instruments were deployed at stations LCA, LCB, LCE, LCI, and LCP (fig. 2-30b). The objective of the moorings at LCP was to investigate processes near the canyon rim. Mean flow during D3 at LCB was similar to the flow observed during D1 and D2. Flow was down-canyon 5 mab and up-canyon 55 mab. Mean flow at LCB above the level of the adjacent shelf was more up-canyon than cross-canyon. At LCP, less than 2 km away on the canyon rim, flow at 19 and 1 mab was directed across the canyon axis. The observations at LCB and LCP show a large change in the

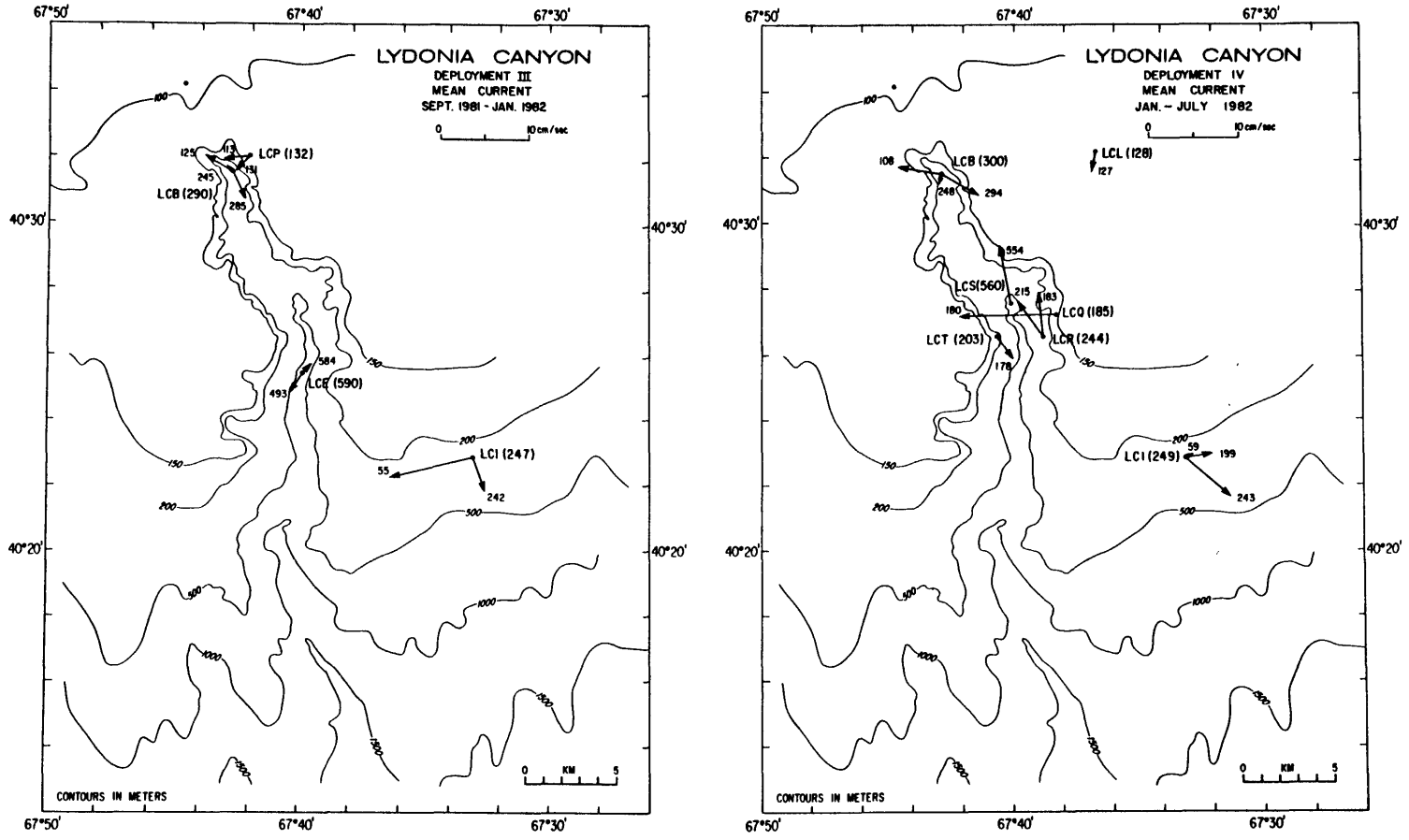

Figure 2-30b. Mean Eulerian current for D3 and D4 (see figure 2-29a for explanation of symbols).

direction of the currents near the head of the canyon as they flow from the shelf toward the canyon axis. At LCE, mean flow was up-canyon at a few cm/s 6 mab, and down-canyon 103 mab. At LCI, mean flow was westward parallel to the shelf isobaths at 55 m and almost directly off-shelf 5 mab.

In D4 (January to July 1982), instruments were again deployed at the long-term stations LCA, LCB, and LCI (fig. 2-30b). In addition, instruments were deployed at three new stations, LCQ, LCR, and LCT, to investigate the cross-canyon structure of the flow to the north of the canyon mouth. Measurements were also made near the bottom at a LCS to provide additional information along the floor of the canyon axis. Mean flow at LCB was again cross-canyon above the level of the adjacent shelf and down-canyon 6 mab. Flow at LCB was also slightly down-canyon 50 mab, in contrast to previous observations. At LCI, flow was approximately parallel to the shelf isobaths at mid-depth and directed off-shelf 6 mab.

The mean flow observed in the cross-canyon array was particularly interesting. Flow at LCQ(5 mab) was westward toward the canyon axis. On the east wall of the canyon at LCR, only a few kilometers away and at the same level in the water column, the mean flow was northward (up-canyon). On the west wall of the canyon at LCT, flow was southward (down-canyon). These observations suggest that the mean flow turns northward as it flows across the east rim and may circulate around the canyon at about 200 m.

The mean flow at LCS(6 mab) was strongly up-canyon at about 6 cm/s. This observation at LCS is a crucial measurement in that it shows a divergence of the mean Eulerian flow between LCB (down-canyon flow) and LCS (up-canyon flow) along the canyon floor. This divergence has major implications for the net transport of sediments within the canyon (see chapter 3) and is a notable difference between Oceanographer and Lydonia Canyons.

In D5 (July to November 1982), instruments were deployed at LCA and LCB and a single near-bottom instrument was deployed at LCU at 144 m in the west arm of the canyon. The flow at LCB was as observed in previous deployments: across canyon above the sill depth, weak at 50 mab, and down-canyon near the bottom (fig. 2-30c). The near-bottom mean flow at LCU was southwestward, suggesting flow around the northern tip of the canyon.

Relationship to high-frequency fluctuations

A correlation between the strength of the high-frequency current fluctuations (at periods faster than about 30 hours) and the net Eulerian downslope flow near the bottom is clearly established on the continental slope (see chapter 7). The same correlation is observed in the Lydonia Canyon Experiment at LCU, LCB, and LCE in the canyon axis, at LCQ on the canyon rim, and at LCI on the slope. At these stations, net down-canyon or downslope flow occurs during periods of increased current fluctuations. This net Eulerian flow may result from oscillatory flow along a sloping boundary where the water column is stratified. During upslope flow, the fluid near the bottom is retarded by friction; heavier water runs over lighter water and vertical mixing occurs as the lighter water rises through the boundary layer. Because of enhanced vertical mixing, the bottom boundary layer is thicker and the flow at a fixed height above the bottom is weaker than observed in the constant density case. As water flows down-canyon, lighter water runs over heavier water. The boundary layer is stably stratified, consequently thinner, and there is stronger flow at a fixed height above the bottom than in the constant density case. Thus the near-bottom current meters record a net Eulerian down-canyon flow because they are located in a slow-velocity region of a relatively thick boundary layer during up-slope flow and in the outer fast-velocity

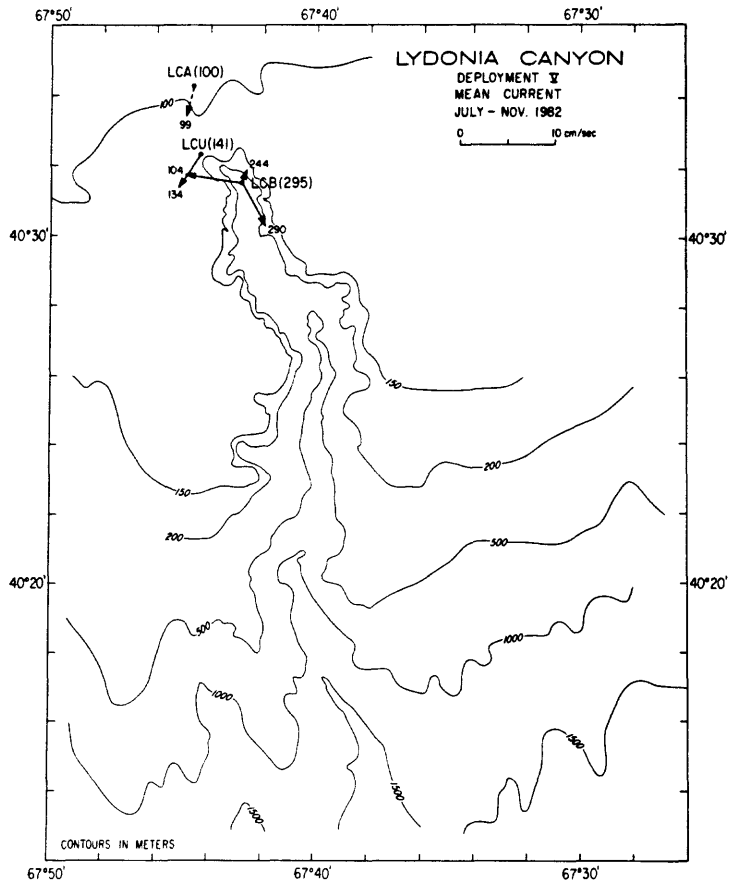

Figure 2-30c. Mean Eulerian current for D5. (see figure 2-29a for explanation of symbols).

region of a thinner boundary layer during downslope flow. The Eulerian mean flow could also result from a complicated spatial current field caused by flow through topographic constrictions within the canyon. The correlation between the strength of the low-passed flow and the amplitude of the fluctuations indicates some non-linear driving. Whatever the cause, the residual Eulerian current may not indicate a net Lagrangian transport of water or sediment. Until these processes are resolved, the net flows, primarily in the canyon axis and near the bottom, should only be interpreted as a measure of the local net flow.

Summary and discussion of the mean flow

The Eulerian mean flow observed in the various moored arrays shows several persistent features (fig.2-31). It is convenient to separate the flow into currents on the shelf (stations LCA, LCL, LCM, and LCB above the canyon sill depth), currents on the continental slope (stations LCI, LCJ, LCK, and at LCN and LCH above the canyon rim), and currents in Lydonia Canyon along the axis and along the walls. At all locations, the mean flow was generally parallel to the isobaths, except near the sea floor on the shelf and slope where there was a significant off-shelf or downslope component.

On the continental slope, the currents were strongly influenced by Gulf Stream eddies (fig. 2-31a). At mid-depth, the monthly mean flow was primarily parallel to the isobaths, and both northeastward and southwestward flow was observed. Near the bottom at LCI, there was a persistent off-shelf component of flow of a few cm/s. On the shelf (LCA, LCL, and LCM), mean flow at mid-depth was southwestward parallel to the local isobaths. At LCB at depths above the canyon rim, the mean flow was southwestward, similar to the flow on the adjacent shelf.

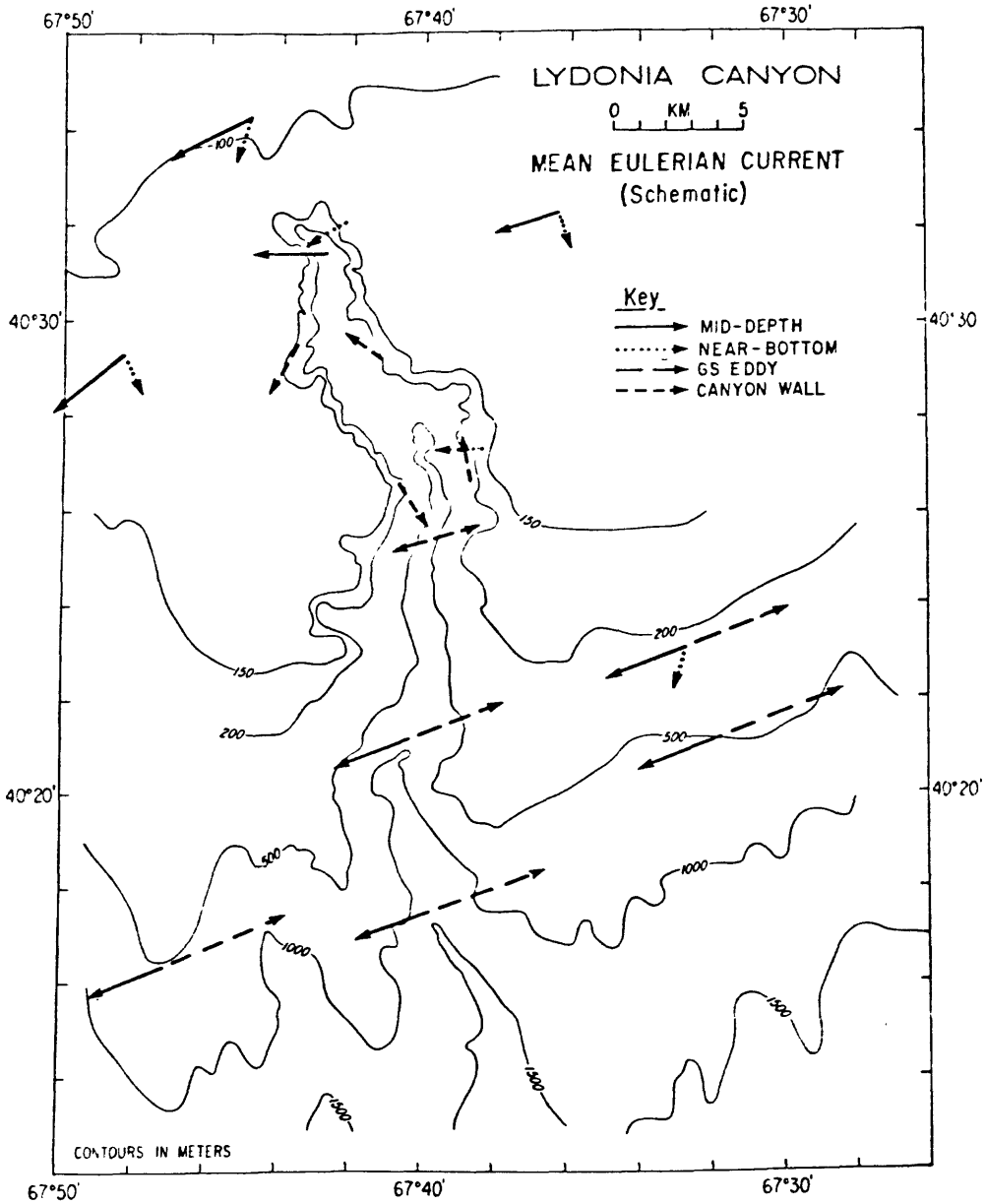

Figure 2-31a. Preliminary schematic of the Eulerian mean flow on the shelf and slope adjacent to Lydonia Canyon and along the walls of the canyon. Solid lines indicate the mid-depth flow and dotted lines indicate the near-bottom flow. On the slope, the arrows indicate flow in the upper 100-200 m. The heavy dashed lines indicate the mean flow when Gulf Stream eddies are located to the south of the canyon and the solid lines indicate flow in the absence of eddies. The light dashed lines indicate flow along the canyon wall just below the level of the adjacent shelf (at about 150 m at the two locations in the head of the canyon, and at about 200 m at the two stations near the mouth of the canyon).

Along the axis of Lydonia Canyon, the near-bottom Eulerian mean flow observed at LCB, LCE, and LCS during D1 through D4 suggest a complex Eulerian circulation pattern (fig. 2-31b). The mean Eulerian flow 6 mab at LCB was consistently down-canyon at speeds on the order of 5 cm/s and the flow 50 mab was generally up-canyon at 1-2 cm/s. At LCE the near-bottom Eulerian mean flow was weaker than at LCB, but there was a weak and variable upcanyon flow 6 mab, and a down-canyon flow about 100 mab. At LCS, near-bottom flow was up-canyon at 5 cm/s. There is clearly a convergence of the Eulerian mean flow between LCB and LCS, which to conserve mass requires outflow at depths between about 300-400 m if the Eulerian and Lagrangian flows are equal. The up-canyon flow at LCB 50 mab, and down-canyon flow 100 mab at LCE may indicate recirculation in small cells in the bottom 200 m near the canyon floor. The convergence of the Eulerian mean flow occurs approximately in the region of fine sediments along the canyon axis, and this convergence may be one of the causes of the sediment accumulation there (see chapter 3).

As mentioned above, the amplitude of the Eulerian mean flow measured at a fixed point may not be the same as the transport of water particles or sediment, especially in the canyon axis where there were large high-frequency current fluctuations. The amplitude of the mean flow which is on the order of 5 cm/s, would transport water from LCS to LCB in only a few days. In addition, the mean flow is perpendicular to the lines of constant temperature, salinity, and density; the relatively stable hydrography is inconsistent with such a strong mean flow perpendicular to isopleths of density.

Finally, the observations on the eastern rim of the canyon (LCP, LCQ) suggest flow from the shelf across the canyon at depths above the canyon rim. The data also suggest that at about 200 m, flow is northward into the canyon along the eastern wall (LCR, LCD) and southward out of the canyon on

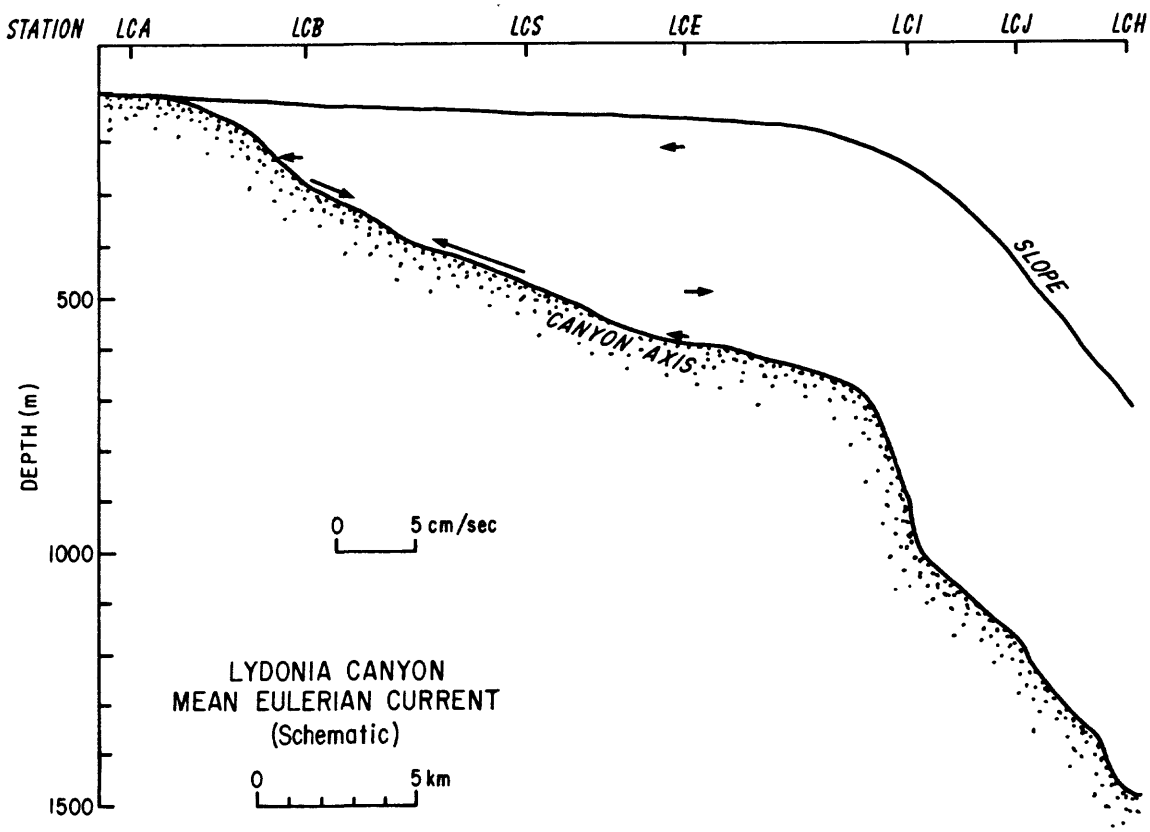

Figure 2-31b. Preliminary schematic of Lydonia Canyon showing upcanyon-downcanyon component the mean Eulerian current at LCB, LCS, and LCE along the canyon axis. Note that the mean Eulerian current may not indicate actual Lagrangian water-particle trajectories. The convergence in the near-bottom flow between LCS and LCB may partially cause the deposit of fine-grained sediments which occur in the upper part of the canyon. If the Eulerian and Lagrangian mean flow are equivalent, the convergence also suggests outflow between 300-400 m, or small closed recirculation cells along the bottom. Data on the adjacent shelf and slope suggests westward flow across the canyon above the level of the rim.

the west wall (LCC, LCT). This may be a mechanism for exchange of water between the outer shelf and canyon head.

Effects of Gulf Stream Warm Core Rings

The monthly mean flow during D1 and the record-averaged means during D2-D5 clearly show the occasional major influence of Gulf Stream WCRs on the flow on the outer shelf. Several questions concerning the WCRs are of particular interest: How often do the rings affect the flow at the edge of the shelf? How far onto the shelf and how deep on the slope do the rings affect the flow? Do the rings at the shelf edge affect the flow within the canyon? What are the strengths of the near-bottom flow associated with eddies? Most of these questions must be addressed by examining individual periods when rings affect the flow; there are not enough WCR events, even in the long-term observations made as part of the canyon experiment, to statistically characterize the flow.

Frequency

Mooring LCI was maintained from D1 through D4 and the observed currents provide a good measure of the length of time that WCRs affected the flow on the slope adjacent to Lydonia Canyon. The low-passed along-slope flow at LCI clearly shows several WCR events, identified by the sustained net eastward current (fig. 2-32). The flow is affected for periods as short as 10 days (WCR 81-C), and as long as several months. Typical low-passed current speeds at 60 m were 40-60 cm/s at 60 m, and 10-30 cm/s at 5 mab. The presence of WCRs was subjectively determined from the Oceanographic Frontal Analysis charts and the occurrence of sustained net eastward flows 5 mab at LCI. Eight periods of WCR influence were identified during the first four deployments of

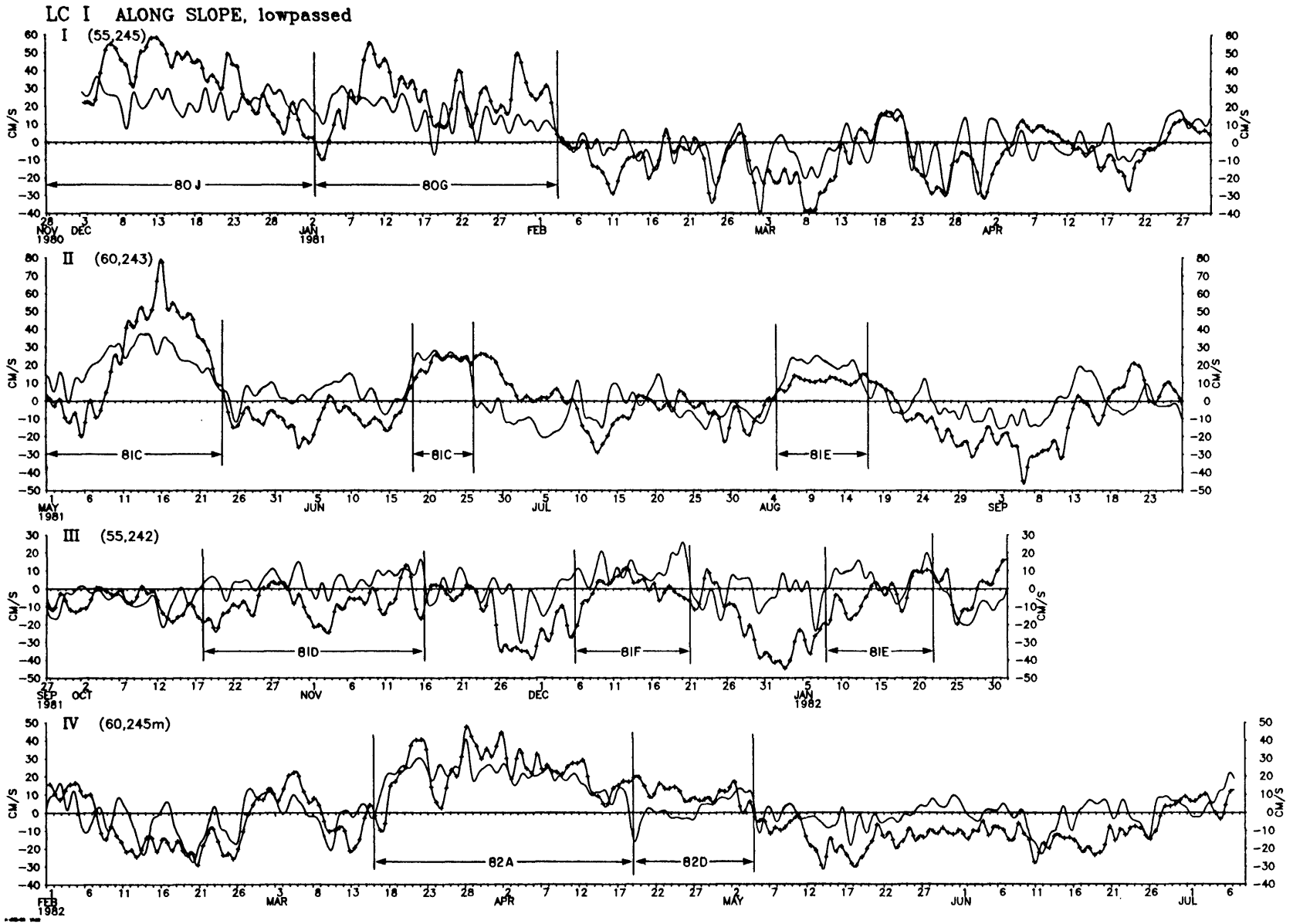

Figure 2-32. Low-passed along-slope component of flow at LCI(55) (pluses) and LCI(5 mab) for D1 through D4. Periods of WCR influence, based on oceanographic analysis charts and sustained eastward flow, are indicated. Positive flow is toward 75°, negative flow toward 225°.

the Lydonia Canyon array, the largest being the nearly two-month period in December 1980 and January 1981 already illustrated by the monthly mean flow during D1. During the 579-day observation period, eddies affected the flow at LCI about 32 percent of the time. This estimate, based on the near-bottom flow at LCI is somewhat subjective, but clearly shows that WCRs affect the flow on the outer edge of the shelf for substantial periods of time. A long-term inventory of WCRs is needed to determine if the 1981-1982 period was typical for WCR frequency and size.

Effects on the shelf and canyon

The array in place during D1 provided good spatial coverage on the shelf and slope and shows that the strong eastward along-slope flow associated with WCR 80-J and 80-G also caused eastward flow of LCE(116), but not at LCA(80), LCB(92) or LCL(65) (fig. 2-33). The near-bottom flow at LCM(119) and LCL(105) was toward the southeast in December 1980 and January 1981, indicating some influence of the WCRs near the bottom. A hydrographic section made across the shelf and slope passing through LCL and LCI in January 1981 (fig. 2-15a) shows that these near-bottom instruments were in slope water, just seaward of the shelf-water/slope-water front. In this case, the eastward flow associated with WCRs apparently extended to but not across the front.

The observations made along the slope in D1 show the depth to which WCRs affect the net along-slope flow. At LCI, the net eastward flow was observed 5 mab during both WCRs 80-J and 80-G. In fact, the net eastward flow was most persistent below the shelf-water/slope-water front at LCI(195) and LCI(245). The flow was more variable, especially at 10 m, as the apparently sharp front separating ring and shelf-water moved slightly on-shelf and off-shelf (see fig. 2-32). At LCJ, the net eastward flow was observed during WCR 80-J and

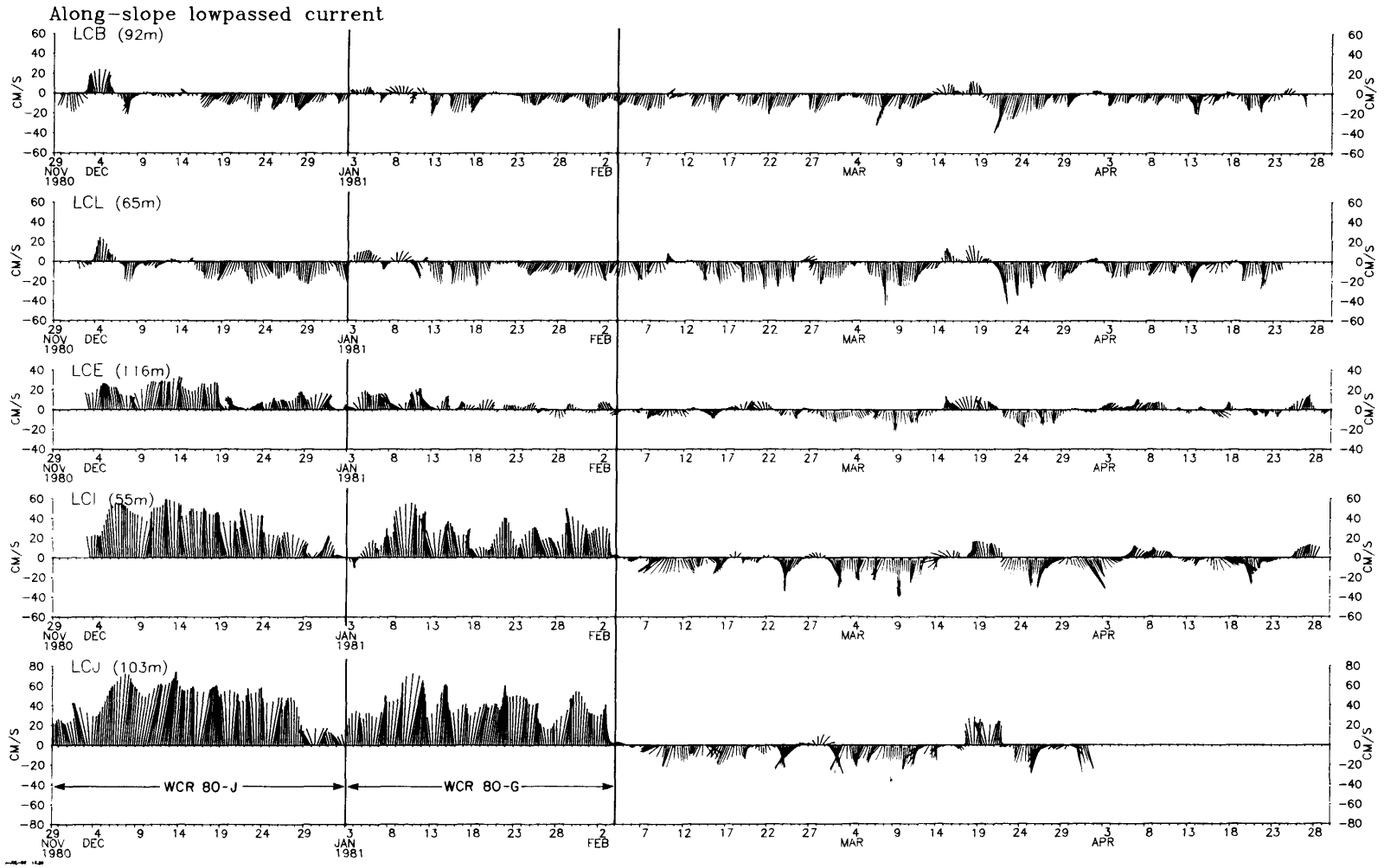

Figure 2-33. Vector stickplot of low-passed current at LCB(92), LCL(65), LCE(116), LCI(55), and LCJ(103) during D1. Periods of WCR 80J and 80G are indicated. Eastward flow on the slope extends to LCE, but not to LCB. Positive along-slope is up, positive cross-slope to the left.

80-G at 83 and 223 m, but not at 471 m. Eastward flow was observed at LCK(204) and LCH(290) during both rings, and there was some suggestion of eastward flow associated with the rings at LCK(454) and LCH(590). Thus for those two WCRs, effects were observed to about 500 m to the west of Lydonia Canyon, and to less than 400 m to the east.

The array of instruments at LCB, LCL, LCQ, LCR and LCT in place during D4 (January to July 1982) provide a limited picture of the circulation at a depth of about 200 m in the outer part of the canyon associated with a WCR. The weekly National Weather Service Oceanographic Analysis charts show WCR 82-A to southeast of station LCI on March 9, 16 and 23, and to the south of LCI on March 30 and April 6. The ring was about 150 km in diameter between March 9 and 30, and about 100 km in diameter on April 6. Between April 6 and 20, WCR 82-A was involved with a northward meander of the Gulf Stream and was displaced southeastward of Lydonia Canyon on April 13 and eastward on April 20. WCR 82-D formed from this northward meander and is first shown on the oceanographic analysis chart of April 20. WCR 82-D remained south of Lydonia Canyon until about May 11.

The flow at LCI clearly reflects the eastward flow on the north side of these eddies (fig. 2-32). At LCI(59) sustained eastward flow occurred from March 18 to May 2, and at LCI(245) the low-passed flow was consistently eastward from March 18 to April 18. Between April 18 and May 5, the flow was weaker but still eastward, apparently influenced by WCR 82-D. Between March 18 and April 2, the net flow at LCT(178), just below the rim on the western side of the canyon, was southeastward. On the eastern side of LCR(183), flow was northward (fig. 2-34). At LCQ(180), the flow was consistently westward with an increased northward component during the period of time the eddy was to the south of the canyon. At LCB(108) and LCL(124), there were periods of

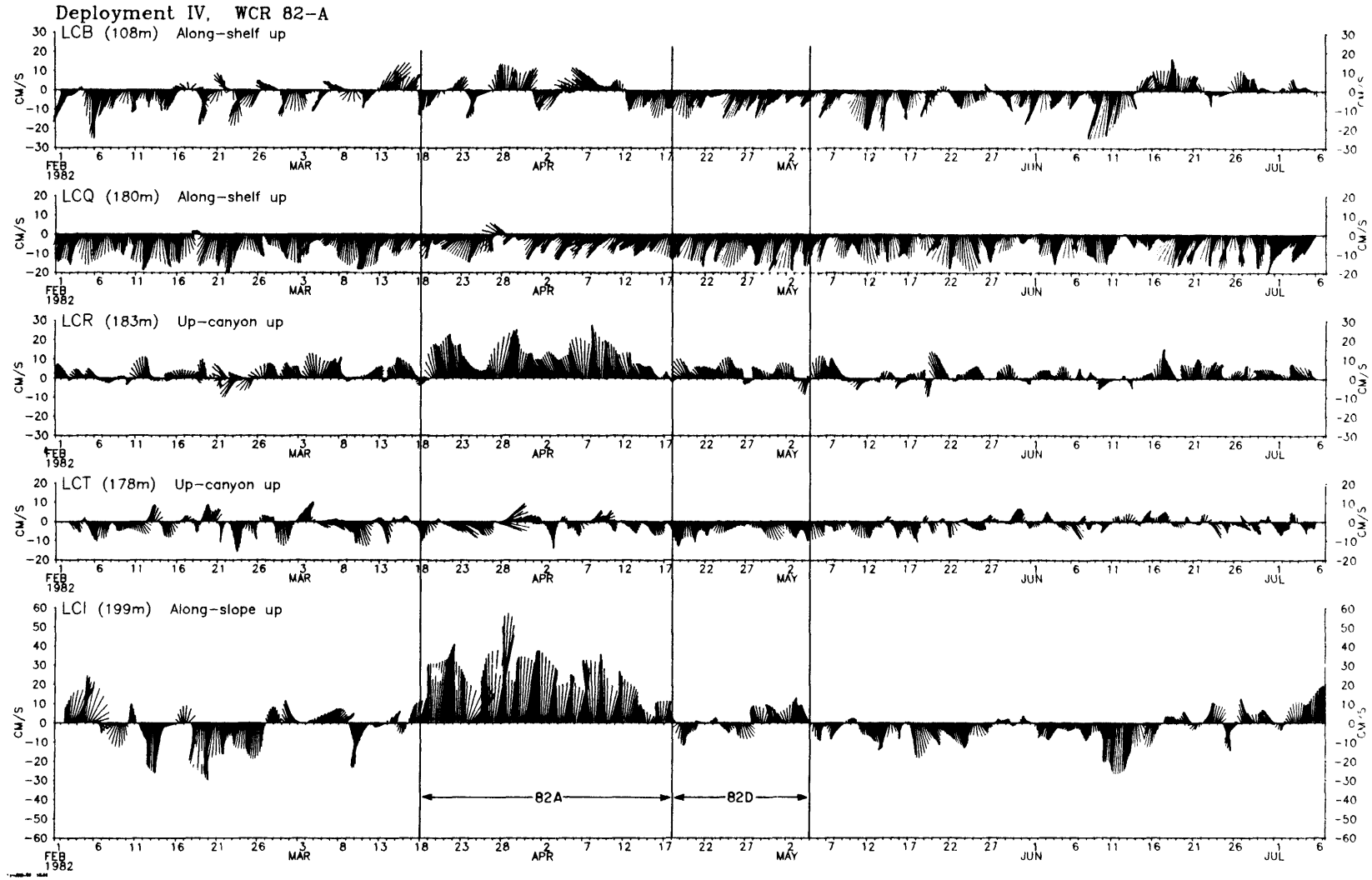

Figure 2-34. Vector stickplot of low-passed current at LCB, LCQ, LCR, LCT and LCI during D4. Positive alongshelf at LCB and LCQ is toward 75°, positive upcanyon at LCR and LCT is toward 10° and 0° respectively, and positive along-slope at LCI is toward 75°.

both eastward and westward alongshelf flow. At LCI, there were fluctuations in the along-slope flow of order 20 cm/s superimposed on the sustained eastward current. Increases in flow to the east at LCI(199) were correlated with eastward (cross-canyon) flow at LCT(178), northward (up-canyon) flow at LCR(183), and eastward flow at LCB(108) (fig. 2-34). Temperature at 200 m at all mooring sites was well correlated throughout the canyon during D4 and during the period of WCR 82-A and 82-D (fig. 2-35). The warmest water was at LCI and on the western side of the canyon. At all stations the water was warmest during the first 15 days of the eddy period (March 18 to April 2), when WCR 82-A was located to the southeast of Lydonia Canyon.

A measure of the flow induced by WCR 82-A was determined by subtracting the mean flow during the non-WCR period (January 31 to March 17 and May 5 to July 7) from the mean flow during the WCR 82-A event (March 18 to April 14). These ring-induced flows are a strong eastward flow at LCI of about 30 cm/s, weak eastward flow of about 1 cm/s at LCB(108) and LCT(178), and a moderate northward flow of about 5 cm/s on the eastern rim at both LCR and LCQ (fig. 2-36). There is also a weak down-canyon flow at LCB(294), suggesting an influence of WCR's deep in the canyon near the head.

Effect on near-bottom current speeds

The strong eastward currents associated with eddies causes strong current speeds near the bottom on the upper slope. At LCI the average near-bottom speed during the periods of WCR influence was about 22 cm/s, but only 13 cm/s during non-eddy periods (fig. 2-37). The strongest speeds occur during WCR events; speeds 5 mab exceeded 30 cm/s about 20 percent of the time when rings were present and only about 3 percent of the time when rings were not present. The modal bottom current speed during rings is shifted upward about 15 cm/s, driven by the net eastward flow of about the same order.

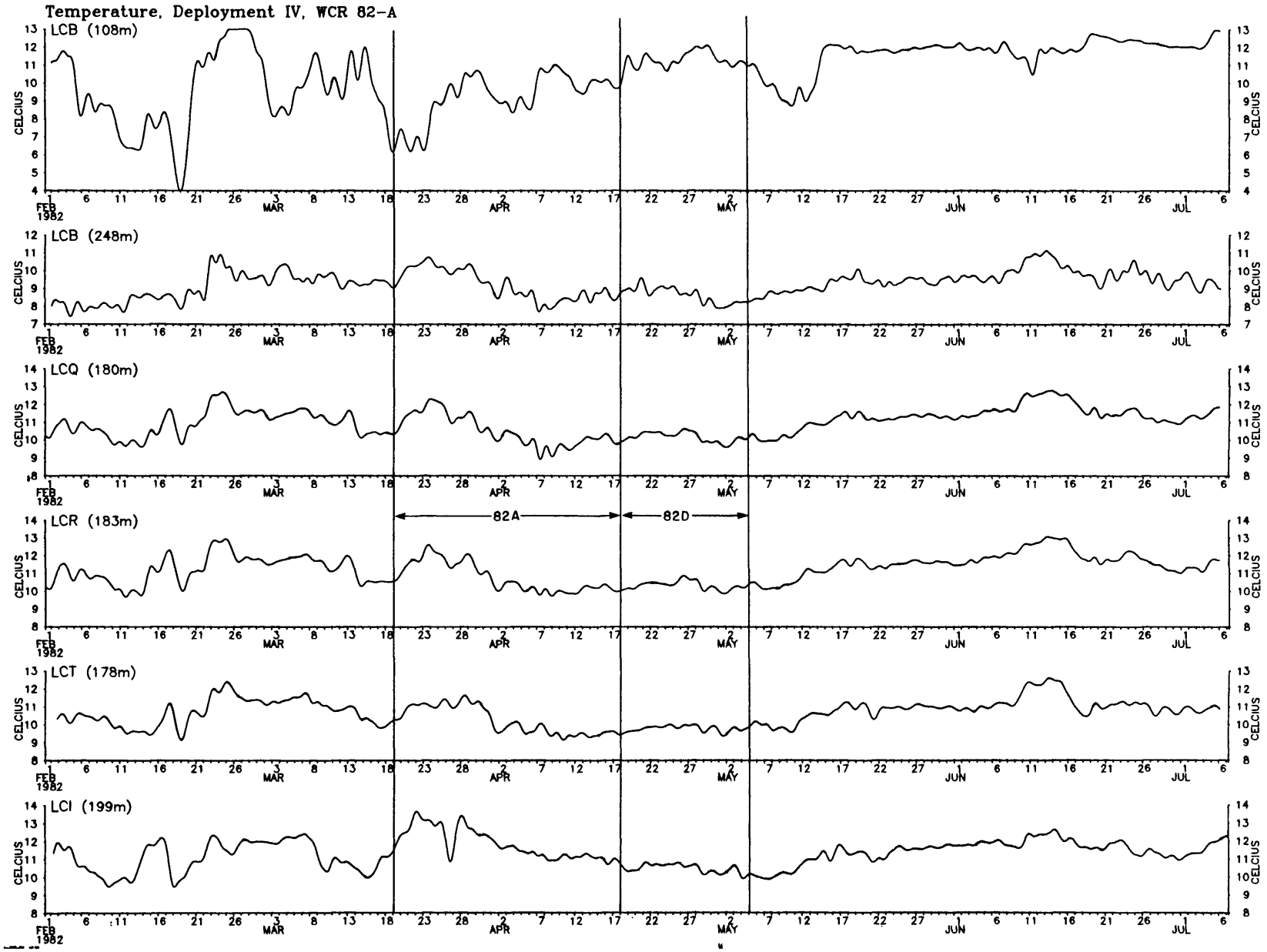

Figure 2-35. Low-passed temperature at selected stations during D4. Periods of WCR 82-A and 82-D are indicated.

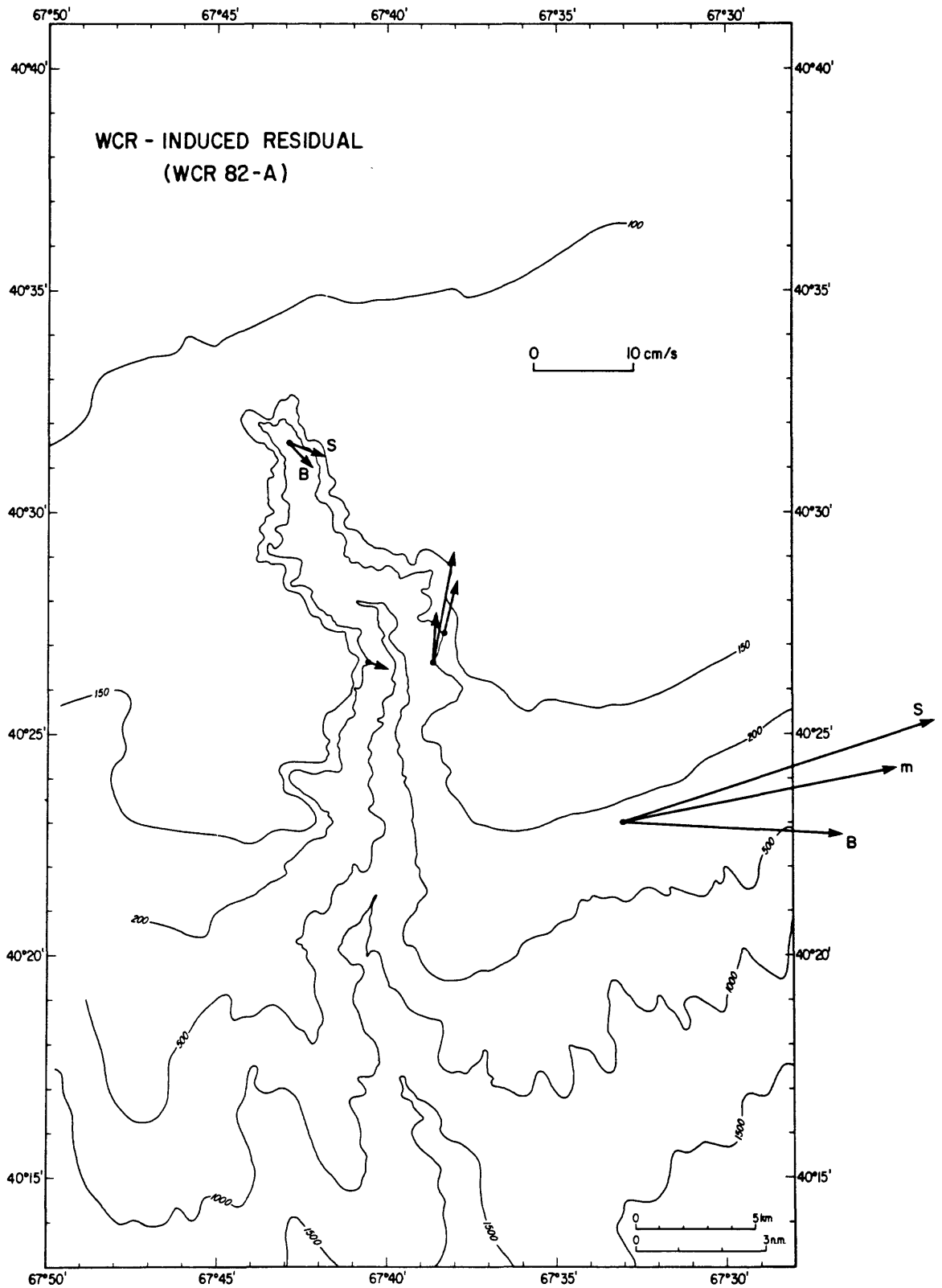

Figure 2-36. Schematic of flow induced by WCRs around the mouth of Lydonia Canyon at about 200 m based on observations made during WCR 82-A.

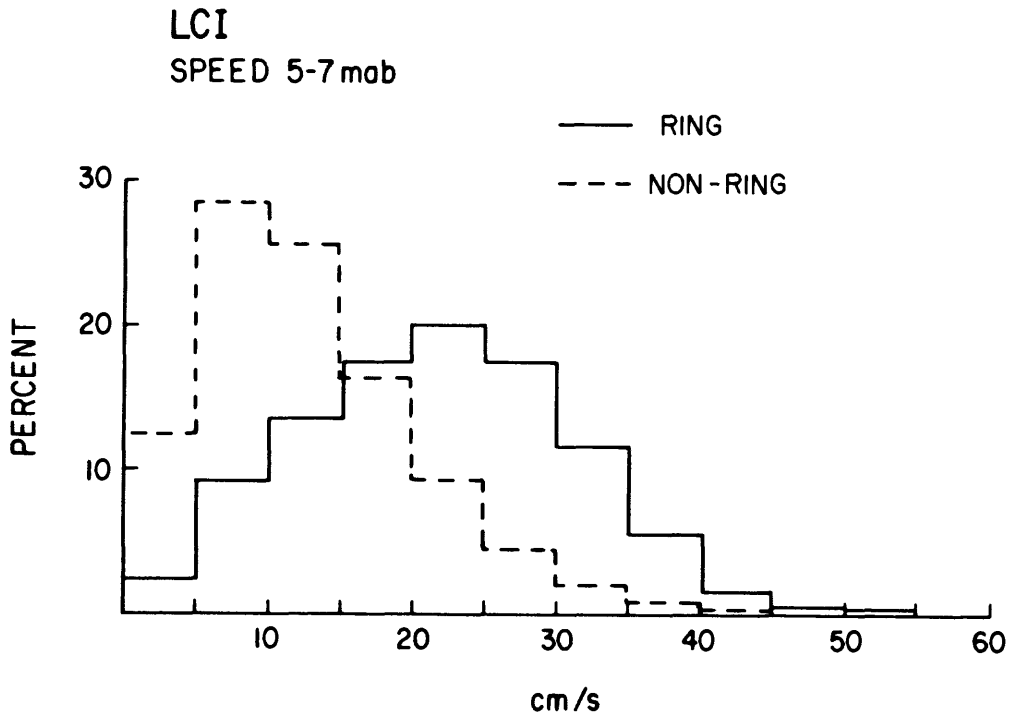

Figure 2-37. Histogram of current speeds 5 mab at LCI during ring and non-ring periods.

Currents near the bottom and sediment transport

The previous statistical analyses of the current observations suggest an orderly flow pattern within the canyon, composed of fluctuating components at various frequencies aligned with the canyon axis superimposed on a mean flow. However, time series of temperature, current, and beam attenuation show that the near-bottom flow in the canyon is often not symmetric and changes rapidly with time. The near-bottom currents at some locations, especially in the axis, are quite chaotic, and there is evidence for vertical and horizontal mixing and sediment resuspension. Although it is beyond the scope of this overview to present an exhaustive analysis of these flows, data selected from a few stations along the canyon axis are presented to illustrate the asymmetry of the current fluctuations and the implications for sediment transport.

The current speeds near the bottom in the canyon axis are strongest at LCE and LCS where they exceed 40 cm/s about 10 percent of the time (fig. 2-38). The currents are weaker at LCB and LCU where they exceed 40 cm/s less than about 3 percent of the time. The currents are weakest at LCH where they never exceed 20 cm/s. Qualitatively, the speed statistics match the surficial sediment texture along the axis; coarser grain sands with little silt and clay occur at LCE and LCS where the currents are strong, while finer grained sand occurs at LCB and LCU. The finest sediments occur at LCH where the currents are weakest.

In the canyon axis at LCU, LCB, LCS, and LCE, the near-bottom flow is characterized by fluctuations in the inertial and semidiurnal bands and at a broad range of higher frequencies primarily oriented along the canyon axis. The current fluctuations are spiky; there are periods of moderate flow in one direction of the axis, followed by a shorter period of stronger flow in the other direction. For example, at LCB1(277) there is moderately weak down-

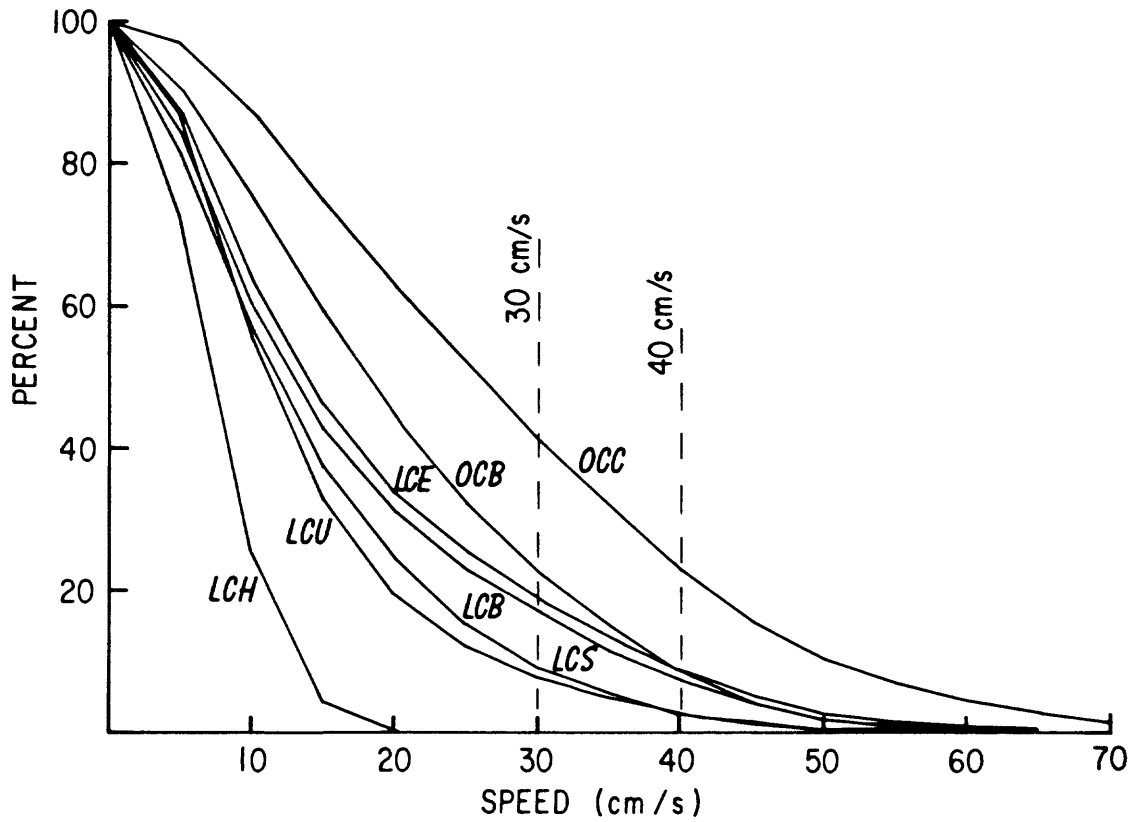

Figure 2-38. Cumulative speed distribution curve for stations along the canyon axis showing percent occurrence in excess of given speed. All measurements at 5 mab.

canyon flow of 10-20 cm/s followed by short up-canyon pulses that sometimes exceed 40 cm/s (fig. 2-39a). The temperature fluctuations associated with this flow are also not symmetric. There is a gradual increase in water temperature during the down-canyon flow, but the temperature falls rapidly, sometimes as much as 3°C as the flow changes to up-canyon. There are also rapid and large changes in beam attenuation, some of which occur during strong speed events. At LCB4(294), the up-canyon flow is smoother and clearly defined increases in beam attenuation at maximum up-canyon flow (fig. 2-39b). There is no increase in beam attenuation during the following down-canyon flow, even though the near-bottom speeds are comparable. (See chapter 3 for a more detailed discussion of these fluctuations).

At LCE1(595), the up-canyon component of flow is more symmetrical than at LCB (fig. 2-39c). However, there are some periods when the temperature is nearly constant in time which occur at maximum up-canyon flow, suggesting vertical mixing. The beam attenuation shows rapid changes, many of which occur at peak current speed in a tidal cycle. During one period at LCU(134), maximum beam attenuations occur at maximum off-shelf water particle excursions, suggesting a direction of the more turbid shelf-water past the instrument site at least during some parts of the observation period (fig. 2-39d). The observations of near-bottom beam attenuation and flow along the axis suggest a range of sediment transport processes; at some stations advection controls the concentration of suspended particles, at others local resuspension occurs, and at others the cause of beam attenuation changes are unclear.

The interpretation of the beam-transmissometer observations is complicated by the varying sensitivity of the instrument to grain size. For example, a change of 1 mg/L of very fine silt (4-μ diameter) will cause a

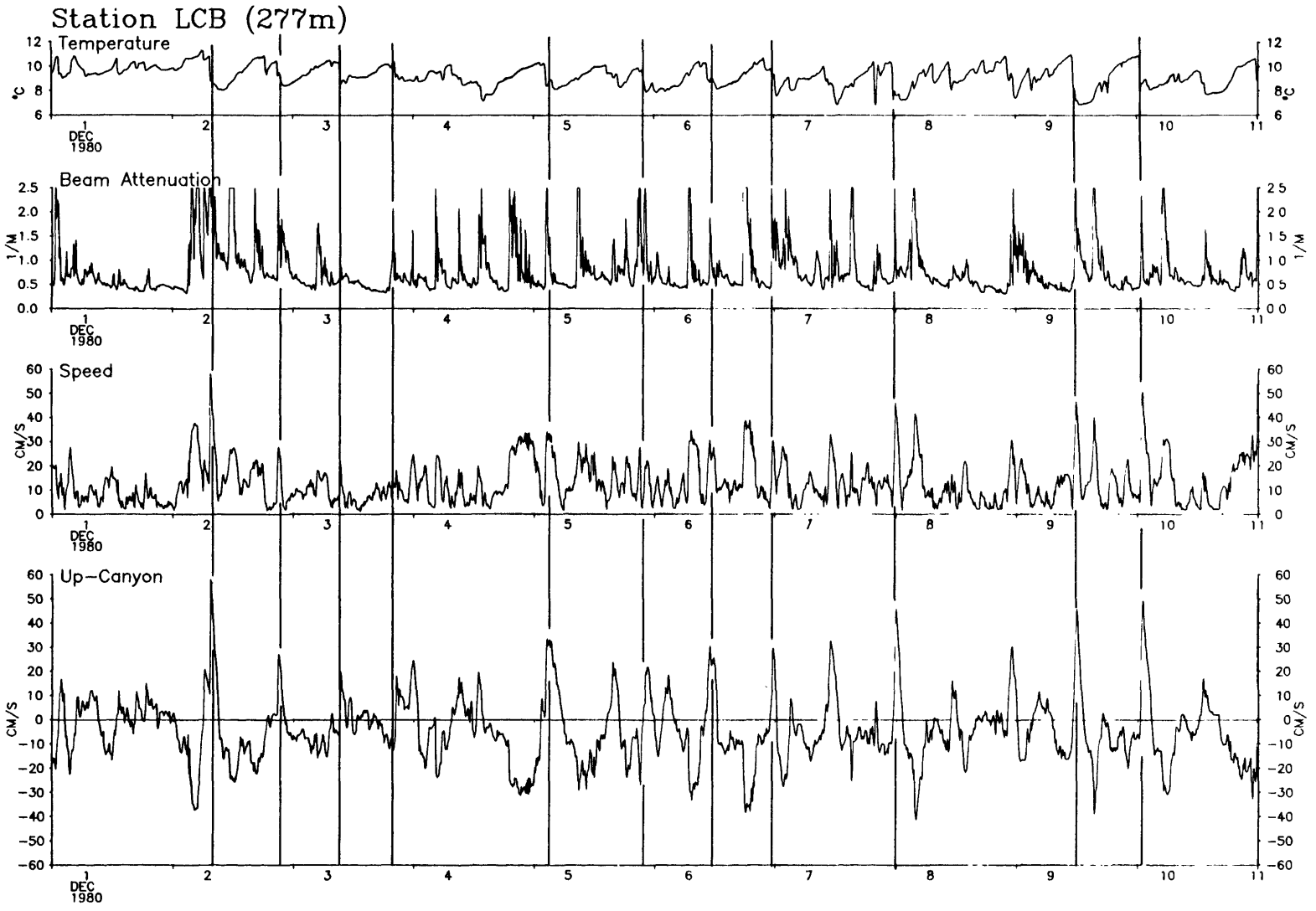

Figure 2-39a. Time series of temperature, beam attenuation, speed and upcanyon current at LCB1(5 mab). Selected events are joined by vertical lines. Data are every 7.5 minutes.

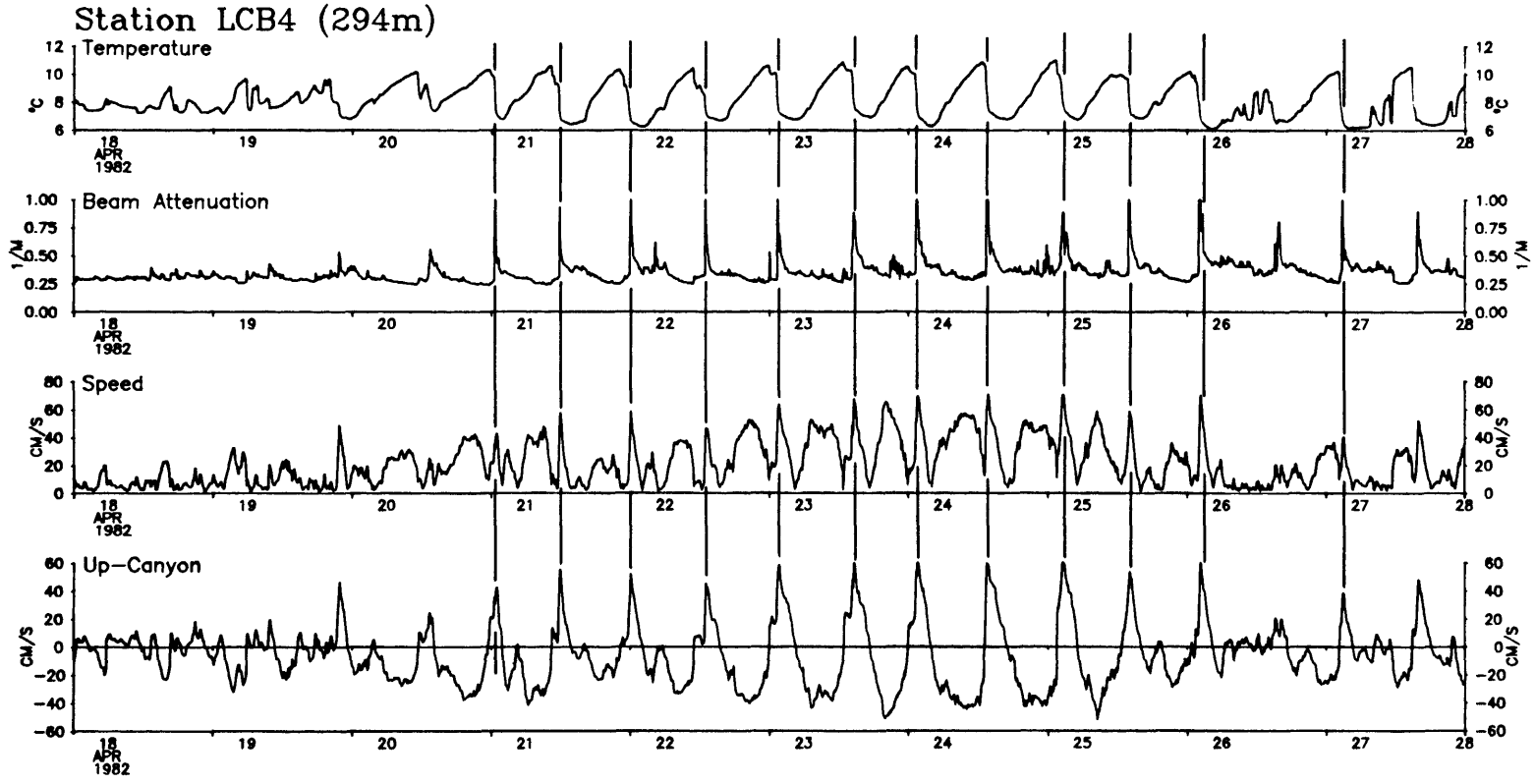

Figure 2-39b. Time series of temperature, beam attenuation, speed and upcanyon current at LCB4(5 mab). Selected events are joined by vertical lines. Data are every 7.5 minutes.

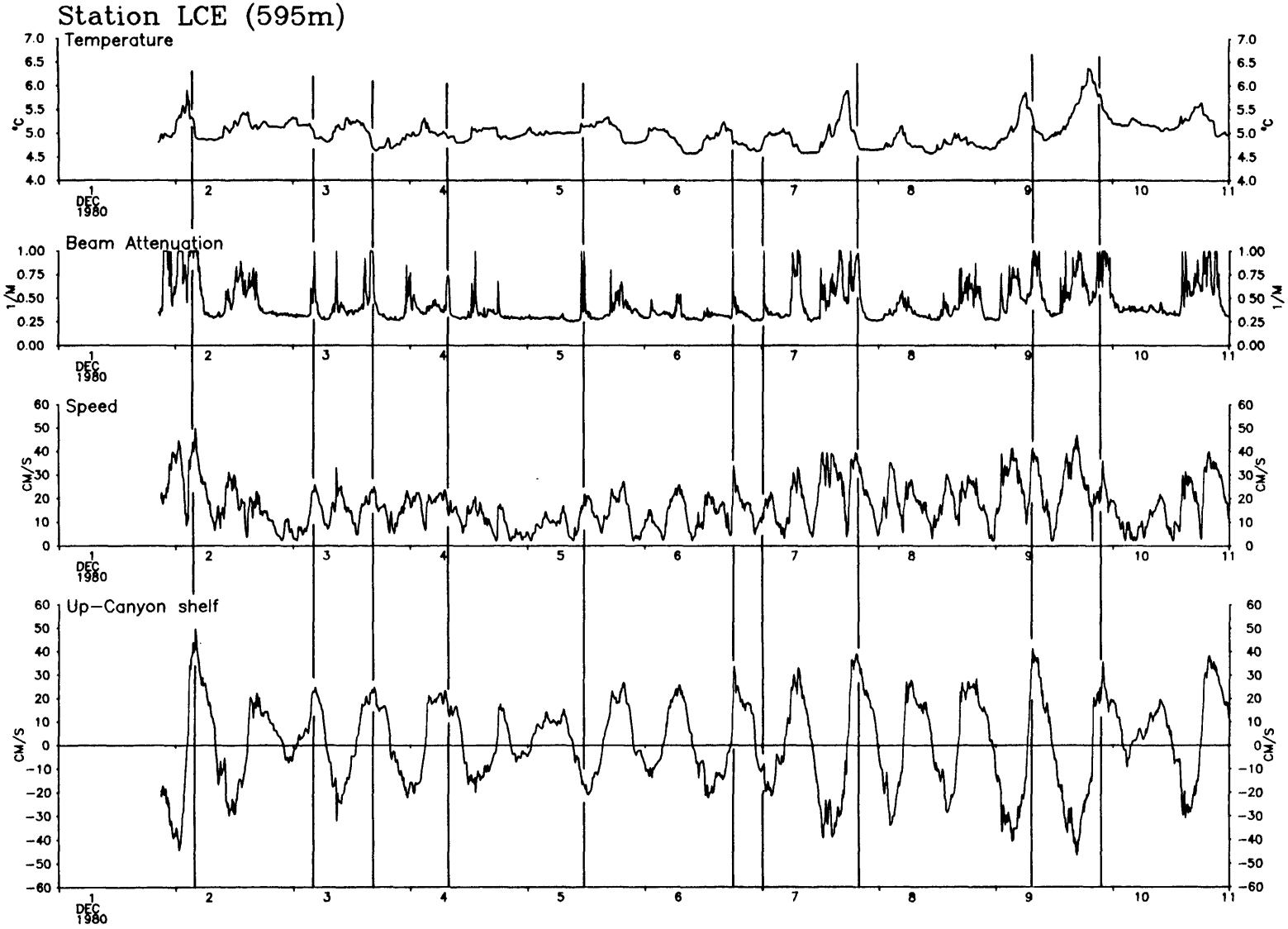

Figure 2-39c. Time series of temperature, beam attenuation, speed and upcanyon current at LCE1(5 mab). Selected events are joined by vertical lines. Data are every 7.5 minutes.

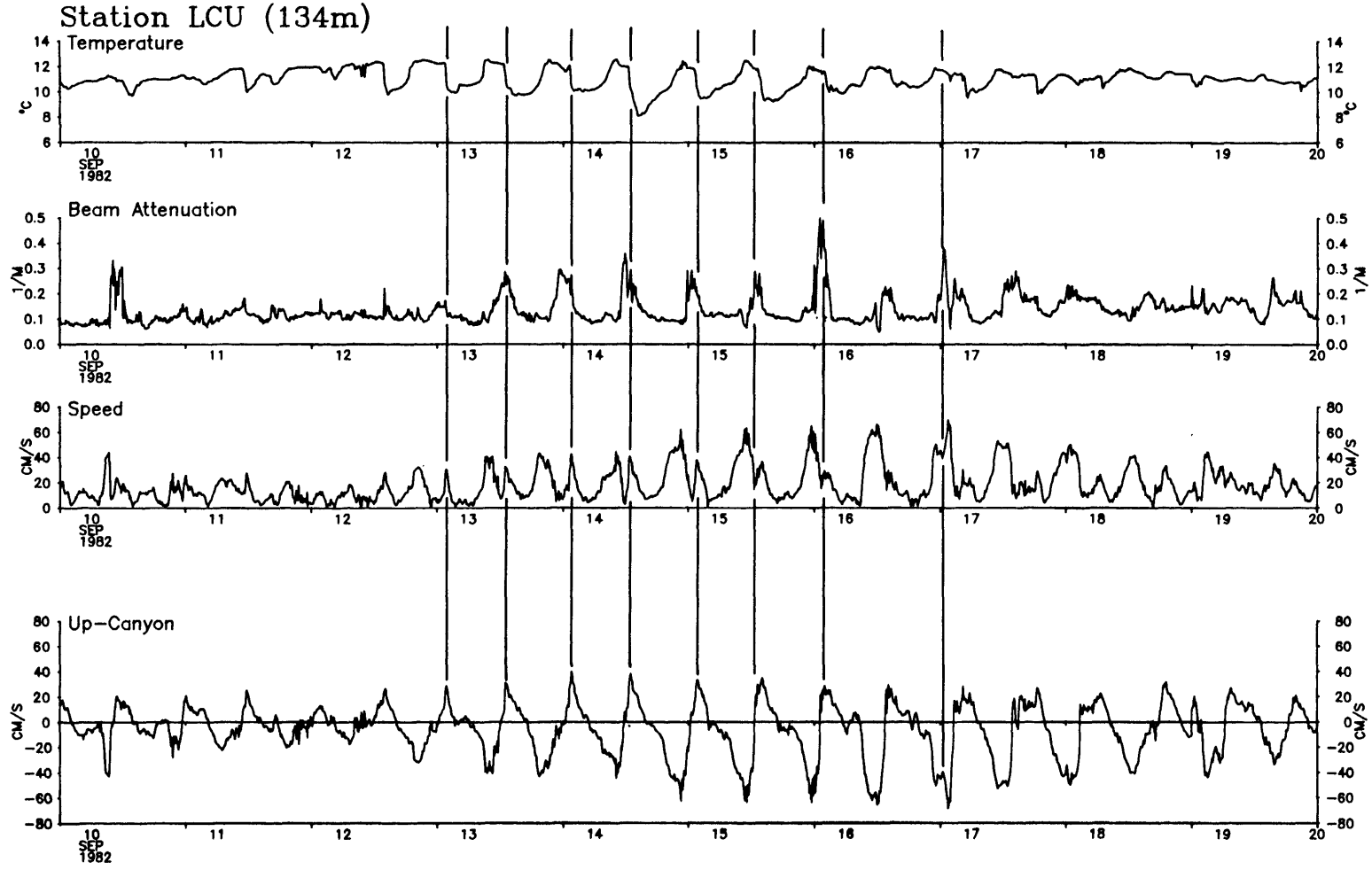

Figure 2-39d. Time series of temperature, beam attenuation, speed and upcanyon current at LCU(5 mab). Selected events are joined by vertical lines. Data are every 7.5 minutes.

change in beam attenuation of about 0.25 m^{-1}, while an equivalent change of very fine sand (62-μ diameter) will cause a change of only about 0.016 m^{-1} (see chapter 9). Because of this sensitivity to fine particles, which fall slowly and remain in suspension for long periods of time, the beam attenuation measurements reflect not only local processes (resuspension and mixing) but also advection from distant sources.

Scatter plots of the currents along the axis show some asymmetry in flow direction, especially for the strongest speeds (fig. 2-40). At LCB and LCS, the scatter plots are S-shaped. At LCB, maximum down-canyon flow has a significant eastward component and maximum up-canyon flow has a westward component. These direction changes may partially reflect the canyon geometry; water particle displacements during some of the strongest flows are easily 3-4 km, a significant fraction of the canyon's axis length.

The asymmetry in the flow direction of the strongest speeds changes along the axis of the canyon and determines the direction of bedload transport of sediment. The percentage of speeds greater than 30 cm/s and between 20 and 30 cm/s as a function of direction is shown in figure 2-41. At LCU and LCB, the strongest currents are in the down-canyon direction; at LCS, the strongest currents are in the up-canyon direction. At LCE, the strength of currents in the up-canyon and down-canyon direction are about equal. The asymmetry implies down-canyon transport of sediments that move as bedload at LCU and LCB, and up-canyon transport at LCS. The convergence in along-canyon transport suggests that the canyon head between LCB and LCS is a region of accumulation of sands. More detailed calculations of the transport along the axis using a one-dimensional model confirm this convergence (see chapter 3). The transport of finer grained silts and clays, which remain in suspension for long periods of time, are more influenced by the mean circulation. However,

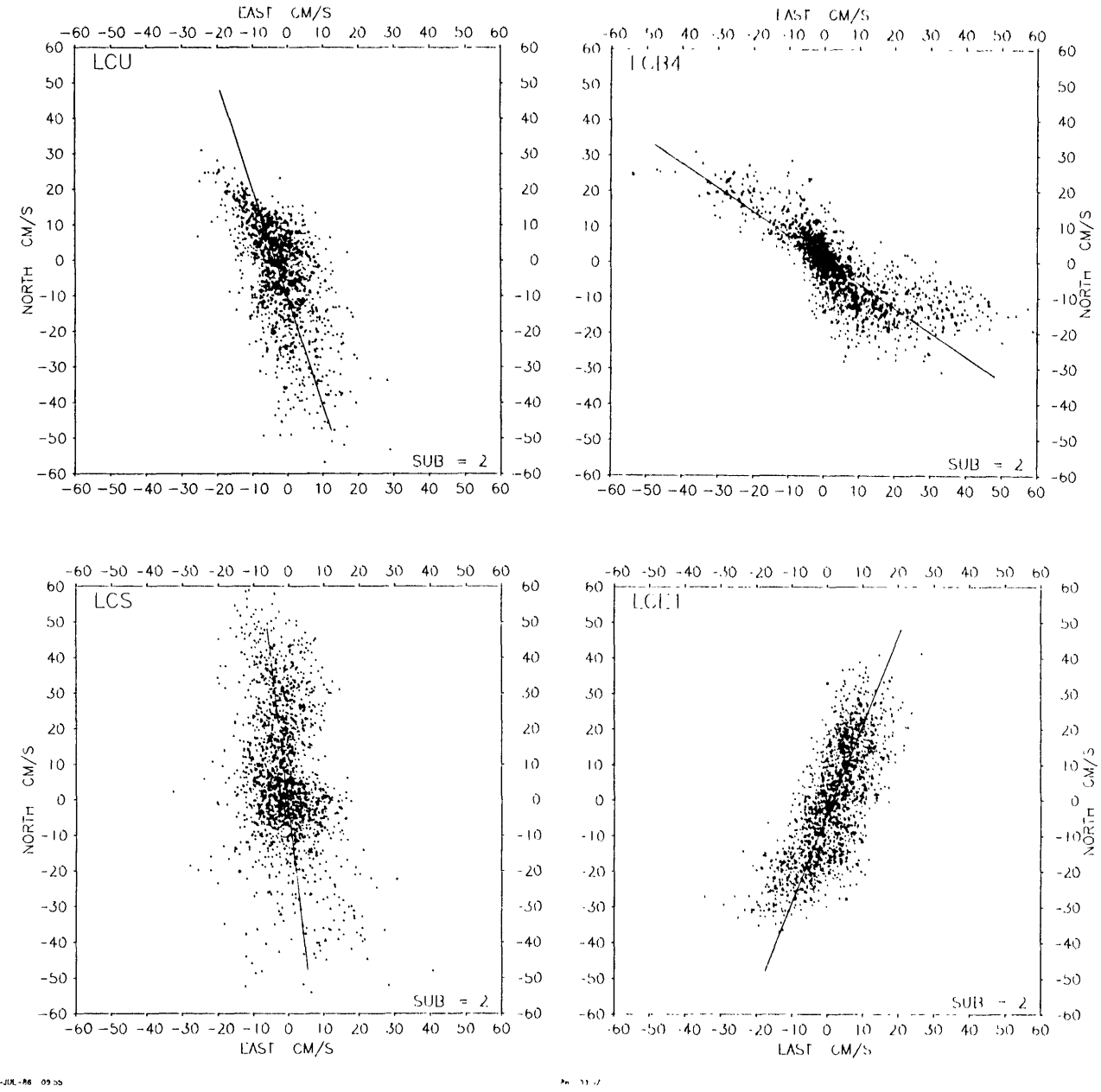

Figure 2-40. Scatterplot of hour-averaged currents at LCU, LCB, LCS, and LCE.

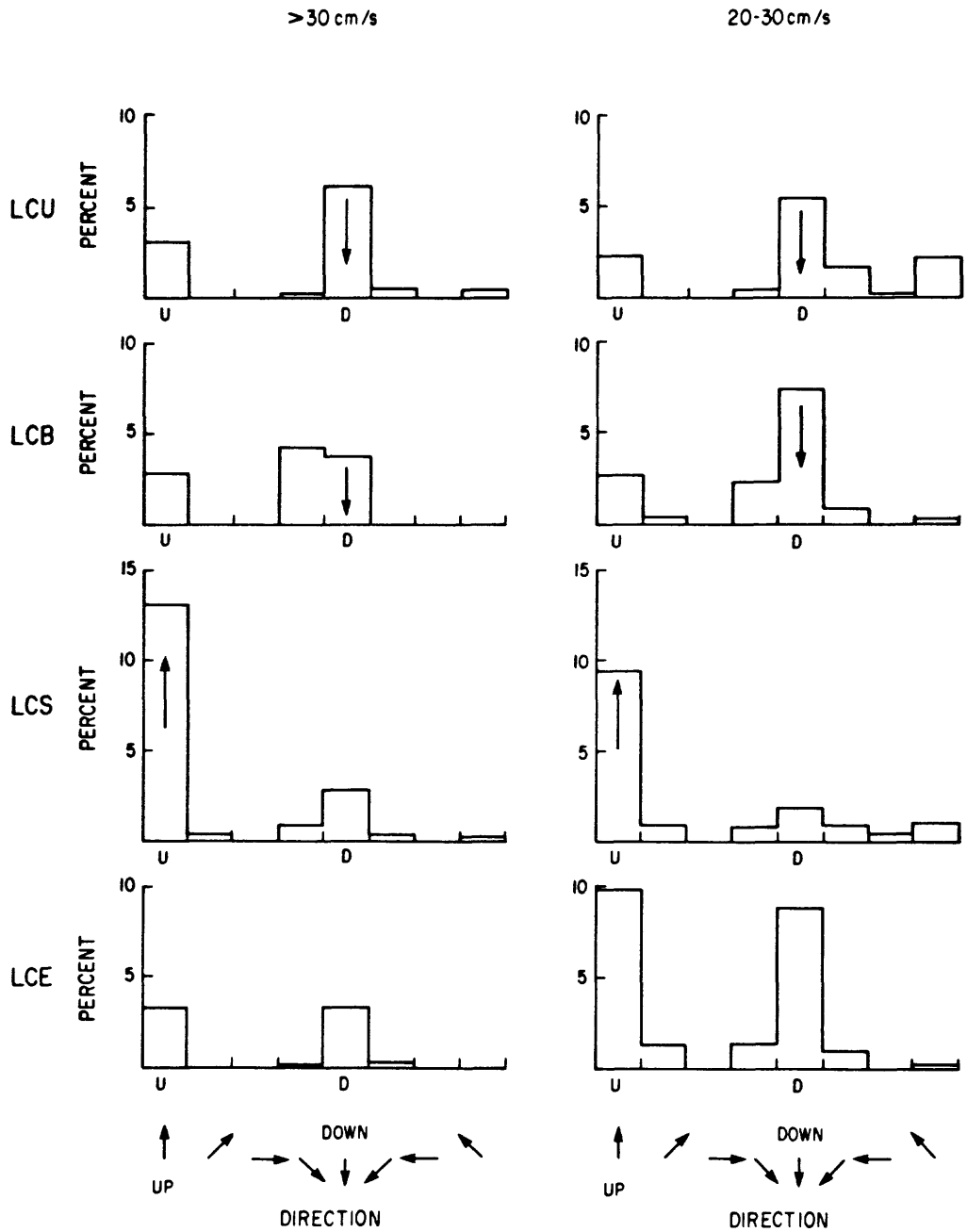

Figure 2-41. Histogram of near-bottom currents greater than 30 cm/s and between 20 and 30 cm/s as a function of direction for stations along the axis of Lydonia Canyon. At stations with a much higher percentage of strong upcanyon (downcanyon) current, the net transport of sediment as bedload is in the upcanyon (downcanyon) direction. Where there is a clear asymmetry, arrows indicate the net transport direction.

the Lagrangian transport pattern is not well defined because of the many non-linear processes implied by the current observations.

Effect of Storms

Storms are one of the most important processes causing sediment resuspension on the outer shelf (see chapter 3 and Butman, in press). The oscillatory currents associated with surface waves increase the bottom stress, and net flows associated with the shelf-wide response to the wind can transport the finer sediments over long distance. Over the southern flank of Georges Bank, currents are primarily driven by the alongshelf component of wind stress. Canyons may intercept and capture this alongshelf transport, especially for flow to the southwest when flow near the bottom should be off-shelf. In addition, the alongshelf flow is in geostrophic balance with a cross-shelf pressure gradient (Noble and others, 1983). In the simplest model, this shelf-wide pressure gradient may drive up-canyon flow when the alongshelf flow is toward the northeast and down-canyon flow when the alongshelf flow is toward the southwest. The strength of the current response in the canyon depends on the cross-shelf pressure gradient and any internal readjustment of the density field. Again, down-welling events would be most favorable for transport into the head of the canyon. Statistical analysis of the low-frequency currents during D1 did not show much coupling between the shelf and canyon (see chapter 5), but individual major storms may affect the flow within the canyon which is not captured in the record-averaged statistics.

The burst pressure measurements obtained by the tripods on the shelf indicate the occurrence of pressure fluctuations associated with storms near the bottom (fig. 2-42). These fluctuations are caused by swell waves, at

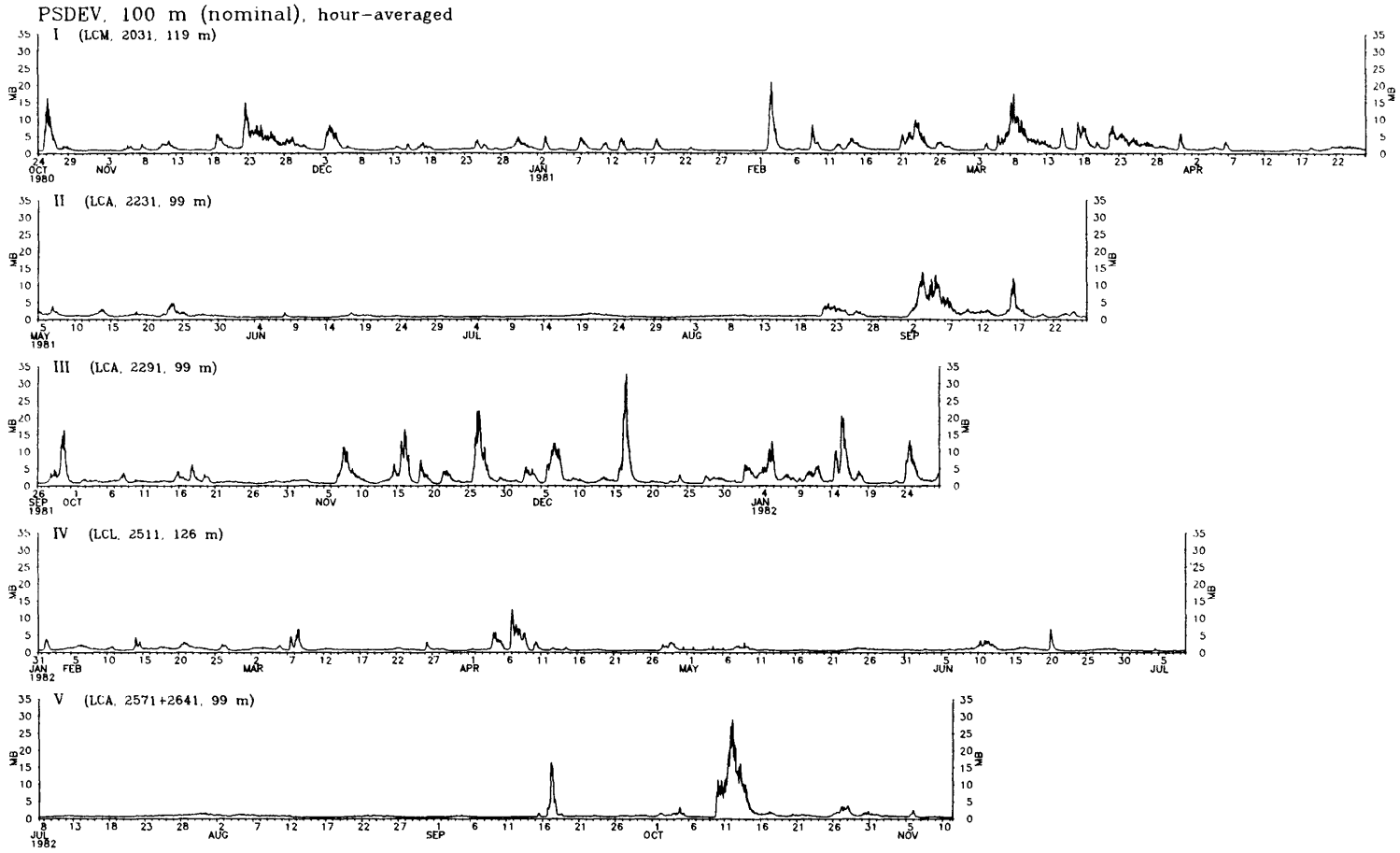

Figure 2-42. Standard deviation of bottom pressure at shelf stations during D1 through D5 indicating periods of major wave activity near the bottom.

periods longer than about 12 sec., and qualitatively show the frequency and intensity of major storms. The storms are strongest and most frequent in fall and winter (November through March) and weaker and less frequent in spring and summer.

The available temperature, salinity, beam attenuation and current records were examined for the major storms which occurred on March 8, 1981, November 20, 1981, and October 11, 1982. These three storms were selected for analysis because they caused mixing within the head of the canyon (see chapter 4) and major resuspension of sediment as found in the sediment traps on the shelf (see chapter 6). Several questions are of interest: Is there evidence that sediment suspended on the shelf during storms is carried over or into the canyon? Are there changes in the temperature, salinity, beam attenuation, and currents in the canyon during these storms?

During all three storms the peak near-bottom swell, as measured by the tripod systems, followed the peak wind-stress as measured at Nantucket Lighhship and at EB63 (located near Great South Channel). The generation of swell is determined by the strength, fetch, direction and duration of the wind systems, and local wind stress is not always a good measure of local swell. As an example, during the October 11 storm, peak swell occurred on October 12, 1981, but local wind stress reached a maxima on October 9. This storm intensified as it traveled eastward off the continental land mass. At least for swell, some of the strongest waves which cause sediment movement propagate from distant storms and thus do not occur at times of maximum wind stress.

Near bottom beam attenuation measurements on the shelf show sediment resuspension during all storms, and a net alongshelf flow across the canyon axis. During both the March 8, 1981 and November 26, 1981 storms, increased beam attenuations were observed at LCB(100), confirming a transport

resuspended shelf sediment over the canyon axis. For the storms with southwestward flow across the axis above the canyon rim, the bottom of the shelf/slope front moves slightly off-shelf, based on decreased salinity and temperature measured at LCB(100). Most of the high beam attenuations are associated with this colder shelf water.

It is difficult to unambiguously correlate changes at depths below the rim in the canyon with major storms on the shelf. The clearest signal is the increased salinity anomalies at LCB near the bottom which indicate freshening or warming of the near-bottom water (see chapter 4). At LCE(5 mab) there were increased fluctuations in temperature and beam attenuation 1 to 2 days following the March 8 storm, and the strongest low passed down-canyon flow observed at LCE during D1 occurred on March 9. Otherwise, the fluctuations in temperature, current and beam attenuation were typical of everyday conditions. In the canyon time series observations, the storms are not major signals, as they are in the shelf observations.

In summary, there is evidence that resuspended shelf sediment is carried across the canyon axis above the rim during storms. Some of this material must settle and be captured in the canyon head. Most of the flux into the canyon should occur toward the shallowest part of the shelf where the waves are strongest, thus most effective in resuspending sediment and during downwelling-favorable (southwestward) flow. Within the canyon, further analysis is needed to separate any (weak) storm signals from the everyday currents.

Currents in Oceanographer Canyon

Near-bottom current observations were made in the axis of Oceanographer Canyon at about 230 m and 600 m, locations in the axis comparable to stations

LCB and LCE in Lydonia Canyon, to compare the current and sediment transport regimes in the two canyons. The currents in Oceanographer Canyon were similar in frequency and orientation to those in Lydonia but were more energetic, primarily at semidiurnal periods. Average current speeds 5 mab were 19 and 27 cm/s at OCB and OCC, respectively, compared to about 12 and 15 cm/s at LCB and LCE (table 2-8). The speeds at OCC were the strongest observed in the canyon experiment and exceeded 40 cm/s about 23 percent of the time (fig. 2-38). Strongest speeds were in the down-canyon direction, suggesting down-canyon transport of sediment at both OCB(223) and OCC(554) (fig. 2-43). At OCB and OCC, the net Eulerian flow was also down-canyon at about 5 cm/s (fig. 2-44).

One of the most striking current records made as part of the canyon experiment was obtained in the axis of Oceanographer Canyon at OCC(554) (fig. 2-45). Here the current fluctuations at semidiurnal period sometimes exceeded 80 cm/s in the down-canyon direction. The beam attenuation observations show increased suspended sediment concentrations during these fluctuations and the amplitude of the temperature changes, using the hydrographic sections to estimate the mean temperature gradient, suggests internal wave amplitudes as large as 150 m. The near-bottom measurements show that Oceanographer Canyon is an extremely active canyon; the semidiurnal tidal currents are strong and there is a net down-canyon transport of sediment as bedload at 220 and 600 m.

DISCUSSION

The topography of Lydonia Canyon, its location at the transition between continental shelf and open ocean, and the density stratification make the currents in and around the canyon especially complex. The currents fluctuate over a wide range of frequencies, and the amplitude and orientation of the

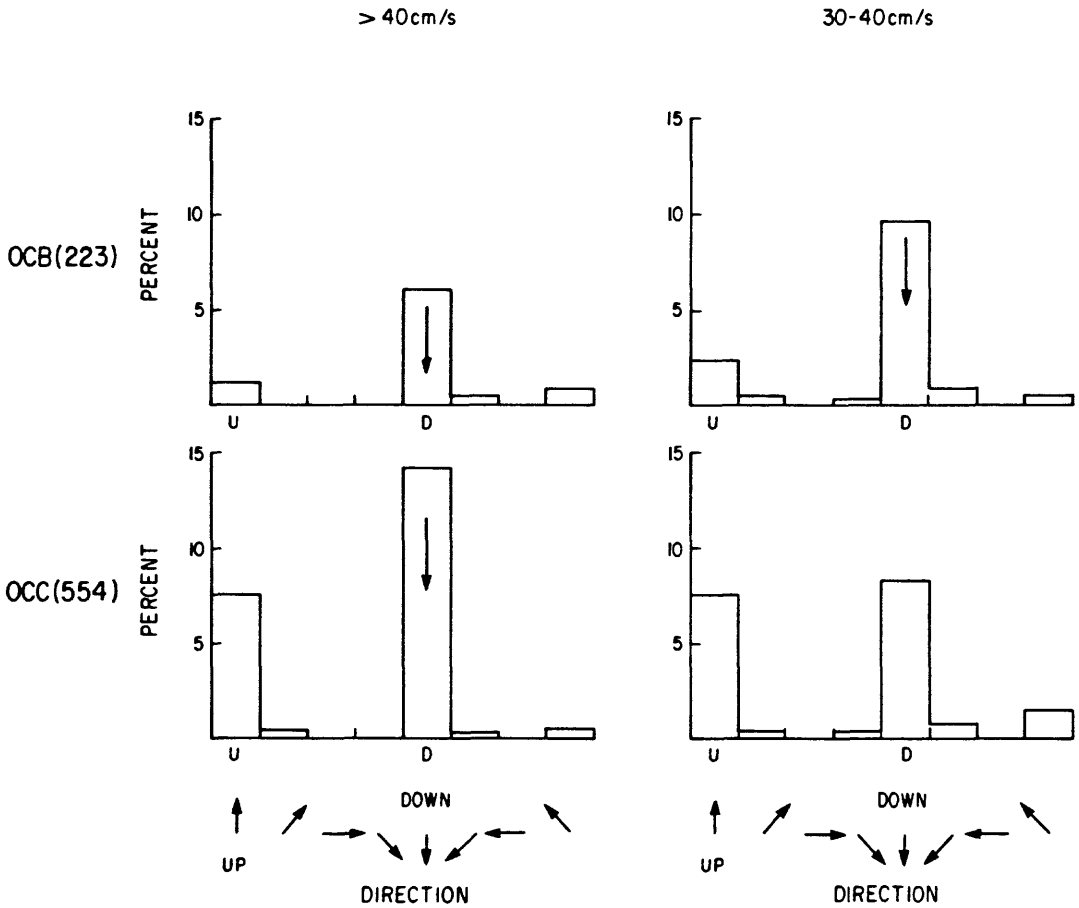

Figure 2-43. Histogram of near-bottom currents greater than 40 cm/s and between 30 and 40 cm/s at stations OCB and OCC in the axis of Oceanographer Canyon. For explanation see fig. 2-41.

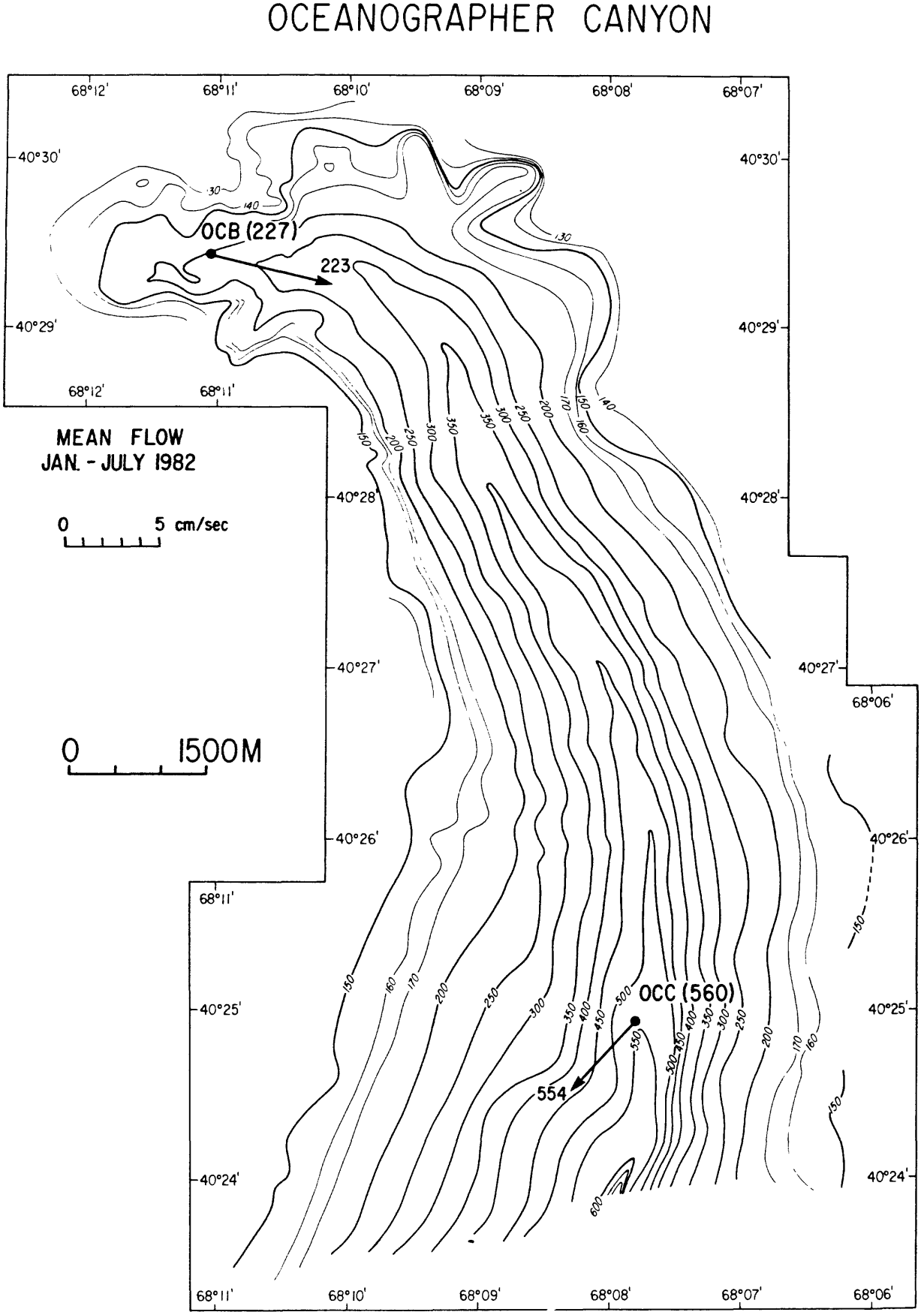

Figure 2-44. Net Eulerian near-bottom flow in Oceanographer Canyon at OCB and OCC.

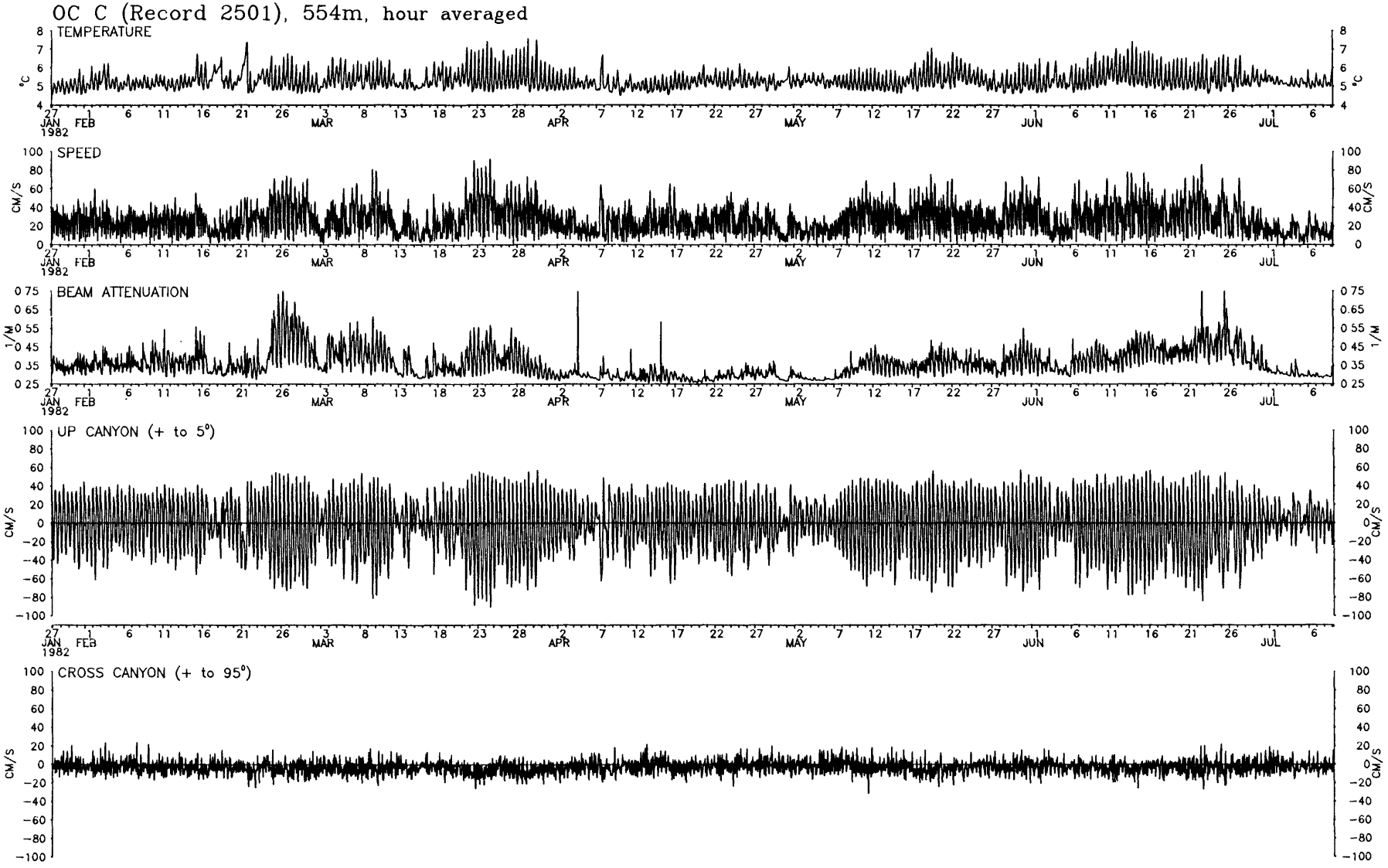

Figure 2-45. Time series of observations made at 6 mab at station OCC. Note current speeds in excess of 60 cm/s, and fluctuations in beam attenuation.

fluctuations change over short spatial scales. Within the canyon, the currents are channeled by the topography. Some of the fluctuations are apparently either locally trapped or generated by the interaction of the density field and the topography. Others are generated by processes outside the canyon -- for example, by the tidal currents on the shelf and by Gulf Stream WCRs on the upper slope. Some of the low-frequency fluctuations in the canyon are apparently driven by the higher frequency currents at least near the bottom.

A major issue that remains to be resolved is the net transport of water and suspended particles through the canyon. The moored observations have shown the Eulerian flow pattern, but the Lagrangian flow is probably not the same, especially in the axis of the canyon where the flow changes over short vertical and horizontal scales. The convergence of near-bottom flow near the head of the canyon (down-canyon flow at LCB at 300 m and up-canyon flow at LCS at 550 m) is consistent with the observed accumulation of finer-grained sediments near the head (see chapter 3 and 6). However, the strong Eulerian mean flow is perpendicular to the persistent isopleths of temperature, salinity, and density; these features could not be maintained in this Eulerian flow field without strong mixing. The measured near-bottom Eulerian mean is probably not the Lagrangian mean but the result of differential vertical mixing in the bottom boundary layer during upslope or downslope flow, an asymmetry in the up-canyon and down-canyon fluctuations caused by the geometry of the canyon, or a net flow to balance a Reynolds flux caused by the internal wave field (Wunsch, 1971; Ou and Maas, 1986). The direction of bedload transport of sediment determined from the Eulerian observations is probably correct, however, because these particles remain near the bottom. The transport of water may be much different than the Eulerian mean, recirculating

in smaller local vertical or horizontal cells. More closely spaced measurements in the vertical and horizontal and a model of flow in the bottom mixed layer over a slope in a stratified water column are needed. Near-bottom observations using neutrally-buoyant floats in the axis would be of interest (Voorhis and others, 1976).

The currents are intensified near the bottom and there is active sediment resuspension and movement to depths of at least 600 m in both Oceanographer and Lydonia Canyons. Based on profiles of beam attenuation (and the sediment trap data, chapter 6) particles are suspended at least 50-100 mab. Time series of beam attenuation in the axis show frequent, short-duration, large-amplitude changes in suspended sediment concentration, some caused by local resuspension and some by vertical and horizontal advection.

There is near-bottom sediment resuspension on the shelf during storms which is carried over the canyon rim at shelf depths, especially during downwelling favorable flows; some of this material must be trapped by the canyon, especially the coarser sediments which move as bedload. Enhanced bottom stress associated with waves is a major cause of sediment resuspension on the shelf. There must also be a continual flux of particles to the canyon which are carried across the canyon axis by the persistent westward residual mean flow.

Long-term observatons have been made in four major canyons along the U.S. east coast: Lydonia and Oceanographer (this study), Hudson (Hotchkiss and Wunsch, 1982) and Baltimore (Gardner, 1983; Hunkins, 1983). Although Hotchkiss and Wunsch (1982) do not present basic statistics of the flow in Hudson Canyon, they do show that the energy in the internal wave band increases toward the sea floor and the canyon head, consistent with the distribution observed in Lydonia Canyon. In Lydonia, Oceanographer, and

Baltimore Canyons, currents were measured at common depths of about 250 m and 550 m in the axis (table 2-13). At 250 m there was a net Eulerian down-canyon flow of order 5 cm/s near the head in all three canyons. The average near-bottom speeds at this depth in Lydonia were only about 70 percent of the speeds measured in Oceanographer and Baltimore. At about 550 m, the net Eulerian flow in Oceanographer was down-canyon at about 5 cm/s; in Baltimore Canyon, the net flow was up-canyon. In Lydonia, up-canyon flow of order 5 cm/s was observed at LCS(550) and weak flow at LCE(600). At 550-600 m, near-bottom speeds in Baltimore and Lydonia were about the same, but average current speeds in Oceanographer were almost twice as strong. The differences in current speeds in these canyons must result from canyon geometry (side wall and axis slope, mouth and top opening) and the internal wave characteristics. The near-bottom Eulerian residual currents in the heads of the canyon may converge, as in Lydonia or Baltimore, or be down-canyon, as in Oceanographer. There may be several Eulerian cells in these canyons which are not resolved by the available measurements; as discussed above, modelling and additional measurements along the axis are needed.

One important consequence of the concentration of energy at periods faster than about 30 hours is that relatively short-duration observations are sufficient to characterize the flow. As an example, the basic statistics of the flow near the bottom were not much different between the five deployments at LCB. Very long data records are needed to address infrequent events, such as the effect of storms on the shelf or Gulf Stream WCRs, but much of the dynamics of the flow is resolved by the internal wave band.

The Lydonia Canyon Experiment was conceived as a pilot study to describe the currents and processes of sediment transport in one East Coast submarine canyon. The results illustrate the complexity and variability of the flow.

Table 2-13. Average ($\bar{S}$), standard deviation (SD), maximum current speed (MAX), and net up-canyon flow ($\bar{U}$) near the bottom at about 250-300 m and 550-600 m in the axis of Lydonia, Oceanographer, and Baltimore canyon. All speeds in cm/s. For $\bar{U}$, positive is up-canyon, negative is down-canyon.

	250 m				550 m			
Canyon	$\bar{S}$	SD	MAX	$\bar{U}$	$\bar{S}$	SD	MAX	$\bar{U}$
Lydonia	13	10	65	-4	15	9	61	-1
					16	13	66	6
Oceanographer	19	12	65	-6	27	16	92	-5
Baltimore	19	12	73	-5	16	12	78	5

Some common features of canyons, such as the bottom intensification of energy in the internal wave band, increased fluctuations near the head, and the net Eulerian flows near the bottom, have been identified. The observations provide a sound basis for modelling the flows and for future detailed field measurements designed to examine the dynamics.

ACKNOWLEDGEMENTS

I thank the officers and crew of the RV OCEANUS, who endured major mooring and hydrographic cruises, often in rough North-Atlantic winters, for their skill, patience, and hard work. I thank B. Strahle, F. Musialowski, V. Wilson, and J. Larson, who built most of the moorings and skillfully prepared the instruments. I thank the Buoy Group of the Woods Hole Oceanographic Institution for loan and preparation of some of the VACMs used in deployment 1, and the National Marine Fisheries Service for the loan of some of the VACMs used in other deployments. P. Shoukimas and S. Conley processed the data. M. Noble, V. Lyne, and J. Moody provided helpful analysis and advice. J. Moody did the M_2 tidal computations. In addition to those listed above M. Bothner, C. Parmenter, R. Rendigs and A. Eliason provided skillful assistance on all the cruises. E. Imamura first proposed the canyon experiment and provided continual support and encouragement.

REFERENCES

Baker, E.T., and Hickey, B.M., 1986, Contemporary sedimentation processes in and around an active west coast submarine canyon: Marine Geology, v. 71, p. 15-34.

Beardsley, R.C., Chapman, D.C., Brink, K.H., Ramp, S.R., and Schlitz, R., 1985, The Nantucket Shoals flux Experiment (NSFE79). Part I: A basic description of the current and temperature variability: Journal of Physical Oceanography, v. 15, p. 713-748.

Bothner, M. H., Spiker, E. C., Johnson, P. P., Rendigs, R. R., Aruscavage, P. J., 1981, Geochemical evidence for modern sediment accumulation on the continental shelf off southern New England: Journal of Sedimentary Petrology, v. 51, p. 281-292.

Bothner, M. H., Rendigs, R. R., Campbell, E., Doughten, M., Aruscavage, P. J., Dorrzapf, A., Johnson, R., Parmenter C., Pickering, M., Brewster, D., and Brown, F., 1982, The Georges Bank Monitoring Program: analysis of trace metals in bottom sediments: Final report to the U.S. Bureau of Land Management under Interagency Agreement AA851-IA2-18.

Butman, B., Processes causing surficial sediment movement, Chapter 13 in Backus, R. H. (ed.), Georges Bank: Cambridge, MA. MIT Press, in press.

Butman, B., Moody, J. A., and Conley, S. J., 1986a, Hydrography of the New England Shelf and Slope: Data report for R/V OCEANUS cruise 130, November 1982: U.S. Geological Survey Open-File Report 86-101, 241 p.

Butman, B., Moody, J.A., and Conley, S.J., 1986b, Hydrography of Lydonia Canyon: Data Report for OCEANUS cruise 104, September 29 - October 1, 1981: U.S. Geological Survey Open-File Report 86-504, 211 p.

Butman, B., and Conley, S.J., 1984, Lydonia Canyon Experiment: Data Report for moored array deployment 1, October 1980-April 1981: U.S. Geological Survey Open File Report 84-201, 223 p.

Butman, B., and Moody, J.M., 1984, Bathymetric map of Lydonia Canyon, U.S. Atlantic Outer Continental shelf: U.S. Geological Survey Miscellaneous Field Studies Map MF-1710, 3 plates.

Butman, B., Beardsley, R.C., Magnell, B., Frye, D., Vermersen, J.A., Schlite, R., Limeburner, R., Wright, W.R., and Noble, M.A., 1982, Recent observations of the mean circulation on Georges Bank: Journal of Physical Oceanography, v. 12, p. 569-591.

Butman, B., and Folger, D.W., 1979, An instrument system for long-term sediment transport studies on the continental shelf: Journal of Geophysical Research, v. 84, p. 1215-1220.

Cacchione, D.A., and Wunsch, C., 1974, Experimental study of internal waves over a slope: Journal of Fluid Mechanics, v. 66, p. 223-229.

Carpenter, G.B., Cardinell, A.P., Francois, D.K., Good, L.K., Lewis, R.L., and Stiles, N.T., 1982, Potential geologic hazards and constraints for blocks in proposed North Atlantic OCS Oil and Gas Lease Sale 52: U.S. Geological Survey Open-File Report 82-36, 51 p., 3 plates.

Carson, B., Baker, E.T., Hickey, B.M., Nittrouer, C.A., DeMaster, D.J., Thorbjarnarson, K.W., and Synder, G.W., 1986, Modern sediment dispersal and accumulation in Quinault Submarine Canyon - A summary: Marine Geology, v. 71, p. 1-13.

Erickson, C.G., 1982, Observations of internal wave reflection off sloping bottoms: Journal of Geophysical Research, v. 87, p. 525-538.

Gardner, W.D., 1983, Suspended sediment transport in Baltimore Canyon and adjacent slope, chapter 2 in Canyon and Slope Processes Study, V 2, Physical Processes; Final Report for U.S. Minerals Management Service, contract 14-12-0001-29178: Palisades, N.Y., Lamont-Doherty Geological Observatory, p. 135-243.

Grant, W.D., and Madsen, O.S., 1979, Combined wave and current interaction with a rough bottom: Journal of Geophysical Research, v. 84, p. 1797-1808.

Hathaway, J. C., 1971, Data file, Continental Margin Program, Atlantic coast of the United States, Woods Hole Oceanographic Institution Reference 71-15, 496 p.

Hecker, B., Logan, D. T., Gandarilles, F. E., and Gibson, P. R., 1983, Megafaunal assemblages in Lydonia Canyon, Baltimore Canyon, and selected slope areas, chapter 2 in Canyon and Slope Process Study, V. 3, Biological Processes: Final Report to U.S. Minerals Management Service, contract 14-12-0001-29178: Palisades, N.Y., Lamont Doherty Geological Observatory, p. 1-117.

Hickey, B.M., Baker, B., Kachel, N., 1986, Suspended particle movement in and around Quinault submarine canyon: Marine Geology, v. 71, p. 35-83.

Hotchkiss, F.S., and Wunsch, C.W., 1982, Internal waves in Hudson Canyon with possible geological implications: Deep-Sea Research, 29, p. 415-442.

Hunkins, K.H., 1983, Physical Oceanography in Baltimore Canyon and adjacent slope, chapter 1, in Canyon and Slope Processes Study, V.2, Physical Processes; Final Report to U.S. Minerals Management Service, contract 14-12-0001-29178: Palisades, N.Y., Lamont-Doherty Geological Observatory, p. 135-243.

Moody, J. A., Butman, B., Beardsley, R. C., Brown, W. S., Daifuku, P., Irish, J., Mayer, D. A., Mofjeld, H. O., Petrie, B., Ramp, S., Smith, P. and Wright, W. R., 1984, Atlas of tidal elevation and current observations on the Northeast American Continental Shelf and Slope: U.S. Geological Survey Bulletin 1611, 122 p.

Moody, J.A., Butman, B., and Conley, S.J., 1986a, Hydrography of Lydonia Canyon: Data Report for R/V OCEANUS cruise 91, January 1981: U.S. Geological Survey Open-File Report 86-174, 142 p.

Moody, J.A., Butman, B., and Conley, S.J., 1986b, Hydrography of Lydonia Canyon: Data Report for R/V OCEANUS cruise 95, April-May, 1981: U.S. Geological Survey Open-File Report 86-286, 224 p.

Moody, J.A., Butman, B., and Conley, S.J., 1986c, Hydrography of the New England Shelf and Slope: Data Report for R/V OCEANUS cruise 113, January 29 - February 3, 1982: U.S. Geological Survey Open-File Report 86-343, 271 p.

Noble, M., Butman, B., and Williams, E., 1983, On the longshelf structure and dynamics of subtidal currents on the eastern United States Continental Shelf: Journal of Physical Oceanography, v. 13, p. 2125-2147.

Noble, M., Butman, B., and Wimbush, M., 1985, Wind-current coupling on the southern flank of Georges Bank: Variation with senson and frequency: Journal of Physical Oceanography, v. 15, p. 604-620.

Scanlon, K.M., 1984, The continental slope off New England: A long-range sidescan sonar perspective: Geo-Marine Letters, v. 4, p. 1-4.

Schlee, J. S., 1973, Atlantic continental shelf and slope of the United States, sediment texture of the northeastern part: U.S. Geological Survey Professional Paper 529-L, 64 p.

Shepard, F.P., Marshall, N.F., McLaughlin, P.A., and Sullivan, G.G., 1979, Currents in submarine canyons and other sea valleys: American Association of Petroleum Geologists Studies in Geology, no. 8, Tulsa, OK, 173 pp.

Shepard, F.P., and Dill, R.F., 1966, Submarine Canyons and other sea valleys: Chicago, IL, Rand McNally, 381 p.

Stanley, D.J., and Kelling, G., (eds.), 1978, Sedimentation in Submarine Canyons, Fans and Trenches: Stroudsberg, PA, Dowden, Hutchinson, and Ross, 395 p.

Strahle, W.J., and Butman, B., 1985, Modification of EG&G vector-averaging current meter to record light transmission and water conductivity: U.S. Geological Survey Open-File Report 85-106, 22 p.

Twichell, D. C., McClennen, C. E., and Butman, B., 1981 Morphology and processes associated with accumulation of fine-grained sediment deposit on the southern New England Shelf: Journal of Sedimentary Petrology, v. 51, p. 269-280.

Twichell, D.C., 1983, Geology of the head of Lydonia Canyon, U.S. Atlantic Outer Continental shelf: Marine Geology, 54, p. 91-108.

U.S. Department of Commerce, Oceanographic Analysis Charts. National Weather Service, National Earth Satellite Service.

Valentine, P.C., Cooper, R.A., Uzman, J.R., 1984, Submarine sand dunes and sedimentary environments in Oceanographer Canyon: Journal of Sedimentary Petrology, 54, p. 704-0715.

Valentine, P.C., Uzman, J.R., Cooper, R.A., 1980, Geology and Biology of Oceanographer Submarine Canyon: Marine Geology, 38, p. 283-312.

Voorhis, A. D., Webb, D. C., and Millard, R. C., 1976, Current structure and mixing in the shelf/slope water front south of New England: Journal of Geophysical Research, v. 81, p. 3695-3708.

Wunsch, C., 1969, Progressive internal waves on slopes: Journal of Fluid Mechanics, v. 35, p. 131-144.

CHAPTER 3

SAND TRANSPORT AND FINE PARTICLE SUSPENSION WITHIN AND AROUND LYDONIA CANYON

By

Vincent D. Lyne and Bradford Butman

CHAPTER 3

Table of Contents

	Page
Abstract	3-1
Introduction	3-2
Field data	3-4
Mooring information	3-4
Bottom roughness observations	3-6
Wave and current measurements	3-14
Beam transmissometer fouling	3-15
Sediment transport model	3-17
Model application	3-23
Comparisons of measured and model attenuation	3-25
Predicted sand transport rates	3-31
Fine sediment transport	3-41
Relation to hydrography	3-43
Attenuation time-series interpretation	3-46
Vertical and horizontal interrelationships	3-46
Internal wave packets and sediment suspension	3-53
Discussion on internal wave effects	3-62
Conclusions	3-66
Acknowledgements	3-68
References	3-69

ABSTRACT

Sediment transport within and around Lydonia Canyon is examined with a one-dimensional sediment transport model that utilizes observations of near-bottom current and beam transmission. Separate analyses are provided for the transport of sand fractions and fine particulate matter. Within the canyon, energetic internal waves associated with Warm Core Rings are inferred to be a prime mover of sediment. On the surrounding shelf, wave-current interaction enhances sediment transport.

Computed sand transports indicate active sediment accumulation at the head of Lydonia Canyon and along the canyon floor. At the canyon head, for depths shallower than 300 m, an accumulation rate of 3.6 m/1000 years is predicted. Between 300 m to 450 m depth the accumulation declines to 2.4 m/1000 years. The observed coarse patch of sand along the axis floor between 450 m to 650 m depths occurs in an area of predicted erosion. The bulk of the sand transport on the shelf and in the canyon is due to energetic currents that prevail for less than a few percent of the time.

Temporal changes in near-bottom beam attenuation at LCB and LCE, not attributable to sand suspension, are explained as suspension changes due to fine particles with settling velocities equivalent to that for fine sand. The amount of this suspended fine particulate matter is greatest at LCB but varies from deployment to deployment and was most abundant during the first deployment.

Highly peaked attenuation signals were observed during energetic upcanyon flows associated with internal wave packets at LCB. The lack of attenuation peaks during downcanyon flows, equally as energetic as the upcanyon flows, is hypothesized to be due to upwelling and downwelling during upcanyon and downcanyon flows respectively. Models predictions for sand suspension, with

upwelling speeds comparable to that for fine sand, produce attenuation signals in reasonable agreement with observations. The hypothesised upwelling/downwelling imply large upcanyon transport of sand and sediment.

INTRODUCTION

The transport of sand and fine particulate matter within and around Lydonia Canyon is examined here using a one-dimensional sediment transport model and measurements of beam attenuation. A one-dimensional sediment transport model is used for modelling medium and fine sand (377 μm to 47 μm) transport because the vertical distribution and transport of these sand fractions is largely controlled by local processes and because the beam transmission signal attributable to sand suspension may be masked by the bias of beam transmission signals towards finer particles (see chapter 9 and Moody and others, 1986). Fine particulate and organic matter can remain suspended in the water column for hours or days and hence the local concentration of such particles is not entirely due to local processes; a one-dimensional sediment transport model may not therefore be appropriate for analysing particles that settle slowly. Instead, measured beam attenuation, measured currents, hydrographic data, and sediment trap data (see chapter 6) are used to analyse the transport of fine particulate matter.

Sand transport is affected by the strength of the current, the bottom roughness, the surficial sediment distribution, and the erodability of the sediments which in turn is affected by such processes as bed amoring and bioturbation. A further important factor is surface gravity waves; in particular swell waves that produce oscillatory flows at depths down to 200 meters (Miller and Komar, 1980). The sediment transport model used here parametrizes the effect of wave-current interaction and stratification of the

water column by suspended sediment. For stations on the shelf less than about 125 m in depth, wave-current interaction enhances the stress and roughness experienced by the mean current, and also enhances the skin friction stress on sediment particles at the bed. The combined influence of these processes is to substantially increase the load of suspended sediment. However, the work required to suspend sediment reduces turbulence levels and alters the vertical distribution of sediment. This coupling between the turbulence and suspended sediment distribution adds considerable complexity to sediment transport computations. Recent modelling studies (Lyne and others, 1986b) have, however, suggested that limitations to the amount of sediment that can be eroded from the bed, due perhaps to bed armoring, almost totally eliminate the effect of water-column stratification by suspended sediment. Nonetheless, the stratification effect is built into the model and is used in the simulations reported here. Model predictions of sediment transport are also sensitive to the specification of bottom roughness and surficial sediment size distribution. The selection of these parameters and their influence on predicted sediment transport rates is discussed.

In this chapter we first describe the location of the stations examined here in relation to the surficial sediment distribution and present selected observations made at stations on the shelf, in the canyon axis, and along the canyon rim. The sediment transport model is then described and results of the model are discussed. Measured beam attenuation signals are used to infer the dynamics of fine particulate matter suspension. Lastly, we examine the role of internal wave packets on sediment resuspension and transport.

FIELD DATA

Mooring Information

The locations of the Lydonia Canyon stations examined here are described in chapter 2. We will discuss sediment transport results derived from data collected at stations LCA, LCL, LCM, LCP, and LCU, which will be referred to as the shelf stations, LCB, LCE, LCS, and LCH, which will be referred to as the canyon axis stations, LCQ on the eastern canyon rim, and LCI on the eastern upper slope. Data from the shelf stations, with the exception of LCU, were obtained by bottom tripods, which measure pressure fluctuations due to waves, in addition to temperature, current, and beam transmission (Butman and Folger, 1979). Station LCU in about 140 m of water is the deepest of the shelf stations; no pressure measurements were made here because wave-current interaction was not expected to be significant at this depth. Measurements at other stations were obtained by either the deep instrument package (DIP) or a VACM modified to measure light attenuation (see chapter 2). Table 3-1 presents the mooring information for the stations.

The shelf stations are located in general within the coarse silt-very fine sand patch around the head of Lydonia Canyon; LCA is located at the northern edge of the patch. Within the canyon axis, LCB is in the area where the concentration of very fine sand exceeds 50 percent. The surficial sediment at LCS contain about 40 percent of medium sand. Further south at LCE the surficial sediments again contain very fine sand. In this region of the axis, the surficial sediment composition is highly variable. At LCH, the deep station within the canyon, the surficial sediments are greater than 90 percent silt-plus-clay. LCI on the upper slope has a sediment composition coarser than those of the shelf stations.

Table 3-1. Location and deployment information for bottom tripods and moorings, within and around Lydonia Canyon, selected for analysis of sediment transport. Station locations are shown in the chapter 2.

Station	Mooring	Deployment period	Water depth (m)	Latitude (N.)	Longitude (W.)	Inst. type*
LCA	2041A	24 Oct'80 - 12 Dec'81	100	40°34.20'	67°44.81'	T
	2041B	16 Feb'81 - 24 Apr'81	100	40°34.20'	67°44.81'	T
	2231	5 May'81 - 26 Sep'81	100	40°34.25'	67°44.76'	T
	2571	8 Jul'82 - 12 Aug'82	104	40°33.83'	67°44.21'	T
LCB	2083	28 Nov'80 - 28 Apr'81	282	40°31.55'	67°42.82'	DIP
	2263	29 Apr'81 - 26 Sep'81	288	40°31.56'	67°42.83'	SSP
	2311	27 Sep'81 - 27 Jan'82	290	40°31.54'	67°42.79'	DIP
	2413	31 Jan'82 - 7 Jul'82	300	40°31.52'	67°42.83'	SSP
	2583	8 Jul'82 - 11 Nov'82	295	40°31.49'	67°42.29'	SSP
LCE	2114	1 Dec'80 - 1 Jul'81	600	40°25.38'	67°39.88'	DIP
	2322	29 Sep'81 - 30 Jan'82	590	40°25.40'	67°39.84'	SSP
LCH	2211	20 Jan'81 - 28 Apr'81	1,380	40°17.59'	67°39.54'	DIP
LCI	2154	2 Dec'80 - 29 Apr'81	250	40°22.84'	67°33.14'	DIP
	2341	27 Sep'81 - 31 Jan'82	247	40°23.11'	67°32.60'	SSP
LCL	2511	31 Jan'82 - 9 Jul'82	127	40°32.40'	67°36.52'	T
LCM	2031	24 Oct'80 - 26 Apr'81	120	40°29.57'	67°48.55'	T
LCP	2371	26 Sep'81 - 28 Jan'82	131	40°32.02'	67°42.07'	T
LCQ	2431	30 Jan'82 - 7 Jul'82	185	40°27.25'	67°38.27'	DIP
LCS	2451	29 Jan'82 - 7 Jul'82	560	40°27.61'	67°40.03'	SSP
LCU	2591	8 Jul'82 - 11 Nov'82	141	40°32.37'	67°44.37'	SSP

* For instrument type, T stands for bottom tripod, DIP stands for deep instrument package and SSP stands for suspended sediment package.

Bottom roughness observations

The roughness of the bottom was determined from bottom photographs obtained from the near-bottom instrument package and from photographs taken during the ALVIN submersible dive (Butman and Bothner, unpublished transcripts and photographs). Photographs of the seabed are shown in figures 3-1 to 3-7. At the shelf stations, much of the roughness is due to bioturbation, shell hash and small ripples (figures 3-1, 3-2). Sand ripples have a typical spacing of about 10 cm and their crests are generally rounded except after periods of active sediment transport when sharp-crested ripples appear. The bottom is obscured by suspended sediment during storms so that bottom features cannot be observed. At LCB along the canyon axis the seafloor is generally smooth with lightly scattered fragments of shell and an occasional fish, crab, or lobster (figure 3-3). Ripples of about 15 cm length appear after active sediment suspension. The formation of these ripples may have been aided by the presence of the circular anchor weight. The most distinct and regular ripples were observed at LCE in about 600 m water depth along the canyon axis (figure 3-4). Here, the average ripple spacing is about 18 cm and no shells or shell hash were observed. At LCS, no photographs were obtained from the mooring but the site was surveyed during an ALVIN dive (dive 1037, August 28, 1980). As the ALVIN proceeded westward across the canyon axis, isolated patches of ripples were observed and a layer of light and fluffy organic matter was found on the surface, covering tan-colored sand underneath (figure 3-5). The crests of sand ripples appeared to be composed of a darker black sand. In some areas, the bottom was literally covered by Ophiuroids (brittle stars), their arms almost touching each other. Occasionally, depressions 10-20 cm deep and up to half a meter wide were observed. At the deep station LCH, the seafloor was relatively smooth (figure 3-6) on the upper slope

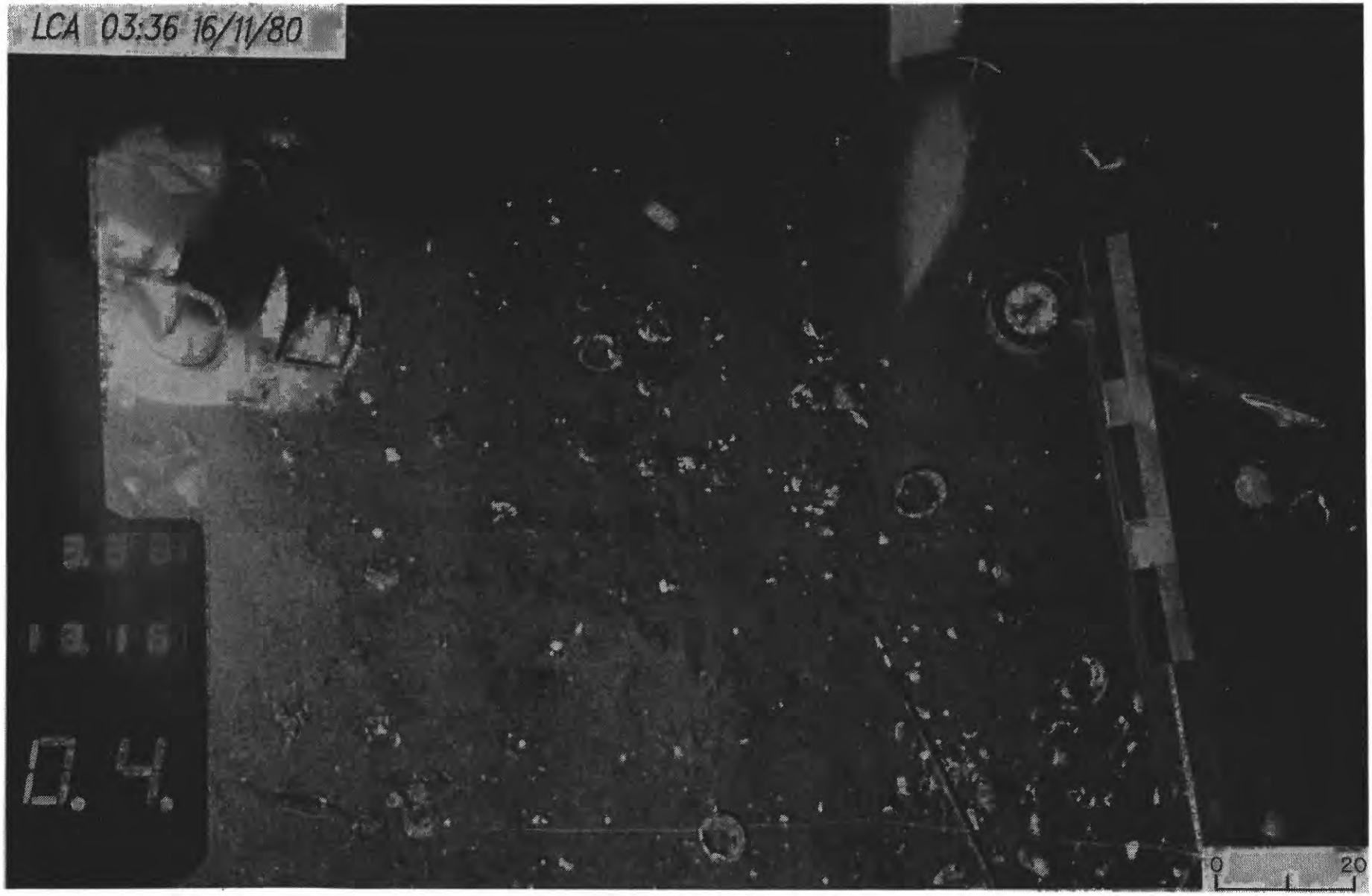

Figure 3-1. Bottom photograph at station LCA.

Figure 3-2. Bottom photograph at station LCM.

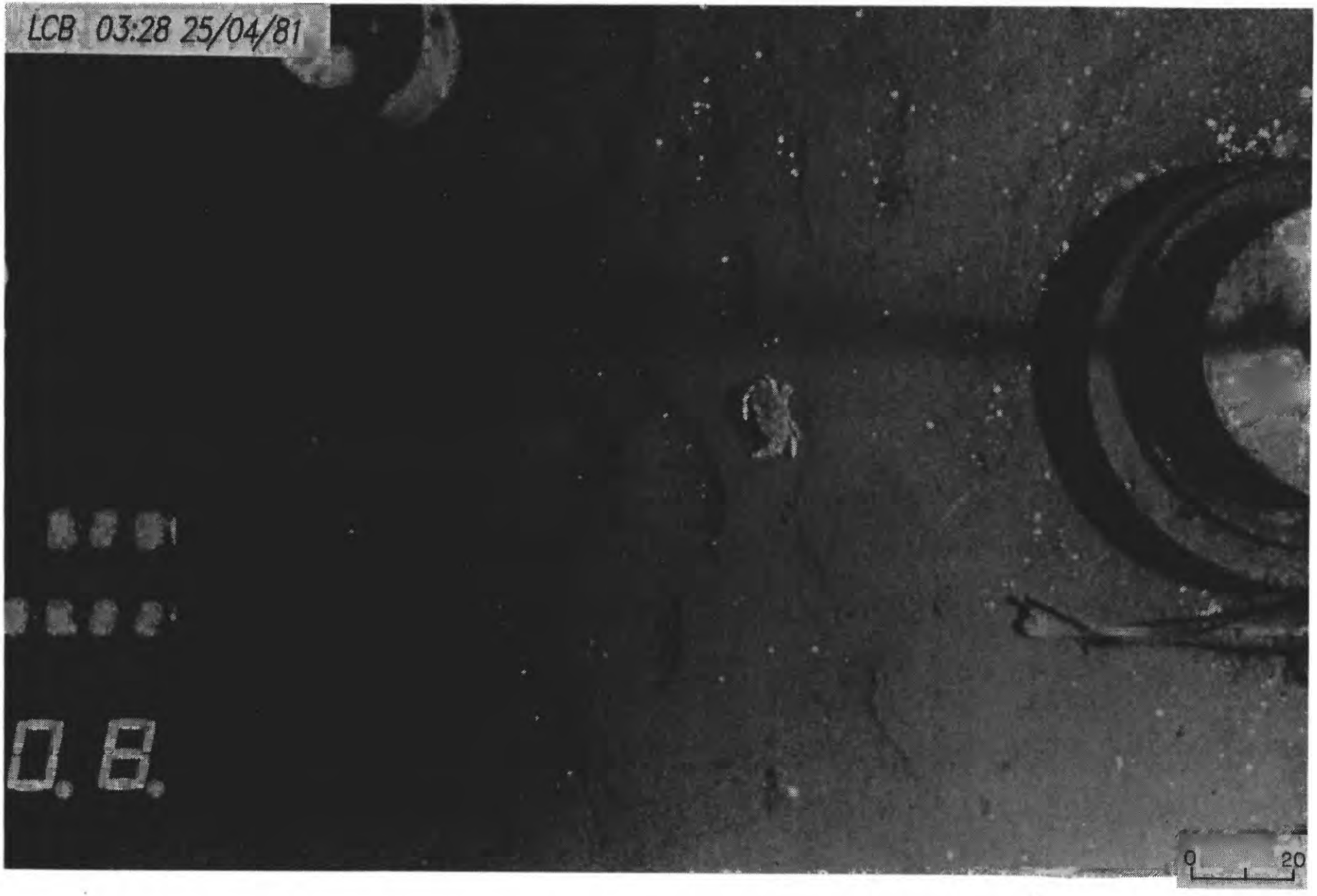

Figure 3-3. Bottom photograph at station LCB.

Figure 3-4. Bottom photograph at station LCE.

Figure 3-5. Bottom photograph near station LCS taken through the porthole of the submersible ALVIN. The width of the field of view is approximately 2 meters.

Figure 3-6. Bottom photograph at station LCH.

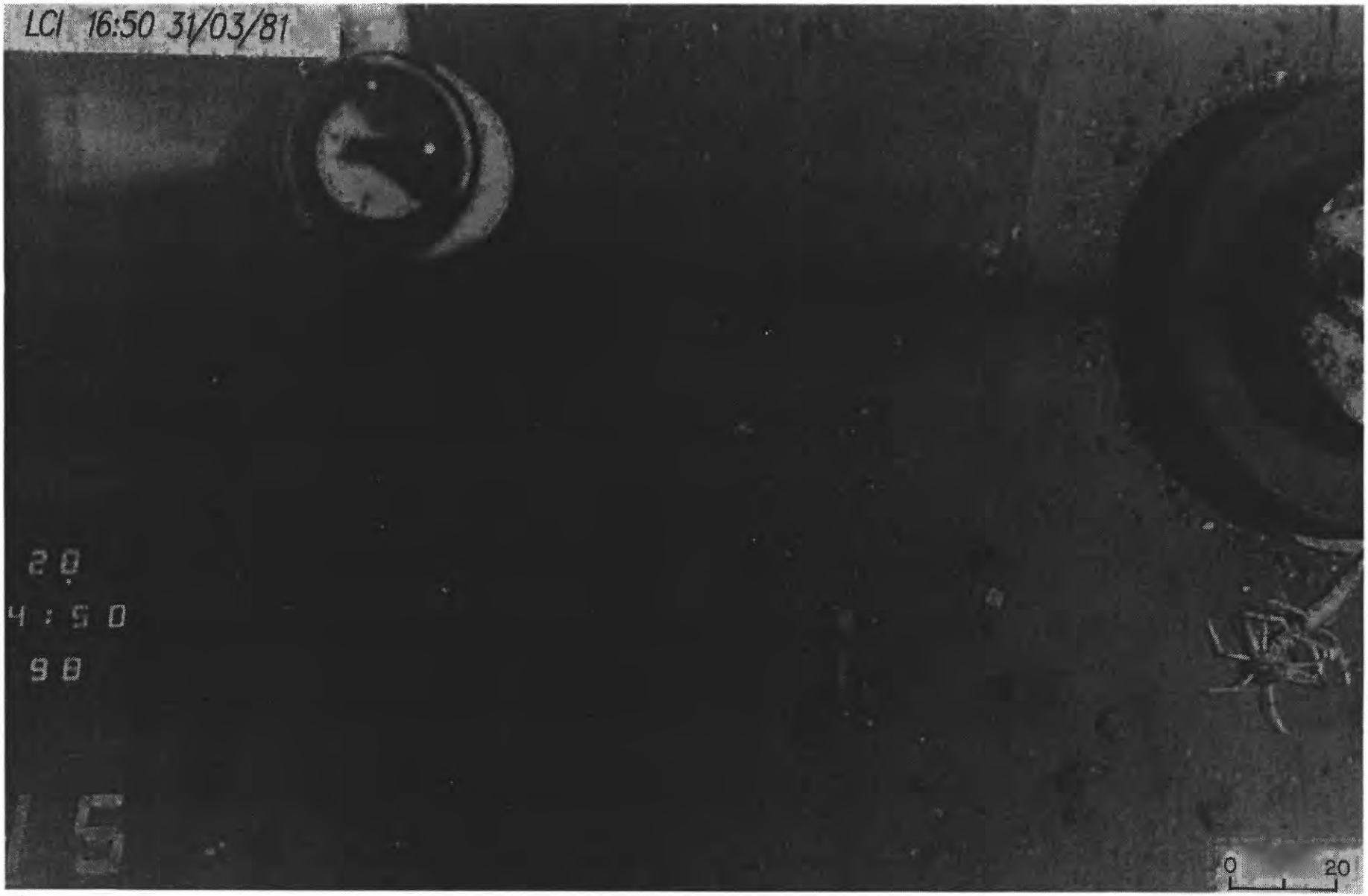

Figure 3-7. Bottom photograph at station LCI.

station LCI the seafloor was also relatively smooth (figure 3-7) although, gravel and some pebbles appeared to have been uncovered around the area of the anchor weight. At LCQ on the canyon rim, the dominant roughness elements were gravel; more than 7 percent of the bottom sediment is comprised of gravel larger than 1.6 cm in size.

Wave and current measurements

The most uncertain aspect of the current measurements are the measurements of the wave and current statistics from the bottom tripods during storm periods (Lyne and others, 1986a). In brief, the major problem with the wave measurements is that the wave groupiness signal is aliased because of the relatively short (48 s) burst measurement. Lyne et al. (1986a) present corrections to the measurements to account for the reduced wave energy in the measured pressure standard deviation (PSDEV) due to the sampling scheme and an aliased wave groupiness signal. Typically such corrections are about 20 percent of the PSDEV measurements used here. For shelf stations in less than 80 m water depth, wave periods derived from the measurements are good to within 1 to 2 s during storms when the wave period is typically longer than 12 s. An empirical relation between PSDEV and wave period, derived from NOAA surface buoy wave data (Lyne and others, 1986a), was found to give better estimates of wave period than measured, except for the cases of distant swell waves propagating into the observation site or during the tail end of storms when the PSDEV decayed but wave periods were still longer than predicted by the empirical relation.

Errors in the current speed and direction are acceptable (~10% error for speed, ~10^{o} for direction), provided the current speed is at least as large as the bottom wave speed. Fortuitously, during storms, this is often the case.

However, at times the storm-generated currents may oppose the tidal currents during some phase of the tidal cycle which produces a weak total mean current (relative to the wave) and therefore large uncertainties in current speed and direction

Beam Transmissometer Fouling

Fouling of beam transmissometers results in a attenuation signal whose apparent background signal increases with time. Figure 3-8 shows an example of a transmissometer signal, taken at LCM, that has a background signal almost constant in time up to the end of December when fouling causes a continual rise of the attenuation signal. Our objective is to eliminate the constant background and fouling signal. Suspended sediment would cause an incremental attenuation, above the background, that we would like to retrieve.

The filter used here is essentially a digital recursive filter whose output signal is constrained to be not larger than the input signal (- hence the name Constrained Digital Filter (CDF)). Devised originally by Lyne (1981), the filter employs a forward and then a reverse filtering procedure so as not to introduce, or minimize phase shifts in the filtered output. The basis of the CDF is a recursive exponential filter which for forward filtering, is of the form:

$$y_1 = x_1$$

$$y_n = \alpha y_{n-1} + (1-a)x_n \qquad n = 2, 3 \ldots L$$

with constraints:

$$\text{if } y_n > x_n \text{ then } y_n = x_n$$

where, x_n denotes the sequence of observed attenuation values

y_n is the filter output of background attenuation

α is the filter parameter.

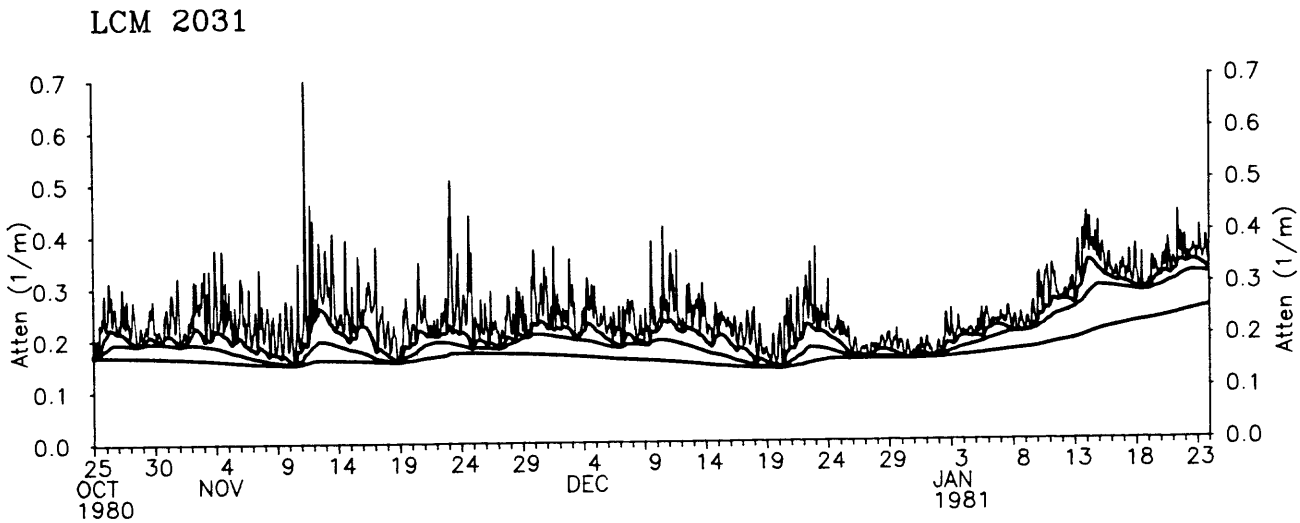

Figure 3-8. Illustration of constrained digital filter output (thick lines) for filter parameters of 0.9, 0.99, and 0.995. Larger filter parameters produce smoother output. Required signal is original minus filtered signal. Note "leakage" of fouling signal towards the end of the record for output from using the largest filter parameter.

The reverse recursion employs essentially the same steps in reverse:

$$z_L = x_L$$

$$z_n = \alpha z_{n+1} + (1-\alpha)y_n \qquad n = L-1,\ L-2,\ldots,1$$

with constraint

$$\text{if } z_n > y_n \text{ then } z_n = y_n$$

The series of output z_i (i =1, 2, ...L) is the background and fouling signal which when subtracted off from the original attenuation series (x_i) gives the desired output.

An example of the filter ouput is shown in figure 3-8. Choosing an appropriate filter parameter (α) involves subjective judgement of what the background noise is. Too small an α will eliminate some non-background signal from attenuation events that last for more than a few days; e.g., the output for $\alpha = 0.9$ for the November 10-19th attenuation event in figure 3-8. Whereas, too big an α will allow some background signal to pass through and also prevent the proper operation of the reverse filter towards the end of the record. For example, for $\alpha = 0.998$ in figure 3-8, the output in January is that from the the forward filter because the reverse filter output for that period is larger than the forward filter output. Thus, the filter will not provide a good output of the signal due to fouling if the filter parameter is too large. We chose $\alpha = 0.99$ as a compromise for the filtered attenuation signals presented in this chapter.

SEDIMENT TRANSPORT MODEL

The modelling studies are based on a modified version of the sediment transport model described by Grant and Glenn (1983) and Glenn (1983), hereafter referred to as GG 83. The model parametrizes the effects of stress enhancement due to non-linear wave-current interaction, movable bed effects of

sand ripple formation and near-bed sediment transport, and inhibition of vertical mixing due to the earth's rotation and density stratification from temperature, salinity, and suspended sediment. Not all of these features of the model are employed in this study, and it is important to understand what conditions require each feature.

The vertical profile of both velocity and sediment concentration are affected by turbulent stirring of the water column, generally characterized by the shear speed u_{*c} - an indicator of turbulent velocity fluctuations. The velocity profile and sediment suspension are coupled through movable bed effects which change the physical bottom roughness, and through the inhibition of vertical momentum transport by sediment stratification. It is difficult to intuitively understand the workings of the full model because of all the non-linear feedback; GG 83 present simplified model studies which illustrate one major component of the model at a time. In addition to the importance of wave-current interaction, two principal conclusions of these studies are that the model results are most sensitive to the specification of the physical bottom roughness, and at skin friction stresses beyond the breakoff point where sand ripples degrade, the roughness due to the near-bed sediment transport layer and sediment stratification dominate the feedback interaction between the velocity and sediment dynamics.

For shelf stations, wave-current interaction is the most important aspect of the flow field that must be treated in the sediment transport model. The wave boundary layer (WBL) has scales of up to a few tens of centimeters and is embedded within a larger planetary boundary layer (PBL) of a few tens of meters. The heights of these two layers are limited by their characteristic oscillatory time scales: of order seconds for the WBL and of order one day for the PBL. The current in the PBL sees a roughness greater than the

physical bottom roughness because of vertical stirring of mean momentum in the WBL. The concept of an enhanced apparent bottom roughness is introduced in Grant and Madsen (1979).

In the absence of sediment stratification, the solution for the mean velocity profile within and above the WBL is logarithmic and subject to zero velocity conditions at $z = z_o$ for the WBL and, at $z = z_{oc}$ for the PBL, i.e.,

$$u_c = \frac{u_{*c}}{u_{*cw}} \cdot \frac{u_{*c}}{\kappa} \ln\left(\frac{z}{z_o}\right) \qquad \text{for } z \leq \delta_{cw} \tag{1}$$

$$u_c = \frac{u_{*c}}{\kappa} \ln\left(\frac{z}{z_{oc}}\right) \qquad \text{for } z > \delta_{cw} \tag{2}$$

where, κ is Von Karman's constant = 0.4, u_{*c} is the current shear speed, u_{*cw} is the combined wave-current shear speed within the WBL, z_o is taken to be $k_b/30$ for fully rough flow and k_b is the physical bottom roughness The WBL scale is $\delta_{cw} = 2\kappa u_{*cw}/\omega$ (see discussion in Grant and Madsen, 1986) where ω is the wave radian frequency. Eddy viscosities used in deriving these profiles are time invariant and proportional to the characteristic shear speed for the respective layers and distance from the bottom:

$$\nu_T = \kappa u_* z \tag{3}$$

$$\text{and} \quad u_* = u_{*cw} \qquad \text{for } z \leq \delta_{cw}$$

$$= u_{*c} \qquad \text{for } z > \delta_{cw}$$

Above the WBL, the mean sediment concentration for each sediment size class is determined by a balance between the settling flux and vertical turbulent diffusion, i.e.,

$$\nu_{Ts} \frac{\partial C_n}{\partial z} = -w_{fn} C_n, \tag{4}$$

where C_n is the sediment volume concentration of the n^{th} size class, w_{fn} is the fall velocity (positive) of the n^{th} size and ν_{Ts} is the vertical diffusivity = ν_T/γ (γ=0.74)(see later discussion for a more general formulation that parametrizes stratification). Integrating (4) yields a concentration profile

$$C_n(z) = C_n(\delta_\omega)\left(\frac{z}{\delta_\omega}\right)^{-\beta_n} \tag{5}$$

with, $$\beta_n = \frac{\gamma\omega_{fn}}{\kappa u_{*c}}$$

where $C_n(\delta_\omega)$ is the concentration of the n^{th} size class at the wave boundary layer height (δ_ω).

For weak sediment stratification, the principal feedback between stresses in the WBL and the sediment is through bedform generation. Sand ripples first appear at skin friction stress equal to the critical value for initiation of motion (e.g. Madsen and Grant, 1976). Grant and Madsen (1982) have recast laboratory results from oscillatory flow in terms of the maximum skin friction stress (as opposed to the total stress derived from water surface slope which includes bedform pressure drag). Ripples are steepest at the point of incipient motion and, within the equilibrium range, have a wavelength about one fifth the wave orbital excursion amplitude. The equilibrium range terminates at stresses greater than the breakoff value where ripple steepness decreases and near-bed sediment transport increases. The resulting roughness experienced by the flow within the WBL is due to both ripples and near-bed sediment transport; Grant and Madsen (1982) derive a semi-empirical expression for the total roughness:

$$k_b = 160\ (s + C_m)d\ \psi_c[(\psi'/\psi_c)^{1/2} - 0.7]^2 + 27.7\ \eta^2/\lambda \tag{6}$$

$$\text{with } \psi'/\psi_c > 1.$$

where s is the specific gravity of the sediment, C_m is the added mass coefficient, d is the sediment diameter, ψ' is the maximum value of the Shield's parameter, ψ_c is the critical value of the Shield's parameter for initiation of sediment motion, η is the sand ripple height and λ is the ripple wavelength. The first term in (6) is the contribution to the roughness from the near-bed transport layer, and the second term is the form drag contribution from ripples.

As yet, there is no satisfactory method for computing skin friction stress for wave-current flows over seabeds with composite roughness elements. For unidirectional flow, the drag partition approach of Einstein and Barbarosa (1952) is often used. Laboratory measurements by Paola (1983) of spatially averaged skin friction over immobilized sand ripples agree to within 10 percent with the Einstein-Barbarosa method. For wave-current flows, GG 83 calculate skin friction stress by replacing the total physical roughness with the sand grain roughness but otherwise retain the same wave and current velocities above the WBL. It is not certain how to calculate skin friction in going from unidirectional to wave-current flows. Partly to circumvent this problem, we have extended the Einstein-Barbarosa method to wave-current flows as follows: for logarithmic velocity profiles, the mean velocity over a depth H is:

$$\frac{u}{u_*} = \frac{1}{\kappa}\left(\ln\left[\frac{H}{z_o}\right] - 1\right) \tag{7}$$

where u_* in the total shear speed, and z_o is the total roughness parameter. Using the Einstein-Babarosa drag partition theory, the mean velocity is also expressed as:

$$\frac{u}{u_{*sf}} = \frac{1}{\kappa}\left(\ln\left[\frac{H}{z_{os}} \cdot \left(\frac{u_*}{u_{*sf}}\right)^2\right] - 1\right) \tag{8}$$

z_{os} is that part of z_o due to sand grain roughness and u_{*sf} is the predicted skin friction shear speed. We choose H (normally the hydraulic radius) to be $10\ k_b = 10(30z_o)$ which gives good agreement with Paola's (1983) results. Since H is within the logarithmic term in (7), the results are not too sensitive to its exact magnitude as long as it is larger than k_b. For wave-current flows, the near bottom layer ($z < 0.1\delta_{cw}$) is logarithmic to a good approximation (GM 79) and the same approach is applicable with u_* being replaced by u_{*cw}. The method is ad hoc but provides a consistent formulation for wave-current and unidirectional flows.

With active sediment suspension, the turbulent buoyant flux of sediment attenuates vertical momentum transport. GG 83 take this into account by modifying the turbulent diffusivities through their dependence on the Monin-Obukhov stability parameter z/L. L is the Monin-Obukhov length, which for steady sediment stratification is:

$$L = u_*^3/[\kappa \sum_n g\,(s_n-1)\,w_{fn}C_n] \tag{9}$$

where g is the gravity constant, s_n is the specific density of sediment, w_{fn} is the fall velocity for sediment class n, and C_n is the concentration for sediment class n. Momentum and sediment eddy diffusivities are modified according to:

$$\underline{\text{Momentum}} \qquad \nu_{Tm} = \nu_T/(1 + \beta z/L) \tag{10}$$

$$\underline{\text{Sediment}} \qquad \nu_{Ts} = \nu_T/(\gamma + \beta z/L)$$

where $\gamma = 0.74$ and β is approximately 5.

Although the attenuation of eddy diffusivities due the earth's rotation is included in the model dynamics, it is not discussed here because it does not significantly affect the near-bottom (< 10 m) sediment and velocity profile.

The bottom boundary condition for the sediment distribution is based on the Smith and McClean (1977) formulation for the reference concentration at z_o:

$$C_n(z_o) = C_{bn}\frac{\gamma_o S_n}{1+\gamma_o S_n} \tag{11}$$

C_{bn} is the bed concentration, S_n is the normalized excess shear stress = $(\tau_{sf}-\tau_c)/\tau_c$, τ_{sf} is the skin friction stress and τ_c is the critical shear stress to initiate sand movement. GG 83 chose $\gamma_o = 0.002$ based on comparisons of model predictions with transport measurements from laboratory oscillatory flows. We chose $\gamma_o = 0.0007$ to account for the higher predicted transport rates with the modified skin friction calculation procedure adopted here.

The velocity and concentration profiles are obtained by integrating upwards (on a logarithmic grid) from the top of the WBL (GG 83 show by scaling analysis that stratification is unimportant within the WBL).

A further imposed boundary condition introduced by Lyne and others (1986) is a limitation on the depth to which sediments can be eroded. Such a condition is thought to be necessary to account for the winnowing effect or, bed armoring of sediments. In addition, the fine and very fine sediments which are suspended during a storm must come from a limited depth of the bed determined by either the depth to which the coarser sediments are eroded or, the disturbed or stirred layer on the seabed due, for example, to migrating sand ripples or bioturbation. The simulation results by Lyne and others (1986) suggest an appropriate erosion depth limit of 2 mm for midshelf stations along the Mid-Atlantic Bight shelf and southern flank of Georges Bank. This erosion limit is used in our studies.

Model Application

Model simulation results are described here for the transport of sand of four sizes ranging from 32 to 500 μm in diameter. Table 3-2 shows the percentage of each sediment size class and the bottom roughness parameter used in the model runs for each station.

The estimates of the bottom roughness are somewhat subjective because they are based on bottom photographs and thus the vertical scale of the roughness elements must be estimated. For ripples, however, there are constraints on the range of possible steepnesses. The relation between ripple geometry and roughness is obtained from concentation-dependent scaling, summarized by Wooding and others (1970), which accounts for the relative contributions to the overall roughness by individual boundary elements and the

Table 3-2. Magnitude of the bottom roughness and percentages of surficial sediment, of four sand size classes, used in the model studies for Lydonia Canyon. Coarse sand, gravel, fine silt and clay fractions are not included in the model studies.

Station	Roughness k_b (cms)	Percentages				Sediment sample*
		375 μm	188 μm	94 μm	47 μm	
LCA	1	30.0	30.0	20.0	8.0	SG
LCB	5	2.0	19.0	53.0	3.0	A
LCE	10	1.0	50.0	35.0	15.0	A
LCH	0.5	0	5.0	13.0	20	A
LCI	0.5	14.8	43.5	27.7	6.5	SG
LCL	4	7.1	24.8	55.8	3.5	SG
LCM	2	2.6	43.1	40.6	3.5	SG
LCP	4	8.1	27.2	53.4	2.7	SG
LCQ	1	29.0	10.4	2.2	0.3	SG
LCS	5	34.0	20.0	5.0	18.0	A
LCU	4	0	6.3	72.3	10.0	SG

*SG indicates sediment sample is from surface grab, and A indicates sample from ALVIN submersible dive.

intervening surface area between elements. For sand ripples, the equivalent roughness is as given in equation 6. The percentage of the seafloor area roughened by shell hash, sand ripples and pebbles and, their respective roughness heights were estimated from the bottom photographs and then averaged to obtain the roughness numbers in Table 3-2. LCE had the largest roughness, - caused by the sand ripples there. The deepest station in the axis LCH and LCI on the slope have the smallest roughnesses. Movable bed effects are not incorporated in this study due to uncertainities in model formulation and lack of field verification (see Lyne and others, 1986b).

Sediment grain size classes are usually reported by the largest (coarsest) particle retained on the sieve. For example, 125 μm material is the material retained on the 125 μm sieve, but contains sediment between 125 and 250 μm in diameter. The sand sizes used in the model simulations in (Table 3-2) are the average sieve size. For non-uniform sediment distributions, the magnitude of the calculated sediment transport is sensitive to the selection of sediment size (see model comparisons section).

Comparison of Measured and Model Attenuation

It is not possible to present all the comparisons between measured and model attenuation time-series; a selection of representative comparisons for periods of high stress are provided. As noted previously, high values of measured attenuation are not necessarily due to high sediment concentration because measured attenuation signals are biased towards the finer sediment particles (e.g., chapter 9 and Moody and others, 1986). The measured attenuation signal places an upper bound on the signal that would be produced by the sand components modelled here. In analysing the measured attenutation signal the persistent background signal, and the signal due to fouling of the transmissometer sensor, are eliminated with the constrained digital filter.

Figure 3-9 shows comparisons of measured and model attenuation time-series for station LCA for a 20-day period that includes a period of high current stress associated with a winter storm. Model predictions are shown for sediment size defined in two ways: The lower sieve size and the mid-sieve size. The predicted attenuation for the lower sieve size, during the high stress event on November 22 is about four times larger than measured, whereas for the mid-sieve size they are comparable. Both model predictions do not reproduce the high attenuation signal measured toward the end of November, suggesting that the measured signal is due to fine silt and clay sized particles. The model for LCB (fig. 3-10) underpredicts the observed attenuation signal. Note the regularity of the measured attenuation spikes which occur at about half the frequency of the current stress peaks, suggesting that attenuation peaks may not all due to local resuspension. This segment of the record from LCB is discussed in more detail in the section on fine particle transport. The comparison between model and observed attenuation at LCE (fig. 3-11) is good for the largest stress event on the November 15. Most of the other measured high attenuation signals are not reproduced and the attenuation predictions of the model for other high stress events is at about the noise level of the instrument. For LCM (fig. 3-12), predicted attenuation during the high stress events of November 11-13 are out of phase with the measured attenuation which has relative maxima at times of minimum current stress. This peculiar phenomenon of maximum attenuation at minimum stress has also been observed at a number of other locations on the shelf and Georges Bank and it is thought to be due either to the movement of a turbidity front, or more likely, due to "inverse resuspension" where sediment suspended during high stress events settles during periods of low stress to produce a highly turbid near-bottom sediment layer. A separate study of this

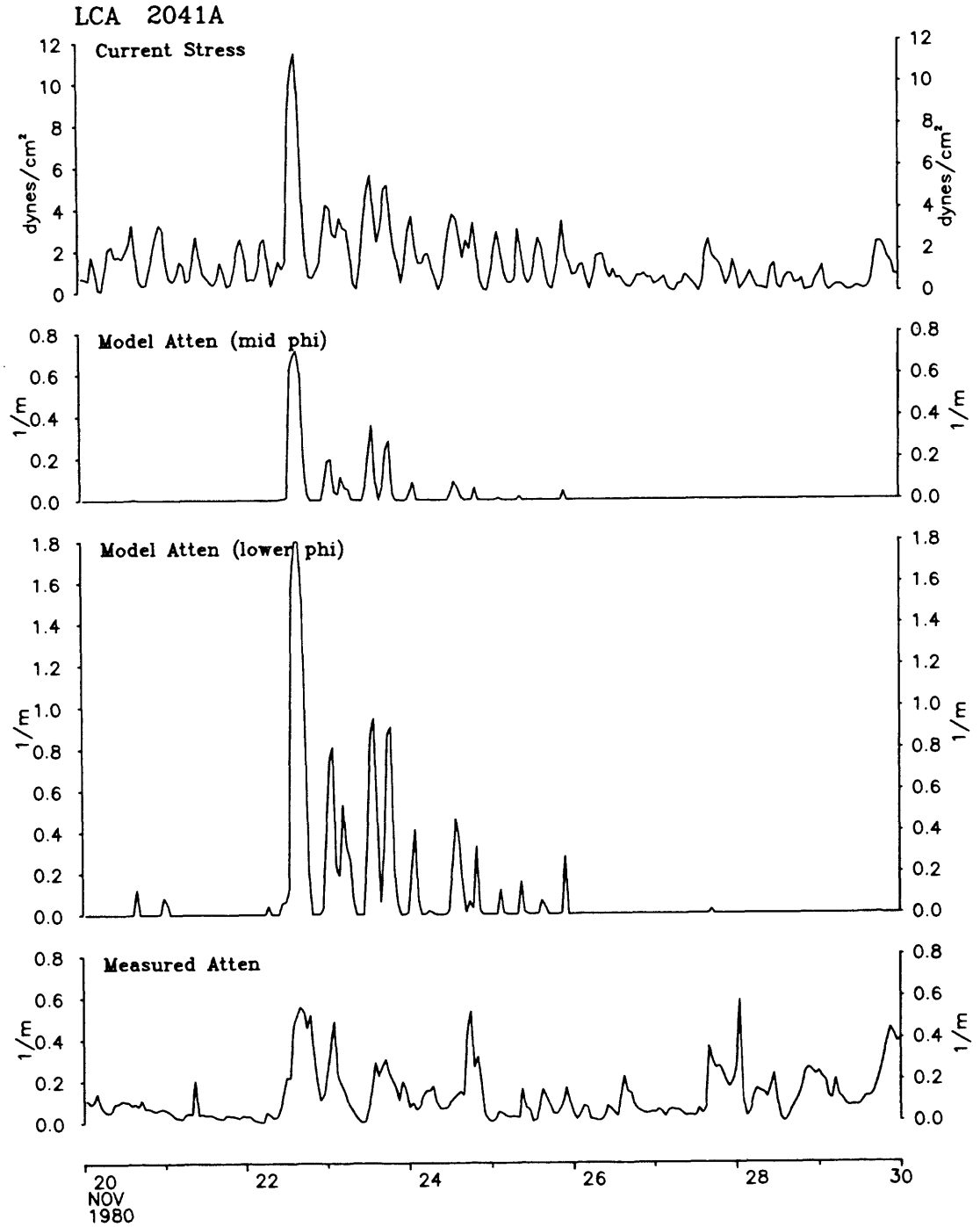

Figure 3-9. Time-series of measured attenuation 1.9 mab at LCA (deployment I, tripod mooring 2041), attenuation predicted by the sediment transport model using four sand grain sizes, and current stress τ_c calculated by the model. The curve labelled "lower phi" refers to sand grain sizes defined as the smallest size retained on the sieve (32, 64, 128 and 250 μm) whereas for the "mid phi" curve the middle sizes are used (47, 94, 188, and 375 μm). The background signal from the measured attenuation was removed using the constrained digital filter.

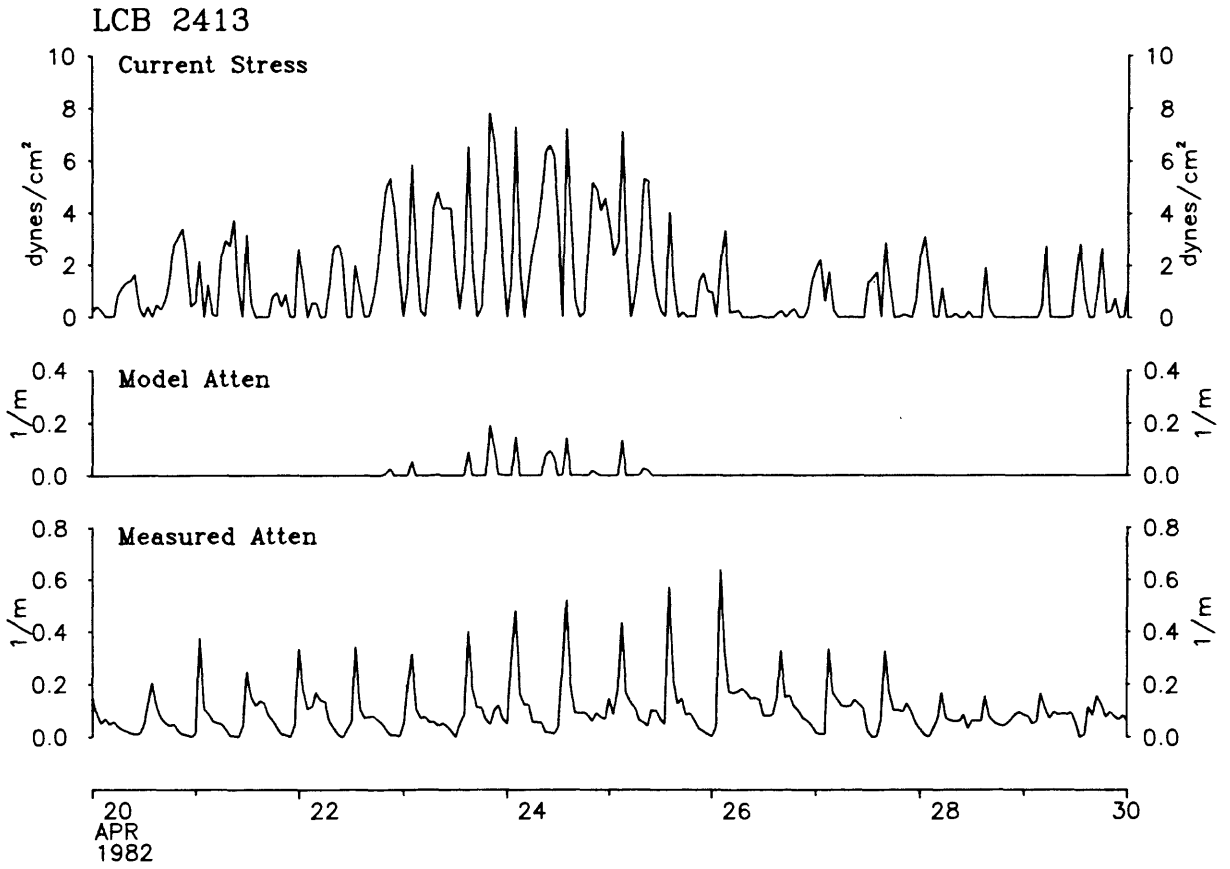

Figure 3-10. As for figure 3-9 but for LCB (deployment IV) using the mid-phi size definition for model calculations.

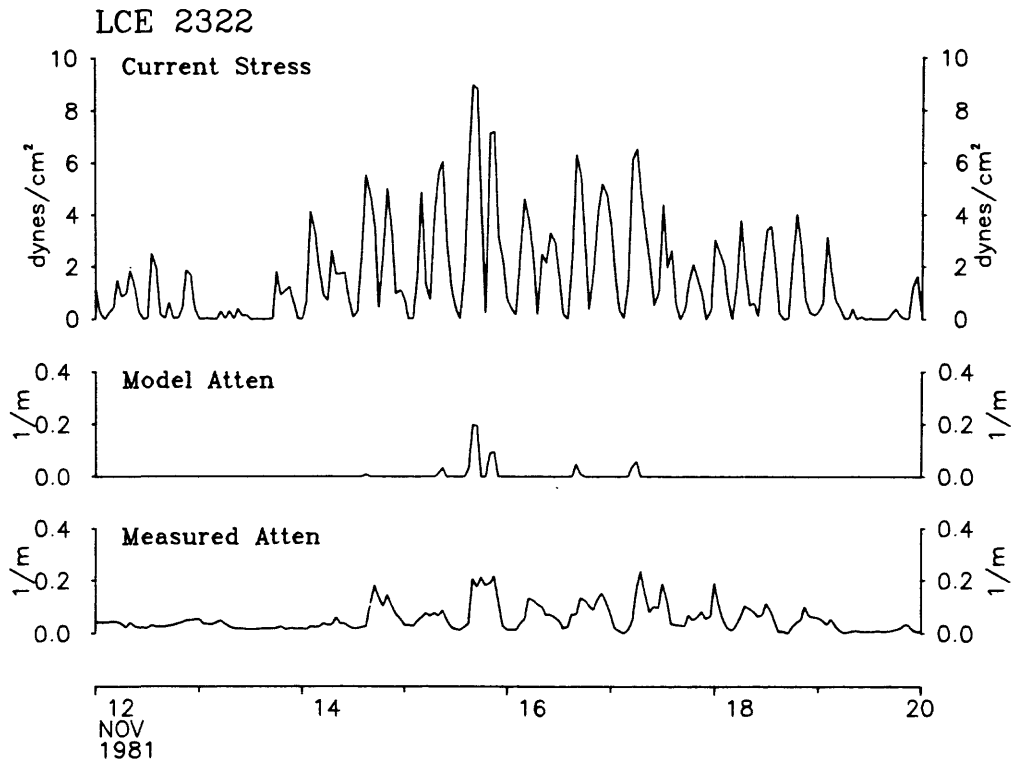

Figure 3-11. As for figure 3-9 but for LCE (deployment III) and for the mid-phi sand sizes.

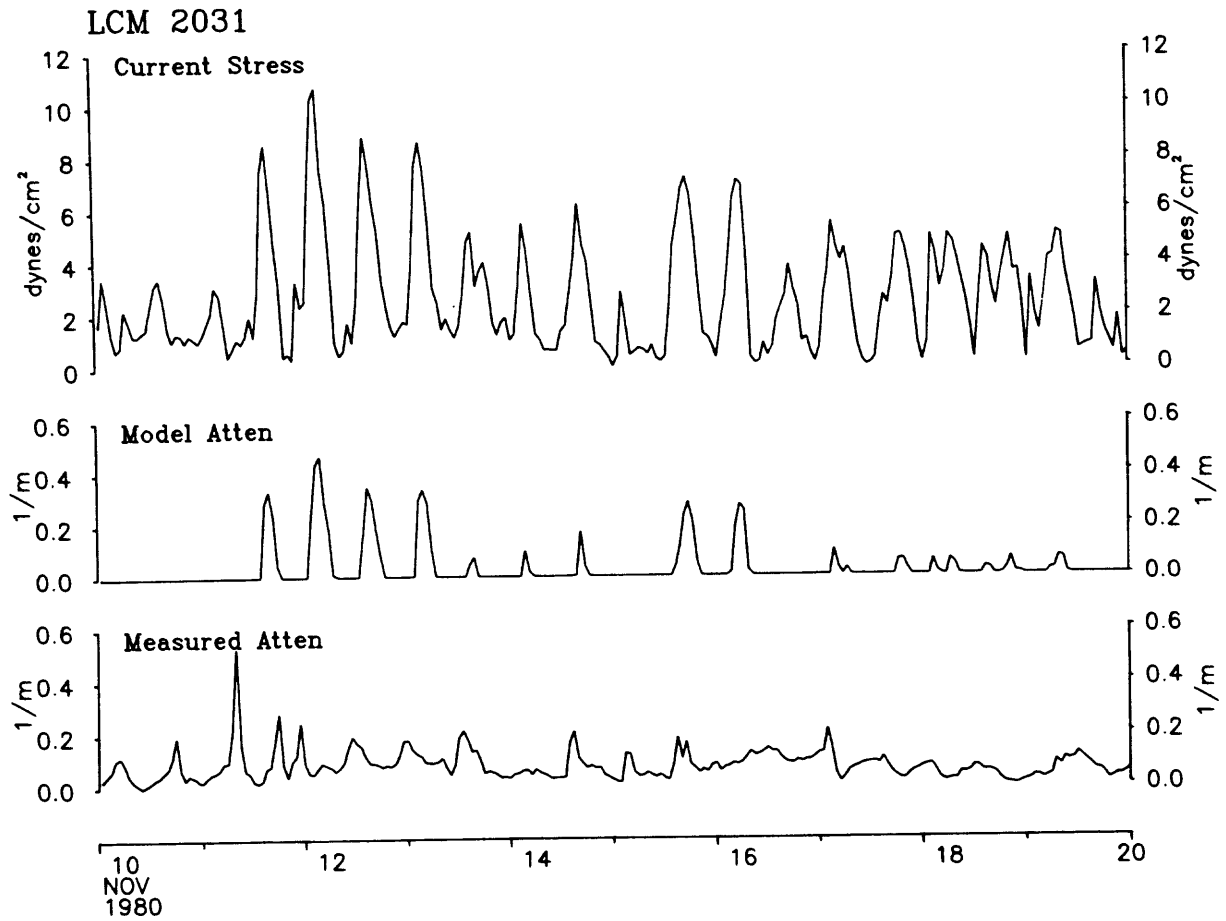

Figure 3-12. As for figure 3-9 but for LCM (deployment I) and for the mid-phi sand sizes.

phenomenon is underway. However, the overprediction of attenuation during high stresses at LCM is disconcerting. The bottom photographs at this site show a highly bioturbated bottom with very little loose sand or sand ripples that would indicate active sediment movement. Also, more than 10 percent of the sediment at LCM is finer than 8 μm in size. We conclude that the surficial sediment is more erosion-limited than predicted for cohesionless sand (Shield's curve) due perhaps to biological processes.

In summary, with the exception of LCM, the predicted attenuation, due to the sand components analysed here, is comparable to the observed attenuation during periods of high current stress. Interpretation of the beam transmissometer measurements is complicated by signals due to suspended fine material and by the low predicted attenuation signals for many stress events that are at the background level of variability. At LCM, the surficial sediment appears to be more compacted and erosion-limited than we have assumed.

Predicted Sand Transport Rates

Transport rates for the four sand sizes were computed using the model for the bottom 10 m of the water column (table 3-3). Transport rates for the 375 μm size class were small or zero and are not presented in table 3-3. Fig. 3-13a shows sediment transport roses for stations located around Lydonia Canyon and Fig. 3-13b shows the sediment transport roses for stations within the canyon axis. At LCA, LCB and LCE, transport roses are shown for two mooring deployments to give some indication of temporal variability. Transports are shown without regard to season; note that observations on the shelf at LCA and LCM were made during winter.

Table 3-3. Components of net sand transport predicted by the sediment transport model for stations within and around Lydonia Canyon. Eastward and northward components are listed for the four sand size fractions and the total sand transport. Transports are calculated for the bottom 10 m. Transport units are mg/cm/s.

SEDIMENT TRANSPORT RATES FOR LYDONIA CANYON

Station (mooring)		SEDIMENT SIZE 188μm 125-250		94μm 64-125		47μm 32-64		Total	
LCA	Deploy.	East	North	East	North	East	North	East	North
2041	I	-0.007	-0.007	-1.498	-1.609	-5.767	-6.461	-7.272	-8.077
2042	I	-0.003	-0.002	-1.346	-1.044	-17.703	-12.060	-19.052	-13.106
2231	II	0.000	0.000	0.000	0.000	-0.038	-0.149	-0.039	-0.149
2571	V	0.000	0.000	0.000	0.000	0.167	-0.433	0.167	-0.433
LCB									
2083	I	0.000	0.000	-0.008	0.003	-0.016	0.035	-0.024	0.037
2263	II	0.000	0.000	-0.038	0.027	-0.041	0.059	-0.080	0.086
2311	III	0.000	0.000	0.385	-0.299	1.138	-0.771	1.523	-1.070
2413	IV	0.000	0.000	0.250	-0.066	0.739	-0.153	0.989	-0.219
2583	V	0.000	0.000	0.053	-0.016	0.267	-0.108	0.320	-0.124
LCE									
2114	I	0.000	0.000	-0.006	-0.006	-0.013	-0.021	-0.019	-0.028
2322	III	-0.001	-0.002	-0.021	-0.289	-0.384	-0.940	-0.506	-1.231
LCI									
2154	I	0.000	0.000	0.000	0.001	0.000	0.003	0.000	0.005
2341	III	0.000	0.000	0.000	0.000	-0.006	-0.081	-0.006	-0.081
LCP									
2371	III	0.000	0.000	-0.122	-0.028	-0.303	-0.094	-0.426	-0.122
LCS									
2451	IV	0.000	0.003	-0.033	0.197	-0.693	3.835	-0.726	4.035
LCQ									
2431	IV	0.000	0.000	-0.053	-0.003	-0.416	0.024	-0.469	0.021
LCL									
2511	IV	0.000	0.000	0.042	-0.149	0.143	-0.355	0.186	-0.504
LCM									
2031	I	0.003	-0.004	1.253	-1.889	3.633	-6.797	4.889	-8.691
LCU									
2591	V	0.000	0.000	0.104	-0.246	1.000	-3.276	1.104	-3.522

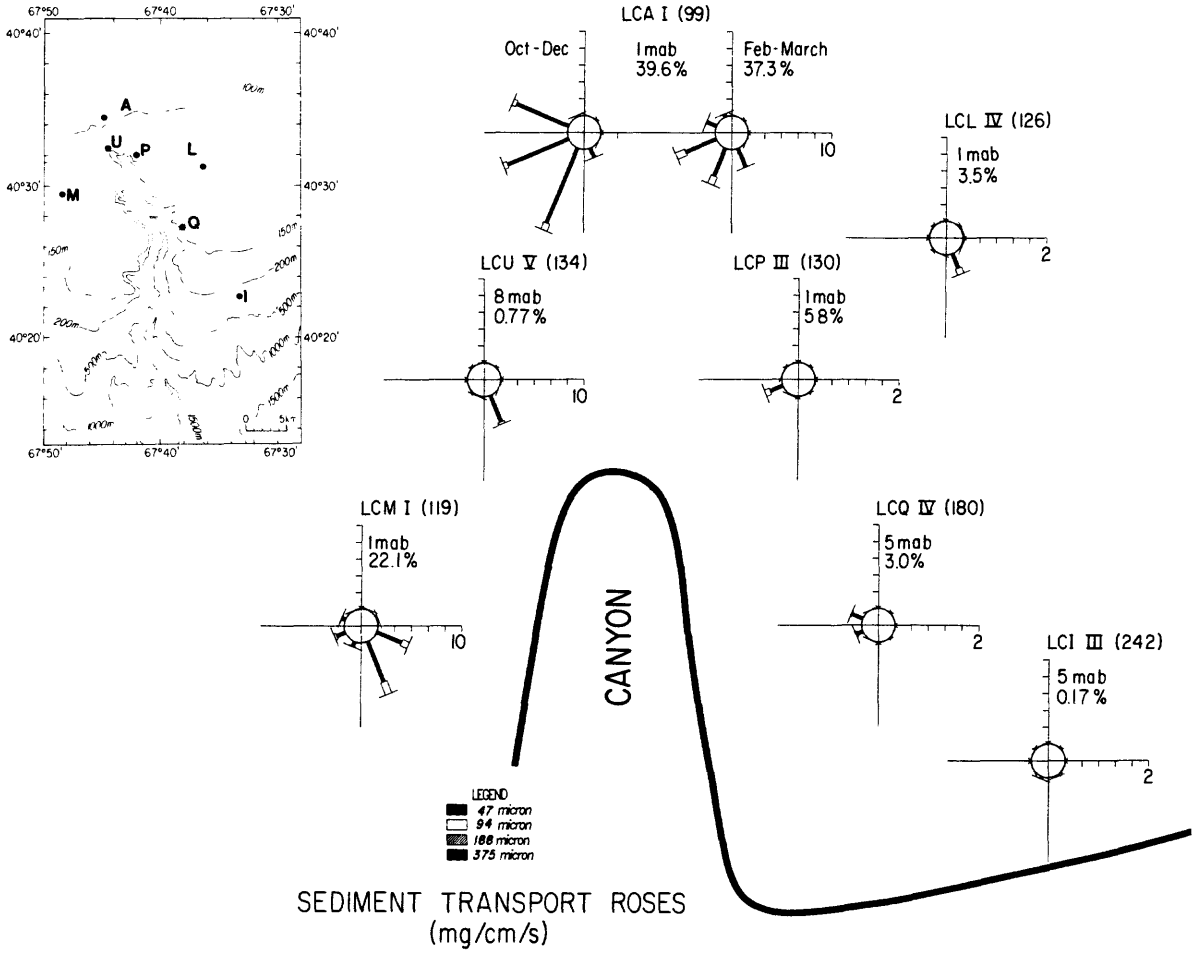

Figure 3-13a. Selected sand transport roses for stations surrounding Lydonia Canyon. Insert map shows station locations. Sand transport rates are sorted by direction, in 45° bins, and averaged over the whole record to provide the record averaged sand transport in each direction bin. The total length of each bar vector is the total sand transport and the contribution for each sediment class is indicated by the shaded bars. The percentage number is the percent of time of non-zero sand transport. Note changes in scale.

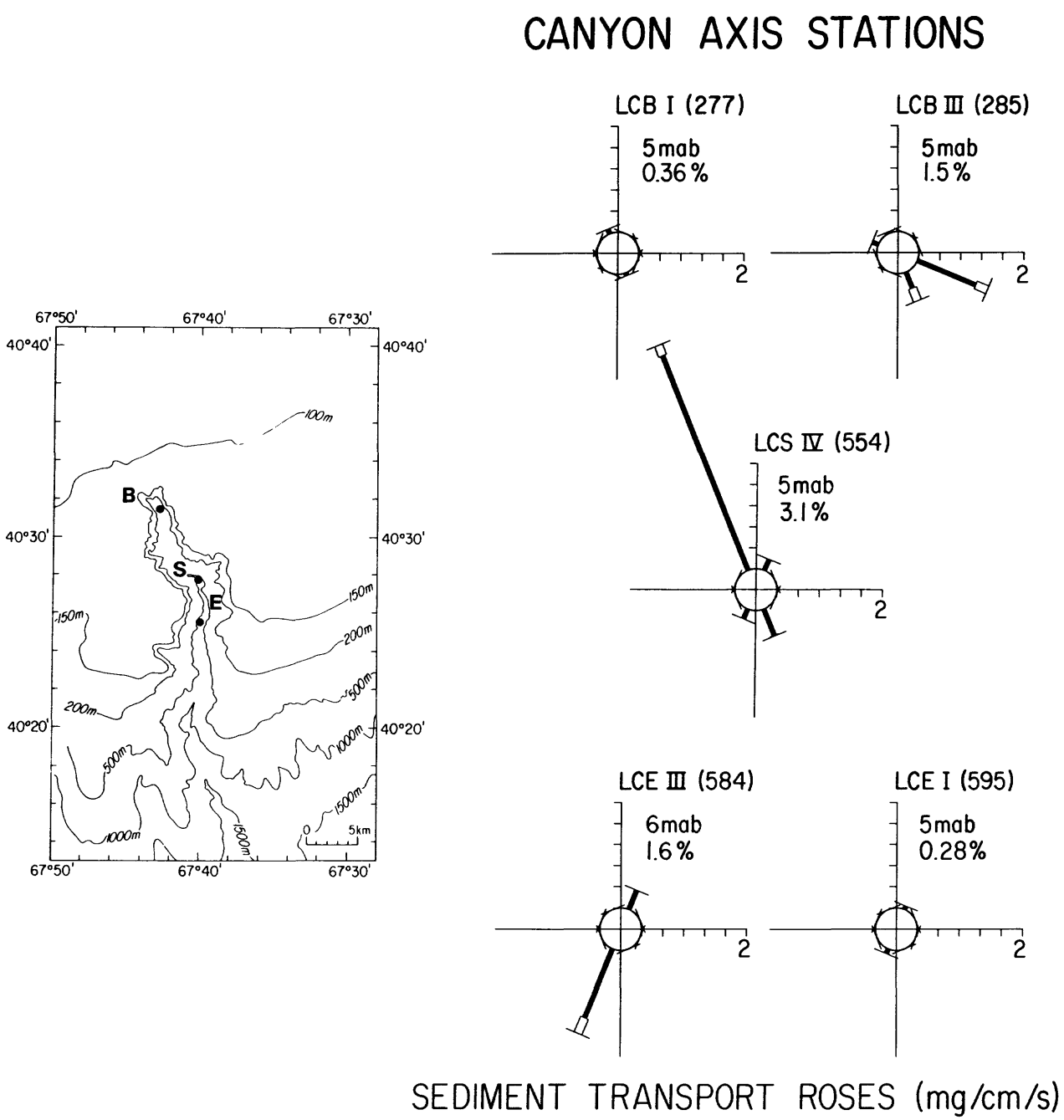

Figure 3-13b. Selected sand transport roses for Lydonia Canyon axis stations. Insert map shows station locations. Sand transport rates are sorted by direction, in 45° bins, and averaged over the whole record to provide the record averaged sand transport in each direction bin. The total length of each bar vector in the total sand transport and the contribution by component is indicated by the shaded bars. The percentage number is the percent of time of non-zero sand transport.

The percentage of time sediment transport is non-zero, (figs. 3-13c 3-13d), shows most active sediment transport at the shelf stations where surface gravity waves increase the skin friction and current stress. LCA and LCM are the two most active stations during winter; non-zero sediment transport occurs more than 20% of the time. At LCU, in slightly deeper water than LCA and LCM, non-zero sediment transport occurred less than 1% of the time, yet the sediment transport rate was about the same order as at LCA and LCM. For much of the time sediment transport at LCA and LCM is small (<10 mg/cm/s) and the bulk of the sediment transport is caused by a few strong current (or wave and current) events which occur only for a few percent of the time. While the percent of non-zero sediment transport at LCU is small, the transport is due to large current events. Similarly, along the canyon axis, sediment transport events occur less than a few percent of the time. LCS is the most active station where sand transport occurred 3 percent of the time. The more persistent sediment transport at the shelf stations during winter is due to the increased skin friction stress associated with surface gravity waves.

The largest transport rates are predicted for LCA and LCM due to the influence of waves. For the four records at LCA (Table 3-3), winter sediment transport rates are at least an order of magnitude larger than transport during summer. At LCB and LCE where wave effects are not significant, there was also a clear temporal variabilty, with maximum transport rates in the fall/winter deployment (2311) of 1981-1982 and minimum transport rates for the winter/spring deployment I of 1980-1981 (2083).

Transport roses for stations around the canyon (fig. 3-13a) show large sediment transport rates for stations at the head of Lydonia Canyon (LCA, LCU) and to the west (LCM). At LCA, the net sediment transport is towards the southwest. At LCU the net transport is towards the canyon head and at LCM

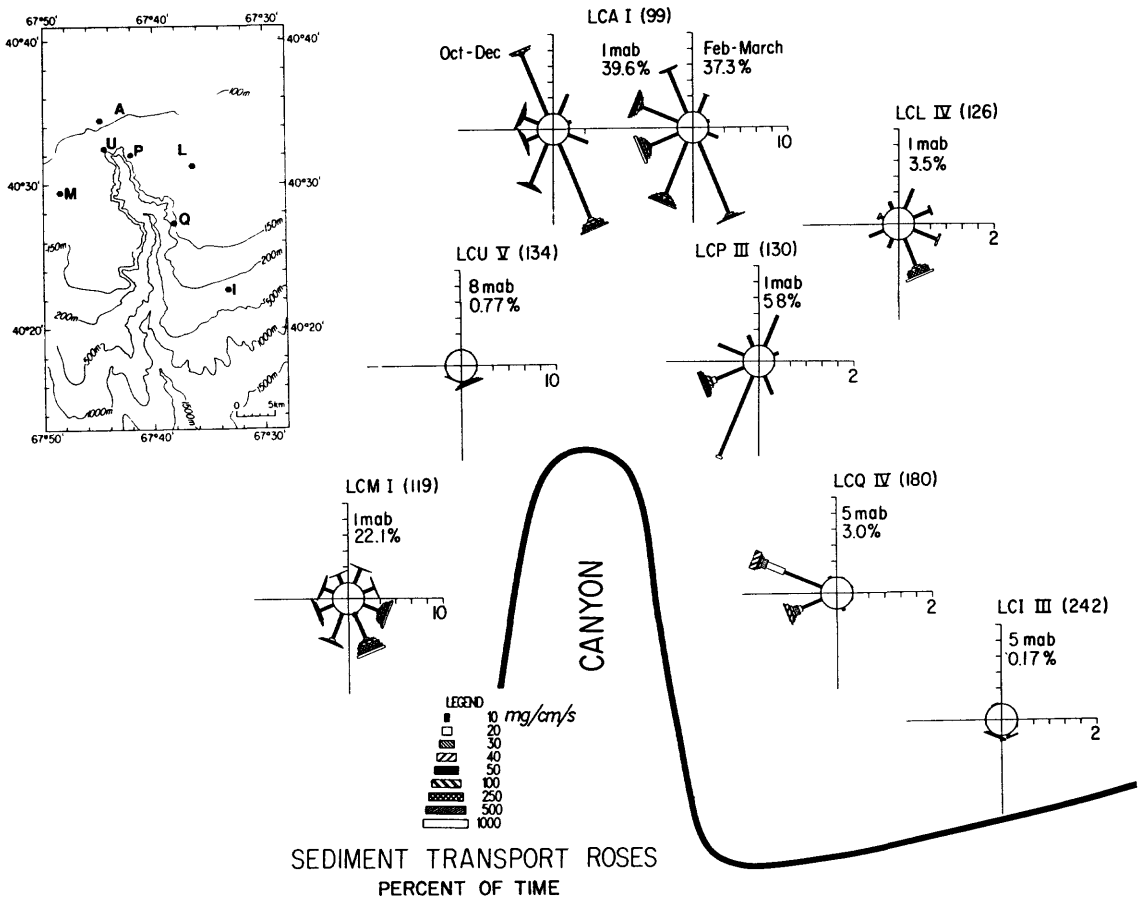

Figure 3-13c. Percentage of time of sediment transport magnitude, for stations surrounding the canyon. The total length of the stacked bars in each direction bin represents the percent of the measurement time that sediment transport was non-zero. The length of each of the different stacked bars indicates the contribution to the total percent of time from transport events of various magnitude ranges indicated in the legend.

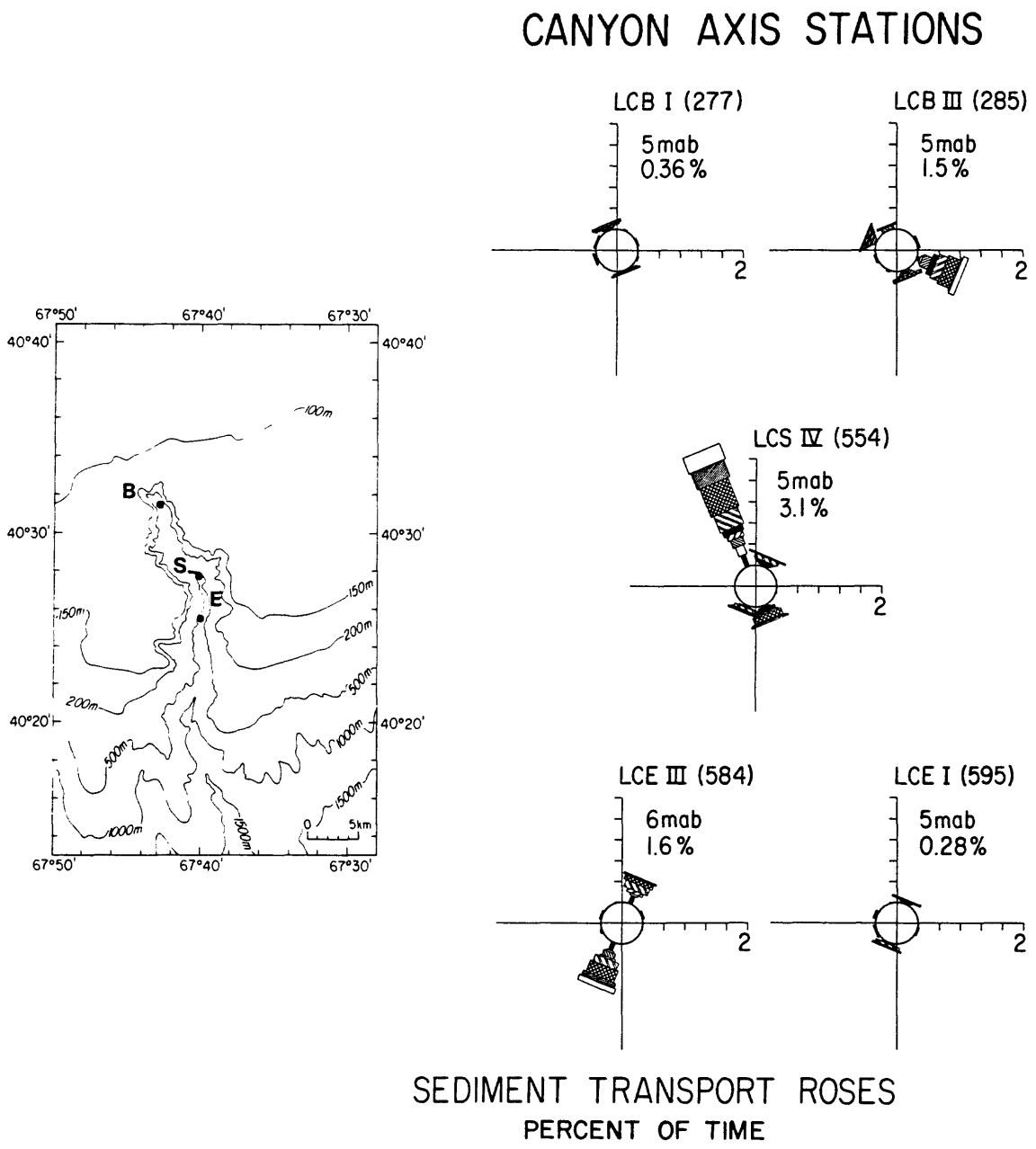

Figure 3-13d. Percentage of time of sediment transport, sorted by direction and sediment transport magnitude, for stations along the canyon axis. See caption to figure 3-13c for explanation of legend. Note net down-canyon transport at LCB and up-canyon transport at LCS.

there is an eastward component transporting sediment towards the western rim of the canyon. The net transport at both stations LCP and LCQ, situated on the eastern rim, is towards the canyon. The net southeastward transport at LCL is somewhat surprising as we expect currents on the shelf to be westward in general. However there is an off shelf near-bottom flow over the outer shelf, some associated with Warm Core Rings (see chapters 2 and 7). Transports at LCI on the upper slope are relatively small in comparison to the other stations. Along the canyon axis, the sediment transport roses (fig. 3-13b) indicate net up-canyon transports for periods of weak transport (2083) and net down-canyon transport for periods of strong transport (2311) (evident also from table 3-3); suggesting that strong currents and hence sediment transport events are in the down-canyon direction. At LCS, the net transport is very clearly large and upcanyon while at LCE there is net down-canyon transport.

Some rough estimates can be made of the sediment accumulation rates along the canyon axis using the computed transports. North of the canyon head at LCA the average sediment transport rate (average of 2042, 2231, and 2571) is 7.8 mg/cm/s roughly downshelf towards the southwest; it is not clear that any of this sediment gets into the canyon. The single observation at LCU suggests a transport of 3.7 mg/cm/s directly toward the canyon head. At LCB, the average transport for the five deployments (table 3-3) is about 0.6 mg/cm/s giving an accumulation of about 3.1 mg/cm/s between LCU and LCB. Spreading this divergence in sediment transport evenly between LCU and LCB yields an accumulation rate equivalent to 2.3 m/1,000 yr (assuming a volume fraction of 0.6 for sand). Adding to this accumulation is the over-the-rim transport at LCP which we expect will reach the canyon floor due to the steep sides. Spreading the transport from LCP across a canyon floor width of 750 m adds

about 1.3 m/1,000 yr giving a total of 3.6 m/1,000 yr for the canyon head region. Much of this transport at LCP occurred during a single large winter storm; yearly averaged flux might be a factor of 2 or more less.

There is also a convergence of sediment transport between LCB and LCS. A uniform spread of this convergent sediment transport amounts to about 1.2 m/1,000 yr with an additional over-the-rim transport, estimated from LCQ, resulting in an accumulation of 1.2 m/1,000 yr giving a total of 2.4 m/1,000 yr. Between LCS and LCE, the sediments appear to be eroding at a rate comparable to the rate at which sediment is coming across the eastern rim.

Geological observations of sediment erosion and deposition in Lydonia Canyon can be used to place our calculations in perspective. Twichell (1983) has inferred from Uniboom profiles that the youngest sediment fill, of Holocene age, in Lydonia Canyon occurs along the canyon floor and gullies shoreward of the shelf break and especially at the head of the canyon. In some places, the fill was more than 25 m thick and appeared to be draped over the existing topography. The observation of sediment accumulation shoreward of the shelf break agrees with the model results which show sediment influx from LCP and LCQ, and convergence near LCB. Direct comparison of sediment fill thickness is not appropriate as the sea level during the beginning of the Holocene period was low enough for waves to affect sediment transport at the head of the canyon. However, the prediction that much of the accumulation is at the canyon head is in qualitative agreement with Twichell's (1983) observations. The predicted accumulation rates of 2.4 m/1,000 yr for the region between LCB and LCS agrees well with the sediment fill thickness of about 25 m or more estimated by Twichell (1983) given accumulation for the last 10,000 years. However, our records are of very short duration (and

active sediment transport events are even shorter) compared to time scales for geologic processes which produce identifiable sediment distribution changes and thus any comparisons are qualitiative. Based on the observed draped nature of the sediment fill, Twichell (1983) suggests that sediment deposition is from suspension rather than bedload. The model predicts that sediment is resuspended to 8 m or more above bottom during high stress events. Also, the sediment coming from the eastern rim may be advected across a substantial distance before being deposited. For example 64 μm sand, which has a settling velocity of 0.26 cm/s, would take about 11 hours to settle through 100 m of water. If this sediment were advected from LCP towards the canyon axis, which is some 180 m deeper, a 10 cm/s mean current would carry the sediment about 7 km horizontally - which is more than the canyon width (but note that the direction of flow below the canyon rim is primarily along the canyon axis). This simple calculation shows that some sediment may not slump down the walls of the canyon, but rather is being advected across the rim and along the axis before being deposited.

The observation of a fine sand patch between the 250-450 m depth along the canyon axis agrees with model prediction of sediment accumulation there (See Chapter 2). Also, the coarse patch of sand observed between the 450 and 650 m depth is in keeping with the model predictions of erosion at this site.

As part of the Lydonia Canyon Experiment, piston cores were obtained in the head of the canyon near LCU to measure sediment accumulation rates (see chapter 6). Accumulation rates in these cores, based on C_{14} dates, ranged from 50-70 cm/1000 years. These rates are a factor of 3-5 times lower than the rate obtained by uniformly distributing the predicted transport convergence between LCU and LCB. But, the predicted transport estimates (table 3-3) suggest that the area between LCA and LCU is eroding so that the

predicted accumulation rate between LCU and LCB will overestimate the local accumulation at LCU. Given the short duration of the observations, the model uncertainities, and possible local variability of deposition, the agreement between model and observation is extremely encouraging.

The up-canyon transport at LCS and the net convergence of sediment toward the canyon head were unexpected. However, both the time-series observations, the surficial sediment texture, the high resolution profiles as well as the piston cores all indicate deposition in the axis. The dynamics of the current structure which causes the divergence is not clear at present, but is probably associated with internal waves in the canyon (see chapter 2).

In summary, model predictions and geological observations both suggest accumulation of sand-sized material in the head of Lydonia Canyon and along the canyon floor down to about the 450 m depth. Sediment accumulation results primarily from suspended sediment transport during high stress events. Sediment influx from the eastern rim is of comparable magnitude to convergent sediment transport along the canyon axis. Sediment influx across the western rim was not measured. The coarse sand between 450 and 650 m depth in the canyon axis appears to be an area of erosion where sediment influx across the rim is of comparable magnitude to sediment transport divergence along the canyon axis.

FINE SEDIMENT TRANSPORT

We describe here the transport of fine particles as inferred from beam transmission data, hydrographic data, and computed values of bottom stress. Beam transmission measurements provide a quantitative measure of the changes in water transparency but no information about the causes. Bottom photographs and observations made during the ALVIN submersible dives show that

transparency changes may not only be due to suspended sediment but also occasionally by fish, swarms of shrimp and floating debris (including garbage bags!). Nonetheless, beam transmission measurements provide important information about the transport of fine particles that cannot be obtained from a one-dimensional model.

Fine particles that settle slowly are mixed higher into the water column than coarse particles and also are advected over long distances. In addition, the stress necessary to cause cohesionless fine sediment to move is relatively large, so that once movement occurs, there is rapid suspension of the sediment - without the initial stage evident for sediment coarser than medium sand, where the grains roll or hop along the bed before suspension. The occurs because the stress to cause sediment motion decreases much less rapidly with sediment size than settling velocity. For example, a 500 μm coarse sand has a settling velocity w_f = 7 cm/s and a critical shear speed u_{*crit} = 1.6 cm/s whereas a 31 μm coarse silt has w_f = 0.06 cm/s and u_{*crit} = 0.86 cm/s Thus, the critical shear speed decreases by less than a factor of two but the settling velocity decreases by more than a factor of 100.

For fine particles, the settling velocity and critical stress are sensitive to certain biological and physical factors. For example, stirring of fine sediment due to benthic foragers could suspend sediment even if the shear stress were much less than that necessary to cause incipient motion. Alternately, adhesive mucus secreted by some benthic animals can raise the critical stress for incipient motion. Particle adhesion or flocculation also raises the settling velocity of fine sediment. Thus, although there are considerable uncertainties in determining how fine particles are transported throughout the canyon, we present an analysis of the available observations to gain some insights.

Relation to hydrography

Figure 3-14 shows a representative winter-time section of salinity and beam transmission, expressed as an attenuation coefficient, taken along the canyon axis. The salinity section shows the presence of the distinctive shelf/slope front marked for example by the 34 psu and 35 psu salinity contours in the upper 150 m of the water column. Onshore of this front near the bottom, is a shelf turbidity layer (note that the details of this layer between stations 31 and 3 are interpolated by the contouring routine). The top 50 m of the water column is well mixed in both salinity and attenuation coefficient. There is deeper surface mixing in the slope water (due to greater heat losses and deep convective mixing) and attenuations are relatively low. A second turbid layer occurs along the canyon axis floor separated from the shelf turbidity layer by the shelf/slope front. In the canyon turbidity layer, the vertical decrease rate of attenuation is much less than that for the shelf.

Given the vertical profile of attenuation and estimates of bottom stress, a settling velocity of the particles can be calculated assuming a local balance between settling and vertical mixing of sediment. At station 31 which is near LCA, the attenuation decays by a factor of about two from 8 mab to 20 mab. Unfortunately, wave and near-bottom (1 mab) velocity measurements are not available at LCA for this period but velocity measurements 20 mab are available and during this period, observations at other shelf stations show no appreciable wave activity. Thus stress can be estimated from current observation alone. At LCA, the hourly velocity 20 mab was about 45 cm/s and the model predicts a u_{*c} = 1.34 cm/s for a bottom roughness of 1 cm. A few trials with the model yields an estimate of 0.34 cm/s for the sediment fall velocity which is equivalent to that for 70 μm size sand. However, the skin

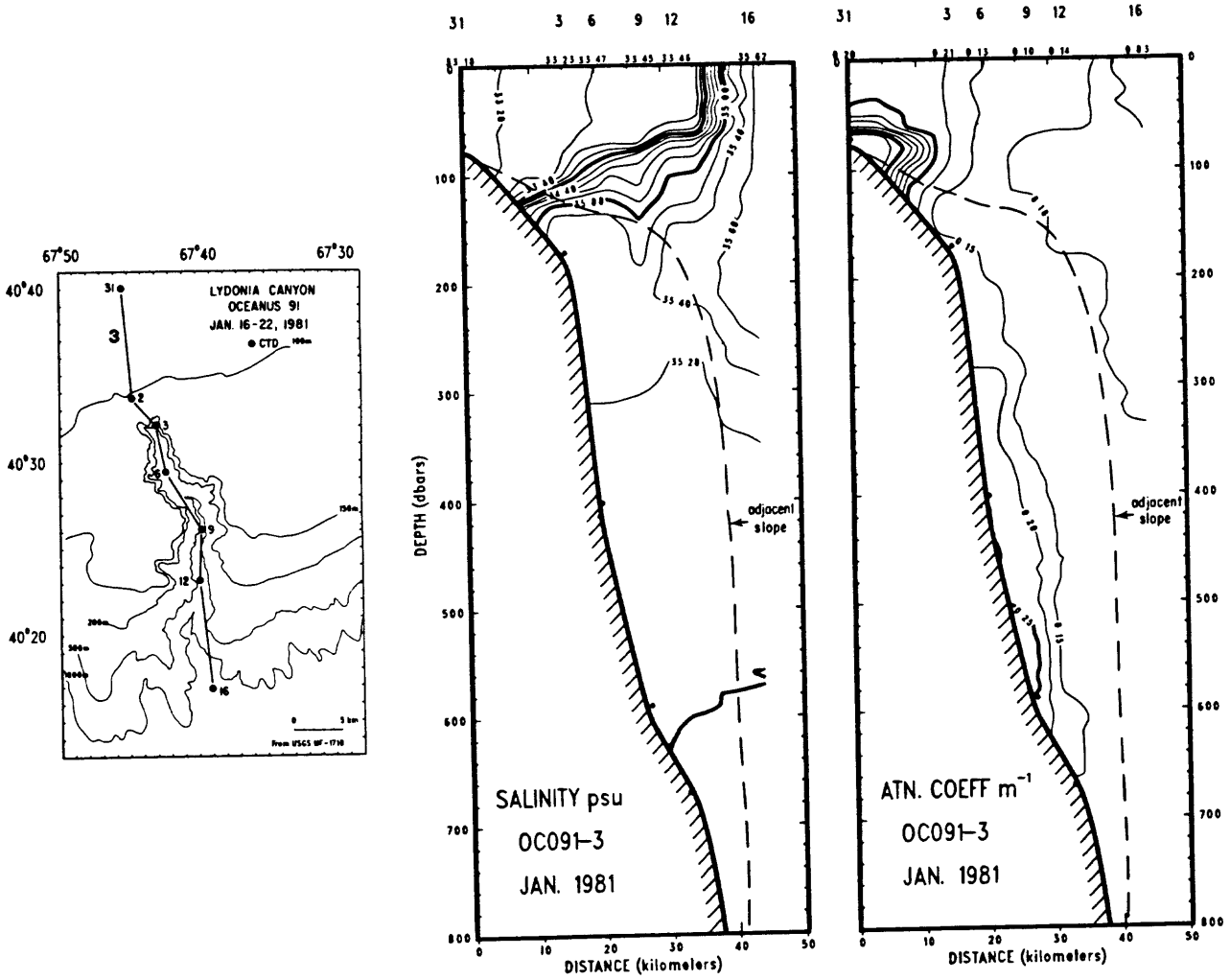

Figure 3-14. Section of salinity and beam attenuation coefficient from OCEANUS cruise 91. Insert map shows station locations.

friction stress (which in this case is about half u_{*c}) is not large enough to move sand of this size. Even if sand of this size were suspended, the concentration at 20 mab would be orders of magnitude too small to cause the observed beam transmission signal. Thus, the shelf turbidity layer must be caused by fine particles having a settling velocity of about 0.34 cm/s.

By contrast to the shelf turbidity layer, the canyon axis turbidity layer has small attenuation coefficients but has a larger vertical scale (100 m or more for attenuation to decrease by 0.05 m^{-1}). Note that in the slope water, there is a background of about 0.1 m^{-1}. Currents were decreasing at LCB during the period when the profile at station 6 was obtained. The shear speed decreased from about 1.4 cm/s half an hour before the profile commenced to 0.6 cm/s half an hour after the profile commenced. There appears to be little fine material at LCB during this time and any fine material appeared to be relatively well mixed. This suggests, in conjunction with the calculated shear speeds, that any material at LCB had small settling velocities or that, the mixing at LCB was more intense than we calculated - due for example to mixing along the walls of the canyon. At station 9, near LCE, the shear speed was about 0.8 cm/s at the time of the profile and increased to 1.3 cm/s an hour later. Again, a much thinner turbid layer would be expected if the particles had a fall velocity of order 0.3 cm/s. The large vertical scale over which the attenuation decays at the axis stations prevents use of the near-bottom model. However, we can conclude that the particles in the canyon settle more slowly than the particles on the shelf and/or that there is increased mixing within the canyon (that is not reflected by the u_{*c} from the near-bottom model) and sediment injection from flow along the canyon walls. Attenuation observations along the canyon axis show enhanced vertical variability of turbidity that may be the result of mixing from the canyon walls.

Attentuation Time-Series Interpretation

Time-series of beam attenuation measured at a number of locations illustrate the vertical and horizontal coherence of fine particle suspension, the settling velocity and critical threshold stress, and the role of storms and energetic current events in the canyon in transporting fine sediment. As it is not possible to present and analyse all of the time-series obtained in the canyon experiment we will present selected observations that illustrate the essential dynamics of fine particle suspension and transport within and around the canyon. The attenuation time-series were all filtered with the constrained digital filter to remove any background and fouling signal.

Vertical and Horizontal Interrelationships

Figure 3-15 shows a selection of time-series made during deployment I at LCA, LCB, and LCE. One of the prominent features of the time-series is the high and spiky attenuation observed at the near-bottom instruments - especially during the month of December 1980. By contrast, the observations away from the bottom show relatively smaller beam attenuations. At LCB(2081) a prominent feature is the increase in the attenuation signal in February and March caused presumably by the spring bloom of phytoplankton. An empirical-orthogonal-function (EOF) analysis of the time-series (Wallace and Dickinson, 1972) shows that most of the variance in the low-passed data is explained by two modes - essentially the two features of the data just described. The signal at LCE (2112) above the bottom is relatively small all the time. Thus, the observations show that much of the fine particle signal occurs along the near-bottom and around the head of Lydonia Canyon, with a possible spring bloom signal in the surface waters near the canyon head and above the canyon rim.

The intriguing question as far as near-bottom sediment-transport is

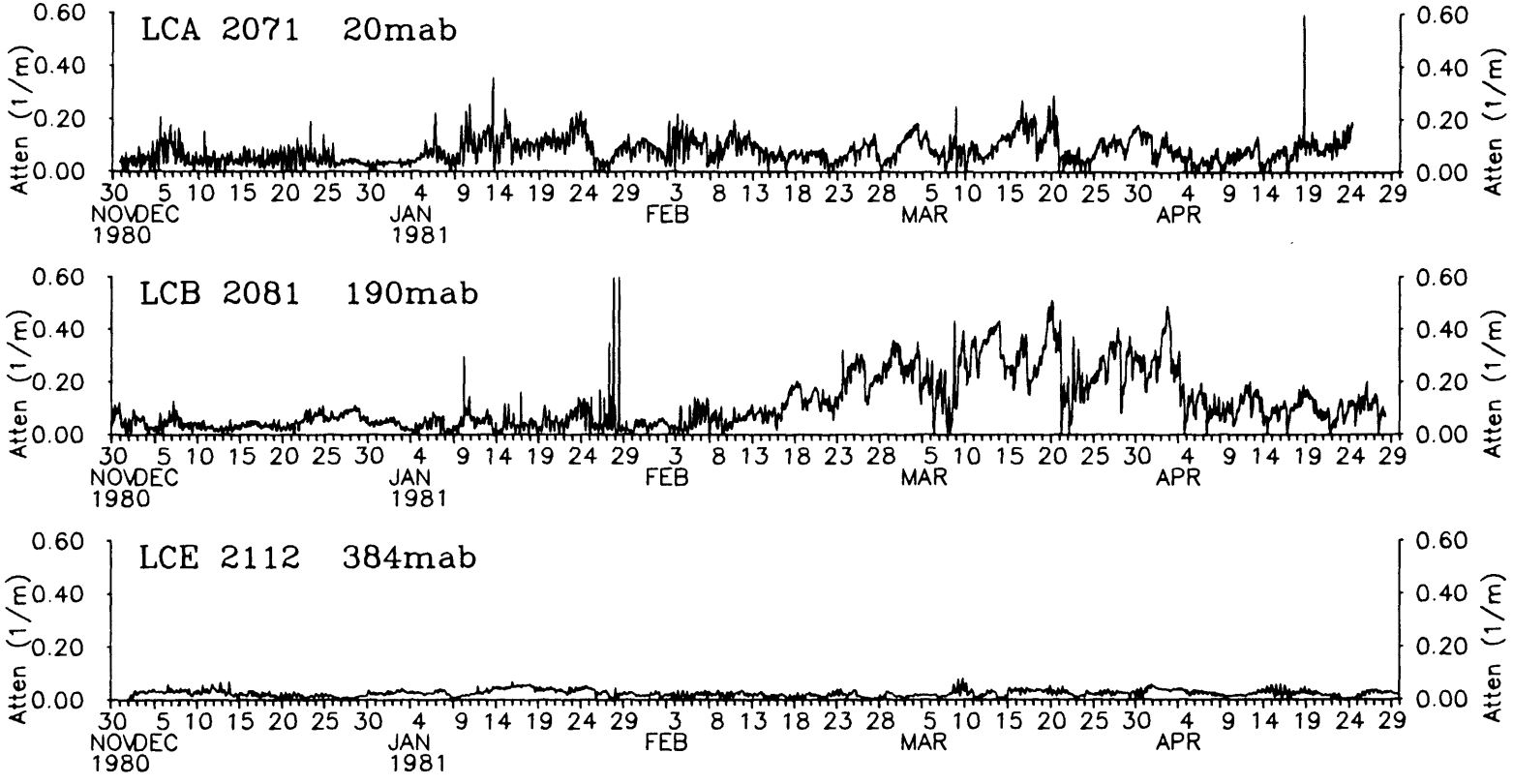

Figure 3-15a. Time-series of beam attenuation measured to LCA, LCB and LCE during deployment I for stations 20 mab or more. The background attenuation signal and transmissometer fouling signal has been removed from each time-series using the constrained digital filter.

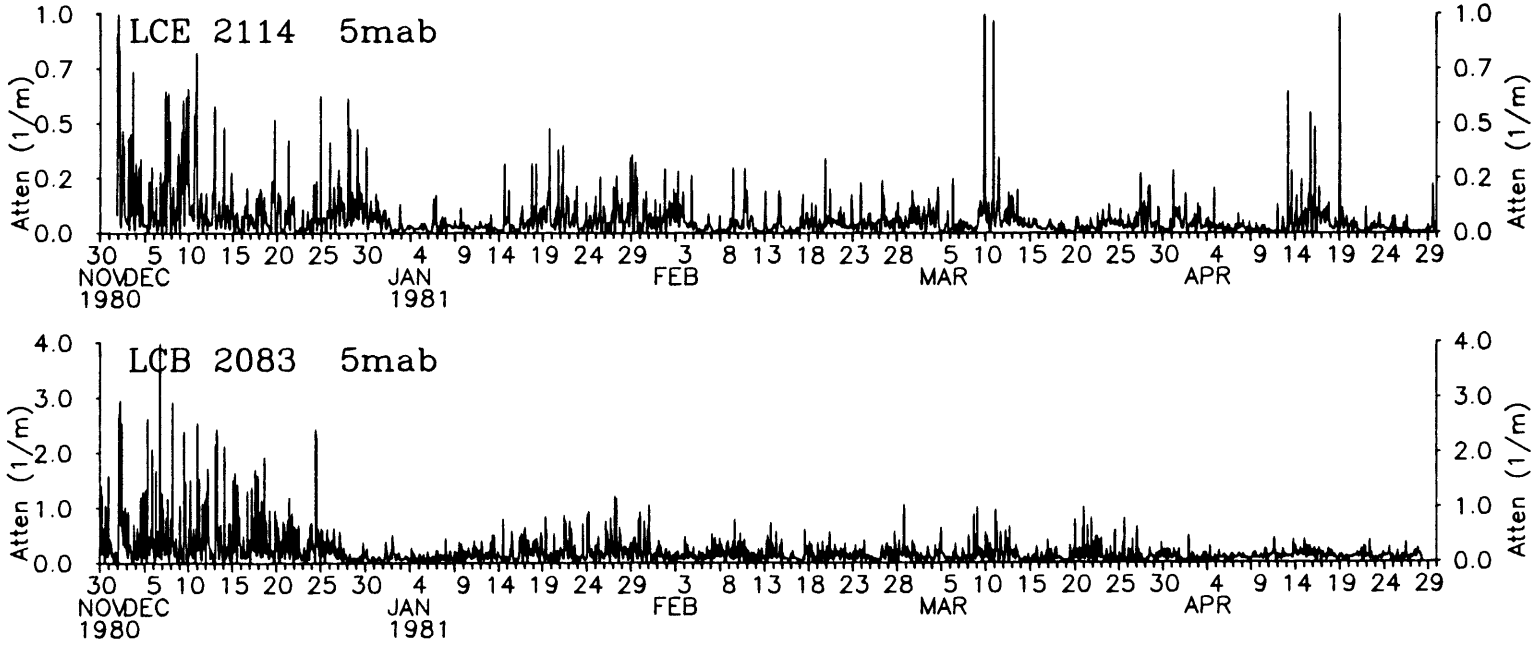

Figure 3-15b. Time-series of beam attenuation measured at LCB and LCE during deployment I for stations 5 mab. The background attenuation signal and transmissometer fouling signal has been removed from each time-series using the constrained digital filter. Note change of scale.

concerned is, what is responsible for the large and rapidly varying signals at LCB and LCE? Bottom photographs at both sites confirm that turbid waters occur at the times of high attenuation seen in the time-series. When the bottom was visible, loose dark sediment was seen scattered over the seafloor; this dark sediment was especially noticable within the troughs of sand ripples at LCE. The amount of the dark sediment varied over time and appeared to be loose and flocculant. However sediment traps deployed at LCB do not show increased capture of organic particles for this deployment (Bothner and Parmenter, pers. comm.).

The rapid attenuation changes suggest rapid settling of sediment and raises the question of whether it is possible to use the time-series of attenuation and bottom stress to calculate settling velocities. Figure 3-16 shows a segment of the observed attenuation at LCB (December 2-10, 1980), computed current stress and predicted attenuation. The surficial sediment was assumed to be comprised only of fine particles having a small critical threshold for sediment movement (one percent of that for 70 μm sand). An erosion limit of 5mm was used. By trial-and-error a settling velocity of 0.34 cm/s gave reasonable agreement between model and observations; the model parameters were not adjusted to optimise the predictions. However, the predictions illustrate that there is local resuspension and deposition and that the settling velocity of the fine particles is relatively large - comparable to fine sand. The same model parameters used for the LCB simulations were also used to simulate the record at LCE. However the maximum amount of material capable of being suspended had to be reduced by a factor of almost 4 to reproduce the observed beam attenuation. As figure 3-17 shows, the overall pattern of predicted attenuation at LCE is in reasonable agreement with observations; there is overprediction of attenuation (perhaps the assumed

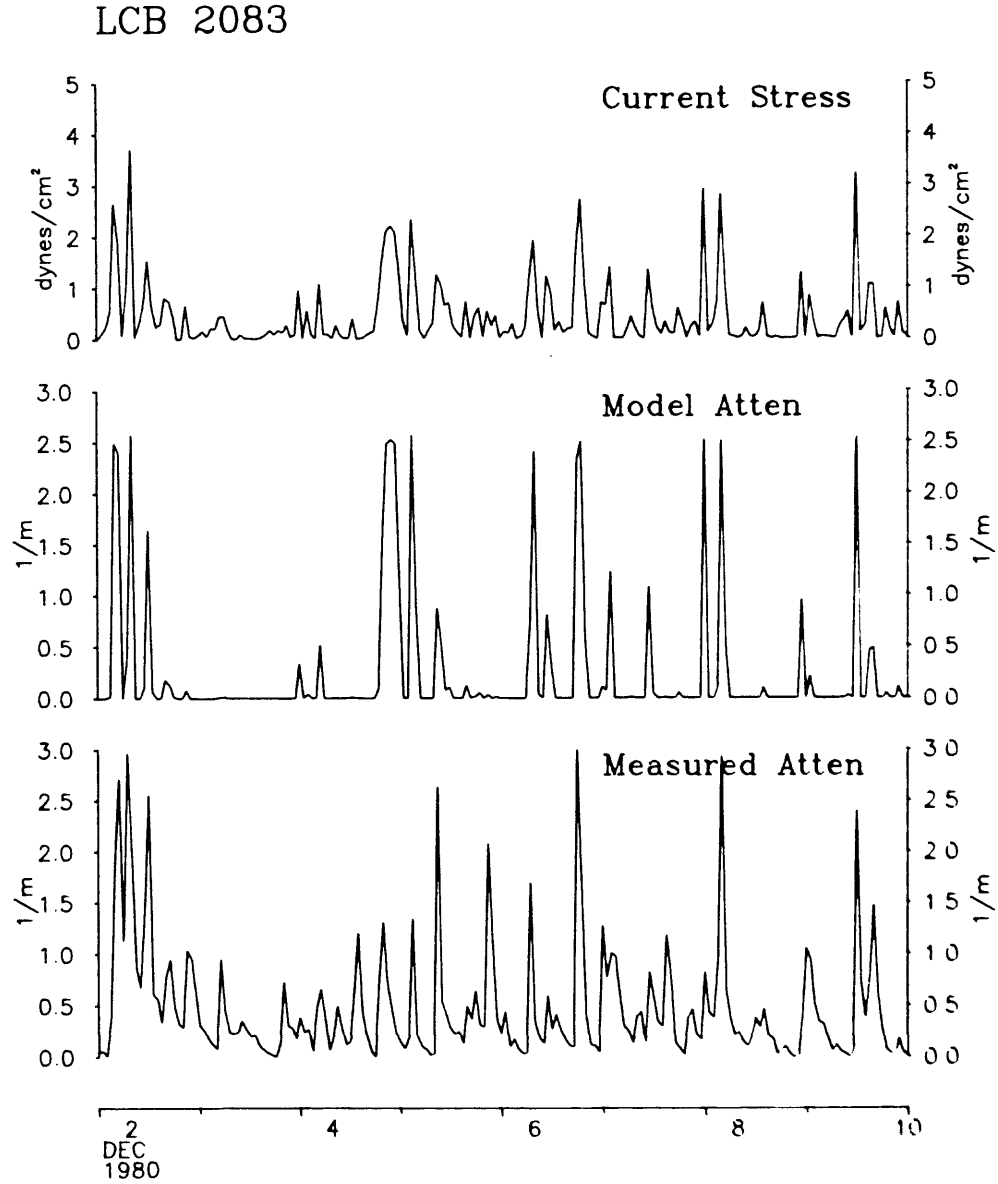

Figure 3-16. Time-series at LCB of measured attenuation, attenuation predicted by the model for fine particles and current stress τ_c calculated by the model. For the model predictions, the sediment is assumed to fall at the rate of 70 μm sand. Sediment concentrations are low enough so that no significant stratification effects are introduced.

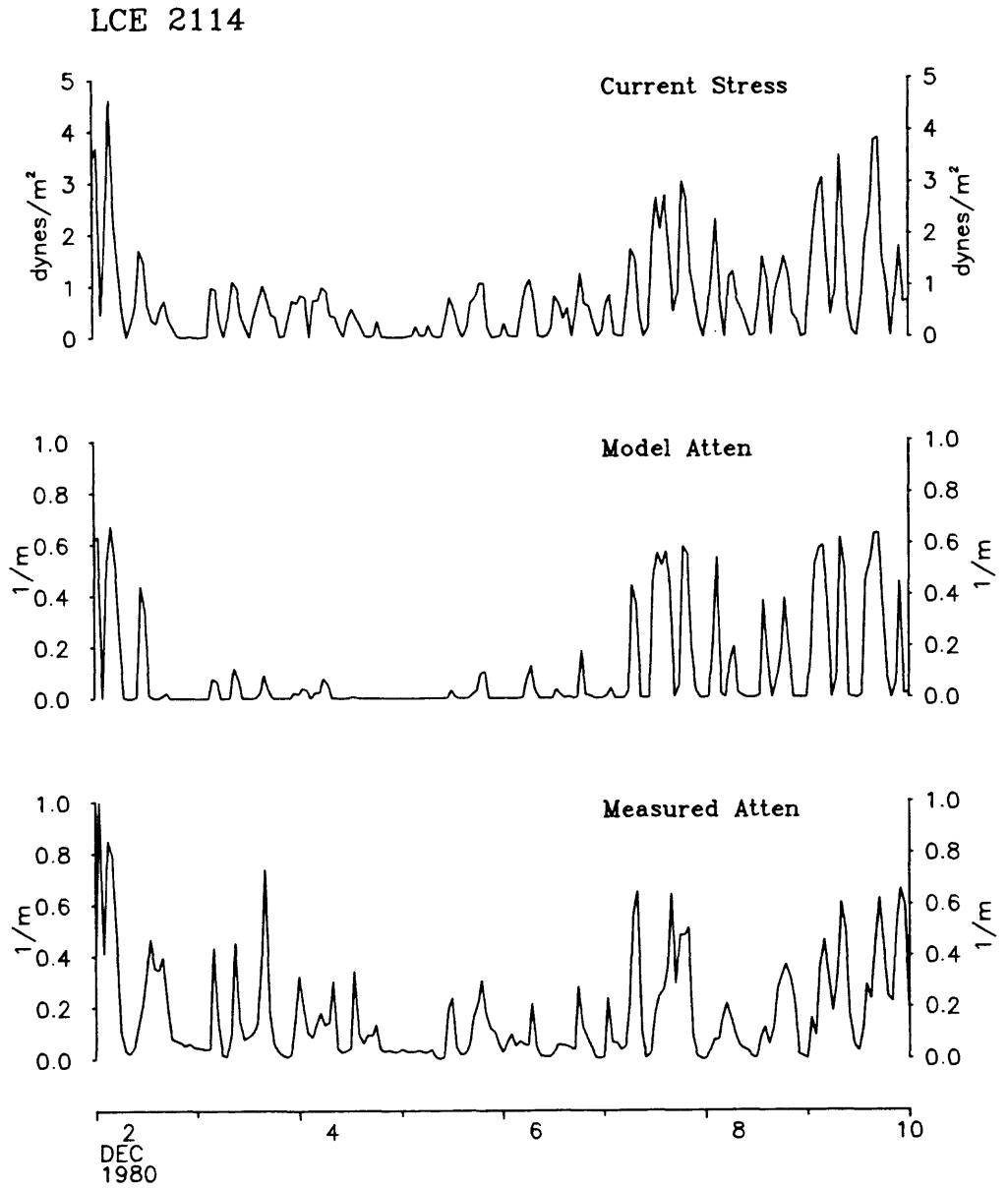

Figure 3-17. As for figure 3-16 but for LCE and assuming total amount of suspended fines is one-fourth that at LCB.

settling velocity is not high enough) for the latter third of the record, but the comparison supports the hypothesis that much of the observed variability is caused by local resuspension. At LCB, the comparison is not as good as at LCE but there are a number of large attenuation events which are simulated by the model. Of course, there are many aspects of the real situation that are not included in our model: time dependence; particles with a distribution of settling velocities; patchiness in the amount of particles and so on. The principal conclusion however is that at these axis stations fine particles settle relatively fast, and attenuation changes can be interpreted as resulting from a local resuspension and settling balance. This is the same conclusion reached with the analysis of the fine particle profile on the shelf (previous section).

Where do these fine particles come form and where do they go? At this stage, we speculate that the particles are derived from the shelf. First, because during December 1980 and January 1981, Warm Core Rings (WCR) 80J and 80G were offshore of Lydonia Canyon and appeared to cause the near-bottom flow at LCM, to flow southeastward (see chapter 2). The near-bottom flow at LCA also changed from southeast to southward. This apparent convergence of the flow may have carried shelf particles from the shelf into the canyon. Second, the attenuation section across the shelf (fig. 3-14) shows a source of fine particles on the shelf above the canyon head, and we have found that the particles both in the canyon and on the shelf have relatively fast settling velocities.

The available records at LCB show that while the December 1980 attenuation fluctuations were large and persistent, large but not as persistent fluctuations were also observed in November 1981 until the end of data record (2311) on the 27th of January 1982. This record was also from a

deep instrument package with a transmissometer 3.4 m above bottom. Records from transmissometers at 8.5 m above bottom (SSP) show some evidence of attenuation fluctuations, but they are not as large (generally less than 1 m^{-1}) as observed 3.5 mab. Some decrease in the fine-particle signal between 3.5 and 8.5 mab is expected if particles settle at the rate we have calculated. For example, if particles settle at 0.3 cm/s and given a current shear speed u_{*c} = 1 cm/s, the signal 8.5 mab will be sixty percent of the 3.4 mab signal. Thus, even though the transmission signals observed at 8.5 mab may not be large, there may well be substantial amounts of fine particles closer to the bottom. The net transport of these particles is unresolved. However, bottom photographs at LCH, in about 1,400 m water depth along the canyon axis, did not show the presence of the particles at least for January-April 1981, so it does not appear that they are transported away from the canyon head down the canyon axis. The almost complete reversal of the mean flow at 50 mab at LCB (see chapter 2) suggests that any particles which do get suspended that high above the bottom during high stress events will be transported shelfward.

INTERNAL WAVE PACKETS AND SEDIMENT SUSPENSION

Unique fluctuations in suspended sediment occur at LCB during periods of large amplitude internal waves. A characteristic feature of such internal waves (fig. 3-18 shows a clear example of energetic internal waves) is that the near-bottom (< 10 m) velocity is asymmetrical in time; the up-canyon flow is sharply peaked while the down-canyon flow is smoother and of longer duration. During down-canyon flows, the waveform of current speed is erratic at times - suggesting enhanced turbulence. At 50 mab, the up-canyon flow is of comparable speed to that at 8 mab but during down-canyon flows there is a

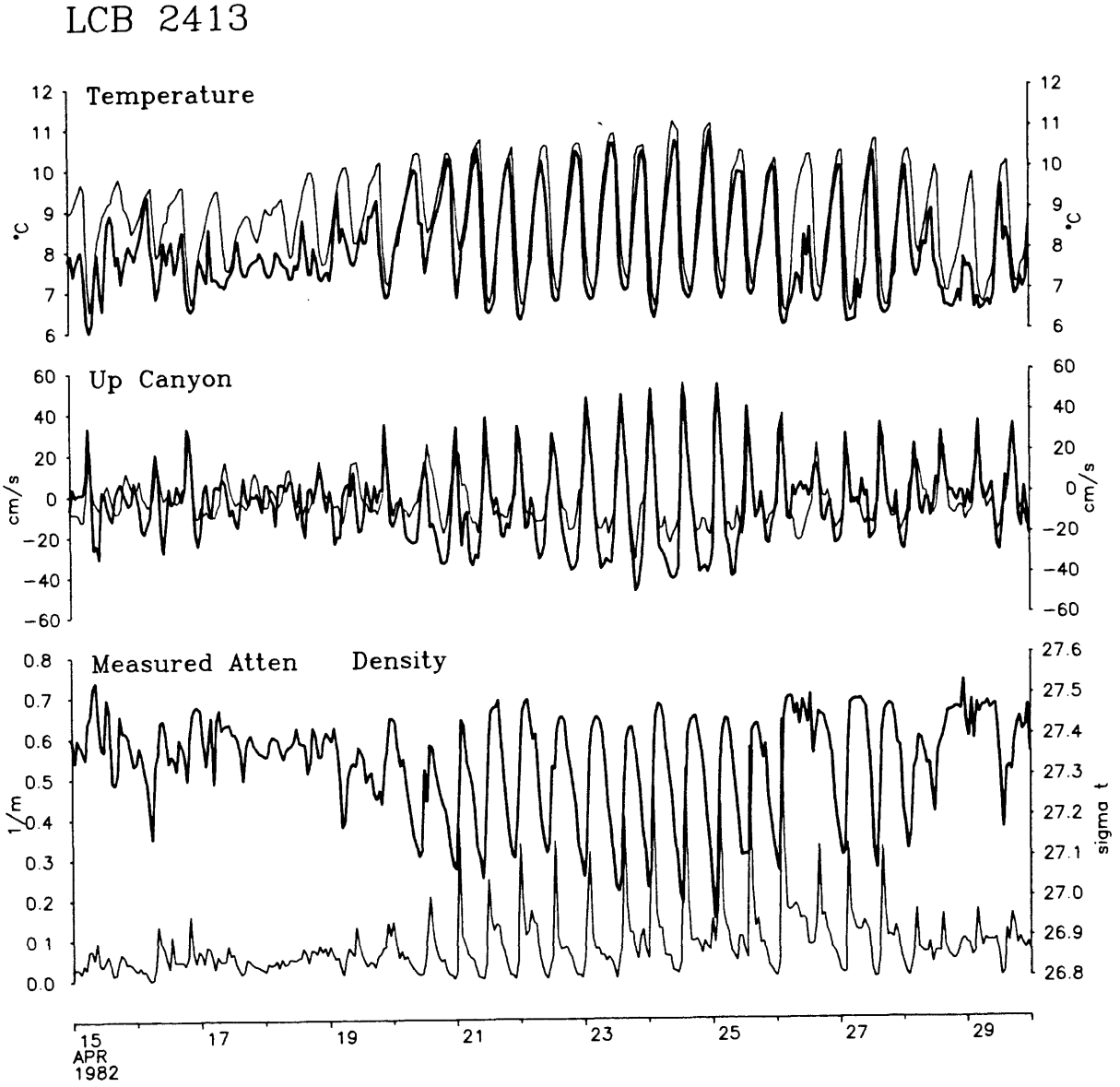

Figure 3-18a. Time-series at LCB during a period of energetic internal wave activity. The bottom graph displays measured attenuation and density (thicker curve) measured 5 mab. Upcanyon flow (middle graph) and temperature (top graph) are shown for measurements taken at two levels: 5 mab and 50 mab (thicker curves). The background attenuation has been removed from the measured signal with the constrained digital filter.

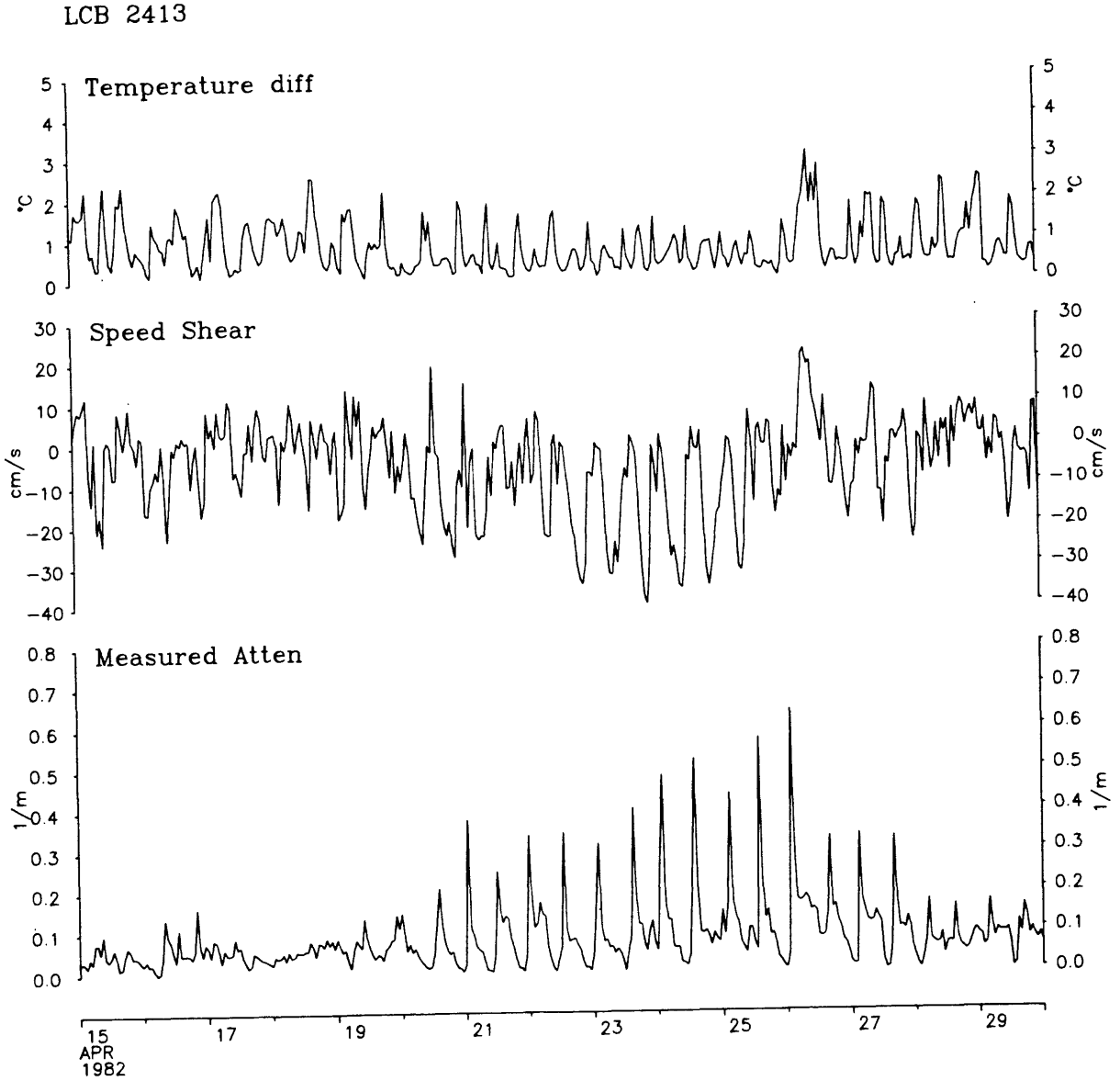

Figure 3-18b. Time-series of measured attenuation at LCB as in 3-18a, difference between current speed (not upcanyon speed) measured 50 mab and 5 mab and, difference between temperature measured 50 mab and 5 mab. Note reduced amplitude of temperature fluctuation during internal wave events and large speed shear during downcanyon flows.

large vertical shear with a bottom-intensified flow. Density oscillations are also intensified during the internal wave events and temperature at 8 mab and 50 mab undergo coherent large oscillations. The temperature difference between 8 and 50 mab is reduced, possibly because of enhanced mixing. While the source of such wave packets has been qualitatively associated with the passage of Warm Core Rings, the mechanism causing the apparently highly non-linear asymmetrical internal waves is unresolved (see chapter 2).

The time-series of beam attenuation (fig. 3-18) shows a remarkable periodicity of sharply-peaked attenuation events that occur only during periods of up-canyon flow. Down-canyon flow speeds are comparable to the upcanyon speeds. These peaks cannot be explained by advection of a turbidity front because the front would pass the observation site during both the up-canyon flow and down-canyon flow. It is also obvious that a local resuspension model, as we have used it, is untenable because high stresses and attenuations would be predicted during both up and down-canyon flows.

One hypothesis which explains these unique attenuation signals during periods of internal waves is that during up-canyon flows there is upwelling and during downcanyon flows there is downwelling. Note that we refer to upwelling [downwelling] as the vertical velocity which is in excess [deficit] of the component of the up-canyon [down-canyon] flow in the vertical direction. In other words, particles are not just moving parallel to the sloping bottom. We have no definite physical explanation of why there should be upwelling/downwelling but we discuss later some laboratory results of Cacchione (1970) that provide some insights. The other alternative is that there is enhanced mixing during upcanyon flows which would mix the sediments vertically. The enhanced turbulence could not be due to flow acceleration as accelerated flows tend to damp turbulence causing "relaminarisation" (e.g.

Hinze, 1975). Turbulence changes caused by stratification (due to temperature or salinity) is inconsistent with observations which indicate vertical homogenization in the bottom 50 m. Thus, by a process of elimination, the upwelling/downwelling scenario appears to be the most reasonable hypothesis.

The upwelling/downwelling hypothesis can be diagnostically analysed to determine whether it explains the observed beam attenuations. We use the previous boundary layer model, and assume a vertical fluid velocity which depends linearly on the up-canyon flow, so that the particle velocity is given by:

$$w - V\sin\alpha = -w_f - 0.34a\ V/60 \qquad (12)$$

where, w is the particle's vertical velocity (positive up),

V is the upcanyon speed (negative for downcanyon),

α is the angle of the bottom of the canyon axis,

w_f is the fall velocity (positive) of the particle,

0.34a is a calibration factor, (0.34 cm/s is about the fall velocity of 70μm sand).

The left hand side of (12) is the vertical velocity relative to a particle moving parallel to the sloping bottom. Using hourly-averaged data and assuming the particles to be the same fine particles found at LCB during the first deployment (2083) we tried simulations with the calibration parameter ranging from 0.5 to 1.25. Reasonable predictions were produced only when the critical threshold stress was at least one-fifth of that for 70μm sand, otherwise, large attenuations during downcanyon flows were predicted. The fact that the critical threshold stress was a significant fraction of that for fine sand indicated, if our hypothesis is correct, that the particles were not the same as those found previously and led us to tentatively conclude that indeed the peak attenuation during internal wave events were caused by sand!

Consequently, we used the model with the sand size fractions for LCB in

Table 3-2 and the upwelling/downwelling formulation. Figure 3-19 shows comparisons of model predictions with observations for hourly data and α = 0.9. The model predictions appear to be too large and predict attenuation spikes only during the high stress events of 23-26 April. One reason why the model does poorly during low stress events is because the hourly-average current speed data input into the model substantially underestimates the highly-peaked up-canyon flows. An example of this underestimation is shown in figure 3-20 which compares the hourly current speed data with data obtained every 450s. For example, the sharp current peak on the 26th of April, evident in the 450s data in figure 3-20, is underestimated by almost a factor of two. These rapid changes in current also imply that a time-dependent sediment suspension model, using finely resolved (in time) data, is required to adequately model the observations. However, the present model is adequate to demonstrate the feasibility of the hypothesis because now we are dealing with sand and upwelling/downwelling speeds comparable to the fall velocity of 70μm sand, that can adjust the sediment profiles relatively rapidly compared to typical stress changes. A simulation with the 450s data shows good agreement of predictions and observations (fig. 3-21). The lack of predicted attenuation during a few low stress events indicates either that the 450s sampling is not fast enough to capture the highest speeds or, that in addition to the smallest assumed size of 47 μm there may be smaller sand or coarse silt components or, roughness increases due to movable bed effects coming into play.

Sediment transport rates for this period, computed over the bottom 20 m show large up and downcanyon transports for the 94μm and 47μm size fractions with the 47μm size transport being about double that for the 94μm size. Total sediment transport rate for the period 20-28 April is 51 mg/cm/s down-canyon

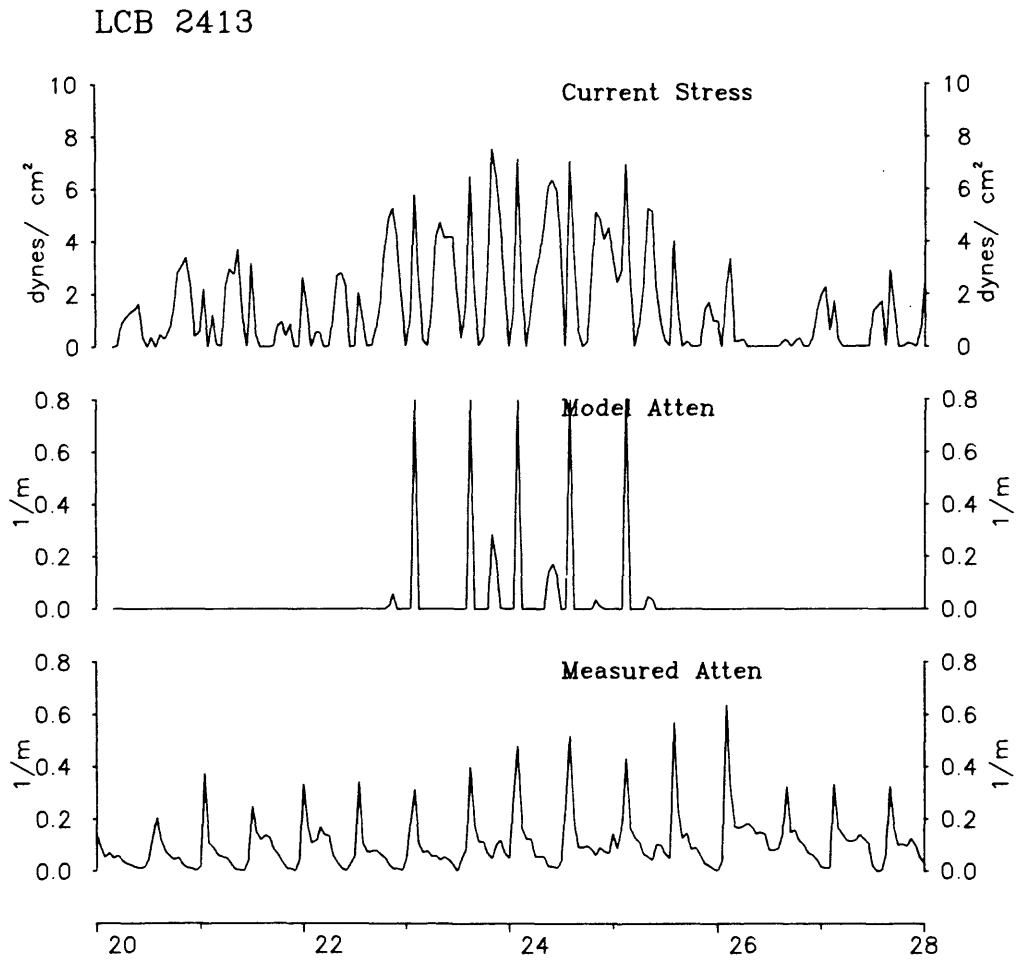

Figure 3-19. Hourly time series at LCB during energetic internal wave events of measured attenuation, model prediction of attenuation using the sand size fractions in table 3-2 for LCB and the upwelling/ downwelling model and, current stress calculated by the model.

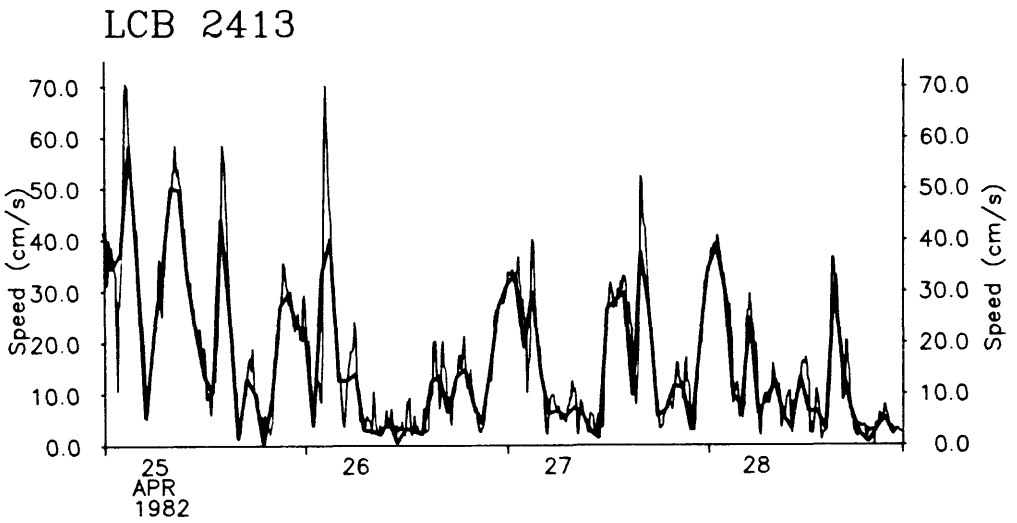

Figure 3-20. Composites of 450s and hourly (thicker curve) current speed for a segment of the internal wave event at LCB (see fig. 3-18).

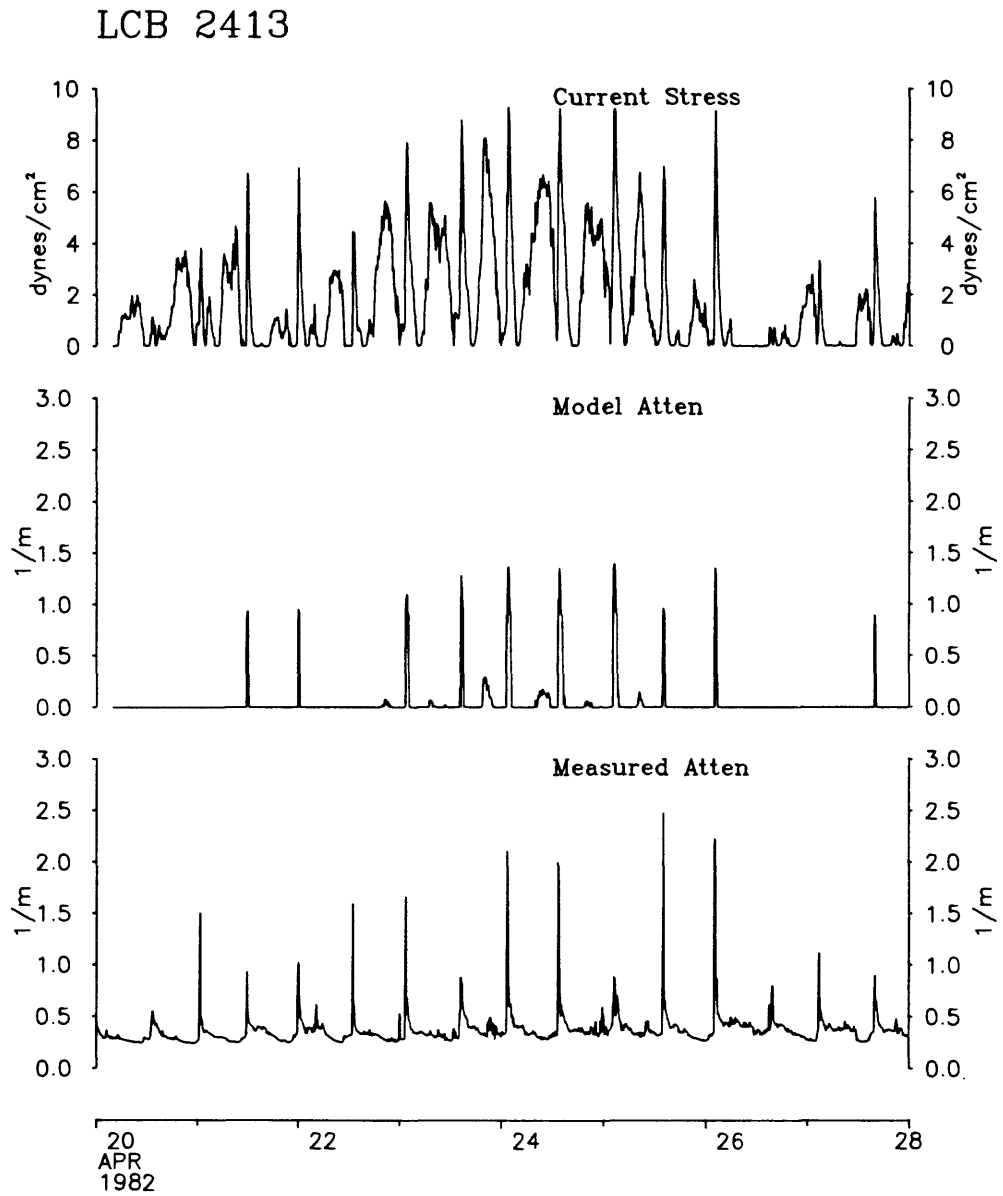

Figure 3-21. As for figure 3-19 but using 450s data instead of hourly data.

and the up-canyon rate is about four times larger at 210 mg/cm/s. Thus, even though the period of up-canyon flow is shorter, it is a prime mover of sediment. These estimates based on the revised model bring into question the estimates of sand transport for LCB during periods where internal waves were active. In particular the conclusion of net down-canyon sediment transport for records with high stresses may no longer be valid.

Sediment trap data (this volume, Chapter 6) provide some evidence of increased sand capture by traps when large internal waves were observed.

Discussion on internal wave effects

We have tried to explain the observations of up-canyon attenuation spikes using a simple hypothesised upwelling/downwelling model. Since the model results imply a large reversal from previous expectations of sediment transport it is important to collect detailed high-quality field data on these internal waves and their influence on sediment transport.

The model used to explain the attenuation is oversimplified. For example, any upwelling or downwelling must clearly go to zero at the bottom and the vertical structure of the flow must depend on the non-linear acceleration terms that introduce further pressure gradient length scales (Yaglom, 1979) that must be considered in the bottom boundary layer formulation. The downslope bottom-intensified flow, perhaps a consequence of density driven flow caused by sediment suspended during the up-canyon flow, is not represented in our model.

Laboratory studies by Thorpe (1966) and Cacchione (1970) of internal waves progressing up a slope may provide some insights on the mechanism causing upwelling/downwelling. The real canyon is of course much more complex than a simple slope especially in terms of topographic influences. In

particular, the lateral contraction effect does not appear to have been studied. Disintegration of internal waves progressing up a slope is documented by Cacchione (1970). Upon progressing into shallow depths, internal waves decrease in wavelength and their amplitude increases. In the case of critical and supercritical internal waves, Cacchione (1970) observes the formation of regularly spaced horizontal vortices during upslope flow. Mixing takes place within the vortices with subsequent ejection of mixed water in the form of thin streamers intruding into the interior of the slope water. During downslope flow, the vortices relax and flatten out. Clearly then complex and little understood phenomenon of energetic internal waves may also take place in the canyons. Could the upheaval of water masses, by vortex formation, and the subsequent relaxation explain the proposed upwelling/downwelling hypothesis? Alternatively, could it be due to the so called "wave run up" phenomenon observed for subcritical flow? The answers to these questions must await further definitive detailed studies.

The connection of these internal waves with Warm Core Rings (chapter 2) suggests that the internal waves will have a significant long-term influence on sediment transport. Figure 3-22 shows a clear connection of the semi-diurnal wave packets and semi-diurnal attenuation events for the second half of the record. Note however that the hourly data used in figure 3-14 does not represent the large rapid attenuation spikes and the apparent lack of correspondence between the wave packets and attenuation during the late March and the first half of April may be due to the use of hourly data.

The modelling results have important implications for the transport of fine particles along the canyon. First, it is important to realize where measurements are being made in relation to bottom turbid layers that form during upwelling/downwelling. There is a need for current and attenuation

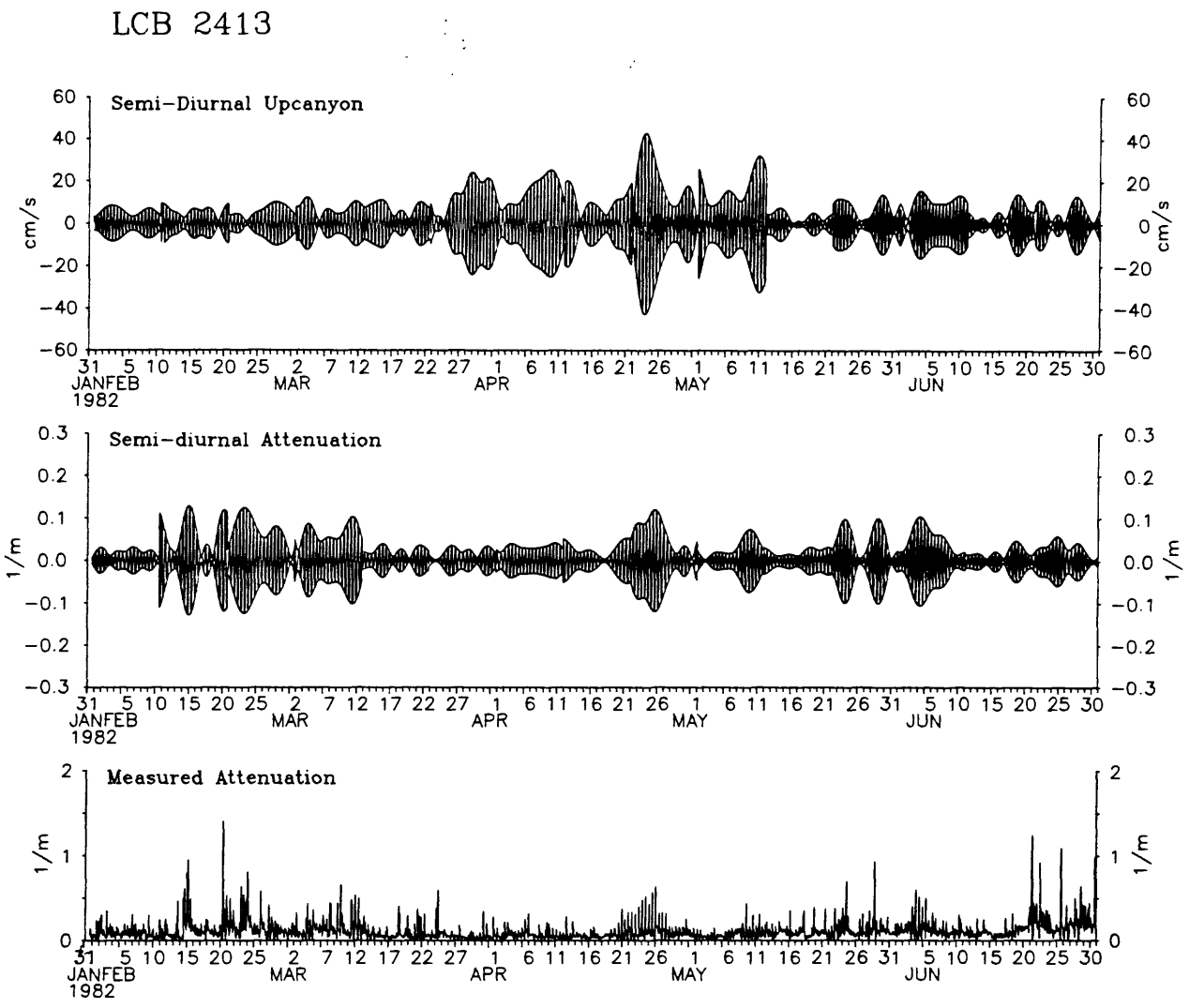

Figure 3-22. Hourly time-series at LCB of measured attenuation with background and fouling signal removed and semi-diurnal component of measured attenuation and upcanyon speed. Semi-diurnal component is reconstituted from spectral estimates for periods of 10.4 to 13.3 hours, calculated every 10 days.

measurements with greater vertical resolution within the bottom 10 m or so, to verify the model predictions and to further our limited understanding of the bottom boundary layer current structure. Second, a theoretical framework for explaining the asymmetrical internal wave current structure, the hypothesised upwelling/downwelling and corresponding improvements in the bottom boundary model formulations are clearly needed. Third, it is erroneous to use the product of current and beam attenuation measured at one level to infer the direction of sediment transport without knowing what particles are causing the observed attenuation and the structure of the vertical sediment and current profile. Lastly, we need to understand the generation and propagation charateristics of these internal waves in order to asssess the long-term impact of such waves on sediment transport in the canyon.

CONCLUSIONS

Model studies using measurements of near-bottom current, waves, beam transmission and surficial sediment have provided sediment transport rates for stations within and around Lydonia Canyon. For the shelf stations, the most uncertain aspect of the model computations is the specification of the erodability of the sediment bed. For stations in the canyon axis non-linear acceleration and intense mixing during energetic internal wave events may invalidate the simple dynamics assumed for the vertical current structure and sediment suspension.

Wave-current interaction enhances sediment transport over the shelf, especially during winter when sediment transport occurred about 40% of the time at station LCA above the canyon head and 22% of the time at LCM on the western shelf. The bulk of sediment transport is however the result of large wave-current events that occur for less than a few percent of the time. The combined influence of waves, tides and the westward mean flow biases sand transport towards the west at LCA. At LCU, just above the canyon head, the largest sediment transport is almost directly into the canyon head. Strong southward veering of near-bottom currents at the shelf stations, associated with Warm Core Rings, produces a convergence of sediment transport into the canyon.

The head of Lydonia Canyon is predicted to be an area of sediment accumulation due to sediment influx from the shelf above the canyon head, from the eastern rim and, from weaker sediment export down the canyon axis. Sand influx across the eastern rim is of comparable magnitude to sand transport convergence along the canyon floor. Sand is predicted to accumulate at a rate of 3.6m/1000 years along the canyon floor for depths less than 300 m. Between 300 m to 450 m, the accumulation rate declines to 2.4 m/1000 years. The

observed coarse patch of sand between 450 m to 650 m depth is an area where sand influx from the eastern rim roughly balances sand transport divergence along the canyon floor.

Temporal changes in near-bottom beam transmission at LCB and LCE, not attributable to sand suspension, are explained as suspension changes due to fine particles with settling velocities equivalent to that for fine-sand. During the first deployment of the moored arrays, the flow into the canyon associated with a Warm Core Ring may have been responsible for injecting substantial quantities of these particles into the canyon.

Energetic internal wave events at LCB are observed to produce highly peaked attenuations only during up-canyon flow. The lack of attenuation peaks during down-canyon flows, equally as energetic as up-canyon flows, is hypothesized to be due to upwelling and downwelling during up-canyon and down-canyon flow respectively. Model predictions for sand suspension with upwelling speeds comparable to that for fine sand, produce attenuation signals in reasonable agreement with observations, provided 450s rather than hourly data are used. These internal waves may enhance the accumulation of sand at the canyon head.

This description of sediment transport in Lydonia Canyon has relied heavily on GG83, a one dimensional model of the bottom boundary layer and sediment resuspension. Despite the many assumptions, the model is essential to the interpretation of the field observations. For example, all the conclusions about the transport of sand in the axis are based on the model simulations. Efforts to refine and verify models of sediment transport should continue.

There is a clear need for more detailed data that resolves the vertical current structure and sediment profile during energetic internal waves

events. Similarly detailed measurements are also required at the shelf stations to answer questions such as the erodability of the seabed. Warm Core Rings are of major importance to sediment transport due to the internal waves and convergent near-bottom currents associated with them.

ACKNOWLEDGMENTS

W.D. Grant kindly provided the original version of the sediment transport model. Further development of the model was partly funded by the Coastal Research Center under a Mellon Research grant 25/96.08 to VDL.

REFERENCES

Butman, B. and Folger, D. W., 1979, An instrument system for long-term sediment transport studies on the Continental Shelf: Journal of Geophysical Research, v. 84, p. 1215-1220.

Butman, B. and Conley, S., 1983, Lydonia Canyon experiment, data report, moored array deployment I, October 1980-April 1981: U.S. Geological Survey Open-File Report 84-201.

Butman, B., Noble, M. A., Moody, J. A., and Bothner, M. H., 1983, Lydonia canyon dynamics experiment: preliminary results. In: Environmental Geologic Studies on the United States Mid and North Atlantic Outer Continental Shelf Area, 1980-1982, Vol. III Final Report to the Bureau of Land Management .

Cacchione, D. A., 1970, Experimental study of internal gravity waves over a slope, Ph.D. Thesis, Massachusetts Institute of Technology, Cambridge, Ma., 238 p.

Einstein, H. A. and Barbarossa, N. L., 1952, River channel roughness, American Society of Civil Engineers, Transactions, Paper No. 2528, p. 1121-1132.

Glenn, S. M., 1983, A Continental Shelf bottom boundary layer model: The effects of waves, currents and movable bed, D. Sc. Thesis, Massachusetts Institute of Technology, Cambridge, MA., 237 p.

Grant, W. D. and Madsen, O. S., 1979, Combined wave and current interaction with a rough bottom: Journal of Geophysical Research, v. 84, p. 1797-1808.

Grant, W. D. and Glenn, S. M., 1983, A Continental Shelf bottom boundary layer model. Vol. 1, Theoretical development: Technical Report to the American Gas Association, 167 p.

Grant, W. D., and Madsen, O. S., 1986, The Continental Shelf bottom boundary layer: Annual Review of Fluid Mechanics, v. 18, p. 265-305.

_____, 1982, Movable bed roughness in unsteady oscillatory flows: Journal of Geophysical Research, v. 87, p. 469-482.

Hinze, J. O., 1975, Turbulence: Second Edition, McGraw-Hill, Inc., New York, Chapter 7.

Lyne, V. D., 1981, Recursive modelling of sluggish and time-varying streamflow responses: Master of Sc. Thesis, Dept. of Civil Engineering, University of Western Australia, Perth.

Lyne, V. D., Butman, B., and Grant, W. D., 1986a, Computations of bottom stress for Georges Bank and the Mid-Atlantic Bight Continental Shelf. (Draft).

Lyne, V. D., Butman, B., Grant, W. D., 1986b, Model and field studies of sediment transport on Georges bank and the Mid-Atlantic Bight Continental Shelf. (Draft).

Madsen, O. S., and Grant, W. D., 1976, Sediment transport in the coastal environment. Ralph M. Pearson Laboratory, Massachusetts Institute of Technology Report No. 209, p. 105.

Miller, M. C., and Komar, P. D., 1980, A field investigation of the relationship between oscillatory ripple spacing and the near-bottom water orbital motions: Journal of Sedimentary Petrology, v. 50, p. 183-191.

Moody, J. A., Butman, B., and Bothner, M. H., 1986, Near-bottom suspended matter concentration on the continental shelf during storms: Continental Shelf Research (accepted).

Paola, C., 1983, Flow and skin friction over natural rough beds. D. Sc. Thesis, Massachusetts Institute of Technology, Cambridge, MA., p. 347.

Smith, J. D., and McLean, S. R., 1977, Spatially averaged flow over a wavy surface: Journal of Geophysical Research, v. 82, p. 1735-1746.

Thorpe, S. A., 1966, Internal gravity waves. Ph.D. Thesis, Trinity College, Cambridge, England.

Twichell, D. C., 1983, Geology of the head of Lydonia Canyon, U.S. Atlantic outer shelf: Marine Geology, v. 54, p. 91-108.

Wallace, J. M. and Dickinson, R. E., 1972, Empirical orthogonal representation of time series in the frequency domain. Part I: Theoretical considerations: Journal of Applied Meterology, v. 11, p. 887-892.

Wooding, R. A., Bradley, E. F., and Marshall, J. K., 1973, Drag due to regular arrays of roughness elements of varying geometry: Boundary Layer Meteorology, v. 5, p. 285-308.

Yaglom, A. M., 1979, Similarity laws for constant-pressure and pressure-gradient turbulent wall flows: Annual Review of Fluid Mechanics, v. 11, p. 505-540.

CHAPTER 4

MIXING OF WATER IN SUBMARINE CANYONS INDICATED BY CHANGES IN TEMPERATURE-SALINITY CURVES

By

John A. Moody and Bradford Butman

Chapter 4

Table of Contents

Page

Abstract....4-1

Introduction....4-1

Water masses....4-3

Georges Bank water....4-4

Scotian Shelf water....4-4

Winter water....4-6

Western North Atlantic water....4-6

Methods....4-8

Field measurements....4-8

Reference TS curve....4-8

Mixing types....4-10

Results....4-21

January 1981 (OCEANUS Cruise 91)....4-21

April 1981 (OCEANUS Cruise 95)....4-23

October 1981 (OCEANUS Cruise 104)....4-23

January 1982 (OCEANUS Cruise 113)....4-26

November 1982 (OCEANUS Cruise 130)....4-26

Mixing time scales....4-26

Other canyons (OCEANUS Cruise 130)....4-30

Summary....4-32

References....4-35

ABSTRACT

The mixing of water below 200 m within a submarine canyon is investigated by examining changes in the temperature and salinity properties of water along the canyon axis. The water mass which penetrates submarine canyons is Western North Atlantic (WNA) water and local salinity maxima and minima occur at depths below 200 m. Vertical mixing increases [decreases] the salinity of water in the canyon relative to the source of Western North Atlantic water outside the canyon depending upon whether or not a salinity minima [maxima] is within the mixing region. Vertical mixing across density surfaces was evident in Lydonia and Oceanographer canyons over several hundred meters and resulted in salinity changes of ~ 0.1 o/oo. External mixing of WNA water with shelf water resulted in salinity changes of approximately 0.3 o/oo - 1.0 o/oo and was evident between 200-300 m (just below the canyon rim) and at the head of Lydonia Canyon.

Mixing was greater along the canyon than along the continental slope and large mixing events at the head of the canyon seem to be associated with either the passage of large atmospheric storms or warm core rings which had time scales of 1-2 months.

INTRODUCTION

Numerous submarine canyons cut into the eastern United States continental shelf along the shelf break from Cape Hatteras to the Northeast Channel (fig. 4-1). Lydonia Canyon is a typical canyon located on the south flank of Georges Bank which varies in width and depth, from approximately 5 km at the head of the canyon where the canyon floor is 100-150 m below the level of the adjacent shelf (100 m), to 10 km at the shelf break where the canyon floor is about 1000 m below the adjacent shelf. Submarine canyons are located at the

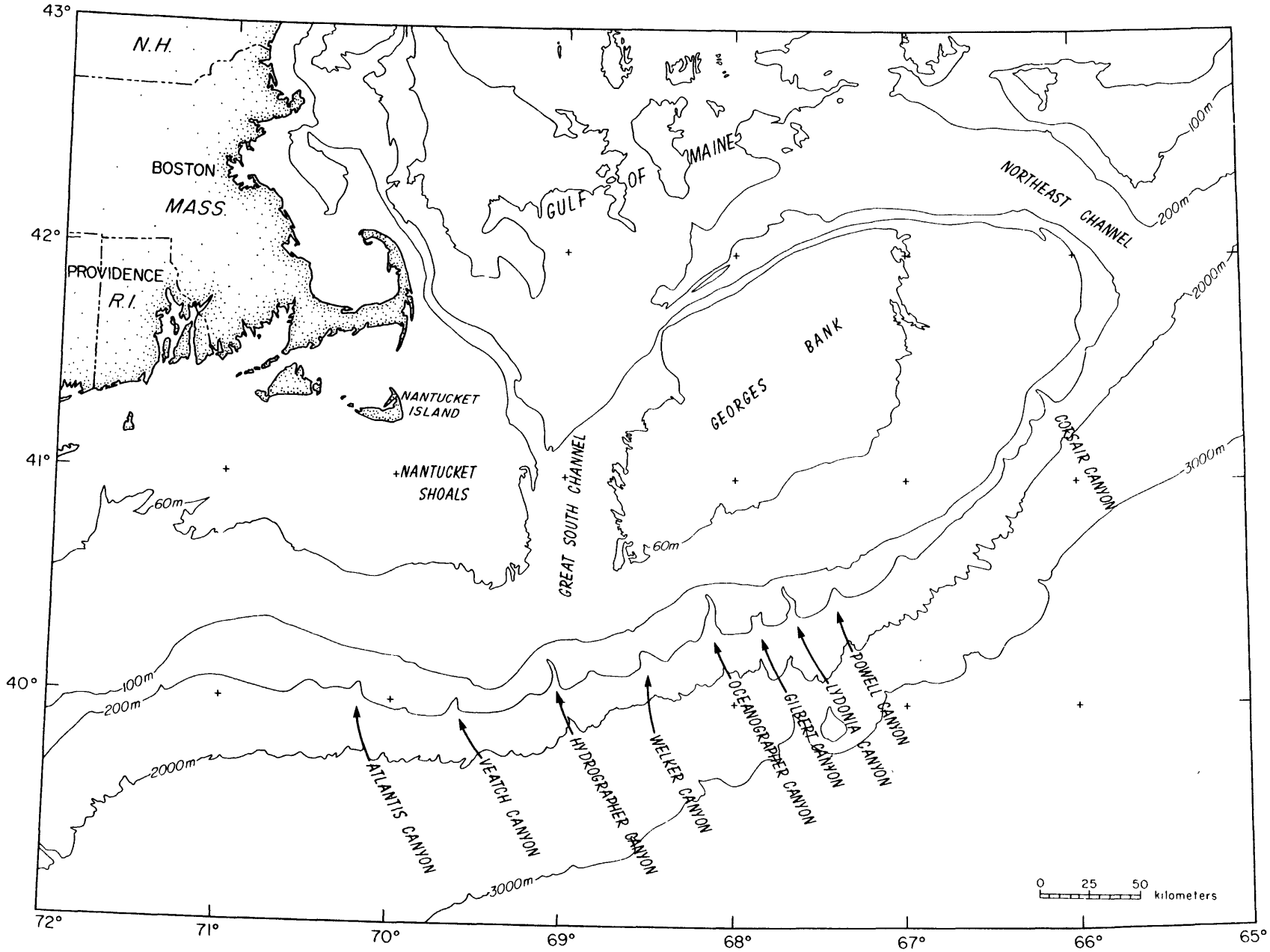

Figure 4-1. Location of submarine canyons along the continental shelf south of Georges Bank and Nantucket Shoals. The shelf break is at about 200 m.

shelfbreak, a transition region between water of shelf origin and water formed in the western north Atlantic. The canyons provide a passageway for deep ocean water to reach well landward of the shelf break. Changes in the temperature and salinity (TS) properties of this water in the canyon are indicators of mixing that occurs between shelf and deep ocean water as well as internal mixing of water within the canyon. Canyons have been cited as possible sites for mixing and exchange of water between shelf and slope. According to theory (Wunsch, 1969) a critical slope of the canyon walls and bottom will focus internal wave energy toward the head and bottom of submarine canyons and result in a decrease in wavelength and an increase in wave amplitude as the bottom shoals. This has been observed in laboratory experiments (Cacchione and Wunsch, 1974) where breaking internal waves and associated turbulent mixing occurred near the intersection of the bottom slope and the water surface. The increase in internal wave energy from the mouth toward the head of canyons has been observed in Hydrographer, Hudson and Lydonia Canyons by Wunsch and Webb (1979), Hotchkiss and Wunsch (1982) and Butman (chapter 2).

We investigate the mixing of deep Western North Atlantic water as an indicator of mixing processes within submarine canyons. This chapter presents evidence of such mixing in Lydonia and Oceanographer Canyon based on hydrographic observations made during five cruises conducted between January 1981 and November 1982.

WATER MASSES

There are three primary sources of water with salinities less than 34 o/oo on the eastern North American Continental Shelf: Georges Bank water (GBW), Scotian Shelf water (SSW) and winter or "cold pool" water (Bigelow,

1933 or Ketchum and Corwin, 1964; Houghton and others, 1982;). The water seaward of the continental shelf is characterized by salinities greater than 35 o/oo. Gulf Stream water (GSW) occurs near the surface and the deep Western North Atlantic water (WNA) occurs below about 700 m. Shelf water and GSW water meet near the shelf break to form the shelf/slope front. This front intersects the surface about 30 km offshore of the shelf break (Mooers, 1979) and intersects the bottom within 6-17 km of the 100 m isobath (Wright, 1976). The front is a region of mixing often characterized by calving of detached parcels of shelf water (Wright, 1976; Posmentier and Houghton, 1981) but this mixing takes place in water above the major portion of submarine canyons which have rim depths of 100-200 m. The temperature and salinity characteristics of each of the water masses are briefly described below.

Georges Bank water

The Georges Bank water (GBW) mass is formed north of Lydonia Canyon on the relatively isolated and shallow Georges Bank which is less than 60 m deep. The water is well mixed by tidal currents, ranges in salinity between 32.1 and 32.9 o/oo (Hopkins and Garfield, 1981) and has a wide temperature range (2-17°C) due to the shallowness of Georges Bank which allows rapid heating in summer and cooling in winter (see fig. 4-2).

Scotian Shelf water

The Scotian Shelf water (SSW) mass is fresher and cooler than GBW; salinity ranges from 31.1 to 33.0 o/oo and temperature from 0-12 °C (fig. 4-2). The source of SSW is northeast of Lydonia Canyon and the flow is generally south westward along the shelf break (Chapman and others, 1986).

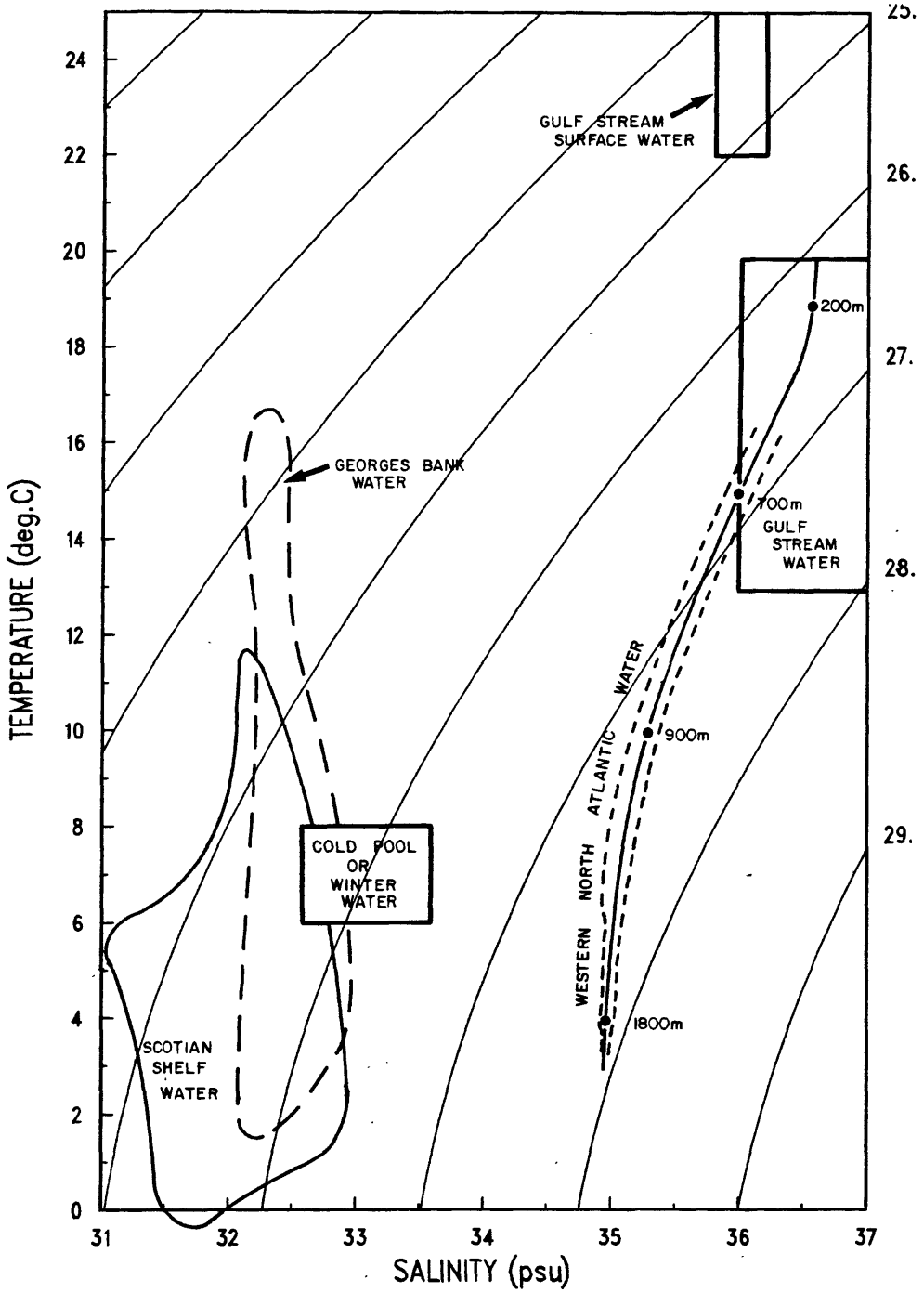

Figure 4-2. Characteristics of water masses on the eastern North American continental margin. Values of sigma-t are labelled along the right side of the figure. The Georges Bank and Scotian Shelf water mass characteristics are from Flagg (1982). The TS curve for Western North Atlantic (WNA) water is from Armi and Bray (1982); the dashed line on either side indicates the variability of WNA water based on Wright and Worthington (1970). Temperature and salinity characteristics of Gulf Stream water are discussed in Wright and Parker (1976) and Wright (1976) and characteristics of the "cold pool" are from Houghton and others (1982).

Cold pool or winter water

Cold pool water is formed during the winter by vertical mixing of shelf water and then is isolated near the bottom by summer warming of the surface water. The cold pool is characterized by salinities of 32.6-33.6 o/oo and typical temperatures of 6-8 °C (fig. 4-2) with minimum temperature of 4 °C (Houghton and others, 1982).

Western North Atlantic water

The source of Western North Atlantic (WNA) water at the surface is primarily GSW (fig. 4-2) with salinities greater than 36 o/oo and temperatures greater than 18°C at 100 m, and greater than 15°C at 200 m (Wright, 1976). Below 200 m WNA water has a well defined temperature-salinity (TS) relation, developed by Iselin (1936) for temperatues between 4 and 18°C and extended by Worthington and Metcalf (1961) for potential temperatures below 4°C. Armi and Bray (1982) fit a cubic spline to these historical standard curves, and presented an analytic function of salinity vs potential temperature (see WNA curve in fig. 4-2). The source of this deep WNA water along the shelf break is frequently Gulf Stream warm core rings (see chapter 2) which have TS curves below 200-450 m that are identical to the standard curve for WNA water (see Joyce, 1984; Stalcup and others, 1985; EG&G, 1978).

The variability of the salinity of WNA water was determined by using the volumetric results of Wright and Worthington (1970) and computing the standard deviation of salinity for ten temperature ranges (17-18, 15-16, 13-14, 11-12, 9.5-10.0, 7.5-8.0, 5.5-6.0, 4.5-5.00, 3.8-4.0 and 2.8-3.0°C). The variability is about 0.04 o/oo for temperatures less than 5.0 °C and about 0.10 o/oo for temperatures greater than 5.0 °C (fig. 4-3).

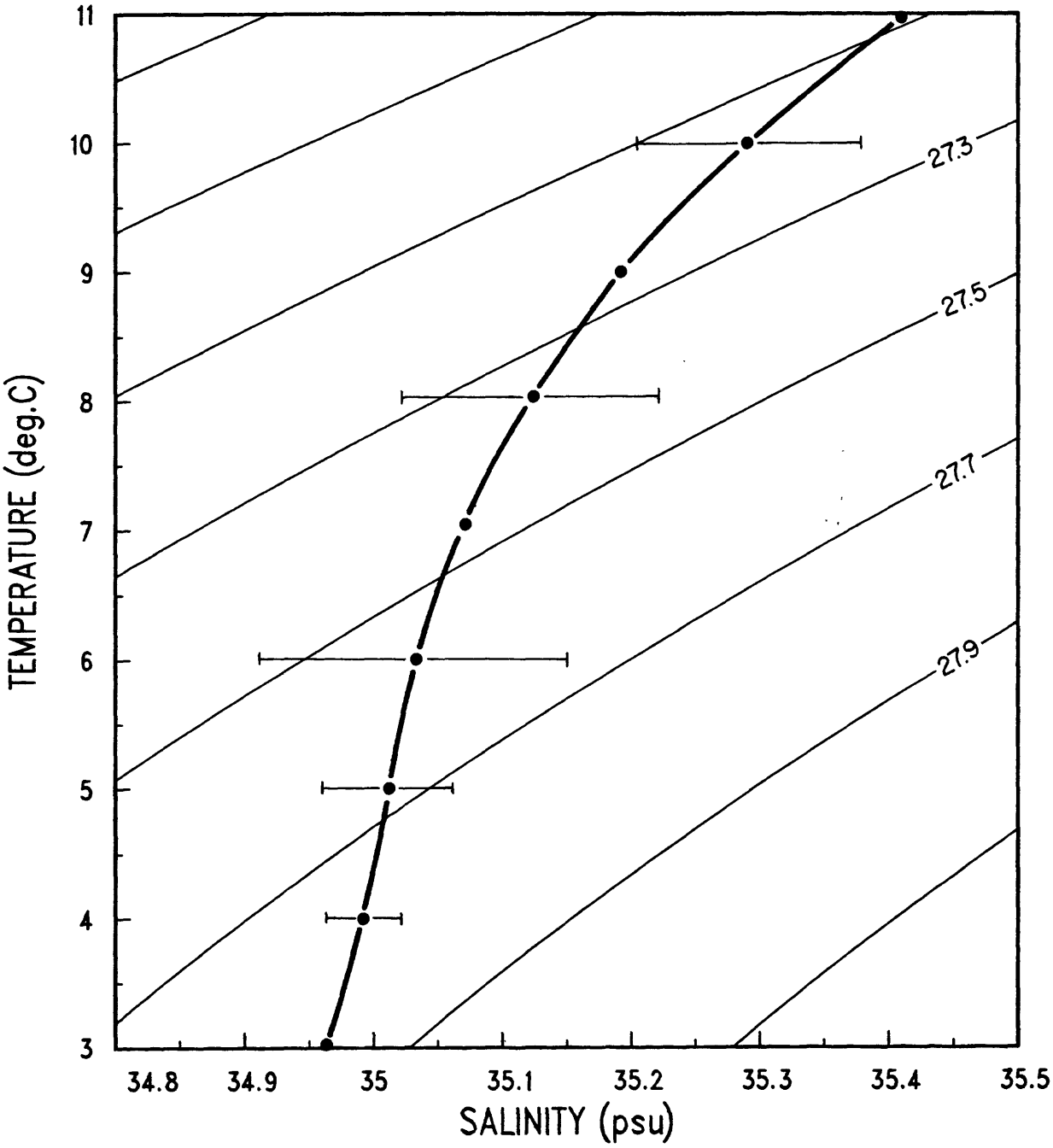

Figure 4-3. An expanded plot of the lower portion of the standard WNA TS curve (fig. 4-2). The bars indicate the standard deviation of the salinity for the following temperature ranges (2.8-3.0, 3.8-4.0, 4.5-5.0, 5.5-6.0, 7.5-8.0, 9.5-10.0, 11-12, 13-14, 15-16 and 17-18^{o}C).

METHOD

Field measurements

Four hydrographic cruises (OCEANUS cruise 91, 95, 104, and 113,) were conducted between January 1981 and January 1982 around Lydonia Canyon and one cruise in November 1982 (OCEANUS 130) surveyed Welker and Oceanographer canyons as well as Lydonia Canyon (fig. 4-4). Cruise 91 and 113 were during the winter (January 16-22, 1981 and January 29-February 3, 1982 respectively). Cruise 95 was during the spring (April 24-May 5, 1981), cruise 104 was during the late summer-early fall (September 25-October 2, 1981) and cruise 130 was during the fall (November 16-22, 1982). The hydrographic measurements (pressure, temperature, salinity, oxygen and light transmission) were made with a NBIS (Neil Brown Instrument Systems, Mark III) CTD profiler. The CTD data were processed ashore and then bin-averaged at 2-dbar pressure or depth intervals (1 dbar is approximately equal to 1 meter) except OCEANUS 91 which was averaged at 10 dbar intervals. For details of the processing and sections and lists of all data see Moody and others, (1986a).

Reference TS curve

To investigate mixing within the canyon based on changes of the TS curve, a TS curve representative of the unmixed, source water outside the canyon is needed. The variability of the TS properties of water outside the canyon was investigated using the WNA salinity anomaly (defined as the observed salinity minus the standard WNA salinity at the observed sigma-t). In general, the WNA anomalies at stations outside the canyon were almost identical, and within the variability of WNA water (fig. 4-3). The deviations changed from cruise to cruise; for example during January 1981 the WNA salinity anomaly at stations 16 and 20 was nearly zero at all depths except for a negative anomaly (fresher

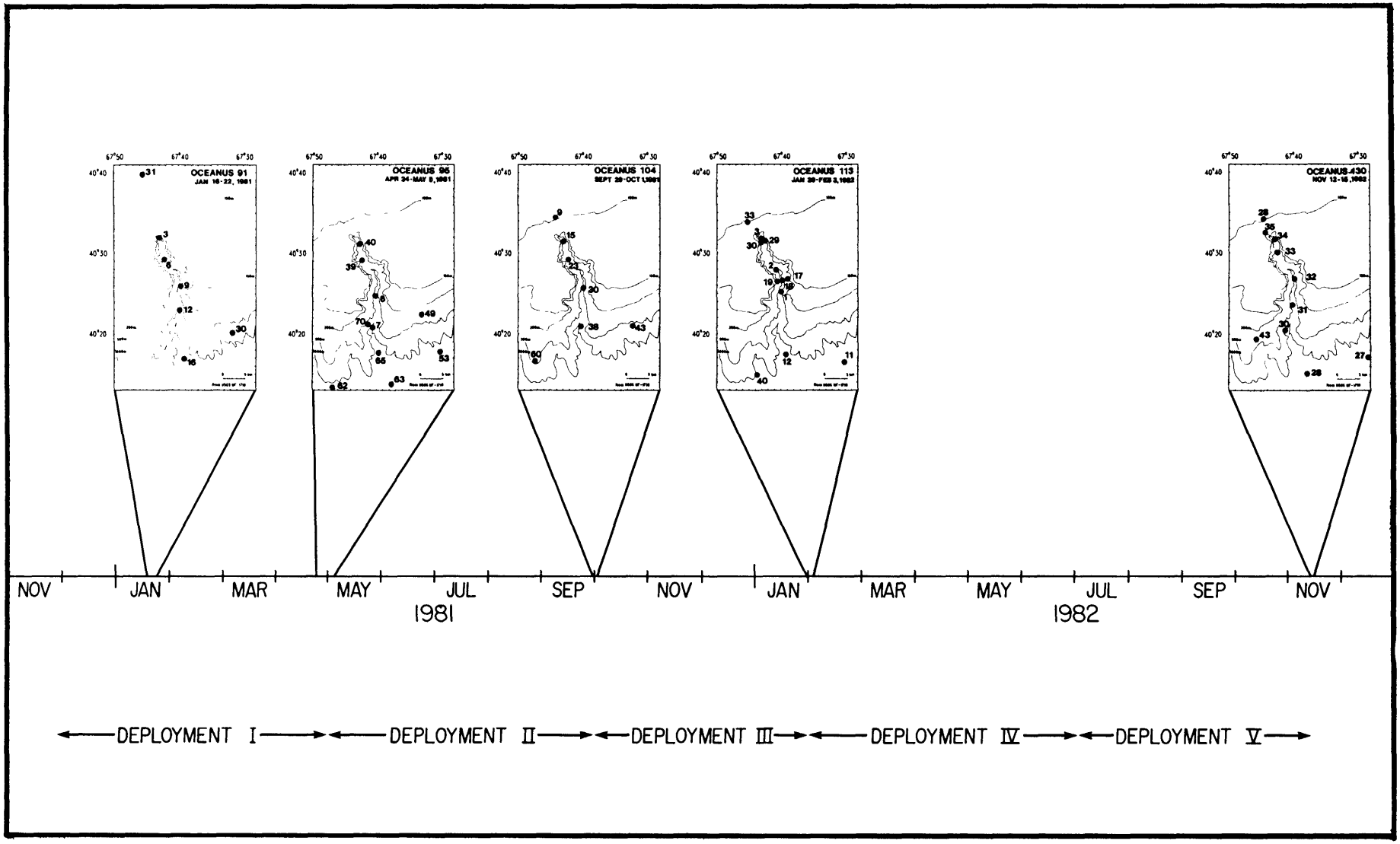

Figure 4-4. Location and time of hydrographic stations for each cruise that are referenced in this chapter and the deployment periods for moored instruments (see chapter 2 for mooring locations).

than WNA water) of about 0.03 o/oo near the bottom and a small positive anomaly at 425 dbar (station 20) and 460 dbar (station 16) where the water was 0.03 to 0.05 o/oo saltier than WNA water (fig. 4-5a). This positive anomaly at both stations occurs at the same sigma-t; stations 16 and 20 have nearly identical anomaly curves, when the WNA anomaly is plotted vs sigma-t, indicating little change in TS properties along the outer shelf (fig. 4-5b). In April 1981, the WNA anomaly was much larger than in January but still similar at 3 stations outside the canyon. One negative anomaly of about 0.05-0.12 o/oo was centered between sigma-t values of 27.2 and 27.4 and a second anomaly (0.05-0.09 o/oo) was centered between 27.6 and 27.7 (fig. 4-5c).

Based on the relatively small differences observed in the TS curves for stations outside the canyon, a reference station was selected for each cruise which had a WNA anomaly similar to stations along the slope (for example station 16 for OCEANUS 91 and station 63 for OCEANUS 95, see figs. 4-5b and 4-5c). We did not use the standard WNA TS curve as a reference curve because changes in salinity between stations in the canyon were of the same order as the variability of standard WNA water. Thus, changes in salinity due to canyon mixing could not be separated from typical spatial and temporal changes in WNA water. Changes are measured relative to the TS properties observed at the mouth of the canyon during each hydrographic survey. We thus tacitly assume that the water in the canyon is derived from this source.

Mixing types

Two types of mixing can be identified from the TS curves, which we call internal vertical mixing (within a water mass), and external mixing (between two masses). Internal vertical mixing between two depths which bound a salinity minimum [maximum] will result in a straightening of the TS curve and

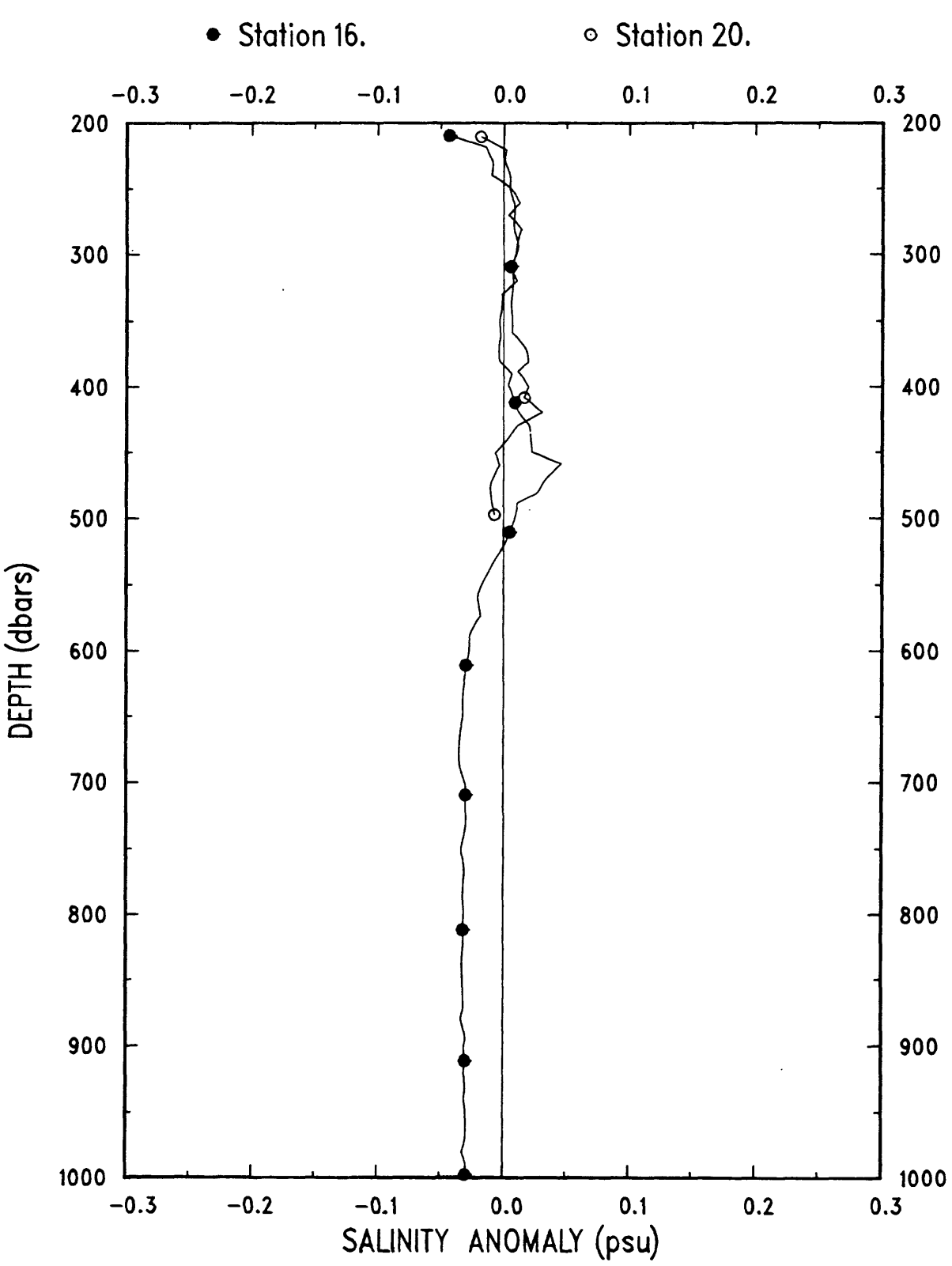

Figure 4-5a. Western North Atlantic (WNA) salinity anomaly (observed salinity minus reference salinity of same sigma-t) plotted versus depth for station 16 (OCEANUS 91) in the canyon axis (water depth 1355 m) and station 20 (OCEANUS 91) on the adjacent slope (water depth 755 m). Negative (positive) values indicate the water is fresher (saltier) than WNA water.

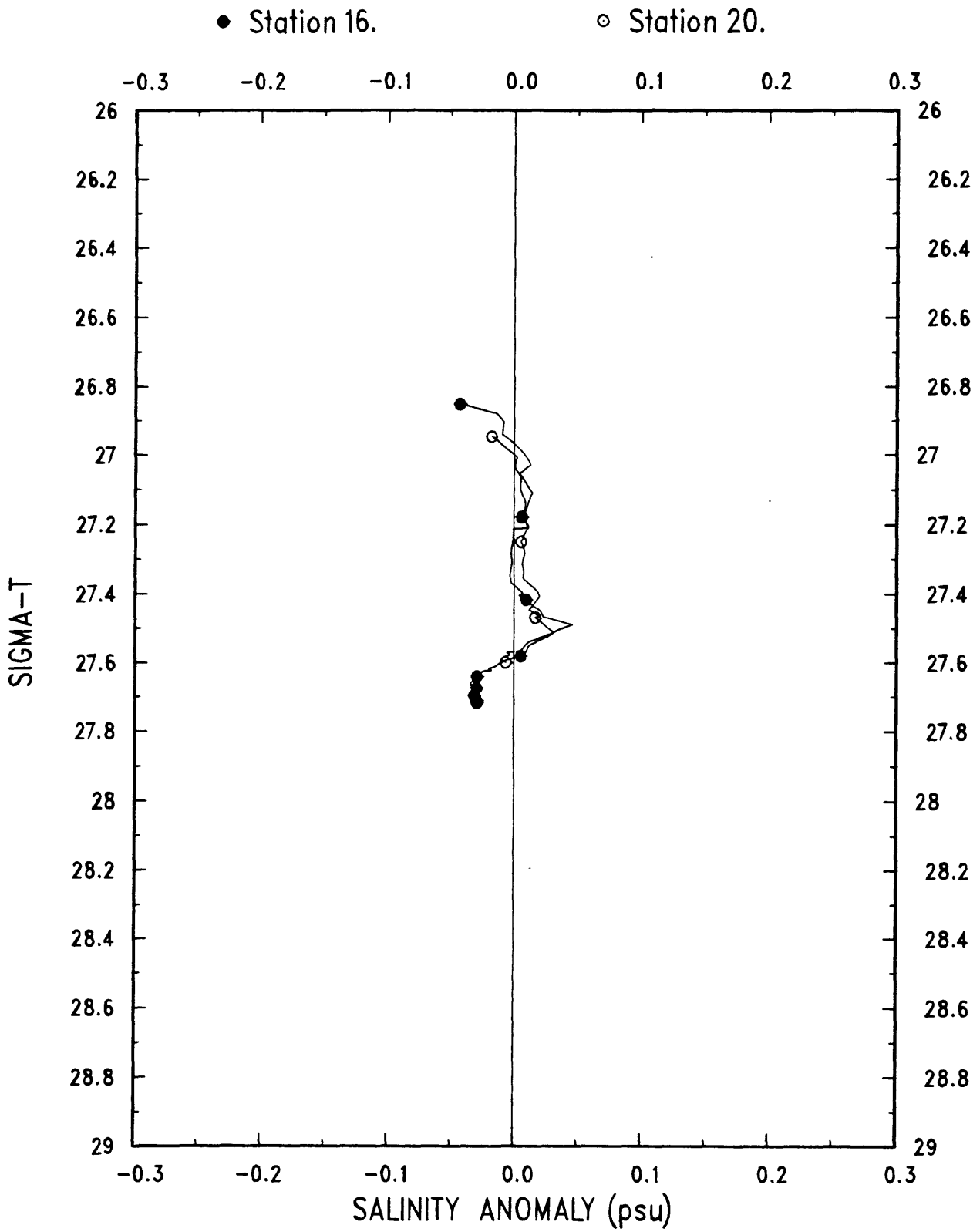

Figure 4-5b. The WNA salinity anomaly (observed salinity minus reference salinity of same sigma-t) for stations 16 and 20 (OCEANUS 91) plotted versus density or sigma-t. Note that the positive salinity anomaly that occurs at different depths in figure 4-5a is at the same sigma-t value (27.5).

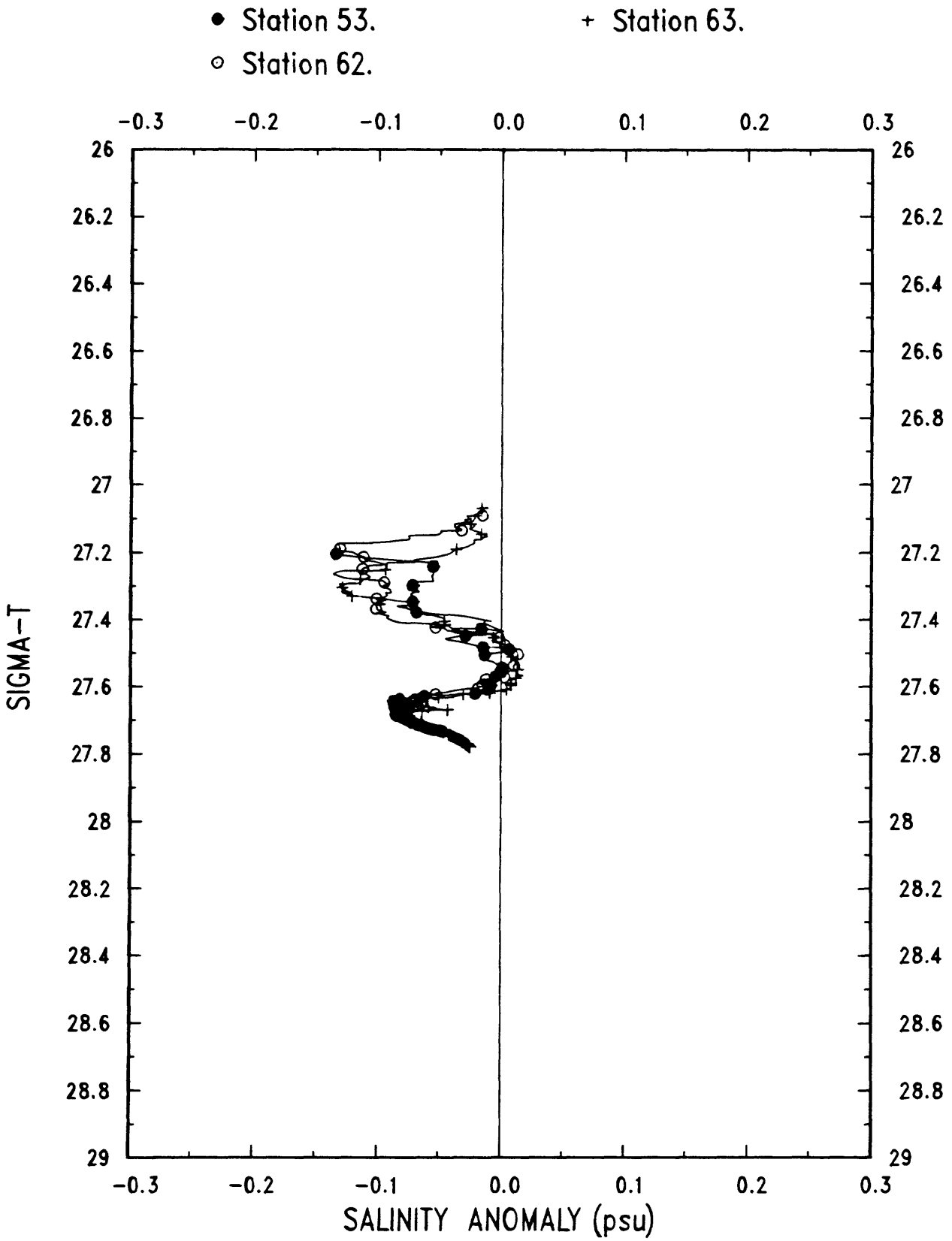

Figure 4-5c. A WNA salinity anomaly (observed salinity minus reference salinity of same sigma-t) plot for OCEANUS 95. See figure 4-4 for station locations.

an increase [decrease] in the salinity of the water relative to the reference station (see fig. 4-6). This straightening of TS curves indicates vertical mixing across sigma-t surfaces and evidence for it is found at several stations in Lydonia Canyon. For example at station 9 (OCEANUS 91), vertical mixing resulted in an increase in salinity of about 0.1 o/oo between approximately 240 dbars and the bottom when compared to the reference station (see fig. 4-7a). At station 6 (OCEANUS 95) between 320-500 dbars there is a decrease in salinity due to vertical mixing of about 0.1 o/oo relative to the reference station (see fig. 4-7b). Station 70 (OCEANUS 95) illustrates vertical mixing which caused an increase in salinity between 262-310 dbar and a decrease in salinity between 310-540 dbars (fig. 4-7c). Vertical mixing between two depths makes the water more uniform in temperature and salinity, and thus the spacing between points on the TS curve is reduced. Regions of enhanced vertical mixing are thus qualitatively identified by the clustering of points on a TS curve as around 400 dbar on the TS curves for station 6 (fig. 4-7b) and station 70 (fig. 4-7c).

External mixing with another water mass will result in a TS curve that intersects the reference TS curve at one point (see curve 1, fig. 4-6) or the TS curve may be shifted so that it does not intersect the reference TS curve at any point (see curve 2, fig. 4-6). This type of mixing probably occurs along sigma-t surfaces; Stations 2, 29 and 30 (OCEANUS 113) illustrate external mixing of GSW and shelf water between 200 and 300 dbar at the head of Lydonia Canyon (fig. 4-8a, 4-8b).

The type of mixing regions within Lydonia Canyon were identified by examining TS curves for each cruise. To quantify the intensity of mixing, and to help differentiate between vertical mixing and mixing between water masses a canyon salinity anomaly (observed salinity minus reference salinity of same

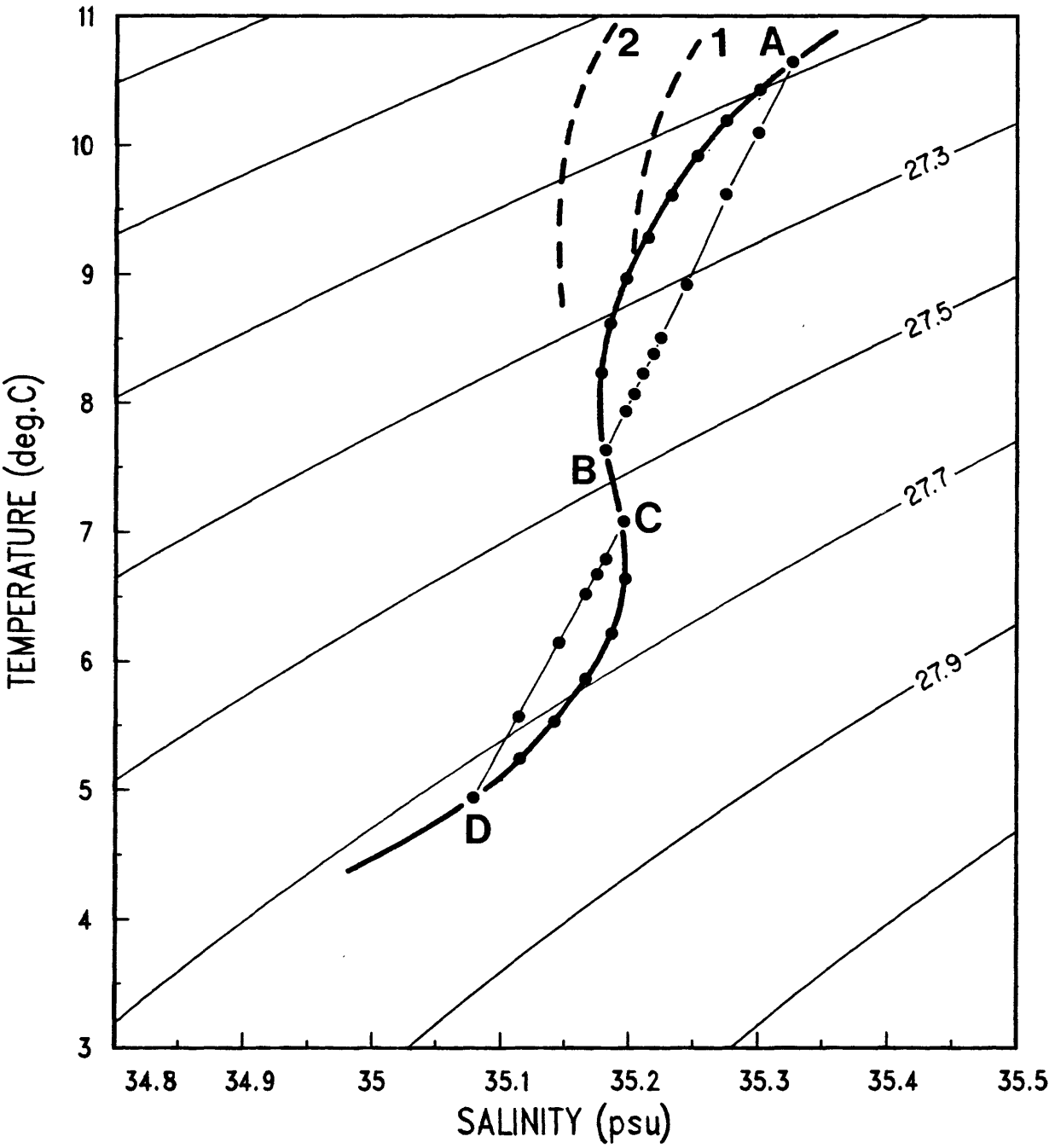

Figure 4-6. Hypothetical TS curve showing internal vertical mixing between depths A and B (a local salinity minimum). This results in a straightening of the TS curve between depths A and B, an increase in the salinities at intermediate depths and a reduced spacing between points on the TS curve. Vertical mixing between depths C and D (a local salinity maximum) results in a decrease in salinity at intermediate depths, straightening of the TS curve and a reduced spacing between points on the TS curve. Curves 1 and 2 illustrate external mixing with another water mass which is fresher.

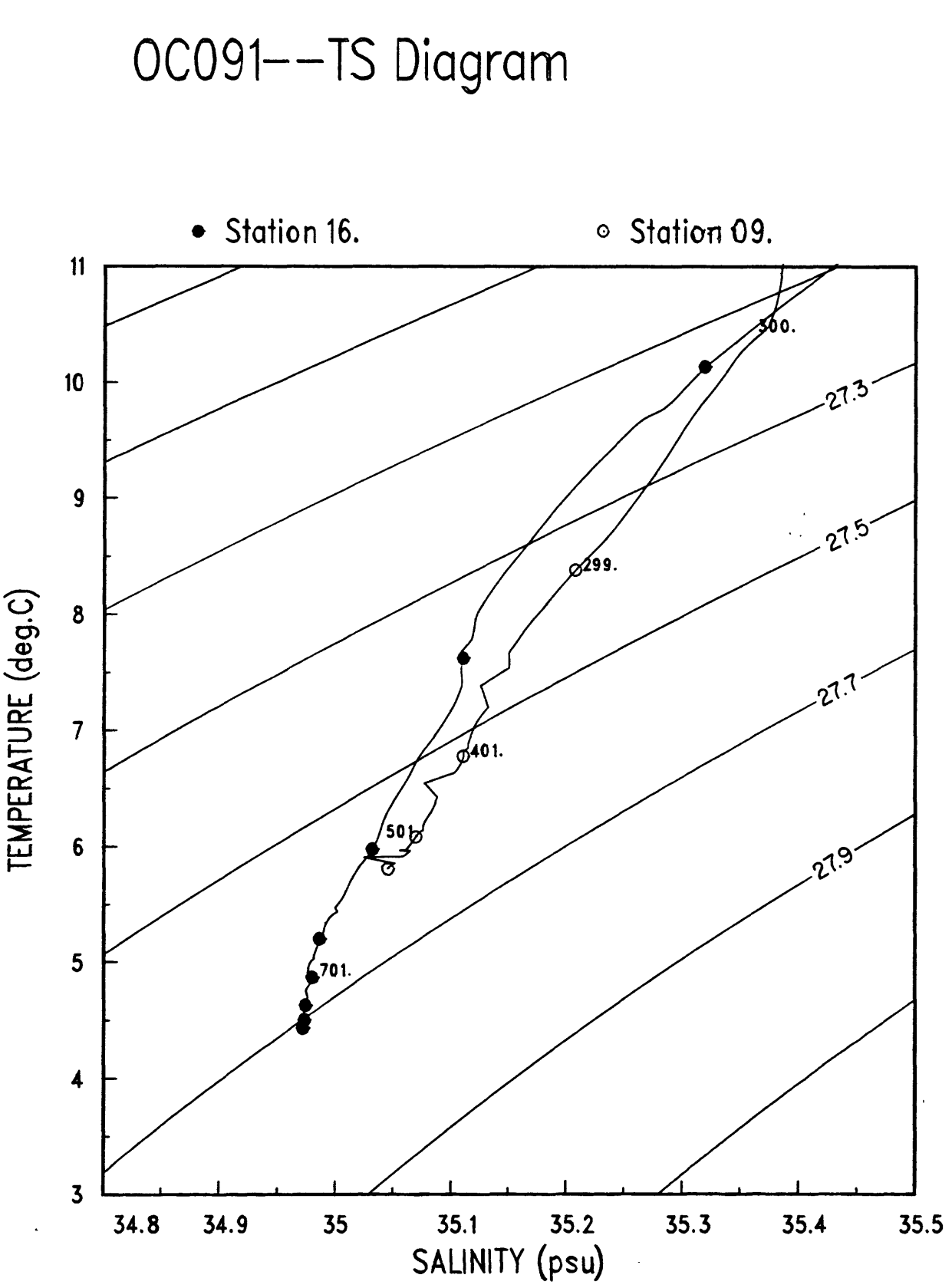

Figure 4-7a. Example of vertical mixing of a local salinity minimum resulting in an increase in salinity between 240 dbars and the bottom (January 1981). Station 16 is the reference station and station 9 is approximately halfway between the reference station and the head of Lydonia Canyon. Depth annotations are in dbars.

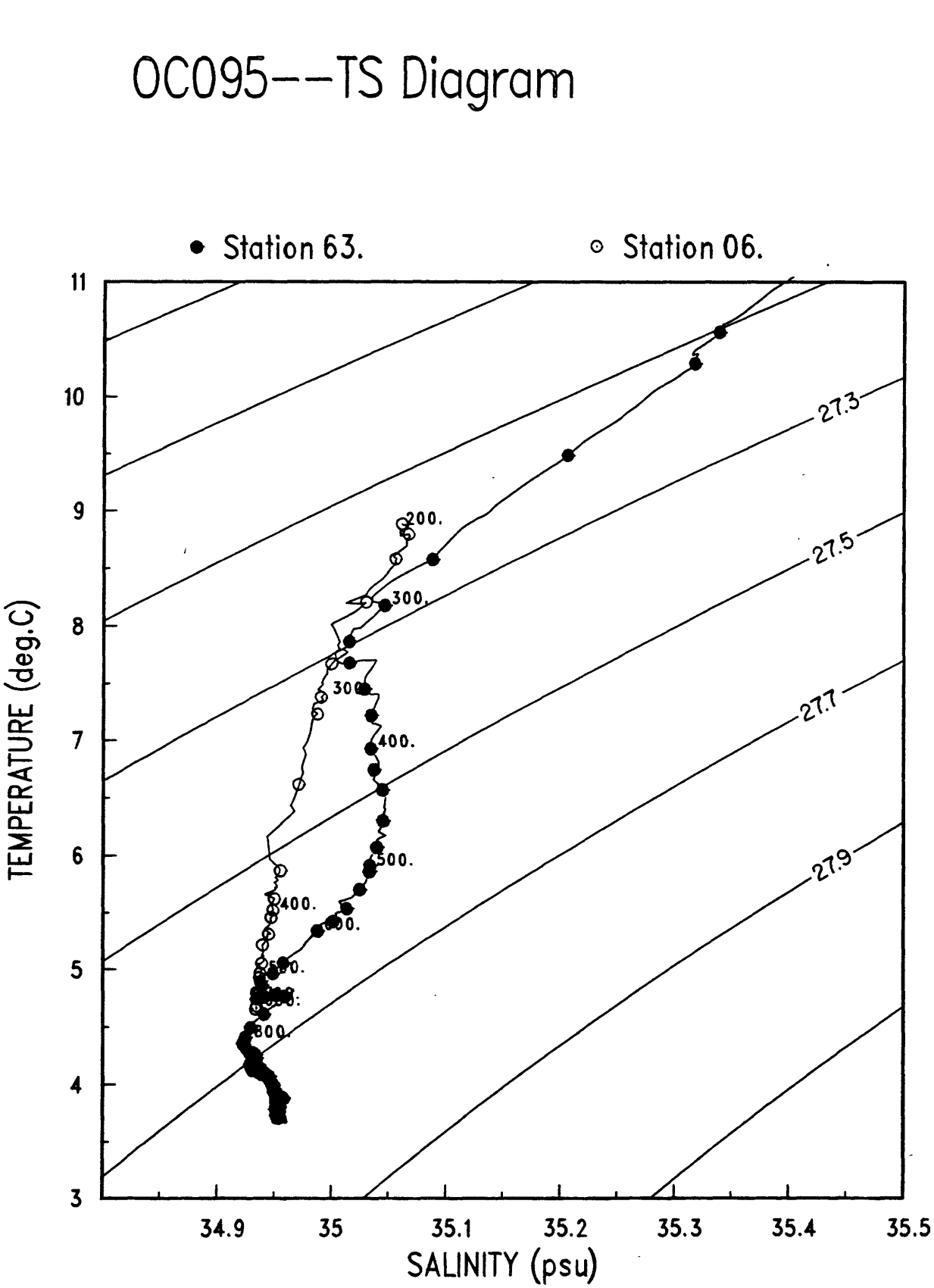

Figure 4-7b. Example of vertical mixing of a local salinity maximum resulting in a decrease in salinity between about 320-500 dbars (April-May, 1981). Station 63 is the reference station and station 6 is at about the same location as station 9 (fig. 4-7a). Note the decreased spacing between points on the TS curve near 400 dbars which indicate a region of greater mixing.

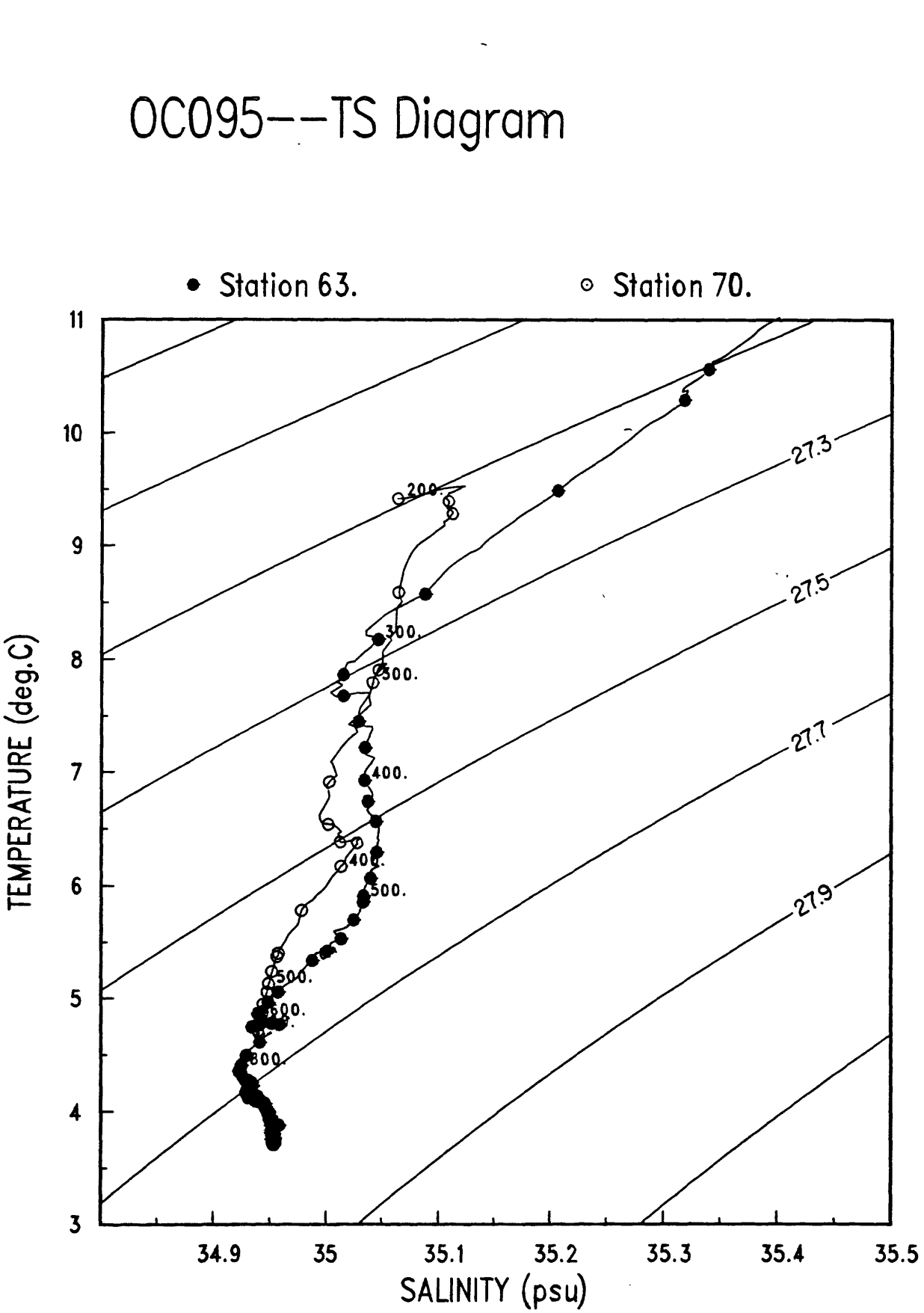

Figure 4-7c. Example of vertical mixing resulting in an increase in salinity between 262-310 dbars and a decrease in salinity between 310-540 dbars (April-May, 1981). Station 70 is located approximately midway between station 6 and the reference station 63 (fig. 4-7b).

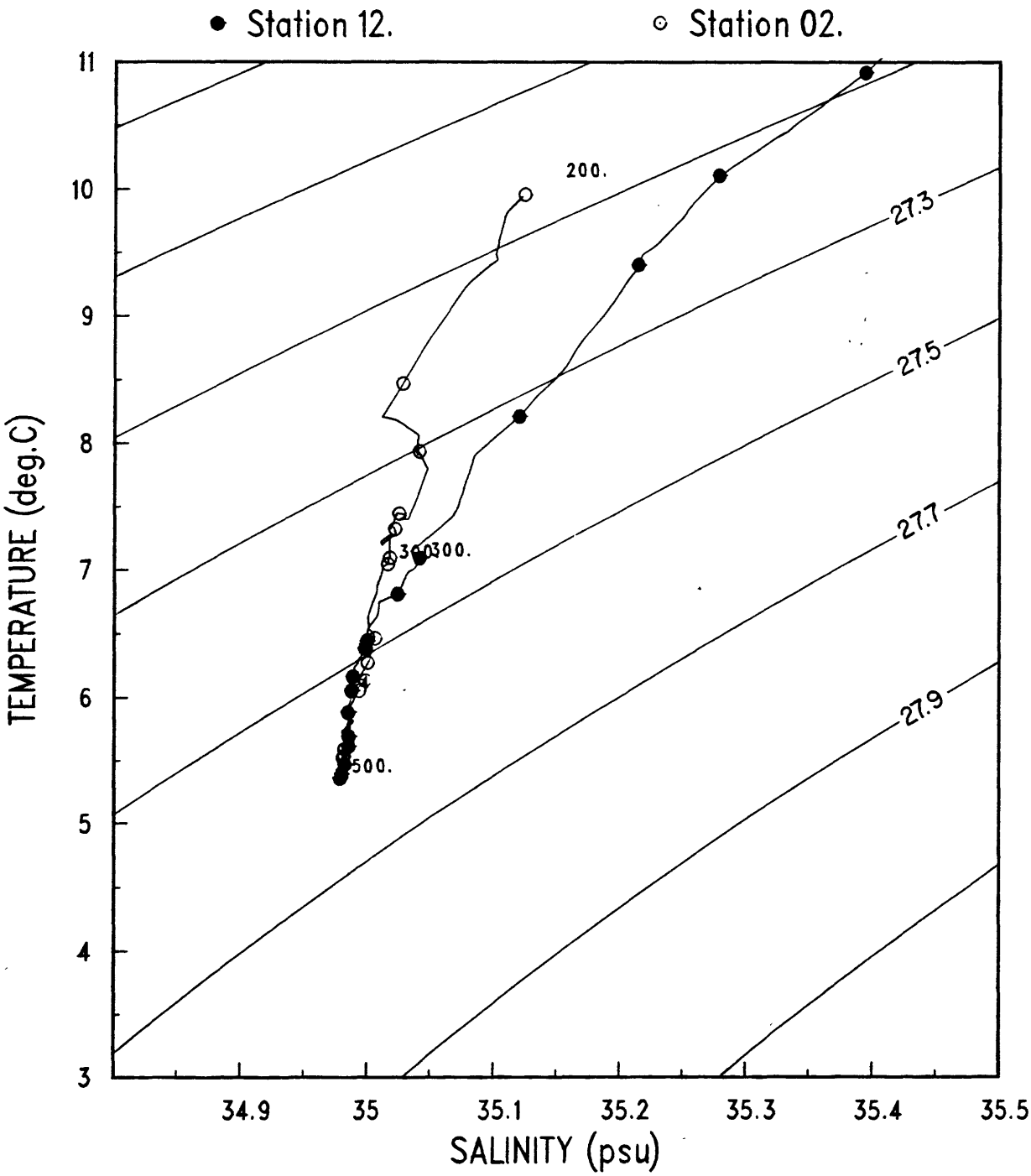

Figure 4-8a. Example of external mixing with less saline water. The mixing is greatest between 200-300 dbar. The water below 320 dbars gradually becomes Western North Atlantic water below about 340 dbars. Station 12 is the reference station (January-February, 1982).

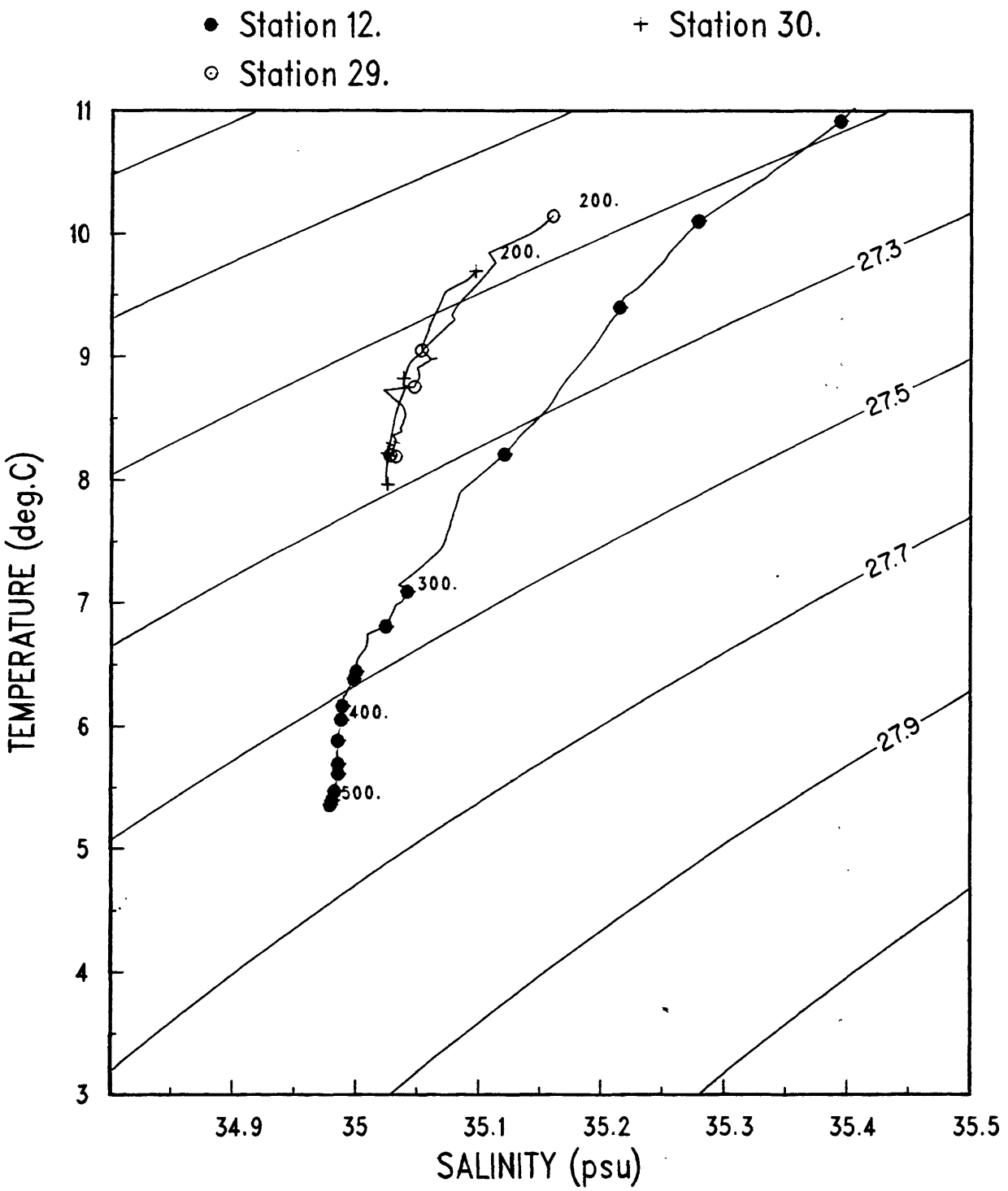

Figure 4-8b. Example of external mixing with a second water mass which extends from 200 dbars to the bottom and there is no evidence of Western North Atlantic water. Station 12 is the reference station and stations 29 and 30 are in the head of Lydonia Canyon (January-February, 1982).

sigma-t) was computed using the reference station for each cruise. A positive canyon salinity anomaly indicates that the water within the canyon is saltier than the water at the reference station outside the canyon on the same isopycnal and that there is internal vertical mixing across sigma-t surfaces. A negative anomaly indicates that the water within the canyon is fresher than the water outside the canyon on the same isopycnal. A negative anomaly could be due to internal vertical mixing across sigma-t surfaces (fig. 4-7b) or due to external mixing along sigma-t surfaces (fig. 4-8) of low salinity shelf water (near the 200 m depth or around the head of the canyon) with deep WNA water offshore.

RESULTS

January 1981 (OCEANUS 91)

Warm core ring 80G (see chapter 2) was located just to the south of Lydonia Canyon. The water within Lydonia Canyon was slightly saltier than standard WNA water and a maximum WNA anomaly of 0.05 o/oo occurred at about 400 dbars between stations 6 and 9. The most intense internal vertical mixing occurred near the head of Lydonia Canyon (~ station 6) at depths of about 300 dbars (fig. 4-9) where the canyon salinity anomaly exceeded 0.05 o/oo. External mixing of shelf water with WNA water (probably supplied by the Warm Core Ring 80G) occurred between 200-300 dbars which is below the canyon rim and the shelf/slope front (see chapter 2). The sigma-t surfaces dip sharply offshore due to the presence of the warm core ring (chapter 2) and thus WNA water at 300-400 dbar is mixed with shelf water at 200-300 dbar.

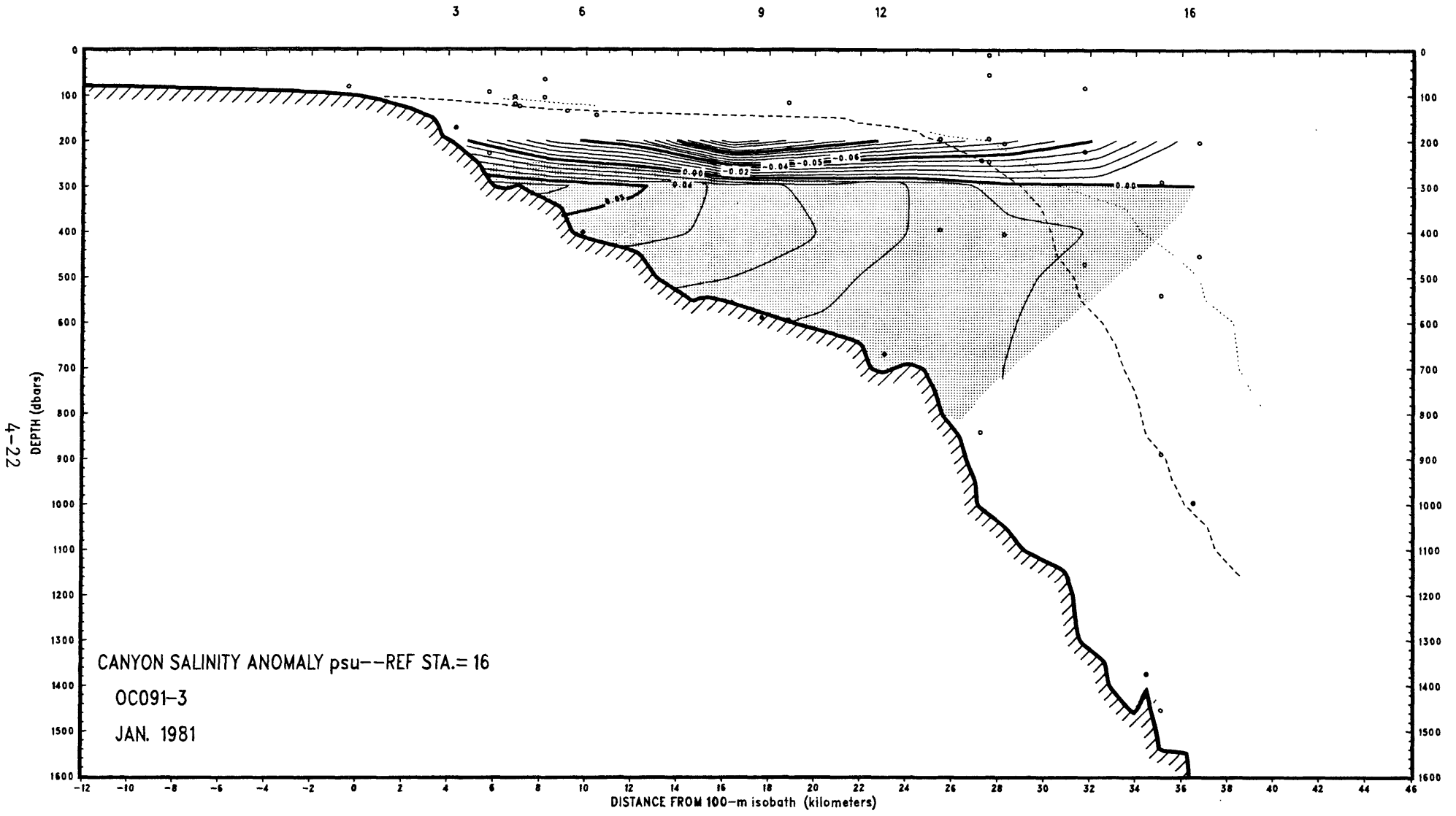

Figure 4-9. January 1981 canyon salinity anomaly (observed salinity minus reference salinity of the same sigma-t). Negative (positive) salinity anomaly indicates the water is fresher (saltier) than water at reference station outside the canyon. Regions where internal vertical mixing is evident have been stippled. Station numbers are shown across the top. The solid circle below the station number is the location of the deepest measurement obtained by the CTD and the open circles are the location of moored instruments (see chapter 2). The dashed line is the profile of the shelf and slope east of the canyon and the dotted line is the profile of the shelf and slope west of the canyon.

April 1981 (OCEANUS 95)

Intense vertical mixing as well as mixing between water masses was observed in the canyon during OCEANUS 95. Internal vertical mixing in the canyon occurred seaward of station 6 and below 300 dbar (see fig. 4-10). The vertical mixing generally resulted in lower salinities than the reference station (negative salinity anomaly) because there was a relative salinity maximum within the mixing zone. At station 63 this was between 320 and 600 dbar or sigma-t values of 27.31 and 27.62 (see fig. 4-7b). If the mixing zone had occurred between sigma-t values of 27.2 and 27.5 then the resulting water probably would have been saltier than the reference station rather than fresher.

External mixing was again evident between 200-300 dbar, just below the canyon rim, and in the upper canyon between stations 6 and 40. The TS curves for stations 39 and 40 resembled curves 1 and 2 in figure 4-6 indicating mixing with an external source of low salinity water available around the head of the canyon (chapter 2). The TS curve for station 49 on the slope (fig. 4-3) which was in approximately the same water depth as stations 39 and 40 was nearly identical to the reference curve (station 63, fig. 4-7c) indicating that shelf water was mixed with WNA water at stations 39 and 41. The salinity anomaly was generally stronger than in January.

October 1981 (OCEANUS 104)

Vertical mixing was evident in most of the canyon below about 250 dbar between stations 23 and 38 (see fig. 4-11). There was no hydrographic station in the deeper part of the canyon so that station 43 (see fig. 4-3) on the slope east of the canyon was used as the reference station. External mixing occurred only within a small area at the head of the canyon and in a narrow band of water between 200-250 dbars.

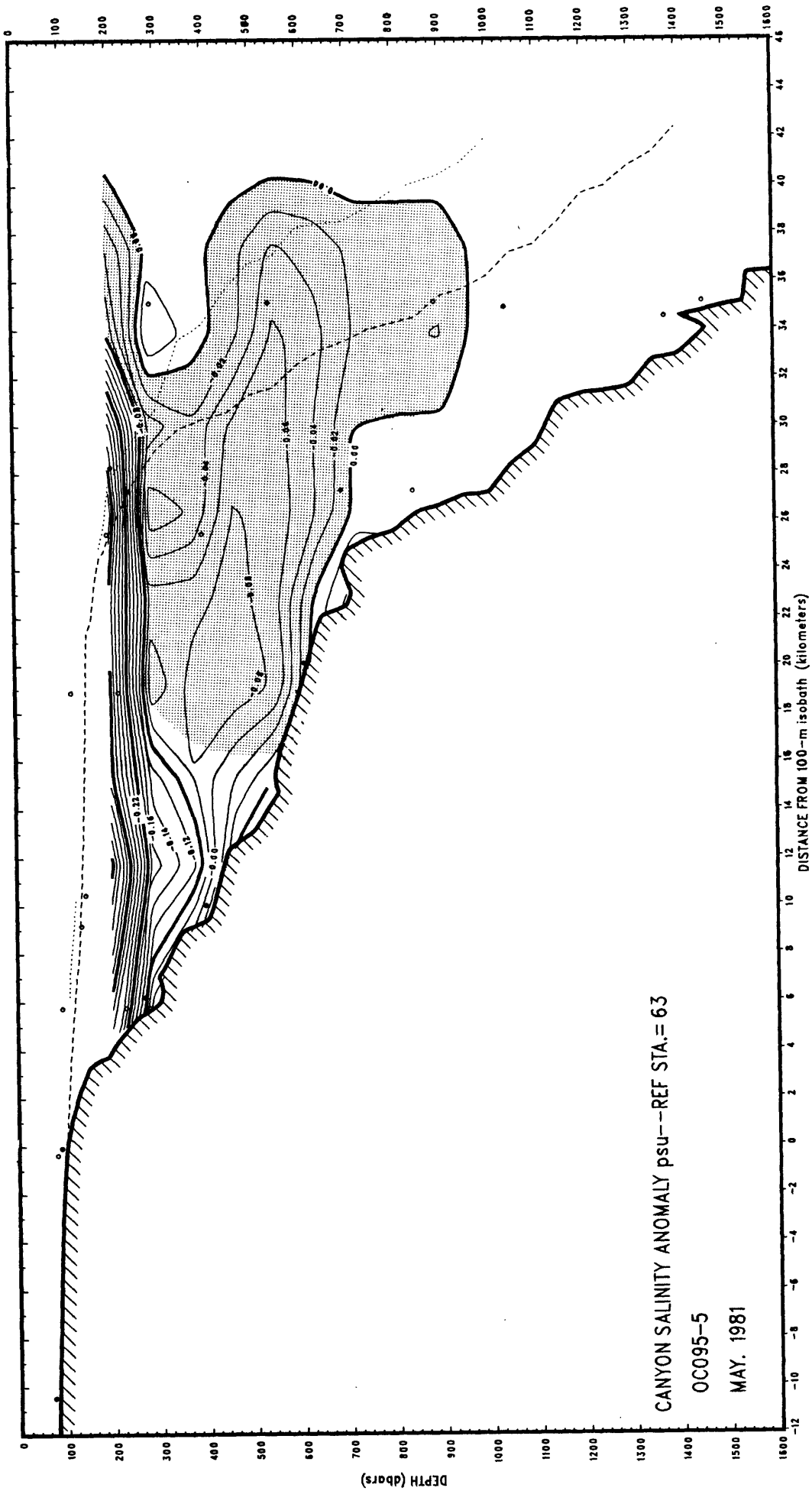

Figure 4-10. April-May 1981 canyon salinity anomaly. See figure 4-9 for explanation.

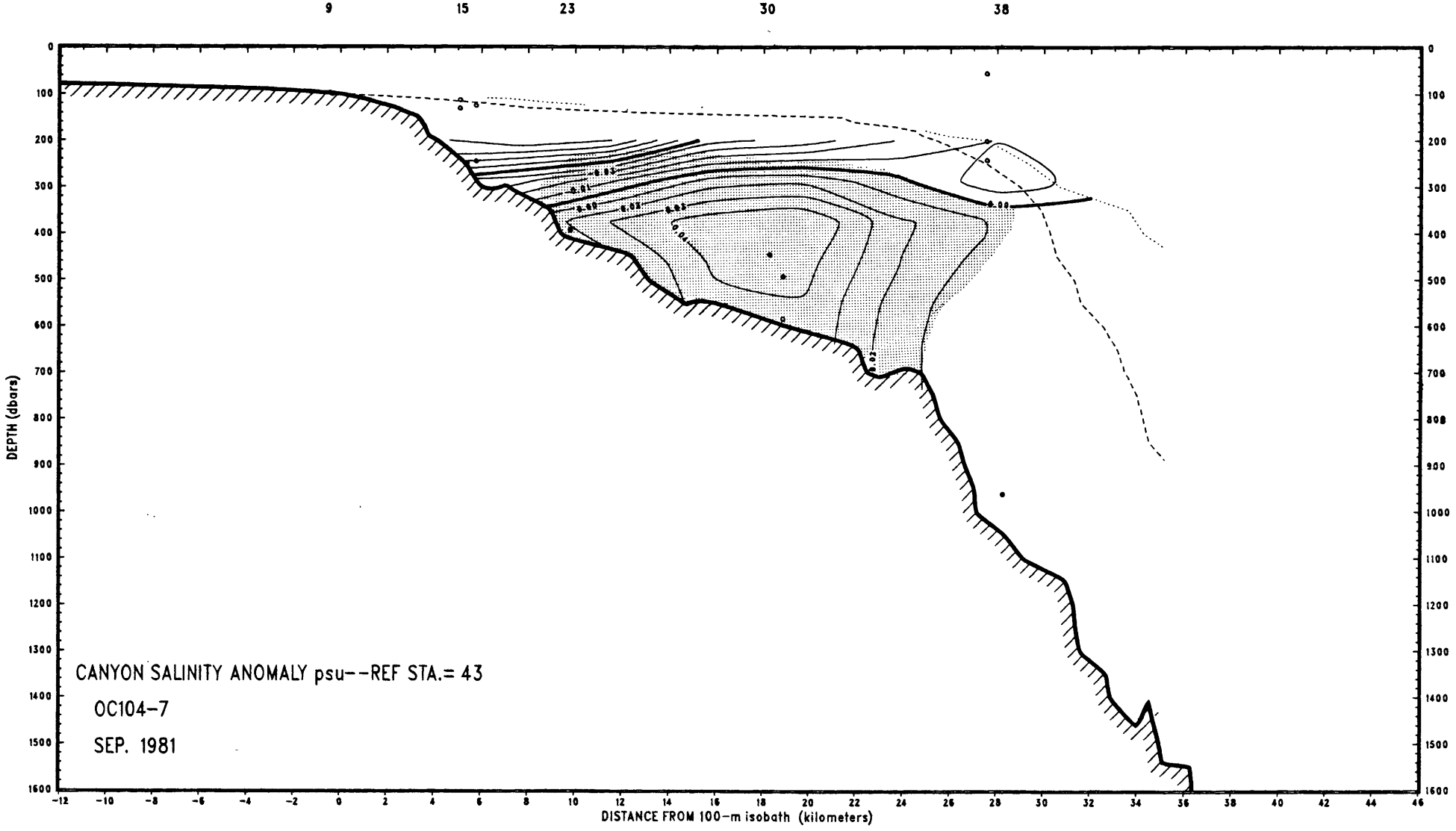

Figure 4-11. September-October 1981 canyon salinity anomaly. See figure 4-9 for explanation.

January 1981-82 (OCEANUS 113)

CTD hydrocasts stopped above 500 dbar along the canyon axis. The only mixing defined by these measurements was external mixing which decreased the salinity between 200 and 400 dbar throughout the canyon (fig. 4-12).

October 1982 (OCEANUS 130)

Internal vertical mixing occurred within the entire canyon below 200 dbar; even at the head of Lydonia Canyon where previous cruises showed external mixing (fig. 4-10, 4-11, and 4-12). The TS curves for stations 32-34 were similar to the curve AB in figure 4-6 but terminated at the bottom before recrossing the reference curve. Each successive TS curve was shifted to the right and indicated additional mixing toward the head of the canyon.

Mixing Time Scales

The hydrographic data gives a synoptic picture of deep mixing in Lydonia Canyon at five different times over a period of two years. To obtain some measure of the variability at shorter time scales a time series of the WNA anomaly was computed for temperature and salinity data recorded at depths of 227 m and 277 m (50 and 5 meters above bottom) near the head of Lydonia Canyon (station LCB, chapter 2).

The WNA anomaly time series was low passed (>33 hours) and the time series was predominately negative, indicating water fresher (shelf water) than standard WNA water mixing with WNA water during deployments I, III and IV (see fig. 4-4 and 4-14). The water in the head of Lydonia Canyon from November 30, 1980 to about January 26, 1981 had TS characteristics within the variability of WNA water. During March 8-13, 1981 there was a strong negative anomaly

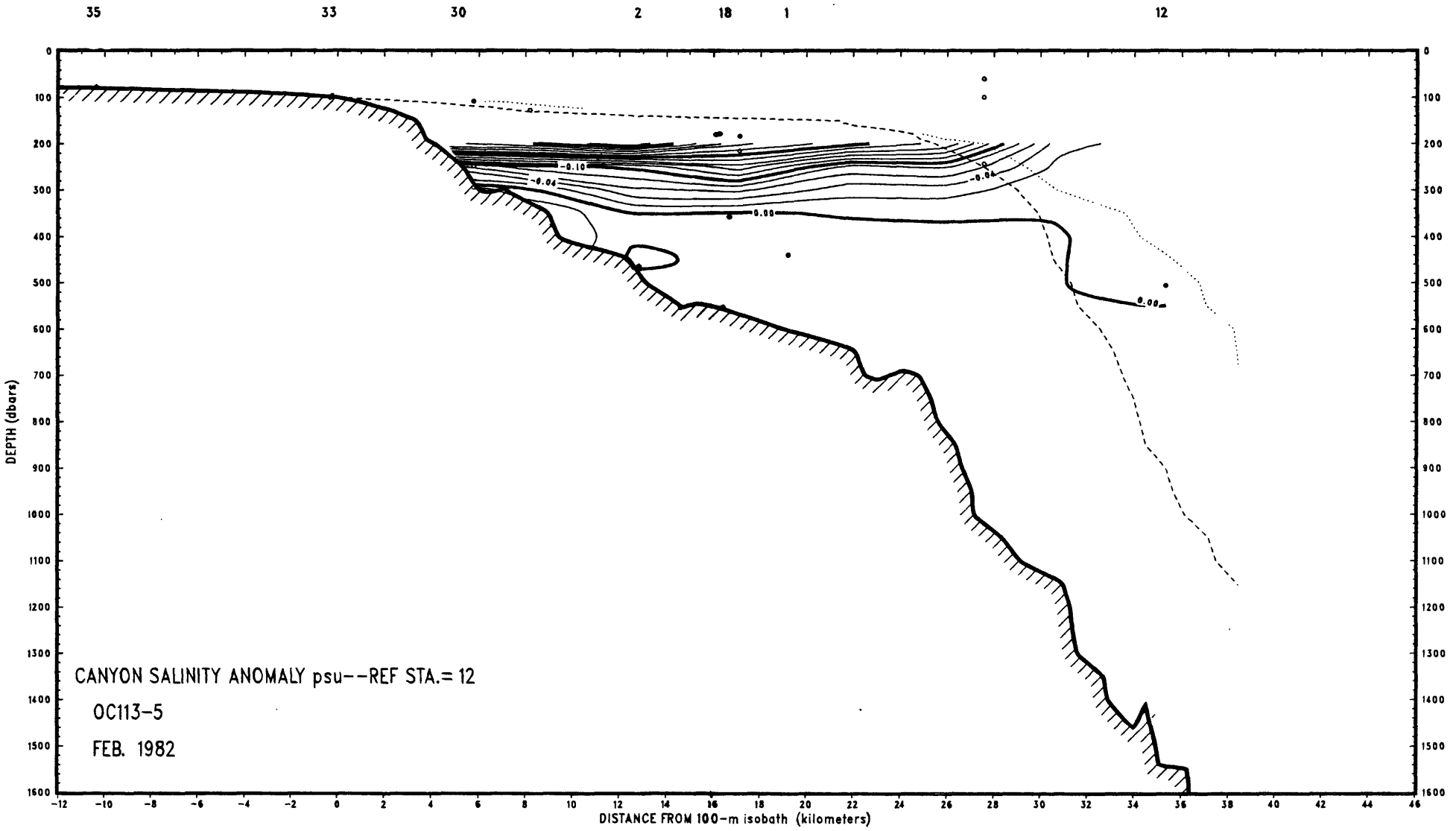

Figure 4-12. January-February 1982 canyon salinity anomaly. See figure 4-9 for explanation. Note that there is no data below about 500 dbars.

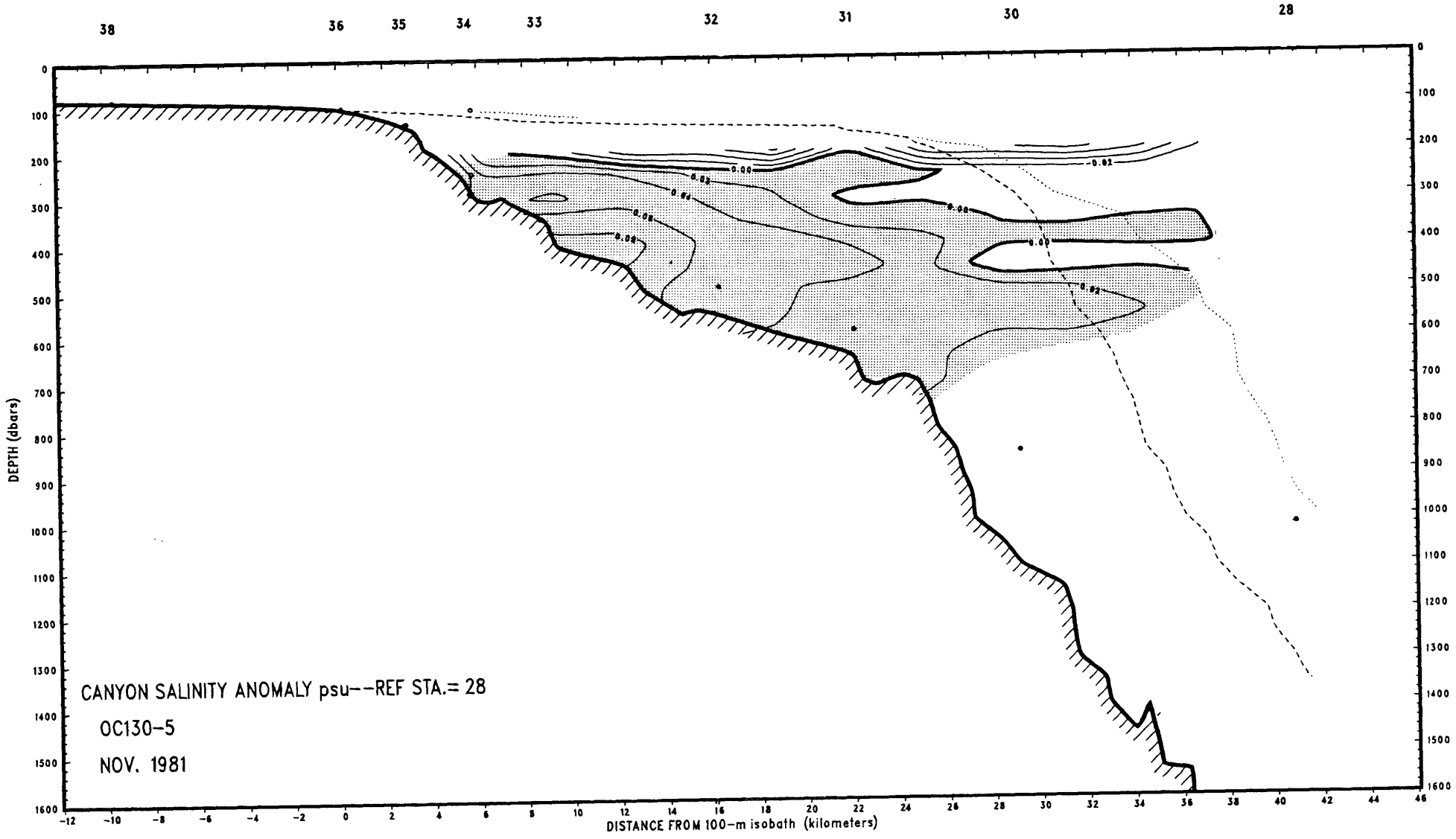

Figure 4-13. November 1982 canyon salinity anomaly. See figure 4-9 for explanation.

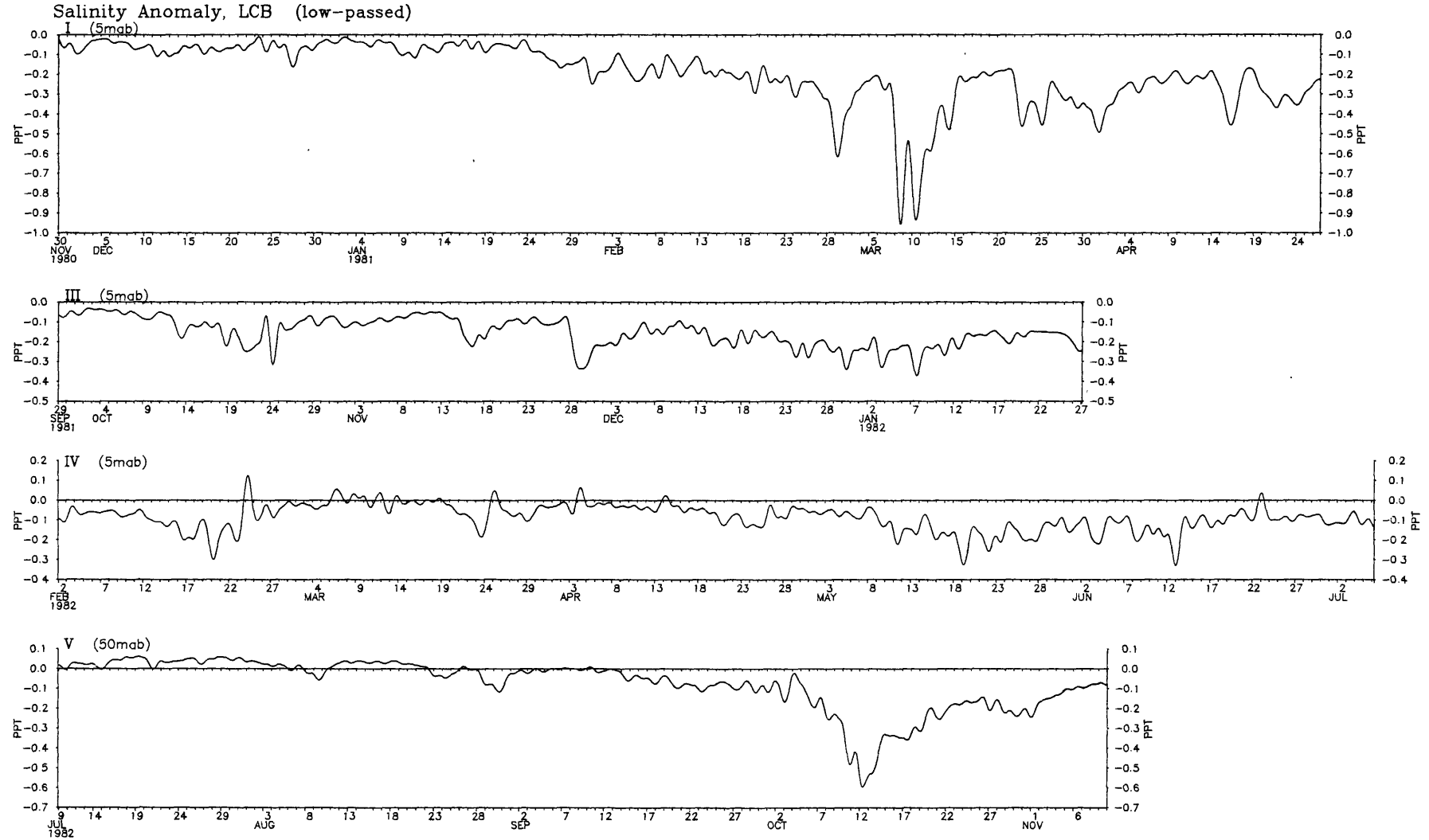

Figure 4-14. Time series of Western North Atlantic (WNA) salinity anomaly (observed salinity minus the standard WNA salinity at the observed sigma-t) for a long-term mooring at the head of Lydonia Canyon (station LCB, fig. 2-2). Salinity measurements for deployments I, III, and IV were 5 meters above bottom (5 mab) and at 50 mab for deployment V. Negative (positive) anomaly indicates water which is fresher (saltier) than WNA water of the same density.

(~0.8 o/oo) followed by smaller amplitude, negative anomalies on March 23-24, April 1-2 and April 16th. The March 8-13 anomaly is associated with strong down canyon flow during the passage of a cyclonic storm across the continental shelf (see also chapter 2). During deployment III there are two additional large amplitude anomalies occurring about one month apart (October 20-23 and November 28-30, 1981); during the November 28-30 negative anomaly there was again a pulse of downcanyon flow indicating significant amounts of shelf water transported and mixing downcanyon. Several positive anomalies occurred during deployment IV and seemed to be correlated with upcanyon flow of 0-1 cm/s (February 24, March 6-7, March 18-19, April 4, 1982) or very weak downcanyon flow (March 25 and April 13-14). The reversal from predominantly downcanyon flow of shelf water to upcanyon flow of WNA water is probably associated with warm core rings 82-A (February 18-March 18, 1982; chapter 2) and 82-D (March 18-April 16, 1982) which passed the mouth of Lydonia Canyon (see chapter 2). During the first part of deployment V (July 9-September 12, 1982) there was a uniform mass of WNA in the head of the canyon. This was followed by a large storm (chapters 2 and 6) on October 10-14 which resulted in a large decrease in salinity at the head of the canyon (fig. 4-14) indicative of shelf water flowing down the canyon. Large amplitude anomalies on the order of 0.3 to 0.8 o/oo appear to occur on time scales of 1-2 months and are associated with either the passage of atmospheric storms or warm core rings.

Other canyons

On OCEANUS 130, one CTD hydrocast was made in Welker Canyon and four in Oceanographer Canyon. Along the axis of Oceanographer Canyon (fig. 4-15a) the TS curves showed an increase in salinity toward the head of the canyon relative to station 28 the reference station used for calculating the canyon

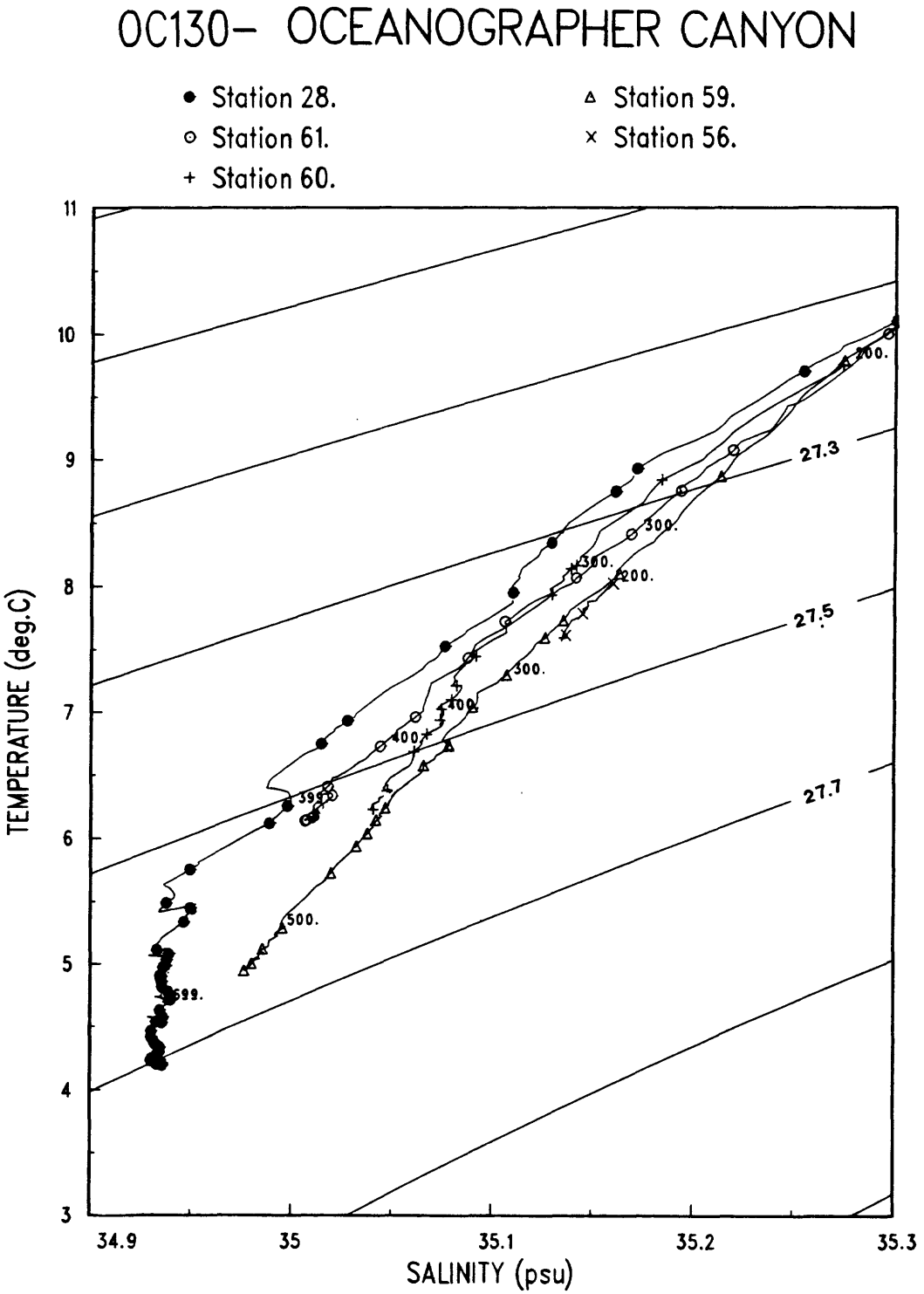

Figure 4-15a. TS curves for stations in the axis of Oceanographer Canyon. Station 28 is the reference station used for Lydonia Canyon. Station 61 is at the mouth of Oceanographer Canyon where the water depth is 1240 m, station 60 is in 695 m, station 59 is in 560 m, and station 56 is at the head of Oceanographer Canyon in 226m.

OC130- WELKER CANYON

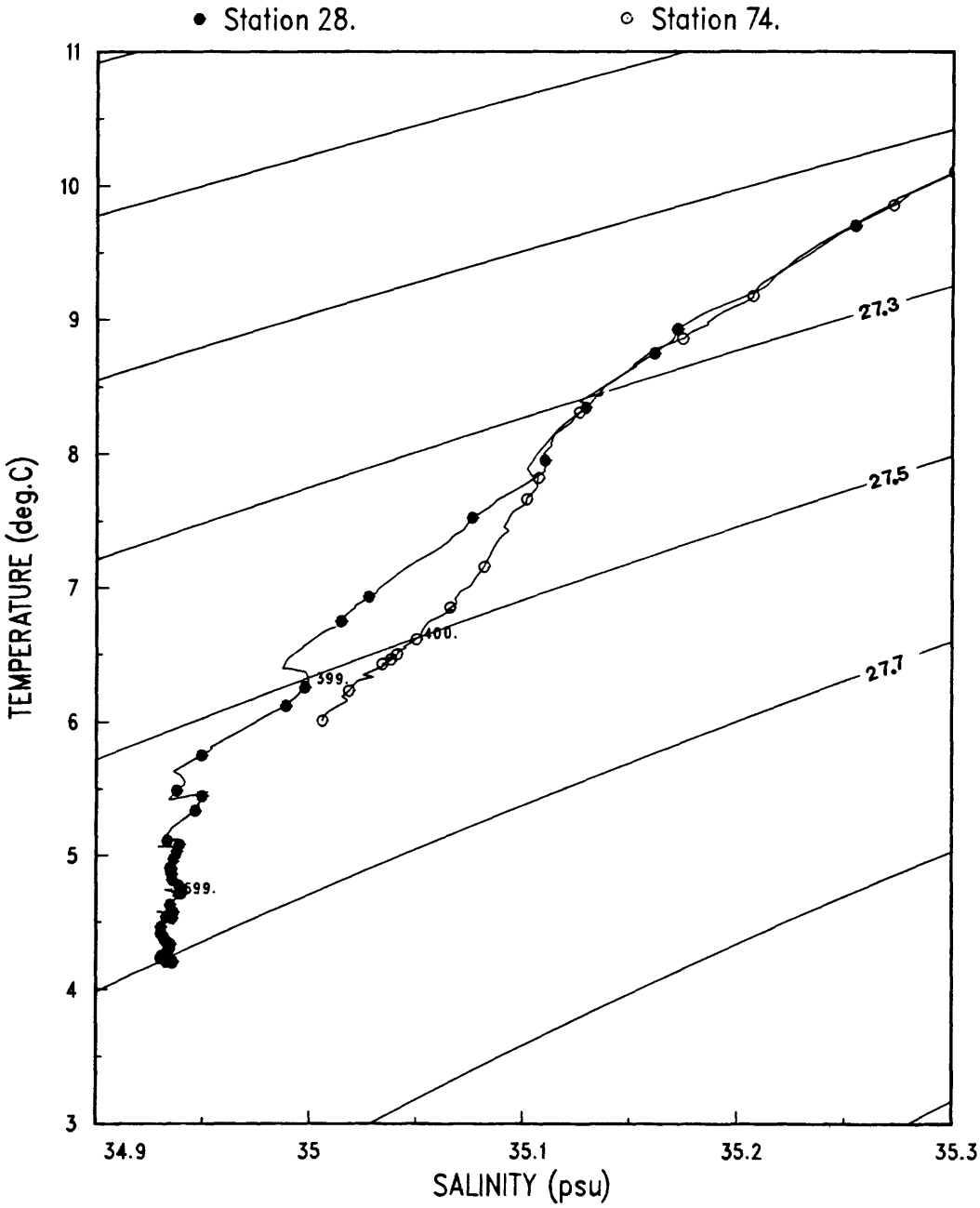

Figure 4-15b. TS curve for station 74 is about 6 km off the axis of Welker Canyon in 478 m of water.

salinity anomaly for Lydonia Canyon (fig. 4-13). The TS curve for Welker Canyon also indicated internal vertical mixing (fig. 4-15b). Satellite surface temperatures and hydrograph sections (chapter 2) indicated a warm core ring along the shelf break and at the entrances to these three canyons. The close proximity of the ring may have increased the internal vertical mixing such that it occurred throughout the length of all three canyons.

DISCUSSION AND SUMMARY

Changes in TS curves indicated that vertical mixing occurred below 300 dbars and over vertical distances of several hundred meters within Lydonia Canyon and increased toward the head of the canyon. External mixing with shelf water predominated between 200-300 dbar and at the head of the canyon where several strong downcanyon flows associated with storms mixed shelf water with WNA.

The time scales (1-2 months) for large changes in salinity in the canyon (0.3-0.8 o/oo) due to external mixing seem to be associated with the occurrence of atmosphere storms and warm core rings. Vertical mixing was also evident in other canyons such as Oceanographer and Welker canyon. These observations agree with Hotchkiss (1982) who defined a salinity anomaly for water corresponding to a sigma-t of 27.3 and found that nine of the twelve stations with salinity anomalies between 0.08 o/oo and 0.14 o/oo were in canyons, and that the salinity anomalies on the adjacent shelf were negligible.

Canyon mixing may be responsible for observed increases in near-bottom nutrient concentrations (Stepien, 1983) which correlate well with high abundance of plankton biomass and epifaunal distribution in the upper regions of Baltimore Canyon (Stepien, 1983 and Hecker and others, 1983). The vertical

mixing is probably an indicator of internal wave which have been shown to be amplified near the bottom and capable of moving sediment (see chapters 2 and 3; Cacchione and Southard, 1974).

Increased mixing relative to the open slope does occur within submarine canyons but the physical cause is not clear. Additional analysis of the available data is required to asses the relative importance of internal waves, storms and the presence of warm core rings in the canyon mixing. The rates of mixing associated with each process needs to be addressed as well as the mixing above 200 m where calving processes are common but require a closer spacing of hydrographic stations than used in this study.

References

Armi, L., and Bray, N. A., 1982, A standard analytical curve of potential temperature versus salinity for the Western North Atlantic: Journal of Physical Oceanography, v. 12, p. 383-387.

Bigelow, N. B., 1933, Studies of the waters on the continental shelf, Cape Cod to Chesapeake Bay, I The cycle of temperature: Papers in Physical Oceanography and Meteorology, v. 2, p. 1-135.

Butman, B., Moody, J. A., and Conley, S. J., 1986a, Hydrography of the New England Shelf and Slope: Data report for R/V OCEANUS Cruise 130, November 1982: U.S. Geological Survey Open-file report no. 86-101, p. 241.

Butman, B., Moody, J. A., and Conley, S. J., 1986b, Hydrography of Lydonia Canyon: Data report for R/V OCEANUS Cruise 104, September 25-October 2, 1981: U.S. Geological Survey Open-file report no. , p. .

Cacchione, D., and Southard, J. B., 1974, Incipient sediment movement by shoaling internal gravity waves: Journal of Geophysical Research, v. 79, p. 237-242.

Cacchione, D., and Wunsch, C., 1974, Experimental study of internal waves over a slope: Journal of Fluid Mechanics, v. 66, part 2, p. 223-239.

Chapman, D. C., Barth, J. A., Beardsley, R. C., and Fairbanks, R. G., 1986, On the continuity of mean flow between the Scotian Shelf and the Middle Atlantic Bight: Journal of Physical Oceanography, v. 16, p. 758-772.

EG&G Environmental Consultants, 1978, Analysis report: Interaction of a Gulf Stream Eddy with Georges Bank: Appendix D of Eighth Quarterly Progress Report, p. 1-56.

Flagg, C. N., Magnell, B. A., Frye, D., Cura, Jerome, J. J., McDowell, S. E., and Scarlet, R. I., 1982, Interpretation of the physical oceanography of Georges Bank, Final Report, v. 1, chapters 1 and 2: EG&G Environmental Consultants.

Hecker, B., Logan, D. T., Gandarillas, F. R., and Gibson, P. R., Megafaunal assemblages in Lydonia Canyon, Baltimore Canyon and selected slope areas, in Final Report: Canyon and Slope Processes Study, Volume III, Biological Processes, Lamont-Doherty Geological Observatory, p. 1-140.

Hopkins, T. S., and Garfield, N. III, 1981, Physical origins of Georges Bank Water: Journal of Marine Research, v. 39, p. 465-500.

Hotchkiss, F., 1982, Observed circulation and inferred sediment transport in Hudson Submarine Canyon, Ph.D. Thesis, M.I.T., 224 p.

Hotchkiss, F. S., and Wunsch, C., 1982, Internal waves in Hudson Canyon with possible geological implications: Deep-Sea Research, v. 29, p. 415-422.

Houghton, R. W., Schlitz, R., Beardsley, R. C., Butman, B., and Chamberlin, J. L., 1982, The Middle Atlantic Bight Cold Pool: Evolution of the temperature structure during Summer 1979: Journal of Physical Oceanography, v. 12, p. 1019-1029.

Iselin, C. O'D., 1936, A study of the circulation of the Western North Atlantic: Papers in Physical Oceanography, v. 4, p. 1-101.

Joyce, T. M., 1984, Velocity and hydrographic structure of a Gulf Stream Warm Core Ring: Journal of Physical Oceanography, v. 14, p. 936-947.

Ketchum, B. H., and Corwin, N., 1964, The persistence of "winter" water on the continental shelf south of Long Island, New York: Limnol. Oceanography, v. 9, p. 467-475.

Moody, J. A., Butman, B., and Conley, S. J., 1986a, Hydrography of Lydonia Canyon: Data report for R/V OCEANUS Cruise 91, January 1981: U.S. Geological Survey Open-file report no. 86-174, 142 p.

Moody, J. A., Butman, B., and Conley, S. J., 1986b, Hydrography of Lydonia Canyon: Data report for R/V OCEANUS Cruise 95, April-May, 1981: U.S. Geological Survey Open-file report no. 86-286, 224 p.

Moody, J. A., Butman, B., and Conley, S. J., 1986c, Hydrography of the New England Shelf and Slope: Data report for R/V OCEANUS Cruise 113, January-February, 1982: U.S. Geological Survey Open-file report no. 86-343, 271 p.

Mooers, C. N. K., Garvine, R. W., and Martin, W. W., 1979, Summertime synoptic variability of the Middle Atlantic shelf water/slope water front: Jounral of Geophysical Research, v. 84, p. 4837-4854.

Posmentier, Eric S., and Houghton, Robert W., 1981, Springtime Evolution of the New England shelf break front: Journal of Geophysical Research, v. 86, p. 4253-4259.

Stalcup, M. C., Joyce, T. M., Barbour, R. L., and Dunworth, J. A., 1985, Hydrographic data from Warm Core Ring 82-B: Woods Hole Oceanographic Institution Technical Report 85-29, 225 p.

Stepien, J. C., 1983, Nutrients in Baltimore Canyon and adjacent slope in Final Report: Canyon and Slope Processes Study, Volume II, Physical Processes, Lamont-Doherty Geological Observatory, p. 243-319.

Worthington, L. V., and Metcalf, W. G., 1961, The relationship between potential temperature and salinity in deep Atlantic water: Rapp. Conseil Perm. Explor. Mer., v. 149, p. 122-128.

Wright, W. R., and Worthington, L. V., 1970, The water masses of the North Atlantic Ocean, a volumetric census of temperature and salinity: Serial Atlas of the Marine environment, Folio 19, American Geographical Society.

Wright, W. R., 1976, The limits of shelf water south of Cape Cod, 1941 to 1972: Journal of Marine Research, v. 34, p. 1-14.

Wunsch, C., 1969, Progressive internal waves on slopes: Journal of Fluid Mechanics, v. 35, part 1, p. 131-144.

CHAPTER 5

THE REGIONAL STRUCTURE OF SUBTIDAL CURRENTS WITHIN AND AROUND LYDONIA CANYON

By

Marlene Noble

Chapter 5

Page

Abstract.....5-1

Introduction.....5-2

Data Set.....5-4

Results.....5-12

The regional structure in the subtidal current field.....5-12

Subtidal currents over the shelf.....5-12

Subtidal currents over the slope.....5-19

Subtidal currents in Lydonia Canyon.....5-28

Coupling among the regional current fields.....5-36

Wind-driven currents.....5-40

Discussion.....5-46

Summary.....5-53

Acknowledgments.....5-55

References.....5-56

ABSTRACT

Beginning in October 1980, 14 current-meter moorings were deployed within Lydonia Canyon and over the continental shelf and slope around the canyon for nearly six months. The observations show that the subtidal current field is partitioned into four distinct regions: currents over the shelf, over the slope in water depths shallower and deeper than 300 m, and within the canyon. Subtidal currents over the shelf and slope are strong and have well-defined spatial structures that are fairly independent from each other. Subtidal currents within the canyon are much smaller, exhibiting a weakly organized flow pattern only at mid-canyon sites. Although the canyon's presence does not alter the along-isobath flow over the shelf and slope, enhanced cross-isobath current fluctuations are observed to occur at slope sites above and slightly below the canyon rim. A moderate to weak coupling is also observed among the regional currents, indicating that along-isobath currents which flow northeastward [southwestward] over the shelf and upper slope tend to be associated with onshelf [offshelf] flow above and within the canyon. Wind stress drives a 2 to 4 cm/s per dyne/cm^2 current along-isobaths over the shelf and upper slope. Wind stress does not drive currents over the deep slope or currents within the canyon.

INTRODUCTION

Along the northeastern United States, the outer continental shelf and upper slope is convoluted; many small and medium-size canyons cut across the slope into the shelf. Between October 1980 and November 1982, the U.S. Geological Survey conducted a field program to study the circulation within one of these submarine canyons and to investigate the effects of the canyon on the shelf/slope circulation. During the first portion of the field program,

14 current-meter moorings were deployed in and around Lydonia Canyon for 5 to 6 months. Lydonia, a medium-size canyon on the New England shelf south of Georges Bank, cuts northward approximately 20 kilometers into the shelf (fig. 5-1).

Previous measurements of currents within submarine canyons have usually been confined to fairly short observations of currents within the canyon themselves. Current records were often less than a week long. Shepard and others (1979) provides a nice summary of many short current records obtained from a wide variety of canyons on both coasts of the United States. Their data indicate that currents within submarine canyons are mainly tidal and that packets of internal waves can propagate along the canyon axis. The loss of several current meters after strong storm events led them to infer that storms triggered turbidity currents in canyons that were filled with sediment because they headed near river mouths.

Current records obtained over a longer period in Hudson canyon, a major canyon on the eastern U.S. continental shelf, support previous observations that baroclinic and barotropic tidal currents are a major component of the current field within a submarine canyon (Hotchkiss and Wunsch, 1982). The subtidal currents observed in Hudson canyon were relatively weak and were not obviously correlated with wind forcing. Only one along-canyon current event could be associated with the passage of a very strong storm.

Because earlier current records were of short duration, and because canyons were sparsely instrumented, previous studies could not describe the subtidal circulation patterns within a canyon. Nor could they directly measure interactions between the currents in the canyon and currents over the shelf and slope. In this chapter, we will describe the subtidal circulation within Lydonia Canyon and over the outer shelf and upper slope near the canyon

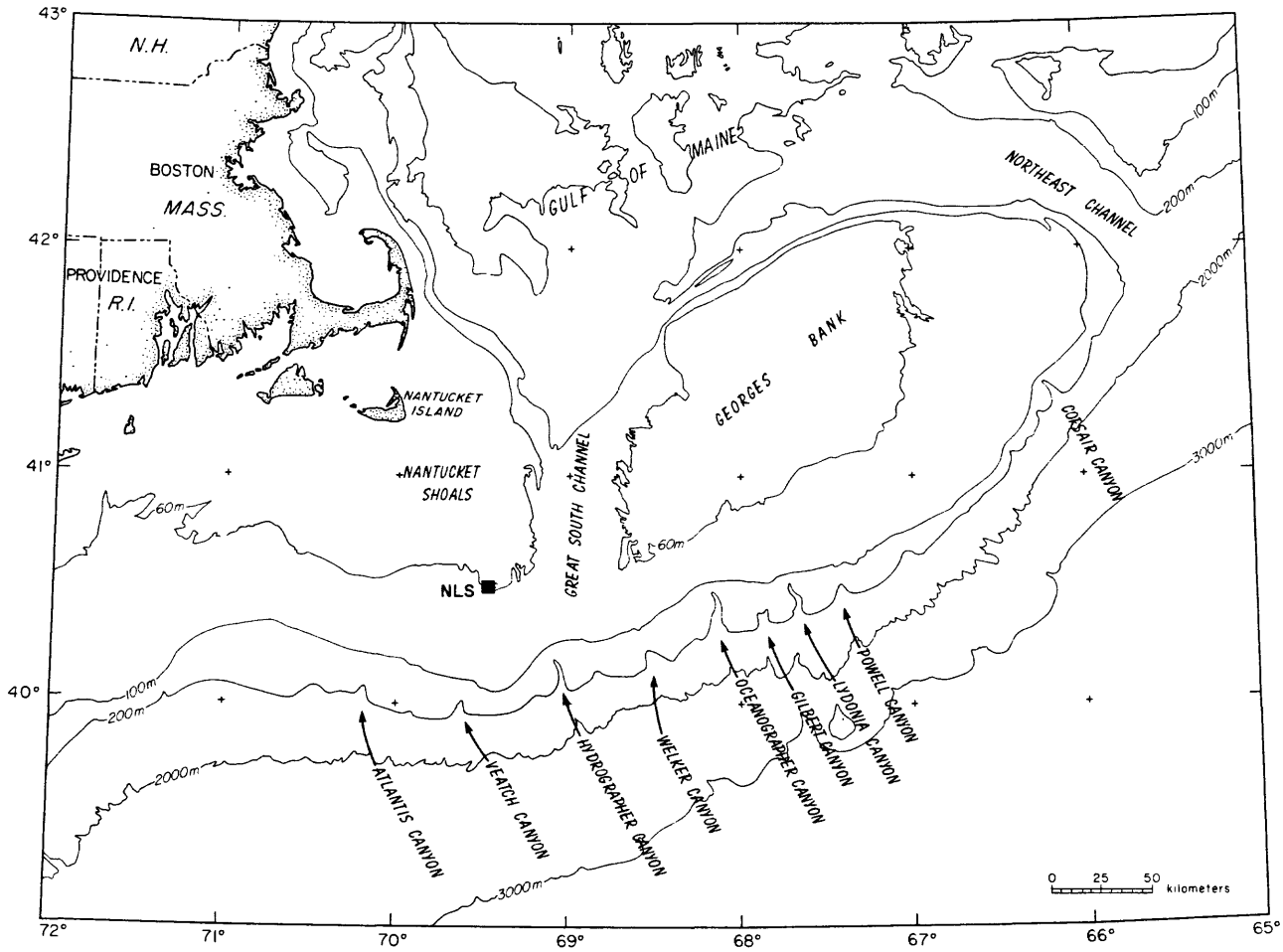

Figure 5-1. Location of Lydonia Canyon and the Nantucket Lightship (NLS).

We investigate the coupling between subtidal currents in these three regions, and determine the strength of the wind-forced flow within the regions. (See Chapter 2 for an overall description of the canyon experiment).

DATA SET

During the first deployment of the moored array, from October 1980 through April 1981, fourteen current-meter moorings were deployed in a dense array on the shelf and slope around Lydonia Canyon and within the canyon itself (table 5-1, fig. 5-2). Based primarily on instrument location, data from the vector-averaging current meters (VACMs) on the moorings were grouped into three categories, representing the shelf, slope, and canyon regions. For instruments located near the boundary of two regions, the character of the current record determined the instrument category. Data records are referenced as LCB(277) when LCB is the station name, and 277 is the depth in meters.

Seven current meters were deployed on the shelf to monitor the mid-depth and near-bottom currents and to measure the flow above and slightly within the canyon. These instruments were located either directly above the seabed (on moorings LCA, LCM and LCL), over the shelf but above the canyon rim (on mooring LCB), or slightly below the canyon rim (on moorings LCC and LCD). Sixteen current meters were deployed at nine locations on the upper slope (on moorings LCK, LCI, and LCJ), in the canyon but above the canyon rim (on moorings LCE, LCG, LCN, LCF, and LCH), or slightly below the rim (current meter LCE(216)). These instruments monitored currents over the slope on both sides of the canyon and currents above the canyon itself. Eight current meters were deployed within the canyon, well below the depth of the rim (fig. 5-3). The current meters on moorings LCB, LCE, LCN, and LCH monitored

Table 5-1. Locations of the current meters in and around Lydonia canyon. For each current meter, the letters denote the mooring name and the numbers denote the depth of the instrument. The Shelf, Slope, and Canyon categories represent measurements over the shelf, over the slope and within the canyon. All current meters are VACMs.

Station	Location	Depth instrument	Depth water	Current[1] direction	Topographic direction	Observation period
			Shelf			
LCA(80)	40°34.2'N 67°44.5'W	80m	100m	75°	76°	Dec 02 1980 Apr 22 1981
LCM(103)	40°29.5'N 67°48.2'W	103m	123m	81°	70°	Nov 29 1980 Apr 26 1981
LCB(92)	40°31.6'N 67°42.8'W	92m	282m	85°	--	Nov 30 1980 Apr 26 1981
LCL(70) LCL(110)	40°31.7'N 67°36.5'W	70m 110m	130m	84°	85°	Dec 01 1980 Apr 23 1981
LCC(134)	40°29.4'N 67°43.5'W	134m	184m	75°	--	Oct 26 1980 Mar 24 1981
LCD(143)	40°29.3'N 67°41.3'W	143m	193m	75°	--	Oct 29 1980 Mar 08 1981
			Slope			
LCE(116) LCE(216)	40°25.4'N 67°39.9'W	116m 216m	600m	75°	--	Dec 03 1980 Apr 29 1981
LCG(195)	40°21.4'N 67°41.6'W	195m	495m	75°	--	Oct 28 1980 Apr 25 1981
LCN(243)	40°21.3'N 67°40.4'W	243m	1041m	75°	--	Dec 01 1980 Apr 25 1981
LCF(205)	40°21.2'N 67°39.0'W	205m	505m	75°	--	Oct 29 1980 Apr 14 1981
LCI(10) LCI(55) LCI(195) LCI(245)	40°22.9'N 67°33.0'W	10m 55m 195m 245m	250m	75°	75°	Dec 03 1980 Apr 28 1981
LCK(204) LCK(454)	40°16.3'N 67°47.0'W	204m 454m	554m	75°	75°	Nov 29 1980 Apr 26 1981
LCH(290) LCH(540)	40°17.6'N 67°39.5'W	290m 540m	1554m	75°	--	Dec 02 1980 Apr 25 1981
LCJ(83) LCJ(223)	40°21.2'N 67°32.0'W	83m 223m	571m	75°	75°	Nov 29 1980 Apr 01 1981 Apr 27 1981

LCJ(471)		471m				
			Canyon			
LCB(227)	40°31.6'N	227m	282m	333°	330°	Nov 30 1980
LCB(277)	67°42.8'W	277m				Apr 22 1981
LCE(595)	40°25.4'N	595m	600m	20°	15°	Dec 03 1980
	67°39.9'W					Apr 29 1981
LCG(395)	40°21.4'N	395m	495m	49°	35°	Oct 28 1980
	67°41.6'W					Apr 25 1981
LCN(841)	40°21.3'N	841m	1041m	49°	35°	Dec 01 1980
	67°40.4'W					Apr 25 1981
LCF(405)	40°21.2'N	405m	505m	49°	35°	Oct 29 1980
	67°39.0'W					Apr 25 1981
LCH(890)	40°17.6'N	890m	1554m	0°	350°	Dec 02 1980
	67°39.5'W					Apr 25 1981
LCH(1454)		1454m				Apr 08 1981

[1] for Shelf, current direction is alongshelf
for Slope, current direction is alongslope
for Canyon, current direction is alongcanyon

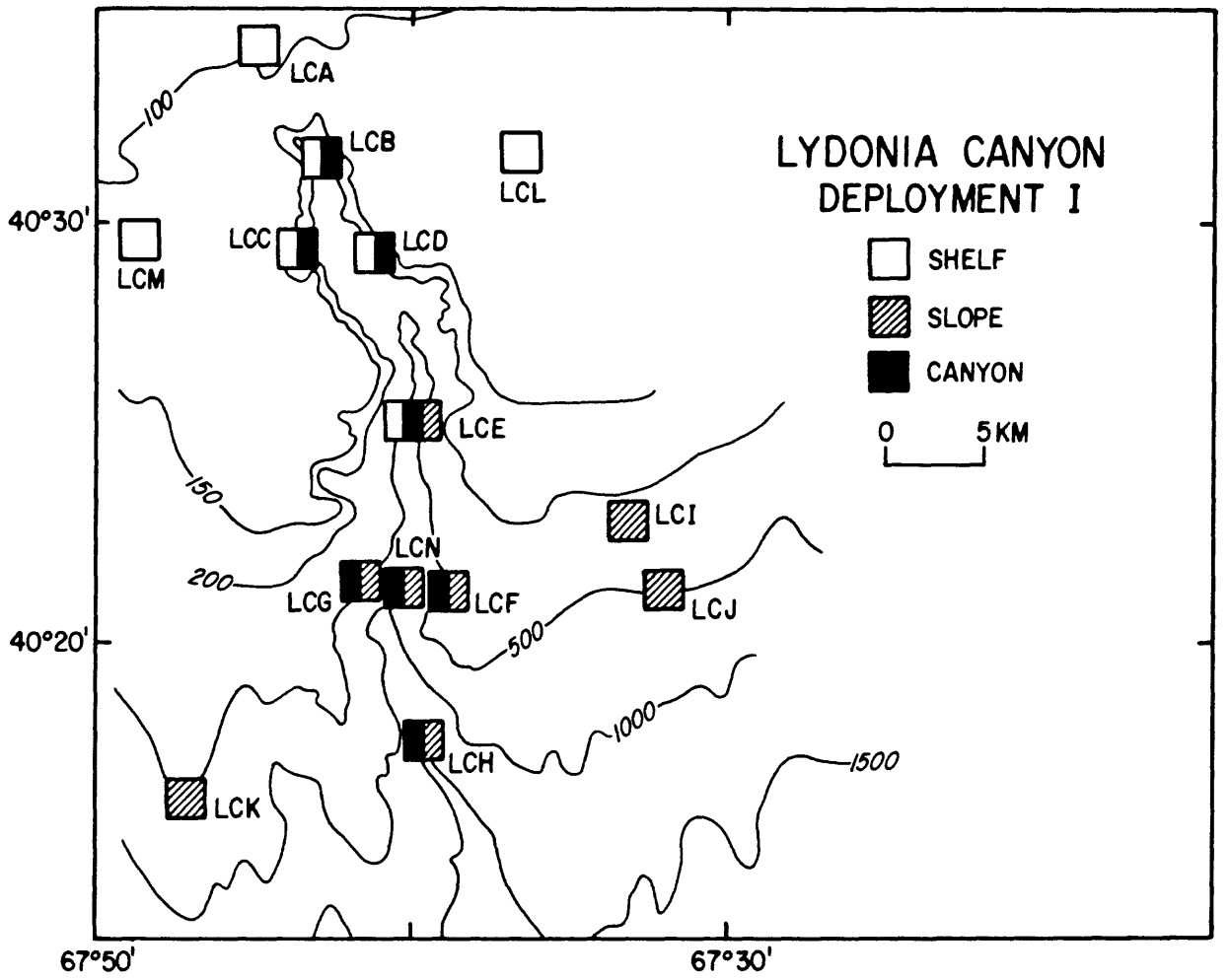

Figure 5-2. Locations of the current-meter moorings deployed in and around Lydonia Canyon. The shelf, slope and canyon classifications represent the categories of the current meters on the mooring.

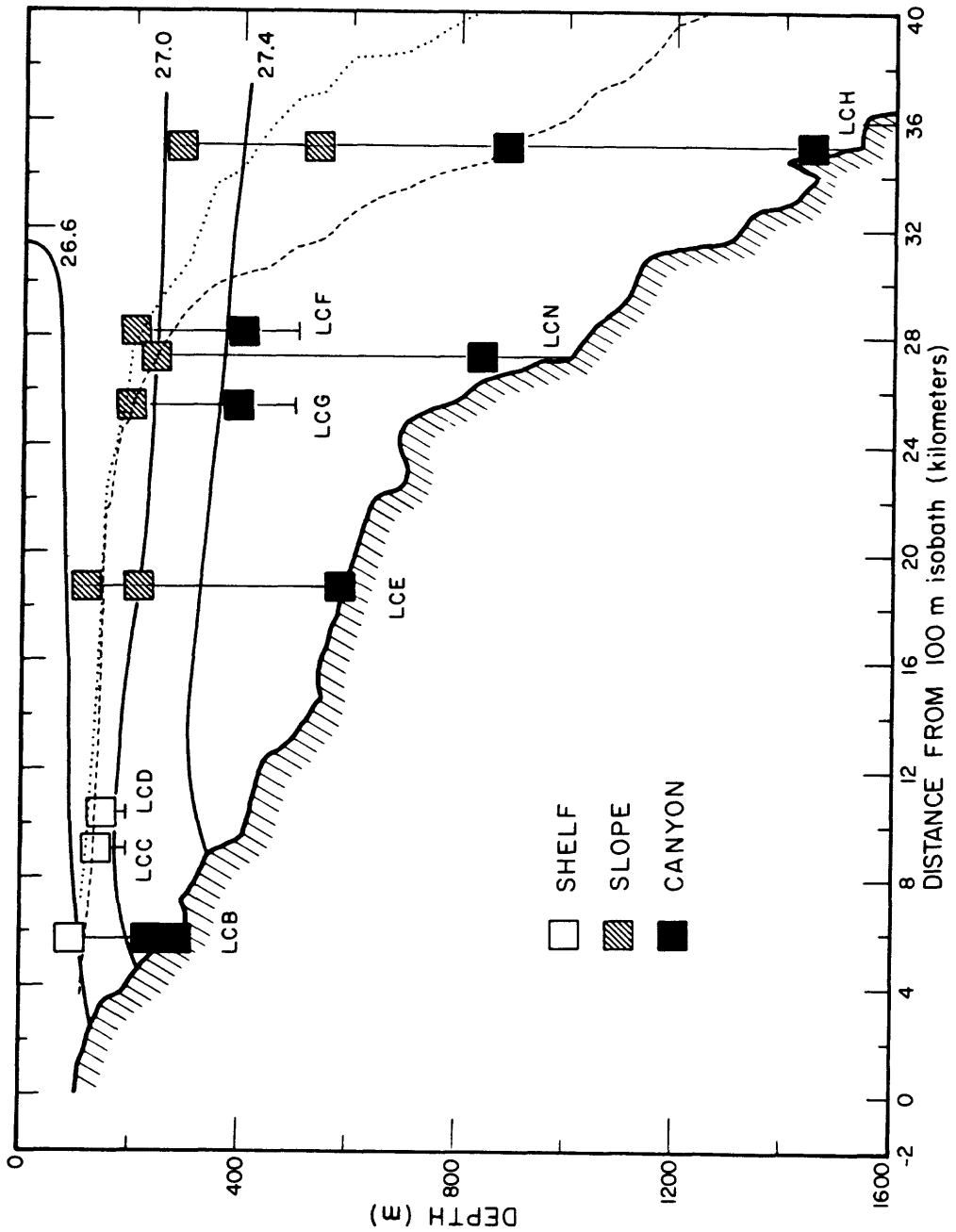

Figure 5-3. Locations of the current meters within and above Lydonia Canyon showing the mooring name and current-meter category (shelf, slope or canyon). A schematic density section is superimposed.

the flow within 5 to 200 m of the seabed along the canyon axis. Currents in the axis were also measured at site LCH(890), which was at about the same depth as site LCN(841), but further down the canyon axis. Two current meters, LCG(395) and LCF(405), measured the flow along the canyon walls 100 m above the bottom.

All current observations were lowpass filtered to remove fluctuations with periods shorter than 40 hours. The subtidal currents (i.e. currents with frequencies between 1/2.5 and 1/32 cycles per day (cpd) were rotated into new coordinate systems that were appropriate to each site (table 5-1). The currents over the shelf were decomposed into an alongshelf/cross-shelf coordinate system. The alongshelf orientation, which is positive toward the northeast, is aligned nearly parallel with both the orientation of the individual subtidal current ellipses and with the local shelf topography (tables 5-1, 5-2). The positive cross-shelf direction is to the northwest. The currents over the slope were decomposed into a 75^{o}-345^{o} coordinate system, with along-slope currents positive toward the northeast. The along-slope orientation is aligned with the regional slope topography and is within a few degrees of the axis of the subtidal current ellipses (tables 5-1, 5-2). The currents within the canyon were decomposed into an along-canyon/cross-canyon coordinate system, with positive directions northward into the canyon (along-canyon) and eastward (cross-canyon). Since the canyon meanders as it cuts into the shelf, the along-canyon orientation changes from 0^{o} at LCH in the outer canyon, to 49^{o} at LCN in the mid canyon, to 333^{o} at LCB in the canyon head.

Observations of wind speed and direction at Nantucket Lightship, located approximately 200 km northwest of Lydonia Canyon, were obtained from the National Climatic Center (fig. 5-1). Because the alongshelf scale of wind

Table 5-2. Ellipse statistics of the subtidal flow field. The statistical parameters are described in Gonella, 1972.

Station	Ellipse orientation	Ellipse stability	Rotary coefficient
	Shelf		
LCA(80)	74°	0.89	0.26
LCM(103)	82°	0.79	0.15
LCB(92)	87°	0.80	0.12
LCL(70)	83°	0.81	0.10
LCL(110)	86°	0.80	0.19
LCC(134)	--	--	--
LCD(143)	--	--	--
	Slope		
LCE(116)	70°	0.63	-0.12
LCE(216)	0°	0.60	0.10
LCG(195)	68°	0.91	0.10
LCN(243)	69°	0.87	0.02
LCF(205)	77°	0.95	0.06
LCI(10)	70°	0.65	-0.02
LCI(55)	73°	0.84	0.03
LCI(195)	76°	0.96	0.02
LCI(245)	77°	0.82	0.04
LCK(204)	79°	0.84	0.13
LCK(454)	74°	0.96	0.02
LCH(290)	70°	0.90	0.06
LCH(540)	75°	0.89	0.03
LCJ(83)	83°	0.91	-0.03
LCJ(223)	72°	0.94	0.04
LCJ(471)	81°	0.94	-0.12
	Canyon		
LCB(227)	333°	0.66	0.05
LCB(277)	317°	0.73	0.14
LCE(595)	22°	0.68	-0.16
LCG(395)	53°	0.75	0.07
LCN(841)	50°	0.72	0.14
LCF(405)	45°	0.76	-0.12
LCH(890)	75°	0.50	0.13
LCH(1454)	11°	0.85	0.02

systems over the New England Continental Shelf is longer than 500 km, wind at Nantucket Lightship is considered to be representative of the low-frequency wind over Lydonia Canyon. Wind stress is defined to be

$$\tau = \rho C_D W \, |W|$$

where ρ is the air density (0.0012 gm/cm^3), C_D the wind-stress drag coefficient, and W the wind velocity. The wind-stress drag coefficient increases with wind speed

$$C_D = (0.8 + 0.065 \, |W_{10}|) \times 10^{-3}$$

where $|W_{10}|$ is the wind speed 10 m above the surface in m/s (Wu, 1980). The wind stress records were lowpass filtered and decomposed into an alongshelf/cross-shelf coordinate system. The positive alongshelf wind stress direction is 60^o, which is parallel to the large-scale shelf topography. The positive cross-shelf wind stress direction is 330^o.

Hydrographic observations were made over the shelf, the slope and in the canyon when the moorings were deployed, on one cruise in the middle of the deployment period (January 1981), and when the moorings were recovered. Though these observations are semisynoptic pictures of the density structure, they can be used to describe the approximate location of the major hydrographic features in the region (fig. 5-3; see chapter 2). In winter, the shelf water is relatively cold and fresh; temperatures are near 5^{o}C and σ_t values are less than 26.6. The shelf-water/slope-water front intersects the seabed near the 120-m isobath, along a line running roughly through stations LCM, LCB, and LCL. These stations, and stations above the canyon (LCB(92) and LCE(116)), are close to the shelf-water/slope-water front and may be affected by frontal excursions. In January 1981, a lens of warm, salty (12^{o}C and 35.4 0/00) relatively light water was found in the canyon centered at about 180 m. This lens was apparently associated with a large Gulf Stream warm core

ring located to the south of the canyon. The intruding lens caused the isopycnals in the canyon to deepen seaward below 180 m. In May 1981, at the end of Deployment 1, the isopycnals were flatter seaward of the canyon head (Moody and others, 1986a, 1986b; see chapter 2). Instruments at about 200-m water depth in the outer canyon -- LCE(2112), LCG(195), LCN(241), and LCF(205) -- may be affected by intrusions associated with the eddies. Below 400 m, the isopycnals are rather flat and spaced farther apart.

RESULTS

The spatial structure in the subtidal current field

The subtidal currents over the shelf, the slope, and in the canyon share few common characteristics. Subtidal currents tend to be aligned with the topography in all three regions, but the current amplitudes vary significantly. In the canyon, subtidal current speeds typically range from 5 to 10 cm/s, while currents over the upper slope reach speeds of 40 to 60 cm/s (fig. 5-4). Major current events are often observed only in one region. For example, a warm core ring passed through part of the instrumented array during December 1980 and January 1981. Currents above 250 m over the upper slope moved rapidly and uniformly toward the northeast, while currents over the shelf, currents below 250 m over the upper slope, and currents in the canyons were apparently unaffected by the ring (fig. 5-4, see also chapter 2). Wind stress, which drives current along the shelf, is not obviously correlated with subtidal currents over the slope or within the canyon.

Subtidal currents over the shelf

Within each of the four regions, subtidal currents share many common features. Over the shelf, most currents are stably aligned with the

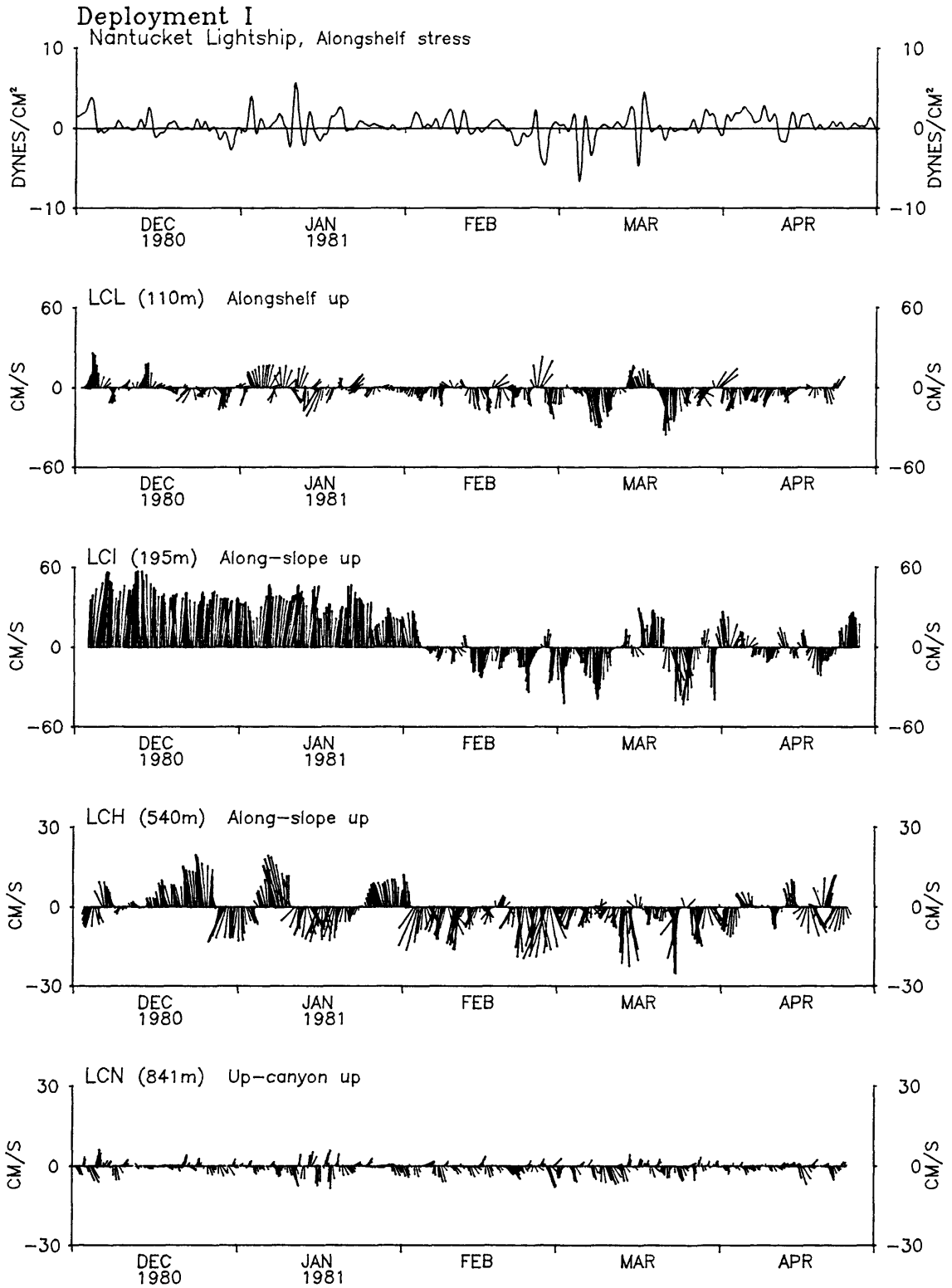

Figure 5-4. Wind stress and typical current-meter records illustrating the flow on the shelf, slope, and in the canyon. LCL(110) is a shelf site, LCI(195) and LCH(540) are slope sites. LCN(841) is a canyon site. Note change in scale for LCH and LCN.

topography, along 80° (table 5-2). Currents over the shelf lose their stability only at LCC(134) and LCD(143), sites that were located near the canyon rim, slightly below the depth of the adjacent shelf. The mean current flows steadly toward the southwest (table 5-3). The mean alongshelf current has an amplitude of 11 cm/s in the middle of the water column at LCL(70); the amplitude is reduced to between 4 cm/s and 8 cm/s within 20 m of the seabed. The mean cross-shelf current has no consistent direction at the shelf sites.

Alongshelf currents are highly correlated. Near the seabed, the joint correlations among the set of alongshelf currents are greater than 0.8, with no significant phase lags. Cross-shelf currents are in phase but less well correlated, with correlation amplitudes less than 0.4 among these same sites.

Because the correlations among the alongshelf currents are high, alongshelf currents and, to some extent, cross-shelf currents, can be represented by the first mode of an empirical orthogonal function (table 5-4, fig. 5-2). The first mode is a spatial average of the correlated portion of the current field, weighted by the current amplitudes at each instrument site. The first mode in the subtidal alongshelf current contains 70 percent of the total variance in the data set and represents over 75 percent of the variance at sites over the shelf or above the canyon head. Mode 1 is less representative of the alongshelf current further out over the canyon, and contains 40-70 percent of the available current variance at sites LCC(134), LCD(143) and LCE(116). The alongshelf Mode 1 currents fluctuate together, and have an amplitude near 10 cm/s at most shelf sites (fig. 5-5, table 5-4). Mode 1's alongshelf amplitude is reduced only at sites below the canyon rim, at LCC(134) and LCD(143). Although the alongshelf Mode 1 currents were derived from currents within 20 m of the seabed, the mode also represents the mid-depth currents over the shelf. The alongshelf Mode 1 currents are in

Table 5-3. The mean and variance of the subtidal currents at each site. Positive alongshelf and positive alongslope are toward the northeast. Positive alongcanyon is up canyon. Shelf denotes currents over the shelf. Slope(200) and Slope(500) denote currents over the slope above and below 300m. Canyon denotes currents in the canyon. The number of independent points in each data record is the record length divided by the autocorrelation scale.

Shelf

Station	Alongshelf mean	Alongshelf variance	Autocorrelation scale	Cross shelf mean	Cross shelf variance	Autocorrelation scale
	cm s^{-1}	cm^2 s^{-2}	days	cm s^{-1}	cm^2 s^{-2}	days
LCA(80)	-8.5±2.5	91.6	2.3	-0.1±0.8	13.3	1.5
LCM(103)	-4.4±2.5	105.2	2.3	-2.6±0.8	17.4	1.5
LCB(92)	-8.0±2.2	77.1	2.3	1.0±0.7	12.8	1.5
LCL(70)	-10.9±2.9	112.6	2.3	0.0±0.8	15.2	1.5
LCL(110)	-3.6±2.5	98.7	2.3	-0.4±0.8	16.4	1.5
LCC(134)	-3.8±1.5	38.3	2.3	-2.2±0.7	12.9	1.5
LCD(143)	-2.3±1.2	23.1	2.3	3.0±0.8	14.5	1.5

Slope(200)

Station	Alongslope mean	Alongslope variance	Autocorrelation scale	Cross slope mean	Cross slope variance	Autocorrelation scale
	cm s^{-1}	cm^2 s^{-2}	days	cm s^{-1}	cm^2 s^{-2}	days
LCE(116)	3.3±6.2	111.6	10	0.0±0.9	19.2	1.5
LCE(216)	-1.5±0.8	11.1	2	3.5±1.1	32.2	1.5
LCG(195)	3.4±6.4	165.3	10	0.4±0.5	9.0	1.5
LCN(243)	10.4±10.9	372.5	10	2.1±0.9	18.5	1.5
LCF(205)	14.9±12.3	568.8	10	1.7±0.8	16.2	1.5
LCI(10)	-8.3±8.2	374.3	6.3	-3.9±2.0	97.8	1.5
LCI(55)	7.6±13.3	558.1	10	0.4±1.2	35.0	1.5
LCI(195)	12.1±13.9	612.9	10	-0.4±0.6	7.5	1.5
LCK(204)	11.3±12.3	489.2	10	1.0±1.1	29.5	1.5
LCH(290)	12.0±12.8	505.4	10	2.1±0.9	18.4	1.5
LCJ(83)	18.3±18.8	904.8	10	0.3±3.7	35.6	1.5
LCJ(223)	18.0±15.3	761.2	10	0.5±0.7	14.2	1.5

Slope(500)

Station	Alongslope mean	Alongslope variance	Autocorrelation scale	Cross slope mean	Cross slope variance	Autocorrelation scale
	cm s^{-1}	cm^2 s^{-2}	days	cm s^{-1}	cm^2 s^{-2}	days
LCK(454)	-1.4±5.3	145.9	6.3	-1.2±0.4	4.0	1.5
LCH(540)	-2.3±3.7	72.8	6.3	0.7±0.5	5.2	1.5
LCJ(471)	-0.4±2.5	34.8	6.3	0.4±0.3	2.1	1.5

Canyon

Station	Alongcanyon mean	Alongcanyon variance	Autocorrelation scale	Cross-canyon mean	Cross-canyon variance	Autocorrelation scale
	cm s^{-1}	cm^2 s^{-2}	days	cm s^{-1}	cm^2 s^{-2}	days
LCB(227)	2.1±0.5	6.2	1.5	-0.2±0.3	1.4	1.5
LCB(277)	-3.3±0.7	10.3	1.5	-1.1±0.3	2.6	1.5
LCE(595)	0.0±0.7	11.7	1.5	1.4±0.3	2.2	1.5
LCG(395)	-0.5±0.3	3.4	1.5	-0.7±0.1	0.7	1.5
LCN(841)	-0.9±0.5	6.0	1.5	-1.1±0.2	0.8	1.5
LCF(405)	-2.1±0.5	7.1	1.5	-0.0±0.2	1.5	
LCH(890)	-0.2±0.4	4.2	1.5	-0.3±0.6	7.3	1.5
LCH(1454)	0.0±0.7	9.7	1.5	0.8±0.3	1.3	1.5

Table 5-4. The first mode in the along and cross-shelf currents. Stations that have less than 6% of their variance contained in the mode are deleted from the mode. The 95% confidence level for zero correlation squared is 0.06. The modal amplitude is defined to be the square root of twice the variance of the mode at each site.

Shelf_EOF

Station	Alongshelf amplitude cm s^{-1}	Percent variance %	Cross-shelf amplitude cm s^{-1}	Percent variance %
LCA(80)	11.1	76	3.3	39
LCM(103)	12.6	85	3.5	38
LCB(92)	10.7	81	2.6	28
LCL(110)	12.0	81	3.7	46
LCC(134)	6.1	69	--	--
LCD(143)	5.0	51	2.4	25
LCE(116)	10.0	43	2.3	14
Mode 1		70		29

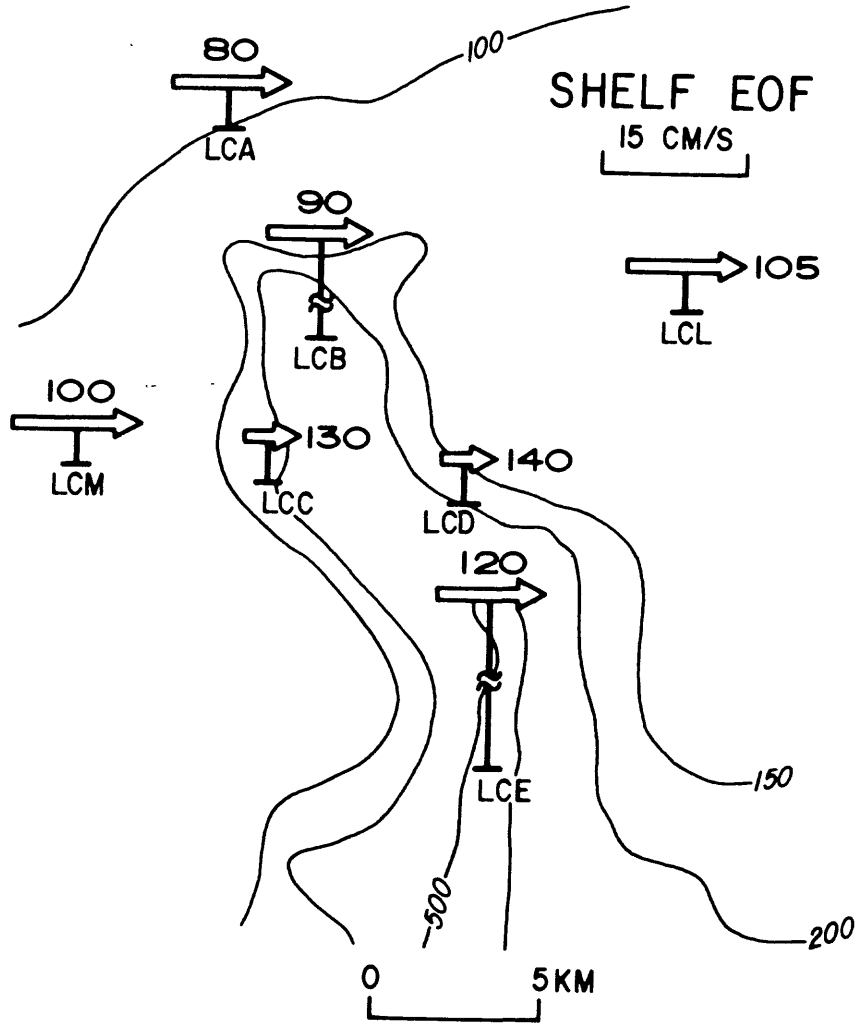

Figure 5-5. The first mode for alongshelf currents over the shelf (shelf EOF). The numbers next to the current arrows are the depth of the current measurement in meters.

phase with and highly coherent with alongshelf currents at LCL(70) across the entire subtidal frequency band (fig. 5-6).

The first mode for cross-shelf currents is less representative of the cross-shelf current field, for it contains only 29 percent of the total cross-shelf variance. The Mode 1 cross-shelf currents fluctuate together, with amplitudes around 3 cm/s (table 5-4). Mode 1 cross-shelf currents do not represent the mid-depth cross-shelf flow field, for the mode is not well correlated with cross-shelf currents at LCL(70) (fig. 5-6).

The currents at a typical shelf site, LCL(110), and the Mode 1 currents have very similar spectra (figs. 5-7a,b). Both current records have much stronger currents alongshelf than cross-shelf. Most of the alongshelf current energy is at periods longer than six days. However, a significant alongshelf spectral peak does exist at the 2.7 day period.

Most of the spectral energy in the alongshelf wind stress is found at periods shorter than four days. The strong spectral peak at 2.7 days found in the alongshelf current record also occurs in the wind stress record (fig. 5-7a).

Subtidal currents over the slope

The currents over the slope can be divided into two distinct subsets, which are designated Slope(200) and Slope(500) (table 5-5). The Slope(200) observation sites are in water depths shallower than 300 m. The majority of Slope(200) sites are located below the shelf-water/slope-water front and are, for at least part of the time, located in the lens of warm, salty water below the shelf-water/slope-water front (fig. 5-3).

The mean along-slope Slope(200) currents are strong, with amplitudes generally between 10 and 20 cm/s, and are directed toward the northeast (table

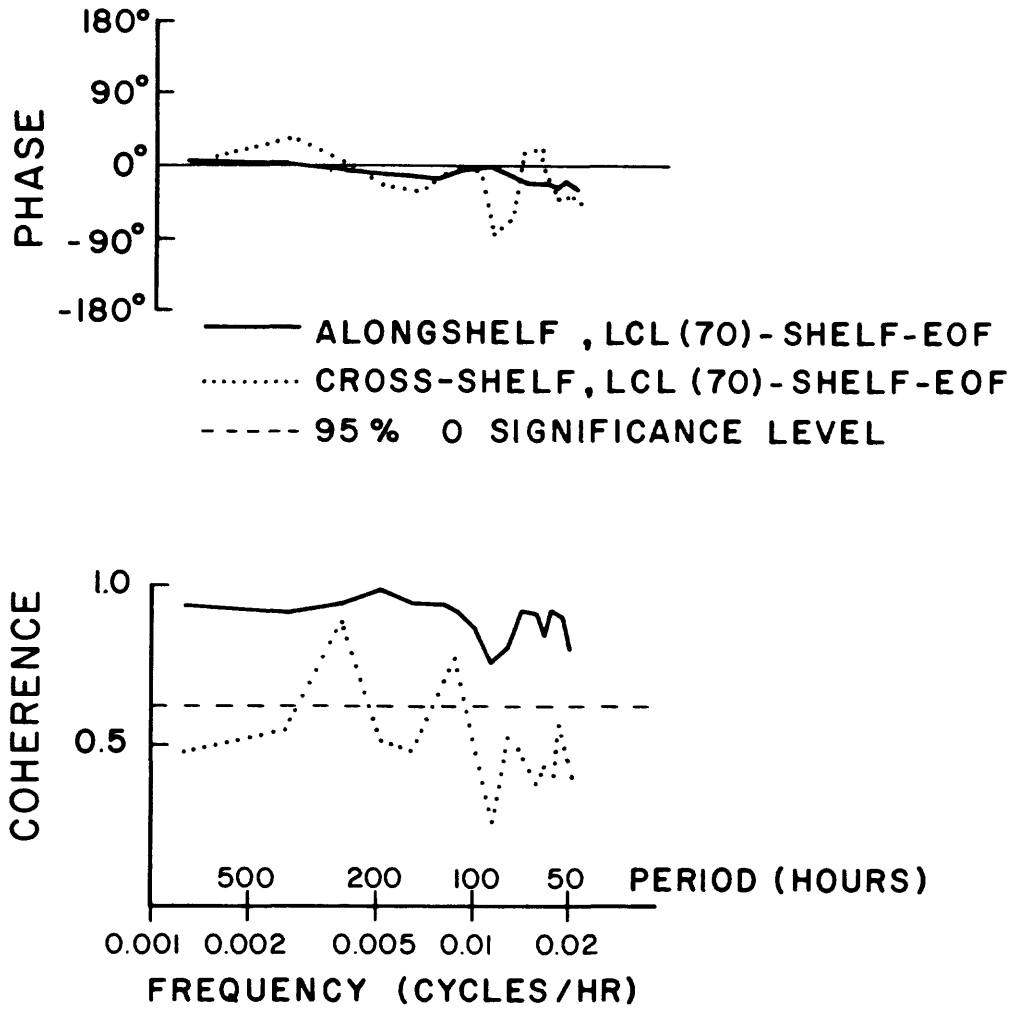

Figure 5-6. Coherence between mid-depth currents at shelf site LCL(70) and the first mode shelf EOF currents. A positive phase indicates that currents at LCL(70) lead shelf EOF currents.

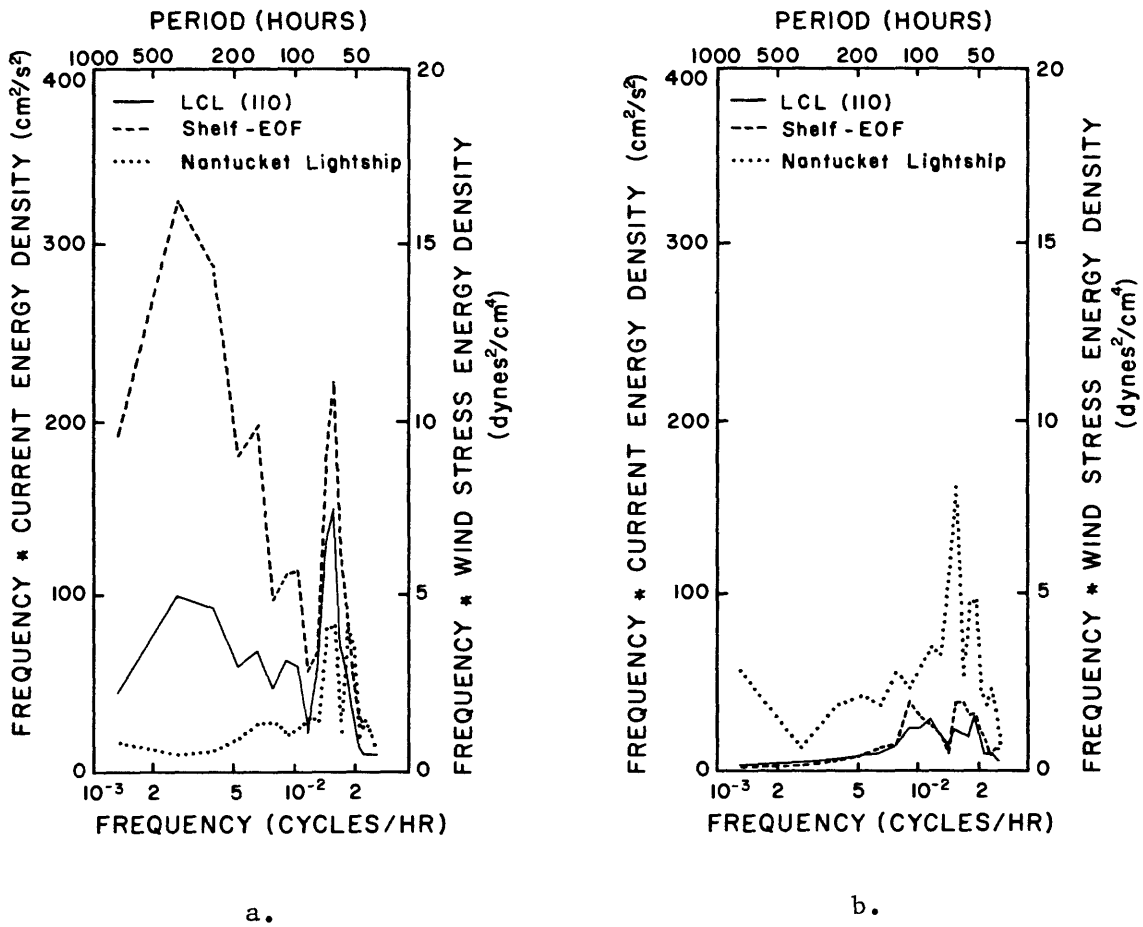

Figure 5-7. Variance-conserving spectra of alongshelf currents and wind stress (a) and cross-shelf currents and wind stress (b).

Table 5-5. The first modes in the along and cross-slope currents over the slope. Slope(200) and Slope(500) represent currents above and below 300m. Stations with less than 6% of their variance contained in the mode are deleted from the mode. The 95% confidence level for zero correlation squared is 0.06. The modal amplitude is defined to be the square root of twice the modal variance at each site. For the second cross-slope Slope(200) mode, the modal amplitudes at each site for the 17 and 46% variance calculation are approximately equal.

Slope(200)_EOF

Station	Alongslope amplitude cm s^{-1}	Percent variance %	Cross-slope amplitude cm s^{-1}	Percent variance %	Cross-slope amplitude cm s^{-1}	Percent variance %
LCE(116)	12.7	67	1.8	8	2.2	12
LCE(216)	--	--	--	--	7.3	76
LCG(195)	15.7	68	--	--	2.0	21
LCN(243)	25.7	84	-1.9	9	4.8	59
LCF(205)	34.2	95	--	--	3.0	28
LCI(10)	20.3	52	12.6	89	--	--
LCI(55)	32.5	90	5.2	44	--	--
LCI(195)	33.9	89	--	--	--	--
LCK(204)	29.8	85	--	--	--	--
LCH(290)	31.5	94	--	--	3.4	30
LCJ(83)	43.3	100	4.4	27	--	--
LCJ(223)	39.3	96	--	--	--	--
Mode 1		89		33		
Mode 2						17(46)[1]

Slope(500)_EOF

Station	Alongslope amplitude cm s^{-1}	Percent variance %	Cross-slope amplitude cm s^{-1}	Percent variance %
LCK(454)	17.0	96	1.4	26
LCH(540)	11.2	86	-3.0	87
LCJ(471)	3.1	14	--	--
Mode 1		82		50

[1] Mode 2 accounts for 46% of the variance for currents in the mode.

5-3). But the mean current orientation is not stable, for the means are not significant at the 95 percent confidence level. During this observation period, the mean along-slope current was flowing opposite to its usual southwesterly direction over the slope (Beardsley and others, 1976, Butman and others, 1982). These strong northwesterly mean currents are associated with the passage of a warm core ring through the array during the first half of the deployment (fig. 5-4). The along-slope currents return to a southwesterly flow after the ring passes.

The mean Slope(200) cross-slope currents are significantly different from zero only at a few locations. The mean flow is 3 cm/s off-shelf at the shallowest instrumented site, LCI(10), and is 2-3 cm/s on-shelf at the sites above the canyon rim (table 5-3). Cross-shelf currents at LCI(195) and LCK(204), slope sites at the same depth but to the side of the set of sites above the canyon, have no significant mean.

The along-slope Slope(200) currents are highly correlated; the first along-slope mode contains 89 percent of the total current variance and usually contains over 80 percent of the current variance at each individual site (table 5-5). In the first along-slope mode, all currents fluctuate in the same direction and current amplitudes are largest at depths between 60 m and 300 m (fig. 5-8). The modal amplitude is smaller near the surface at LCI(10), and onshore, above the canyon at LCE(116). With current amplitudes around 35 cm/s, the first along-slope mode is nearly 3 times stronger than the alongshelf Mode 1 currents over the shelf. The energy in the along-slope currents at a typical Slope(200) site, LCI(195), is concentrated at the longest periods (fig. 5-9). Several spectral peaks occur at shorter periods, but these peaks are not significant at the 95 percent confidence level.

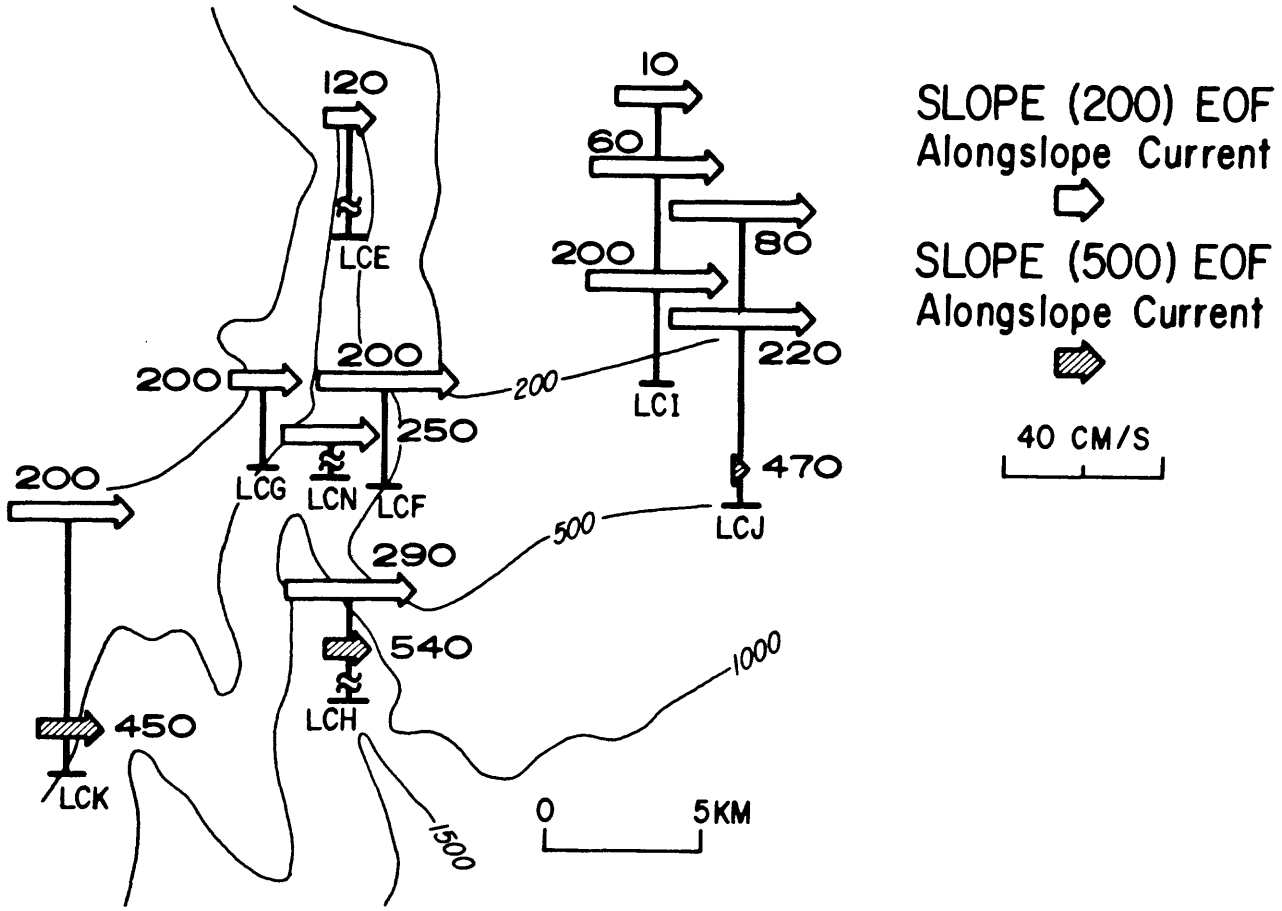

Figure 5-8. The first mode along-slope currents for Slope(200) EOF and Slope(500) EOF. The numbers next to the current arrows are the depth of the current measurement in meters.

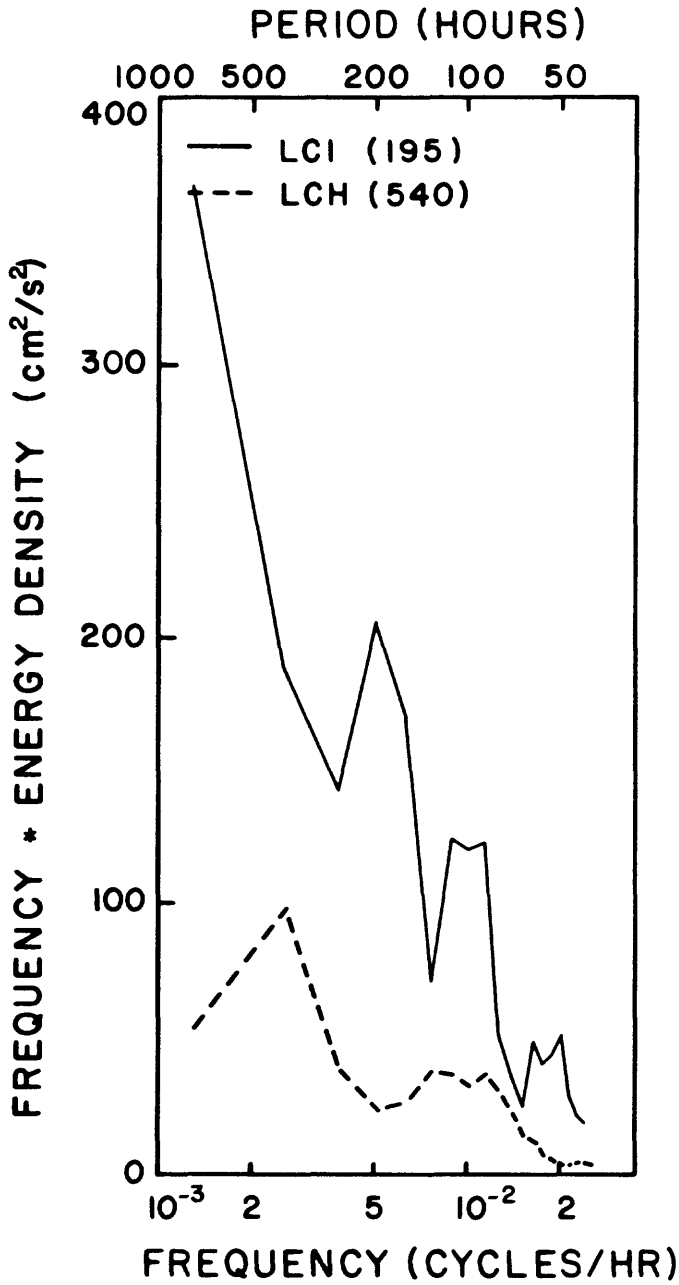

Figure 5-9. Variance-conserving spectra of along-slope currents at typical Slope(200) (LCI(195)) and Slope(500) (LCH(540)) sites.

The Slope(200) cross-slope currents are smaller in amplitude and are more weakly correlated than the along-slope; the first two cross-slope modes together account for 50 percent of the total cross-slope current variance (table 5-5). The first cross-slope mode contains 33 percent of the variance and represents the near-surface flow field at LCI and LCJ. This first mode is dominated by flow at LCI(10), where currents with average amplitudes near 12 cm/s flow on and off the slope. The mode decays quickly with depth; modal amplitudes are reduced to 4 or 5 cm/s between 55 and 83 m.

The second Slope(200) cross-slope mode represents enhanced cross-slope fluctuations at the sites above and just below the canyon rim (fig. 5-10, table 5-5). The locations of the Mode 2 sites are the same locations that have significant mean on-shelf currents. Currents at equivalent depths, but at slope stations located to the sides of the canyon (LCI(195), LCK(204), and LCJ(223)), have neither a correlated cross-shelf flow structure or a significant mean cross-shelf flow. The cross-slope currents represented by Mode 2 are moderately coupled. Though Mode 2 accounts for only 17 percent of the cross-slope variance summed over all Slope(200) sites, it does represent 46 percent of the variance within the subset of sites in the second mode. The Mode 2 cross-slope current structure, which is dominated by strong 7 cm/s fluctuations at LCE(216), is confined to the outer shelf. Cross-shelf currents at the same depth, but further toward the canyon head (at sites LCB(92), LCC(134), and LCD(143)), are not correlated with Mode 2.

Deeper over the slope, at the Slope(500) sites, the along-slope currents are weaker than the Slope(200) currents. The mean along-slope Slope(500) flow is less than 2.5 cm/s, with no significant orientation (table 5-3). The variance in the Slope(500) along-slope currents, represented by site LCH(540), is much smaller than is observed higher in the water column and it is dominated by the longest period fluctuations (fig. 5-9).

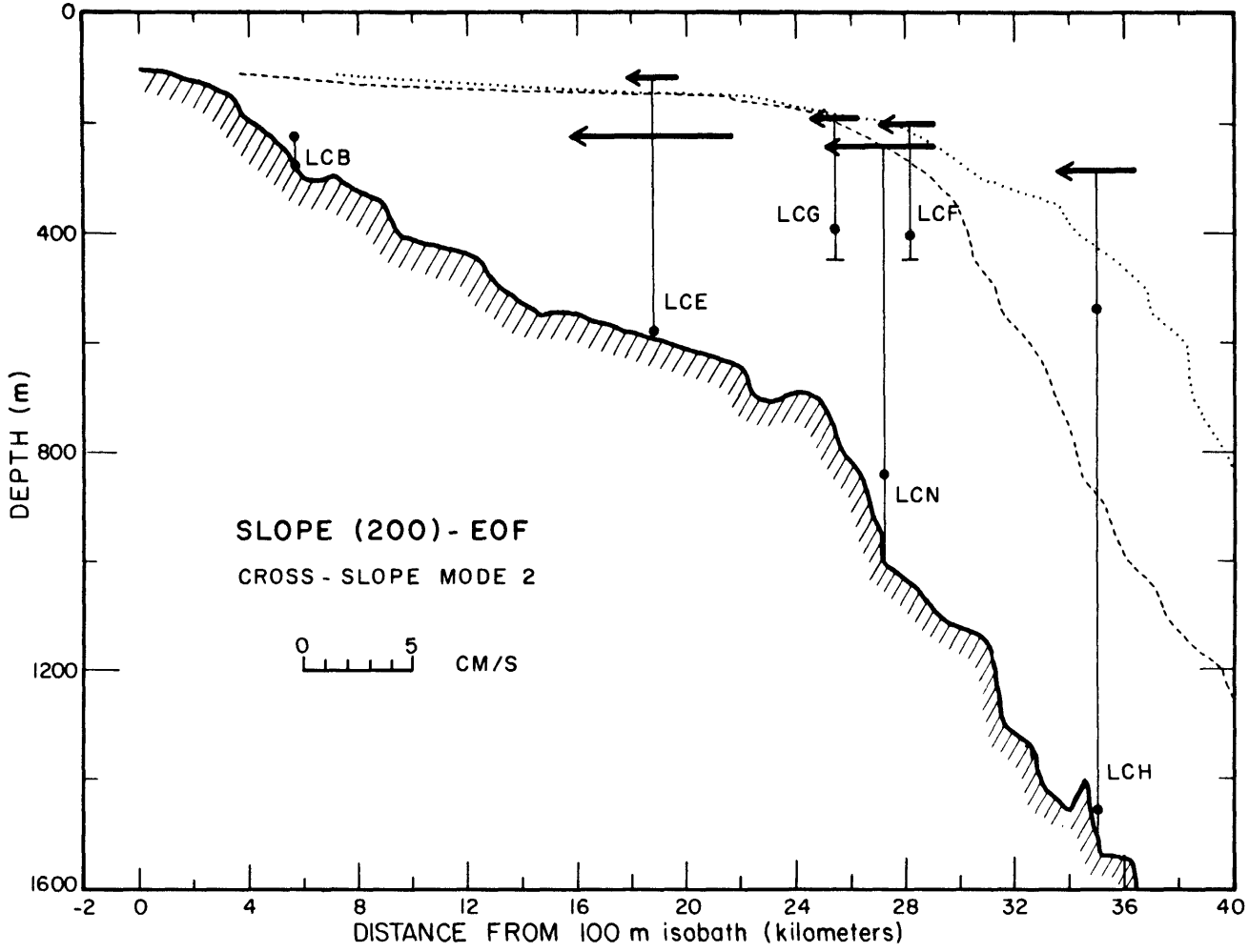

Figure 5-10. Cross-slope current amplitudes at sites in the second Slope(200) EOF mode.

Along-slope currents at the Slope(200) sites are more correlated than along-slope currents at the Slope(500) sites. The along-slope currents at sites LCK(204), LCH(290), and LCJ(223) have coherence amplitudes between 0.81 and 0.91 (table 5-6). The strong correlations among these currents are determined by energetic fluctuations at periods longer than 5.3 days, for the coherences are weak for fluctuations with shorter periods. Along-slope currents on the same moorings, but observed deeper in the water column, have an average coherence amplitude between 0.64 and 0.86. At both depths, the currents at the eastern sites lead currents to the west. At the deeper slope sites, the amplitude of the along-slope coherences is spread more evently over the frequency band. For periods between 2.5 and 5.3 days, coherences range between 0.55 and 0.65. At longer periods (5.3 to 32 days), coherences are 0.69 to 0.90.

Because along-slope currents at Slope(500) sites are more weakly correlated, the first mode in the along-slope flow does not represent the three slope sites uniformly. Mode 1 is dominated by alongshelf currents at LCK(454) and LCH(540), with current amplitudes between 11 and 17 cm/s (fig. 5-7, table 5-5). At LCJ(471), the amplitude of all Mode 1 currents drops to 3 cm/s. The cross-slope Slope(500) currents are even more weakly correlated than the along-slope. The first cross-slope mode essentially represents current fluctuations only at LCH(540) (table 5-5).

Subtidal currents in Lydonia Canyon

Subtidal currents within Lydonia Canyon flow parallel to the canyon axis, but the current orientations are only moderately stationary. The subtidal current ellipses tend to be aligned within 20^{o} of the canyon axis; ellipse stabilities range from 0.50 to 0.85 (table 5-2). The subtidal currents in the

Table 5-6. Coherences among the Slope(200) and Slope(500) alongslope currents. A positive phase indicates that the first member of a station pair leads the second. Coherences below the 95% significance level are not reported.

Station pair		Frequency Band: 5.3 - 32 days coherence	5.3 - 32 days phase	2.5 - 5.3 days coherence	2.5 - 5.3 days phase	2.5 - 32 days coherence	2.5 - 32 days phase
				Vertical seperation			
Slope(200)	Slope(500)	--	--	--	--	--	--
LCK(204)	LCK(454	0.66	9°±20°	0.38	21°±42°	0.64	9°±14°
LCH(290)	LCH(540)	0.56	-1°±26°	0.47	2°±31°	0.55	0°±17°
LCJ(223)	LCJ(471)	0.53	-23°±28°	0.40	-2°±40°	0.48	-21°±21°
				Horizontal sepatations			
LCK(204)	LCH(290)	0.93	-8°±7°	0.39	-34°±41°	0.91	-9°±5°
LCK(204)	LCJ(223)	0.83	-17°±12°	--	--	0.81	-18°±8°
LCH(290)	LCJ(223)	0.90	-8°±8°	0.63	-44°±20°	0.89	-9°±6°
LCK(454)	LCH(540)	0.90	-7°±8°	0.65	-40°±19°	0.86	-10°±7°
LCK(454)	LCJ(471)	0.72	-49°±17°	0.55	-95°±25°	0.64	-54°±14°
LCH(540)	LCJ(471)	0.69	-47°±18°	0.62	-83°±20°	0.64	-53°±14°

canyon are relatively weak; amplitudes range between 3 cm/s and 5 cm/s. There is a slight tendency for the largest currents to be found near the bottom at sites LCB(277), LCE(595), and LCH(1454) (fig. 5-11).

Mean along-canyon currents have significant spatial structure (fig. 5-12, table 5-3). The mean flow is 2 cm/s toward the canyon head at LCB(227) and 50 m deeper on the same mooring, is 3 cm/s toward the canyon mouth. At LCG(395) and LCF(405), sites 5 km apart on the west and east canyon walls, mean flows are weakly down canyon at 2.3 and 0.5 cm/s, respectively. Along-canyon mean flows are either insignificant or down-canyon at the other sites.

The energy in subtidal currents in the canyon occurs primarily at periods shorter than six days (figs. 5-13a,13b). At a period of 2.7 days, an energetic spectral peak, significant at the 95 percent confidence level, occurs in the along-canyon currents at most sites. The cross-canyon currents are weak except at LCH(890), where along-slope flow penetrates below the rim and slightly into the canyon.

Within Lydonia Canyon, subtidal currents have a weakly organized spatial structure. Only six of a possible 28 instrument pairs are correlated with each other (table 5-7a). The along-canyon fluctuations at the mid-canyon sites LCE(595), LCF(405), LCN(841), and LCH(890) are positively correlated. The along-canyon current at LCB(227) is negatively correlated with the mid-canyon sites. Currents at the deeper mid-canyon sites LCN(841) and LCH(890) tend to lead LCB(227) (in the canyon head) and LCF(405) (high on the canyon wall). For this correlated subset of sites, the along-canyon currents in the individual frequency bands are not coherent with each other except at the energetic 2.7-day period. For this period, coherence amplitudes range between 0.63 and 0.86 (table 5-7a). No significant coherence amplitudes at the 2.7-day period occur between the other instrument pairs in the canyon.

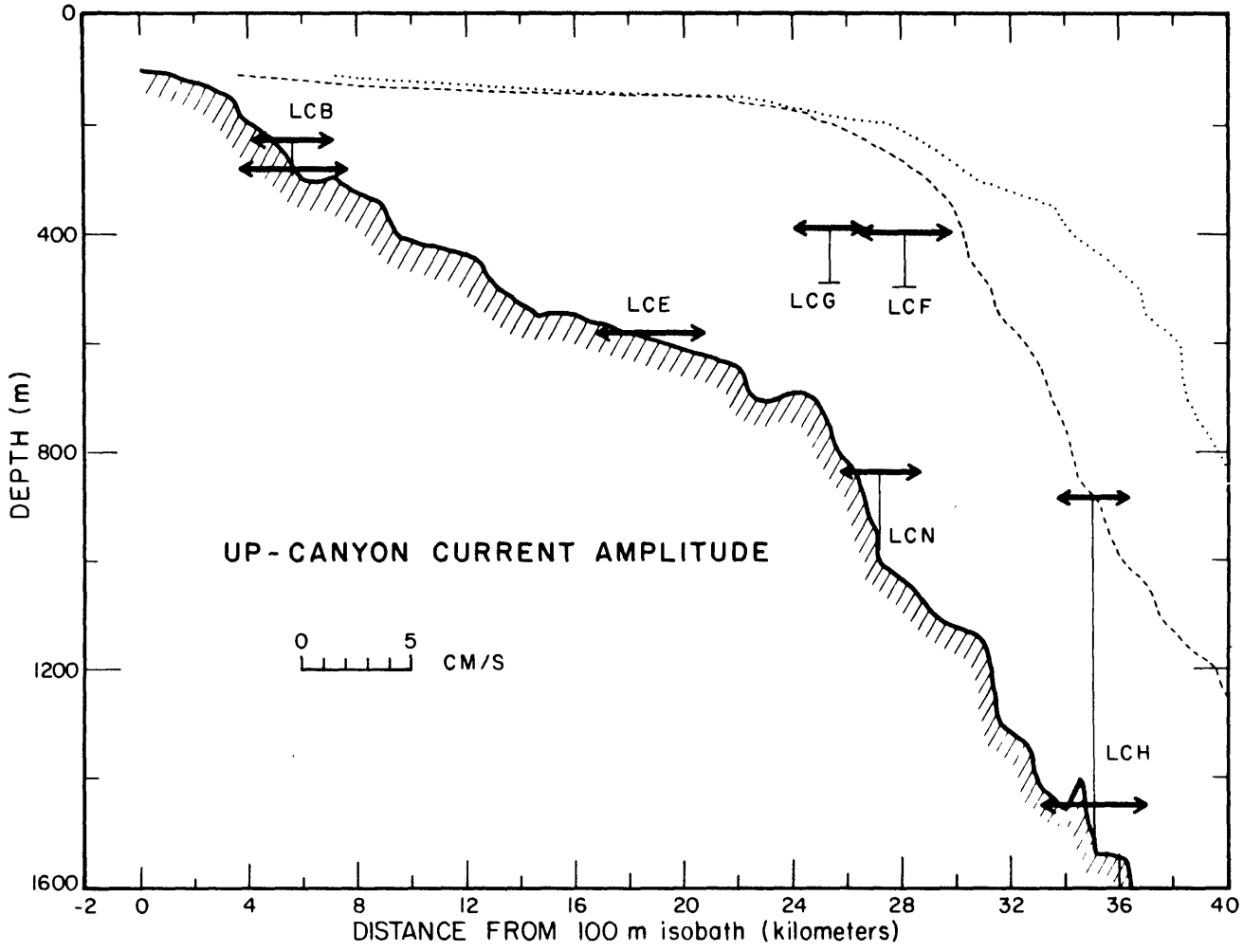

Figure 5-11. Subtidal along-canyon current amplitudes at all canyon sites.

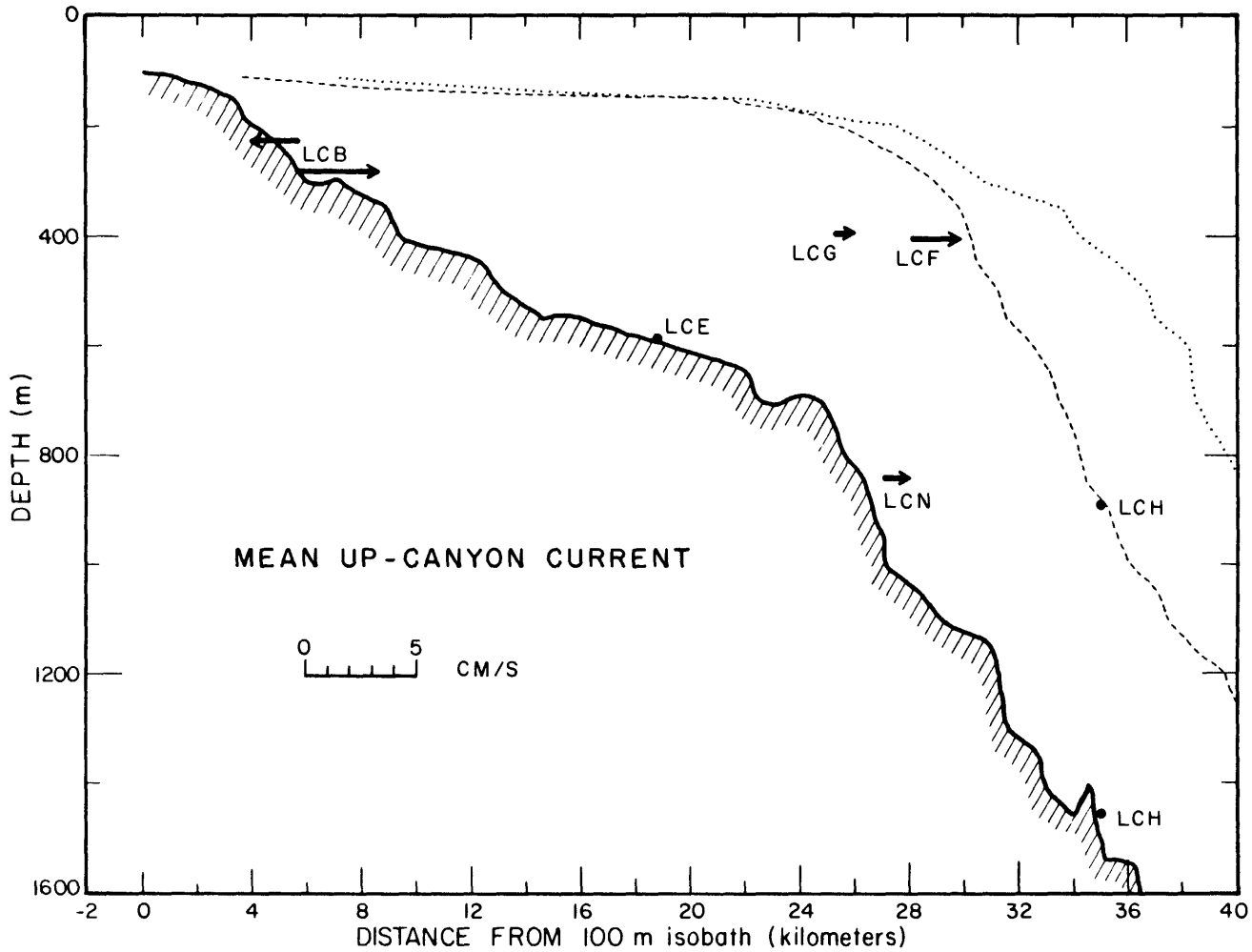

Figure 5-12. Mean along-canyon current amplitudes at canyon sites. Means not significantly different from zero are not shown.

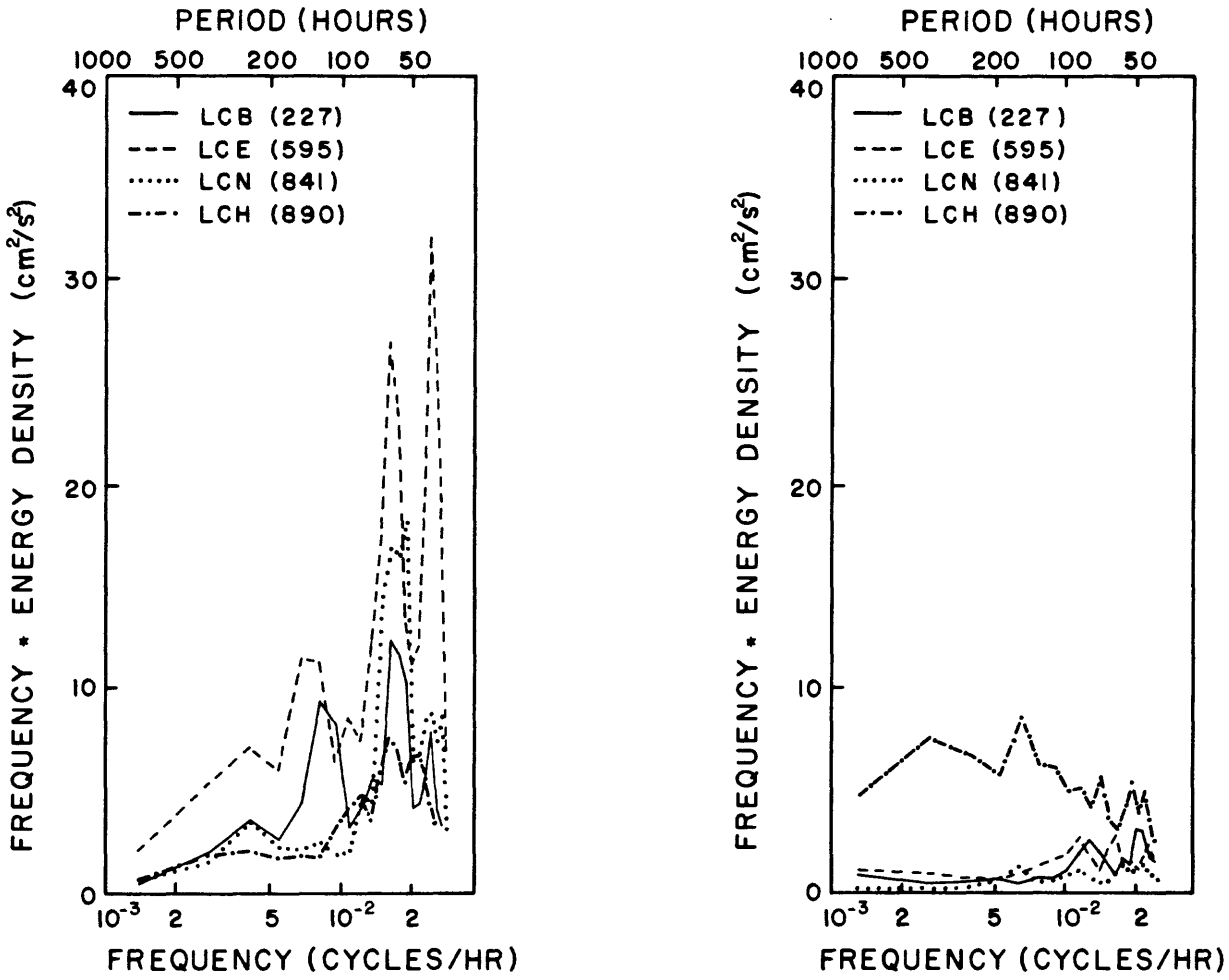

Figure 5-13. Variance-conserving spectra of along-canyon (a) and cross-canyon (b) currents at selected sites.

Table 5-7a. Correlations and coherences among the alongcanyon currents. A positive phase indicates that the first member of a station pair leads the second. Coherences below the 95% confidence level for zero coherence are not reported. The 2.7 day spectral band was the only individual band that had significant coherence levels.

Station pair	correlation		2.7-day coherence	
	amplitude	phase lag* hours	amplitude	phase lag* degrees
LCB(227)-LCE(595)	-0.28	-6	0.84	106°
LCB(227)-LCN(841)	-0.25	-18	--	--
LCB(227)-LCH(890)	--	--	0.75	98°
LCE(595)-LCN(841)	0.41	-6	0.63	-48°
LCE(595)-LCF(405)	0.33	18	--	--
LCE(595)-LCH(890)	0.35	0	0.70	-19°
LCN(841)-LCH(890)	0.58	0	0.86	8°

Table 5-7b. First mode for alongcanyon currents. Stations that have less than 6% of their variance contained in the mode are not reported. The 95% significance level for zero correlation squared is 0.06. The modal amplitude is defined to be the square root of twice the modal variance at each site. For the time-adjusted mode, the x's denote instrument sites not included in the modal analysis.

	Simultaneous set		Time-adjusted subset	
Station	Alongcanyon amplitude cm s^{-1}	Percent variance %	Alongcanyon amplitude cm s^{-1}	Percent variance %
LCB(227)	-1.5	18	-1.7	20
LCB(277)	--	--	x	x
LCE(595)	4.7	88	4.6	86
LCG(395)	--	--	x	x
LCN(841)	1.8	25	2.2	38
LCF(405)	--	--	1.5	16
LCH(890)	1.6	31	1.5	28
LCH(1454)	--	--	x	x
Modal		25		46

Not surprisingly, this correlated set of currents forms the first mode for along-canyon currents, which contains approximately 25 percent of the total variance in the along-canyon currents (table 5-7b). In the first mode, mid-depth canyon currents flow down-canyon [up-canyon] when currents at the canyon head flow up-canyon [down-canyon]. When canyon sites not in the mode are removed from the analysis and covariance amplitudes are adjusted for the phase lag among the instrument sites, the modal structure is more evident. The first mode of the time-adjusted subset accounts for 46 percent of the available variance (fig. 5-14, table 5-7b). Currents in the mid-canyon flow down-canyon with speeds between 1.5 and 4.6 cm/s when currents at LCB(227), in the canyon head, flow up-canyon at 1.7 cm/s. The first-mode current pattern is similar to the mean along-canyon current flow structure (figs. 5-11,12). The mid-depth mean current flow is down-canyon, while mean flow at LCB(227) is up-canyon.

Coupling among the regional current fields

In general, subtidal currents representative of the shelf, the upper and mid-slope, and the canyon are uncorrelated with each other. A moderate to weak coupling only exists between subtidal currents over the shelf and upper slope and between shelf and canyon currents. A northeasterly [southwesterly] along-isobath current over the shelf and slope is loosely associated with on-slope [off-slope] flow for currents above and slightly within the canyon (table 5-8).

The along-slope current in the first shelf mode, Shelf EOF, is coherent with both the Slope(200) EOF along-slope current and the second mode Slope(200) cross-slope current, with average coherence amplitudes across the entire subtidal band (2.5 to 32 days) of 0.51 and 0.42 respectively (table 5-

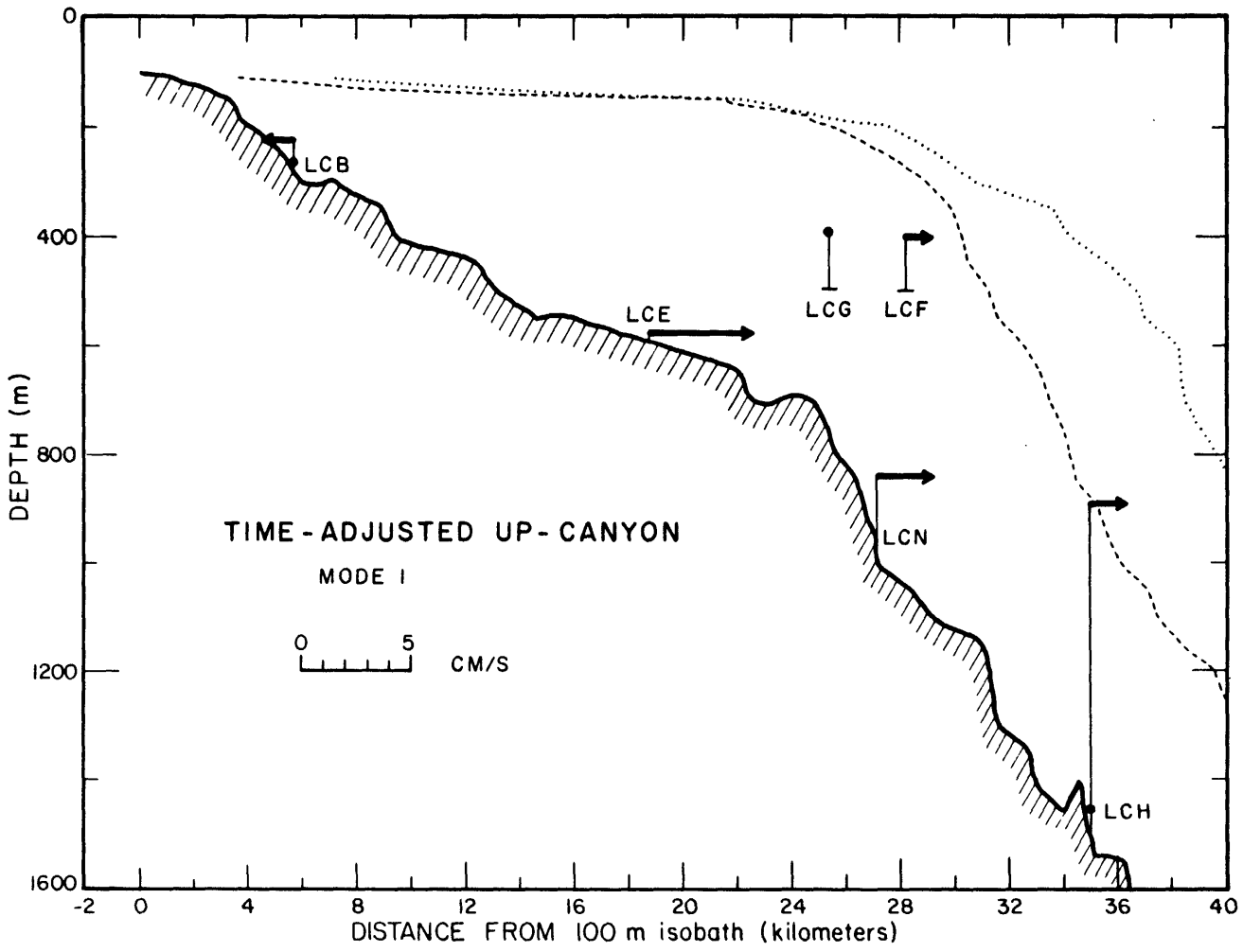

Figure 5-14. The amplitude of Mode 1 along-canyon currents. The time of each current record has been adjusted for maximum joint correlations among the instrument pairs.

Table 5-8. Coherences among the regional currents. A positive phase indicates that the first member of a station pair leads the second. A dash denotes that the measured coherence was below the 95% significance level.

Station pair		Frequency Band					
		5.3 - 32 days		2.5 - 5.3 days		2.5 - 32 days	
		coherence	phase	coherence	phase	coherence	phase
Shelf_EOF alongslope	Slope(200)_EOF alongslope	0.54	29°±33°	--	--	0.51	29°±23°
Shelf_EOF alongslope	Slope(200)_EOF cross slope (mode 2)	--	--	0.61	-30°±25°	0.42	-13°±30°
Slope(200)_EOF alongslope	Slope(200)_EOF cross slope (mode 2)	0.44	-22°±46°	--	--	0.34	-20°±39°
Shelf_EOF alongslope	Canyon_EOF alongcanyon	0.42	64°±49°	0.48	67°±36°	0.42	65°±30°

8). The shelf current flows in the direction of and leads the along-slope current by 29°, or 9 hours. The alongshelf, along-slope coherence decreases with frequency; it is largest in the low-frequency band (5.3 to 32 days) and is only marginally significant at the higher frequencies (2.5 to 5.3 days). This low-frequency band is the same band that contains the majority of the alongshelf and along-slope current variances (figs. 5-7a, 5-8).

As alongshelf current flows northeastward [southwestward], the cross-slope current over the slope, but above the canyon tends to flow onshore [offshore] (table 5-8). The alongshelf, cross-slope coherence increases with frequency; coherence amplitudes are not significant in the low-frequency band and amplitudes average 0.61 at the higher frequencies. In the high-frequency band, the cross-slope current leads the shelf current by 30°. These coherent fluctuations in the cross-slope current field are confined to currents in the shallow waters over the outer canyon, for the cross-slope Mode 2 current is not correlated with the cross-slope current over the shelf (Shelf EOF cross slope), with cross-slope currents at similar depths over the canyon head (at LCB(92), LCC(110), or LCD(143)), or with cross-slope current at depth (at LCH(540)).

Over the upper slope, the Slope(200) EOF along-slope and cross-slope Mode 2 currents are in phase, weakly correlated and have an average coherence of 0.34 across the subtidal band. As along-slope current flows northeastward [southwestward], the cross-slope current tends to flow onshore [offshore]. The slope coherence decreases with frequency; high frequency coherence amplitudes are below the 95 percent significance levels.

The spatially averaged current fields above and below 300 m on the upper slope are independent from each other. Neither the along-slope or cross-slope Mode 1 Slope(200) EOF currents are coherent with the Mode 1 Slope(500) EOF

currents, even though moderate coherence amplitudes around 0.5 to 0.6 exist at the individual moorings (table 5-6). The along-slope Slope(500) current is also independent of the flow over the shelf and in the canyon; there was no significant coherences among currents in these regions.

The along-canyon currents at the individual instrument sites tend to be weakly correlated with the spatially averaged flow along the shelf (table 5-9). The correlations that do exist are weak and appear only at the canyon sites that together form the first canyon mode (Canyon EOF). The Shelf EOF along-slope current is more highly correlated with the Canyon EOF current than with the along-canyon currents at the individual sites (correlation amplitudes of 0.43 vs. maximum individual correlations of 0.34), which supports the assumption that the Canyon EOF mode represents an organized flow pattern that is extracted from the generally disorganized canyon currents (table 5-8). The alongshelf current leads the along-canyon currents by 12 to 36 hours. No gross frequency structure exists in the coupling between currents over the shelf and within the canyon; the coherence amplitudes for the low and high frequencies are nearly equal. Currents in the canyon are not correlated with cross-shelf flow.

The Canyon EOF current is not coupled to currents over the slope. At only one site, LCH(890), are along-canyon currents correlated with the Slope(500) along-slope flow (table 5-9). However this correlation is weak, 0.26, and though statistically significant, it may not represent a stable relationship over time.

Wind-driven currents

Even though the regional subtidal currents are not clearly related to wind stress (fig. 5-4), the winds do drive 10 to 25 percent of the along-

Table 5-9 Correlations of the alongisobath shelf and slope modal currents with the alongcanyon currents. A positive phase indicates the shelf or slope currents leads the canyon currents. Correlations below the 95% level are denoted by a dash.

Canyon station	Shelf_EOF		Slope(500)_EOF	
	Correlation	Phase lag hours	Correlation	Phase lag hours
LCB(227)	-0.29	20	--	--
LCB(277)	--	--	--	--
LCE(595)	0.34	20	--	--
LCG(395)	--	--	--	--
LCN(841)	0.31	18	--	--
LCF(405)	0.30	36	--	--
LCH(890)	0.22	12	0.26	30
LCH(1454)	--	--	--	--
CN_EOF	0.43	18	--	--

isobath currents over the shelf and upper slope (tables 5-10a-c). Over the shelf, the alongshelf currents are primarily driven by the alongshelf component of wind stress. Average wind-driven current amplitudes range from 2 to 4 cm/s per dyne/cm^2 (table 5-10a). The wind-current coupling is strongest at the lower frequencies; currents from 4.7 to 6.2 cm/s per dyne/cm^2 account for 28 to 49 percent of the alongshelf current variance. The wind is less effective at higher frequencies, where the wind-driven currents between 1.5 and 2.1 cm/s per dyne/cm^2 account for less than 20 percent of the current variance. The coupling between alongshelf wind stress and the first mode in alongshelf currents (Shelf EOF) reflects the wind-current coupling at the individual sites. The coupling is strongest at the lower frequencies, accounting for 40 percent of the modal variance. At the higher frequencies, the wind-driven variance drops to 14 percent of the total.

At many sites on the shelf, alongshelf currents are also driven northeasterly [southwesterly] along the shelf by the off-shelf [on-shelf] component of wind stress (table 5-10b). The coupling of alongshelf current to cross-shelf wind is weaker than its coupling to alongshelf wind. On average, the cross-shelf wind stress drives a 1 to 2 cm/s per dyne/cm^2 current, accounting for approximately 10 percent of the alongshelf current variance. Again, the current coupling to cross-shelf wind is strongest at the lowest frequencies. Neither component of wind-stress is significantly correlated with cross-shelf flow.

Over the upper slope, the wind-driven along-slope currents account for 6 to 12 percent of the total current field, even though no significant decrease is observed in the amplitude of the wind-forced current between the shelf and slope (table 5-10a, 10b). The cross-shelf component of wind stress, rather than the alongshelf, is slightly more effective at forcing along-slope

Table 5-10a. Coherences between the alongshelf wind stress and alongisobath currents. A positive phase means the wind stress leads the currents. γ^2 is the coherence squared. Dashes denote coherences below the 95% level for zero coherence.

	Frequency Band								
	5.3 - 32 days			2.5 - 5.3 days			2.5 - 32 days		
Station	Frequency response cm^3/dyne-s	Phase	γ^2	Frequency response cm^3/dyne-s	Phase	γ^2	Frequency response cm^3/dyne-s	Phase	γ^2
Shelf									
LCA(80)	6.2±2.7	19°	0.49	2.1±1.7	55°	0.17	4.4±1.7	25°	0.31
LCM(103)	5.8±2.9	32°	0.35	1.9±1.6	32	0.14	4.1±1.7	27°	0.25
LCB(92)	4.6±2.6	21°	0.30	1.5±1.3	50°	0.12	3.2±1.5	26°	0.22
LCL(70)	5.7±3.7	30°	0.28	--	--	--	4.0±2.1	34°	0.20
LCL(110)	4.7±3.1	38°	0.28	--	--	--	3.6±1.9	41°	0.21
LCC(134)	2.5±1.5	70°	0.29	--	--	--	1.7±0.9	73°	0.19
LCD(143)	--	--	--	--	--	--	1.2±0.8	72°	0.12
Slope									
LCE(116)	3.6±2.8	51°	0.19	--	--	--	2.3±1.6	42°	0.12
LCG(195)	3.7±3.4	41°	0.12	2.0±1.6	13°	0.13	2.7±1.9	26°	0.09
LCN(243)	--	--	--	--	--	--	2.5±2.5	25°	0.06
LCF(205)	7.5±6.7	74°	0.13	--	--	--	4.3±3.4	74°	0.08
LCI(10)	6.6±5.6	71°	0.16	--	--	--	3.9±3.3	62°	0.08
LCI(55)	--	--	--	--	--	--	--	--	--
LCI(195)	--	--	--	--	--	--	--	--	--
LCK(204)	--	--	--	--	--	--	--	--	--
LCH(290)	--	--	--	--	--	--	--	--	--
LCJ(83)	--	--	--	--	--	--	--	--	--
LCJ(223)	--	--	--	--	--	--	--	--	--
Modes									
Shelf_EOF	--	33°	0.40	--	33°	0.14	--	33°	0.29
Slope(200)_EOF	--	--	--	--	--	--	--	--	--

Table 5-10b. Coherences between cross-shelf wind stress and alongisobath currents. A positive phase means the wind stress leads the currents. γ^2 is the coherence squared. Dashes denote coherences below the 95% level for zero coherence.

	Frequency Band								
	5.3 - 32 days			2.5 - 5.3 days			2.5 - 32 days		
Station	Frequency response cm^3/dyne-s	Phase	γ^2	Frequency response cm^3/dyne-s	Phase	γ^2	Frequency response cm^3/dyne-s	Phase	γ^2
Shelf									
LCA(80)	--	--	--	--	--	--	--	--	--
LCM(103)	2.7±2.2	180°	0.17	--	--	--	1.8±1.3	-174°	0.10
LCB(92)	2.8±1.8	171	0.25	--	--	--	1.5±1.1	176°	0.10
LCL(70)	3.4±2.5	166°	0.19	--	--	--	--	--	--
LCL(110)	3.1±2.0	168°	0.28	--	--	--	1.9±1.3	177°	0.13
LCC(134)	1.2±1.1	152°	0.14	--	--	--	0.7±0.6	157°	0.10
LCD(143)	--	--	--	--	--	--	--	--	--
Slope									
LCE(116)	--	--	--	--	--	--	--	--	--
LCG(195)	--	--	--	--	--	--	--	--	--
LCN(243)	--	--	--	--	--	--	--	--	--
LCF(205)	--	--	--	--	--	--	--	--	--
LCI(10)	--	--	--	--	--	--	2.3±2.2	-72°	0.06
LCI(55)	--	--	--	--	--	--	--	--	--
LCI(195)	--	--	--	--	--	--	--	--	--
LCK(204)	3.9±3.7	-98°	0.13	--	--	--	2.2±2.0	-100°	0.07
LCH(290)	--	--	--	--	--	--	--	--	--
LCJ(83)	--	--	--	--	--	--	3.3±3.0	-110°	0.09
LCJ(223)	4.4±4.2	-120°	0.13	--	--	--	2.7±2.3	-122°	0.08
Modes									
Shelf_EOF	--	152°	0.16	--	--	--	--	161°	0.08
Slope(200)_EOF	--	--	--	--	--	--	--	--	--

Table 5-10c. Coherences between 110° wind stress and alongisobath currents. A positive phase means the wind stress leads the currents. γ^2 is the coherence squared. Dashes denote coherences below the 95% level for zero coherence.

	Frequency Band								
	5.3 - 32 days			2.5 - 5.3 days			2.5 - 32 days		
Station	Frequency response cm^3/dyne-s	Phase	γ^2	Frequency response cm^3/dyne-s	Phase	γ^2	Frequency response cm^3/dyne-s	Phase	γ^2
				Shelf					
LCA(80)	3.6±2.2	-7°	0.29	--	--	--	2.3±1.4	6°	0.16
LCM(103)	4.1±2.1	14°	0.35	--	--	--	2.8±1.3	16°	0.23
LCB(92)	4.0±--	3°	0.42	--	--	--	2.3±--	10°	0.20
LCL(70)	4.7±2.5	2°	0.37	--	--	--	2.9±1.5	13°	0.20
LCL(110)	4.0±2.0	5°	0.40	--	--	--	2.7±1.3	16°	0.22
LCC(134)	1.2±1.1	13°	0.14	--	--	--	0.8±0.6	18°	0.09
LCD(143)	--	--	--	--	--	--	--	--	--
				Slope					
LCE(116)	2.6±2.2	15°	0.15	--	--	--	1.7±1.2	12°	0.11
LCG(195)	--	--	--	1.2±1.1	-13°	0.11	1.7±1.3	17°	0.07
LCN(243)	3.4±3.2	24°	0.14	--	--	--	2.3±1.8	25°	0.08
LCF(205)	5.1±4.3	54°	0.15	--	--	--	2.8±2.2	53°	0.08
LCI(10)	5.1±3.9	84°	0.19	--	--	--	3.0±2.2	90°	0.10
LCI(55)	--	--	--	--	--	--	--	--	--
LCI(195)	--	--	--	--	--	--	2.5±2.4	8°	0.06
LCK(204)	4.7±3.9	73°	0.17	--	--	--	2.7±2.1	71°	0.09
LCH(290)	--	--	--	--	--	--	--	--	--
LCJ(83)	--	--	--	--	--	--	3.2±3.0	73°	0.08
LCJ(223)	4.9±4.5	66°	0.14	--	--	--	2.9±2.4	62°	0.08
				Modes					
Shelf_EOF	--	0°	0.31	--	--	--	--	8°	0.19
Slope(200)_EOF	--	--	--	--	--	--	--	--	--

currents. At slope sites LCI, LCK, LCH, and LCJ, the most effective wind-stress orientation for forcing along-slope currents is aligned 60° to 70° clockwise from the along-slope flow (table 5-11).

The correlation between wind and current is a slowly varying function of wind-stress orientation. Wind stress decomposed along 110° accounts for the largest percentage of along-slope current variance, approximately 20 percent of the slope currents (similar to the alongshelf wind forcing), and 10 percent of the along-slope variance (table 5-10c). Wind-stress oriented perpendicular to 110° is not correlated with either alongshelf or along-slope currents.

An alongshelf wind stress also drives a cross-isobath flow over the shelf and slope (table 5-12). In the shallow surface waters, represented by Mode 1 Slope(200) EOF cross-slope current, 11 percent of the current variance is forced to the right of the wind by the alongshelf wind stress, an orientation consistent with Ekman dynamics. At LCI(10), a site 10 m below the surface, a 2.5 cm/s current is driven off shore by a northeasterly wind stress. The enhanced cross-isobath flow observed on the slope, over the canyon (Mode 2 Slope(200) cross-slope flow), is also weakly correlated with wind-stress. On average, 18 percent of the current in Mode 2 is forced onshore, opposite to the surface current, by a northeasterly wind stress. Wind-driven currents range between 1 and 2 cm/s per dyne/cm^2 at sites where Mode 2 is strong.

Wind stress was not a significant forcing function for currents over the mid slope or currents in the canyon.

DISCUSSION

The currents over the shelf observed during this study are similar to currents observed elsewhere on the flanks of Georges Bank (Flagg and others, 1982; Butman and Beardsley, 1985; Noble and others, 1985). Typical subtidal

Table 5-11. Angle between wind stress and alongisobath current that represents the maximum coherent-current forcing. A negative angle indicates that the wind is rotated clockwise from the alongisobath current. For consistency among the reported angles, the alongisobath current direction is defined to be 75° in this table.

Shelf Station	Frequency band 5.3 - 32 days Orientation	Frequency band 2.5 - 32 days Orientation	Slope Station	Frequency band 5.3 -32 days Orientation	Frequency band 2.5 - 5.3 days Orientation
LCA(80)**	-35°	-31°	LCE(116)*	-56°	-53°
LCM(103)**	-56°	-52°	LCG(195)*	-48°	-46°
LCB(92)**	-65°	-57°	LCN(243)	-58°	-52°
LCL(70)**	-67°	-61°	LCF(205)*	-44°	-39°
LCL(110)**	-72°	-66°	LCI(10)*	-51°	-54°
LCC(134)**	28°	23°	LCI(55)	-70°	-68°
LCD(143)*	-63°	-68°	LCI(195)	-69°	-67°
Shelf_EOF**	-46°	-42°	LCK(204)*	-69°	-65°
			LCH(290)	-55°	-59°
			LCJ(83)	-64°	-70°
			LCJ(223)*	-68°	-70°

* A significant coherence was measured between the alongshelf or alongslope current and one component of wind stress.

** A significant coherence was measured between the alongshelf or alongslope current and both components of wind stress.

Table 5-12. The coherence between alongisobath wind stress and cross-slope currents. A positive phase indicates that the wind stress leads the current. γ^2 is the coherence squared. Dashes denote coherences below the 95% level for zero coherence.

	Frequency Band								
	5.3 - 32 days			2.5 - 5.3 days			2.5 - 32 days		
	Frequency response cm^3/dyne-s	Phase	γ^2	Frequency response cm^3/dyne-s	Phase	γ^2	Frequency response cm^3/dyne-s	Phase	γ^2
Slope(200)_EOF									
Cross slope Mode 1	--	--	--	--	131°	0.28	--	117°	0.11
LCI(10)	--	--	--	3.7±2.0	133°	0.31	2.5±1.7	137°	0.13
Slope(200)_EOF									
Cross slope Mode 2	--	30°	0.21	--	--	--	--	25°	0.18
LCE(216)	--	--	--	1.7±1.5	17°	0.14	1.6±1.1	22°	0.13
LCN(243)	1.2±1.1	20°	0.16	--	--	--	0.9±0.8	14°	0.08

currents flow northeasterly or southwesterly over the shelf, approximately parallel to isobaths, have average amplitudes from 5 to 20 cm/s, and are partially driven by wind stress. Analytic models of shelf circulation (Csanady, 1978; Allen, 1980; Brink, 1983) and previous observations (Butman and others, 1979; Ou and others, 1981; Noble and Butman, 1983) have shown that the alongshelf currents are correlated over large distances alongshelf, separations often greater than 600 km. Since the moorings in the canyon experiment were separated by less than 30 km, it is not surprising that the first alongshelf mode for shelf currents contains 70 percent of the alongshelf current variance.

The amplitude of the wind-driven current over the shelf and upper slope is comparable to wind-driven current amplitudes observed in the winter and early spring at other sites on Georges Bank and over the continental shelf just west of the bank (Flagg and others, 1982; Beardsley and others, 1985; Noble and others, 1985). Several numerical and analytic models exist that predict the characteristics of the wind-driven current over the New England shelf and within the Gulf of Maine (Csanady, 1978; Isaji and others, 1982; Wright and others, 1986). Though the models differ in the predicted amplitude of the wind-driven current, all models agree that the wind-driven flow is forced primarily by the alongshelf component of wind stress, where the alongshelf orientation is determined from spatially averaged topography over a region tens of kilometers long rather than from the strictly local topography. Previous observations from several years of current record collected at a site 40 km northeast of Lydonia Canyon, in a shallower water depth of 85 meters, confirm model predictions. The highest correlations were found between alongshelf current and wind stress at Nantucket Lightship oriented along 60°, which is parallel to the spatially averaged topography (Noble and others, 1985).

The majority of the currents flowing along the shelf and slope around Lydonia Canyon have their strongest correlations with wind stress oriented 50^{o} to 70^{o} clockwise from the 75^{o} average topographic orientation. There is a slight tendency for the winds to be more parallel to the currents in the shallower water, for the smallest angle between the wind and current is found at LCA(80). In the deeper water, either the orientation of the Nantucket Lighship wind stress is not representative of the wind-forcing for the Georges Bank region for this particular time period or the onshelf component of wind stress drives significant alongshelf flow, as is predicted by one model of wind-forced flow over a submarine bank (Brink, 1983).

For along-slope currents at the 200- and 500- m depths, the currents on the individual moorings are vertically coherent. The currents observed at the western sites are correlated with and lead currents at the eastern sites. The correlated alongshelf current separated by equivalent alongshelf distances showed no significant phase shifts, indicating that the process responsible for the phase shift over the slope is not a dominate feature of the shelf circulation.

Even though the spatial resolution of this data set is too limited to allow one to determine the mechanisms responsible for the westerly phase propagation over the slope, one can determine that several mechanisms potentially responsible for the observed westward phase shift are unlikely candidates. The observed westward phase shift is not associated with the slow, westward advection of the Gulf Stream eddy past the site. The phase shift is present whether the eddy is present or not. Theoretical models predict that even though westwardly propagating, subtidal, coastally trapped shelf waves (Mysak, 1980) and subtidal waves trapped over a submarine bank (Brink, 1983) have their largest amplitudes shoreward of the shelf break,

a weak, along-slope current also exists over the slope. Along the New England coast, coastally trapped waves are predicted to have phase speeds on the order of 33 km/hr and bank wave phase speeds are on the order of 13 km/hr. Not only are the predicted phase speeds significantly larger than the observed phase speed of 1-2 km/hr, but the amplitude of the wave over the shelf would have to be larger than the observed shelf current in order to account for the strength of the signal at the slope sites.

Bottom-intensified topographic Rossby waves exist at subtidal frequencies: they are predicted to have their largest along-slope current amplitudes near the seabed at the shelf break and at the slope-rise junction, and may propagate westward with phase speeds of a few kilometers per hour (Ou, 1980; Ou and Beardsley, 1980). Previous studies have provided evidence that topographic Rossby waves do exist on the New England slope (Thompson, 1977; Ou and Beardsley, 1980). However, in this data set, the slope currents are not dominated by bottom-intensified topographic Rossby waves, for the currents are not bottom-trapped. Current amplitudes at the 200-m sites are more than double the current amplitudes at the 500-m sites. A simple statistical model, which assumes favorable characteristics for a common signal in the current records (i.e., that only one signal exists at each mooring site, that the signal amplitude is depth independent and that the record at 500 m is noise-free), predicts that coherences amplitudes between the 200- and 500- m nstruments would be half the observed vertical coherence amplitudes reported in table 5-6. In order for the model to predict coherence amplitudes as large as are observed, the current amplitude must decrease with depth.

The currents in the canyon have no obvious direct, linear driving mechanisms. Wind stress is not coherent with canyon currents at any individual site nor is wind stress coherent with the Mode 1 along-canyon

currents. The Gulf Stream eddy, which advected past the canyon mouth for the first half of the current record, did not affect currents in the canyon at periods shorter than 32 days. Canyon current statistics for the periods when the eddy was or was not present are not significantly different from each other. Neither along-slope or alongshelf currents penetrate more than 50 m below the canyon rim.

However, along-canyon currents may be indirectly coupled to the flow along the shelf through the shelf pressure field. In a study of currents over the shelf and slope off Vancouver, Canada, Freeland and Denman (1982) attribute the formation of an anomalous body of dense, low-oxygen water on the shelf to upwelling through a narrow, nearby canyon. Though no observations of canyon currents were presented, a theoretical model of upwelling through the canyon driven by the shelf pressure gradient in geostrophic equilibrium with shelf current roughly reproduced the hydrographic observations.

In this data set, direct current measurements also suggest that along-canyon currents are driven by the shelf pressure-gradient field. Over the shelf, the pressure gradient associated with a southwestward alongshelf current decreases toward the slope. Above the canyon, this pressure gradient is balanced by the Coriolis force on the alongshelf flow. Within the canyon, the canyon walls inhibit alongshelf (or cross-canyon) flow, hence the pressure gradient will tend to drive flow out of the canyon. Both the mean current orientation, generally down-canyon, and the nearly zero phase shift between the along-canyon and alongshelf currents are in the proper sense to balance the pressure gradients associated with the southwesterly mean and the fluctuating alongshelf current.

However, the simplest barotropic, frictionless, linear model of flow along a wedge, forced by an along-wedge pressure imposed at the top of the

wedge predicts that the along-wedge (or along-canyon) current would have an amplitude equal to or greater than an alongshelf current in geostrophic equilibrium with the along-wedge pressure gradient. Measured along-canyon current amplitudes are on the order of a few cm/s, significantly smaller than the 10 cm/s alongshelf current. It is probable that the largest portion of the pressure gradient over the shelf is balanced in the canyon, far from the canyon head, by baroclinic adjustment of the canyon density field.

SUMMARY

The subtidal currents over the shelf and slope have well-defined spatial structures that, for the most part, are unaffected by the presence of Lydonia Canyon. The sizes of the Rossby and Burger numbers (0.3 and 30, respectively) both indicate that the along-isobath flow will tend to ignore variations in topography that have typical canyon along-isobath length scales (on the order of 20 km). Alongshelf currents at stations on the shelf have approximately the same amplitude and are highly coherent with currents at similar depths located above the canyon rim. High correlations and uniform amplitudes are also observed for the slope currents above 300-m water depth located on either side of the canyon.

Although the canyon's presence does not alter the along-isobath flow over the shelf and slope, enhanced cross-isobath current fluctuations are observed to occur at sites above and slightly below the canyon rim. The Mode 2 Slope(200) EOF cross-slope currents flow on and off the shelf in an organized pattern that is weakly correlated with the alongshelf flow field and with wind stress. Cross-slope currents at sites at similar depths over the slope show no enhanced cross-isobath fluctuations or correlation with the alongshelf current or wind stress.

Approximately 20 percent of the alongshelf current and 8 to 10 percent of the along-slope current at depths above 300 m is driven by wind stress oriented along 110°. Wind stress does not drive significant flow over the deeper slope or flow within the canyon. The wind-driven currents have fairly uniform amplitudes over the shelf and upper slope, generally between 2 and 4 cm/s per dyne/cm^2. Even though the wind-driven current amplitudes are consistent with other observations of wind-driven currents in this region, the angle between the wind and along-isobath current, 40° clockwise from the alongshelf orientation, is much larger than is either predicted or commonly observed. With this data set, it cannot be determined whether the observed angle between the wind and the currents is a real feature or an artifact caused by using winds observed at Nantucket Lightship. Subsequent analysis of the currents, relating them to winds observed within the Gulf of Maine and off Nova Scotia, Canada, will determine whether large angles between wind stress and along-isobath currents are a consistent feature of the flow field around Lydonia Canyon.

The wind-driven currents account for only a small percentage of the energy in the alongshelf and along-slope current field. For shelf and slope depths greater than 150 m, the characteristics of the along-isobath currents are mainly determined by processes which drive the very energetic slope flow. The along-slope currents at water depths less than 300 m are well-correlated across vertical separations of a few hundred meters and horizontal separations of 30 km. The along-slope currents at the 500-m level are reduced in amplitude by 50 percent or more from the alongshelf currents above 300 m, but are still correlated along the slope.

In contrast to the strong, organized flow over the shelf and slope, the subtidal canyon currents are weak and disorganized. Along-canyon currents in

the canyon head that are separated vertically by 50 m are not correlated, nor are currents along the canyon wall separated horizontally by 4 km. Only along-canyon currents at the mid-canyon sites have a weakly organized flow structure. Subtidal currents in the outer canyon flow down-canyon as currents in the canyon head, at LCB, flow upcanyon.

The current observations presented here show that currents over the slope and shelf around a submarine canyon and, to a lesser extent, currents within a submarine canyon, have well-defined flow patterns. Unfortunately, models which can predict the complicated subtidal current regime in and around the canyons still need to be developed. This data set offers several clues as to what driving forces may need to be included in subsequent models. It is consistent with the observations to assume that along-canyon currents are driven by cross-shelf pressure gradients that are in equilibrium with the alongshelf flow. Subsequent analysis of data from pressure sensors deployed on the shelf and within Lydonia Canyon will help determine the significance of pressure gradient forcing and how deeply into the canyon the cross-shelf pressure gradients reach. Subtidal canyon currents may also result from rectification of the relatively strong tidal and internal wave fields in the canyon. Preliminary analysis of the current records indicates that pulses in the subtidal currents may be associated with pulses in the internal wave field (see chapter 2).

ACKNOWLEDGMENTS

We are grateful for the assistance of the Woods Hole Oceanographic Institution Buoy Group in the design of the current moorings, and of the officers and crew of the R/V Oceanus in the deployment and recovery of the current-meter moorings. M. Shoukimas and S. Conley assisted in the processing of the current records.

REFERENCES

Allen, J. S., 1980, Models of wind-driven currents on the continental shelf: Annual Review of Fluid Mechanics, v. 12, p. 389-433.

Beardsley, R. C., Boicourt, W. C. and Hansen, D. V., 1976, Physical oceanography of the Middle Atlantic Bight: American Society of Limnology and Oceanography, Special Symposium, v. 2, p. 20-34.

Beardsley, R. C., Chapman, D. C., Brink, K. H., Ramp S. R., and Schlitz, R., 1985, The Nantucket shoals flux experiment (NSFE79). Part 1: A basic description of the current and temperature variability: Journal of Physical Oceanography, v. 15, p. 713-748.

Brink, K. H., 1983, Low-frequency free wave and wind-driven motions over a submarine bank: Journal of Physical Oceanography, v. 13, p. 103-116.

Butman, B., Noble, M. and Folger, D. W., 1979, Long-term observation of bottom current and bottom sediment movement on the Mid-Atlantic Continental Shelf: Journal of Geophysical Research, v. 84, p. 1187-1205.

Butman, B. and Beardsley, R. C., 1986, Long-term observations on the southern flank of Georges Bank: Seasonal cycle of currents, temperature, stratification, and wind stress: Journal of Physical Oceanography (submitted).

Csanady, G. T., 1978, The arrested topographic wave: Journal Physical Oceanography, v. 8, p. 47-62.

Flagg, C. N., Magnell, B. A., Frye, D., Cura, J. J., McDowell, S.E. and Scarlet, R. E., 1982, Interpretation of the physical oceanography of Georges Bank: EG&G Environmental Consultants, Final Report to the Bureau of Land Management, EG&G Report 82-B4569, 901 p.

Freeland, H. J. and Denman, K. L., 1982, A topographically controlled upwelling center off southern Vancouver Island: Journal Marine Research, v.40, p. 1069-1093.

Gonella, J., 1972, A rotary-component method for analyzing meteorlogical and oceanographic vector time series: Deep-Sea Research, v. 19, p. 833-846.

Hotchkiss, F. S. and Wunsch, C., 1982, Internal waves in Hudson canyon with possible geological implications: Deep-Sea Research, v. 29, p. 415-442.

Isaji, T., Spaulding, M. L., and Swanson, J. C., 1982, A three-dimensional hydrodynamic model of wind and tidally-induced flows on Georges Bank. Appendix A in Flagg, C. N., Magnell, B. A., Frye, D., Cura, J. J., McDowell, S. E., and Scarlet, R. I., Interpretation of the physical oceanography of Georges Bank: EG&G Environmental Consultants, Final Report to the Bureau of Land Management, EG&G Report 82-B4569, p. A1-A67.

Mysak, L. A., 1980, Topographically trapped waves: Annual Review of Fluid Mechanics, v. 12, p. 45-76.

Noble, M. A., Butman, B., and Williams, E., 1983, On the longshelf structure and dynamics of subtidal currents on the eastern United States Continental Shelf: Journal of Physical Oceanography, v. 13, p. 2125-2147.

Noble, M. A., Butman, B., and Wimbush, M., 1985, Wind-current coupling on the southern flank of Georges Bank: variation with season and frequency: Journal of Physical Oceanography, v. 15, p. 604-620.

Ou, H. W. 1980, On the propagation of free topographic Rossby waves near continental margins, Part 1: Analytical model for a wedge: Journal of Physical Oceanography, v. 10, p. 1051-1060.

Ou, H. W. and Beardsley, R. C., 1980, On the propagation of free topographic Rossby waves near continental margins. Part 2: Numerical model: Journal of Physical Oceanography, v. 10, p. 1323-1339.

Ou, H. W., Beardsley, R. C., Mayer, D., Boicourt, W. C., and Butman, B., 1981, An analysis of subtidal current fluctuations in the Middle Atlantic Bight: Journal of Physical Oceanography, v. 11, p. 1383-1392.

Shepard, F. P., Marshall, N. F., McLoughlin, P. A., and Sullivan, G. G., 1979, Currents in submarine canyons and other sea valleys: Tulsa, OK, American Association of Petroleum Geologists, Studies in Geology, No. 8, 173 pp.

Thompson, R. O. R. Y., 1977, Observations of Rossby waves near site D: Progress in Oceanography, V. 7, Pergamon Press, p. 1-28.

Wright, D. G., Greenberg, D. A., Loder, J. W., and Smith, P. C., 1986, The steady-state barotropic response of the Gulf of Maine and adjacent regions to surface wind stress: Journal of Physical Oceanography, v. 16, p. 947-960.

Wu, J., 1980, Wind-stress coefficients over the sea surface near neutral conditions: Journal of Physical Oceanography, v. 10, p. 727-740.

CHAPTER 6

THE FLUX AND COMPOSITION OF RESUSPENDED SEDIMENT IN SUBMARINE CANYONS OFF THE NORTHEASTERN UNITED STATES: IMPLICATIONS FOR POLLUTANT SCAVENGING

by

Michael H. Bothner, Carol M. Parmenter, Richard R. Rendigs, and Meyer Rubin

Chapter 6

Table of Contents

	Page
Abstract	6-1
Introduction	6-2
Equipment and methods	6-5
Sediment traps	6-5
Poison dispensers	6-5
Deployment and recovery	6-8
Laboratory methods	6-8
Results and Discussion	6-10
Comparison of different size traps	6-10
Sediment flux in different physiographic areas	6-11
Depth profile of resuspended sediment flux	6-19
Time variability in flux	6-19
Trace-metal concentrations in sediment-trap samples	6-30
Sediment sources	6-42
Potential of pollutant adsorption by resuspended sediments	6-48
Conclusions	6-55
References	6-58

ABSTRACT

Sediment traps were used to estimate the flux of resuspended sediments in Lydonia and Oceanographer Canyons and on the adjacent Atlantic Continental Shelf and Slope. The axes of both canyons are sites of much higher resuspension activity than areas of comparable depth outside of the canyons. The highest resuspended flux (157 $g/m^2/day$) was measured 5 meters (m) off the bottom in Lydonia Canyon axis at 300 m water depth. For traps located at the head of Lydonia Canyon in water depths of 100-125 m, the variability in the flux and texture of the trapped sediment correlates with the timing and strength of major storms. Traps deeper in the canyon axis show textural differences over time that are similar to those at the head of the canyon, but the textural record is more complicated. The greater variability indicates that additional processes, such as internal waves, can cause resuspension in the canyons.

The hypothesis that shelf-derived material is being transported into Lydonia Canyon is supported by two new sets of data. First, the concentration of Ba, a major element in drilling mud, increased in the resuspended sediment collected in the axis of Lydonia during the period in which eight exploratory wells were drilled on Georges Bank. The magnitude of Ba increase was analytically detectable but environmentally insignificant. The concentrations of other trace metals in resuspended sediment did not increase during the drilling period. Second, ^{14}C dating of piston cores from the head of Lydonia Canyon indicates sediment is accumulating at an average rate of 60 cm/1,000 yr.

The more intense resuspension and higher accumulation rates in the canyons as compared to the open continental slope suggests that the canyon sediments have a higher potential for the adsorption of sediment-reactive

pollutants. This hypothesis is supported by higher specific activities and higher inventories of lead-210 and plutonium-239,240 that are found in sediments from the canyon axis. More frequent resuspension increases the opportunity for particulates to adsorb dissolved materials and strip them from the water column. This process may make the canyons a more effective sink for pollutants than the open slope.

INTRODUCTION

Submarine canyons are major topographic features of the upper continental slope along the southern flank of Georges Bank from Northeast Channel to Great South Channel (Vol. 1, fig. 1). Recent analysis of long-range sidescan-sonar data in this region indicates that approximately 80 percent of the upper continental slope is dissected by a combination of gullies and canyons (Scanlon, 1984). This topography is likely to have played a major role in the transport of sediment to the deep sea during times of glacially lowered sea level. There is growing evidence that the dynamics of modern sedimentary processes may vary significantly in different canyon systems (Gardner, 1983; Baker and Hickey, 1986).

Increased interest in exploration and development of potential offshore oil and gas deposits on the continental shelf and slope necessitates an understanding of the physical processes which control the transport and distribution of any pollutant associated with resource development. Because pollutants are often adsorbed by and transported with suspended particulate matter (Benninger and others, 1975; Huggett and others, 1980) a major objective of this study was to investigate the relative intensity of processes which increase the concentration of particulate matter in the water column within Lydonia and Oceanographer Canyons and on the adjacent shelf and

slope. Our study complements an on-going investigation of biological processes on the slope and rise, which includes a number of stations in Lydonia Canyon (Maciolek and others, 1986).

In this chapter we discuss measurements of the resuspended sediment flux using sediment traps. The term "flux" is used synonymously with sediment-collection rate. Although experiments have shown that sediment traps of certain design accurately reflect bottom sedimentation rates in flumes (Gardner, 1980), at high current speeds, the absolute efficiency of sediment traps is less than 100 percent and strongly dependent on hydrodynamics of the traps and flow (Butman and others, 1986). We therefore use the measured sediment flux in a relative sense to compare sediment transport processes in different parts of the study area.

Traps were positioned at various heights above the sea floor along the axes of Lydonia and Oceanographer Canyons, on the adjacent continental slope, and on the continental shelf at the head of each canyon. At some locations in Lydonia Canyon, traps were deployed over a two-year period beginning November 1980 (fig. 6-1). Our specific objectives were: (1) to define the relative magnitude of sediment resuspension in the different physiographic areas; (2) to determine the correlation between events causing increased bottom stress and increases in sediment flux; (3) to define the distance above the bottom affected by resuspension; and (4) to determine the concentration of selected chemical constituents of the collected material in order to infer the potential for pollutant adsorption.

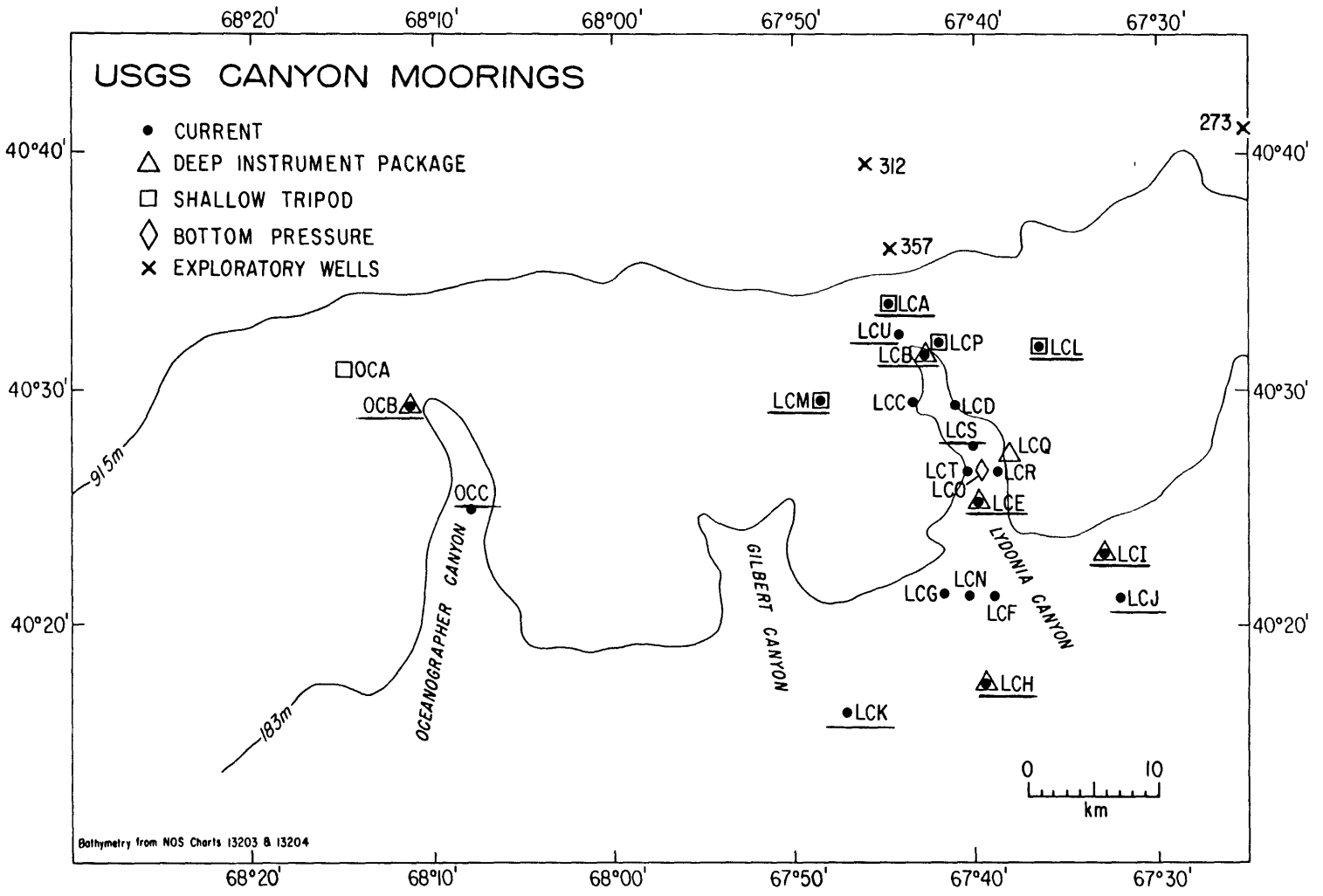

Figure 6-1. Sediment traps discussed in this report were deployed on moorings designated by underlining.

EQUIPMENT AND METHODS

Sediment traps

Because the resuspended sediment flux in Lydonia and Oceanographer Canyons was unknown at the start of our experiment, we used four different size traps (fig. 6-2a) to insure collection of a large sample. The smallest trap, referred to as a tube trap, was constructed from polybuterate tubing that was 6.6 cm internal diameter (id) 60 cm in length, and 3.2 mm wall thickness. The bottom of the trap was sealed with a securely taped plastic cap. The other three traps, referred to as cone traps, had mouth openings of 25, 33, and 50 cm id and had the shape of a cone or of a cylinder tapering to a cone (fig. 6-2a). All of the cone traps were connected by adapters to a small (2-3 cm id round, and in some cases, square) sampling tube about one meter long. A protective outer barrel consisting of schedule-80 polyvinyl chloride pipe was fitted over the sample tube and attached to the fiberglass cone of the trap with standard threaded fittings.

In order to better focus on discrete time intervals during a collection period, some of the traps were fitted with an instrument that discharged approximately 1 gram of teflon powder (fig. 6-2a) at preselected time intervals, typically 10 or 20 days (Anderson, 1977). The teflon made a layer that was visible within the sediment column and could often be identified in X-radiographs.

Poison Dispensers

A poison dispenser (fig. 6-2b) was bolted on the side of each trap. The dispenser consisted of a 175-mL, screw-capped plastic jar containing 50 g of powdered sodium azide and about 150 g of sodium chloride. A plastic holder containing both a Millipore and Nuclepore filter (47-mm diameter and 0.4-μm

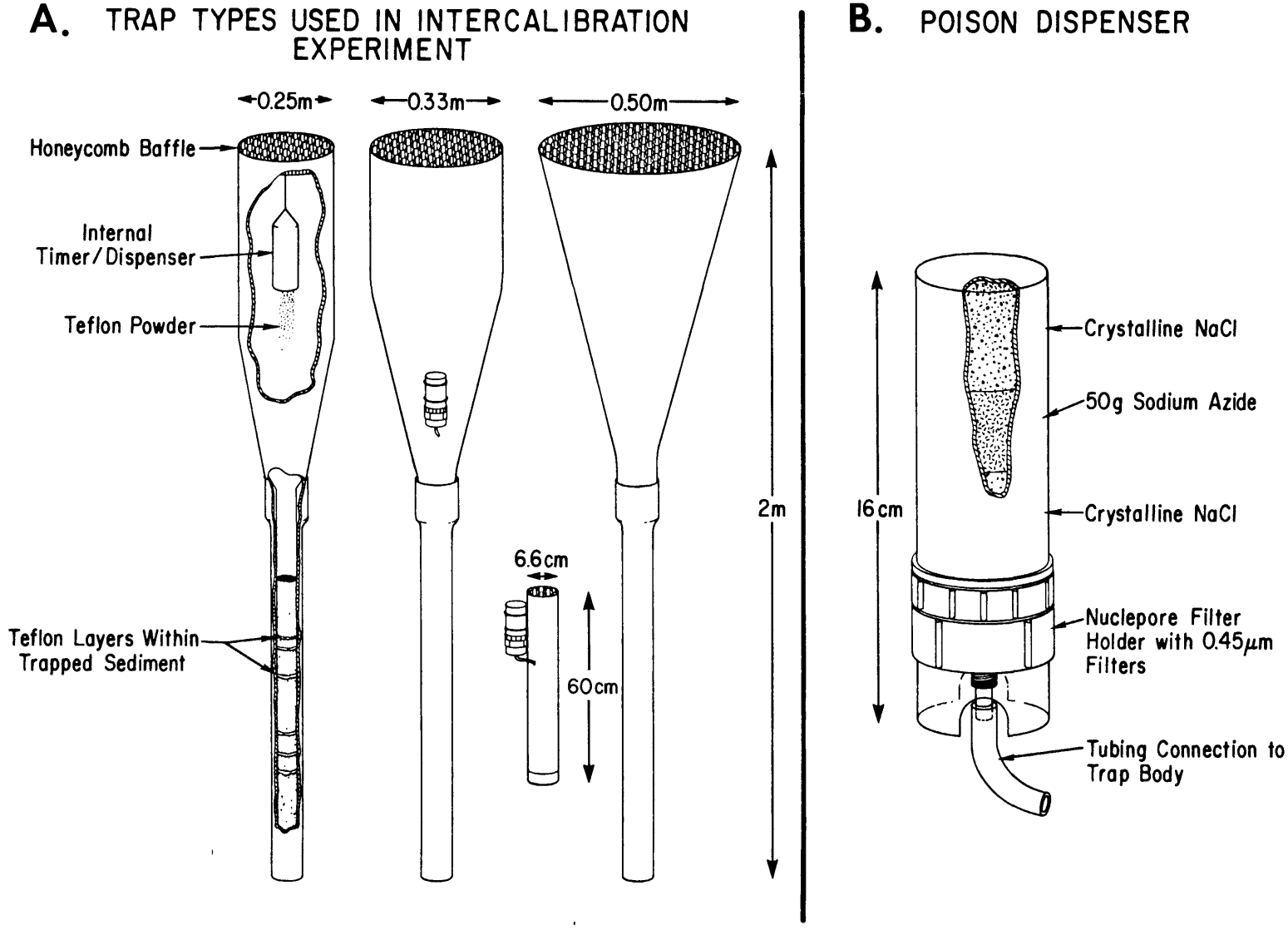

Figure 6-2. A. Dimensions of four types of sediment traps used in this experiment. Internal teflon dispensers were used in some traps to add layers of teflon at a specified time interval. B. Configuration of poison dispenser. At time of deployment, the poison dispenser floods with seawater and the resulting brine slowly flows from the dispenser to the sample tube.

pore diameter) was threaded into the bottom end of the jar and a short piece of Tygon tubing connected the nipple of the filter holder to a hole in the side of the trap. When submerged, the containers flood with sea water, forming a saturated solution of salt and azide. This solution diffuses through the filters and flows as a density current to the bottom of the trap. These dispensers retain the preservative during deployment operations, even if traps are temporarily upside down, and then release the preservative slowly over a period of a few months.

There were no direct measurements of the concentration of NaN_3 remaining in the traps when they were recovered. However, elevated salinity levels (as high as 60 ppt) were present in the water above the trapped sediment even after a deployment of about six months. Assuming that the NaN_3 diffuses out of the traps at the same rate as the NaCl, the concentration ratio of dissolved azide to excess salinity should be about 230 ppm of NaN_3 for each part per thousand salinity above ambient. The salinity of the water overlying trapped sediments or in interstitial water was typically 2-25 ppt higher than ambient seawater and NaN_3 concentrations are thus estimated to range from about 400 ppm to 5 ppt. Reducing conditions occurred in only a few of the sediment traps that had elevated salinity levels in the water above the trapped sediment.

An additional advantage of the high salinity at the bottom of the traps was the increased stability of the water immediately above the trapped sediment, which minimized resuspension and loss of material during recovery of the traps in rough seas.

Baffles were installed in each of the sediment traps. They consisted of an aramid fiber/phenolic resin honeycomb (HEXCELL) with a cell diameter of 1 cm and a length of 7.5 cm. The material showed no apparent deterioration

during exposure to seawater for periods of at least one year.

The baffles served two functions. First, Gardner's (1980) flume results for traps that had very low Reynolds numbers suggest that baffles increase the collection efficiencies of funnels by reducing turbulence and the associated resuspension of trapped sediment (but see also Butman [1986] for results with cylinders). Secondly, baffles prevent fish or other organsims larger than the mesh size from occupying the trap.

Deployment and recovery

Polyethylene-jacketed steel cable (3/8 or 3/16 in. diameter) was used in each section of the mooring where sediment traps were positioned. The cone traps were attached to the wire by means of stainless steel wire clamps, while the smaller tube traps were fastened to the wire with electrical tape. Mooring recovery was initiated by activating an acoustic release above the anchor. Subsurface flotation spheres were positioned such that the traps remained upright during and after ascent to the surface. Specific characteristics of the mooring design are discussed by Butman and Conley (1984).

Laboratory methods

Upon recovery, water overlying the trapped sediment was siphoned and discarded at sea and the sediment sample was refrigerated until bulk X-rays could be taken (usually within a week of recovery); the sediment samples were then frozen. Samples collected in the tube traps were split using a "T" or a 4-way splitter (Honjo, 1978) until subsamples of an appropriate volume were attained. Frozen samples from the cone traps were extruded from collection tubes, and subsampled at various depth intervals. These were thawed,

homogenized, and subsampled for various analyses. Before drying, a salt correction was calculated from the measured salinity or the salt was removed by repeated rinsing and centrifuging using filtered distilled water.

The material adhering to the inner walls of the cone traps was collected after only one of the deployments. On this occasion the material was removed from the inner walls of the cone traps with a high pressure jet of water, collected, and later centrifuged. The rinsed and dried material weighed between 1 and 3 grams and was not directly correlated with the size of the trap. We have elected not to include the material from the cone trap walls as part of the trap sample because much of this material consisted of algae or other biological growth which would not have fallen out of the water column into the trap. In addition, quantification of the amount is difficult because some material loosely adhering to the inner walls of the cone may have been washed out of the trap during recovery. We point out that biological fouling of trap surfaces is a concern, particularly for long-term deployments within the photic zone.

Textural analyses were made on wet sediment samples using standard sieving and Coulter counting techniques. Organic carbon analyses were made using a LECO carbon analyzer after acid (liquid of vapor) leaching of sediments to remove carbonate. Analytical error for these determinations is less than 10 percent based on the results of analyzing replicate samples.

In selected samples, the concentrations of the following elements were determined: aluminum (Al), barium (Ba), cadmium (Cd), chromium (Cr), copper (Cu), iron (Fe), lead (Pb), manganese (Mn), mercury (Hg), nickel (Ni), vanadium (V), and zinc (Zn). Analyses were carried out by the U.S. Geological Survey Branch of Analytical Laboratories, Reston, Va. The various procedures employed in each of the analyses are detailed in Bothner and others (1985).

Coefficients of variation among replicates was typically less than 10 percent of the mean value, except for concentrations at or near the detection limit of the method.

The activity of $^{239,240}Pu$ was determined on 10 grams of totally dissolved sediments. The samples were spiked with ^{236}Pu to determine chemical yield. The isotopes were concentrated by means of an ion exchange procedure and plated onto stainless steel disks for determination by alpha counting. Details of the procedure are presented in procedures manual number E-PU-06 of the Environmental Measurements Laboratory (U.S. Dept. of Energy), 376 Hudson Street, NY, NY 10014.

^{210}Pb analyses were done on acid leached sediments by plating the granddaughter isotope ^{210}Po on silver disks followed by alpha counting. ^{14}C measurements were made on the total organic carbon fraction after the sediments had been acid leached to remove carbonate carbon. The ^{14}C activity was determined using the acetylene gas counting method (Suess, 1954). The dates were calculated relative to the U.S. National Bureau of Standards oxalic acid standard activity (Stuiver and Polach, 1977). Other details of these procedures are presented in Bothner and others, 1981.

RESULTS AND DISCUSSION

Comparison of different size traps

One of the most interesting findings of this study was that the different sediment traps had reproducibly different trapping efficiencies.

On two occasions during this experiment we compared the relative collection efficiency of four different size traps by positioning an array of sizes on a single mooring line, 3 m apart, 100-116 m above the sea floor. The details of these experiments are presented in Appendix 1 of this report and

will only be summarized here. Because the horizontal flow of water and suspended matter (typically 10 cm/s or more) is much greater than essentially all of the settling particles, we found no shadowing effects from this vertical configuration of the traps.

We found that the smallest traps collected at the highest relative rate (in $g/m^2/day$) and the largest traps collected at the lowest rate. Theoretical considerations predict that collection efficiency is partially dependent on trap Reynolds number (UD/ν, where U = horizontal fluid velocity; D = trap diameter; ν = kinematic fluid viscosity) and, therefore, the nearly linear relationship between the collection rate and trap diameter is expected since values of U and ν are the same for traps of different size on the same mooring (Butman and others, 1986). The high linear correlation between collection rate and trap diameter ($r = -.97$; see appendix 1, fig. A1-4) gave us the basis for normalizing the flux measurements of the three larger traps to that of the tube trap most commonly used throughout our study. The correction factors for the 25-, 33- and 50-cm cone traps are 1.27, 1.60, and 4.17, respectively. The coefficient of variation between replicates was 7.6 percent for the 50-cm cone traps and less than 3.3 percent for the tube traps.

Using these factors, we have normalized the data of the larger traps to that of the tube traps and we have used the normalized data in the illustrations. Both corrected and uncorrected catch rates are presented in table 6-1.

Sediment flux in different physiographic areas

The most extensive sediment-trap array was deployed in the Lydonia Canyon region from November 1980 to April 1981. The normalized sediment flux with

Table 6-1.-Sediment-trap deployments and flux data

Sta.	Water depth (m)	Trap no.	Height above bottom (m)	Date deploy (YrMoDy)	Date recover (YrMoDy)	No. days	Trap type	Trap mouth (m^2)	Volume (cc)	$cc/m^2/d$	Dry wt. (g)	$g/m^2/d$	$g/m^2/d$ (normalized)
Deployment 1													
LCA	100	102	26.0	801130	810424	145	A	0.0490	121.40	17.09	16.00	2.25	2.87
LCA	100	100	5.0	801130	810424	145	A	.0490	490.00	68.97	109.30	15.38	19.58
LCB	290	116	50.0	801128	810428	151	A	.0860	846.00	65.15	215.50	16.59	26.53
LCB	290	103	20.0	801128	810428	151	A	.0860	930.00	71.62	244.00	18.79	30.04
LCB	290	111	5.0	801128	810428	151	A	.0490	2030.00	274.36	441.90	59.72	76.02
LCE	600	104	5.0	801201	810701	213	A	.0490	1545.00	148.03	--	32.40	41.24 est.
LCH	1380	114	20.0	810120	810428	98	A	.0860	127.00	15.07	22.70	2.69	4.31
LCH	1380	107	5.0	810120	810428	98	A	.0490	47.00	9.79	33.30	6.93	8.83
LCH	1425	113	100.0	801201	810427	145	A	.0860	203.00	16.28	34.70	2.78	4.45
LCI	250	115	50.0	801202	810429	148	A	.0860	40.00	3.14	1.70	.13	.21
LCI	250	101	20.0	801202	810429	148	A	.0860	22.00	1.73	1.50	.12	.19
LCI	250	106	5.0	801202	810429	148	A	.0490	49.00	6.76	6.60	.91	1.16
LCJ	535	120	300.0	801127	810429	153	A	.1960	94.00	3.13	11.20	.37	1.49
LCK	554	109	300.0	801127	810427	151	A	.1960	56.00	1.89	5.50	.19	.74
LCL	125	108	26.0	801130	810425	146	A	.0490	72.00	10.06	6.90	.96	1.23
LCL	125	105	5.0	801130	810425	146	A	.0490	202.00	28.24	46.10	6.44	8.20
LCM	125	112	26.0	801202	810425	144	A	.0490	84.00	11.90	11.60	1.64	2.09
LCM	123	110	5.0	801202	810425	144	A	.0490	269.00	38.12	55.80	7.91	10.07
Deployment 2													
LCA	100	230	24.0	810505	810926	144	A	.0860	77.00	6.22	9.20	.74	1.19
LCA	100	223	5.0	810505	810926	144	A	.0860	119.00	9.61	27.70	2.24	3.58
LCA	100	212	2.0	810505	810926	144	SQ	.0052			5.30	7.08	
LCA	100	215	3.0	810505	810926	144	SQ	.0052			4.70	6.28	
LCB	288	233	80.0	810429	810926	150	B	.0034			.40	.78	
LCB	288	232	65.0	810429	810926	150	B	.0034			4.95	9.71	
LCB	288	222	50.0	810429	810926	150	A	.0860	860.00	66.67	152.00	11.78	18.84
LCB	288	218	3.0	810429	810926	150	A	.0490	1936.00	263.40	344.00	46.80	59.58
LCI	250	219	5.0	810503	810927	147	A	.0860			1.87	.15	.24
LCL	125	213	3.0	810426	810926	153	SQ	.0052			2.26	2.84	

* A = Cone-type trap; B = Tube traps; Sq = Square traps, similar in size to tube trap.

Table 6-1.-Sediment-trap deployments and flux data--Continued

Sta.	Water depth (m)	Trap no.	Height above bottom (m)	Date deploy (YrMoDy)	Date recover (YrMoDy)	No. days	Trap type	Trap mouth (m^2)	Volume (cc)	$cc/m^2/d$	Dry wt. (g)	$g/m^2/d$	$g/m^2/d$ (normalized)
Deployment 3													
LCA	100	318	3.5	810926	820128	124	A	.0490	558.00	91.84	100.00	16.46	20.95
LCB	295	322	150.0	810927	820130	125	B	.0034			2.50	5.88	
LCB	295	323	125.0	810927	820130	125	B	.0034			4.30	10.12	
LCB	295	326	57.0	810927	820130	125	B	.0034			20.20	47.53	
LCB	295	302	56.0	810927	820130	125	A	.0860	995.00	92.56	305.20	28.39	45.39
LCB	295	327	25.0	810927	820130	125	B	.0034	102.00	240.00	36.20	85.18	
LCB	295	328	5.0	810927	820130	125	SQ	.0052	188.00	289.23	91.89	141.37	
LCB	290	321	27.0	810927	820128	123	B	.0034			37.80	90.39	
LCB	290	301	20.0	810927	820128	123	A	.0490	1932.00	320.56	616.10	102.22	130.12
LCB	290	320	7.5	810927	820128	123	B	.0034			45.80	109.52	
LCB	290	300	5.0	810927	820128	123	A	.0490	2819.00	467.73	743.00	123.28	156.92
LCI	247	315	141.0	810927	820131	126	A	.0490	19.00	3.08	4.60	.75	.95
LCI	247	314	137.0	810927	820131	126	A	.1960	39.00	1.58	5.90	.24	.96
LCI	247	313	133.0	810927	820131	126	A	.0860	20.00	1.85	2.10	.19	.31
LCI	247	312	129.0	810927	820131	126	A	.0860	31.00	2.86	2.70	.25	.40
LCI	247	311	125.0	810927	820131	126	A	.0490	19.00	3.08	3.40	.55	.70
LCI	247	310	20.0	810927	820131	126	A	.1960	35.00	1.42	2.00	.08	.32
LCP	132	317	26.0	810928	820128	122	A	.0860	89.00	8.48			
LCP	132	316	5.0	810928	820128	122	A	.0490	126.00	21.08	47.40	7.93	10.09
LCP	131	319	3.5	810926	820128	123	A	.0490	270.00	44.80	71.20	11.81	15.04
Deployment 4													
OCB	227	419	55.0	820128	820709	162	A	.0860	849.60	60.98	320.70	23.02	36.80
LCA	100	401	3.4	820128	820707	160	A	.0490	223.00	28.44	40.10	5.11	6.51
LCA	100	401B	2.6	820128	820707	160	B	.0034			5.68	10.44	
LCA	100	401A	.7	820128	820707	160	B	.0034			8.52	15.66	
LCB	300	412	200.0	820131	820707	157	A	.1960	83.70	2.72	7.30	.24	.95
LCB	300	404	50.0	820131	820707	157	A	.0860	990.90	73.39	289.30	21.43	34.25
LCB	300	403	20.0	820131	820707	157	A	.0490	881.60	114.60	249.90	32.48	41.35
LCB	300	402	5.0	820131	820707	157	A	.0490	1861.00	241.91	537.30	69.84	88.90
LCI	249	415	150.0	820131	820708	159	A	.1960	42.00	1.35	2.53	.08	.32
LCI	249	414	50.0	820131	820708	159	A	.1960	58.10	1.86	5.14	.16	.66
LCI	249	413	5.0	820131	820708	159	A	.0860	106.40	7.78	11.48	.84	1.34
LCS	560	405	117.0	820129	820707	159	A	.1960	332.20	10.66	171.80	5.51	22.05
LCS	560	411	113.0	820129	820707	159	A	.0860	737.10	53.91	198.60	14.52	23.22
LCS	560	411A	110.0	820129	820707	159	B	.0034			15.27	28.25	
LCS	560	410	108.0	820129	820707	159	A	.0490	749.80	96.24	180.72	23.20	29.53
LCS	560	409A	102.0	820129	827007	159	B	.0034			15.75	29.13	

*A = Cone-type trap; B = Tube traps; Sq = Square traps, similar in size to tube trap.

Table 6-1.-Sediment-trap deployments and flux data--Continued

Sta.	Water depth (m)	Trap no.	Height above bottom (m)	Date deployed (YrMoDy)	Date recovered (YrMoDy)	No. days	Trap type*	Trap mouth (m^2)	Volume (cc)	$cc/m^2/d$	Dry wt. (g)	$g/m^2/d$	$g/m^2/d$ (normalized)
Deployment 4--Continued													
LCS	560	408	101.0	820129	820707	159	A	.1960	852.80	27.36	191.44	6.14	24.57
LCS	560	408B	80.0	820129	820707	159	B	.0034			18.80	34.78	
LCS	560	408A	40.0	820129	820707	159	B	.0034			27.61	51.07	
LCS	560	407	20.0	820129	829797	159	A	.0490	1358.90	174.42	359.20	46.10	58.69
LCS	560	407B	19.0	820129	820707	159	B	.0034			27.95	51.70	
LCS	560	407A	8.0	820129	820707	159	B	.0034			32.90	60.86	
LCS	560	406	5.0	820129	820707	159	A	.0490	1358.70	174.39	333.98	42.87	54.57
LCS	560	406A	3.0	820129	820707	159	B	.0034			45.14	83.50	
OCB	227	418	5.0	820128	820709	162	A	.0490	1580.00	199.04	823.60	103.75	132.07
OCC	560	421	100.0	820127	820709	163	A	.1960	681.60	21.33	263.20	8.24	32.95
OCC	560	421D	80.0	820127	820709	163	B	.0034			24.12	43.52	
OCC	560	421B	20.0	820127	820709	163	B	.0034			41.95	75.69	
OCC	560	421A	10.0	820127	820709	163	B	.0034			52.74	95.16	
Deployment 5													
LCA	104	541	3.4	820812	821111	91	A	.0490	369.60	82.89	117.50	26.35	33.54
LCA	104	544	3.4	820812	821111	91	B	.0034			7.20	23.27	
LCA	104	541	3.4	820812	821111	91	A	.0490	369.60	82.89	117.50	26.35	33.54
LCA	104	543	2.2	820812	821111	91	B	.0034			6.95	22.46	
LCA	104	542	.7	820812	821111	91	B	.0034			16.73	54.07	
LCB	295	540	196.0	820708	821111	126	A	.1960	62.40	2.53	2.50	.10	.40
LCB	295	525	180.0	820708	821111	126	B	.0034			.16	.37	
LCB	295	526	116.0	820708	821111	126	B	.0034			3.20	7.47	
LCB	295	527	114.0	820708	821111	126	A	.0490	220.40	35.70	40.80	6.61	8.41
LCB	295	528	110.0	820708	821111	126	A	.1960			81.00	3.28	13.12
LCB	295	529	107.0	820708	821111	126	B	.0034	328.17	13.29	4.70	10.97	
LCB	295	530	106.0	820708	821111	126	A	.0860			49.00	4.52	7.23
LCB	295	531	103.0	820708	821111	126	B	.0034	293.3	27.10	69.60	10.26	
LCB	295	531	103.0	820708	821111	126	B	.0034			4.98	11.62	
LCB	295	532	102.0	820708	821111	126	A	.0490	294.20	47.65	56.43	9.14	11.63
LCB	295	533	58.0	820708	821111	126	B	.0034			8.65	20.19	
LCB	295	534	56.0	820708	821111	126	A	.0490	556.00	90.06	117.87	19.09	24.30
LCB	295	535	25.0	820708	821111	126	B	.0034			15.50	36.18	
LCB	295	536	20.0	820708	821111	126	A	.0490	1766.70	286.15	509.32	82.49	105.01
LCB	295	537	10.0	820708	821111	126	B	.0034			19.77	46.15	

*A = Cone-type trap; B = Tube traps; Sq = Square traps, similar in size to tube trap.

depth at stations located in the canyon axis and on the adjacent shelf and slope (fig. 6-3) showed a pronounced increase in flux near the bottom at all locations, clearly reflecting the effects of resuspension. Flux values measured about 300 meters above bottom (mab) on the open slope represent our best estimates of primary flux, about 1 $g/m^2/day$. These are considered maximum values because the trap samples contained some rather large zooplankton, which may have been killed by the poison after swimming into the trap.

The highest flux of resuspended sediment during this deployment period (76 $g/m^2/day$) was measured 5 mab at station LCB in the axis of the canyon (fig. 6-3). The flux at LCB is higher by more than a factor of three than at any of the three stations on the continental shelf. The close agreement between the fluxes measured at moorings LCL and LCM at 125-m water depth on the continental shelf gives additional confidence in the reproducibility of our measurements. The near-bottom resuspended sediment flux in the canyon axis decreases with increasing water depth, and at 1,500 m (sta. LCH), the flux is similar to that measured on the continental shelf. On the slope (LCI), the fluxes are much smaller than at any other of the sampling locations (fig. 6-3).

Figure 6-4 illustrates both the steep gradient of increasing resuspended sediment flux in traps closest to the bottom and the differences in the magnitude of flux at the various mooring locations of this first deployment.

In order to compare the intensity of resuspension in Lydonia Canyon with that in Oceanographer Canyon, two moorings were deployed in each canyon at comparable water depths. At 20 mab in both canyons, at exactly the same water depth, the flux in Oceanographer Canyon was 1.3 times higher than in Lydonia Canyon (fig. 6-5). Higher fluxes were observed in Oceanographer Canyon

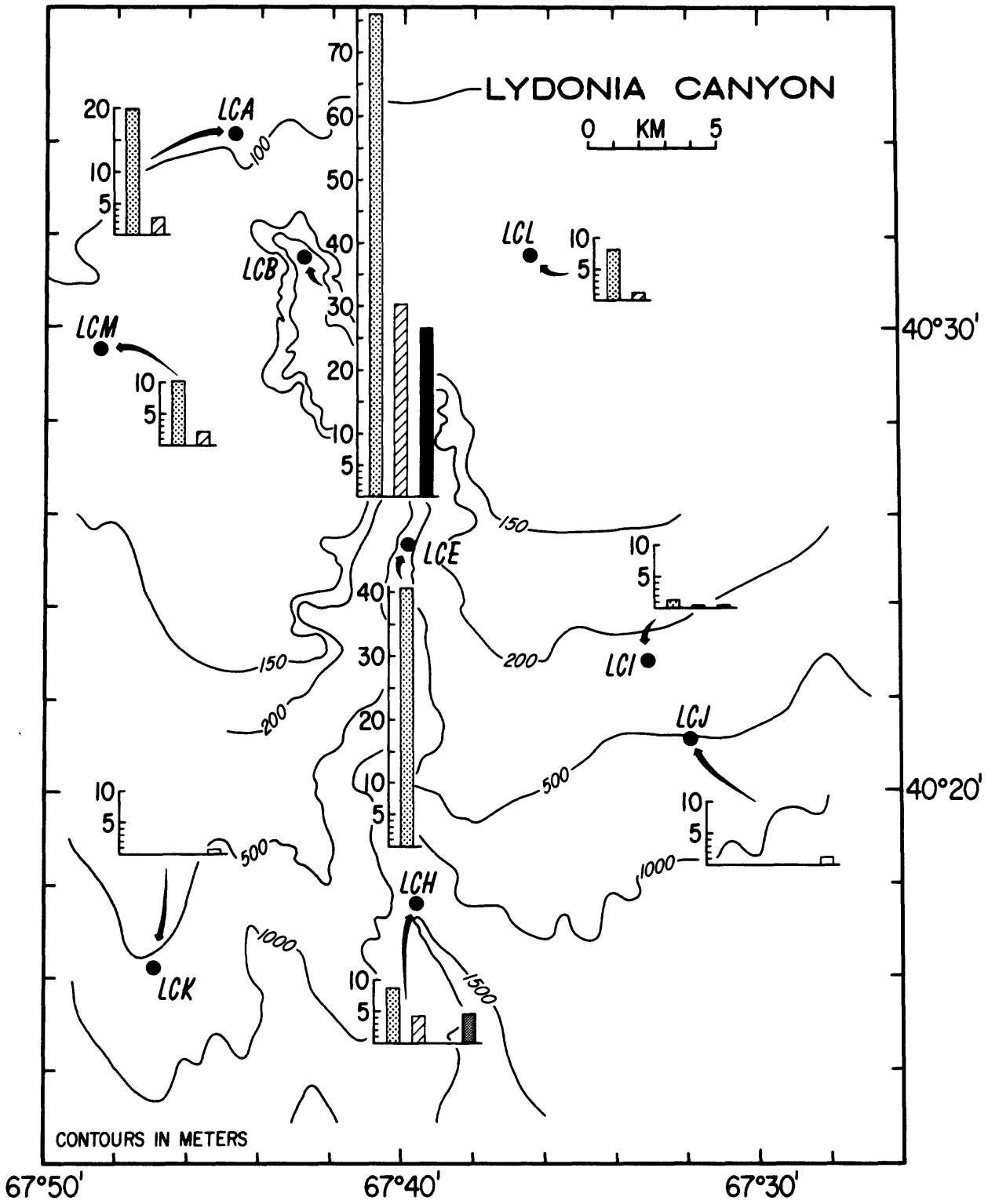

Figure 6-3. Histograms showing the flux of resuspended sediment ($g/m^2/day$) at different heights above the bottom; ▨ = 5 mab; ▨ = 20-26 mab; ■ = 50 mab; ■ = 100 mab; □ = 300 mab.

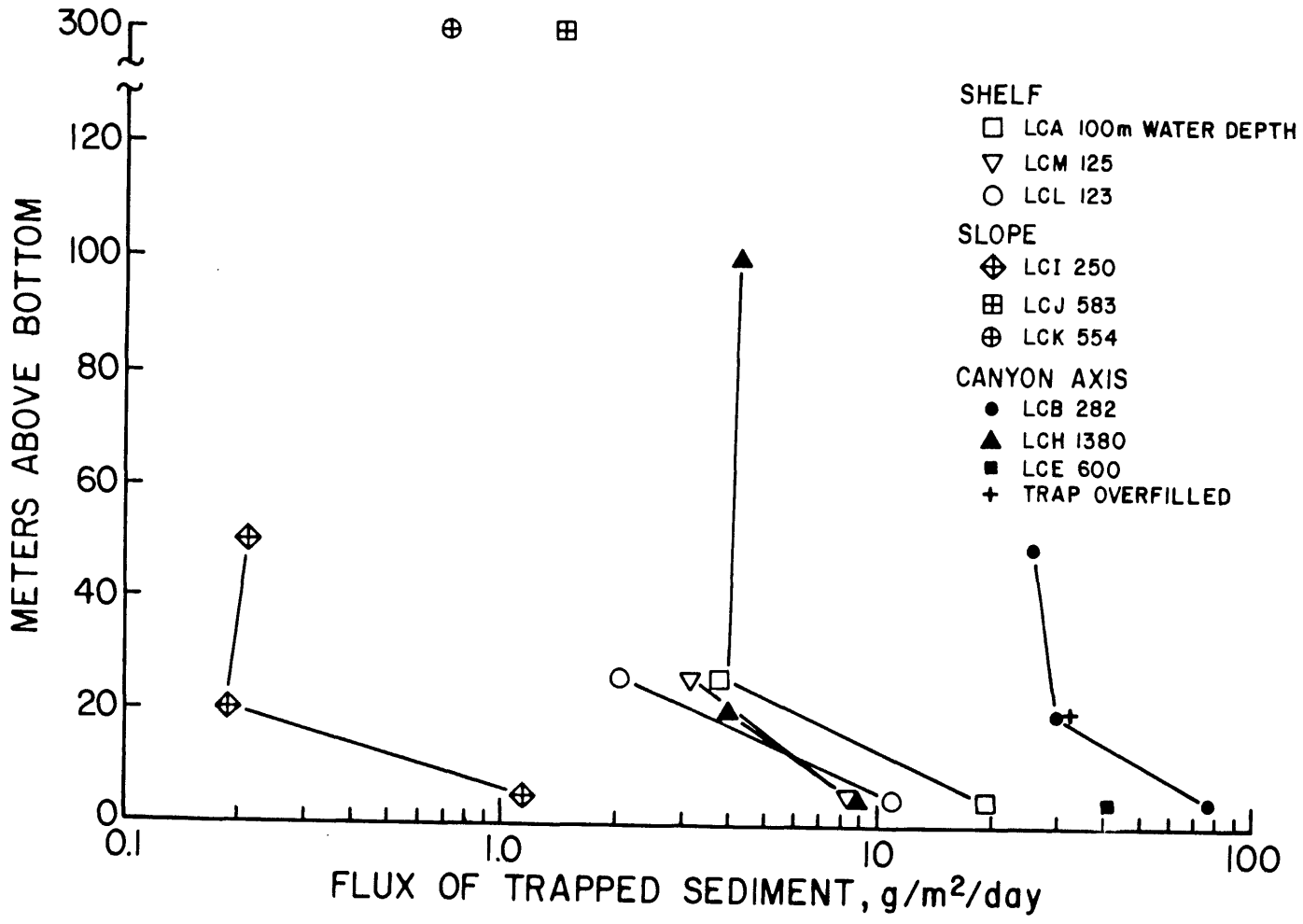

Figure 6-4. Comparison of sediment flux at different locations for a deployment between Nov. 1980 - April 1981. Data point labeled with (+) is a minimum value because collection tube was overfilled.

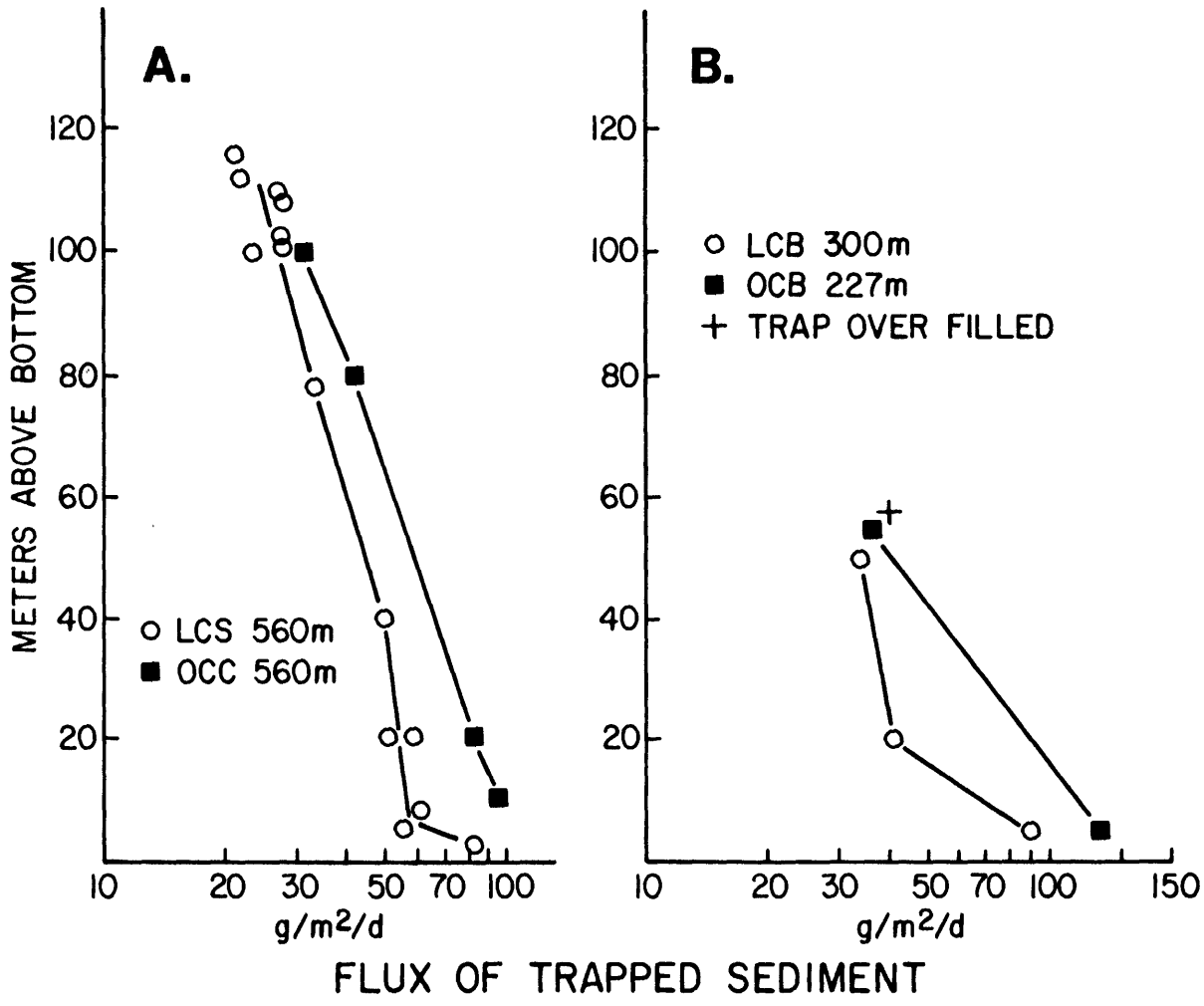

Figure 6-5. Comparison of sediment flux in Lydonia and Oceanographer canyons for a deployment from January to July, 1982. Data point labeled with (+) is a minimum because collection tube was overfilled. A. Moorings at 560 m water depth. B. Moorings at 300 and 227 m water depth.

throughout the lower 100 m of the water column. The higher fluxes and coarser texture of resuspended sediment in Oceanographer Canyon, as compared to those in Lydonia, are clearly a response to the higher current velocities measured in Oceanographer Canyon (Butman, ch. 2 of this volume).

Depth profile of resuspended sediment flux

For each deployment at LCB (fig. 6-6) there is a nearly linear relationship between the log of the sediment flux and trap height above the bottom. This logarithmic increase in the flux of suspended matter is present within the depth range from 3 mab to more than 120 mab. We are presently investigating various models which might account for this rather regular distribution of flux by assuming resuspension from the walls of the canyon, horizontal mixing, and canyon geometry.

The significant increase in near-bottom sediment flux has also been observed in Baltimore Canyon (Gardner, 1983) and is expected in the axis of Hudson Canyon on the basis of high suspended-matter concentrations in the water column (Drake and others, 1978). In contrast, in Quinault Canyon off the Washington coast, Baker and Hickey (1986) found no increase in the flux of trapped sediment as the trap's height above the bottom decreased. They believe this is because in Quinault Canyon, the primary source of suspended sediments is from the overlying water column, originating from a nepheloid layer generated on the continental shelf edge and advected over the canyon at intermediate depth.

Time variability in flux

The variability in resuspended sediment flux can be described on three different time scales. These are: (1) the 4 to 6-month duration of each

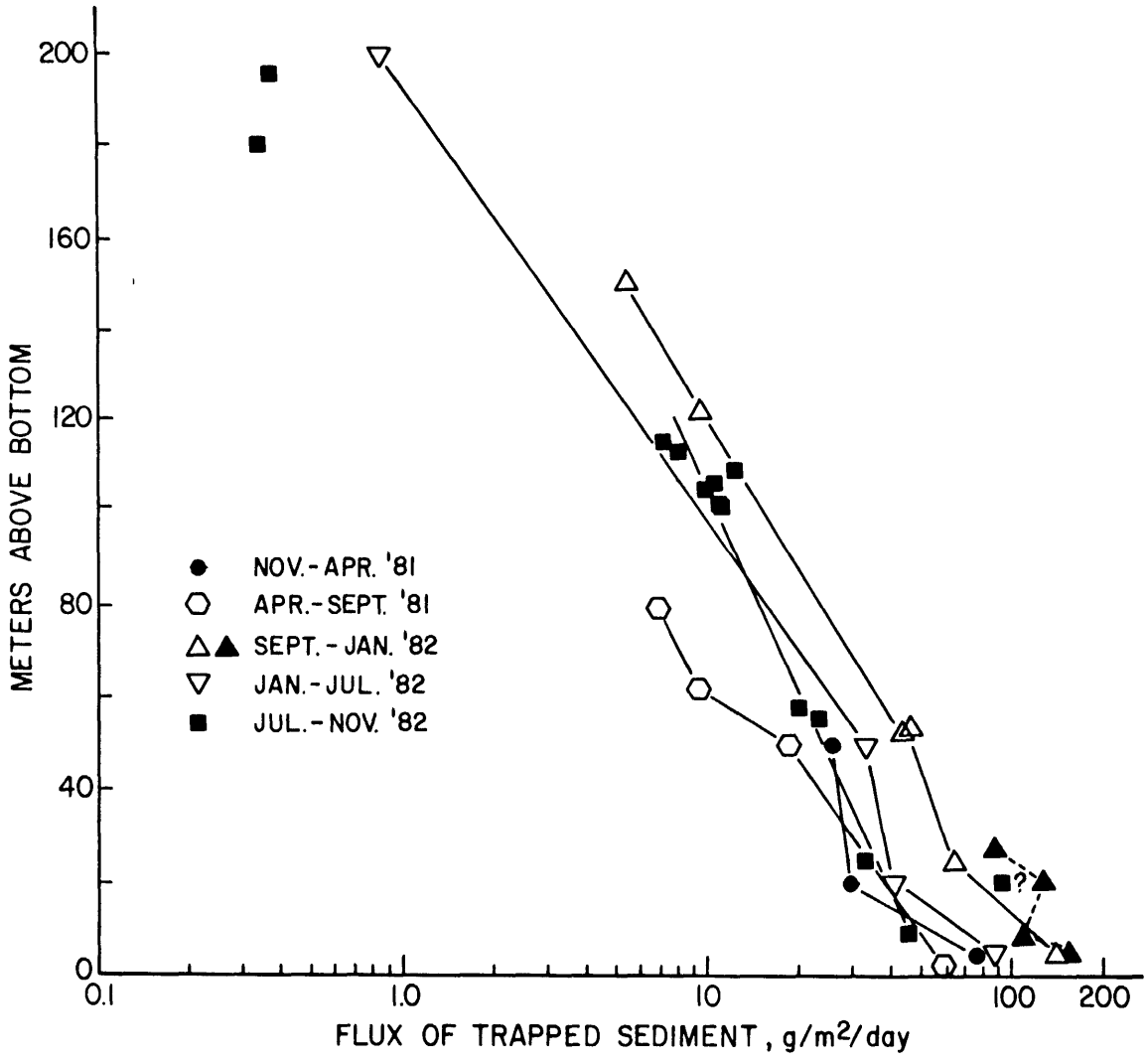

Figure 6-6. Flux of sediments in axis of Lydonia Canyon (LCB, 280 m water depth) during 5 deployment periods. The question mark (?) indicates an unexplained high flux which falls off the linear trend established for the Jul - Nov. '82 deployment (see also Figure 6-7).

deployment; (2) the 5 to 20-day intervals between layers of teflon in some traps; and (3) the shorter but less well defined time intervals represented by the alternating layers of coarse and fine sediment identified in bulk X-rays of the trap samples. There were five successive deployments at station LCB in Lydonia Canyon that give some indication of the variability in resuspended sediment flux on the scale of about five months. In the lower 50 m of the water column, the flux varied by about a factor of 2 for the five deployment periods (fig. 6-7). In the third deployment period, from September 1981 to January 1982, the flux collected in the traps was higher at all depths and the trap at 5 mab collected the highest flux measured in this program, 156 $g/m^2/day$. This period of highest average flux correlates with the deployment period having the greatest number of major storm events per month on the continental shelf (fig. 6-8).

At mooring location LCA at the head of the canyon (125-m water depth) the measured flux of sediment during deployment 3 is greater than during deployments 2 and 4, in agreement with the results at LCB at a depth of 295 m in the canyon axis (fig. 6-9). At LCA the flux during deployment 5 was higher than deployment 4. This trend may reflect local influence of resuspension by a storm which did not impact the deeper station (LCB).

Examination of the teflon time record in this trap sample indicates that the total weight of sediment collected by the trap in a 20-day period varied by a factor of 5. Examination of the record of storm events on the shelf indicates that 50 percent (by weight) of the material was collected during and subsequent to one major storm beginning on October 11, 1982 (fig. 6-10). The bulk X-rays show a layer of relatively coarse sediment at the time of this major storm as well as a layer of coarse sediment correlating approximately with the time of a smaller storm on September 21, 1982.

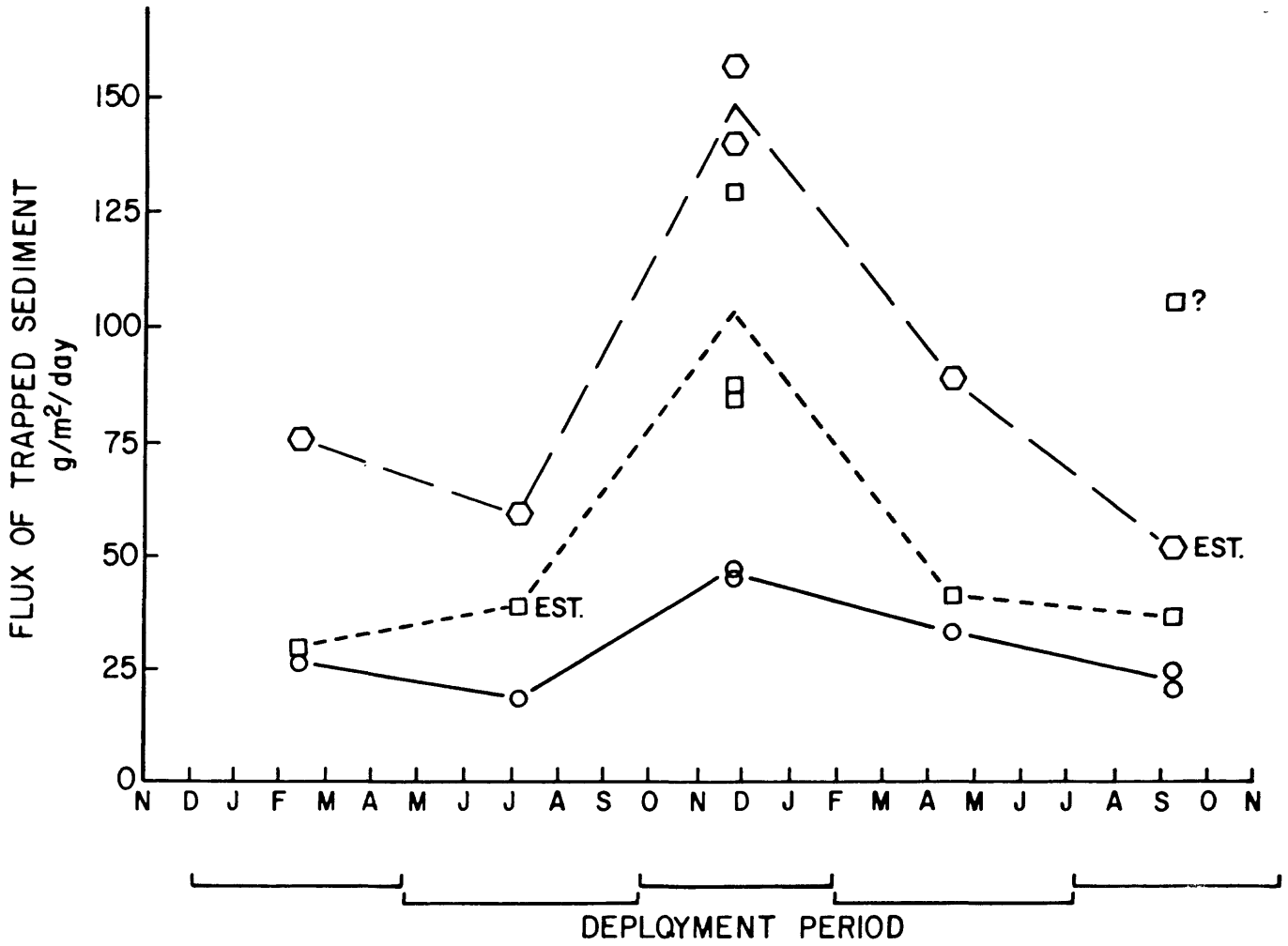

Figure 6-7. Sediment flux at station LCB, Lydonia Canyon axis, 280 m water depth for each deployment period. 3-7 meters above bottom (MAB) = ⬡— — ; 20-27 MAB = □---; 50-58 MAB = ○ ——. Estimated values based on Figure 6-6. One data point marked with ? is much higher than expected based on the trends observed in Figure 6-6.

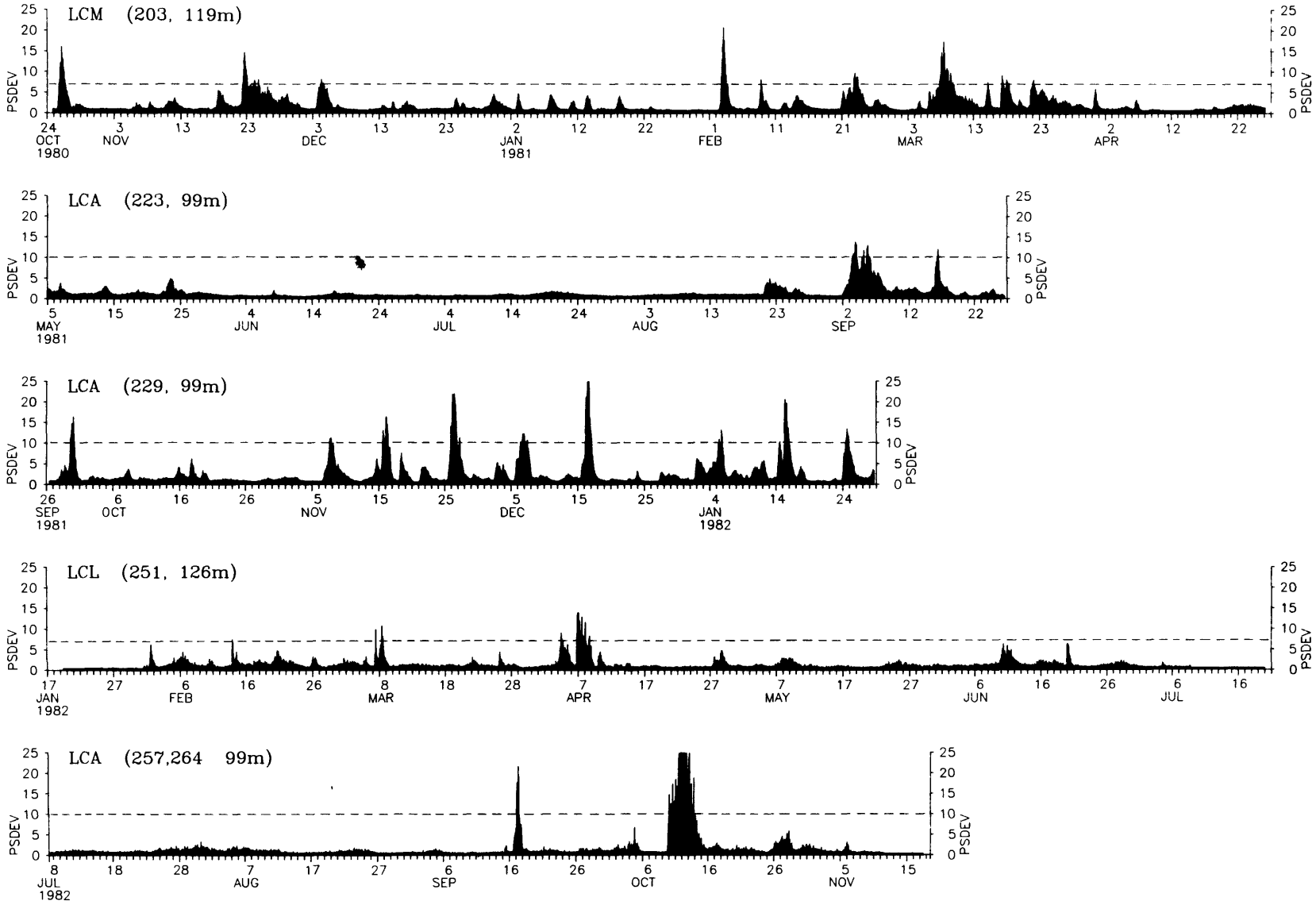

Figure 6-8. Record of pressure standard deviation measured near the rim of Lydonia Canyon for each deployment period. Dashed line represents equivalent level of PSDEV accounting for different water depths.

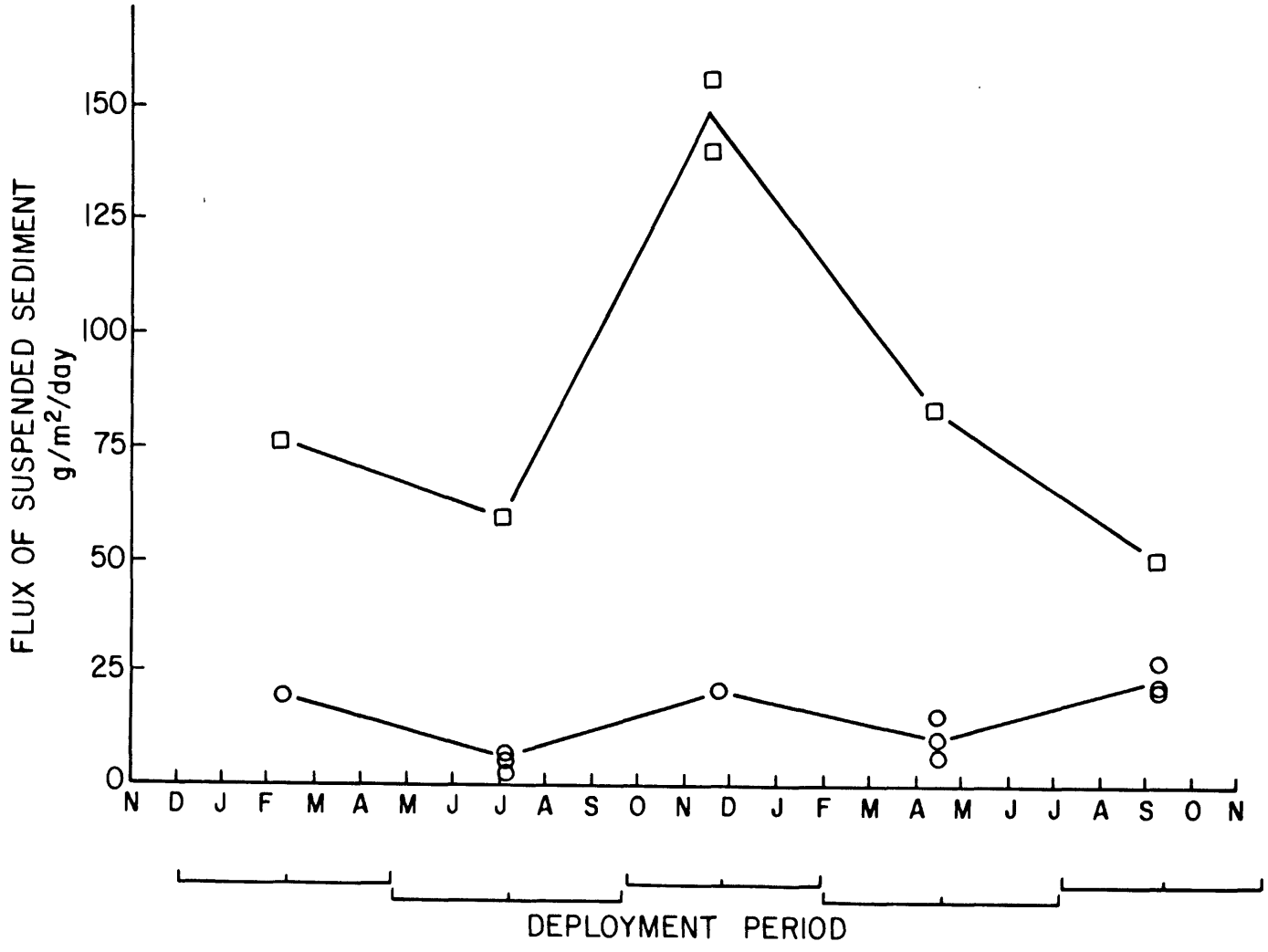

Figure 6-9. Sediment flux in Lydonia Canyon axis (LCB, 293 m average depth, 3-7 meters above bottom = □) and on the Continental Shelf at canyon head (LCA, 100 m, 3-5 meters above bottom = ○).

Figure 6-10.

A. Histogram showing the relative (%) mass of sediment collected at station LCA, 3 meters above bottom, during each 20 day interval between August 12 and November 10, 1982.

B. Schematic diagram showing position of teflon timing layers (open symbols) and layers of coarser sediment (dots). Percent sand is indicated below schematic.

C. X-radiograph of the sediment trap sample showing layers of coarser (darker) and fine sediment. Top of sample is to the left.

D. Record of bottom stress (dynes per cm^2) at station LCA.

E. Calculated flux of trapped sediment using the model described in Chapter 3. The size distribution (%) of particles 8, 32-63, and 64-125 μm in diameter is indicated for periods of increased flux.

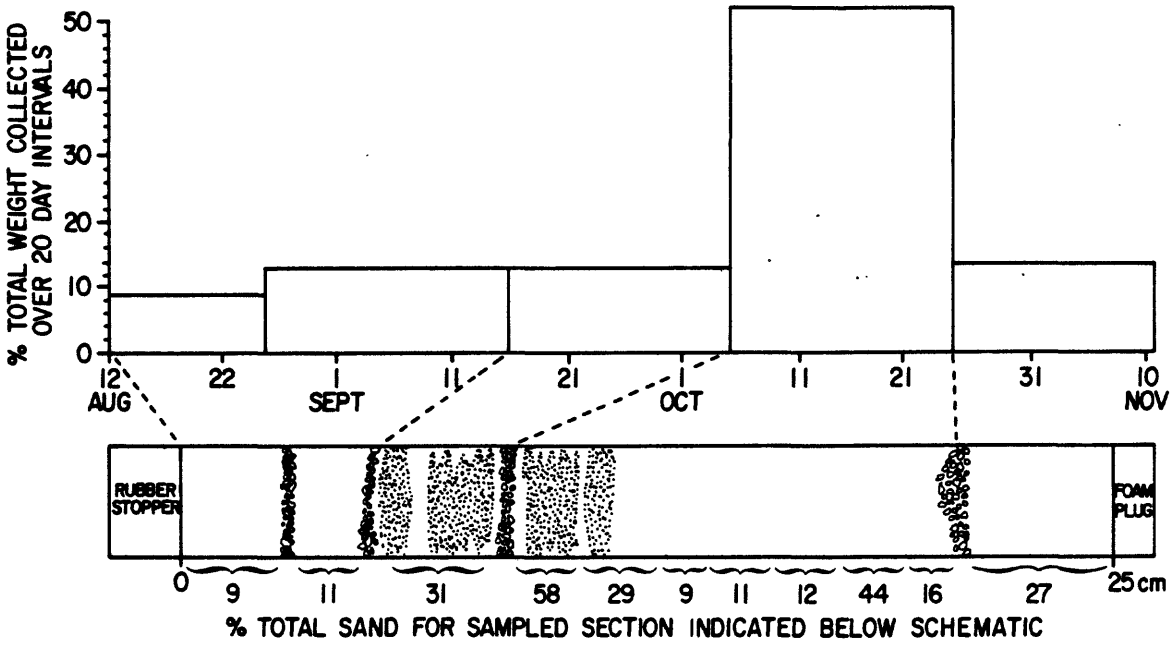
% TOTAL WEIGHT COLLECTED OVER 20 DAY INTERVALS
50
40
30
20
10
0
12 AUG
22
1 SEPT
11
21
1 OCT
11
21
31
10 NOV
RUBBER STOPPER
FOAM PLUG
0
9
11
31
58
29
9
11
12
44
16
27
25cm
% TOTAL SAND FOR SAMPLED SECTION INDICATED BELOW SCHEMATIC

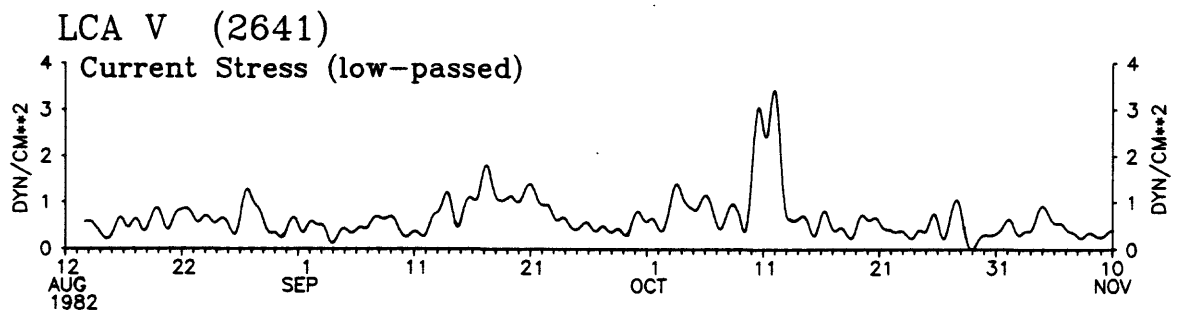
LCA V (2641)
Current Stress (low-passed)
DYN/CM**2
4
3
2
1
0
12 AUG 1982
22
1 SEP
11
21
1 OCT
11
21
31
10 NOV

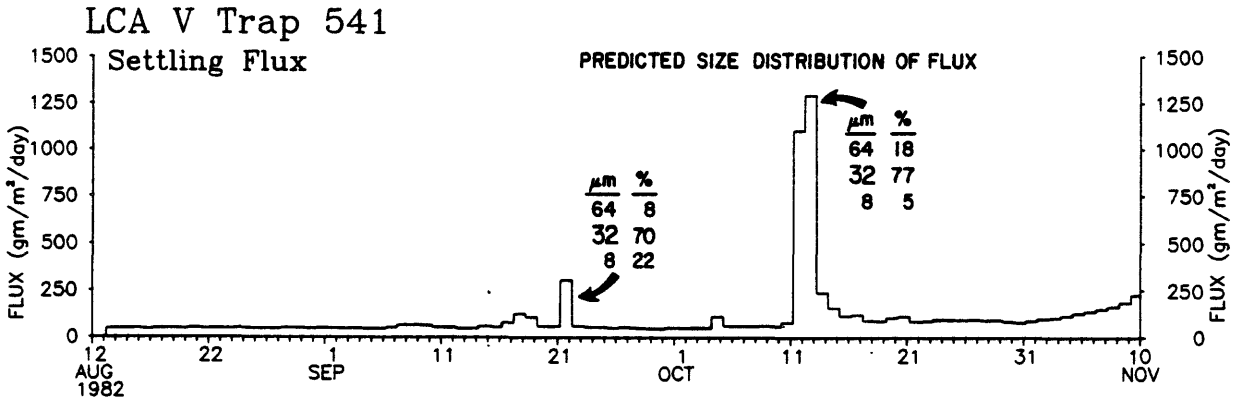
LCA V Trap 541
Settling Flux
PREDICTED SIZE DISTRIBUTION OF FLUX
μm % 64 8 32 70 8 22
μm % 64 18 32 77 8 5
FLUX (gm/m²/day)
1500
1250
1000
750
500
250
0
12 AUG 1982
22
1 SEP
11
21
1 OCT
11
21
31
10 NOV

Analysis of the variability in flux on the time scale of a single storm was investigated using the model discussed in chapter 3. The model uses wave and current data to predict the concentration and size distribution of resuspended sediment in near-bottom water. It uses fall velocities for different size classes of sediment determined from Stokes Law, and then calculates vertical flux. It does not correct for any differences in trap efficiency which may occur at different current speeds.

Figure 6-10d shows the predicted size distribution and vertical flux of the collected sediment as a function of time. The predicted periods of higher flux are in excellent agreement with the measured fluxes during periods defined by the teflon layers. Two periods of relatively coarse sediment resuspension predicted by the model are matched by two sandy layers in the trap sample at the time of storms. The % sand predicted by the model during the largest storm (18%) is somewhat less than the average sand content found in the trap during the storm period (25%). Sand sized biogenic material, not considered in the model, may account for the discrepency.

Excellent agreement between the model's prediction of the timing and composition of storm-derived resuspended sediment was observed in comparing the sediment trapped at LCP (5 mab) during the third deployment and the record of bottom stress (figs. 6-11a-e). This model showed that the increase in the sediment flux during storms can be at least an order of magnitude higher than during non-storm periods.

We examined the X-radiographs from different mooring locations (fig. 6-1) for similarity in the pattern of coarse and fine layers. Similar patterns were observed in near bottom (5 mab) traps for moorings LCA, LCL, and LCM deployed north, west, and east of the canyon head (water depths 100-125 m) during deployment 1. The pattern at LCB for deployment 5 is somewhat similar

Figure 6-11.

A. Histogram showing the relative (%) mass of sediment collected at station LCP, 5 meters above bottom, during each 10 day interval between September 28, 1981 and January 28, 1982.

B. Schematic diagram showing position of teflon timing layers (open symbols) and layers of coarser sediment (dots). Percent sand is indicated below schematic.

C. X-radiograph of the sediment trap sample showing layers of coarser (darker) and fine sediment. Top of sample is to the left.

D. Record of bottom stress (dynes per cm^2) at station LCP.

E. Calculated flux of trapped sediment using the model described in Chapter 3. The size distribution (%) of particles 8, 32-63, and 64-125 μm in diameter is indicated for periods of increased flux.

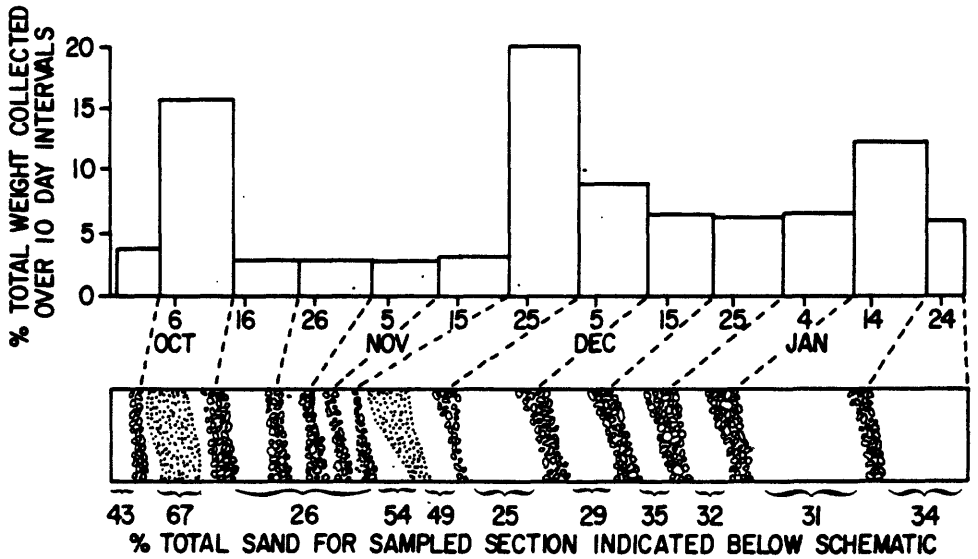
% TOTAL WEIGHT COLLECTED OVER 10 DAY INTERVALS
20
15
10
5
0
6 OCT
16
26
5 NOV
15
25
5 DEC
15
25
4 JAN
14
24
43
67
26
54
49
25
29
35
32
31
34
% TOTAL SAND FOR SAMPLED SECTION INDICATED BELOW SCHEMATIC

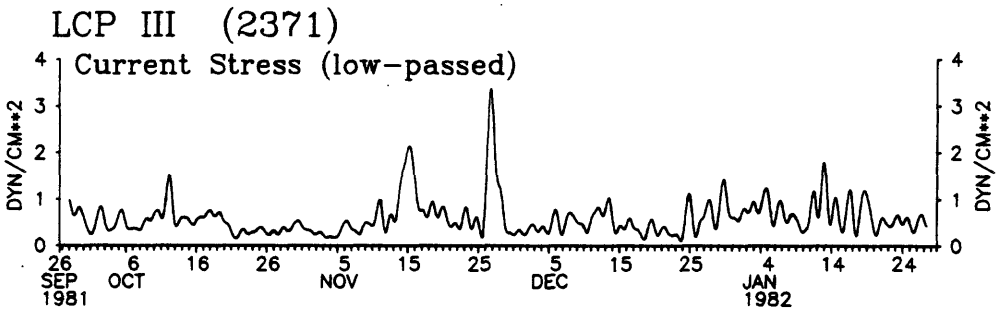
LCP III (2371)
Current Stress (low-passed)
DYN/CM**2
4
3
2
1
0
26 SEP 1981
6 OCT
16
26
5 NOV
15
25
5 DEC
15
25
4 JAN 1982
14
24

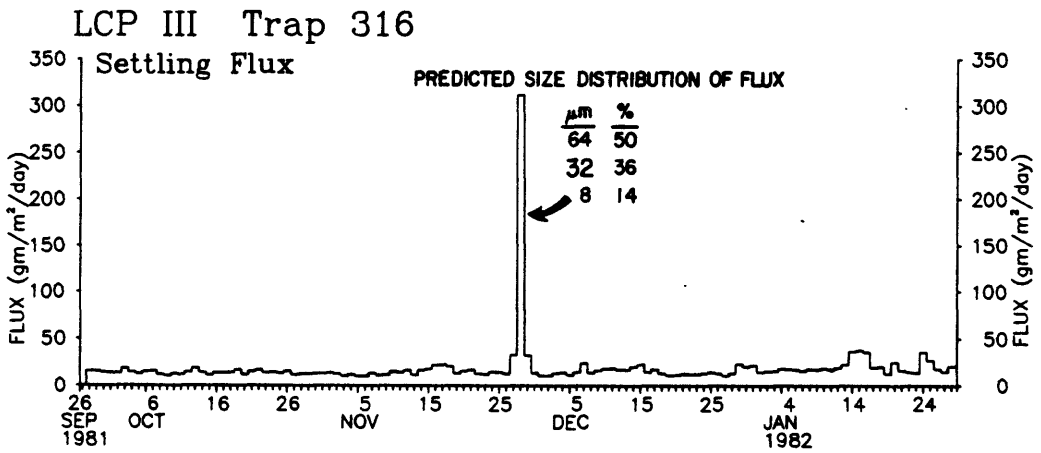
LCP III Trap 316
Settling Flux
PREDICTED SIZE DISTRIBUTION OF FLUX
μm %
64 50
32 36
8 14
FLUX (gm/m²/day)
350
300
250
200
150
100
50
0
26 SEP 1981
6 OCT
16
26
5 NOV
15
25
5 DEC
15
25
4 JAN 1982
14
24

to that of the shelf stations, but the pattern of textural changes in the X-radiographs from the axis are more complicated, probably in response to more frequent resuspension events in the canyon axis. We always hoped for a turbidity flow that would be of sufficient magnitude to leave a unique and identifiable textural record in each trap positioned along the axis, but not so large as to transport all the moorings to the deep sea. In the deployments where two or more moorings were placed along the canyon axis, we have observed no such record.

However, similar textural patterns in the canyon axis can clearly be identified in traps positioned between 20 mab and 120 mab (fig. 6-12). These similar patterns suggest that resuspension events influence at least the lower 120 m of the water column in the canyon axis.

Trace metal concentrations in sediment-trap samples

The concentrations of 12 trace metals were determined in trapped material to help characterize sediment in suspension over the shelf, slope, and canyon (table 6-2). One specific objective of this work was to determine whether or not drilling mud discharged on the continental shelf could be identified in samples from the canyon.

It was possible to address this objective because the sediment-trap deployments for this program included the period before, during, and after exploratory drilling for petroleum resources on Georges Bank. Eight exploratory wells (Vol. 1, fig. 1) were drilled between July 22, 1981 and September 27, 1982. All were classified as dry holes. The location of three wells closest to Lydonia Canyon are plotted in figure 6-1. The traps deployed during this study complimented the Georges Bank Monitoring Program which was designed to determine the environmental effects of offshore drilling (Maciolek-Blake and others, 1985; Bothner and others, 1985).

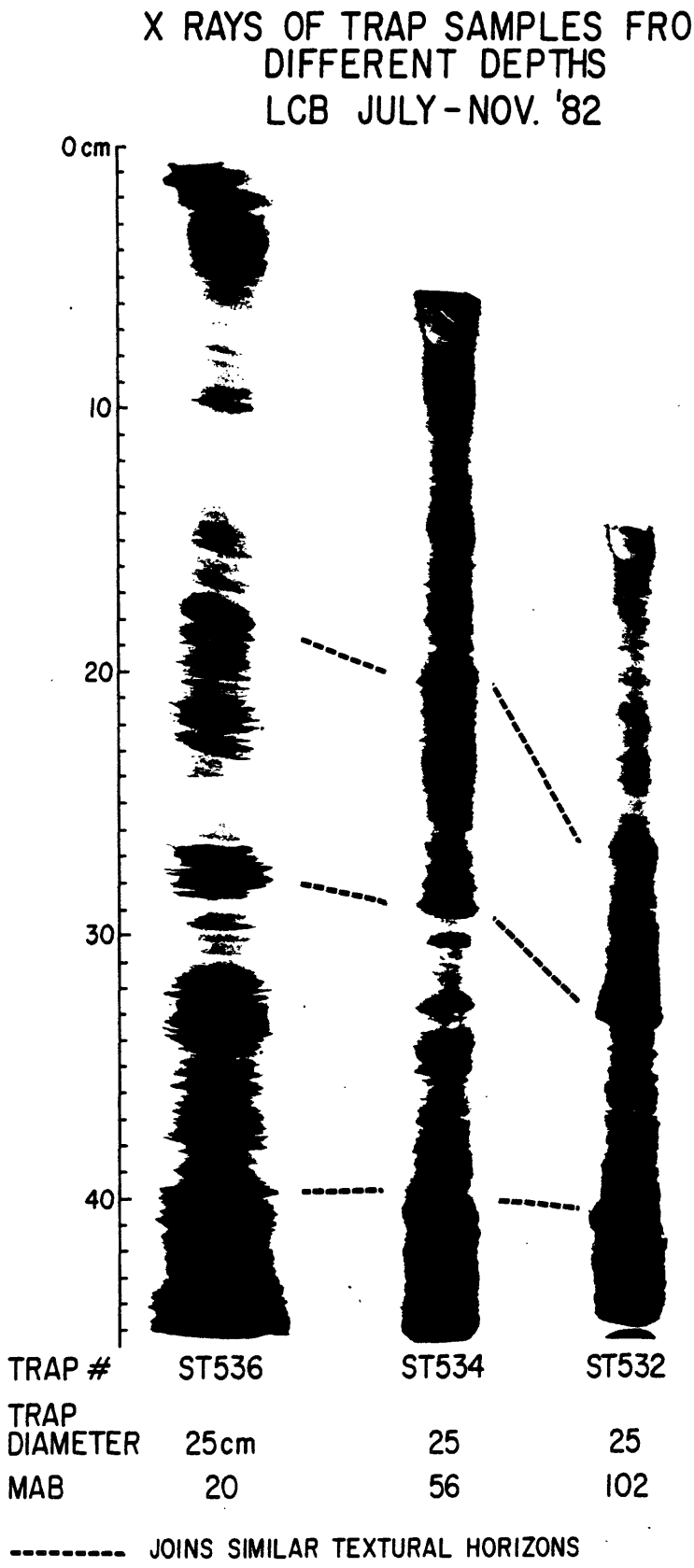

Figure 6-12. X-radiographs (positives) of trap samples from different heights above bottom at station LCB, July-November 1982.

Table 6-2A.-Chemical analyses of sediment-trap samples collected before drilling began

Field number	Lab number	Al (%)	Ba (ppm)	Cd (ppm)	Cr (ppm)	Cu (ppm)	Fe (%)	Hg (ppm)	Mn (ppm)	Ni (ppm)	Pb (ppm)	V (ppm)	Zn (ppm)	OC (%)
ST101-W[1]	W-215131	1.89	170	0.65	550[2]	25	1.44	-	250	19	200[2]	36	133	5.9
ST102-6	W-215132	2.58	160	.83	77	16	1.90	-	400	34	50	95	400	4.3
ST103-20.5	W-215133	3.63	240	.16	74	15	2.31	0.047	520	53	19	110	60	3.2
ST103-40.5	W-215134	3.52	200	.076	71	19	2.34	.043	610	48	32	120	63	3.9
ST103-77.5	W-215135	3.53	210	.076	69	19	2.22	.054	540	52	47	94	110	3.5
ST112-2.2	W-215136	2.33	170	.70	93	10	1.48	.034	380	25	32	61	130	3.2
ST112-6	W-215137	1.89	110	1.3[2]	64	13	1.32	.060	360	22	49	53	410	5.0
ST114-2	W-215138	3.85	310	.053	68	20	2.24	.033	590	45	35	93	71	2.0
ST114-6	W-215139	3.93	320	.038	69	20	2.33	.045	590	53	32	98	58	2.2
ST114-9.8	W-215140	4.13	330	.093	81	20	2.42	.033	610	57	50	110	88	2.3
ST120-11	W-215141	3.11	240	.22	82	47	1.89	.047	470	43	30	84	63	-
ST120-18	W-215142	2.88	240	.16	68	21	1.78	.040	500	39	35	83	79	4.1
T183-GBK-0-26[3]		2.2	230	.10	32	7.5	1.5	-	240	12	24	34	49	2.7
312-425A-W[1]		2.0	760	.87	28	7.8	1.5	-	170	9.5	18	28	68	-
312-427A-W[1]		1.7	247	.56	26	7.3	1.2	-	140	7	18	26	59	-

[1]Whole sample homogenized.
[2]Possibly contaminated.
[3]Depth interval (cm) in sediment-trap sample.

Table 6-2B.-Chemical analyses of sediment-trap samples--Continued

Field number	Lab number	Al (%)	Ba (ppm)	Cd (ppm)	Cr (ppm)	Cu (ppm)	Hg (ppm)	Fe (%)	Mn (ppm)	Ni (ppm)	Pb (ppm)	V (ppm)	Zn (ppm)
Collected after drilling began													
Lydonia Canyon: drilling in progress													
ST222-0-15[3]---W-221248		3.91	304.2	0.08	52.1	10.9	0.05	2.50	348	31.5	32.6	66.3	65.2
ST301-0-4-----W-221249		3.78	266.5	.05	47.7	17.8	.04	2.33	444	27.8	33.3	53.3	64.4
ST403-0-20----W-221285		3.20	260.0	.09	40.0	14.0	.03	1.90	240	18.0	26.0	44.0	46.0
ST536-0-2-----W-221271		3.54	274.2	.16	45.7	16.0	.03	2.06	366	17.1	28.6	41.1	62.8
1 km west of rig: drilling in progress													
ST424-0-4-----W-221251		2.73	1783.6	.39	40.4	11.7	.04	2.14	345	14.3	34.5,	42.8	89.2
ST424-4-7-----W-221252		2.52	1889.1	.38	37.8	8.9	.03	2.14	290	12.6	30.2	45.3	74.3
ST424-7-10----W-221253		2.98	1152.9	.45	40.9	9.4	.04	2.36	310	16.1	27.3	54.5	62.0
ST424-10-15---W-221254		3.11	771.8	.18	40.3	11.1	.03	2.30	357	12.7	30.0	55.3	57.6
ST424-15-17---W-221255		3.34	1224.5	.17	44.5	13.6	.03	2.60	445	18.6	39.6	59.4	73.0
ST424-17-20.5-W-221256		3.40	551.7	.22	51.7	16.4	.03	2.70	481	17.6	64.6	69.3	89.2
6 km east of rig: drilling in progress													
ST426-0-4-----W-221257		2.24	407.0	.51	27.5	10.2	.02	1.73	275	11.2	25.4	34.6	76.3
ST426-6-8-----W-221258		3.09	482.4	.35	44.5	11.1	.04	2.47	346	13.6	30.9	56.9	56.9
ST426-12.5-15-W-221259		3.07	378.1	.45	40.2	11.8	.03	2.48	449	15.4	36.6	59.1	100.4
Rig site: postdrilling													
ST501C-W[1]-----W-221260		2.96	1023.5	1.08	24.2	24.2	.04	2.10	253	5.4	18.3	5.4	121.2
ST502-0-4-----W-221261		3.24	802.7	.30	44.0	23.3	.05	2.46	867	24.6	46.6	62.1	79.0
ST502-4-8-----W-221262		3.48	721.7	.55	43.8	20.6	.10	2.58	760	23.2	46.4	61.9	86.3
ST502-8-12----W-221263		3.42	756.7	.41	43.9	19.5	.07	2.56	622	22.0	43.9	61.0	74.5
ST502-12-14---W-221264		3.18	1070.5	.42	40.0	14.1	.04	2.35	459	15.3	31.8	56.5	69.4
ST505C-W------W-221265		3.49	1070.9	.14	49.8	18.7	.03	2.61	237	27.4	43.6	71.0	72.2
1 km west of rig: postdrilling													
ST506C-W------W-221266		2.30	767.4	.73	26.9	13.6	.03	1.71	230	3.8	30.7	11.5	211.0
ST508C-W------W-221267		3.47	1165.3	.21	48.3	19.8	.04	2.60	198	24.8	44.6	64.5	74.4
ST510C-W------W-221268		1.98	796.0	.03	26.1	10.4	.02	1.46	250	10.4	26.1	23.0	55.3
6 km east of rig: postdrilling													
ST513C-W------W-221269		3.28	625.8	.14	43.2	12.4	.04	2.38	328	11.2	37.2	41.7	76.0
ST515C-W------W-221270		3.28	702.0	.11	45.2	15.8	.03	2.37	226	21.5	33.9	66.7	79.2

Table 6-2C.-Chemical analyses of sediment-trap samples--Continued

<60 µm

Field number	Lab number	Al (%)	Ba (ppm)	Cd (ppm)	Cr (ppm)	Cu (ppm)	Fe (%)	Hg (ppm)	Mn (ppm)	Ni (ppm)	Pb (ppm)	V (ppm)	Zn (ppm)	%<60 (%)
ST103-18-23X	W-226325	4.80	270	0.130	62.0	22.0	3.10	.06	590	48.0	39.0	97.0	120.0	19
ST222-15-20X	W-226326	4.50	280	.300	58.0	23.0	2.70	.00	350	43.0	32.0	89.0	110.0	40
ST301-02-08X	W-226327	4.80	290	.150	64.0	28.0	3.10	.04	570	49.0	37.0	100.0	110.0	25
ST403-00-03X	W-226328	4.50	300	.310	190.0[2]	22.0	2.70	.06	290	48.0	25.0	100.0	110.0	63
ST536-02-04X	W-226330	4.80	350	.170	69.0	22.0	3.20	.04	520	51.0	312.0[2]	100.0	110.0	33
ST537X	W-226331	4.80	380	.280	63.0	34.0	3.20	.04	430	53.0	33.0	100.0	120.0	29

>60 µm

Field number	Lab number	Al (%)	Ba (ppm)	Cd (ppm)	Cr (ppm)	Cu (ppm)	Fe (%)	Hg (ppm)	Mn (ppm)	Ni (ppm)	Pb (ppm)	V (ppm)	Zn (ppm)	%>60 (%)
ST103-18-23Y	W-226333	2.80	240	0.110	44.0	11.0	1.70	.04	310	19.0	17.0	31.0	48.0	81
ST222-15-20Y	W-226334	3.60	250	.320	49.0	17.0	2.40	.03	270	30.0	25.0	62.0	100.0	60
ST301-02-08Y	W-226335	2.90	270	.055	33.0	13.0	1.50	.02	250	15.0	16.0	34.0	43.0	75
ST403-00-03Y	W-226336	2.60	260	.050	760.0[2]	6.0	1.50	.01	200	34.0	13.0	34.0	68.0	37
ST536-02-04Y	W-226338	2.90	270	.096	36.0	11.0	1.60	.03	250	18.0	16.0	31.0	50.0	67
ST537Y	W-226339	2.80	260	.150	33.0	14.0	1.60	.03	280	16.0	15.0	34.0	48.0	71

<60 µm (X) and >60 µm (Y)

Field number	Lab number	Al (%)	Ba (ppm)	Cd (ppm)	Cr (ppm)	Cu (ppm)	Fe (%)	Hg (ppm)	Mn (ppm)	Ni (ppm)	Pb (ppm)	V (ppm)	Zn (ppm)	%>60 (%)
ST424-00-04X	W-226329	3.60	1500	.600	51.0	14.0	2.90	.04	390	33.0	31.0	74.0	170.0	
ST424-00-04Y	W-226337	2.10	870	.380	31.0	10.0	1.50	.03	240	10.0	15.0	31.0	91.0	69
ST001-00-08X	W-226332	3.60	190	.250	54.0	17.0	3.20	.04	350	36.0	30.0	78.0	88.0	
ST001-00-08Y	W-226340	3.00	230	.120	42.0	13.0	2.50	.02	310	24.0	24.0	62.0	55.0	40

[1]W=whole sediment trap homogenized before analysis.
[2]Possibly contaminated.
[3]Depth interval (cm) in sediment-trap sample.

Table 6-2D.-Sediment-trap deployments--Continued

Trap number	Water depth (m)	Trap depth (mab)[1]	Latitude (degrees)	Longitude (degress)	Deployed (Yr Mo Dy)	Recovered (Yr Mo Dy)	General location
ST101	250	20	40°22.95'	67°32.94'	801201	810429	Lydonia Canyon-east slope
ST102	100	26	40°34.21'	67°44.55'	801130	810424	Lydonia Canyon-shelf
ST103	290	20	40°31.55'	67°42.82'	801129	810428	Lydonia Canyon-canyon head
ST112	125	26	40°29.47'	67°48.24'	801129	810425	Lydonia Canyon-shelf west
ST114	1,380	20	40°17.93'	69°39.52'	810120	810428	Lydonia Canyon-canyon axis
ST120	535	300	40°21.18'	67°31.98'	801127	810429	Lydonia Canyon-east slope
T183GBK	64	3	41°02.30'	67°33.49'	791215	800529	Georges Bank shelf-southern flank
312-425A	81	10	40°39.16'	67°46.24'	820202	820611	Lease Block 312-Georges Bank
312-427A	78	10	40°39.76'	67°41.54'	820201	820611	Lease Block 312-Georges Bank

[1]mab=meters above bottom.

Table 6-2E.-Sediment-trap locations and deployment dates--Continued

Trap number	Water depth (m)	Trap depth (mab)[1]	Latitude (degrees)	Longitude (degress)	Deployed (Yr Mo Dy)	Recovered (Yr Mo Dy)	General location
ST001	64	3	41.038333	-67.55817	791215	800525	Georges Bank Shelf-Georges Bank Tripod 183: Predrilling
ST103	290	20	40.52583	-67.71367	801128	810428	Lydonia Canyon axis-Station LCB: Predrilling
ST222	288	50	40.526001	-67.71400	810429	810926	Lydonia Canyon axis: Drilling starts 810724
ST301	290	20	40.526001	-67.71300	810927	820128	Lydonia Canyon axis-Station LCB: Drilling in progress
ST301	290	20	40.526001	-67.71300	810927	820128	Lydonia Canyon axis-Station LCB: Drilling in progress
ST403	300	20	40.525333	-67.71383	820131	820707	Lydonia Canyon axis-Station LCB: Drilling in progress
ST424	81	5	40.652702	-67.77071	820201	820611	1 km west of rig: Drilling in progress
ST426	300	5	40.662704	-67.69229	820201	820611	6 km east of rig: Drilling in progress
ST501	79	25	40.656502	-67.77451	820710	821111	Rig site-Block 312: Postdrilling
ST502	79	20	40.656500	67.76783	820710	821111	Rig site-Block 312: Postdrilling
ST505	79	3	40.656502	-67.76779	820710	821111	Rig site-Block 312: Postdrilling
ST506	79	25	40.657997	-67.77499	820710	821111	1 km west of rig: Postdrilling
ST508	79	10	40.657997	-67.77499	820710	821111	1 km west of rig: Postdrilling
ST510	79	3	40.657997	-67.77499	820710	821111	1 km west of rig: Postdrilling
ST513	77	10	40.662292	-67.69099	820711	821111	6 km east of rig: Postdrilling
ST515	77	3	40.662292	-67.69099	820111	821111	6 km east of rig: Postdrilling
ST536	295	20	40.52480	-67.71321	820708	821111	Lydonia Canyon axis-Station LCB: Drilling in progress
ST537	295	10	40.52483	-67.71317	820708	821111	Lydonia Canyon axis-Station LCB: Drilling in progress

[1]mab=meters above bottom.

As described elsewhere in this chapter, the texture of resuspended sediment is highly variable, largely due to variations in currents and the height above bottom. Concentrations of aluminum in bottom sediments can be considered to be an indicator of the amount of fine sediment on the basis of its high correlation coefficient (r) both with clay (r = .945) and with silt plus clay (r = .969) in surficial sediments from the slope (Bothner and others, 1986; Maciolek and others, 1986). There is also a strong correlation between Al and organic carbon (r = .780) because of the common association between organic carbon and silt plus clay (r = .782; all these correlation coefficients are significant at the 99.9 percent level of confidence). We have calculated the metal-to-Al ratio for each trap sample and determined the mean value for traps in the same geographical/depth area. We then compare trace-metal concentrations of the geographical areas with those of world average shales (Krauskopf, 1967) and plot these values as a comparison to show the level of metal enrichment (fig. 6-13).

For the metals Ba (predrilling), Cu, Fe, Hg, Pb, and V, there is a high degree of uniformity between the metal-to-Al ratios (within two standard deviations) between traps in the different geographical/depth areas. On the basis of metal concentrations, the sources of lithogenic material in traps of different areas cannot be distinguished, which is reasonable because in this area, the surficial sediments from the continental shelf and slope are reworked glacially-derived material from the same general source. The increase in Ba concentration in canyon samples collected after drilling started on the shelf is discussed in the next section.

Zn and Cd ratios in traps at the head of the canyon have unusually high values and high variability, suggesting the possibility of contamination from mooring materials (galvanized chain and linkages in part of the mooring, for example).

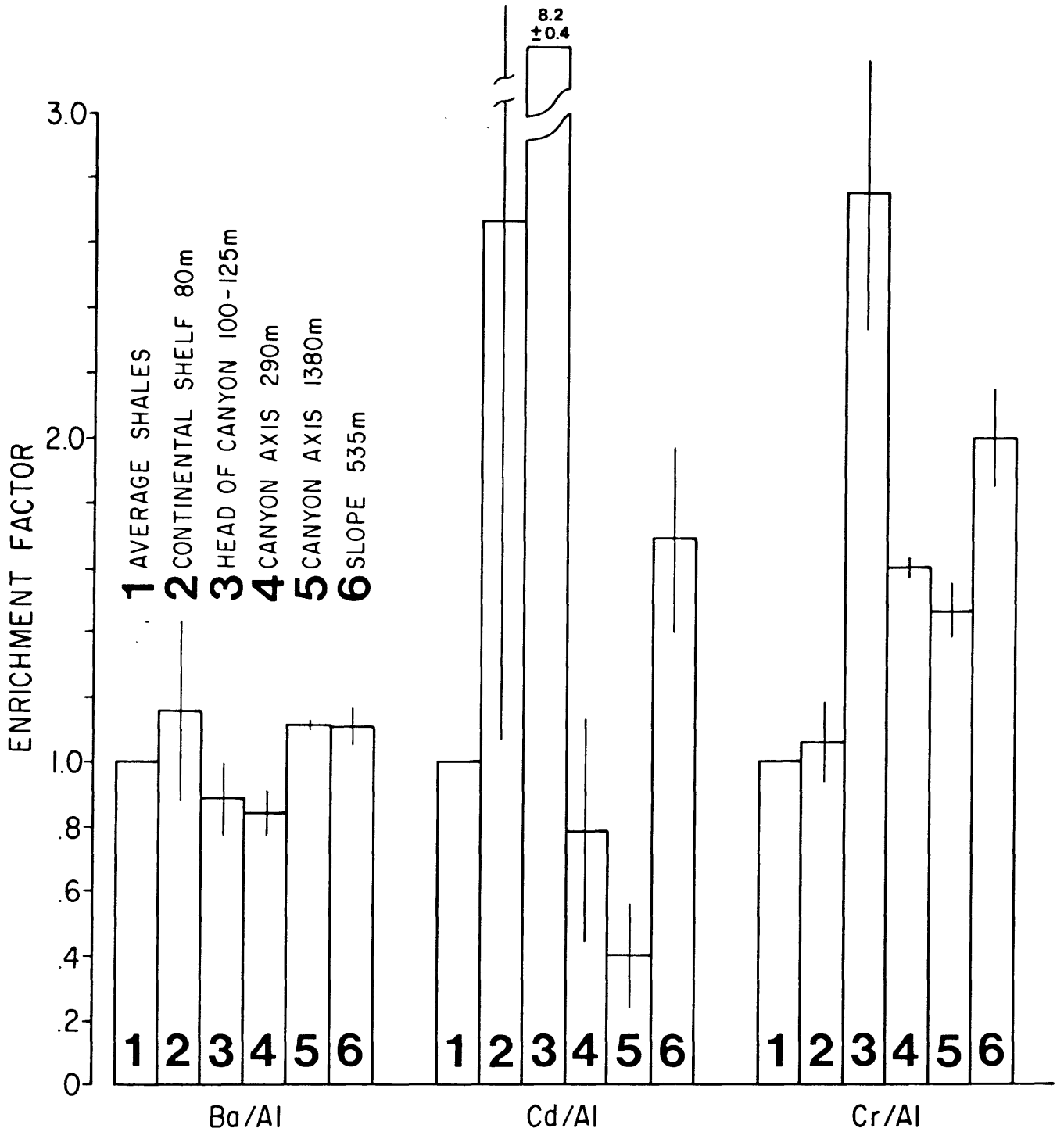

Figure 6-13. A. Histogram showing the average (±1σ) metal to aluminum ratio in sediment trap samples from different geographical/depth areas: calculated as an enrichment factor by using the ratio in world average shales as the comparison value.

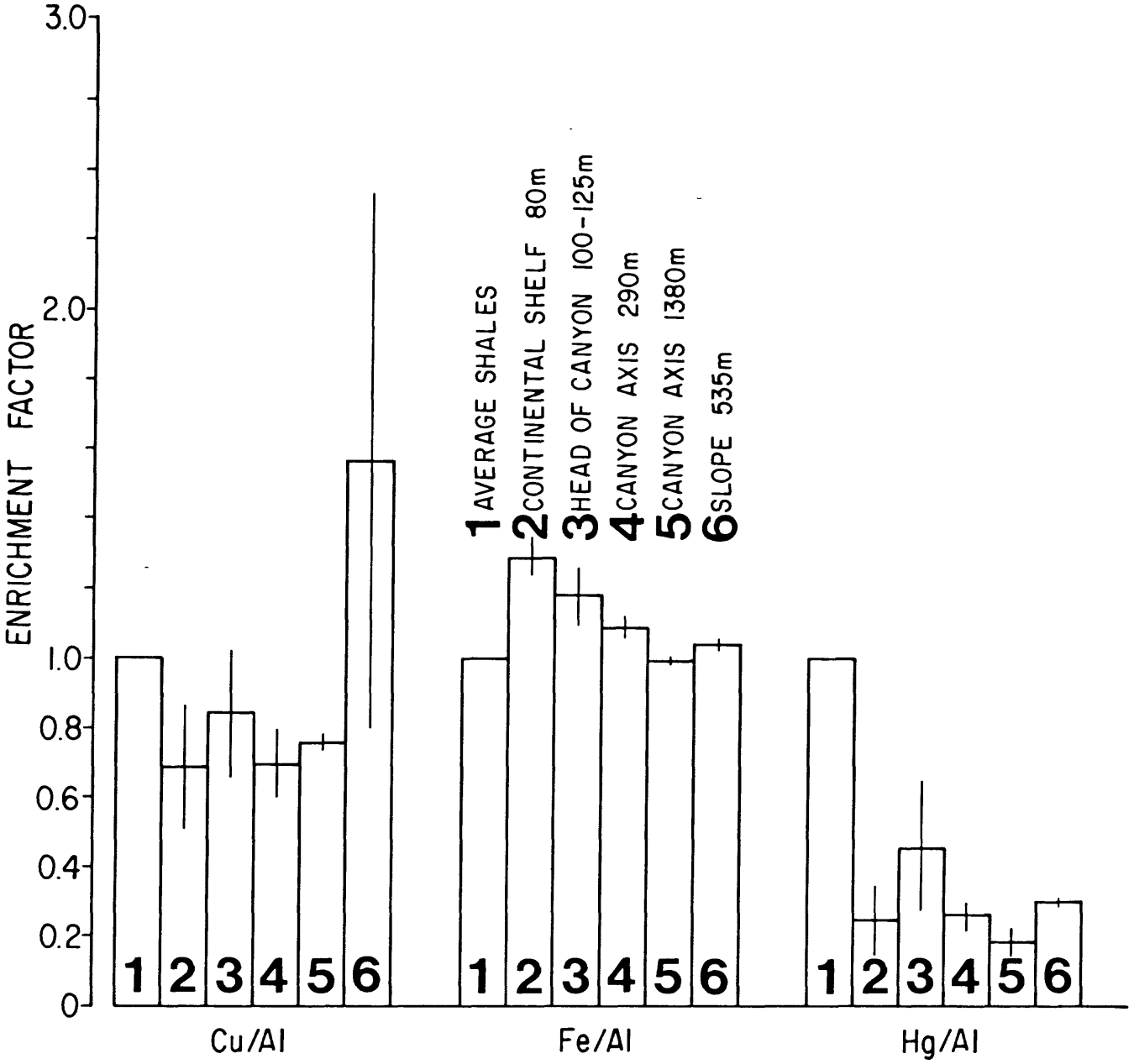

Figure 6-13. B. Histogram showing the average ($\pm 1\sigma$) metal to aluminum ratio in sediment trap samples from different geographical/depth areas: calculated as an enrichment factor by using the ratio in world average shales as the comparison value.

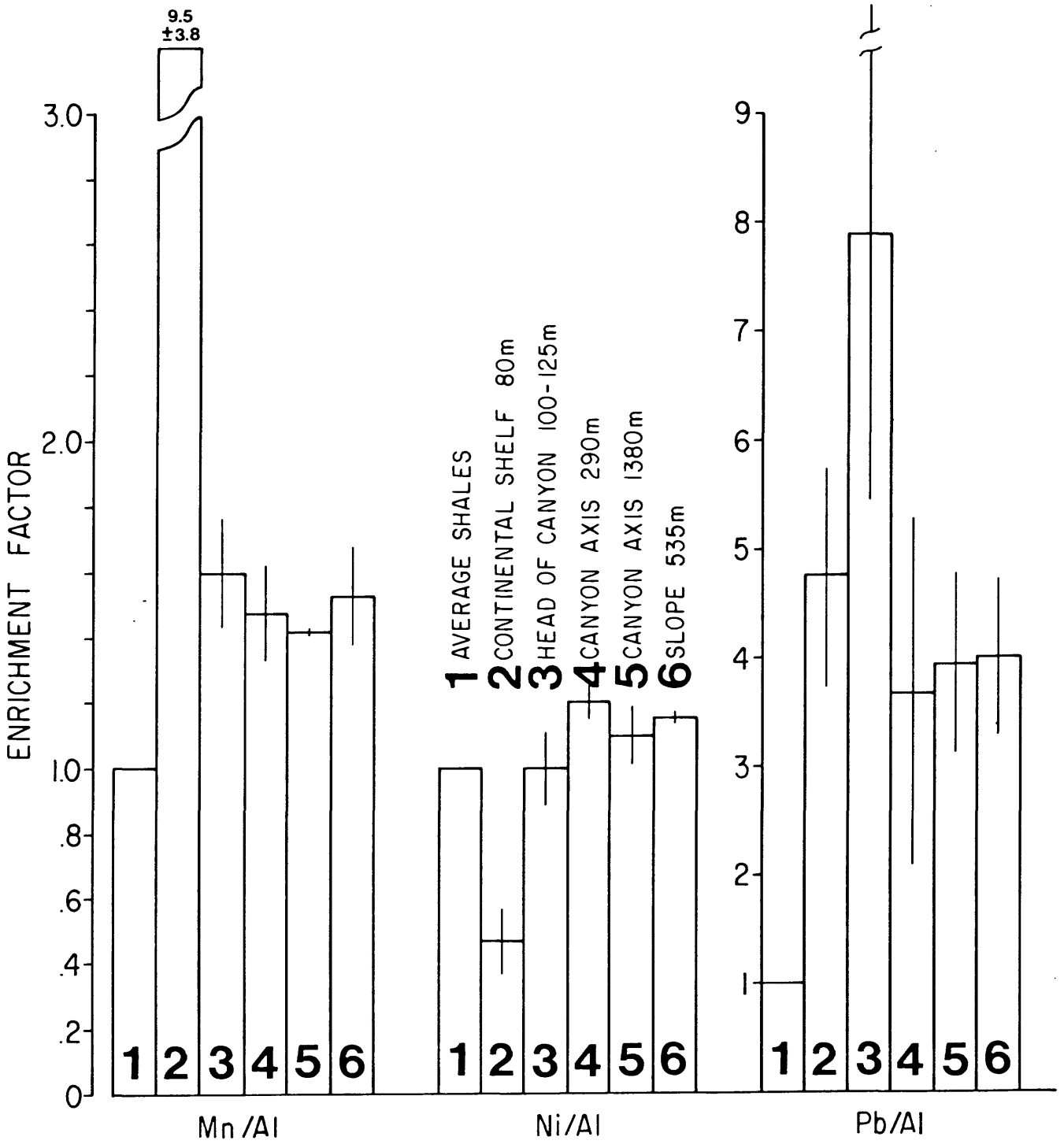

Figure 6-13. C. Histogram showing the average (±1σ) metal to aluminum ratio in sediment trap samples from different geographical/depth areas: calculated as an enrichment factor by using the ratio in world average shales as the comparison value.

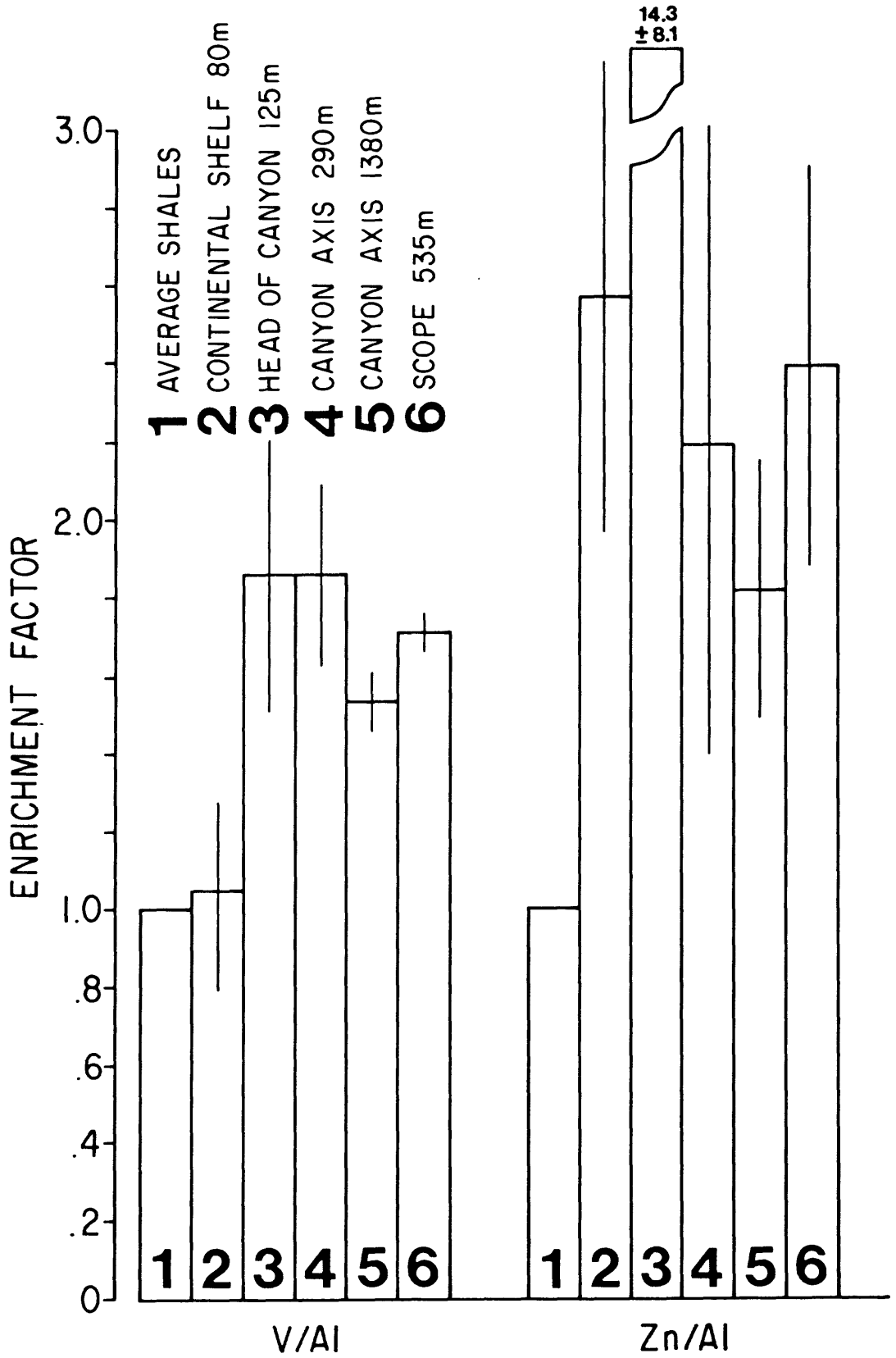

Figure 6-13. D. Histogram showing the average ($\pm 1\sigma$) metal to aluminum ratio in sediment trap samples from different geographical/ depth areas: calculated as an enrichment factor by using the ratio in world average shales as the comparison value.

The sediment trap samples from the continental shelf (table 6-2a) have a higher Mn concentration and much higher enrichment factors than those observed at other trap locations. This is probably related to the occurrence of micromanganese nodules in the bottom sediments in the same area of the shelf as the trap moorings (Poppe and others, 1984). The data suggest that Mn concentrations could serve as a tracer element for resuspended sediment on Georges Bank in a synoptic study of suspended matter in the water column.

At all the trap locations, the Pb enrichment factors are greater than 3.5 (fig. 6-13) compared to world average shales. This level of enrichment for Pb is considerably higher than the enrichment of the other metals (including Zn if one high value is omitted). Pb is also the only metal (of the 12 analyzed here) that is of higher concentration in surficial bottom sediments of the continental slope and muddy areas of the continental shelf than in deeper (>20 cm) sediments (Bothner and others, 1981; Bothner and others, 1986). We interpret the higher concentrations in the surface sediments and in the sediment trap samples to result from anthropogenic discharges of lead to coastal waters and the atmosphere.

Sediment sources

There is geologic evidence indicating that the continental shelf is the source of modern sediments accumulating in the canyons. Valentine and others (1984) have observed bed forms on the walls of Oceanographer Canyon, which suggest transport and entrapment of shelf sediments by this canyon. Twichell (1983) mapped the upper reaches of Lydonia Canyon using high-resolution seismic-reflection and sidescan-sonar techniques. He found Holocene sediments as much as 25 m thick in a distribution pattern that suggested that the shelf was the primary source of sediment. The exact age of this accumulation within

the Holocene and the question of whether or not sediment continues to be deposited at present could not be determined using geophysical techniques.

This study provides geochemical evidence (using Ba concentration data and ^{14}C dating of sediment cores) that material from the continental shelf is entering Lydonia Canyon.

The discharge of fine-grained barite by the drilling operations provided a tracer for the transport of sediments in the Georges Bank area. The results of the Georges Bank Monitoring Program (Bothner and others, 1985) indicate that the Ba enrichment could be detected in bulk sediment (undifferentiated with respect to size) within 6 km of sites of active drilling. In the sediment fraction finer than 60 μm, an increase in the Ba concentrations in sediments was observed to distances as great as 65 km from drilling sites, indicating wide and rapid dispersion.

Elevated concentrations of Ba, found in material collected in sediment traps placed near a well location soon after drilling was completed (table 6-2b), indicated that sediment resuspension was an important mechanism in the redistribution of this Ba (Bothner and others, 1985). The concentration of Ba increased in sediment trap samples (sediment fraction finer than 60 μm) at station LCB (10-50 mab) during the five mooring deployments (fig. 6-14). The increase coincides in time with the beginning of exploratory drilling on Georges Bank. Four wells were completed during the last trap deployment. This group included the two wells closest to mooring station LCB (fig. 6-1). The most intensive drilling activity and a major storm (fig. 6-10) with an initial westward transport (from the rigs toward the canyon) may explain the larger increase in Ba during deployment 5.

During the drilling period, an estimated 5.7×10^6 kg of barite (a major component of drilling mud) was used in drilling operations. Typically more

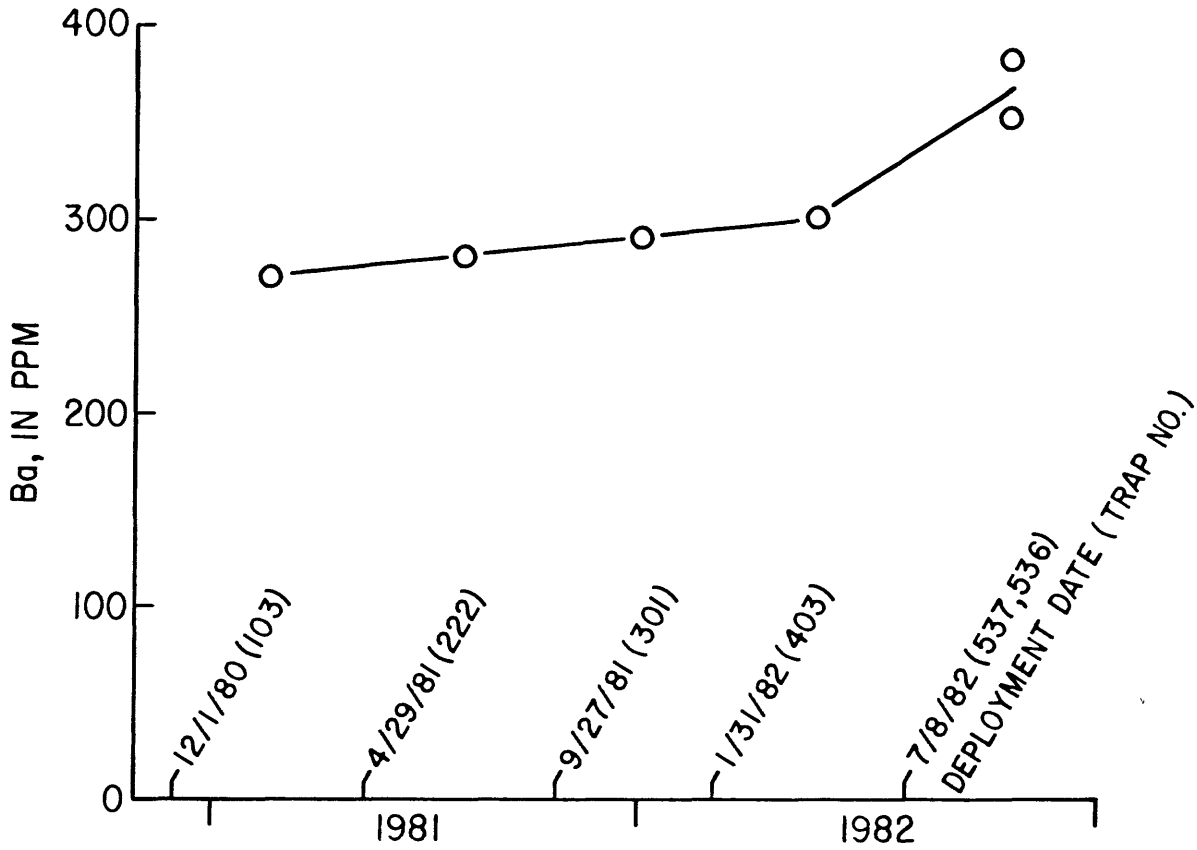

Figure 6-14. Concentrations of barium in the fine fraction of material collected in sediment traps deployed at the head of Lydonia Canyon on different deployment dates. Traps were recovered just prior to the next deployment.

than 50% was lost to formations while drilling or pumped into and sealed in the well before the rig was moved off location (E. P. Danenberger, Minerals Management Service, oral commun. September 21, 1983). The remainder is discharged to the ocean and much of this fraction could be found in the bottom sediments over wide areas of the Bank (Bothner and others, 1985).

It is not possible to compare the relative changes in barium concentrations in the canyon with those on the slope because metal concentrations in the fine fraction of trap samples were determined only on samples from the canyon axis station LCB. Some transport of barium rich particles from the drilling sites to the slope was hypothesized on the basis of increasing concentrations of Ba in bottom sediment from the slope east of Lydonia Canyon at 145 m water depth (Bothner and others, 1983).

The increase in Ba with time in the sediment-trap material from the canyon axis is significant because it is direct evidence that particulates introduced to Georges Bank are transported into the canyon. The Ba signal is observable only after separation and analysis of the fine fraction. No similiar increase was observed in the concentrations of other heavy metals analyzed in the fine fraction. No stress to organisms is expected from these small increases in Ba. Transport of contaminants from the Bank to the canyons could potentially pose an environmental problem, however, depending on the nature and the volume of the contaminant discharged.

The hypothesis that Lydonia Canyon is accumulating sediments eroded from the adjacent continental shelf is supported by ^{14}C profiles from 2 piston cores from the head of the canyon. The analyses were made on total organic carbon contained in sediments composed of muddy sand. The results (table 6-3 and fig. 6-15) indicate a fairly linear increase in age with increasing sediment depth. A linear regession for the data points indicates

Table 6-3. ^{14}C ages determined on total organic carbon in sediment.

Lab No.	Field No. Position Water Depth (m)	Sediment Depth (cm)	^{14}C age (years B.P.)
W-5479	OC124-7A 40°32.4 67°43.4 145 m	0-2	920±230
W-5483	OC122-46 40°27.1 67°44.2 161 m	0-2	800±250
W-5464	OC122-43	54.5-59.5	1880±300
W-5499	40°32.4	112.5-117.5	3150±500
W-5517	67°44.3	184-188.5	3230±300
W-5551	143 m	248.5-253	4540±300
W-5558		309-313	5600±350
W-5465	OC122-45	56-61	2200±500
W-5505	40°32.3	129-134	4550±300
W-5547	67°43.4	211.5-217.5	5440±300
W-5555	148 m	293.5-298	7920±600
W-5561		370.5-375	7640±800

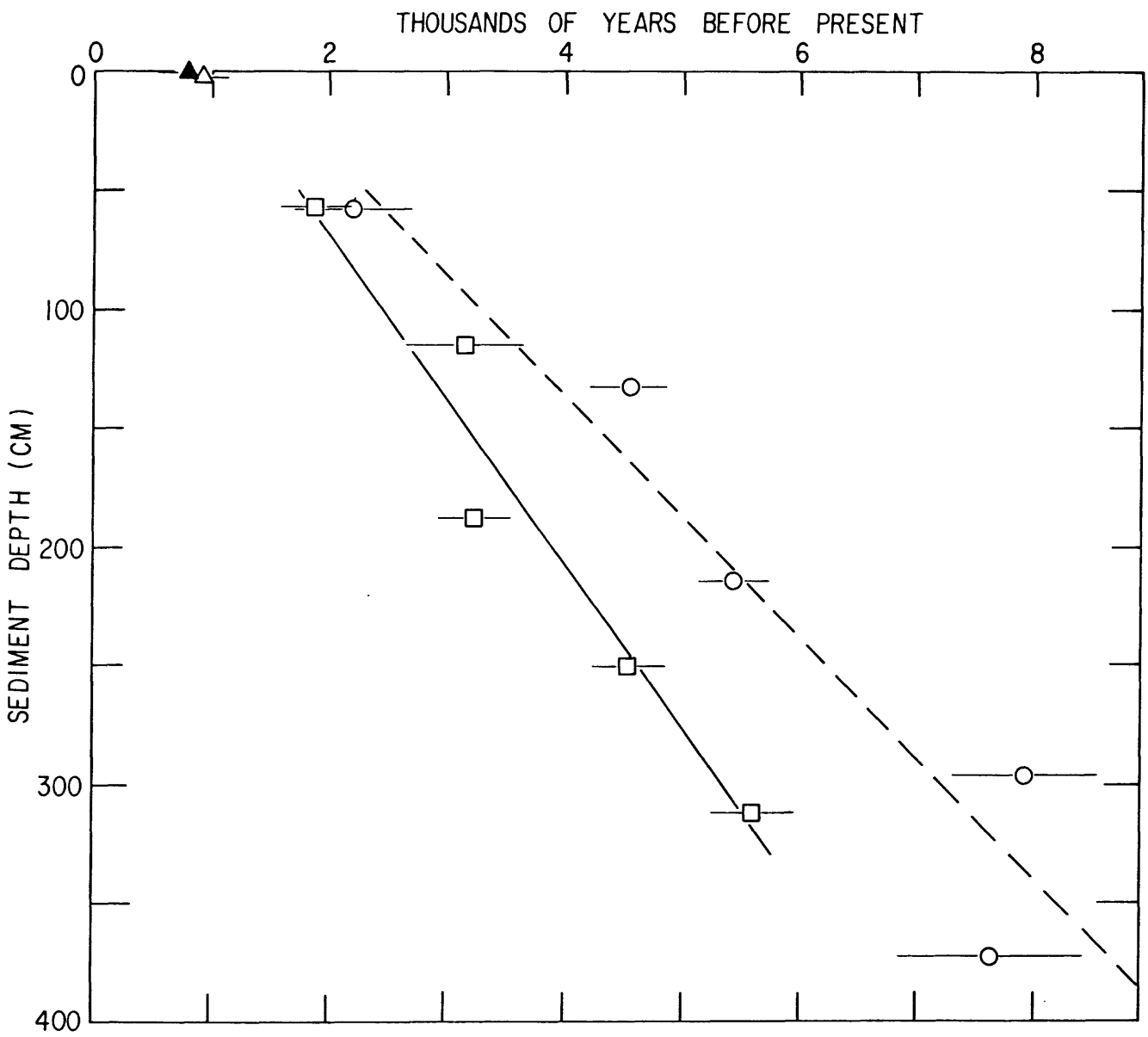

Figure 6-15. ^{14}C age of organic carbon in marine sediments from the head of Lydonia.

▲ = Grab OC122-46, △ = Grab OC124-7A, □ = piston core OC122-43, ○ = piston core OC122-45. Linear regressions indicate accumulation rates of 51 cm/1000 years for OC122-45 and 69 cm/1000 years for OC122-43.

sedimentation rates of 69 and 51 cm/1,000 years for cores 43 and 45, (fig. 6-15), respectively, (correlation coefficient >0.95 for both cores). Taking the average of 60 cm/1,000 years and an assumed uniform dry bulk density of 1.25 g/cc, the mass accumulation rate would be about 2 $g/m^2/day$.

The average resuspended sediment fluxes at LCB and at LCA are higher than the long-term sedimentation rate by factors of 43 and 8, respectively. This indicates that the sediment in the canyons is recycled through the lower water column (resuspended) many times before it is permanently or semi-permanently incorporated into the accumulating sequence of sediments.

The potential of pollutant adsorption by resuspended sediments

The tendency for surfaces of resuspended sediments to act as adsorption sites for certain pollutants in the water column has been well established (Karickoff and others, 1979; Solomons and Forstner, 1984; Forstner and Whittmann, 1979). Given the more frequent and intense resuspension of bottom sediments at stations in the canyon axis compared to stations outside the canyon, one might expect more intense scavenging mechanisms and a higher potential affect of pollutants on benthic organisms living in the canyon.

The distributions of the radioactive isotopes ^{210}Pb and $^{239,240}Pu$ in water and sediments have been effectively used to study the nature and rates of marine geochemical processes (Goldberg and Bruland, 1974; Bacon and others, 1980). These isotopes serve as analogs of sediment reactive pollutants. Their inventories, specific activities (defined as activity per unit weight of dry sediment), and depth distributions can yield important information about pollutant adsorption by sediments and the rates of sediment mixing. In order to address these specific issues, we measured the concentrations and calculated the inventories of ^{210}Pb and $^{239,240}Pu$ in one box core from the

axis of Lydonia Canyon and one box core from the open slope. Both coring locations were positioned at about 630-m water depth.

^{210}Pb is a naturally occurring isotope in the uranium decay series with a half life of 22.3 years and an atmospheric depositon rate to surface waters of the continental margin of about 0.8 dpm/cm^2/yr (Turekian, referenced in Anderson and others, submitted). Once introduced into coastal waters, ^{210}Pb is quickly scavenged by particulate matter (Bacon and others, 1980; Benninger and others, 1975) and may settle to the bottom, depending on the dynamics of the environment. In addition to the atmospheric source, there is a contribution of ^{210}Pb of about 0.01 dpm/cm^2/yr from radioactive decay of ^{226}Ra in slope waters at this depth (Anderson and others, submitted). If this combined flux reaches the bottom sediment and achieves steady-state concentrations, the total inventory of excess ^{210}Pb (defined as the activity above the level supported by ^{226}Ra in sediments) would be about 28 dpm/cm^2. Areas having higher inventories suggest preferential accumulation of ^{210}Pb, either supplied with particulates advected from other areas or transported in solution and more effectively scavenged from the water column by the bottom sediments. Lower inventories imply bypassing of ^{210}Pb or erosion of sediment.

Pu isotopes have been introduced to the oceans largely by atmospheric testing of nuclear weapons. The maximum input occurred about 1962 (based on ^{90}Sr deposition; Hardy, 1977). The Pu inventories in marine sediments are variable depending on the intensity of scavenging processes and the availability of Pu. In one survey of marine sediments off the New England coast, inventories ranged from 4.5 to 0.2 mCi/km^2 (Livingston and Bowen, 1979).

The inventories of both isotopes are about 2.5 times higher in the canyon axis than at the open slope location 63 km to the east (table 6-4A,B). The

Table 6-4A. Sediment Radionuclide Distributions

1. Lydonia Canyon axis, Core 4769, 40°23.87'N, 67°40.13'W
627 m water depth, May 31, 1980

SEDIMENT DEPTH cm	WATER CONTENT %	TOTAL ^{210}Pb dpm/g	EXCESS ^{210}Pb dpm/g	$^{239,240}Pu$ dpm/kg
0-1	36.2	-	-	74 ±3.7
2	31.2	33.7±1.4	32.6±1.4	
3	29.7	25.6±1.1	24.5±1.1	55 ±2.1
4	31.1	-	-	-
5	30.9	22.5±0.1	21.4±0.1	61 ±3.0
6	30.7	-	-	65 ±3.0
7	30.0	11.4±0.4	10.3±0.4	46 ±2.3
8	29.6	-	-	33 ±2.0
9	29.1	8.1±0.3	7.0±0.3	-
10	29.4	-	-	-
11	29.5	6.1±0.2	5.0±0.2	18.5±1.1
12	30.0	6.6±0.2	5.5±0.2	-
13	29.4	4.8±0.2	3.7±0.2	-
14	29.0	-	-	-
15	29.0	3.7±0.1	2.6±0.1	5.3±0.7
16	27.7	-	-	-
17	28.9	3.3±0.1	2.2±0.1	-
18	27.8	-	-	4.5±0.8
19	27.0	3.4±0.1	2.3±0.1	-
20	27.4	-	-	3.1±0.5
21	26.8	3.0±0.1	1.9±0.1	-
22	25.8	-	-	-
23	26.5	1.9±0.1	0.8±0.1	2.0±0.4
24	25.2	-	-	-
25	26.1	1.7±0.1	0.6±0.1	1.6±0.3

Inventory	223 dpm/g	3.2 mCi/km^2
Mixing coefficients cm^2/yr	.92	1.1
Range of 90% confidence	.76 - 1.1	.83 - 1.5

Table 6-4B. Sediment Radionuclide Distributions (continued)

2. Continental Slope, Core 4772, 40°09.43'N, 68°20.12'W, 630 m water depth, May 31, 1980

SEDIMENT DEPTH cm	WATER CONTENT %	TOTAL ^{210}Pb dpm/g	EXCESS ^{210}Pb dpm/g	$^{239,240}Pu$ dpm/kg
0-1	31.8	-	-	43 ±2.2
2	30 7	9.3±0.3	8.1±0.3	38 ±1.
3	29.8	6.8±0.2	7.6±0.3	33 ±2.3
4	29.6	8.9±0.3	7.7±0.3	-
5	29.4	-	-	21.2±1.3
6	28.9	5.6±0.2	4.4±0.2	-
7	29.3	-	-	12 ±0.9
8	29.5	4.7±0.2	3.5±0.2	-
9	28.9	-	-	8.3±0.8
10	29.0	3.5±0.1	2.3±0.2	4.4±0.5
11	28.8	2.5±0.1	1.3±0.1	-
12	28.7	2.4±0.1	1.2±0.1	3.1±0.5
13	28.3	-	-	-
14	27.7	4.9±0.2	3.7±0.2	7.8±0.7
15	28.2	-	-	-
16	28.7	5.0±0.2	3.8±0.2	-
17	28.9	1.1±0.1	0.1±0.1	-
18	26.6	1.3±0.1	0.1±0.1	-

Inventory	86 dpm/cm^2	1.3 mCi/km^2
Mixing coefficient cm^2/yr	.75	.64
Range of confidence	.55 - 1.1	.56 - .75

specific activities of both ^{210}Pb and $^{239,240}Pu$ are also higher in the axis of Lydonia Canyon. Higher specific activities are expected with increasing content of fine sediment (silts and clays). If normalized to the same grain size (table 6-5), the specific activity of sediments in the canyon axis would have an even higher relative value than the slope.

It is not likely that the lower inventories and specific activities at the slope location are a result of the loss of surficial material during sampling. At our slope location, the $^{239,240}Pu$ inventory is 1.3 mCi/km^2. Livingston and Bowen (1979) found the same value at 760-m water depth in the same region. The appearance of the sample at the time of recovery also suggested no loss of the surface material.

The inventory of ^{210}Pb at the slope station is 85 dpm/g, within the range of 50 to 91 dpm/g found on the slope off the northeastern U.S. between 500- and 1,250-m water depth by Buesseler and others (1985). The core from the canyon axis has a ^{210}Pb inventory of 223 dpm/cm^2; considerably higher than the range measured in the "mud patch" southwest of Georges Bank (51-94 dpm/cm^2) by Santschi and others (1981) and Bothner and others (1981) and higher than the range measured in the Hudson Shelf Channel (53-140 dpm/cm^2) by Benninger and Krishnaswami (1981).

The inventories and specific activities of these isotopes suggest that the sediments in the canyon axis are a more effective sink for pollutants in the water column than are sediments on the open slope. These data are consistent with the hypothesis that the higher flux of resuspended sediments results in more frequent and more intense scavenging of sediment reactive constituents from the water column. The higher specific activities in the canyon axis support the hypothesis that local scavenging rather than sediment focusing accounts for the relatively higher inventories of isotopes in Lydonia Canyon.

Table 6-5. - Textural analysis of box cores. [Values accurate to two significant figures]

Field no.	Depth (cm)	Gravel (%)	Sand (%)	Silt (%)	Clay (%)	Mean (ϕ)	Median (ϕ)	St. dev. (ϕ)	Very coarse sand (%)	Coarse sand (%)	Medium sand (%)	Fine sand (%)	Very fine sand (%)	Silt				Clay		
														5phi	6phi	7phi	8phi	9phi	10phi	>10phi
4769	0-1	0.00	62.37	28.62	9.00	4.31	3.60	2.16	0.00	0.00	6.24	24.95	31.18	7.80	8.69	7.05	5.09	4.00	3.10	1.90
4769	1-2	.00	68.41	22.78	8.81	4.12	3.40	2.16	.00	.00	6.84	30.79	30.78	5.27	6.58	5.87	5.06	4.32	2.91	1.58
4769	2-3	.00	68.53	21.99	9.47	4.03	3.23	2.36	.00	.00	13.71	30.84	23.98	4.54	7.07	5.61	4.78	3.46	2.55	3.46
4769	4-5	.00	63.82	27.53	8.61	4.21	3.46	2.13	.00	.00	3.19	35.10	25.53	8.40	8.10	6.15	4.88	4.02	2.75	1.84
4769	5-6	.00	62.67	28.34	8.96	4.09	3.33	2.26	.00	.00	12.53	31.34	18.80	8.51	8.25	6.61	4.96	4.41	3.06	1.49
4769	6-7	.00	61.81	27.19	11.00	4.19	3.04	2.43	.00	.00	12.36	37.09	12.36	5.65	8.52	6.83	6.19	5.42	3.71	1.87
4769	7-8	.00	65.25	25.02	9.73	4.18	3.33	2.25	.00	.00	6.53	35.88	22.84	5.70	7.75	6.29	5.28	4.69	3.37	1.67
4769	8-9	.00	66.33	23.03	10.64	4.13	3.30	2.37	.00	.00	13.27	29.85	23.21	4.35	6.83	6.20	5.65	5.15	3.64	1.85
4769	9-10	.00	61.99	26.27	11.75	4.40	3.52	2.35	.00	.00	6.20	30.99	24.80	5.13	7.83	7.03	6.27	5.74	4.03	1.98
4769	10-11	.00	60.51	27.92	11.53	4.49	3.57	2.28	.00	.00	.00	36.30	24.21	5.53	9.16	7.03	6.20	5.45	3.87	2.21
4769	11-12	.00	62.25	29.26	8.49	3.96	2.86	2.30	.00	.00	12.45	43.57	6.23	8.49	9.33	6.60	4.84	4.04	2.83	1.62
4769	12-13	.00	63.10	25.87	11.00	4.23	3.31	2.37	.00	.00	9.46	34.71	18.93	5.90	7.64	6.57	5.76	5.31	3.65	2.03
4769	13-14	.00	69.87	19.88	10.27	4.15	3.43	2.31	.00	.00	13.97	20.97	34.93	1.75	5.88	5.93	6.33	5.36	3.40	1.51
4769	14-15	.00	59.80	29.03	11.18	4.15	2.97	2.58	.00	.00	23.92	26.91	8.97	5.06	8.12	8.41	7.43	5.75	3.70	1.73
4769	15-16	.00	61.30	25.89	12.81	4.29	3.08	2.62	.00	.00	15.32	33.72	12.26	4.10	8.32	7.16	6.31	5.03	3.56	4.22
4769	16-17	.00	63.96	25.77	10.27	4.13	3.27	2.44	.00	.00	19.19	25.58	19.19	3.74	7.83	7.60	6.60	5.22	3.39	1.66
4769	17-18	.00	64.25	26.28	9.48	4.23	3.45	2.27	.00	.00	9.64	28.91	25.70	5.29	7.33	7.25	6.40	4.87	3.11	1.50
4769	18-19	.00	64.96	25.30	9.74	4.26	3.49	2.22	.00	.00	6.50	29.23	29.23	5.96	7.15	6.51	5.68	4.87	3.19	1.68
4769	19-20	.00	66.47	26.66	6.87	3.82	2.92	2.16	.00	.00	13.29	39.89	13.29	8.08	8.65	5.67	4.26	3.18	2.35	1.34
4769	20-21	.00	63.21	27.74	9.05	4.24	3.40	2.18	.00	.00	3.16	37.93	22.12	7.21	7.65	6.88	6.00	4.71	2.91	1.43
4769	21-22	.00	67.48	25.92	6.57	3.68	2.87	2.23	.00	.00	23.62	30.36	13.50	8.62	7.22	5.95	4.13	2.92	2.05	1.60
4769	22-23	.00	65.42	22.93	11.62	4.20	3.41	2.47	.00	.00	19.63	19.62	26.17	3.04	6.19	6.64	7.06	6.36	3.77	1.49
4769	23-24	.00	67.72	25.24	7.04	3.87	3.13	2.09	.00	.00	10.16	37.25	20.31	8.49	8.14	5.13	3.48	3.23	2.39	1.42
4769	24-25	.00	66.50	25.53	8.01	3.82	2.91	2.24	.00	.00	16.63	36.57	13.30	8.14	8.01	5.32	4.06	3.85	2.81	1.34
4772	0-1	.00	53.49	35.26	11.26	4.67	3.89	2.12	.00	.00	.00	21.40	32.09	14.51	8.65	6.37	5.72	5.54	3.58	2.14
4772	1-2	.00	52.27	34.94	12.79	4.72	3.91	2.22	.00	.00	.00	26.13	26.14	13.12	8.74	6.63	6.45	6.54	4.15	2.10
4772	2-3	.00	49.02	35.63	15.34	5.08	4.08	2.20	.00	.00	.00	9.80	39.22	12.04	9.17	7.19	7.24	7.59	5.25	2.50
4772	3-4	.00	44.68	43.15	12.12	4.88	4.25	2.06	.00	.00	.00	13.40	31.28	21.57	9.79	6.15	5.64	5.81	4.09	2.21
4772	4-5	.00	47.13	39.66	13.22	4.93	4.17	2.12	.00	.00	.00	14.14	32.99	16.44	9.73	6.71	6.77	6.88	4.38	1.96
4772	5-6	.00	45.80	39.95	14.20	4.98	4.34	2.26	.00	.00	.00	22.90	22.90	12.47	11.87	8.13	7.48	7.15	4.72	2.33
4772	6-7	.00	44.57	40.97	14.47	5.11	4.41	2.18	.00	.00	.00	13.37	31.20	13.30	11.09	8.37	8.20	7.54	4.77	2.16
4772	7-8	.00	45.34	39.03	15.58	5.08	4.36	2.29	.00	.00	.00	18.13	27.21	13.12	11.31	7.54	7.06	7.38	4.75	3.45
4772	8-9	.00	46.78	43.38	9.79	4.73	4.20	2.06	.00	.00	.00	23.39	23.39	16.34	13.09	7.82	6.12	4.85	3.14	1.81
4772	9-10	.00	43.61	41.45	14.89	5.19	4.47	2.17	.00	.00	.00	10.90	32.71	13.59	10.32	8.40	9.14	8.06	4.68	2.14
4772	10-11	.00	46.98	40.24	12.72	4.86	4.20	2.20	.00	.00	.00	23.49	23.49	15.32	9.87	7.10	7.95	6.84	4.03	1.86
4772	11-12	.00	45.72	40.33	13.90	4.96	4.29	2.25	.00	.00	.00	22.86	22.86	14.87	9.23	7.98	8.25	7.27	4.51	2.12
4772	12-13	.00	44.85	41.03	14.06	5.02	4.34	2.22	.00	.00	2.24	13.46	29.15	15.33	9.93	7.50	8.27	7.12	4.63	2.31
4772	13-14	.00	44.74	42.39	12.82	4.98	4.31	2.10	.00	.00	.00	13.42	31.32	17.13	10.55	7.63	7.07	6.58	4.20	2.04
4772	14-15	.00	44.93	44.33	10.68	4.76	4.25	2.08	.00	.00	.00	22.46	22.47	20.10	11.23	7.05	5.95	5.18	3.47	2.03
4772	15-16	.00	44.68	40.99	14.33	5.13	4.39	2.12	.00	.00	.00	8.94	35.74	13.72	12.01	7.91	7.35	7.36	4.76	2.21
4772	16-17	.00	47.75	39.45	12.75	4.96	4.17	2.12	.00	.00	.00	14.32	33.43	13.17	11.39	7.57	7.32	6.48	4.33	1.94
4772	17-18	.00	48.14	38.79	13.07	4.99	4.16	2.15	.00	.00	.00	14.44	33.70	11.93	11.20	7.93	7.73	6.59	4.30	2.18

We have made a preliminary estimate of the rates of sediment mixing at these two locations by using a mixing model described by Anderson and others (submitted). The model mathematically treats long-term effects of bioturbation as diffusion within a single mixed layer over the sediment depth range having measurable Pu and excess ^{210}Pb. The effects of sediment accumulation are ignored in this calculation, a simplification that is justified by the observation that Pu has penetrated to the same depth as detectable excess ^{210}Pb. In the absence of significant mixing, levels of ^{210}Pb near the detection limit would occur in 100 year-old sediment, and Pu activity would be nil well above this horizon. Values of ^{210}Pb and Pu significantly higher than the general trend of decreasing activity with depth (probably due to small-scale burrowing) were excluded from the calculation. The results of this model calculation are that mixing coefficients (table 6-4) and therefore the rate of sediment mixing is similar on the continental slope and in the canyon axis at the same water depth.

This is an interesting result which should be tested at other locations inside and outside Lydonia Canyon. Ideal cores to examine are those collected during the MMS-supported program "Study of Biological Processes on the U.S. North Atlantic Slope and Rise" (Maciolek and others, 1986). At the completion of this study, seasonal data will be available on the composition and abundance of benthic infauna for a two year period.

CONCLUSIONS

1. At all locations occupied during this study, the rates of collection by sediment traps greatly increases as the distance between the trap and the sea floor decreases. This gradient indicates that most of the sediment collected in near-bottom traps was resuspended. Similar gradients have been observed in other East Coast canyons (Gardner, 1983).

Near-bottom traps in the axis of Oceanographer Canyon collected at a higher rate than those at a comparable depth in Lydonia Canyon, reflecting the higher current speeds in Oceanographer Canyon. Within the Lydonia Canyon area, highest fluxes of sediment were measured at 300-m water depth in the axis of the canyon. At this location, the same resuspension events could be identified in traps within the lower 120 m of the water column. Intermediate rates were collected in near-bottom traps from the head of the canyon (100 to 125-m water depth) and from the axis of the canyon at 1,500 m. Lowest fluxes of resuspended sediments were measured on the continental slope.

2. The variability in the sediment flux can be evaluated on different time scales. At 300-m water depth in the canyon axis, the flux over a time frame of 4-5 months varies by a factor of 2 and can be correlated with the number of major storms on the continental shelf. The variability resulting from individual storms was at least an order of magnitude greater than during quiet periods. This was determined using dated horizons in the trap sample, bulk X-rays which identify layers of coarse sediment in the trap sample, and a numerical model (chapter 3) which predicts the vertical flux and textural composition of resuspended sediment on the basis of bottom stress. Predictions by the model agreed very well with the date and texture of coarse layers in trap samples.

3. Trace metal-to-aluminum concentration ratios (which normalize for textural variability) for Ba (predrilling), Cu, Fe, Hg, Ni, Pb, and V are similar in the trapped sediment from different geographical/depth areas included in this study. The similar metal ratios support the widely held hypothesis that the surficial sediments on the continental shelf and slope are reworked glacially-derived material from the same general continental source. An enrichment of Mn in trapped material from the continental shelf, compared to the other areas, is probably related to local concentrations of micro-manganese nodules found locally in shelf sediments. Pb/Al ratios in all of the geographical/depth areas are more than 3.5 times higher than the ratio in world average shales. This finding is in agreement with the enrichments that were found in the slope sediments and which have been ascribed to the use of lead in gasoline.

4. New evidence for transport of continental shelf material into Lydonia Canyon is provided by two geochemical measurements. First, accumulation rates of about 60 cm/1,000 years were determined on piston cores recovered from the head of Lydonia Canyon. The rapid rates of accumulation, the proximity to the shelf, the along-shelf current pattern, and the seismic-reflection data of this area all support the hypothesis that shelf sediments are being transported into the head of Lydonia Canyon.

Second, Ba concentrations increased by 40% in the fine fraction (<60 μm) of trapped sediment from the canyon axis during the 2-year period of these deployments. The increase is attributed to the transport of Ba-rich drilling mud from the exploratory drilling on Georges Bank between July 1981 and September 1982. Eight exploratory wells were drilled. The closest was 9 km away from the location where increases in Ba concentration were observed.

This small increase in Ba concentration is not accompanied by an increase in other metals associated with drilling muds, and by itself, the increase in Ba does not constitute an environmental hazard. This opinion is based on the low toxicity of barium sulfate, and the small concentration increase that was observable only in the fine fraction. The concentration of organic additives in drilling mud were not measured in the resuspended sediment, but these constituents would be greatly diluted as indicated by the barium concentrations. The Georges Bank Benthic Infaunal Monitoring Program (Maciolek-Blake and others, 1985) concluded that no changes in benthic infaunal community structure attributed to drilling were observed at locations adjacent to the drilling sites on Georges Bank. Organisms studied in the Georges Bank Monitoring Program were living in sediments having much higher barium concentrations than observed in Lydonia Canyon.

5. There is a higher potential for adsorption of dissolved pollutants by sediments in the canyon axis than on the open continental slope. This conclusion is based on the higher specific activities and higher inventories of excess ^{210}Pb and $^{239,240}Pu$ found in sediments from the canyon axis. The higher fluxes of resuspended sediments in the canyon axis is thought to provide more opportunity for particulates to strip dissolved pollutants from the water column.

References

Anderson, R. Y., 1977, Short term sedimentation response in lakes in western United States as measured by automated sampling: Limnology and Oceanography, v. 22, p. 423-433.

Anderson, R. F., Biscaye, P. E., Bopp, R. F., and Buesseler, K. O., (submitted), Mixing of particles and organic constituents in sediments from the Continental Shelf and Slope off Cape Cod: Seep-1 results.

Bacon, M. P., Spencer, D. W., and Brewer, P. G., 1980, Lead-210 and polonium-210 as marine geochemical tracers: review and discussion of results from the Labrador Sea, in Gesell, T.F., and Lowder, W.F., eds., Natural Radiation Environment III, v. 1, p.473-501.

Baker, E. T., and Hickey, B. M., 1986, Contemporary sedimentation processes in and around an active West Coast Submarine Canyon: Marine Geology, v. 71, p. 15-34.

Benninger, L. K., Lewis, D. M., and Turekian, K. K., 1975, The use of natural lead-210 as a heavy metal tracer in the river-estuarine system: Chapter 12 in Church, T. M., ed., Marine chemistry in the coastal marine environment: American Chemical Society Symposium Series 18, p. 202-210.

Benninger, L. K., and Krishnaswami, S., 1981, Sedimentary processes in the Inner New York Bight: Evidence from excess ^{210}Pb and $^{239,240}Pu$: Earth and Planetary Science Letters, v. 53, p. 158-174.

Bothner, M. H., Spiker, E. C., Johnson, P. P., Rendigs, R. R., and Aruscavage, P. J., 1981, Geochemical evidence for modern sediment accumulation on the Continental Shelf off Southern New England: Journal of Sedimentary Petrology, v. 51, p. 281-292.

Bothner, M. H., Rendigs, R. R., Campbell, E. Y., Doughten, M. W., Parmenter, C. M., O'Dell, C. H., Dilisio, G. P., Johnson, R. G., Gillison, J. R., and Rait, N., 1985, The Georges Bank Monitoring Program: Analysis of trace metals in bottom sediments during the third year: Final report to the U.S. Minerals Management Service, 99 p. (prepared under Interagency Agreement No. 14-12-0001-30153).

Bothner, M. H., Campbell, E. Y., Dilisio, G. P., Parmenter, C. M., Rendigs, R. R., Doughten, M. W., Johnson, R. G., Gillison, J. R., and Rait, N., 1986, Analysis of trace metals in bottom sediments in support of deepwater biological processes in the U.S. Mid-Atlantic Continental Slope and Rise: Second Interim Report to the U.S. Minerals Management Service, 59 p. (prepared under Interagency agreement No. 14-12-0001-30197)

Buesseler, K. O., Livingston, H. D., and Sholkouitz, E. R., 1985, $^{239,240}Pu$ and excess ^{210}Pb inventories along the shelf and slope of the northeast U.S.A.: Earth and Planetary Science Letters, v. 76, p. 10-22.

Butman, C. A., 1986, Sediment trap biases in turbulent flows: Results from a laboratory flume study: Journal of Marine Research, August, 1986.

Butman, B., and Conley, S. J., 1984, Lydonia Canyon Experiment: Data Report for moored array deployment 1, October 1980 - April 1981: U.S. Geological Survey Open-file Report 84-201, 223 p.

Butman, C. A., Grant, W. D., and Stolzenbach, K. D., 1986, Predictions of sediment trap biases in turbulent flows: A theoretical analysis based on observations from the literature: Journal of Marine Research, August 1986 (in press).

Drake, D. E., Hatcher, P. K., and Keller, G. H., 1978, Suspended particulate Canyon, in Stanley, D. J., and Kelling, G., eds., Sedimentation in Submarine Canyons, Fans, and Trenches: Stroudsburg, PA., Dowden, Hutchinson and Ross, Inc., p. 33-41.

Forstner, U., and Wittmann, G. T. W., 1979, Metal pollution in the aquatic environment: Springer-Verlag, New York, 486 p.

Gardner, W. D., 1980, Sediment trap dynamics and calibration: a laboratory evaluation: Journal of Marine Research, v. 38, p. 17-39.

Gardner, W. D., 1983, Suspended sediment transport in Baltimore Canyon and adjacent slope, in Chapter 2, Volume 2, Canyon and Slope Processes Study: Lamont-Doherty Geological Observatory Final Report to the U.S. Minerals Management Service, 106 p. (prepared under contract No. 14-12-0001-29178).

Goldberg, E. D., and Bruland, K., 1974, Radioactive geochronologies, in Goldberg, E. D., ed., The Sea, Ideas and Observations on Progress in the Study of the Seas, Vol. 5, Marine Chemistry: New York, John Wiley & Sons, p. 451-489.

Hardy, E. P., 1977, Final tabulation of monthly ^{90}Sr fallout data, 1954-1976: U.S. Department of Energy, Environmental Quarterly, HASL-329.

Honjo, S., 1978, Sedimentation of materials in the Sargasso Sea at a 5,367 m deep station: Journal of Marine Research, v. 36, p. 469-492.

Huggett, R. J., Nichols, M. M., and Bender, M. E., 1980, Kepone contamination of the James River Estuary: Chapter 2 in Baker, R. A., ed., Contaminants and Sediments, Volume 1, Fate Transport, Case Studies, Modeling, Toxicity: Ann Arbor Science, Ann Arbor, Michigan, p. 33-52.

Karickoff, S. W., Brown, D. S., and Scott, T. A., 1979, Sorption of hydrophobic pollutants on natural sediments: Water Research, v. 13, p. 241-248.

Krauskopf, K. B., 1967, Introduction to Geochemistry: New York, McGraw Hill, 721 p.

Livingston, H. D., and Bowen, V. T., 1979, Pu and ^{137}Cs in coastal sediments: Earth and Planetary Science Letters, v. 43, p. 29-45.

Maciolek-Blake, N., Grassle, J. F., and Neff, J. M., 1985, Georges Bank bethnic infauna monitoring program: Final report for the third year of sampling: Final Report (in three volumes) to the U.S. Minerals Management Service, prepared under contract 14-12-0001-29192.

Maciolek, N., Hecker, B., Butman, C., Grassle, J., Dade, W., Boehm, P., Steinhauer, W., Starczk, V., Baptiste, E., Ruff, R., and Brown, B., 1986, Study of Biological Processes on the U.S. North Atlantic Slope and Rise: Interim Report to the U.S. Minerals Management Service, 201 p. (prepared under Contract No. 14-12-0001-30064).

Poppe, L. J., Commeau, R. F., Commeau, J. A., Manheim, F. T., Aruscavage, P. J., 1984, Ferromanganese micronodules from the surficial sediments of Georges Bank: Journal of Marine Research, v. 42, p. 463-472.

Santschi, P. H., Li, Y. H., Bell, J. J., Trier, R. M., and Kawtaluk, K., 1980, Pu in coastal marine environments: Earth and Planet Science Letters, v. 51, p. 248-265.

Scanlon, K. M., 1984, The Continental Slope off New England: A Long-Range Sidescan-Sonar prospective: Geo-Marine Letters, v. 4, p. 1-4.

Solomons, W., and Forstner, U., 1984, Metals in the hydrocycle: Springer-Verlag, New York, 349 p.

Stuiver, M., and Polach, H. A., 1977, Reporting of ^{14}C data: Radiocarbon, v. 19, p. 355-363.

Suess, H. E., 1954, Natural radiocarbon measurements by acetylene counting: Science, v. 120, p. 5-7.

Twichell, D. C., 1983, Geology of the head of Lydonia Canyon, U.S. Atlantic Continental Shelf: Marine Geology, v. 54, p. 91-108.

Valentine, P. C., Cooper, R. A., and Uzmann, J. R., 1984, Submarine sand dunes and sedimentary environments in Oceanographer Canyon: Journal of Sedimentary Petrology, v. 54, p. 704-715.

CHAPTER 7

DOWNSLOPE FLOW ASSOCIATED WITH HIGH-FREQUENCY CURRENT FLUCTUATIONS OBSERVED ON THE OUTER CONTINENTAL SHELF AND UPPER SLOPE ALONG THE NORTHEASTERN U. S. CONTINENTAL MARGIN

IMPLICATIONS FOR SEDIMENT TRANSPORT

By

Bradford Butman

CHAPTER 7

Table of Contents

Page

Abstract.....7-1

Introduction.....7-1

Field Program.....7-3

Results.....7-9

Hydrographic Setting.....7-9

Mean Flow.....7-16

Currents at Station SF.....7-21

Near-bottom flow at other stations.....7-37

Discussion and Conclusions.....7-46

Acknowledgements.....7-48

References.....7-49

ABSTRACT

Current measurements made 5-7 meters above bottom at six stations along the U.S. east coast continental margin show a net Eulerian downslope flow of 1-5 cm/s. Although the scalar current speed decreases with water depth and toward the bottom, fluctuations in the cross-isobath flow were stronger and increasingly asymmetric near the bottom. Maximum downslope flow exceeded maximum upslope flow by a factor of two to three. The strength of the low-passed downslope flow was proportional to the upslope Reynolds flux of density as well as to the amplitude of the current fluctuations that have periods shorter than 30 hours. These flow characteristics may be caused by differential vertical mixing in the bottom boundary layer where a stratified fluid flows upslope (unstable) and downslope (stable). The asymmetry in current strength clearly favors net downslope transport of sediments that move as bedload.

INTRODUCTION

The Western North Atlantic continental slope is a relatively narrow transition region between the continental shelf and the continental rise. Along the east coast of the United States, the texture of the surficial sediment changes rapidly from primarily sand to silt and clay just seaward of the shelfbreak (Stanley et al, 1983; Schlee, 1973), indicating a change from an active sedimentary environment on the shelf to a more tranquil depositional environment on the upper slope. Csanady and Shaw (1983) have suggested that because of the relatively weak currents on the slope, this region may be a sink for fine-grained particles. Because anthropogenic pollutants often adhere to fine-grained particles, over long periods of time the slope may be a region of accumulation for these contaminants. Csanady and others (submitted)

summarize recent current observations made on the shelf, slope and rise to test this hypothesis.

To leave the continental shelf, particles must cross the shelfbreak. The net direction and rate of sediment transport is the result of many oceanographic processes that operate on different time scales (see Karl and others, 1983; Butman, in press). Although the residual circulation is typically only a few cm/s and is thus not strong enough to resuspend bottom sediments, it often is important in determining the net transport of material over a long period of time. For example, very fine silts and clays that settle slowly are easily transported by a weak mean flow, and resuspension events caused by energetic internal waves or tides which are oscillatory by themselves result in a net transport of material when even a weak mean flow is superimposed. Thus although the residual circulation isn't the whole transport story at the shelfbreak, it is an important component.

Direct measurements of the near-bottom flow over the outer shelf and upper slope south of New England are few. Bumpus (1973) inferred a net off-shelf near-bottom flow seaward of about the 80 m isobath on the basis of bottom drifter data, and Wunsch and Hendry (1972) reported currents measured at about 950 m on the slope that suggested a net downslope flow near the bottom. Beardsley and others (1985) also reported a net downslope near-bottom flow at 200 m in the Nantucket Shoals Flux Experiment. Recent observations on the outer shelf and upper slope, summarized by Butman (in press), also show a net downslope flow near the bottom. Such a net downslope flow would clearly favor transport of sediments from the shelf to slope.

This study presents new near-bottom current observations made along the outer shelf and upper slope south of New England. The measurements confirm the net off-shelf and downslope Eulerian mean flow suggested by previous

studies, but show that it is a wide-spread feature of the near-bottom flow over the slope. The observations also show that the net flow is associated with (or maybe caused by) strong current fluctuations, primarily of tidal frequency. The speeds associated with these fluctuations are sometimes strong enough to resuspend the bottom sediments, especially on the upper slope in water depths of 200-300 m, and are always strongest in the downslope direction.

FIELD PROGRAM

Long-term near bottom current observations were made at six stations along the U.S. Atlantic continental margin between 67° and 70°W (fig. 7-1). Stations T, SF, SE and SG at water depths of 100, 200, 500 and 1150 m form a transect across the shelf and upper slope at approximately 70°W. Stations LCI at 250 m and SA at 500 m provide additional observations to the east of this transect. All of the stations were located in areas of relatively smooth topography or on local topographic highs. However, the slope in this region of the margin is characterized by many large canyons and gullies (Scanlon, 1984; Carpenter et al., 1982; Butman and Moody, 1984), especially below 400 m, and at all stations deeper than 250 m there are topographic features of 100-200 m relief nearby.

The U.S. Geological Survey has conducted two major field experiments on the outer shelf and upper slope: the Lydonia Canyon Experiment from 1980 to 1982 and the Slope Experiment from 1982 to 1984. The data presented here from stations SA, SF, SE, and SG were collected during deployment II (October 1983 to March 1984) and III (March to November, 1984) of the Slope Experiment. The data at station LCI were obtained as part of the Lydonia Canyon Experiment and were obtained in four successive deployments made between December 1980 and

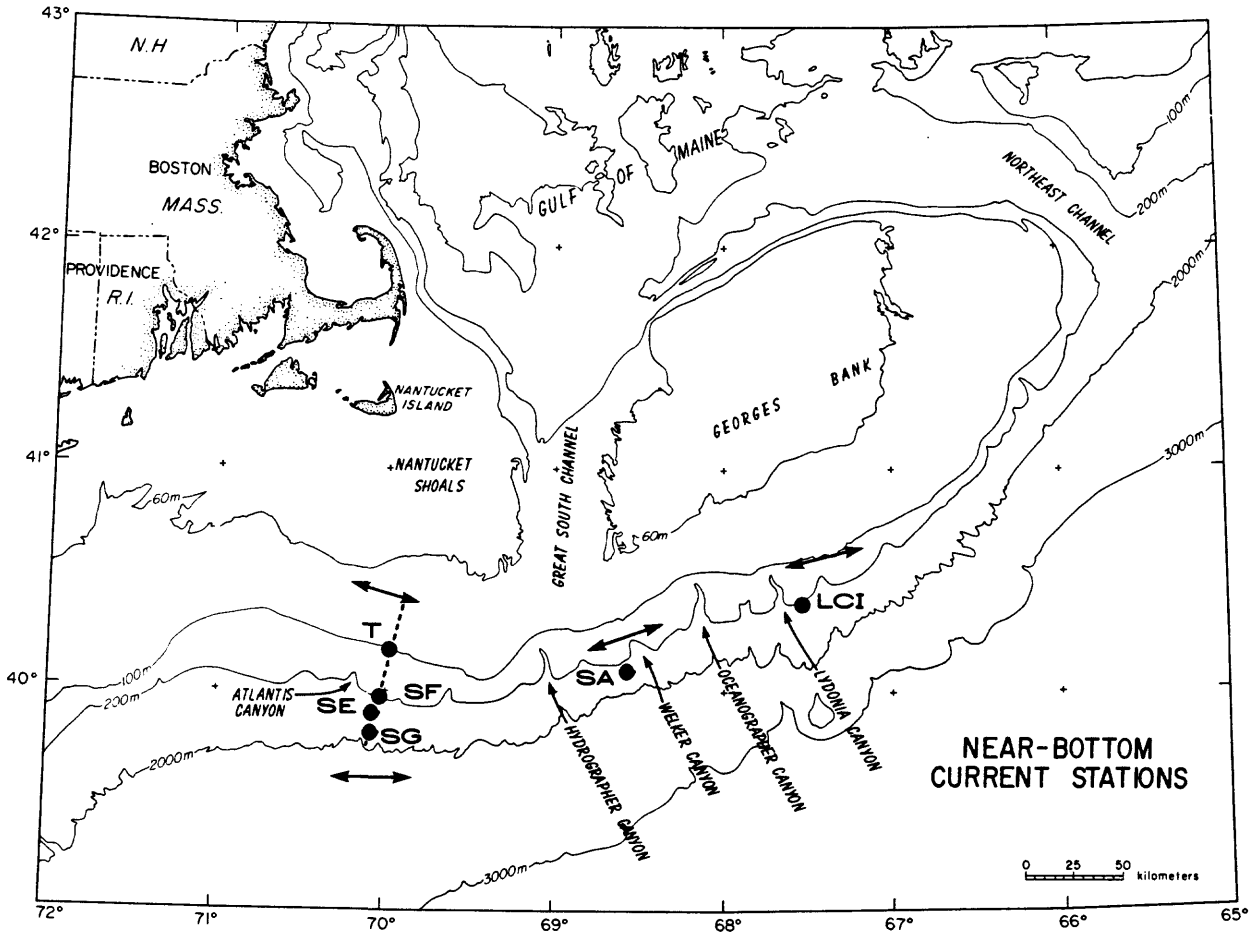

Figure 7-1a. Bathymetric map showing location of current measurements made along the outer shelf and upper slope of New England. Dotted line indicates location of hydrographic section shown in figure 7-2 and two-headed arrows indicate the local along-isobath coordinate system (table 7-1).

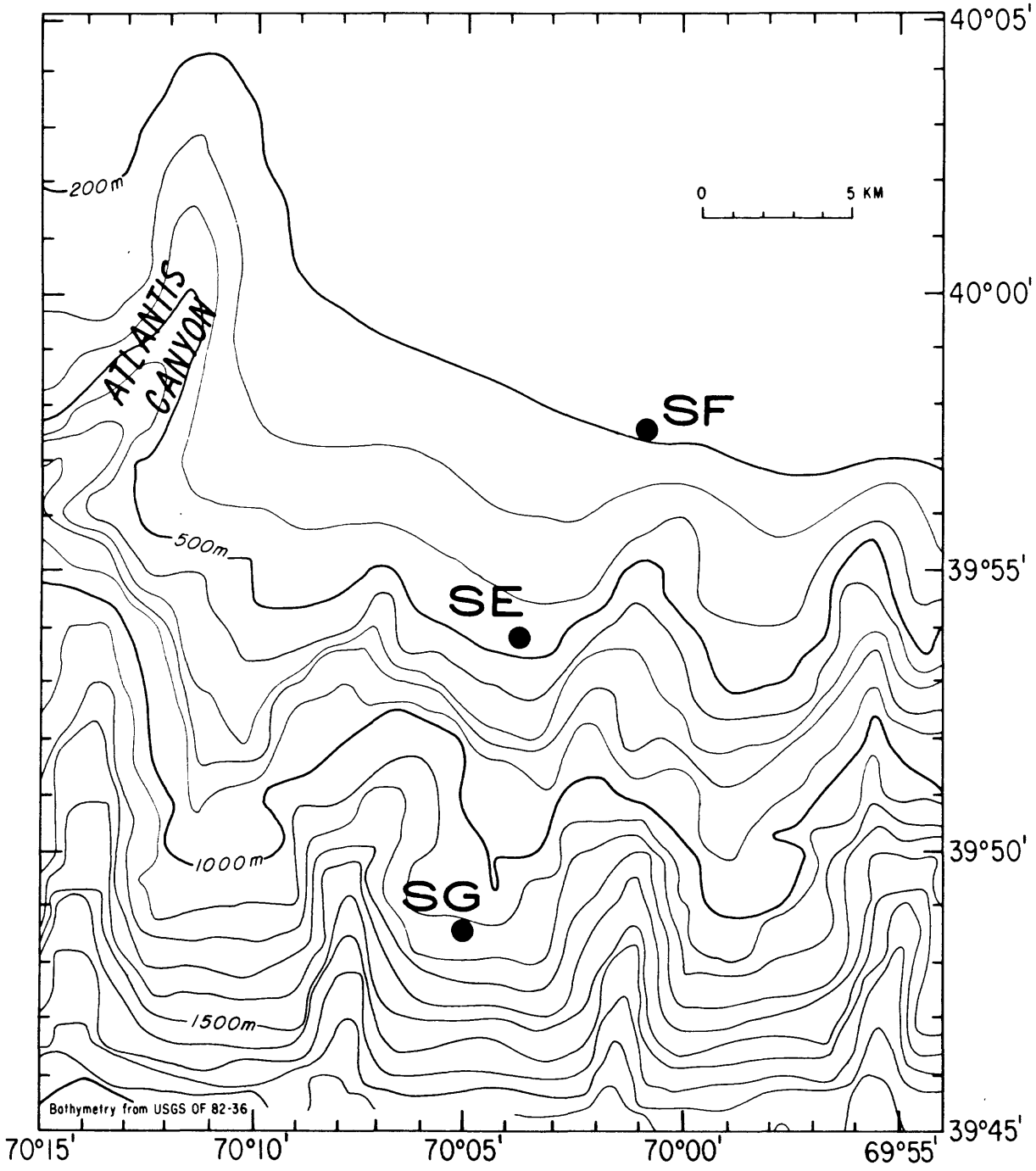

Figure 7-1b. Detailed map showing location of moorings near 70°W (base from Carpenter et al., 1982).

July 1982. At each station currents were measured within 7 meters above bottom (mab) and at at least one additional height (usually between 50 and 200 m) above the seafloor for periods of 3 to 6 months. The currents were measured with EG & G vector averaging current meters (VACM), some of which were modified to also record light transmission and water conductivity (Strahle and Butman, 1985). Station information is tabulated in table 7-1, and deployment periods and instrument depths as part of table 7-2. Only the near-bottom measurements and the measurements at the next closest height above bottom are presented in this analysis of the near-bottom mean flow.

The currents at each station were rotated to a local along-isobath cross-isobath coordinate system determined from scatter plots of the low-frequency currents, the low-frequency ellipse orientations, and the local topography (fig. 7-1a and table 7-1). Currents were low-passed using a digital filter that passed all energy at periods greater than 33 hours. The currents were high-passed by subtracting the low-passed record from the original time series. These "high-frequency" currents include all fluctuations with periods faster than about 30 hours, including the diurnal and semidiurnal tidal currents and inertial currents.

A hydrographic section through the moored array along 70°W was conducted on the instrument deployment and recovery cruises using a Neil Brown Instrument Systems CTD modified to measure light transmission with a Sea Tech 25-cm path length transmissometer (Butman and others, 1985). Brunt-Vaisaila frequency was computed as $(-g/\rho_o)\partial\rho/\partial z$ where g is acceleration due to gravity, ρ_o is the average water density, and $\partial\rho/\partial z$ is the vertical gradient. The density profiles were vertically smoothed to eliminate sharp steps in density.

Table 7-1 Station identifier, water depth, and location of stations where current observations were made (see fig. 7-1). Angle is the positive along-isobath (L) and cross-isobath (C) direction for the rotated coordinate system. The bottom slope at each station was estimated from bathymetric charts (Carpenter and others, 1982).

Sta.	Water Depth (m)	Latitude	Longitude	Angle L	Angle C	Bottom Slope
SA	500	40° 04.8'	68° 33.5'	72	342	0.13
SE	500	39° 53.8'	70° 03.7'	105	15	0.06
SF	200	39° 57.7'	70° 00.9'	105	15	0.04-0.06
SG	1150	39° 48.5'	70° 05.0'	90	0	0.03-0.10
T 100	40° 10.9'		69° 58.3'	105	15	0.002
LCI	250	40° 22.8'	67° 33.1'	75	345	0.09

Table 7-2 Statistics of the hour-averaged along-isobath (u) and cross-isobath (v) currents. Mooring ID is the USGS mooring identification number, SD is standard deviation, 5% is the current speed exceeded 5% of the time, 1% indicates the current speed exceeded 1% of the time when the flow is in the down or upslope direction, and R is the ratio of these two speeds.

Sta.	Water Depth (m)	Inst. Depth (m)	Height above bottom (m)	Mooring ID	Start (YrMoDy)	Stop (YrMoDy)	Duration (Days)	Along U (cm/s)	Along SD (cm/s)	Across V (cm/s)	Across SD (cm/s)	Speed S (cm/s)	Speed SD (cm/s)	Speed 5% (cm/s)	1% Down (cm/s)	1% Up (cm/s)	R (cm/s)
SA	485	184	301	2761	831020	840317	148	6.53	17.27	1.14	9.00	18.0	9.9	38.2	19	14	1.4
		478	7	2762				-3.94	6.50	-1.84	4.55	8.0	4.3	17.7	15	10	1.5
SE	491	390	101	2743	831023	840313	141	-2.44	9.24	-0.27	5.56	9.9	4.9	19.5	12	12	1.0
		484	7	2744				-2.02	4.55	-1.20	6.95	7.5	4.2	16.9	21	13	1.6
	504	403	101	2783	840315	841115	244	-1.19	7.99	-0.22	5.67	8.8	4.5	18.3	13	13	1.0
		497	7	2784				-1.32	3.90	-1.52	6.16	6.2	4.3	16.3	22	10	2.2
SF	202	126	76	2751	831018	840125	98	-7.89	12.77	1.24	9.89	15.9	8.4	30.7	20	13	1.5
		195	7	2752				-6.37	10.13	-4.04	10.36	13.8	8.7	32.1	37	13	2.8
	204	128	76	2793	840316	840724	129	-4.19	9.84	-0.05	7.70	11.7	6.2	24.2	18	16	1.1
		197	7	2794				-5.50	7.94	-3.40	8.69	11.6	6.8	25.7	30	12	2.5
SG	1150	949	201	2811	840313	841115	246	-6.23	7.36	0.45	3.17	8.6	5.4	19.2	6	6	1.0
		1143	7	2812				-4.77	5.80	-1.84	5.27	8.4	4.2	17.1	15	9	1.7
T	100	56	44	2831	840516	841110	177	-12.69	13.06	0.21	12.64	19.5	10.5	39.7	25	25	1.0
		93	7	2832				-4.52	10.52	-1.59	10.95	14.3	7.1	28.3	28	21	1.3
LCI	250	195	55	2153	801202	810429	148	12.24	26.60	-0.41	9.46	26.5	15.6	57.2	19	17	1.0
		245	5	2154				6.83	15.26	-5.08	9.81	17.8	9.2	34.8	29	15	1.9
	250	59	191	2271	810503	810927	146	0.82	22.78	1.30	13.65	22.9	13.6	49.8	38	30	1.3
		245	5	2273				4.57	14.45	-2.77	8.86	15.5	8.6	32.8	25	16	1.6
	251	55	196	2331	810927	820131	125	-9.50	16.86	0.22	13.99	21.1	11.2	43.4	32	30	1.1
	247	242	5	2341				0.39	10.87	-3.89	9.93	13.2	7.6	28.7	34	17	2.0
	249	199	50	2422	820201	820708	157	3.15	17.15	-0.22	8.97	16.5	10.6	39.4	20	18	1.1
		243	6	2423				3.75	13.96	-5.33	11.95	16.3	10.7	37.2	41	19	2.2

RESULTS

Hydrographic setting

Sections of temperature, salinity, density, Brunt-Vaisaila frequency, and beam attenuation coefficient made along the moooring transect at 70°W in October 1983 are shown in fig. 7-2. The instruments at station SF and SE were both located below the shelf-water/slope-water front as indicated by the the 34 0/00 isohaline. The beam attenuation coefficient, roughly proportional to the suspended sediment concentration (Moody and others, submitted), shows increased suspended sediment concentrations near the bottom over the shelf. These increased concentrations occur over the eastern end of a deposit of fine-grained sediments called the mud patch (Twichell and others, 1981, Bothner and others, 1981; Butman, in press). The increased sediment concentrations associated with the mud patch extended to within about 10 km of Station SF at the time this section was made.

Internal wave energy propagates at a slope c to the horizontal given by

$$c^2 = (\sigma^2-f^2)/(N^2-\sigma^2) \qquad (1)$$

where σ is the wave frequency, f is the local inertial frequency, and N is the Brunt-Vaisaila frequency. For waves to exist, the frequency σ must be greater than N but less than f. Waves near the inertial frequency propagate nearly horizontally, and waves near the buoyancy frequency propagate nearly vertically.

The reflection properties of internal waves for constant N over sloping bottoms are well known (Erickson, 1982), and Wunsch (1969) has developed a theoretical description of the propagation of waves into a wedge which has been examined in the laboratory (Cacchione and Wunsch, 1974). The important parameter governing wave propagation is the ratio of bottom slope γ to the angle of wave propagation c. For $\gamma/c<1$ (transmissive case) internal waves are

Figure 7-2. Hydrographic sections made across the outer shelf and upper slope near 70°W passing through the mooring locations (see figure 7-1 for location). The instruments deployed on mooring 275 (station SF) and 274 (Station SE) are superimposed on the section. Station numbers are shown across the top of the section; X indicates XBT, C a CTD station. The dot at the bottom of each cast indicates the deepest measurement depth. The slope of the contours near the bottom should be interpreted with care because of the large changes in depth between stations. Sections redrawn from Butman and others, (1985). [Figures on succeeding pages].

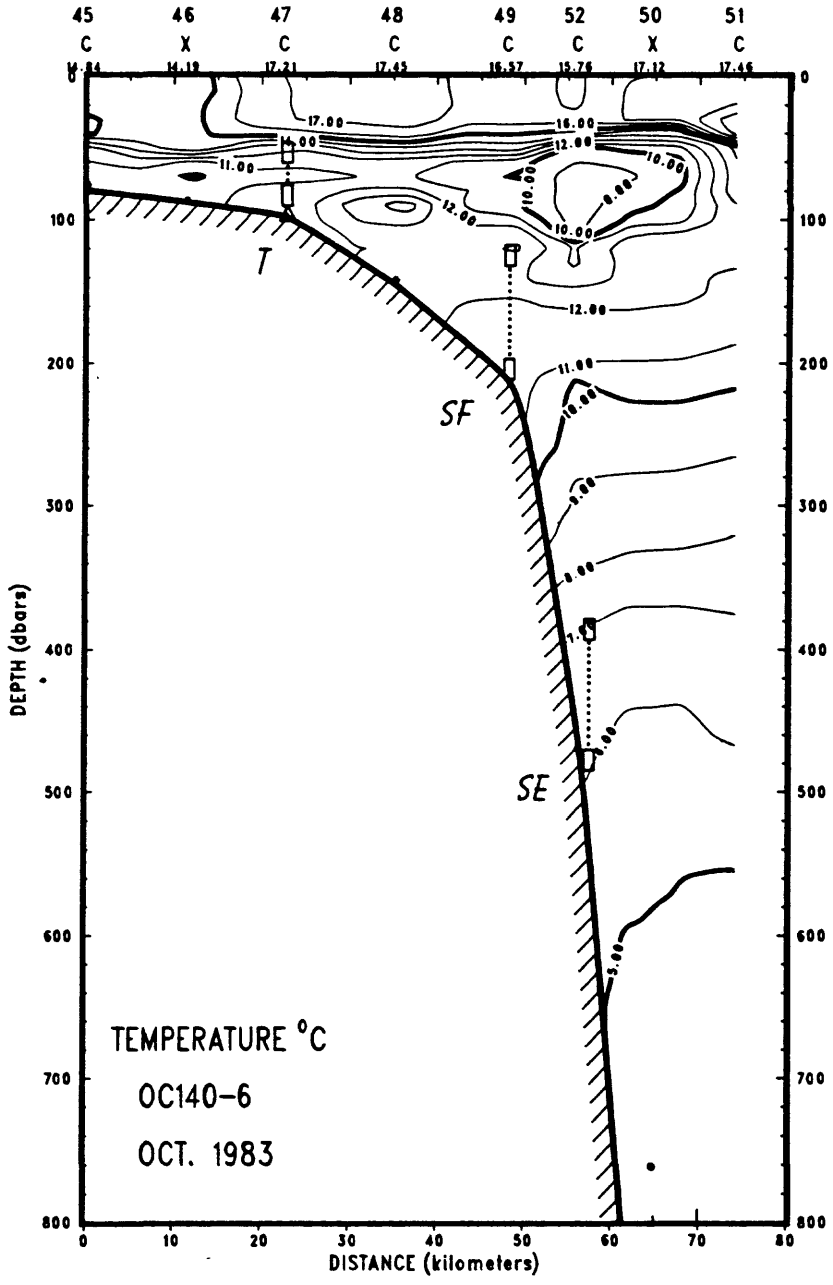

Figure 7-2a. Hydrographic section of temperature made across the outer shelf and upper slope near 70°W passing through the mooring locations (see figure 7-1 for location).

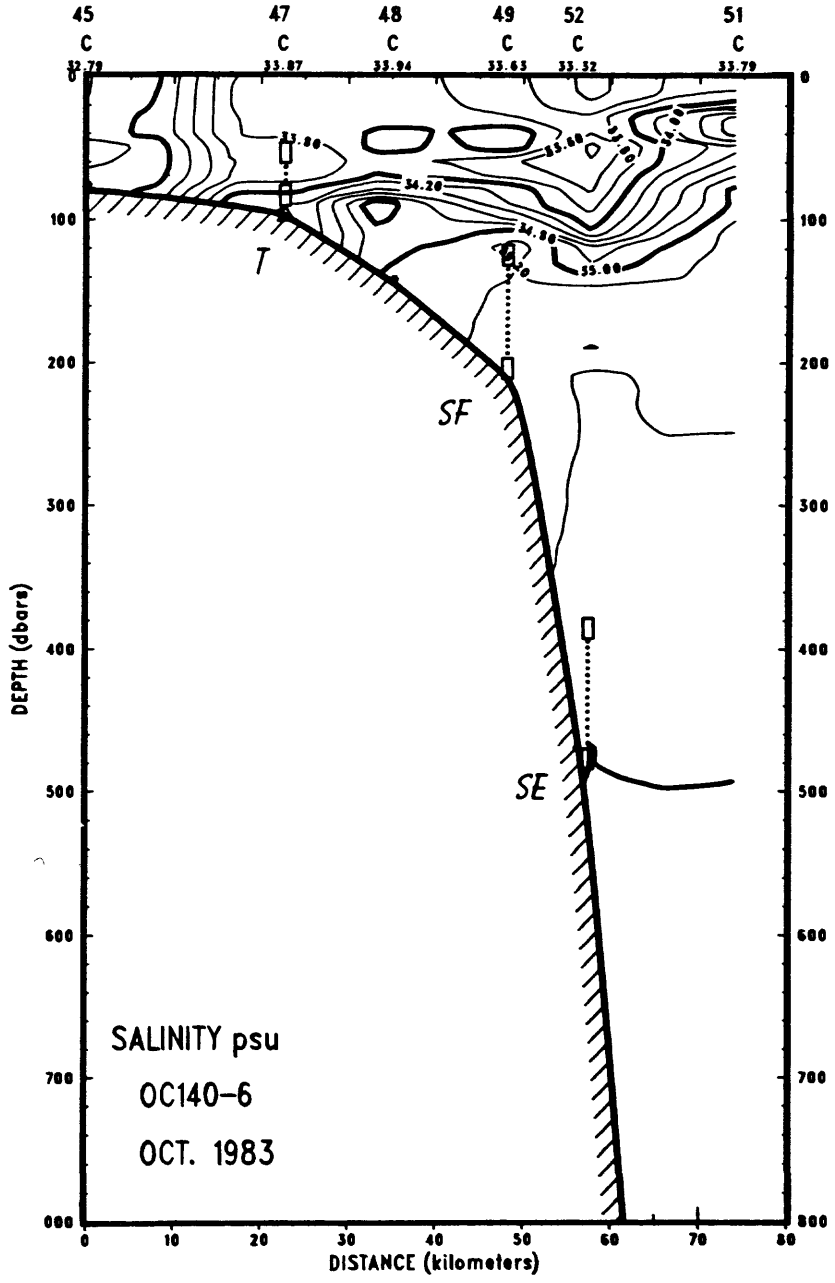

Figure 7-2b. Hydrographic section of salinity made across the outer shelf and upper slope near 70°W passing through the mooring locations (see figure 7-1 for location).

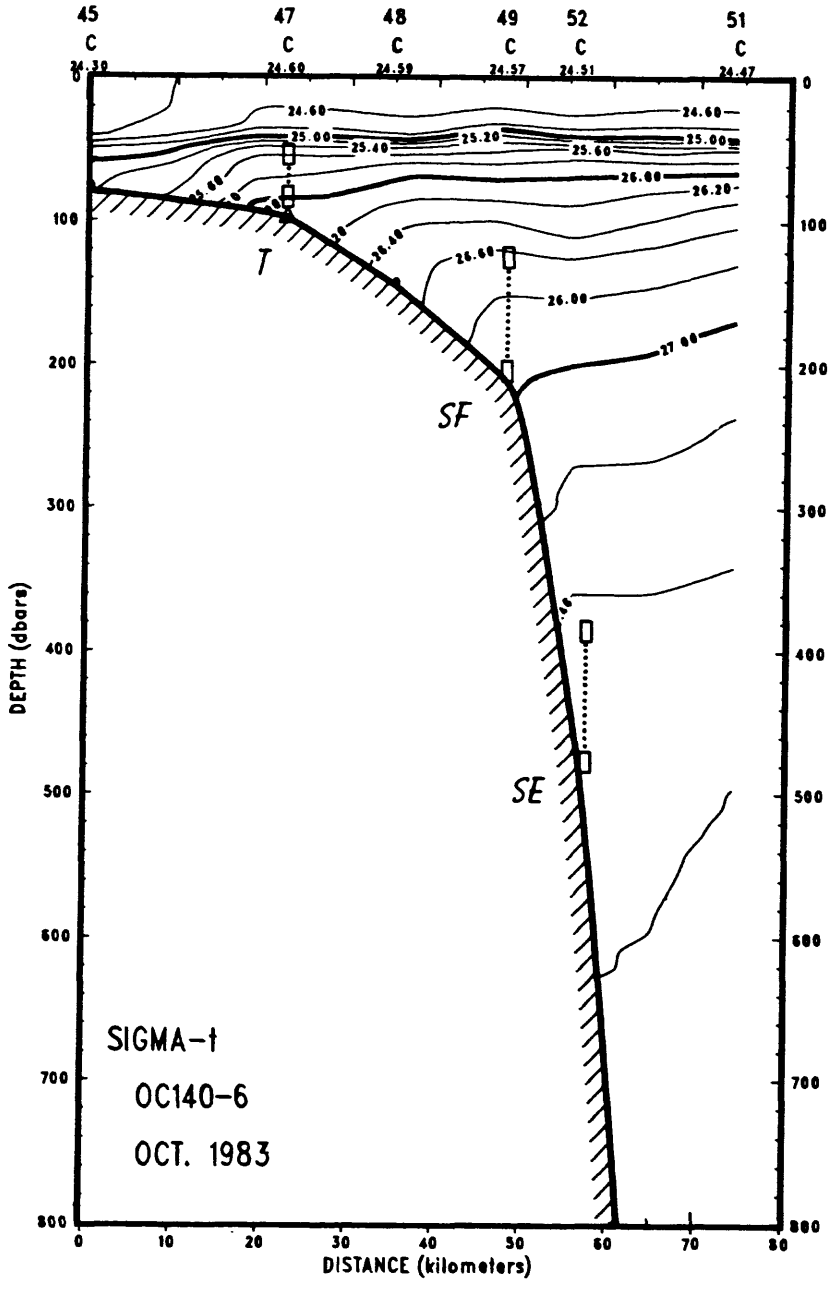

Figure 7-2c. Hydrographic section of sigma-t made across the outer shelf and upper slope near 70°W passing through the mooring locations (see figure 7-1 for location).

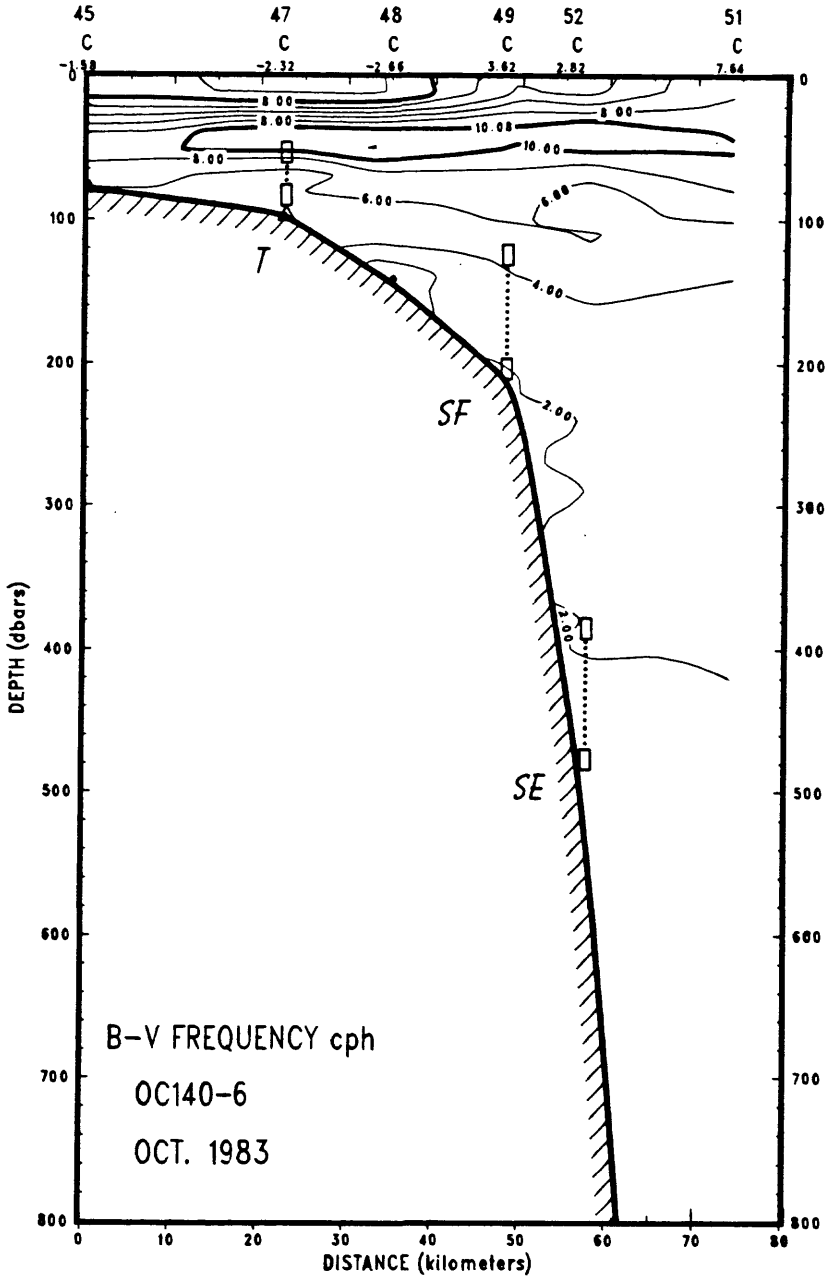

Figure 7-2d. Hydrographic section of Brunt-Vaisaila frequency made across the outer shelf and upper slope near 70°W passing through the mooring locations (see figure 7-1 for location).

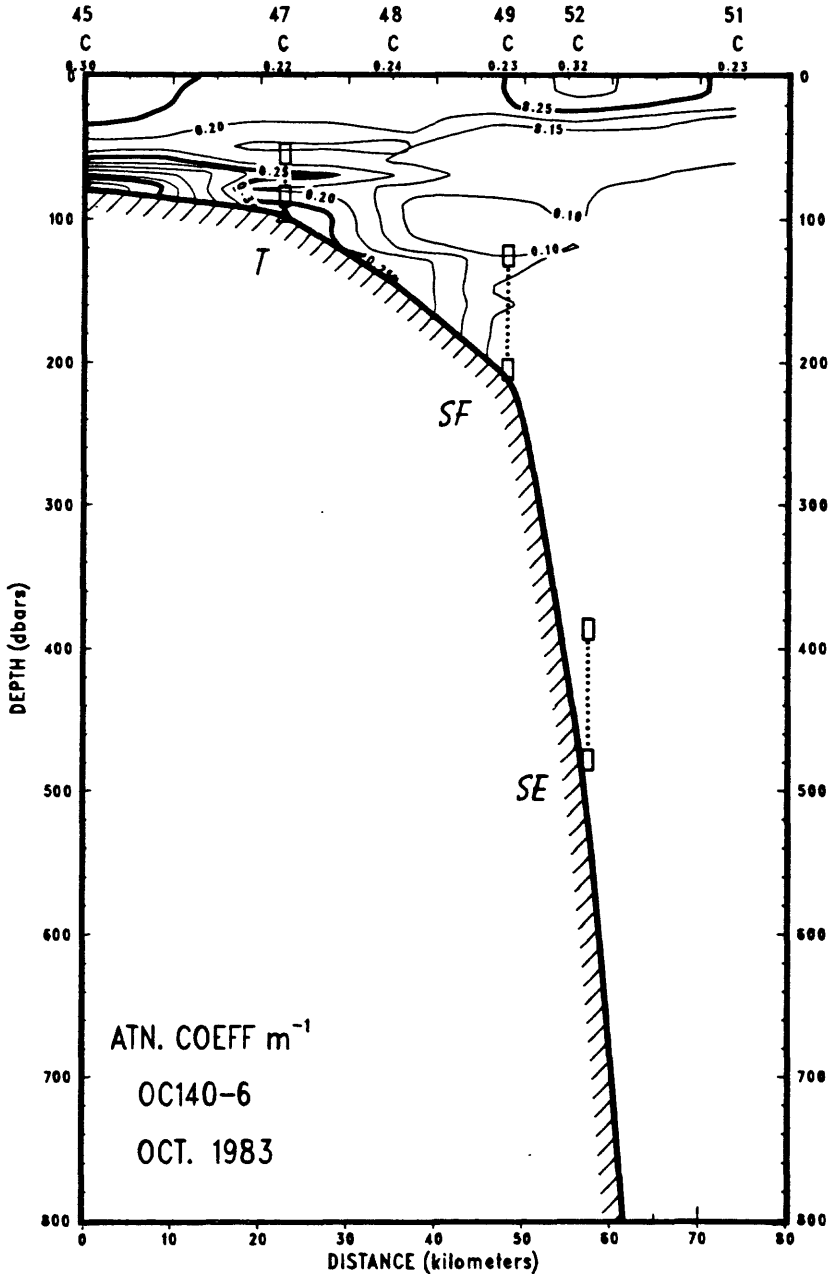

Figure 7-2e. Hydrographic section of beam attenuation made across the outer shelf and upper slope near 70°W passing through the mooring locations (see figure 7-1 for location).

reflected shoreward into the wedge. Linear theory predicts and lab studies confirm an intensification of wave orbital velocities near the bottom and toward the apex. For $\gamma/c = 1$ (critical case), reflected waves travel parallel to the bottom. The frequency at which $\gamma = c$ is called the critical frequency and the slope, the critical slope. For $\gamma/c>1$ (reflective case), wave energy propagating into a wedge is reflected seaward.

The dynamics of internal waves of semidiurnal tidal period is of special interest because of the forced semidiurnal tidal currents which could excite internal waves at the same period. For a Brunt-Vaisaila frequency of 2 cph, characteristic of the upper slope (fig. 7-2d), c is 0.03 for the semidiurnal tide and 0.01 for periods just faster than the inertial. The bottom slope at SF and SE, estimated from bathymetric charts, is about 0.06 or 3-4° (table 7-1). Just landward of SF, the bottom slope decreases rapidly to about 0.003 (0.2°). For a bottom slope of 0.06 and N = 2 cph, the critical period is 7.6 hours; all waves with periods longer than 7.6 hours are reflected seaward, and waves with shorter periods propagate up the slope. Thus amplification of internal tides along the upper slope (water depths of 200 m) caused by propagation from a seaward source is not expected. However, all internal waves with periods between 7.6 and 18.5 hours pass through a critical slope at the shelfbreak just landward of SF; this sharp transition in bottom slope could be a source region for waves (over a wide range of frequencies) which then propagate either landward or seaward.

Mean flow

The Eulerian mean flow computed over the length of the deployment period was on the order of 5 cm/s and was generally parallel to the local topography at 50-200 mab (fig. 7-3 and table 7-2). One of the most striking features of

Figure 7-3. Near-bottom mean flow observed at selected stations. At each station the vector points in the direction of the mean flow (averaged over the entire deployment period). The number in parenthesis following the station identifier is the water depth at the station in meters and the numbers at the tip of the arrow indicate the observation depth in meters from the surface and above the bottom in parenthesis. The mean flow is shown in a rotated coordinate system; westward along-slope is to the left and upslope is up. Note change of scale in figure 7-3c. [Figures on succeeding pages].

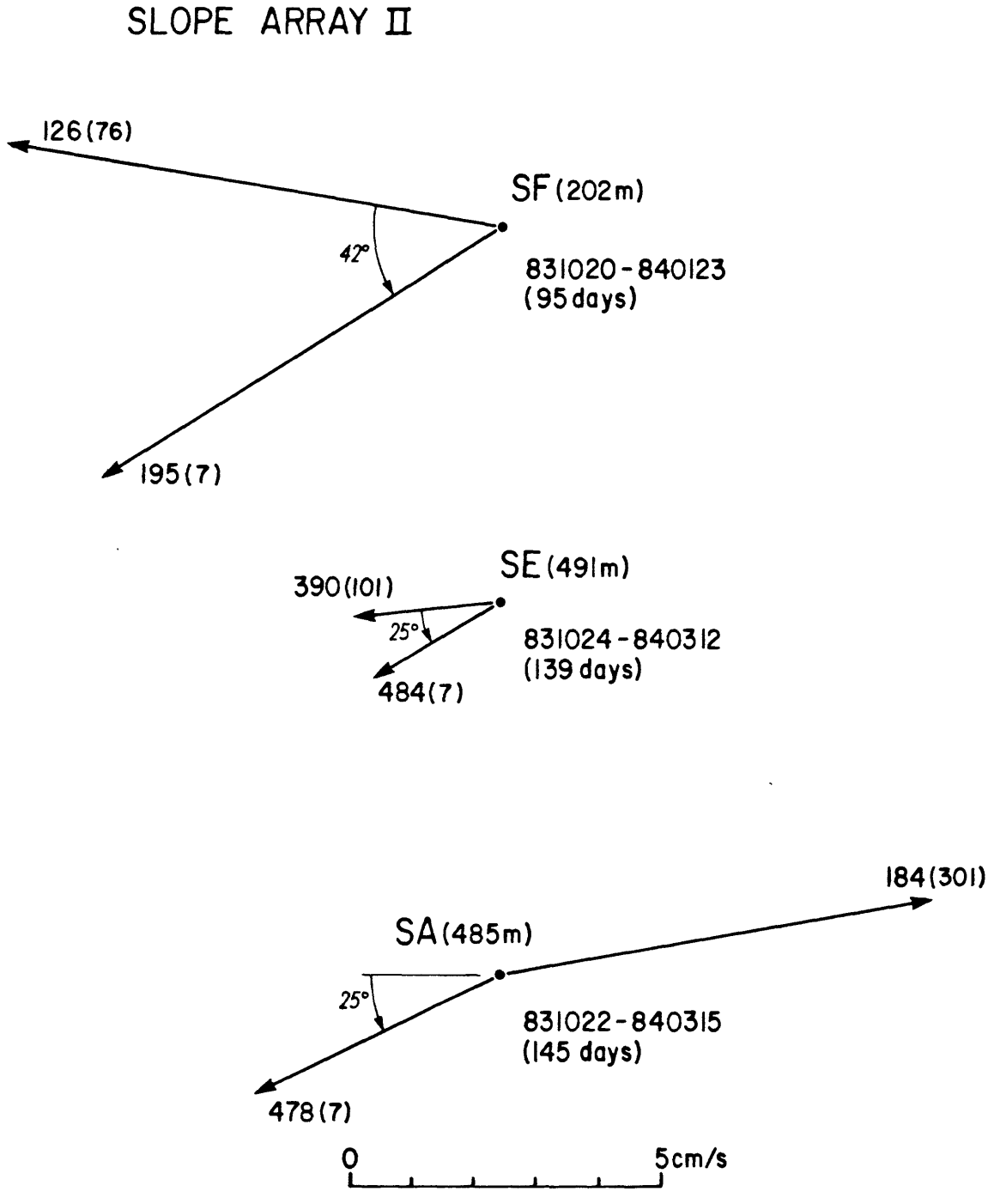

Figure 7-3a. Near-bottom flow observed at selected stations during slope array II.

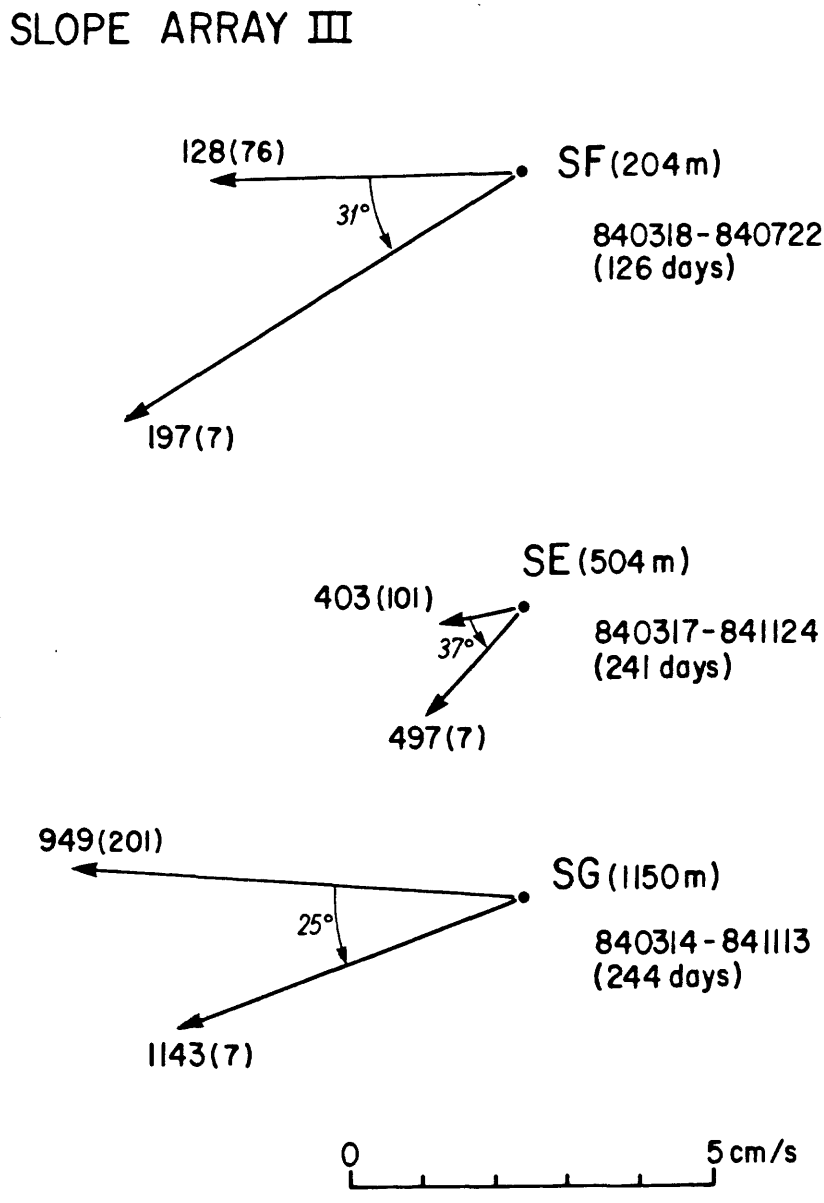

Figure 7-3b. Near-bottom mean flow observed at selected stations during slope array III.

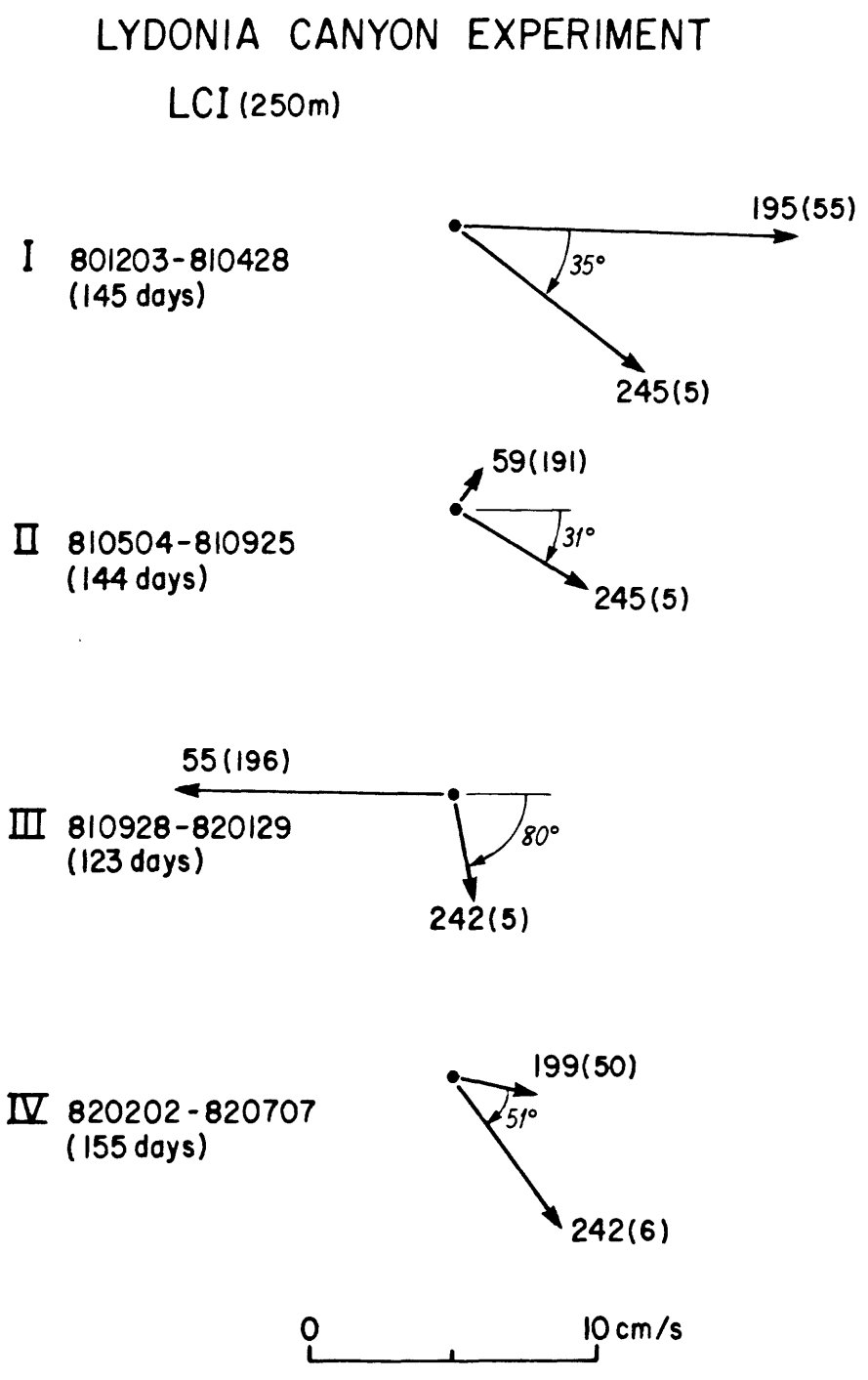

Figure 7-3c. Near-bottom mean flow observed at selected stations during the Lydonia Canyon experiment.

the observations is that the mean Eulerian flow 7 mab was always downslope of the flow 50-200 mab; the angle between the mid-depth and near-bottom flow was on the order of 30^{o}. This downslope near-bottom flow was observed when the mean flow was to the west (fig. 7-3 a,b) or east (fig. 7-3c) and for all of the deployments. In some cases, the net flow near the bottom was stronger than the net flow 50-200 mab.

Currents at Station SF

A portion of record 2751 at 126 m (76 mab) and record 2752 at 195 m (7 mab) obtained at station SF are shown in figure 7-4. Record 2751 is generally typical of current observations on the outer shelf. Hour-averaged current speeds were 10-40 cm/s and fluctuations at tidal and inertial periods dominated the along-isobath and cross-isobath currents. The mean along-isobath flow was westward (consistent with the record-averaged mean), and there were low-frequency fluctuations in the along-isobath component of order 10 cm/s which were occasionally strong enough to cause net flow to the east for periods of a few days. The low-frequency fluctuations in the cross-isobath flow were typically 5 cm/s. The beam attenuation coefficient was between 0.05 and 0.10 m^{-1} and indicated no large changes in suspended sediment concentration.

The currents measured 7 mab at station SF were quite different than the mid-depth currents. The current speeds ranged from 10 to 40 cm/s, but the fluctuations were at somewhat higher frequencies than at mid-depth (for example, the current speed maxima appear spikier). In addition, there were several periods where bottom speeds exceeded 40 cm/s for a few hours (labelled as I, II and III in fig. 7-4). The fluctuations during period I and II occurred at approximately semidiurnal tidal periods, while the speed peaks

Figure 7-4. Time series of temperature, speed, beam attenuation, and hour-averaged and low-passed (heavy line) along-slope and cross-slope current at station SF. Times of large-amplitude current fluctuations are labelled I, II and III (see text).

(a) record 2751 (126 m, 76 mab).

(b) record 2752 (195 m, 7 mab).

[Figures on succeeding pages].

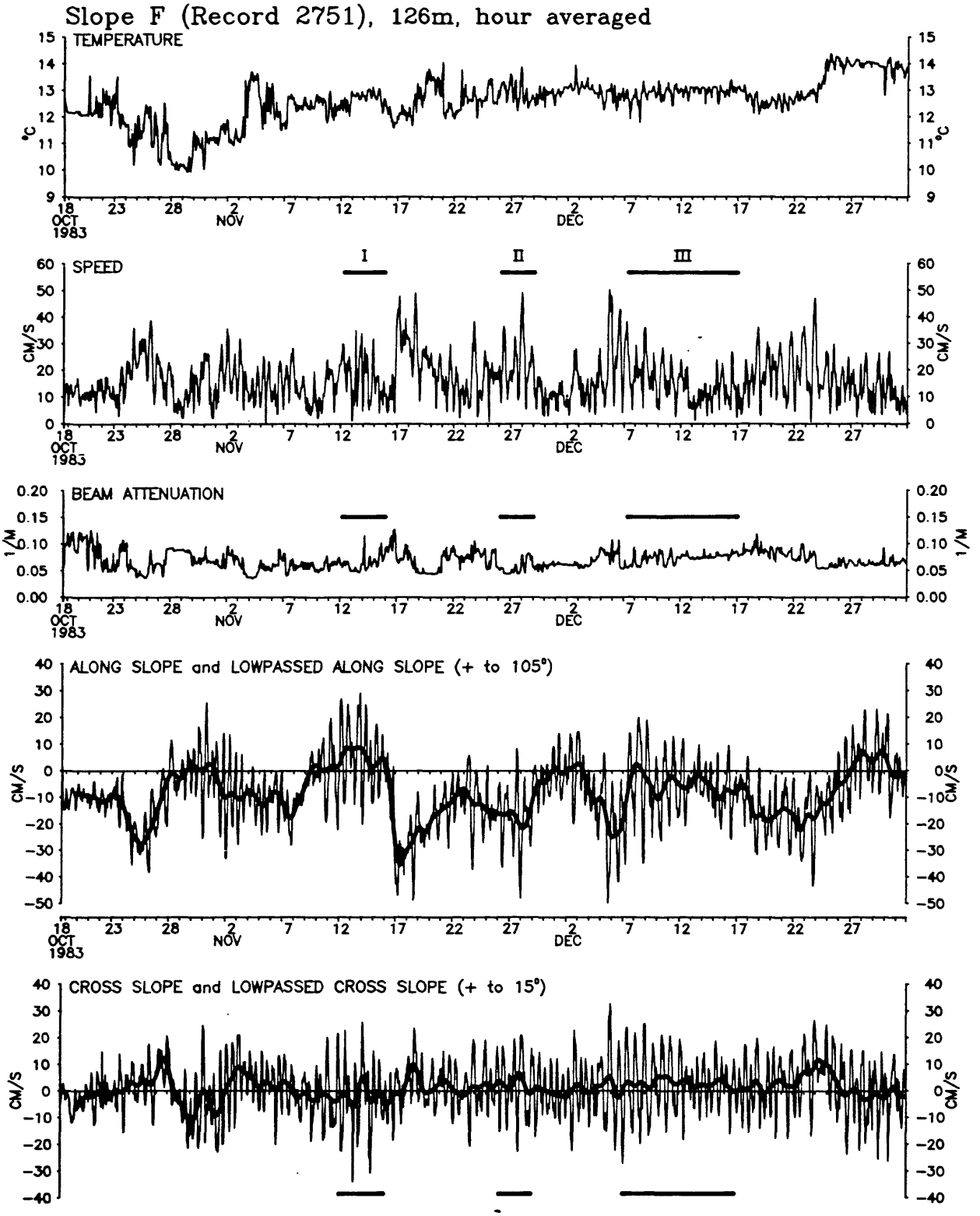
Slope F (Record 2751), 126m, hour averaged
TEMPERATURE
°C
SPEED
I
II
III
CM/S
BEAM ATTENUATION
1/M
ALONG SLOPE and LOWPASSED ALONG SLOPE (+ to 105°)
CROSS SLOPE and LOWPASSED CROSS SLOPE (+ to 15°)
18 23 28 2 7 12 17 22 27 2 7 12 17 22 27
OCT 1983
NOV
DEC

Figure 7-4a.

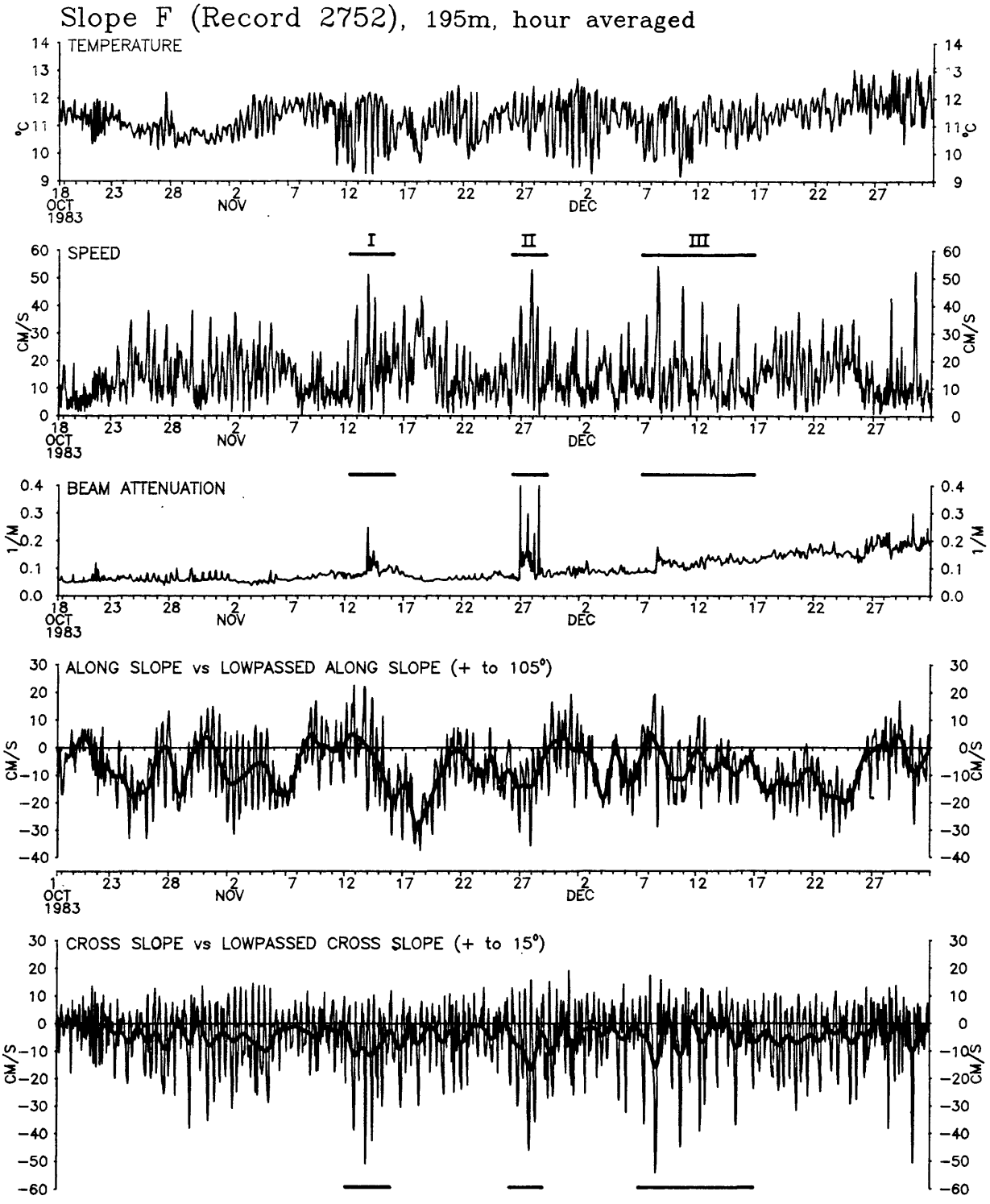
Slope F (Record 2752), 195m, hour averaged
TEMPERATURE
°C
SPEED
CM/S
I
II
III
BEAM ATTENUATION
1/M
ALONG SLOPE vs LOWPASSED ALONG SLOPE (+ to 105°)
CROSS SLOPE vs LOWPASSED CROSS SLOPE (+ to 15°)
18 23 28 2 7 12 17 22 27 2 7 12 17 22 27
OCT 1983
NOV
DEC

Figure 7-4b.

during period III were individual spikes separated by a few days. Note that there is little visual coherence between the large peaks in speed observed 7 mab and the speed at 76 mab.

The beam attenuation coefficient increased during some of the high speed periods (fig. 7-4), suggesting local resuspension of bottom sediments or advection of sediments resuspended elsewhere and advected past the mooring site. Assuming that the resuspended material was fine silt, the proportionality constant between beam attenuation and concentration is about 4 (Moody and others, submitted), and thus the typical changes in beam attenuation of 0.1 to 0.3 m^{-1} are fluctuations in sediment concentration of the order of 1 mg/l. The suspended sediment events are characterized by rapid changes in beam attenuation (fig. 7-5). In the event on November 13, for example, there were three peaks in beam attenuation; the first and third occurred almost at the time of maximum near-bottom speed (52 and 43 cm/s) and maximum off-shelf flow. In the event starting on November 26, the first increase in beam attenuation also occurred at maximum off-shelf flow when the bottom current exceeded 40 cm/s. The succeeding two increases in beam attenuation however were at times of minimum speed (typically 5 cm/s) and maximum up-slope excursion, while the last increase occurred at minimum speed and near-maximum downslope excursion. During the November 13 event the net along-slope flow was near zero, while the along-slope flow during the November 26 event was westward at about 10 cm/s. Observations on the shelf show resuspension during a storm on November 26, and these sediments might have been transported along and off-shelf by the residual flow. Thus although the initial resuspension events were both associated with downslope flow in excess of 40 cm/s, the observed variability of sediment concentration following the initial increase, and speeds in excess of 40 cm/s during other parts of the

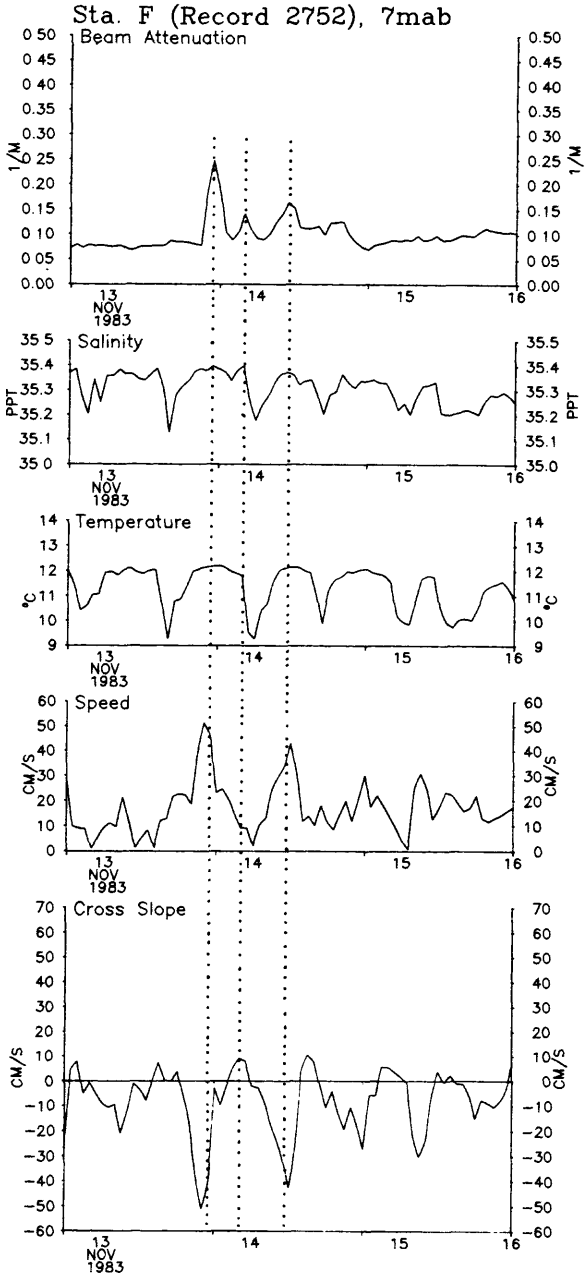

Figure 7-5a. Time series of beam attenuation, salinity, temperature, speed, and cross-slope current at 7 mab at station SF from November 13-15, 1983.

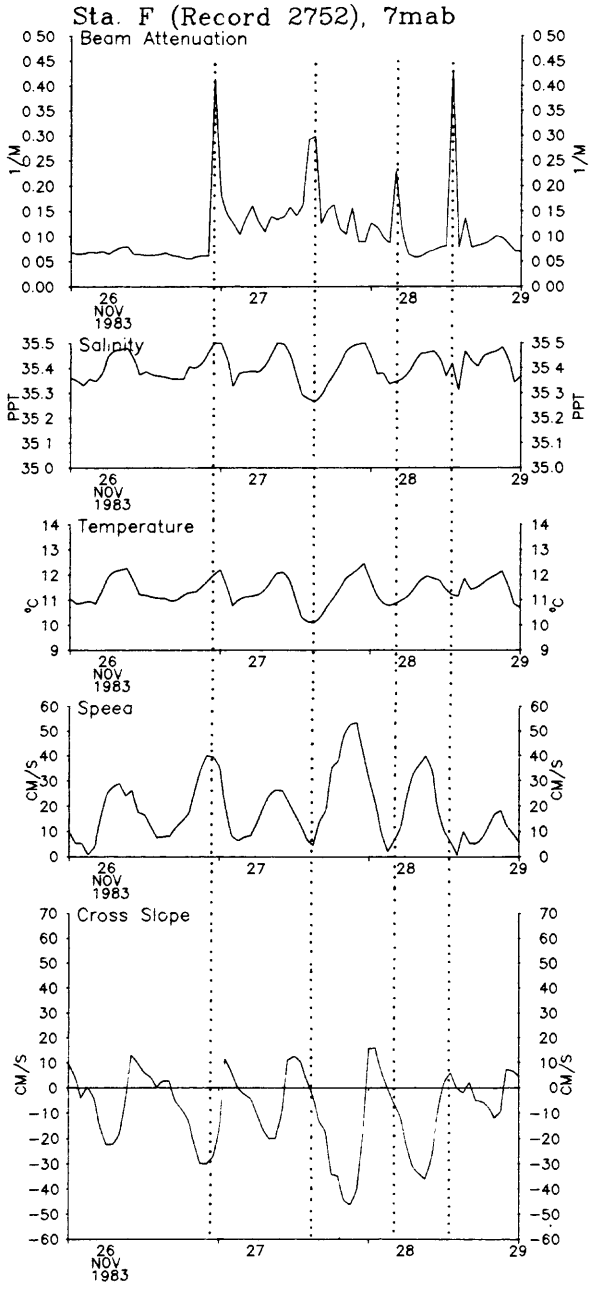

Figure 7-5b. Time series of beam attenuation, salinity, temperature, speed, and cross-slope current at 7 mab at station SF from November 26-28, 1983.

record, without simultaneous increases in beam attenuation, suggest that a complex mixture of processes--resuspension, vertical and horizontal advection and perhaps vertical mixing of suspended material--affects the concentrations at the observation site.

The current fluctuations in the near-bottom cross-isobath flow were very asymmetric; maximum current flow in the upslope direction was typically only 10 cm/s, but maximum flow in the downslope direction occasionally exceeded 40 cm/s (see bottom panel, fig. 7-4b). All of the strong speed events in periods I, II, and III were associated with downslope flow. A visual inspection of the low-passed cross-slope flow suggests that periods of net (i.e., low-passed) downslope flow are correlated with periods of large current fluctuations; this correlation is especially apparent during periods I, II, and III. Both the asymmetry in the strength of upslope and downslope currents, and the net downslope flow during periods of high bottom speeds favors downslope and off-shelf transport of sediment.

A histogram of current speed and sorts of the currents by direction and speed document the asymmetry in the flow direction of the strongest speeds near the bottom (fig. 7-6). While the average speed at 76 mab was slightly larger than at 7 mab (table 7-2), the strongest speeds were observed at 7 mab. The strongest speeds at 76 mab occurred in along-isobath direction but the strongest speeds 7 mab occurred in downslope or down and along-slope direction (toward 180^{o} and 225^{o} in the rotated coordinate system, fig. 7-6).

The spectra and ellipse characteristics of the currents at station SF (fig. 7-7, 7-8, table 7-3) further document the flow characteristics seen in the time series plots. The spectra are characterized by fluctuations in five frequency bands; a low-frequency band (periods longer than about 60 hours), bands centered at the diurnal (24 hours), inertial (18.6 hours), and

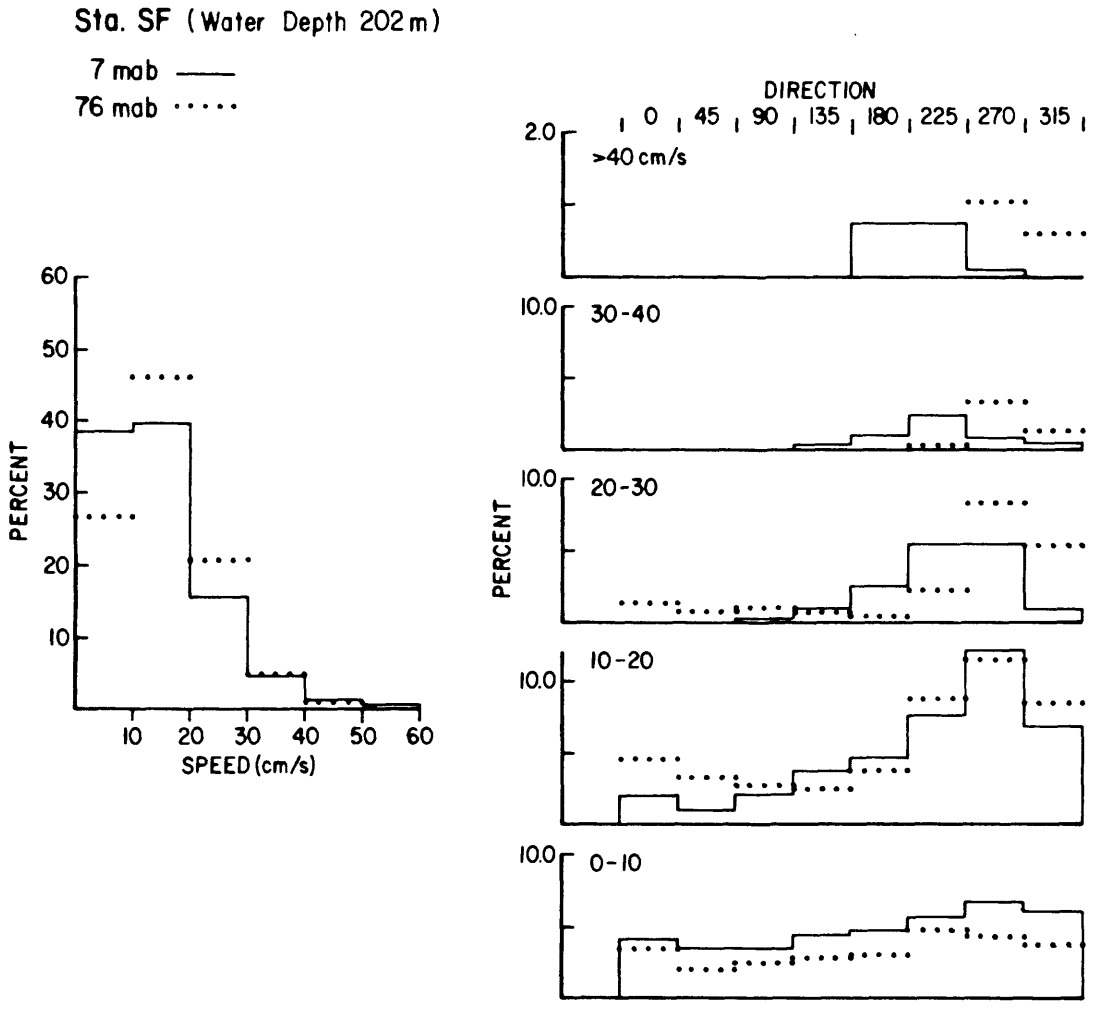

Figure 7-6. Histogram of near-bottom current speed, and histogram of current direction for various speed intervals for currents measured at station SF at 7 and 76 mab. The direction is relative to the local along-isobath coordinate system; 90 and 270 are the along-isobath directions and 0 (on-slope) and 180 (downslope) are the cross-isobath directions.

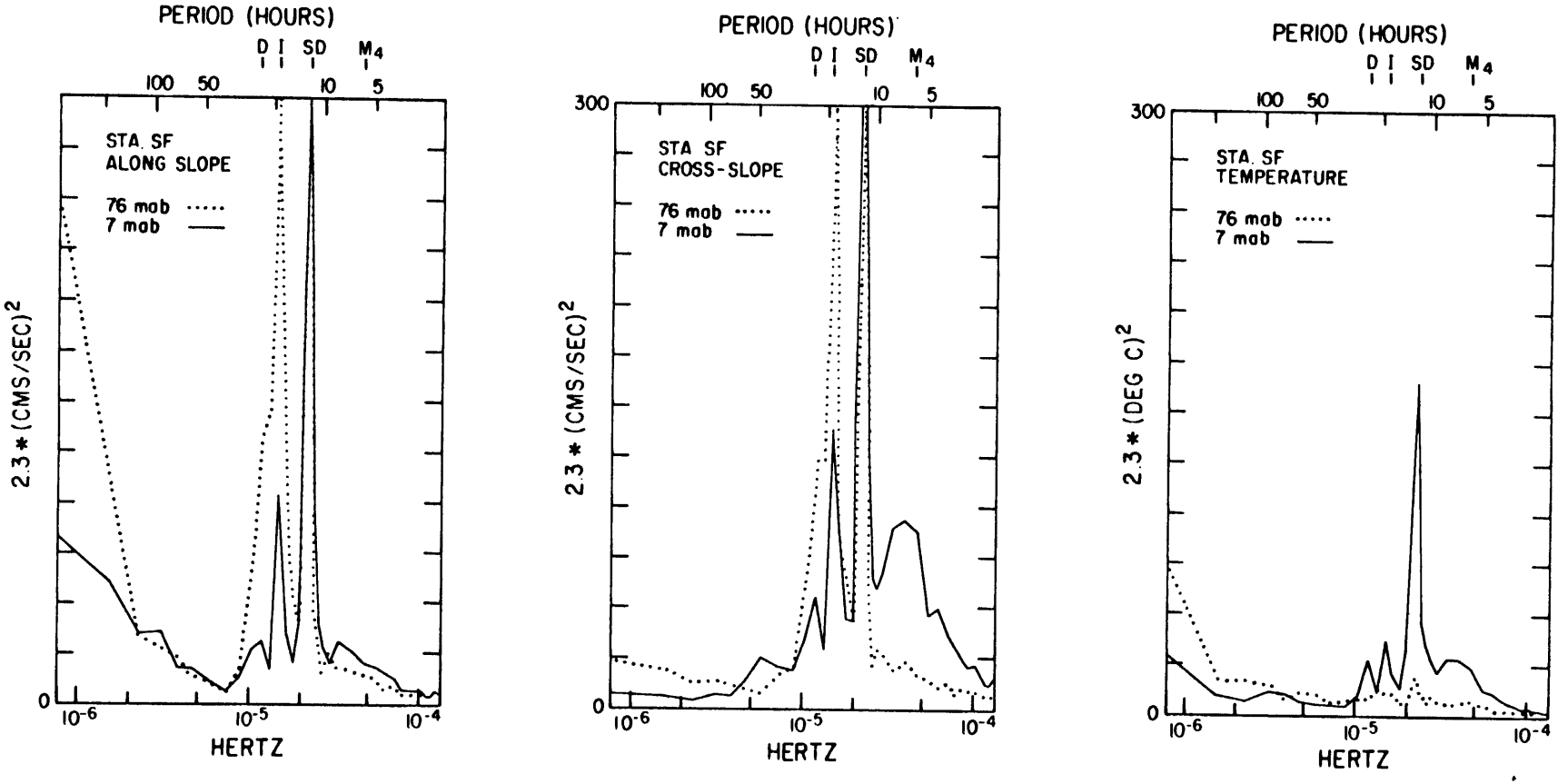

Figure 7-7. Variance conserving kinetic energy spectra for currents observed at station SF at 7 and 76 mab. The diurnal (D), inertial (I), semidiurnal (SD), and M_4 periods are labelled.

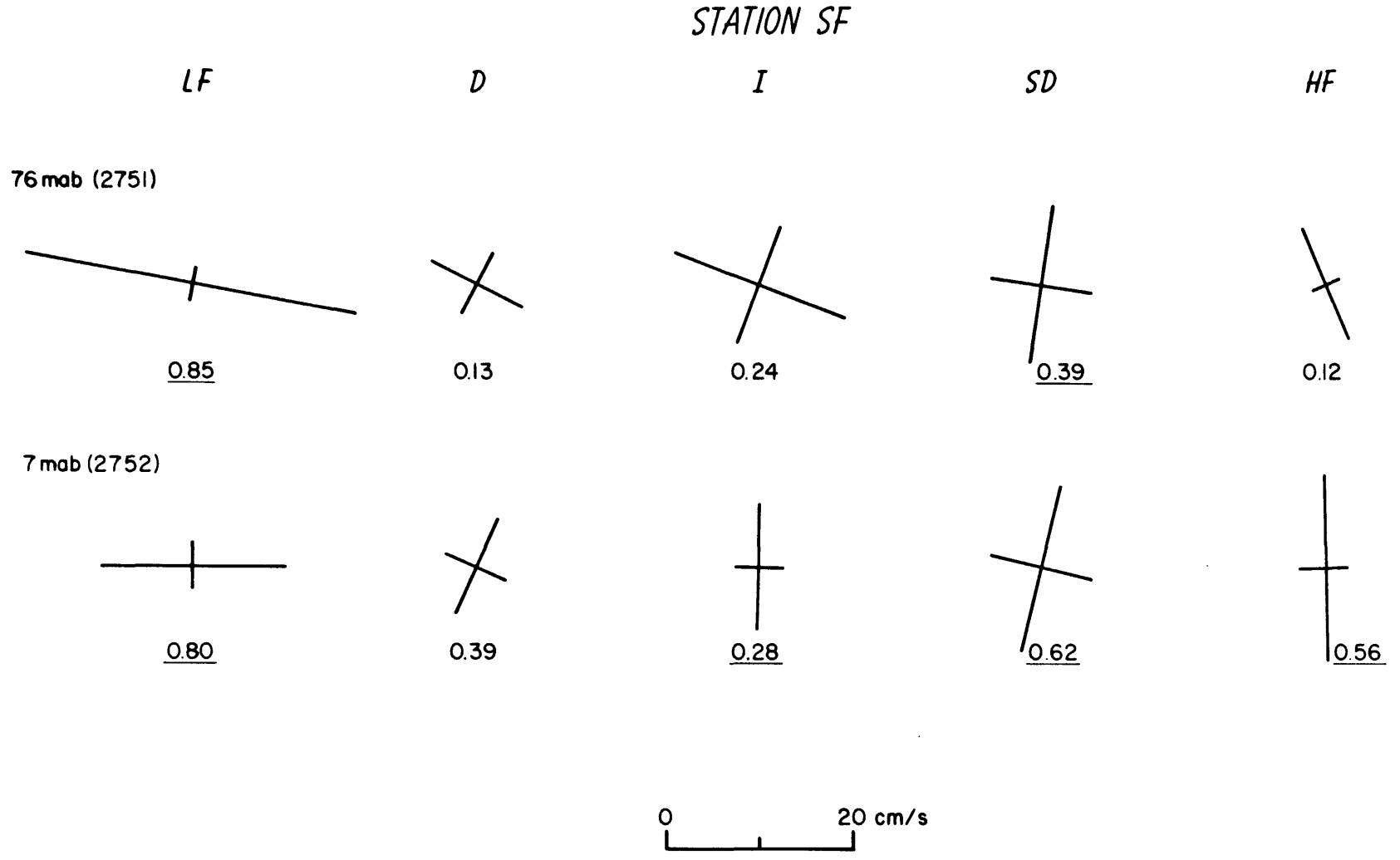

Figure 7-8. Current ellipses at 7 and 76 mab at station SF for energy in the low frequency (LF), diurnal (D), inertial (I), semidiurnal (SD), and high frequency (HF) bands. The number below each ellipse is the stability which is underlined if significant.

Table 7-3a. Total energy (T in cm^2/sec^2), major and minor axis of ellipse (in cm/sec), ratio of minor to major axis (R), ellipse orientation (θ, measured clockwise from north), and ellipse stability (S, underlined if significant) for observations between 7 and 200 mab in 5 frequency bands; low frequency, periods from 360 to 60 hours; diurnal, periods from 25.7 to 22.5 hours; inertial, periods from 21.2 to 13.3 hours; semidiurnal, periods from 12.85 to 11.6 hours; and high frequency, periods from 11.25 to 2 hours. Spectra computed for data prices 360 hours long. A negative u minor indicates ellipse rotates counter-clockwise.

Station	Height above bottom (m)	Record ID	Low Frequency					Diurnal					Inertial				
			T	U_{major}	U_{minor}	R	φ(s)	T	U_{major}	U_{minor}	R	φ(s)	T	U_{major}	U_{minor}	R	φ(s)
SF	76	2751	162.5	17.97	1.49	0.08	100(0.85)	19.6	5.27	3.38	0.64	116(0.13)	64.0	9.39	6.34	0.67	110(0.24)
	7	2752	67.9	9.94	2.29	0.23	90(0.80)	7.4	3.60	1.34	0.37	23(0.39)	26.0	6.72	2.59	0.38	1(0.28)
	76	2793	52.6	10.22	-0.92	-0.09	103(0.64)	15.7	4.60	3.19	0.69	79(0.33)	16.7	4.97	2.94	0.59	115(0.24)
	7	2794	40.6	9.00	0.35	0.04	89(0.78)	5.5	3.23	0.75	0.23	168(0.45)	11.4	4.53	1.49	0.32	159(0.16)
SE	101	2743	99.0	14.06	0.46	0.03	88(0.96)	1.3	1.59	0.26	0.17	117(0.39)	14.2	4.79	2.35	0.49	145(0.40)
	7	2744	6.5	3.60	0.00	0.00	94(0.63)	1.1	1.44	0.12	0.08	132(0.28)	10.3	4.51	0.42	0.09	154(0.55)
	101	2783	49.5	9.95	0.15	0.02	88(0.94)	1.0	1.43	0.07	0.05	78(0.17)	9.4	4.00	1.62	0.41	159(0.21)
	7	2784	3.3	2.56	0.07	0.03	98(0.12)	0.8	1.27	-0.06	-0.04	137(0.28)	6.0	3.41	0.54	0.16	170(0.39)
SG	201	2811	48.9	9.89	-0.17	-0.02	94(0.94)	0.6	1.10	0.14	0.13	163(0.11)	4.0	2.62	0.99	0.38	174(0.34)
	7	2812	28.8	7.59	0.00	0.00	102(0.89)	1.0	1.40	0.07	0.05	78(0.19)	10.4	4.27	1.61	0.38	177(0.56)
LCI	55	2153	190.9	19.53	0.44	0.02	90(0.95)	3.6	2.62	0.59	0.22	82(0.41)	25.2	6.67	2.41	0.36	91(0.17)
	5	2154	73.4	12.11	-0.24	-0.02	92(0.84)	2.4	2.17	-0.12	-0.06	80(0.06)	15.5	5.52	0.66	0.12	172(0.17)
	50	2422	130.6	16.15	0.41	0.03	93(0.91)	1.5	1.72	0.34	0.20	103(0.27)	19.5	5.82	2.26	0.39	88(0.29)
	6	2423	95.5	13.82	-0.07	-0.00	94(0.75)	3.8	2.74	0.27	0.10	178(0.49)	23.7	6.71	1.54	0.23	10(0.37)
T	44	2831	113.6	15.06	0.59	0.04	105(0.56)	39.9	7.47	4.90	0.66	85(0.51)	27.9	6.62	3.48	0.53	17(0.10)
	7	2832	38.3	8.75	0.16	0.02	79(0.67)	27.3	6.30	3.86	0.61	64(0.64)	30.0	6.72	3.84	0.58	24(0.22)

Table 7-3b.

Station	Height above bottom (m)	Record ID	Semidiurnal					High-frequency				
			T	U_{major}	U_{minor}	R	ϕ(s)	T	U_{major}	U_{minor}	R	ϕ(s)
SF	76	2751	49.6	8.22	5.62	0.68	8(0.39)	20.3	6.21	1.42	0.23	157(0.12)
	7	2752	55.4	8.97	5.51	0.61	13(0.62)	52.0	9.94	2.30	0.23	179(0.56)
	76	2793	43.9	7.62	5.44	0.72	15(0.46)	10.1	4.35	1.16	0.27	161(0.13)
	7	2794	31.7	7.16	3.47	0.48	165(0.49)	45.7	9.25	2.40	0.26	172(0.50)
SE	101	2743	17.0	5.57	1.75	0.31	167(0.61)	12.7	4.89	3.36	0.25	167(0.32)
	7	2744	15.9	5.63	0.20	0.07	154(0.71)	33.8	8.13	1.24	0.15	172(0.66)
	101	2783	20.6	6.17	1.79	0.29	168(0.63)	14.3	5.20	1.25	0.24	167(0.40)
	7	2784	10.9	4.66	-0.20	-0.04	163(0.43)	28.6	7.50	0.99	0.13	178(0.63)
SG	201	2811	5.1	3.01	1.02	0.34	160(0.14)	3.4	2.55	0.47	0.19	172(0.30)
	7	2812	13.9	5.02	1.57	0.31	176(0.68)	9.8	4.25	1.27	0.30	2(0.44)
LCI	55	2153	124.7	13.53	8.14	0.60	85(0.36)	34.2	8.13	1.55	0.19	45(0.09)
	5	2154	43.7	8.70	3.41	0.39	6(0.63)	61.5	11.01	1.28	0.12	1(0.52)
	50	2422	99.5	11.66	7.94	0.68	154(0.17)	24.7	6.90	1.34	0.20	28(0.13)
	6	2423	83.1	11.72	5.38	0.46	20(0.68)	65.7	11.23	2.29	0.20	13(0.50)
T	44	2831	145.1	13.99	9.72	0.70	17(0.86)	16.3	5.61	1.08	0.19	154(0.12)
	7	2832	109.5	12.10	8.52	0.70	22(0.82)	25.1	6.80	1.97	0.29	6(0.36)

semidiurnal (12 hours) periods, and a high-frequency band (periods shorter than about 10 hours, centered at M_4 (6.21 hours), the semidiurnal harmonic). In the low-frequency band, the currents were strongly polarized along-isobaths, the ellipse orientation was quite stable, and the energy decreased toward the bottom. In the diurnal and inertial bands, the currents were generally less polarized than in the low-frequency band; although the total energy in these bands decreased toward the bottom, the current ellipses were increasingly stable and orientated in the cross-isobath direction, resulting in slightly increased cross-isobath current fluctuations near the bottom. In the semidiurnal band, the ellipse was more stable near-bottom but the energy, orientation, and polarization remained almost unchanged. In the high-frequency band, the energy near the bottom increased by more than a factor of two, and the currents were strongly polarized across-isobaths. Overall, the effect of the increased polarization and across-isobath orientation of the diurnal and inertial energy and the increased energy in the high frequencies near the bottom is stronger across-isobath currents near the bottom.

The coherence between the along-slope and cross-slope near-bottom and mid-depth currents was high at the diurnal, inertial, and semidiurnal periods, and the near-bottom flow led the flow at mid-depth by about 30-50^{o} in the inertial and semidiurnal bands (fig. 7-9). The along-isobath flow was coherent at low frequencies. At frequencies higher than M_2 (including the M_4 band), both along-isobath and cross-isobath flows were vertically incoherent.

The coherence between sigma-t and cross-slope current was uniformly high for periods from 3 to 24 hours 7 mab and at the diurnal, inertial and semidiurnal periods 76 mab (fig. 7-10). At both depths, the density lagged the cross-slope flow by about 45^{o} and thus there is an upslope Reynolds flux of density at both levels. A time series of the low-passed Reynolds flux,

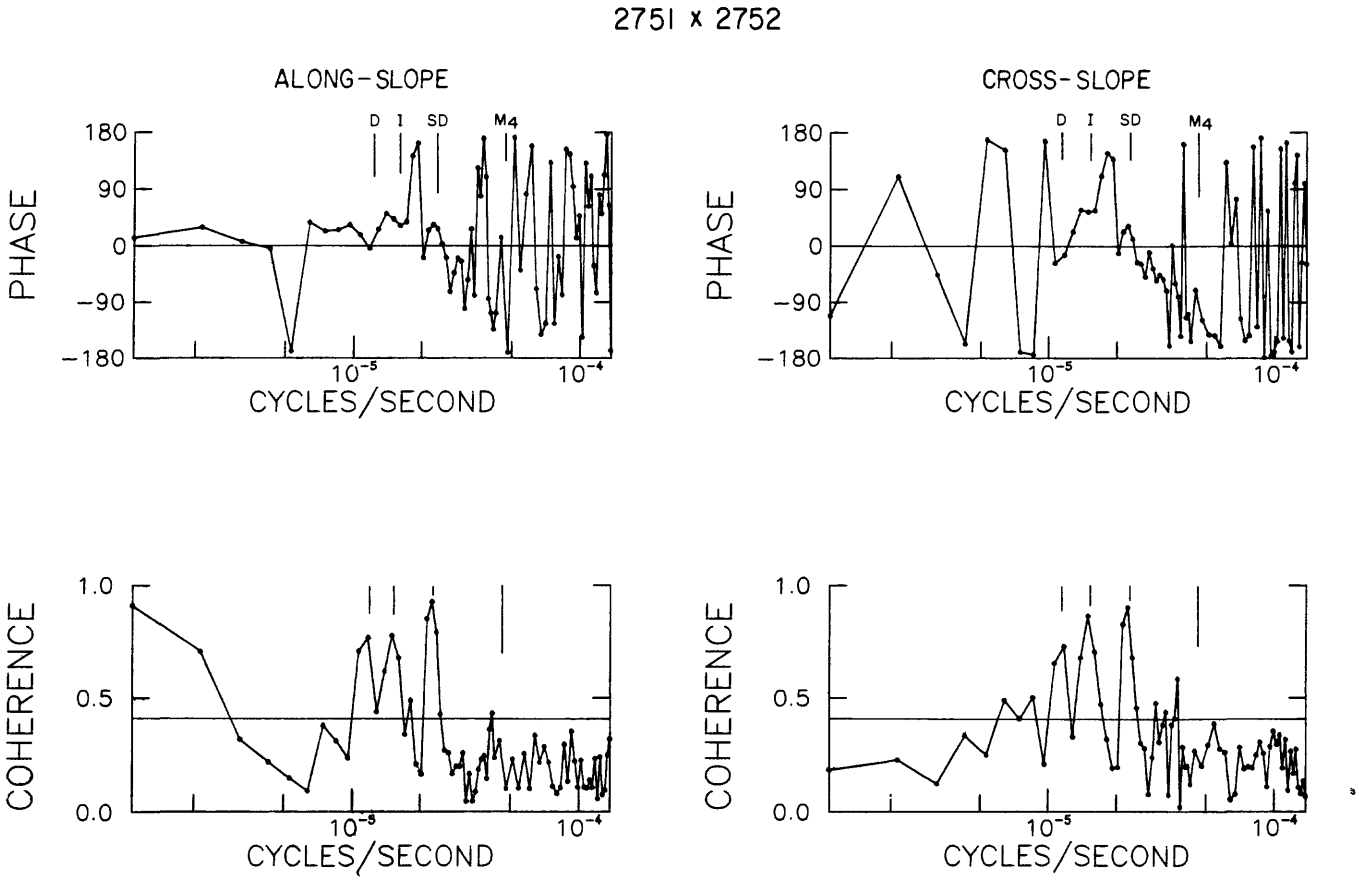

Figure 7-9. Coherence between the along-slope and cross-slope currents at station SF at 7 and 76 mab. Positive phase indicates the current at 7 mab leads the current at 76 mab. The 95% confidence level is shown on the coherence plot. D, I, SD, and M_4 as in figure 7-7.

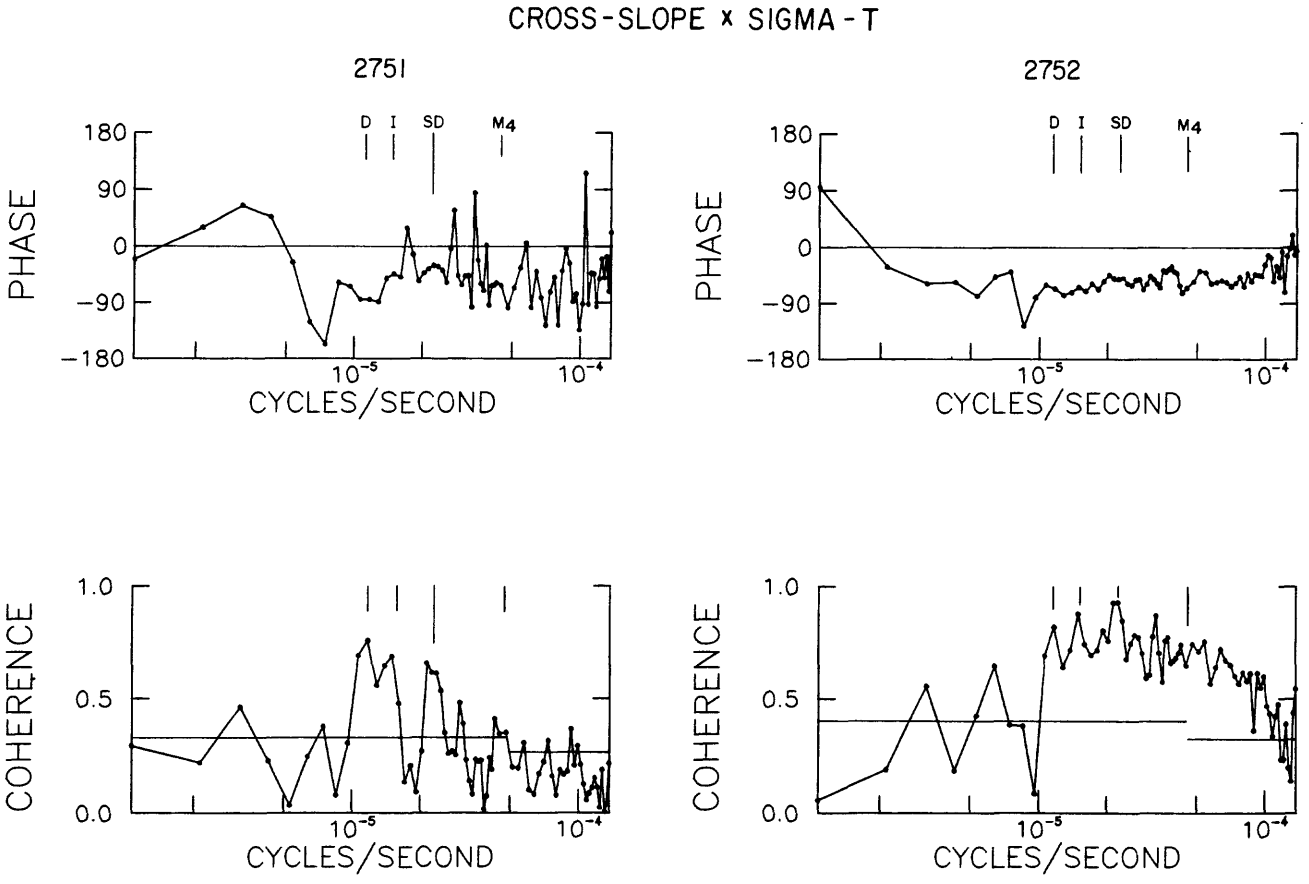

Figure 7-10. Coherence between the cross-slope current and sigma-t at 7 mab and 76 mab at station SF. A negative phase indicates that the density lags the up-slope current. D, I, SD and M_4 as in figure 7-7. The uniformly high coherence and negative phase for fluctuations with periods between about 3 hours and the diurnal period causes an up-slope Reynolds density flux.

$\rho'u'$ where ρ' and u' are the high-passed cross-slope density and current and the overbar indicates low-pass, shows an upslope flux of order 0.5×10^{-3} gm/cm^2-sec at both 76 and 7 mab. At the semidiurnal period the upslope Reynolds flux of density 7 mab was 1.1×10^{-4} gm/cm^2-s. The low-passed downslope flow was extremely well correlated with the upslope Reynolds density flux (fig. 7-11).

A measure of the amplitude of the high-frequency fluctuations as a function of time was obtained by converting the high-passed current components to speed and direction and low-passing the scalor speed (fig. 7-12). There was no correlation between the low-passed cross-slope current and the low-passed amplitude of the high-frequency current at mid-depth, but an excellent correlation near the bottom (fig. 7-13). That the magnitude of the low-passed downslope flow is associated with the amplitude of the high frequency current fluctuations and with the associated upslope Reynolds flux suggests some role of these fluctuations in the dynamics of the downslope flow.

Near-bottom flow at other stations

Most of the characteristics of the flow near the bottom observed at station SF--a net downslope flow, increased high-frequency fluctuations in the cross-slope current, increased asymmetry in strength of upslope and downslope current, and correlation between the net downslope flow and the strength of the high-frequency fluctuations--were also observed at all other stations on the upper-slope, although the effects decreased with water depth (table 7-2, 7-3). Overall, the strength of the current speed decreased with water depth and toward the bottom (fig. 7-14a, table 7-2); speeds exceeded 5% of the time were typically greater than 30 cm/sec on the upper slope, and decreased to about 20 cm/sec at 1150 m. Although the total speed decreased toward the

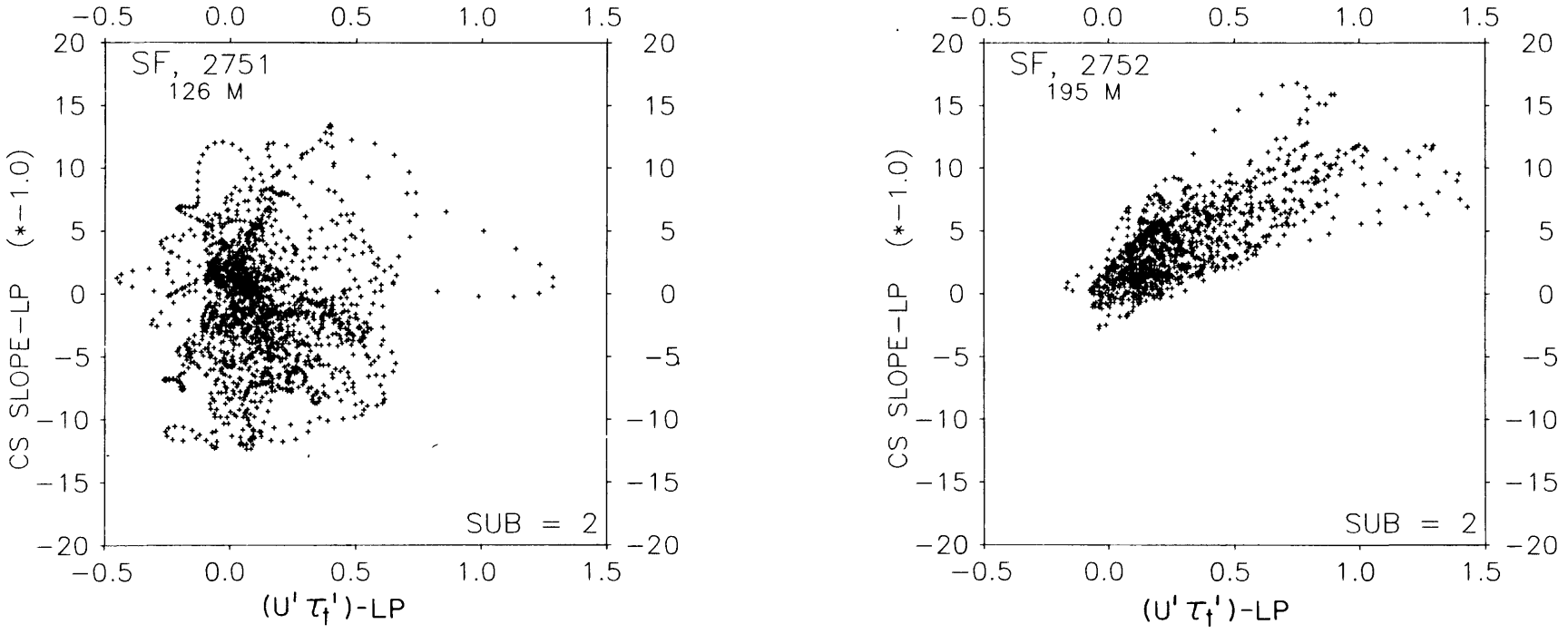

Figure 7-11. Scatter plot of low-passed cross-slope Reynolds flux of density (sigma-t) vs low-passed cross-slope current at station SF at 76 and 7 mab.

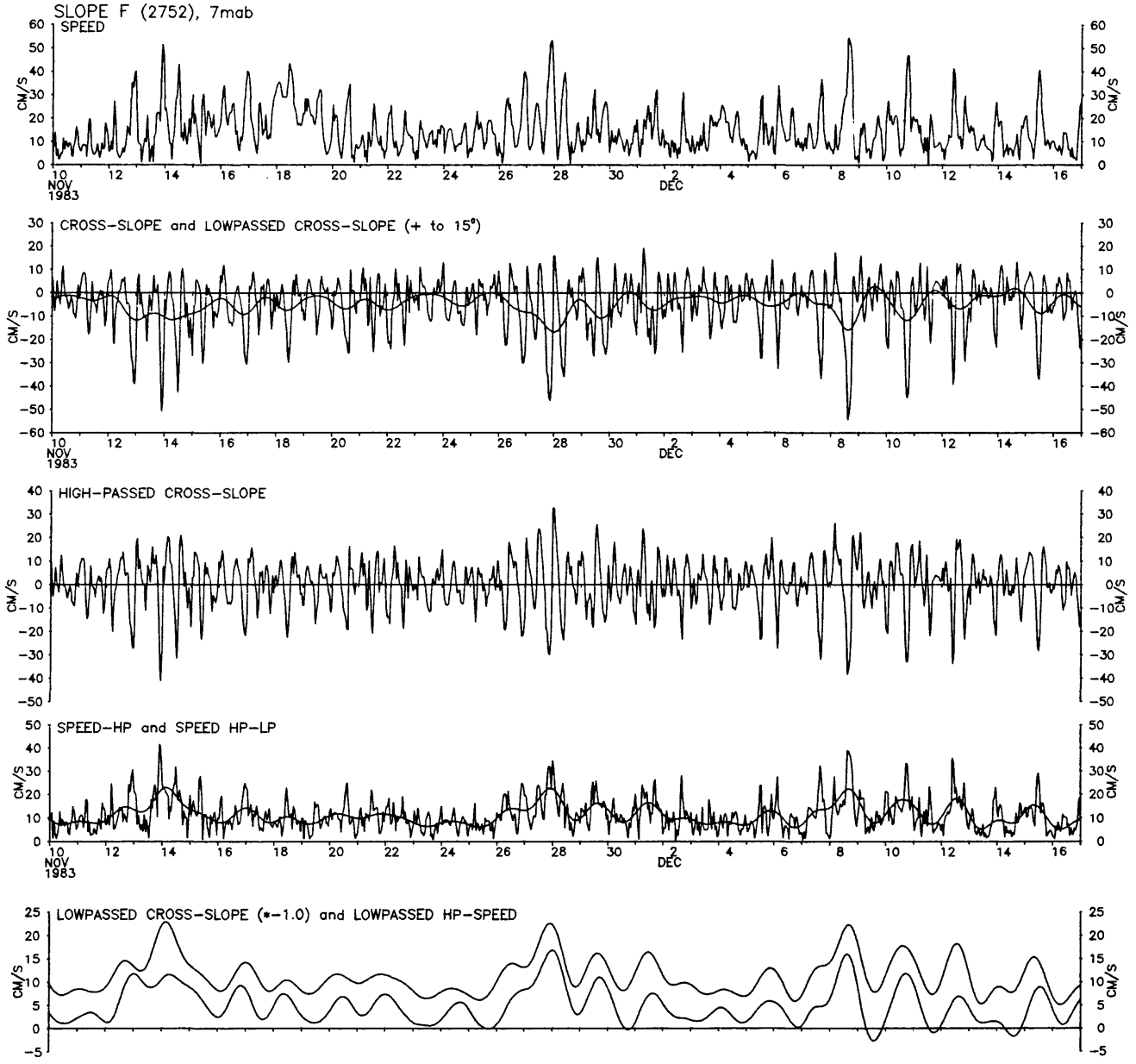

Figure 7-12. Time series of a portion of record 2752 at station SF illustrating the procedure used to estimate the envelope of the high frequency current fluctuations. The upper panel shows the current speed, and the second panel the across-isobath current component with the low-passed flow superimposed. The third panel shows the high-passed component and panel 4 the amplitude of the high-passed flow, and the low-pass of this amplitude. The bottom panel repeats the low-passed amplitude of the high frequency fluctuations along with the low-passed cross-slope flow (positive downslope).

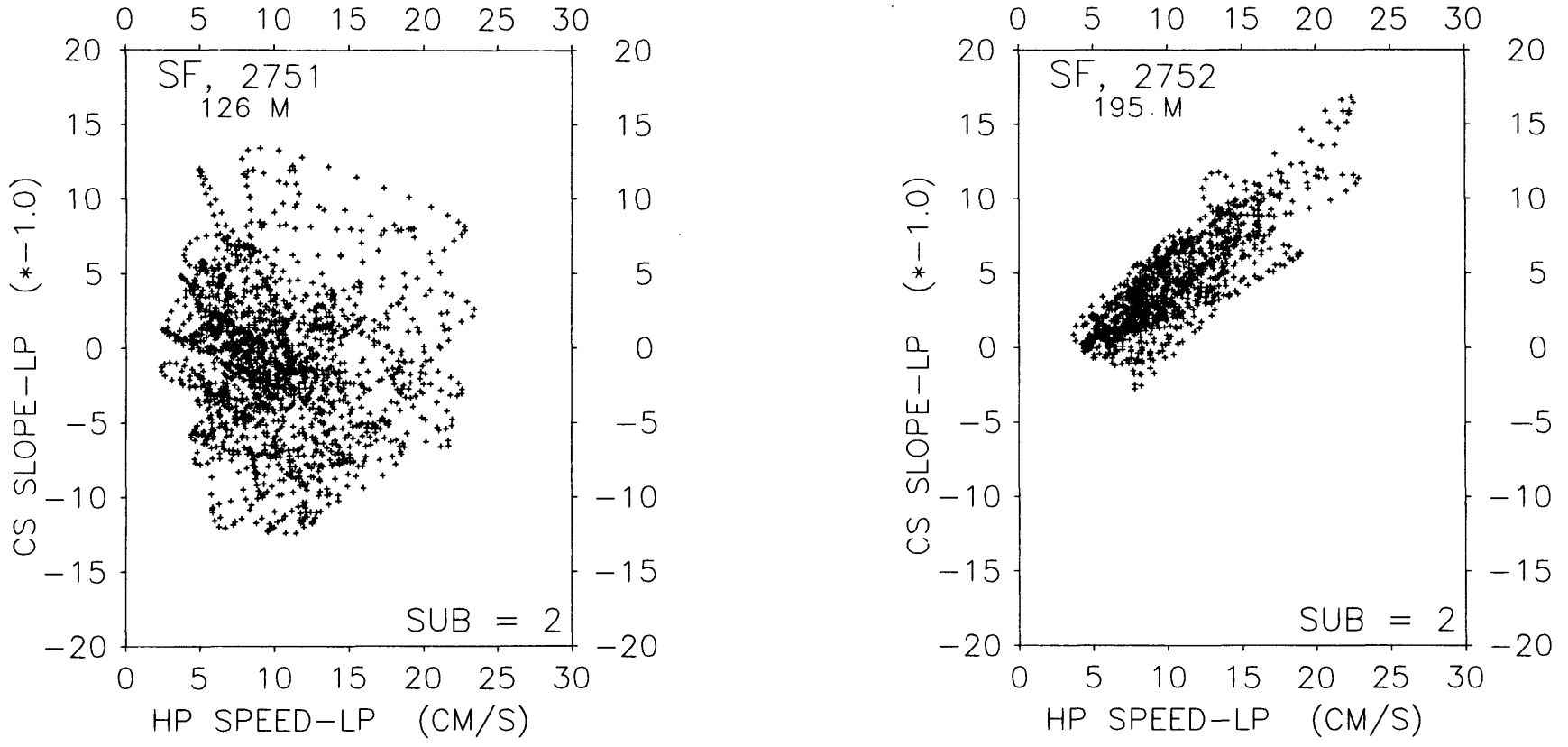

Figure 7-13. Scatter-plot of low-passed across-slope flow vs amplitude of high-frequency fluctuations for currents at 7 and 76 mab at station SF.

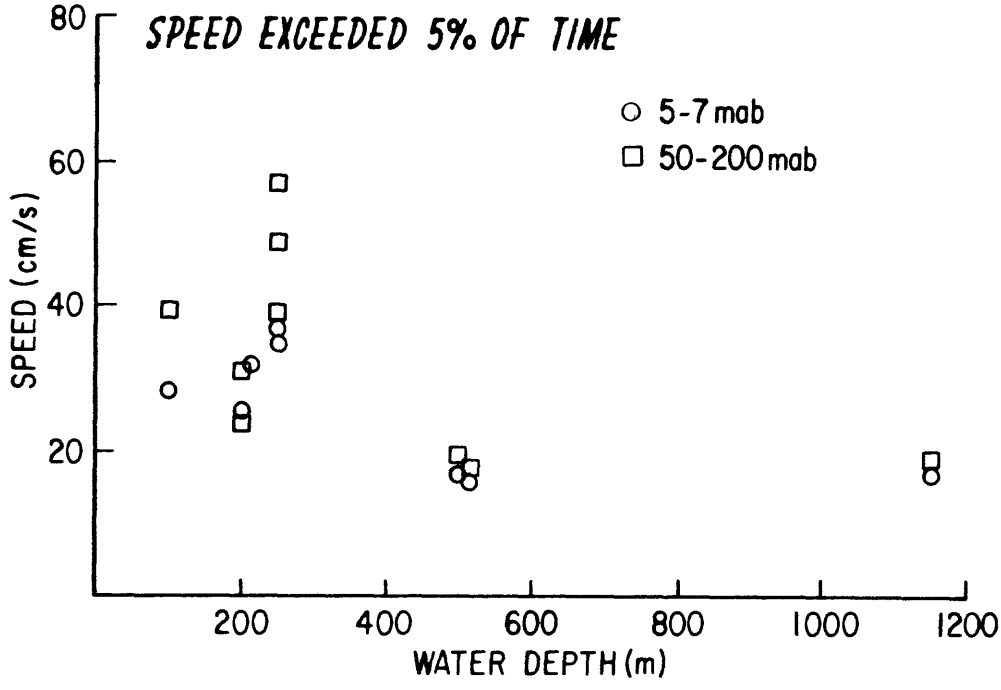

Figure 7-14a. Speed exceeded 5% of the time for measurements at 7 and 50-200 mab as a function of water depth. The stronger speeds at 250 m (station LCI) reflect the increased tides in the Georges Bank region, not necessarily a local maximum at 250 m.

bottom, the standard deviation of the cross-isobath component generally increased slightly toward the bottom (table 7-2) especially at stations where measurements made 5-7 mab could be compared to currents within 100 mab. The near-bottom current speed in the downslope direction (exceeded 1% of the time) was about 37 cm/s at 200 m water depth and decreased to about 16 cm/s at 1150 m (table 7-2, fig. 7-14b). The ratio between near-bottom speed exceeded 1% of the time in the downslope direction to the speed exceeded 1% of the time in the upslope direction was almost 3 at 200 m water depth, and decreased to about 1.5 at 1150 m (fig. 7-14c). In contrast, at 50-200 m from the bottom, the strongest downslope currents were always less than near the bottom, and the ratio between strongest upslope to strongest downslope was greater than one only at 200 m water depth.

The amplitude of the low-passed cross-slope current was correlated with the amplitude of the high frequency currents at all stations (fig. 7-15) and the strength of the high frequency fluctuations and of the low-passed downslope flow generally decreased with depth across the slope. On a record-averaged basis, the net downslope flow was proportional to the total standard deviation (dominated by the high-frequency fluctuations) of the cross-slope component of flow (fig. 7-16).

At all stations, the energy decreased toward the bottom in the low-frequency, diurnal, inertial, and semi-diurnal bands, but increased by a factor of 2 to 3 toward the bottom in the high-frequency band (table 7-3). The current ellipse was oriented nearly parallel to the local isobaths for the low frequencies with little change near the bottom. In contrast, at high frequencies, the ellipse was oriented nearly across-isobaths, and more so at 5-7 mab than at 50-200 mab. Finally, the ellipse stability decreased slightly near-bottom for the low frequencies, but otherwise generally increased near the bottom, especially in the semidiurnal and high frequency bands.

a.

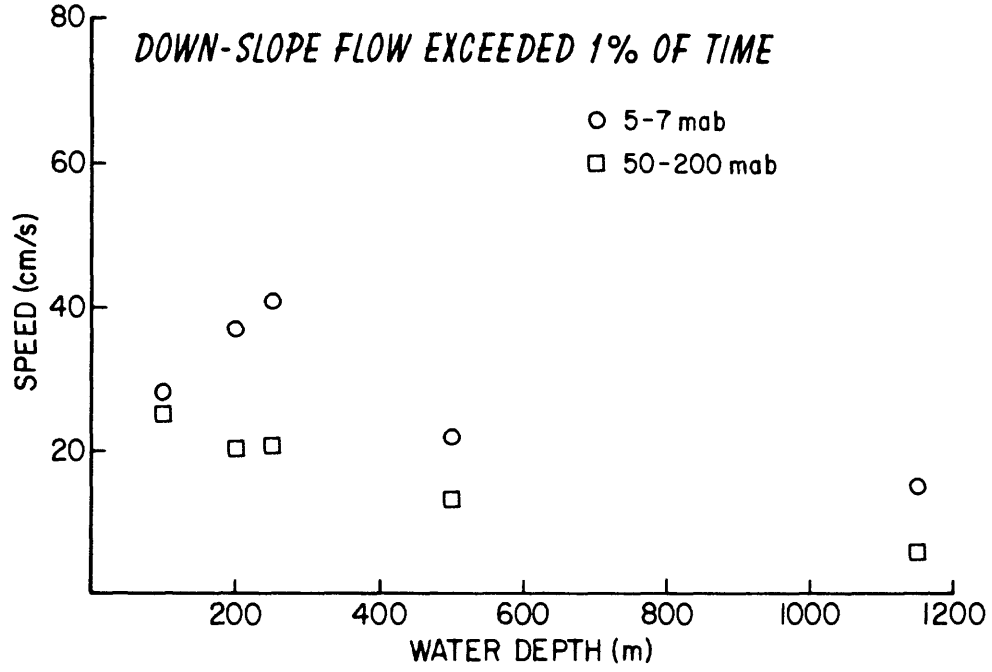

b.

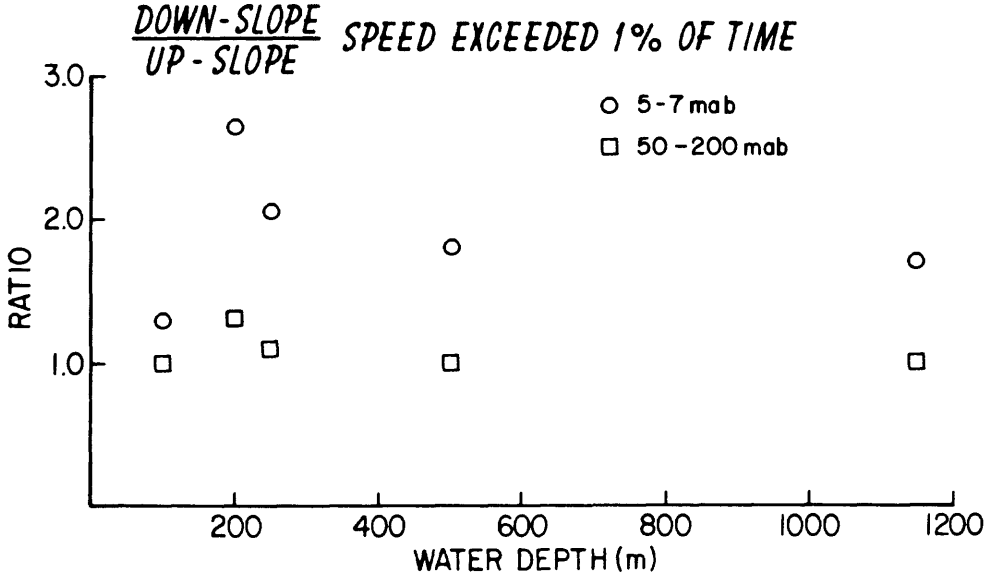

Figure 7-14b. Downslope flow exceeded 1% of the time for measurements at 7 and 50-200 mab as a function of water depth. The stronger speeds at 250 m (station LCI) reflect the increased tides in the Georges Bank region, not necessarily a local maximum at 250 m.

Figure 7-14c. Ratio of downslope flow exceeded 1% of the time to up-slope flow exceeded 1% of the time for measurements at 7 and 50-200 mab as a function of water depth. The stronger speeds at 250 m (station LCI) reflect the increased tides in the Georges Bank region, not necessarily a local maximum at 250 m.

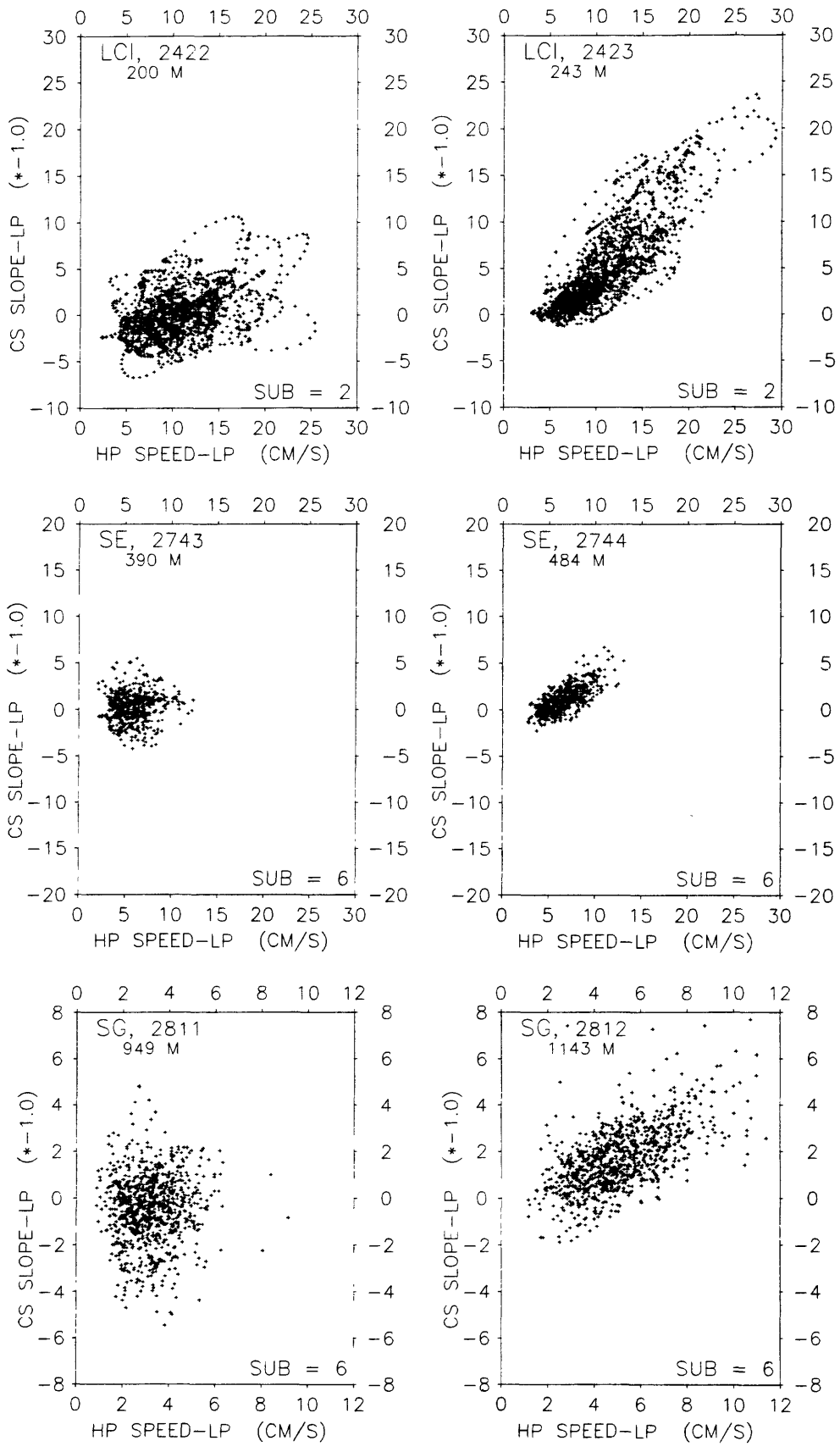

Figure 7-15. Scatter plot of low-passed across-slope flow vs amplitude of high frequency fluctuations for currents at 7 and 50-200 mab at LCI, SE, and SG in water depths of 250, 500, and 1150 m respectively.

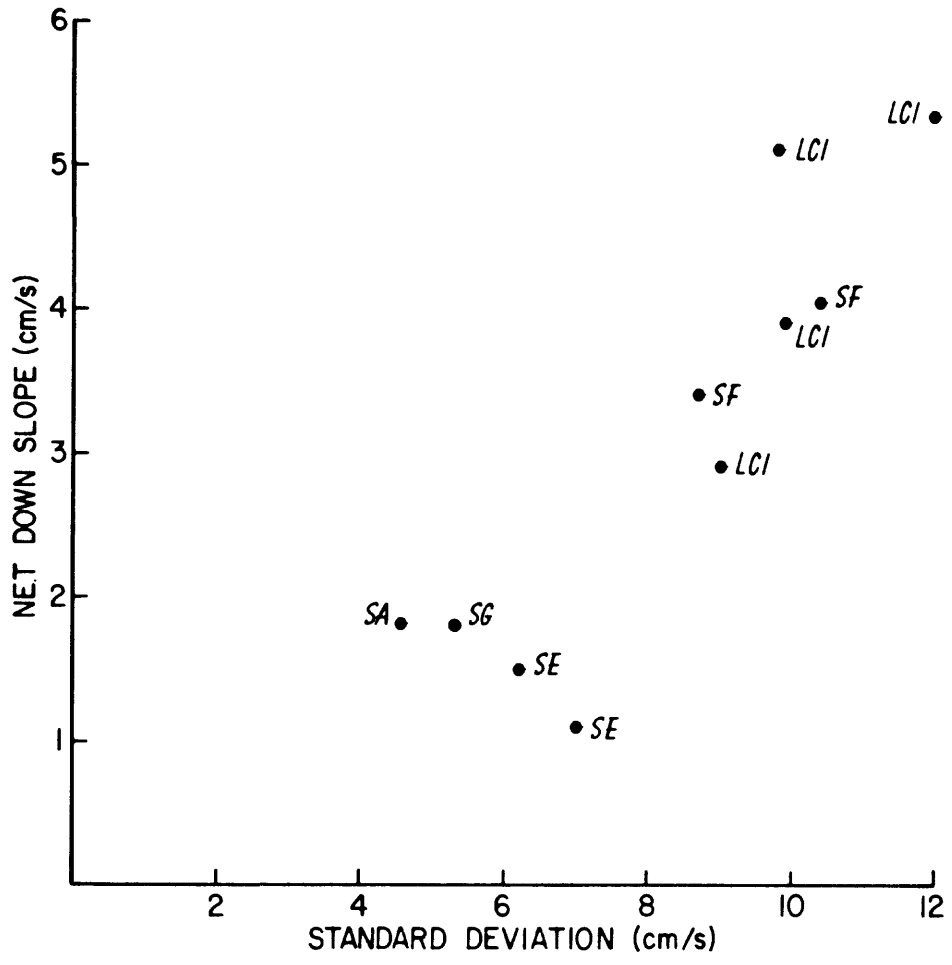

Figure 7-16. Net across-slope flow vs standard deviation of cross-slope flow for current observations 5-7 mab at stations SF, LCI, SA, SE, and SG at nominal water depths of 200, 250, 500 and 1150 m.

DISCUSSION AND CONCLUSIONS

These observations show three characteristics of the near-bottom flow on the outer-shelf and upper slope south of New England: (1) a net Eulerian mean flow of order 5 cm/s generally parallel to the local isobaths but with increased downslope flow near the bottom; (2) fluctuations in the cross-isobath flow that are stronger and increasingly asymmetric near the bottom (i.e., the speed of the downslope flow exceeds the upslope flow by a factor of 2 to 3 caused by increased high-frequency fluctuations and orientation of the current ellipse across-isobaths), and (3) the strength of the low-passed downslope flow near the bottom is proportional to the amplitude of the upslope Reynolds flux of density as well as to the amplitude of the current fluctuations that have periods shorter than 30 hours. These flow characteristics were observed at water depths of 200, 250, 500 and 1150 m on the slope, and at stations separated along-slope by over 200 km. The characteristics are apparently common features of the flow, not influenced by the presence of Gulf Stream rings or major storms. The thickness of the bottom boundary layer in which these flow characteristics occur is at least 7 m, but less than 50 m.

The currents reported here are Eulerian measurements, and do not necessarily indicate the Lagrangian transport of water or sediment. In fact, it is hard to reconcile a net Lagrangian downslope flow in this region where the bottom slope is typically 0.05 to 0.15 (3^o to 9^o). A net downslope flow of 1 cm/s corresponds to a change in depth of almost 100 m/day and is inconsistent with the stable density stratification unless there is outflow of near-bottom water into the interior or mixing.

One mechanism which might maintain the observed density field is that the net Eulerian downslope flow may be balanced by an upslope Stokes drift

associated with the internal tidal wave field (Wunsch, 1971; Ou and Mass, 1986). Estimates of the residual near-bottom cross-wedge flow using the inviscid baroclinic theory in Ou and Mass (1986) are of the right order, but several assumptions of the model do not agree with observation. For example, their theory is for a single fequency, but the observed upslope buoyancy flux occurs over the entire internal wave band (fig. 7-9). In addition, the large increase in energy near the bottom centered at the M_4 tidal period is good evidence for the influence of bottom friction, which is not included in the internal wave model, and the curving sigma-t surfaces near the shelf-break and the large vertical change in N (fig. 7-2d) are not consistent with constant N in the vertical and horizontal. Finally the observation that internal waves in this region of the slope might propagate downslope from a generation region at the shelf break rather than upslope would yield an upslope, not downslope Eulerian mean flow.

Perhaps the simplest explanation for the observed Eulerian downslope flow is vertical mixing in the bottom boundary layer where a stratified fluid flows upslope and downslope. As water flows upslope, the fluid near the bottom is retarded by friction, heavier water runs over lighter water, and vertical mixing occurs as the lighter water rises through the boundary layer. Because of enhanced vertical mixing, the bottom boundary layer is thicker and the flow at a fixed height above the bottom is weaker than would be observed in a constant density case. As water flows downslope, lighter water overruns heavier water. The boundary layer is stably stratified, consequently thinner, and there is stronger flow at a fixed height above bottom than in the constant density case. In addition, the vertical mixing during the upslope flow caused by the unstable stratification will create heavier water along the slope relative to the interior, which may enhance the downslope flow, or drive a

secondary steady circulation. The near-bottom current meters record a net Eulerian downslope flow because they are in a slow velocity region of a relatively thick boundary layer during upslope flow, and in the outer fast velocity portion of a thinner boundary layer during downslope flow. There may be a residual Lagrangian flow associated with this mixing, but it remains to be determined, as well as any associated net transport of water or suspended sediment. However, the strong asymmetry in strength of the near-bottom flow clearly implies net off-shelf transport of material which moves as bedload or which does not remain in suspension for a complete tidal cycle. In addition, the strong near-bottom speeds observed on the upper slope (station SF (200 m) and LCI (250 m)) are occasionally strong enough to resuspend the existing sediments.

ACKNOWLEDGEMENTS

V. Lyne provided helpful analysis and advice.

REFERENCES

Bothner, M. H., Spiker, E. C., Johnson, P. P., Rendigs, R. R., and Aruscavage, P. J., 1981, Geochemical evidence for modern sediment accumulation on the continental shelf off southern New England: Journal of Sedimentary Petrology, v. 51, p. 281-292.

Bumpus, D. F., 1973, A description of the circulation on the continental shelf of the United States: Progress in Oceanography, v. 6, p. 111-157.

Butman, B., Processes causing surficial sediment movement, chapter 13, in Backus, R. H. (ed.), Georges Bank, MIT Press, Cambridge, MA. (in press).

Butman, B., Moody, J. A., and Conley, S. J., 1985, Hydrography of the New England shelf and slope: Data report for R/V Oceanus cruise 140, October, 1983: U.S. Geological Survey Open-File Report 85-505, 199 p.

Butman, B., and Moody, J. A., 1984, Bathymetric map of Lydonia Canyon, U.S. Atlantic outer continental shelf: U.S. Geological Survey Map MF-1710, 2 sheets.

Cacchione, D. A., and Wunsch, C., 1974, Experimental study of internal waves over a slope: Journal of Fluid Mechanics, v. 66, p. 223-229.

Carpenter, G. B., Cardinell, A. P., Francois, D. K., Good, L. K., Lewis, R. L., and Stiles, N. T., 1982, Potential geologic hazards and constraints for blocks in proposed North Atlantic OCS oil and gas lease sale 52: U.S. Geological Survey Open-File Report 82-36, 51 p., 3 plates.

Csanady, G. T., Churchill, J. H., and Butman, B., Near-bottom currents over the Continental Slope in the Mid-Atlantic Bight: Continental Shelf Research. (Submitted)

Csanady, G. T., and D. T. Shaw, 1983, The "insulating" effect of a steep continental slope: Journal of Geophysical Research, v. 88, p. 7519-7524.

Erickson, C. C., 1982, Observations of internal wave reflection off sloping bottoms: Journal of Geophysical Research, v. 87, p. 525-538.

Karl, H. A., Carlson, P. R., and Cacchione, D. A., 1983, Factors that influence sediment transport at the shelfbreak, in Stanley, D. J., and Moore, G. T. (eds.), The Shelfbreak: Critical Interface on Continental Margins: Tulsa, OK., Society of Economic Paleontologists and Mineralogists Special Publication No. 33.

Moody, J. A., Butman, B., and Bothner, M. H., Estimates of near-bottom suspended-matter concentration during storms: Continental Shelf Research. (Submitted)

Ou, H. W., and Mass, L., 1986, Tidal-induced buoyancy flux and mean transverse circulation, Continental Shelf Research, v. 5, p. 611-628.

Scanlon, K. M., 1984, The continental slope off New England: A long-range sidescan-sonar perspective: Geo-Marine Letters, v. 4, p. 1-4.

Schlee, J. S., 1973, Atlantic continental shelf and slope of the United States, sediment texture of the northeastern part: U.S. Geological Survey Professional Paper 529-L, 64 pp.

Stanley, D. J., Addy, S. K., and Behrens, E. W., 1983, The mudline: variability of its position relative to shelfbreak, in Stanley, D. J., and Moore, G. T., (eds.), The Shelfbreak: Critical Interface on Continental Margins: Tulsa, OK., Society of Economic Paleontologists and Mineralogists Special Publication No. 33, p. 279-298.

Strahle, W. J., and Butman, B., 1985, Modification of EG & G vector averaging current meter to record light transmission and water conductivity: U.S. Geological Survey Open-File Report 85-106, 22 p.

Wunsch, C. and Hendry, R., 1972, Array measurements of the bottom boundary layer and the internal wave field on the continental slope: Geophysical Fluid Dynamics, v. 4, p. 101-145.

Wunsch, C., 1971, A note on some Reynolds stress effects of internal waves on slopes: Deep-Sea Research, v. 18, p. 583-591.

APPENDIX 1

A FIELD COMPARISON OF FOUR SEDIMENT TRAPS: CHANGES IN COLLECTION RATE WITH TRAP GEOMETRY AND SIZE

By

Michael H. Bothner, Bradford Butman, and Carol M. Parmenter

Appendix 1

Table of Contents

Page

Abstract.....A1-1

Introduction.....A1-1

Equipment and Methods.....A1-3

Traps.....A1-3

Poison Dispensers.....A1-5

Baffles.....A1-6

Deployment and Recovery.....A1-7

Current Measurements.....A1-10

Laboratory Methods.....A1-10

Results and Discussion.....A1-11

Changes in collection rate with trap type.....A1-11

Influence of mooring tilt.....A1-17

Influence of poison.....A1-18

Conclusions.....A1-19

Acknowledgements.....A1-20

References.....A1-21

ABSTRACT

Sediment traps of four different sizes were deployed in two experiments in the axis of Lydonia Canyon to determine the relative efficiency of sediment collection. Traps were deployed on subsurface moorings about 110 m above the bottom in water depths of 295 m and 560 m for 4-5 months. During this period, the average current speed was about 15 cm/s, and the maximum speed about 50 cm/s. Much of the material collected by the traps was resuspended bottom sediment.

In both experiments a cylindrical trap with the smallest mouth diameter and largest aspect ratio (60 cm long / 6.6 cm in diameter) collected at the highest rate (in grams per square meter per day) and the conical trap with the largest mouth diameter and smallest aspect ratio (200 cm long / 50 cm in diameter) collected at the lowest rate. Trapping rate changed by about a factor of four for the traps tested. The collection efficiency decreased almost linearly with increasing trap diameter, with decreasing aspect ratio and with increasing trap Reynolds number (assuming a constant flow velocity). These results suggest that sediment collection rates determined from traps deployed in different hydrodynamic regimes or from traps of different size and shape may vary considerably and should be interpreted with caution.

INTRODUCTION

An extensive moored array of sediment traps was used to collect suspended sediment as part of a study of current and sediment dynamics in Lydonia Canyon and on the adjacent shelf and slope on the southern flank of Georges Bank (Butman and others, 1983; Butman 1983; Bothner and others, 1983) on the U.S. Atlantic Margin. Because a wide range in the flux of material was expected in

these different physiographic areas, traps of different size and shape were used to ensure that sufficient sediment would be collected for analysis. The comparison study described here was conducted to estimate the relative efficiency of each trap so that sediment collection rate in traps of different size and shape could be compared.

The sediment traps used in this study have not been calibrated in the laboratory under conditions hydrodynamically similar to those encountered in the field (as is the case for some sediment traps; see Butman and others, 1986; Butman, 1986). Thus, the absolute efficiency of these traps is unknown and we can only compare relative rates of sediment collection. In addition, even if these traps were shown to accurately measure particle flux, their use so close to the bottom complicates an estimate of primary flux because frequent resuspension of bottom sediment from the walls and floor of the canyon extends to the depth interval occupied by the traps. Because these traps collected material that was resuspended from the seafloor, the collection rates are considerably higher than the long-term net deposition rates.

In their review of sediment collection by traps, Butman and others (1986) suggest that the efficiency of sediment collection is a function of six dimensionless parameters. The efficiency of traps has been investigated in previous laboratory studies for only three of these six parameters and only over a limited range of values. Based on these limited studies and a theoretical analysis Butman and others (1986) suggest that for fixed values of other parameters, the trap efficiency of cylinders should:

(1) decrease over some range of increasing trap Reynolds number (UD/ν, where U = horizontal fluid velocity; D = trap diameter; ν = kinematic fluid viscosity);

(2) decrease over some range of decreasing particle fall velocity; and

(3) increase over some range of increasing trap aspect ratio (H/D, where H = trap height).

Laboratory flume studies by Butman (1986) show clear evidence for the first and third hypotheses over a limited range of trap Reynolds numbers and aspect ratios (the second hypothesis was not tested). We present the results of the field comparison experiment in the theoretical framework suggested by Butman and others (1986) and find trends which support their working hypotheses that trap efficiency decreases as a function of increasing trap Reynolds number and increases as a function of trap aspect ratio. A change in efficiency with trap Reynolds number is supported by theoretical analysis (Butman and others, 1986), laboratory flume studies (Butman, 1986) and the present field results and strongly suggests that collection efficiencies of a given trap design are not constant over a range of field flow conditions.

EQUIPMENT AND METHODS

Traps

We compared the catch rate of four types of sediment traps (fig. A1-1). The smallest trap, referred to as a tube trap, was constructed from polybutyrate tubing with dimensions, 6.6 cm id, 3.2 mm wall thickness, and 60 cm in length. The bottom of the trap was sealed with a securely taped plastic cap. The other three traps, referred to as cone traps, had mouth openings of 25, 33, and 50 cm id and had the shape of a cone or of a cylinder tapering to a cone (fig. A1-1,). These traps were constructed from molded fiberglass (less than 0.6 cm thick) with a smooth gel coat surface on the inside. All of the cone traps were connected by adapters to a small (2-3 cm id) sampling tube

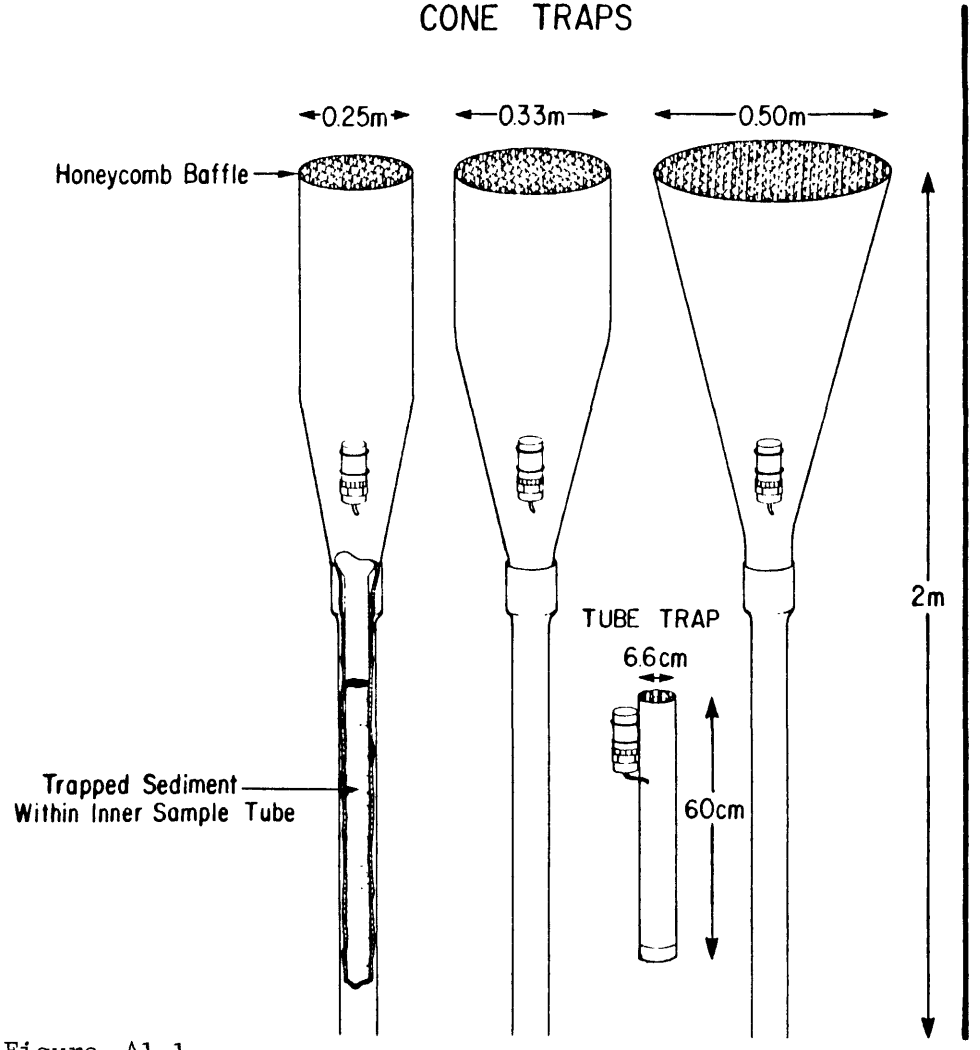

Figure A1-1

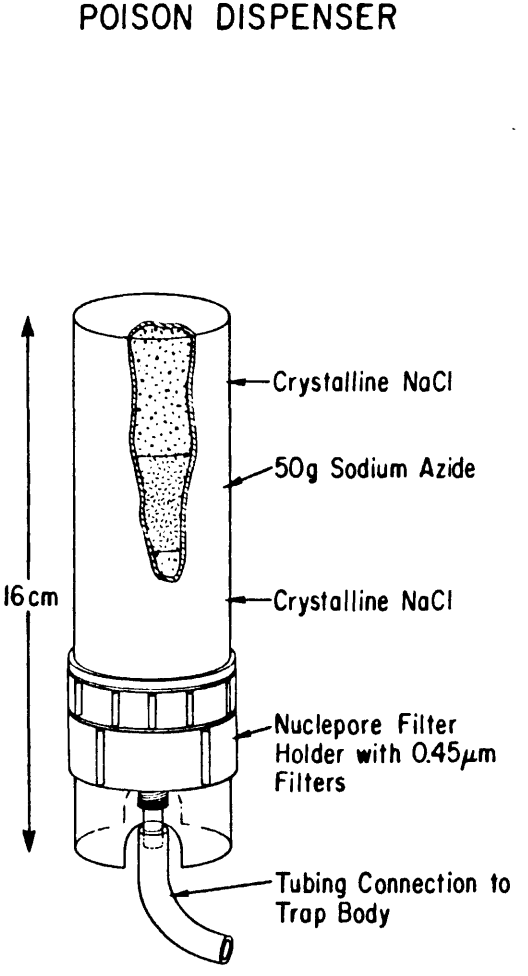

Figure A1-2

Figure A1-1 Dimensions of the four types of sediment traps used in this experiment.

Figure A1-2 Configuration of poison dispenser. At the time of deployment, the poison dispenser floods with seawater, and the resulting brine slowly flows from the dispenser to the sample tube.

about one meter long. Long thin collecting tubes were used so that variations in material entering the trap over time could be investigated by sampling the sediment at different depths within the tube. Sample tubes of different diameters were selected to accommodate anticipated differences in the volume of sediment collected. These tubes were typically round, but occasionally square acrylic tubing was used to improve the quality of x-rays taken of bulk samples. The inner sampling tube was protected by a 5-7.5 cm id polyvinyl chloride (schedule 80) tube that fit over the sampling tube and mated with the fiberglass cone of the trap with standard threaded fittings.

Poison Dispensers

A poison dispenser (fig. A1-2) was bolted on the side of each trap. The dispenser consisted of a 175-ml, screw capped plastic jar containing 50 g of powdered sodium azide (NaN_3)and about 150 g of sodium chloride (NaCl). A plastic holder containing both a millipore and nuclepore filter (47-mm diameter and 0.4μm pore diameter) threaded into the bottom end of the jar and a short piece of tygon tubing connected the nipple of the filter holder to a hole in the side of the trap. When submerged, the containers flood with sea water that forms a saturated solution of salt and azide. This solution diffuses through the millipore and nuclepore filters and flows as a density current to the bottom of the trap. This type of dispenser retains the preservative during deployment, even if traps are temporarily upside down, and releases the preservative slowly over a period of a few months.

There were no direct measurements of the concentration of NaN_3 remaining in the traps when they were recovered. However, elevated salinity levels (as high as 60 ppt) were present in water above the sediment in the tube traps even after a deployment of about 6 months. Assuming that the NaN_3 diffuses

out of the traps at the same rate as the NaCl, the concentration ratio of dissolved azide to excess salinity should be about 230 ppm NaN_3 per ppt salinity above ambient. The salinity of the water overlying trapped sediments or in interstitial water was typically 2-25 ppt higher than ambient seawater and NaN_3 concentrations are thus estimated to range from about 400 ppm to 5 ppt. Reducing conditions occured in only a few of the sediment traps which had elevated salinity levels in the water above the trapped sediment.

Baffles

Baffles were installed in each of the sediment traps. They consisted of an aramid fiber/phenolic resin honeycomb (HEXCELL) with a cell diameter of 1 cm and a length of 7.5 cm. The material showed no apparent deterioration during exposure to seawater for periods of at least one year.

The baffles served two functions. First, Gardner's (1980) flume results for very low trap Reynolds numbers suggest that baffles increase the collection efficiencies of funnels by reducing turbulence and the associated resuspension of trapped sediment (but see also Butman, (1986), for results with cylinders). Secondly, baffles prevent fish or other organsims larger than the mesh size from occupying the trap. During recovery of tripod structures which support current meters or sediment traps on the continental shelf, we have frequently found fish in open pipes and on one occasion we observed a fish coiled inside an unbaffled sediment trap deployed near the sea floor. Material collected in this trap undoubtedly would be disturbed and resuspended when the fish entered or exited the trap and might be further altered while the fish occupied the trap.

Deployment and Recovery

The location of the two comparison experiments described in this paper and the relative positions of the traps on the mooring are presented in Table A1-1 and figure A1-3. The traps were deployed approximately 110 meters above the bottom on taut subsurface moorings. The traps were mounted on the same mooring line with trap openings separated vertically by about 3 meters. Because the horizontal flow of water (typically more than 10 cm/sec) and suspended matter is much greater than esentially all settling particles, the trajectory of the "falling" particles is much less than 5 degrees. We found no evidence that the upper traps were shadowing the lower traps in this mooring arrangement. Polyethylene jacketed steel cable (3/8- or 3/16- in diameter) was used in the section of the mooring where sediment traps were attached. The cone traps were attached to the wire with stainless steel wire clamps and the tube traps were taped to the wire with all-purpose black electrical tape.

Recovery of the mooring and traps was initiated by activating an acoustic release above the anchor. Subsurface flotation, positioned to maintain the traps upright, pulled the mooring to the surface. Specific characteristics of the mooring design are discussed by Butman and Conley (1984). Calculations suggest that the mooring tilt was a maximum of about 5 degrees during the deployment, but was less than 2 degrees most of the time. In rough seas, the traps were unavoidably jolted as they were hauled onboard ship, but in most cases, the saline water above the trapped sediment remained clear, indicating that any disturbance during recovery was insufficient to resuspend the collected sediment

Table A1-1. Deployment data and results of two sediment trap comparison experiments.

Mooring LCS 40°27.6'N., 67°40.0'W., 560 m water depth
deployed January 29, 1982 to July 7, 1982.

Trap no.	Sediment trap diameter (cm)	Meters above bottom	Collection rate ($g/m^2/d$)	Relative[1] collection rate	Aspect ratio (H/D)	Sediment mass (g)
405	50.	116	5.48	0.203	4	172
411	33.	112	14.4	.523	6.1	199
411A	6.6	110	28.1	1.00	9.2	15.3
410	25.	108	23.1	.814	8	181
409A	6.6	104	29.0	.997	9.2	15.8
408	50.	100	6.1	.204	4	191

Mooring LCB 40°31.5'N., 67°42.8'W., 295 m water depth
deployed July 8, 1982 to November 11, 1982

Trap no.	Sediment trap diameter (cm)	Meters above bottom	Collection rate[2] ($g/m^2/d$)	Relative[1] collection rate	Aspect ratio (H/D)	Sediment mass (g)
526	6.6	116	11.5	0.987	9.2	3.2
527	25.	114	9.34	.802	8	40.8
528	50.	110	3.99	.343	4	81.0
529	6.6	107	12.1	1.04	9.2	4.7
530	33.	106	8.48	.728	6.1	49
531	6.6	103	11.37	.976	9.2	5.0
532	25.	102	8.36	.741	8	56.4

[1] Normalized to average of tube trap collection rate.

[2] Normalized to gradient in the mass collected by tube traps at different meters above bottom (column 7). Slope of flux per meter = 2.85%/m, r = .987.

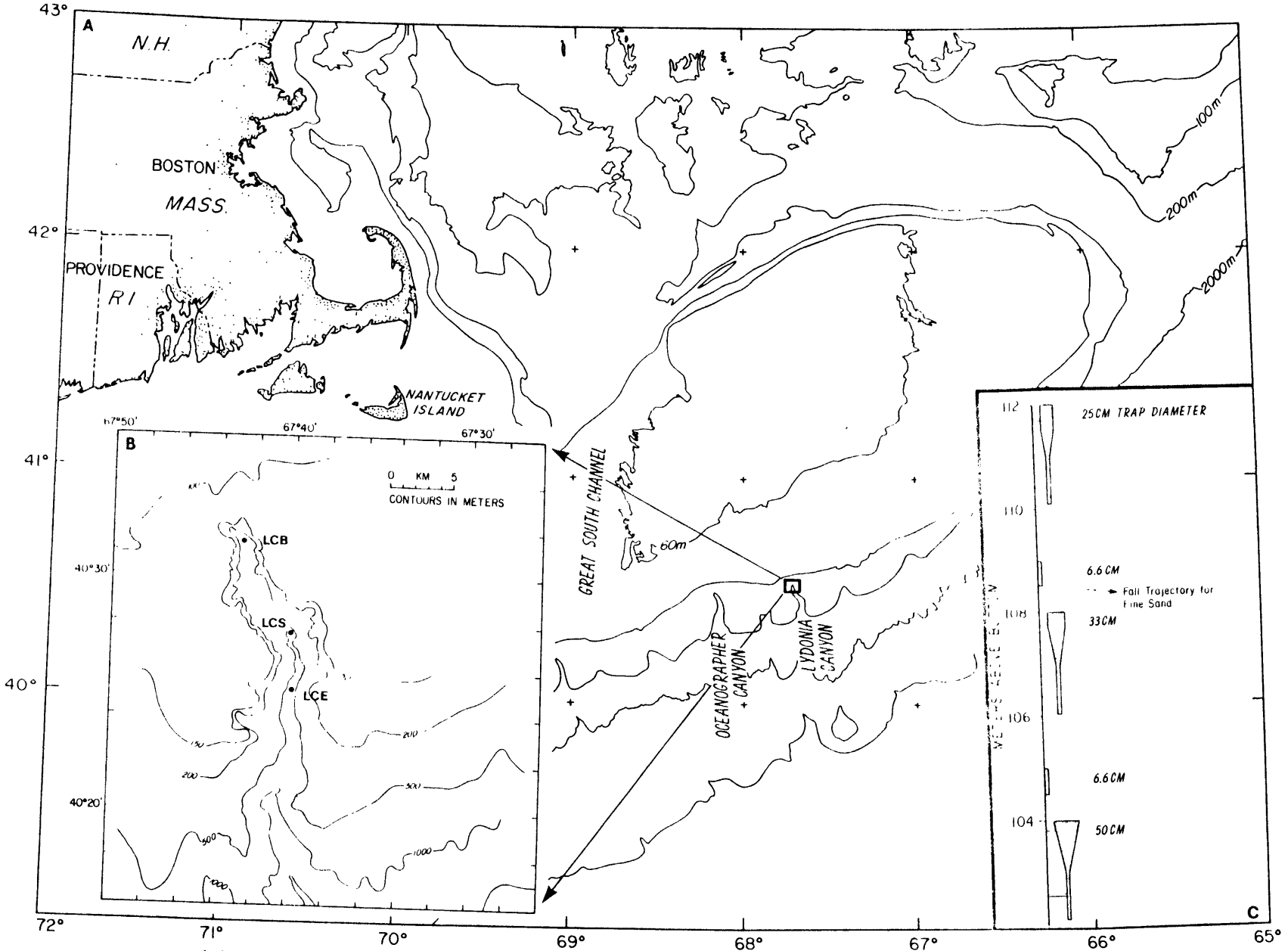

Figure A1-3 (a) Map showing location of Lydonia Canyon on the southern flank of Georges Bank.
(b) Location of moorings in the axis of Lydonia Canyon.
(c) Schematic of sediment trap spacing on the taut mooring wire.

Current Measurements

In experiment 1 at station LCS, currents were measured 6 m above the sea floor or about 94 m below the string of sediment traps by means of an EG&G Sea Link vector averaging current meter. In experiment 2 at station LCB, currents were measured about 75 m above the upper-most trap and 51 m below the lowest trap. Measurements at station LCE (see fig. A1-3) at 6 and 97 m above bottom provide additional statistics of the flow in this canyon. These measurements were made both to characterize the currents experienced by the traps during the collecting period and to provide current data within the array of instruments deployed for the Lydonia Canyon Dynamics Experiment (Butman and others, 1983). Unfortunately, the vertical shear in the currents in the canyon was greater than expected and since the currents were not measured at trap height, the measurements can only be used to estimate the flow near the traps.

Laboratory methods

Water overlying the sediment in traps was siphoned and discarded at sea and the sediment sample was stored in a refrigerator until laboratory analysis began. Samples collected in the tube traps were split using either a Y-splitter or a 4-way splitter (Honjo, 1978) until subsamples of an appropriate volume were attained. The samples from the three larger traps were frozen, extruded from the long sampling tubes, and subsampled at various depth intervals. These were thawed, homogenized, and subsampled as above. A salt correction to the total dry weight was calculated from the measured salinity before drying, or the salt was removed by centrifuging and rinsing with filtered distilled water.

Particles adhering to the inner walls of the cone traps during these experiments were not collected. However, estimates on the amount of this

material was determined from traps recovered after an earlier deployment in Lydonia Canyon. On this earlier occasion the material was removed from the inner walls of the cone traps with a high pressure jet of water, collected, and later centrifuged. The rinsed and dried material weighed between 1 and 3 grams and represented less than 6 percent of the material collected in the sample tubes. This may be an overestimate because some of the material consisted of algae or other biological growth which would not have fallen out of the water column into the trap. Alternatively, the estimate may be somewhat low because some material loosely adhering to the walls of the trap may have been washed off the inner trap surface and transported out of the trap during recovery.

RESULTS AND DISCUSSION

Changes in collection rate with trap type

The physical dimensions of the traps used in this study and the amounts and rates of sediment collected during each experiment are listed in table A1-1. In both deployments, the sediment collection rate ($g/m^2/day$) was highest for the smallest trap and decreased with increasing trap diameter. The collection rate, expressed as a percentage of the rate in the tube trap, decreased almost linearly by about a factor of 4 over the range of trap diameters used (fig. A1-4). Assigning a value of 1 to the flux measured in tube traps, the relative average flux for the 25-, 33- and 50-cm diameter traps was 0.79 ($\pm$0.04, 1 standard deviation), 0.63($\pm$0.15) and 0.25($\pm$0.08) repectively. The variability between replicates (as expressed by the coefficient of variation) was 7.6% for the 50-cm traps in experiment 1 and was 2.2% and 3.3% for the 6.6-cm traps in experiment 1 and 2 respectively (see table A1-1).

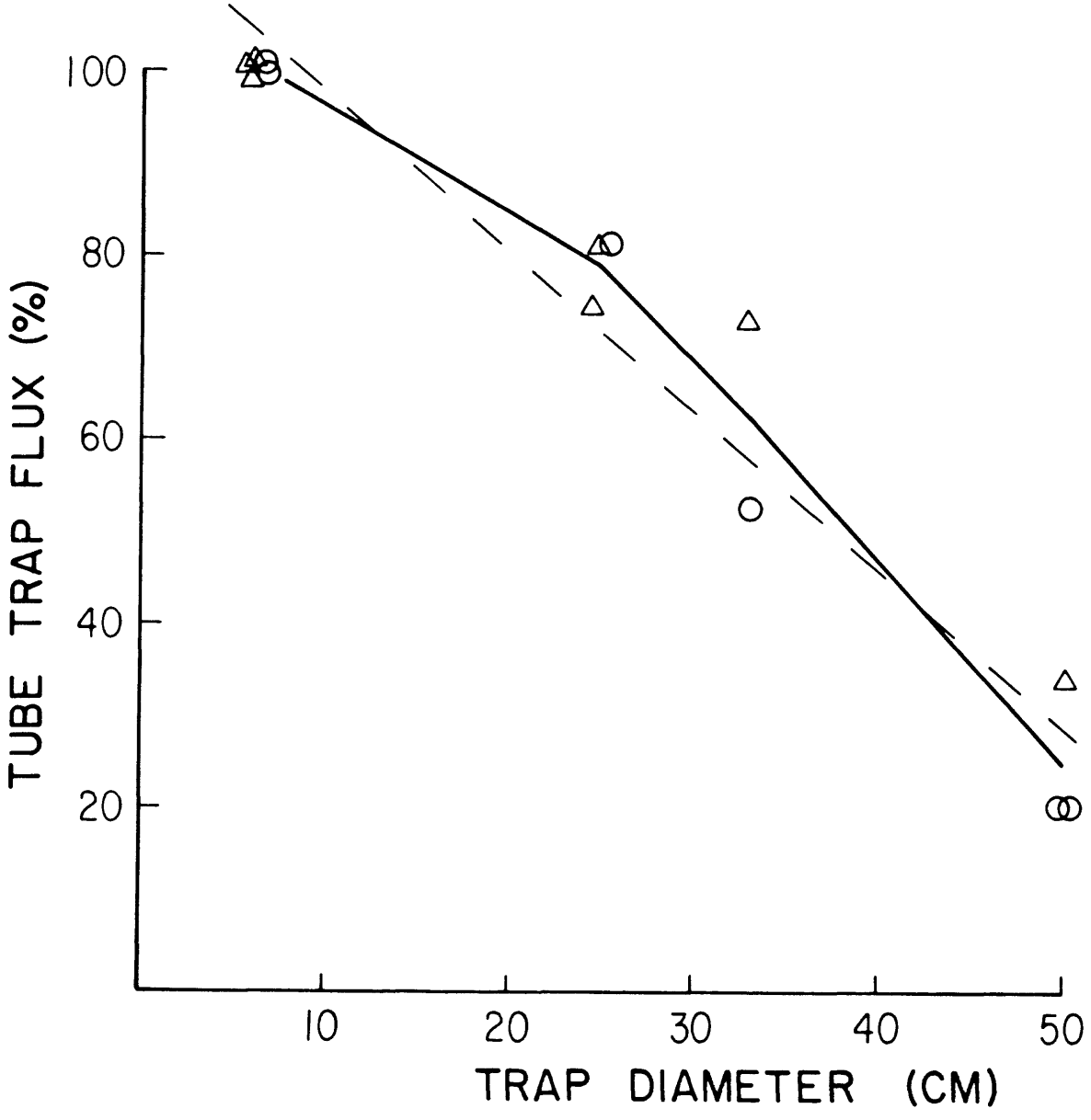

Figure A1-4 Variation in the flux of sediment as a function of trap diameter for two separate deployments in the axis of Lydonia Canyon (Δ= station LCB, O = station LCS). Fluxes ($g/m^2/day$) of the larger traps have been normalized as percentage of the smallest trap. Solid line connects the mean value for each trap size. Dashed line is least squares regression ($r = -.97$). If the average current velocity is assumed for the entire deployment, the plot of flux variation as a function of Reynolds number ($U*D/\nu$) is the same, different only by the constant factor U/ν.

The statistics of the currents measured during experiment 1 and 2 and at an additional nearby station for a different time period are tabulated in table A1-2. Although the instruments were not directly adjacent to the sediment trap array, average current speeds were about 15 cm/s and the standard deviation of the speed was about 10 cm/s. Speeds exceeded 30 cm/s at least 10% of the time and were less than 10 cm/s about 35% of the time.

The traps clearly experienced a wide range of Reynolds numbers and probably a wide range of suspended sediment concentrations during the 4 month deployment. The average collection rate determined from the traps (table A1-1) masks the variations in both Reynolds number and suspended sediment concentration during the deployment period, and thus a trap Reynolds number for comparison with controlled laboratory experiments is difficult to determine. Using the average current speed, trap Reynolds numbers were 1.1 X 10^3 times the trap diameter in cm, or 7.3 X 10^3 for the tube trap and 5.5 X 10^4 for the 50 cm trap (using $\nu = 1.36 \times 10^{-2}$ appropriate for water 35 ppt and 10 ^{o}C). There was a nearly linear decrease in relative efficiency with increasing trap Reynolds number (figure A1-4). These Reynolds numbers are in the range where Tauber (1984), Peck (1972) and Butman, (1986) show a strong Reynolds number dependence in trapping efficiency.

We have plotted the relationship between relative trap efficiency and aspect ratio in two ways (fig. A1-5). In the first case, we have used the entire length of the trap, including the 1-m sample tube; in the second case, we have assumed that the strong salinity gradient that exists in the sample tube and in the lower 24 cm of the tube trap prevented exchange of water below the density interface and thus determined the effective height of the trap. Using either choice (for the effective trap height), there is a nearly linear increase in trapping efficiency as the aspect ratio of the traps increases.

Table A1-2. Statistics of currents measured at station LCS and LCB during experiments I and II, and at station LCE during a different period (see fig. A1-3 for station locations). The average standard deviation, minimum and maximum current speed, and the percent occurrence of speed in 10 cm/s bins is tabulated for each record.

Station	Water depth (m)	Inst. depth (m)	Duration (days)	Avg. (cm/s)	S.D. (cm/s)	Min. (cm/s)	Max. (cm/s)	Occurrence 0-10 (%)	10-20 (%)	20-30 (%)	30-40 (%)	40-50 (%)	>50 (%)
LCB	295	104	125	25.5	10.2	2.0	59.6	5.9	25.3	34.7	24.3	8.6	1.2
		244	125	9.1	5.5	.2	42.1	59.2	34.3	5.8	.7	.1	.0
		290	125	13.6	10.1	.3	59.9	41.4	31.9	16.4	7.9	2.1	.3
LCS	560	554	158	16.8	13.0	.1	66.4	36.2	30.0	15.3	10.1	5.9	2.6
LCE	590	493	123	16.3	11.7	.3	69.3	35.5	32.1	18.3	9.0	3.6	1.4
		584	123	6.1	10.6	.1	60.8	31.5	37.2	18.8	8.4	3.3	.8

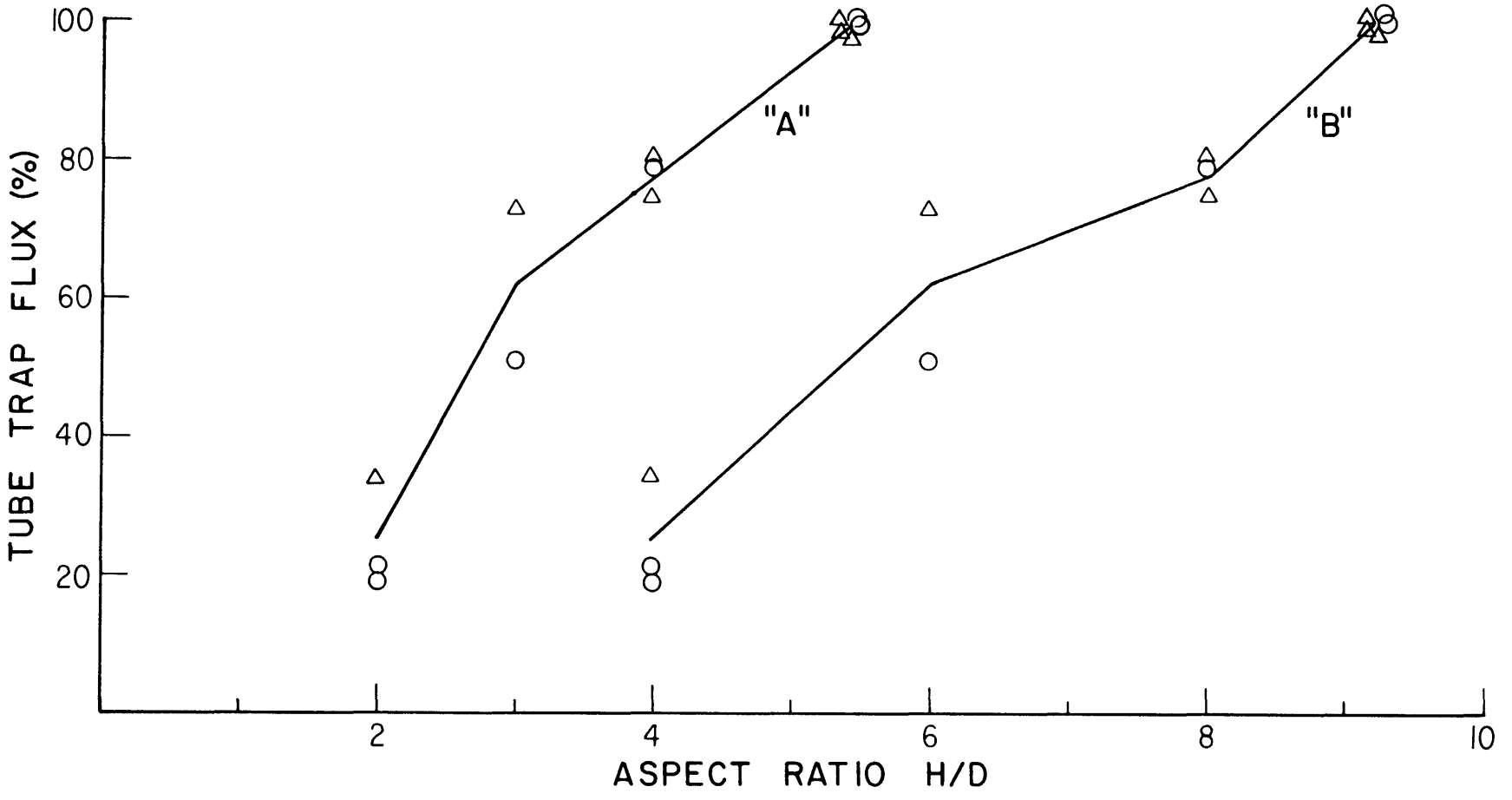

Figure A1-5 Variation in the flux of trapped sediment as a function of aspect ratio. Fluxes of the larger traps have been normalized as a percentage of the smallest trap. Solid lines connect mean value for each trap size. Line "A" assumes the effective trap depth is to the top of the salinity gradient caused by the addition of poison. Line "B" assumes that the trap depth is represented by the overall trap dimensions.

It is interesting that this relationship holds in spite of the markedly different trap shape.

Changes in collection efficiency with aspect ratio and trap Reynolds number were primarily attributed to resuspension effects in the theoretical analysis of Butman and others (1986) and in the lab study using fluids of different density by Lau (1979). The importance of resuspension in aspect-ratio dependent trap collections has been discussed in many previous studies (e.g. Hargrave and Burns, (1979); Gardner, (1980a,b); Bloesh and Burns, (1980); Blomqvist and Kofoed, (1981). During collections in a moving fluid, eddies shed over the trap mouth may penetrate to the trap bottom, resuspending sediments. The eddy length and velocity scales are set by the oncoming flow and by trap mouth diameter. For traps with the same diameter, sufficiently increasing the aspect ratio would eliminate eddy penetration to the trap bottom. The Reynolds number effect is more complex. The depth of eddy penetration inside a trap appears to increase with increasing trap Reynolds number (Lau, 1979); thus the trap aspect ratio required to prevent resuspension increases with increasing trap Reynolds number.

In the present study, it is uncertain whether the observed changes in efficiency are due primarily to Reynolds number or to aspect ratio effects. It is unfortunate that in our field experiments we did not simultaneously test traps with the same Reynolds number and different aspect ratio (i.e. traps with the same mouth diameter but different heights) or traps with the same aspect ratio and different Reynolds numbers. It is also somewhat difficult to attribute differences in collection rate completely to resuspension of trapped material given the restricted sampling tubes of the large traps and the strong salinity gradients observed in all of the traps. Perhaps some or all of the material is first "collected" on the sloping walls of the traps and thus is

subject to resuspension by the flow in the trap for some period of time. The mechanism responsible for the observed differences in trapping must be investigated in laboratory flume experiments.

Butman and others (1986) suggest that for particles with slower fall velocities (i.e. smaller particles), the particle collection rate should decrease over some increasing range of trap Reynolds number. We tried to evaluate this hypothesis by examining the grain size distribution of collected sediments but found no conclusive trends. Part of the problem is the difficulty of estimating fall velocity of particles as they occur in the environment using size analysis procedures which break up fragile flocs and particles aggregated in fecal pellets to a different and unknown degree. Because of this problem, the dependence of efficiency on grain size (fall velocity) should be addressed in laboratory experiments.

Influence of mooring tilt

Subsurface moorings, like those used in this study, tilt in the direction of the current flow. The magnitude of tilt is a function of the current profile, the amount of bouyancy in the mooring, and the drag imposed by various devices on the mooring line. The tilt of moorings was estimated using a computer program (Moller, 1976) that takes into account the position and drag of specific instruments mounted on these moorings and the current speeds measured at various heights above bottom during the deployment. Tilt was calculated assuming that the flow was co-directional throughout the water column and using the statistics of the observed flow at three levels. At the height of the sediment traps in this comparison experiment, the tilt of the mooring is calculated to be approximately 1 degree in response to the average current speed and about 3 degrees in response to one standard deviation above

mean speed. The calculated tilt from maximum speeds is about 5 degrees, but this maximum speed is reached infrequently (table A1-2). These calculations of tilt are confirmed by measurements of the depth of the upper float in the mooring during the deployment and are probably the upper limit on the actual tilt.

We found only one report in the literature that evaluates the effect of tilt on sediment trapping efficiency (Gardner, 1985), and this work evaluates only cylinders. Gardner's data show a 50% increase in the collection efficiency when the tilt has been increased from 0 to 10 degrees, and that the increase in efficiency occurs when the tilt is either toward or away from the direction of flow.

There is another aspect of the mooring design that adds minor uncertainty to our data. The traps were bolted or taped to the mooring wire, which is free to rotate as the tidal currents rotate, but the traps could not independently rotate to a standard position on the wire relative to the flow. As a result, eddies shed downstream by the wire may affect the flow over and through some traps and not others. The smaller traps would probably be more influenced by this process than the larger traps.

Perhaps the best indication that tilt or wire/current position did not compromise the general conclusion of this study is the high reproducibility of the results from two independent experiments where the tilt and orientation of the traps were different.

Influence of poison

In some of the cone trap samples, discrete layers of organisms were distributed throughout the sediment trap sample. The layers often contain a preponderance of one organism (pteropods, euphausids, foraminifera, for

example), in different layers throughout the trap sample. In other traps deployed during the Lydonia Canyon Experiment (Butman and others, 1983) higher concentrations of organisms were found at the bottom of the sampling tube (i.e., collected early in the deployment period) than further up. Two possible explanations, not necessarily independent, might account for these observed layers. The first is that the layers reflect the seasonal succession of zooplankton species in the water overlying the traps. One objective of the future work on these samples is to determine any repetitive seasonal changes of zooplankton and phytoplankton that are well preserved. The second explanation may be an artifact caused by the poison. Zooplankton that swim into the trap in large numbers, may be killed by the poison and accumulate as a discrete layer. Cases where the layers are fewer or absent toward the end of the collection period, might reflect the diminishing strength of the poison due to diffusion, which would allow the zooplankton that enter the trap to escape. This may account for the apparently lower organisms/sediment ratio in the last material collected.

CONCLUSIONS

This long-term comparison of four sediment traps deployed in Lydonia Canyon within a few meters of each other and on the same subsurface mooring showed reproducible differences in the relative efficiencies of sediment collection ($g/cm^2/day$) by traps of different size and shape. Tube traps 6.6 cm id and 60 cm long collected at the highest efficiency, while conical traps 50 cm diameter and 200 cm long collected at the lowest rate. There was a nearly linear decrease in the relative collection rate for increasing trap diameter, and an increase in relative collection rate for increasing aspect ratio (trap length/trap diameter). At the location of these experiments, the average current speed was about 15 cm/s, maximum speed about 50 cm/s.

The differences in collection rates by traps of different size and shape are consistent with the theoretical hydrodynamic considerations discussed by Butman and others (1986), who predict a decreasing trap efficiency over some range of increasing trap Reynolds number and over some range of decreasing aspect ratio. They are also consistent with the lab results of Butman (1986). Our results suggest that catch rates obtained from traps with different hydrodynamic characteristics cannot be compared directly, but that the relative catch rate between different kinds of traps may be determined with good precision for a given set of field conditions.

ACKNOWLEDGMENTS

We thank C.A. Butman for carefully reviewing the manuscript and for many helpful discussions about sediment traps. We also thank the officers and crew of the R/V OCEANUS for expert assistance in deployment and recovery of the moorings.

REFERENCES

Bloesch, J. and Burns, N. M., 1980, A critical review of sedimentation trap technique: Schweiz. Z. Hydrol., v. 42, p. 15-55.

Blomqvist, S. and Kofoed, C., 1981, Sediment trapping - a subaquatic in-situ experiment: Limnology and Oceanography, v. 26, p. 585-590.

Bothner, M. H., Parmenter, C. M., and Butman, B., 1983, Resuspended sediment flux in Lydonia and Oceanographer Canyons off the eastern United States: (abs.) EOS transactions, American Geophysical Union, v. 64, p. 1051.

Butman, B. Noble, N. A., Moody, J. A., and Bothner, M. H., 1983, Lydonia Canyon Dynamics Experiment- Preliminary results: Chapter 8 in McGregor, B. H. (ed), Environmental Geologic Studies on the United States Mid- and North Atlantic Outer Continental Shelf Area, 1980-1982: U. S. Geological Survey Report to the Minerals Management Service.

Butman, B. 1983, Long-term current measurements in Lydonia and Oceanographer Canyons: (abs.) EOS transactions, American Geophysical Union, v. 64, p. 1050.

Butman, B. and Conley, S. J., 1984, Lydonia Canyon Experiment: Data Report for moored array deployment 1, October 1980 - April 1981: U. S. Geological Survey Open File Report 84-201, 223 p.

Butman, C. A., 1986, Sediment trap biases in turbulent flows: Results from a laboratory flume study: Journal of Marine Research, August issue.

Butman, C. A., Grant, W. D., and Stolzenbach, K. D., 1986, Predictions of sediment trap biases in turbulent flows: A theoretical analysis based on observations from the literature: Journal of Marine Research, August issue.

Gardner, W. D., 1980a, Sediment trap dynamics and calibration: a laboratory evaluation: Journal of Marine Research, v. 38, p. 17-39.

Gardner, W. D., 1980b, Field assessment of sediment traps: Journal of Marine Research, v. 38, p. 41-52.

Gardner, W. D., 1985, The effect of tilt on sediment trap efficiency: Deep Sea Research, in press.

Hargrave, B. T., and Burns, N. M., 1979, Assessment of sediment trap collection efficiency: Limnology and Oceanography, v. 24, p. 1124-1136.

Honjo, S., 1978, Sedimentation of materials in the Sargasso Sea at a 5367 m deep station: Journal of Marine Research, v. 36, p. 469-492.

Lau, Y. L., 1979, Laboratory study of cylindrical sedimentation traps: Journal Fisheries Research Board of Canada, v. 36, p. 1288-1291.

Moller, D. A. 1976, A computer program for the design and static analysis of single-point subsurface mooring systems: NOYFB: Woods Hole Oceanographic Institution Technical Report 76-59, 106 p.

Peck, R. M., 1972, Efficiency tests on the Tauber trap used as a pollen sampler in turblent water flow: New Phytology, v. 71, p. 187-198.

Tauber, H., 1974, A static non-overload pollen collector: New Phytology, v. 73, p. 359-369.

APPENDIX 2

NEAR-BOTTOM SUSPENDED MATTER CONCENTRATION ON THE CONTINENTAL SHELF DURING STORMS: ESTIMATES BASED ON IN-SITU OBSERVATIONS OF LIGHT TRANSMISSION AND A PARTICLE SIZE DEPENDENT TRANSMISSOMETER CALIBRATION.

By

John A Moody, Bradford Butman, and Michael H. Bothner

APPENDIX 2

Table of Contents

Page

Abstract.....A2-1

Introduction.....A2-1

Theory.....A2-4

Calibration Methods and Results.....A2-5

Single particle classes.....A2-5

Mixture of particle sizes.....A2-10

Field Measurements.....A2-13

Size distribution of trapped sediments.....A2-21

Estimates of $\bar{B}$ and suspended-matter concentration.....A2-24

Discussion.....A2-29

Summary.....A2-34

Acknowledgements.....A2-35

References.....A2-36

ABSTRACT

A laboratory calibration of Sea Tech and Montedoro-Whitney beam transmissometers shows a linear relation between light attenuation coefficient (c_p) and suspended matter concentration (SMC) for natural sediments and for glass beads. However the proportionality constant between c_p and SMC depends on the particle diameter and particle type. Thus, in order to measure SMC, observations of light attenuation must be used with a time-variable calibration when suspended particle characteristics change with time. Because of this variable calibration, time series of light attenuation alone may not directly reflect SMC and must be interpreted with care.

The near-bottom concentration of suspended-matter during winter storms on the U.S. East Coast Continental Shelf is estimated from light transmission measurements made 2 m above the bottom and from the size distribution of suspended material collected simultaneously in sediment traps 3 m above the bottom. The average concentrations during six storms between December 1979 and February 1980 in the Middle Atlantic Bight ranged from 2-4 mg/l (maximum concentration of 7 mg/l) and 8-12 mg/l (maximum concentration of 22 mg/l) on the south flank of Georges Bank.

INTRODUCTION

Recent interest in near-bottom sediment transport, both on the shelf and in the deep ocean, has produced a number of new instrument systems capable of long-term time series measurements of light transmission using a variety of sensors (Sternberg and Creager, 1965; Butman and Folger, 1979; Drake and Cacchione, 1985; and Williams, 1985). Our laboratory calibrations of some of these sensors (presented in this paper) and those of Baker and Lavelle (1984) have shown that the proportionality constant between light attenuation

coefficient (c_p) and suspended matter concentration (SMC) is a function of particle size. Therefore, a companion time series of suspended particle size is necessary to estimate SMC from these light transmission measurements. With the exception of Sternberg's bag sampler (Sternberg, 1986) the suspended particle sizes are generally not available.

In several long-term deployments of the USGS bottom tripod system (Butman and Folger, 1979) sediment traps were mounted on the tripods. Analysis of the sediment collected over several months in one of these traps showed distinct changes of particle size with time (Parmenter and others, 1983) which was attributed to resuspension of coarser bottom sediments by storms. Extending these results, we have calculated a time series (based on storm periods) of the size of particles in suspension from analysis of the material collected by sediment traps, and used this time-series of particle size with the time-series of light transmission to give estimates of SMC during storms.

There are several limitations to this method. First, the sediment traps may be biased collectors - collection efficiency as a function of particle size and current velocity is not known and thus the material collected in the trap may not accurately represent the size-distribution of the material in suspension at any one time. Second, particles in the water may aggregate or form flocs which are compacted and not preserved in the sediment trap. Finally, the particle size distribution determined from the trap samples is at best an average over time scales of a few days while the light transmission measurements show rapid fluctuations over a few hours. Thus the SMC estimates do not accurately reflect the observed high-frequency variability. We offer this analysis to illustrate the difficulty associated with using transmissometer observations to measure SMC on the Continental Shelf when there is frequent resuspension of bottom sediment and changes in suspended

particle size; the uncertainities in the analysis clearly show that this method should not be adopted as a standard technique for estimating SMC.

Storms are important mechanisms for resuspending and transporting sediments on the Continental Shelf. In order to estimate the magnitude of storm transport, the SMC during storms and calm periods must be known. Measurements made from ships of the near-bottom, background SMC have ranged from 0.1-0.5 mg/l during relatively calm periods along the 60-100 m isobath in the Middle Atlantic Bight off New Jersey and along the southern flank of Georges Bank (Bothner and others, 1982, 1981a; Meade and others, 1975; Manheim and others, 1970). Higher values of SMC, (1.0-3.0 mg/l) during calm periods have been measured by Bothner and others (1981b) in the vicinity of a fine-grained deposit (called the Mud Patch) on the Continental Shelf south of Martha's Vineyard between the Middle Atlantic Bight and Georges Bank. There have been several in situ measurements of SMC during storms but these were all based on optical measurements (Drake and Cacchione, 1985). Some direct measurements (i.e. filtered water samples) of SMC have been made immediately following storms but these probably underestimate the concentrations during storms because suspended sand or coarse silt material (0.250-0.032 mm) settles from the water column in about a day. Manheim and others (1970) reported 7 mg/l of suspended matter in surface waters (20 km off Cape Kennedy) two days after Hurricane Betsy traversed the area in September 1965. Drake (1977) measured maximum near-bottom SMC of 4 mg/l during a moderate November storm in 1973 and Young (1978) reported maximum concentrations of 5-7 mg/l in the same general area of the New York Bight three days after the passage of Hurricane Belle in August 1976. Bothner and others (1981a) reported SMC as high as 15 mg/l in the Mud Patch after a storm in December 1976 and SMC of 3-5 mg/l in the water around Nantucket Shoals one week after a storm in February 1978.

This paper is organized as follows: the first section briefly presents the necessary theory, describes the transmissometer calibration methods, and the calibration results for individual particle sizes and for mixtures of particle sizes. The second section describes the field measurements of light attenuation and suspended matter size distribution, and the third section explains how we estimated the SMC during six winter storms which occurred between December 1979 and February 1980. The last section discusses the problems associated with using this method of estimating SMC.

THEORY

The transmissometer light sensor produces a voltage, TR (volts) proportional to the light intensity at a distance L from the light source given by

$$TR = TR_o \, e^{-cL} \tag{1}$$

where TR_o is the voltage at L = 0 and c (m^{-1}) is the total attenuation coefficient which has contributions from pure water, c_w, from suspended matter, c_p, and from dissolved organic matter (commonly referred to as yellow substance), c_y:

$$c = c_w + c_p + c_y \tag{2}$$

In this study we assume negligible dissolved organic matter ($c_y = 0$). Substituting eq. (2) into eq. (1) gives an equation for computing the light attenuation coefficient, c_p, as a function of light transmission:

$$c_p = \frac{-1}{L} \ln \left(\frac{TR}{TR_{cw}}\right) \tag{3}$$

Where TR_{cw}, is the normalization voltage in "pure water" which contains no suspended matter.

The suspended particle attenuation coefficient, c_p; for a given particle size of diameter D_i is related to the number of particles, N, per unit volume, and to the cross-sectional area by:

$$c_p = \frac{NQ\pi D_i^2}{4} \quad (4)$$

where Q is an effective area coefficient for light attenuation (Spinard and others, 1983). Assuming spherical particles of density, ρ_s, and using eq. (4) the SMC of the ith particle size class is given by:

$$SMC_i = \left(\frac{2\rho_s}{3Q} \cdot D_i\right) \cdot c_{p_i} = B_i \cdot c_{p_i} \quad (5)$$

We will call B_i ($mg/l/m^{-1}$) in eq. (5) the calibration slope; it is theoretically directly proportional to the particle diameter D_i.

CALIBRATION METHODS AND RESULTS

Light attenuation was measured with Montedoro-Whitney (MW) model TMU-3A beam transmissometers and Sea Tech transmissometers. The MW transmissometers use a white light source having a spectral peak near 950 nm, a beam collimated to a diameter of about 30 mm and a 100-cm path length. The light detector is a selenium photovoltaic cell with a maximum response near 555 nm. The Sea Tech transmissometers (hereafter refer to as LED) use a light emitting diode with a wavelength of 660 nm, a beam diameter of 20 mm, and a 25-cm path length (Bartz and others, 1978).

Single particle classes

The MW and LED transmissometers were calibrated in the laboratory using the following procedure. The sensors were placed in a 1 x 2 x 0.5-m tank containing fresh water filtered through 0.2-μm filters. This "pure water" had an average SMC of 0.11 mg/l (method of determing SMC is described below). Natural surficial sediment from the study area and commercial solid glass

beads (Potters Industries, Inc., sizes 1-5 μm, 5-10 μm, and 10-20 μm) were tested. The natural sediment was separated into five size classes by wet-sieving (particle diameters >64μm) and on the basis of particle settling velocity in fresh water for particle diameters <64μ. For each individual size class, the sample was suspended in a nonelectrolytic solution for 3-5 minutes and disaggregated with a sonic probe and then added to the tank in 6-10 increments. As the tank was vigorously stirred to maintain particles in suspension, multiple 400-ml water samples were obtained for each calibration point to directly determine concentration and to measure the size of particles actually in suspension. The SMC was determined by filtering the water samples through pre-weighed paired 0.45-μm Millipore filters, air drying the filters, and then weighing. The particle size distribution was measured using a rapid sediment analyzer (Schlee, 1966) for sizes >64 μm and a Coulter Counter for sizes <64 μm.

For each particle size, a linear correlation (table A2-1) was determined between SMC and the light attenuation coefficient. The measurements of the calibration slope B_i varied systematically with increasing particle size, and a linear relationship for the MW transmissometer (fig. A2-1) between the particle diameter, D_i (in μm), and the calibration slope B_i was determined by regression to be:

$$B_i = 1.12\ D_i \tag{6}$$

The regression was forced through the origin, and the correlation coefficient was 0.998 if the data for 145-μm particles, (which had large uncertainties in particle size), are excluded. This lab calibration shows that in order to determine SMC from beam attenuation observations, the size of material in suspension must be known. For example in the simplest case of the uniform-sized glass beads, a 1.7 mg/l suspension of 3-μm particles has the same beam attenuation (1 m^{-1}) as a 9.8 mg/l suspension of 8-μm particles.

Table A2-1. Calibration slopes B_i and linear correlation coefficient r for different mean particle size.

Sample type	Mean particle diameter (μm ± std. dev)	B_i ($mg/l/m^{-1}$)	r
Natural sediment	5±5	3.1±0.4	0.983
	19±9	16.4±0.4	0.999
	32±15	36.8±2.4	0.996
	82±32	92.5±7.2	0.992
	145±44	199 0±42.0	0.958
Glass beads	3±1	1.7±0.1	0.993
	5±1	4.4±0.3	0.996
	8±2	9.8±0.3	0.998
Diatom culture	2±4	1.3±0.1	0.998

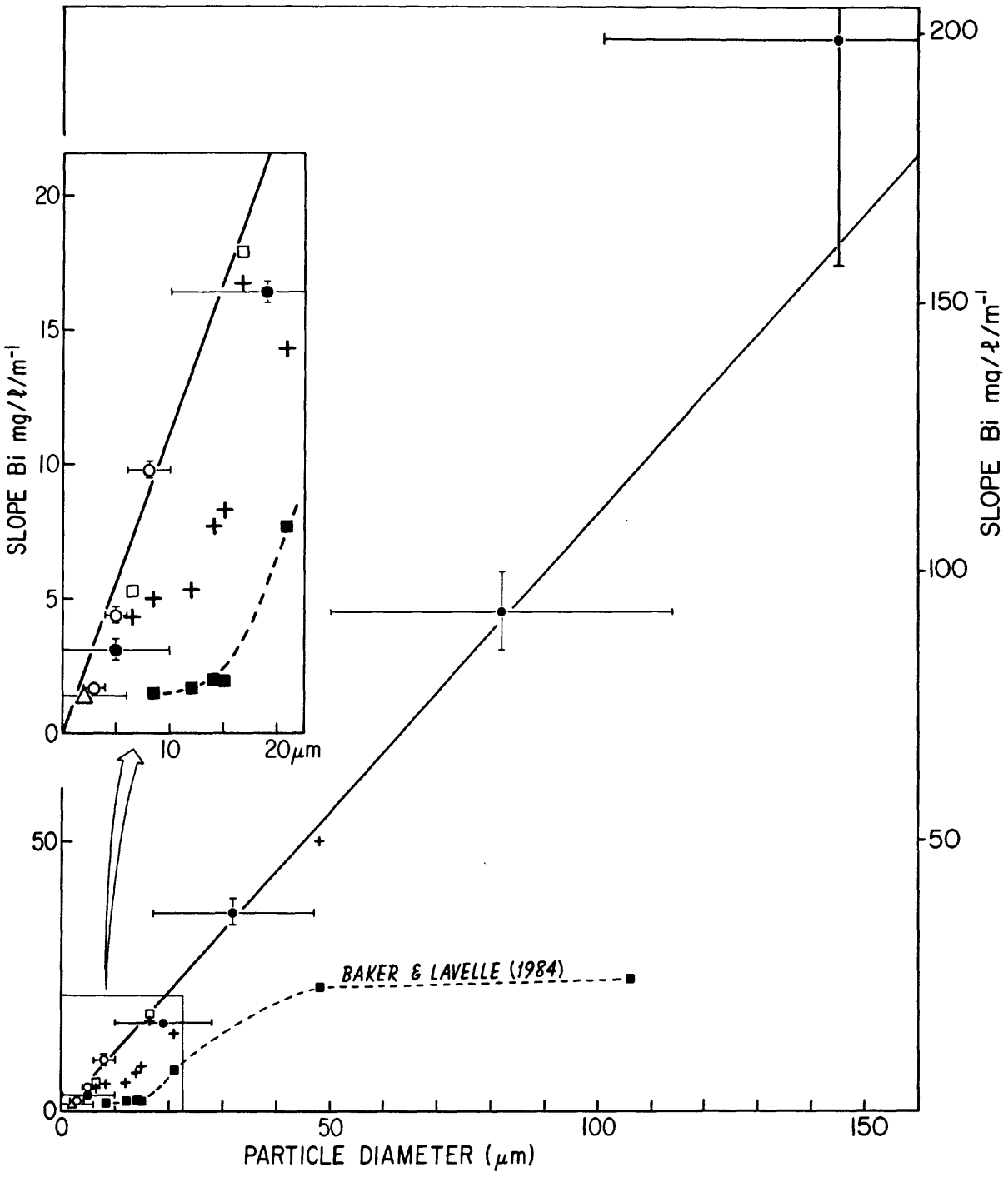

Figure A2-1. MW Transmissometer calibration slope B_i as a function of particle diameter. The data from this paper are plotted using the symbols: ● for natural sediment, o for glass beads, and Δ for diatom culture. Data from Baker and Lavelle (1984) are plotted using the symbols (■) for natural sediment, (□) for glass beads, and + for theoretical predictions. The error bars are ± 1 standard deviation of particle diameter or calibration slope. The results for MW transmissometers are shown in this figure since the light attenuation measurements discussed later were made with this instrument. The results for the LED transmissometer are nearly identical with $B_i = 1.03 D_i$.

Baker and Lavelle (1984) also calibrated beam transmissometers using glass beads and natural sediments. Their glass bead calibrations (open squares in fig. A2-1) agree well with the glass bead calibrations presented here (open circles in fig. A2-1). However, Baker and Lavelle's calibration slopes for natural sediments (solid squares in figure A2-1) are consistently smaller by a factor of 2 or more than the slopes for natural sediments obtained in this study (solid circles in figure A2-1). The different calibrations are not caused by different sensors, since we obtained a similar relationship between particle size and calibration slope ($B_i = 1.03D_i$) for the LED transmissometer used by Baker and Lavelle.

Baker and Lavelle (1984) developed a theory for light scattering by small particles to explain the dependence of the calibration slope B_i on particle size. Predictions from this theory (plotted as +'s in fig. A2-1) fall between the two sets of experimental observations. The discrepancy between the two sets of experimental results is largest for large particles, especially near Baker and Lavelle's experimental point at 106 μm where the mean diameter was estimated as the midpoint of the size range. The differences for natural sediment are probably due to differences in particle shape and the roughness of the natural sediment samples as discussed by Baker and Lavelle (1984).

The different calibration slopes obtained for various particle sizes and shapes emphasize the need to use a calibration appropriate for the material actually in suspension, and suggest extreme caution in interpreting light attenuation measurements as SMC when information about the size and type of particles in suspension is not available.

Mixture of particle sizes

In the field, the particles in suspension are not all one size, but are a mixture of sizes. A calibration slope $\bar{B}$ can be defined for a mixture of particle sizes with a total SMC_t as

$$SMC_t = \bar{B} \cdot c_t \tag{7}$$

where the total attenuation coefficient, c_t, is the sum of the attenuation coefficient, c_{p_i}, for each size class. Expressing the concentration of each size class in terms of the percentage, P_i, of the total concentration SMC_t and using eq. (5) an equation for $\bar{B}$ is:

$$\bar{B} = \left(\sum \frac{P_i}{B_i}\right)^{-1} \tag{8}$$

Finally, by substituting the empirical eq. (6) into eq. (8) we obtain an empirical equation for the calibration slope $\bar{B}$ from a known particle size distribution

$$\bar{B} = 1.12 \left(\sum \frac{P_i}{D_i}\right)^{-1} \tag{9}$$

Equations 8 and 9 were tested in the laboratory for mixtures of 1-5-μm and 10-20-μm glass beads and for samples of sediment collected with a Van-Veen grab near the study area and for one sample taken from a sediment trap. The glass bead mixtures represented only two size classes at the extreme lower end of the size range calibrated in the laboratory and the empirical eq. (6) overestimated the calibration slope B_i for these sizes (see fig. A2-1) so eq. (8) and the individual B_i's (table A2-1) were used to predict the $\bar{B}$ for these mixtures (table A2-2). There was a wider range of size classes in the natural sediment and sediment trap mixtures (fig. A2-2). and eq. (9) was used to predict $\bar{B}$ for these experiments (table A2-2). The predicted values of $\bar{B}$ were within 7 percent of the laboratory measured values of $\bar{B}$ except for the mixture 3-4 which was within 17 percent. Because this mixture contained particles from two sand size classes, the larger difference is expected--the

Table A2-2. Comparison of predicted and measured calibration slopes $\bar{B}$ using eq. (8) for glass beads and eq. (9) for natural sediment. The glass bead mixture is expressed as a ratio of 1-5 μm to 10-20 μm glass beads. The size distribution for the natural sediment and sediment trap samples are shown in figure 2.

Type	Sample	Mixture	$\bar{B}$ Predicted	$\bar{B}$ Measured	Percent difference
Glass bead	1	1:3	4.2	4.5	-6
	2	1:7	5.9	5.5	+6
	3	7:1	1.8	1.7	+2
Natural sediment	4	---	72.0	86.3	-17
	5	---	3.4	3.7	-7
	6	---	15.4	16.5	-7
Sediment trap	7	---	2.8	2.6	+7

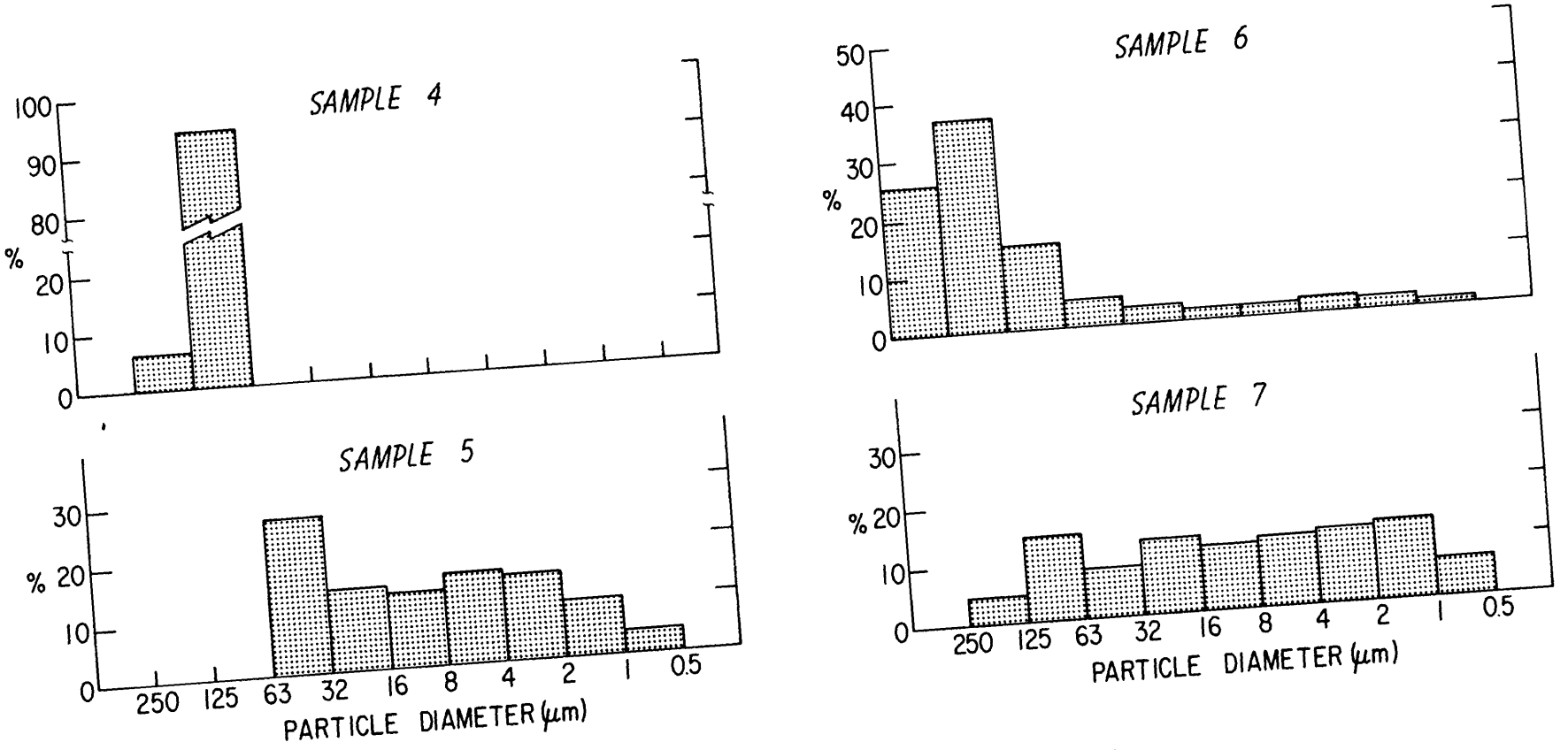

Figure A2-2. Size distribution of suspended sediment mixtures used to test eqs. (8) and (9).

uncertainty in B_i for coarse particles is larger than for fine particles (see table A2-1). The values of $\bar{B}$ predicted by eq. (9) were generally slightly less than the experimentally measured values of $\bar{B}$ for each of the natural samples tested.

FIELD MEASUREMENTS

Tripod instrument systems (Butman and Folger, 1979) were deployed from December 15, 1979 until May 28, 1980 at three locations on the Continental Shelf (fig. A2-3). Station K (lat. 41°04'N., long. 67°34'W.) is located in 63 m of water on the southeast flank of Georges Bank which has a fine sand bottom (fig. A2-4a) exposed to strong tidal currents (28-34 cm/s at 1 m above bottom, Moody and others, 1984). Station Q (lat. 40°30'N., long. 70°12'W.) is in 66 m of water on the eastern edge of a silt and clay deposit called the Mud Patch (Twichell and others, 1981; Bothner and others, 1981b) and in an area of weaker tidal currents (6-14 cm/s). Station MB (lat. 38°42'N., long. 73°39'W.) is in 60 m of water in the Middle Atlantic Bight with a medium sand bottom and the weakest tidal currents (5-9 cm/s).

In this chapter, we attempt to estimate SMC only during storms, when significant resuspension of bottom sediment and large changes in attenuation coefficient are expected. A storm event could be defined in many different ways. We choose to define a storm to be a period of time (longer than 1 day) when the magnitude of the bottom stress exceedes the threshold (10 dynes/cm^2) required to erode 125 μm sediments (Mantz, 1977). The bottom stress (figs. A2-5a, A2-6a) was computed from the near-bottom current and wave measurements using Grant and Madsen's (1979) model of combined wave and current interaction with a rough bottom. The current speeds were measured at 1 m above the bottom (mab), and bottom rms-wave speeds were estimated from

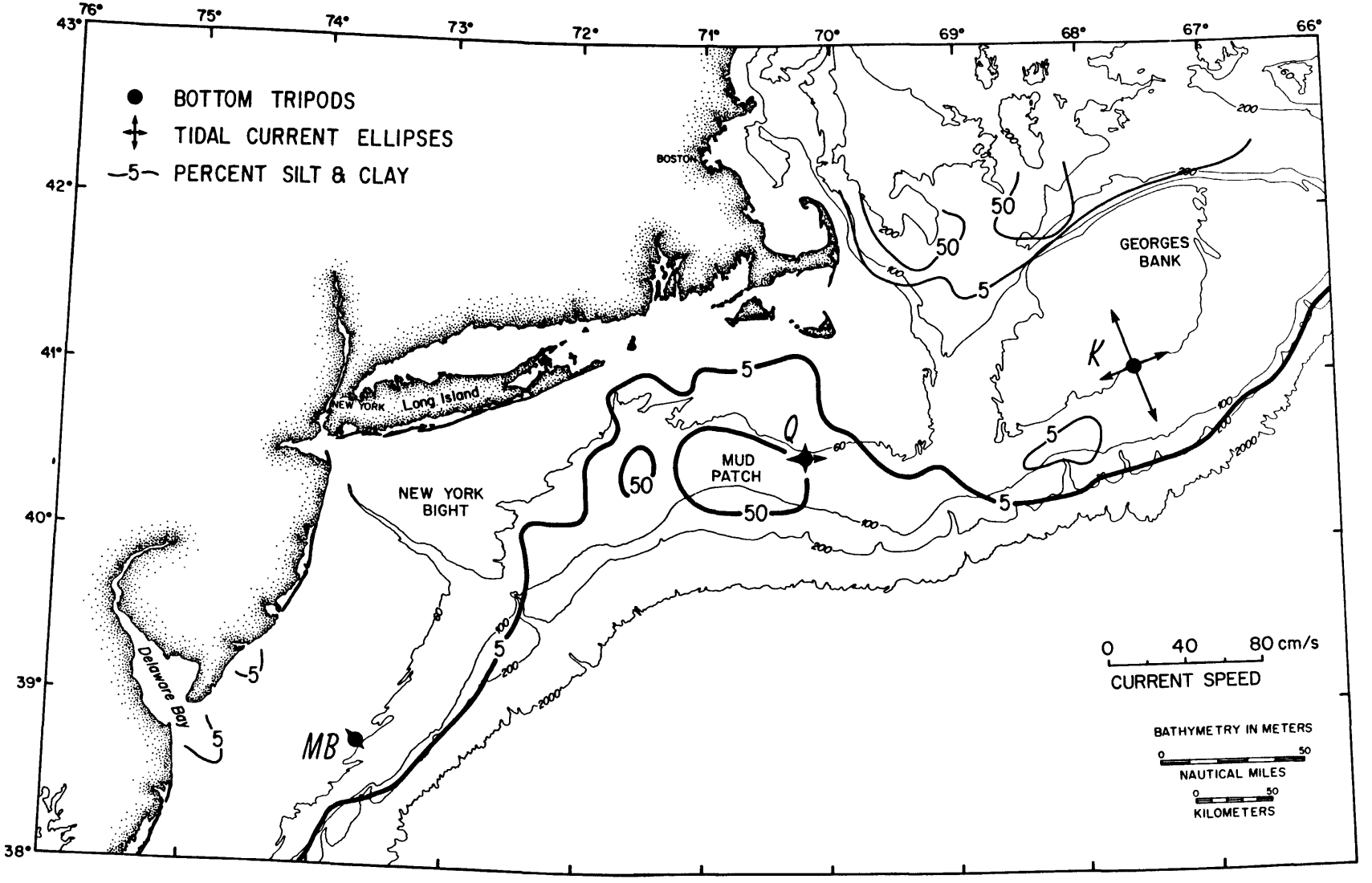

Figure A2-3. Station locations, tidal ellipses, and contours of percent silt and clay in the surficial sediment.

Figure A2-4. Bottom photographs at station K of an area 120 cm by 150 cm. The time of each picture is also indicated by an arrow in figure A2-5b.

Figure A2-4a. Sand bottom with almost no shell cover on December 18 at 0816.

Figure A2-4b. Approximately 80 percent shell cover on January 25 at 0745.

Figure A2-4c. Photograph of suspended sediment, possibly organic matter, on December 20 at 2000.

Figure A2-5 Station K time series.

a. Bottom stress computed using Grant and Madsen's (1979) current-wave interaction theory. Storm periods have been numbered and are periods of time longer than 1 day when the low-passed stress exceeded 10 dynes/cm^2.

b. Light attenuation coefficient computed from light measurement made by a Montedoro-Whitney transmissometer. The dashed line shows the percent shell cover based on the average of 18 visual estimates in squares covering approximately 20 percent of the bottom photograph. The arrows mark times of the three bottom photographs in figure A2-4.

c. Calibration slope $\bar{B}$ as a function of time calculated from the size distribution of material collected in a sediment-trap. B is zero for the calm periods between the storm periods labelled in figure A2-5a. The dotted line between December 20-30 is the value of B based on field measurements of suspended matter containing 75-90 percent non-combustible material (Table A2-4). Triangles indicate release times for teflon flakes.

d. Suspended-matter concentration (in mg/l) estimated as the product of the light attenuation coefficient (fig. A2-5b) and B, assuming that the suspended matter is always inorganic (solid line in fig. A2-5c)

e. Suspended-matter concentration (in mg/l) estimated as the product of the light attenuation coefficient (fig. A2-5b) and B, assuming that the suspended matter between December 20-30 contains 75-90% non-combustible matter (dotted line in fig. A2-5c) but is all inorganic after January 1 (solid line in fig. A2-5c).

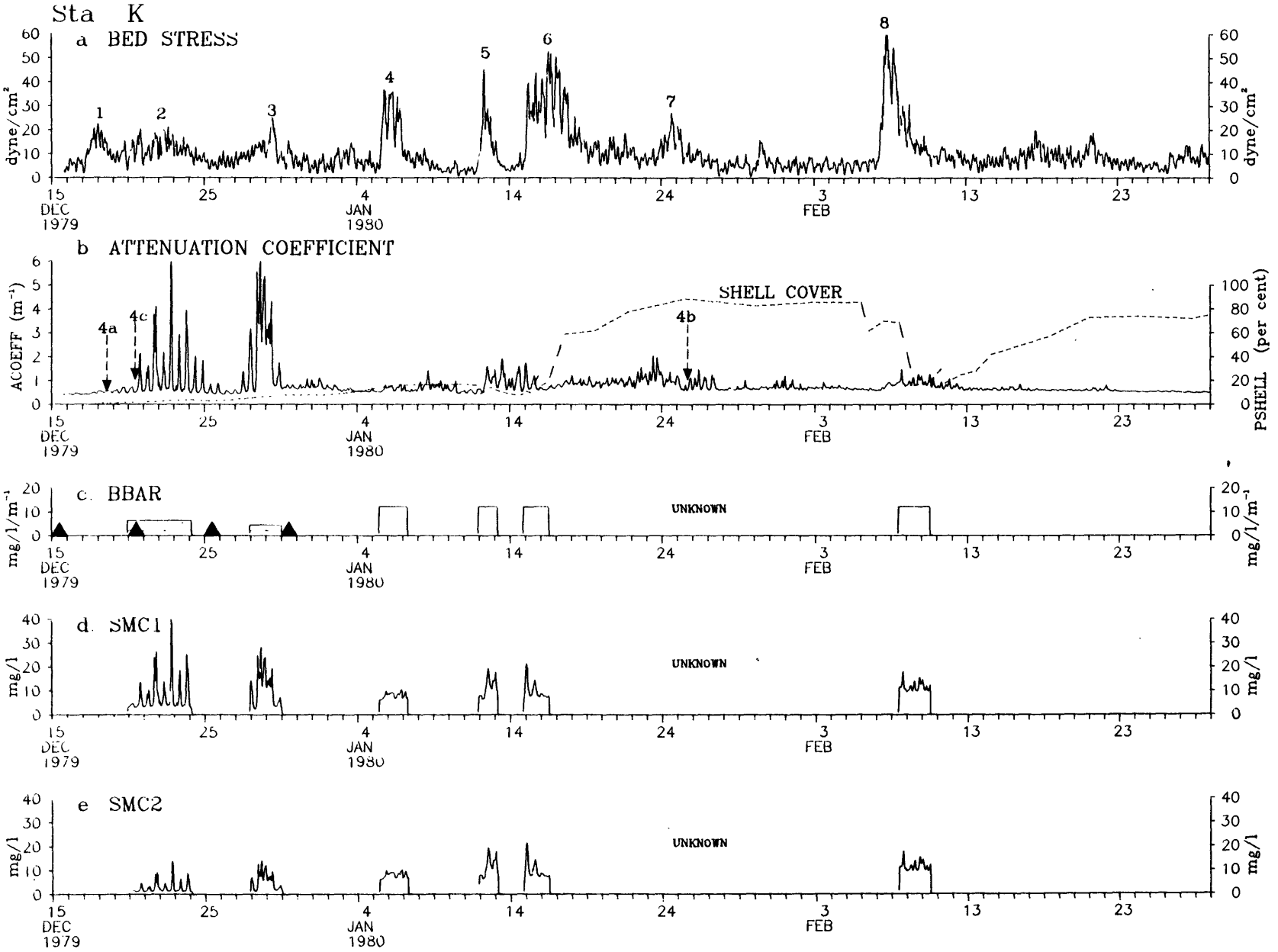
Sta K
a BED STRESS
dyne/cm²
1
2
3
4
5
6
7
8
b ATTENUATION COEFFICIENT
ACOEFF (m⁻¹)
4a
4c
4b
SHELL COVER
PSHELL (per cent)
c. BBAR
mg/l/m⁻¹
UNKNOWN
d. SMC1
mg/l
UNKNOWN
e SMC2
mg/l
UNKNOWN
15 DEC 1979
25
4 JAN 1980
14
24
3 FEB
13
23

Figure A2-5.

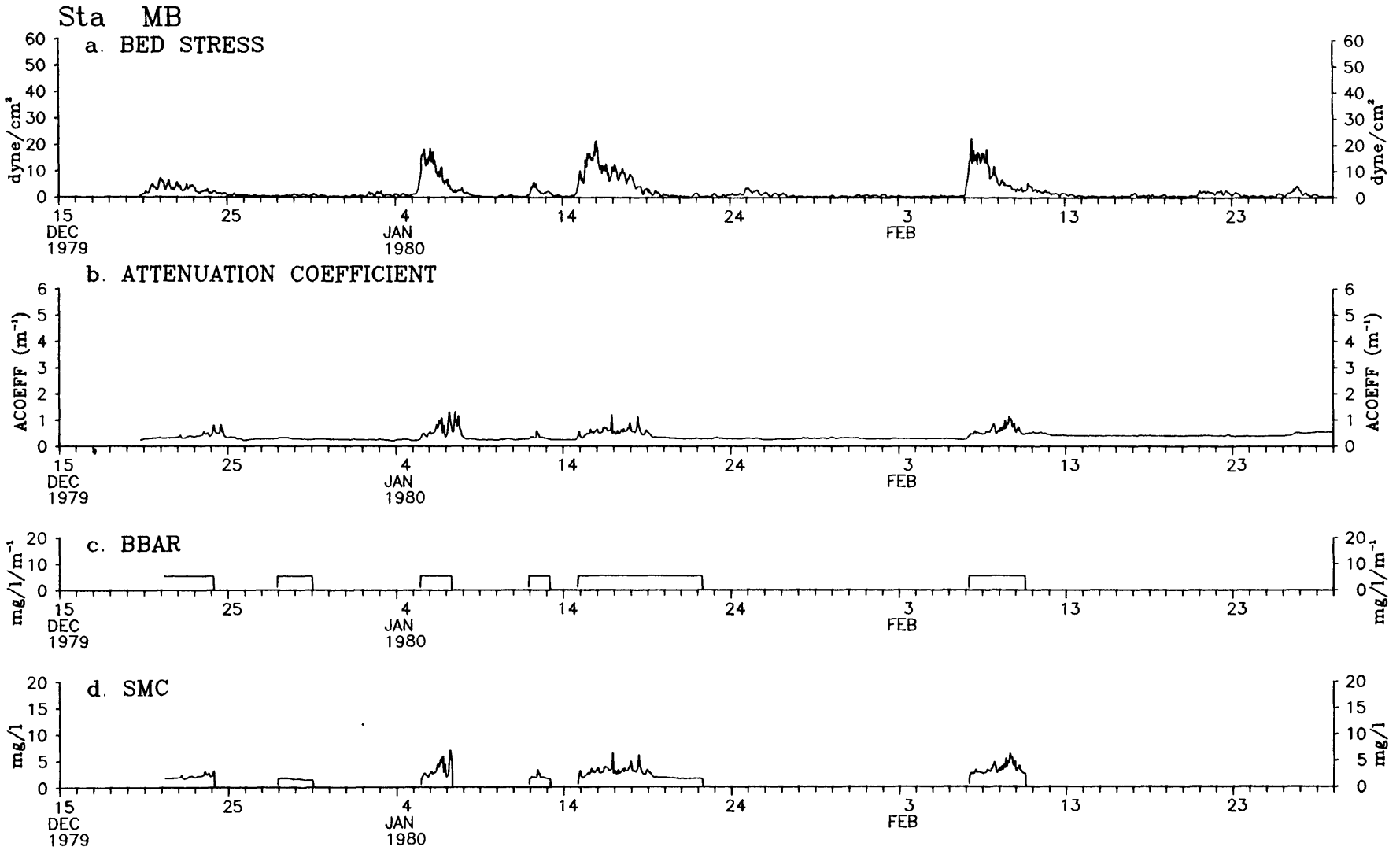

Figure A2-6. Station MB time series. See explanation for figure A2-5.

bottom pressure measurements using linear wave theory. Bottom roughness (10 cm) was determined from measurements of ripples in photographs of the bottom beneath the tripod, and the equation for ripple roughness given in Grant and Madsen (1982) (see Lyne and others for details of the calculation of stress). Bottom stress is not used in this chapter to predict SMC but simply as a semi-quantitative way to identify storms.

Suspended matter was collected by sediment traps mounted on the tripods. The top opening of the trap was about 1 m above the transmissometers and 3.0 above the bottom. The traps had a 25-cm diameter, and 1-m long, baffled collecting funnel connected to a 80-cm long, 4-cm diameter collection tube (Anderson, 1977). This long, small-diameter, collection tube preserves the time-sequence in which sediments entered the trap. Suspended inside the collecting funnel was an instrument (Anderson, 1977) that dispensed about 1 gram of white teflon flakes at 5-day intervals in order to provide "time marks" in the trapped material. During the 166-day deployment period, the entire 81-cm collecting tube at station K was filled with sediment (1,184 cm^3) and an additional 3,328 cm^3 of "overflow" was collected in the trap funnel. A graphic representation of a positive X-ray photograph of the material in the collecting tube and a 24 cm core recovered from the overflow material (hereafter called the overflow core) is shown in figure A2-7.

Size distribution of trapped sediments

The size distribution of the trapped material was determined for 5-cm long samples (approximately 30 grams wet weight) taken every 5 cm in the overflow core and every 10 cm in the collecting tube (see fig. A2-7). Grain size was determined by first wet sieving. Each coarse fraction (>64 μm) was collected on a pre-weighed 0.45 μm Millipore filter, air dried, and then

Figure A2-7. Graphic representation of an X-ray photograph of sediment trap overflow core and collection tube at station K with 5-day timing marks shown as +++ lines. Depths are measured in cm from the bottom of the tube and core. Size distributions of sediment over various intervals in the trap are shown opposite each sample location. This black and white graphic representation makes all layers appear equally distinct. The layers between the December 20th and 25th teflon timing marks were not as distinct as those before and after the December 30th timing mark and those in the overflow core.

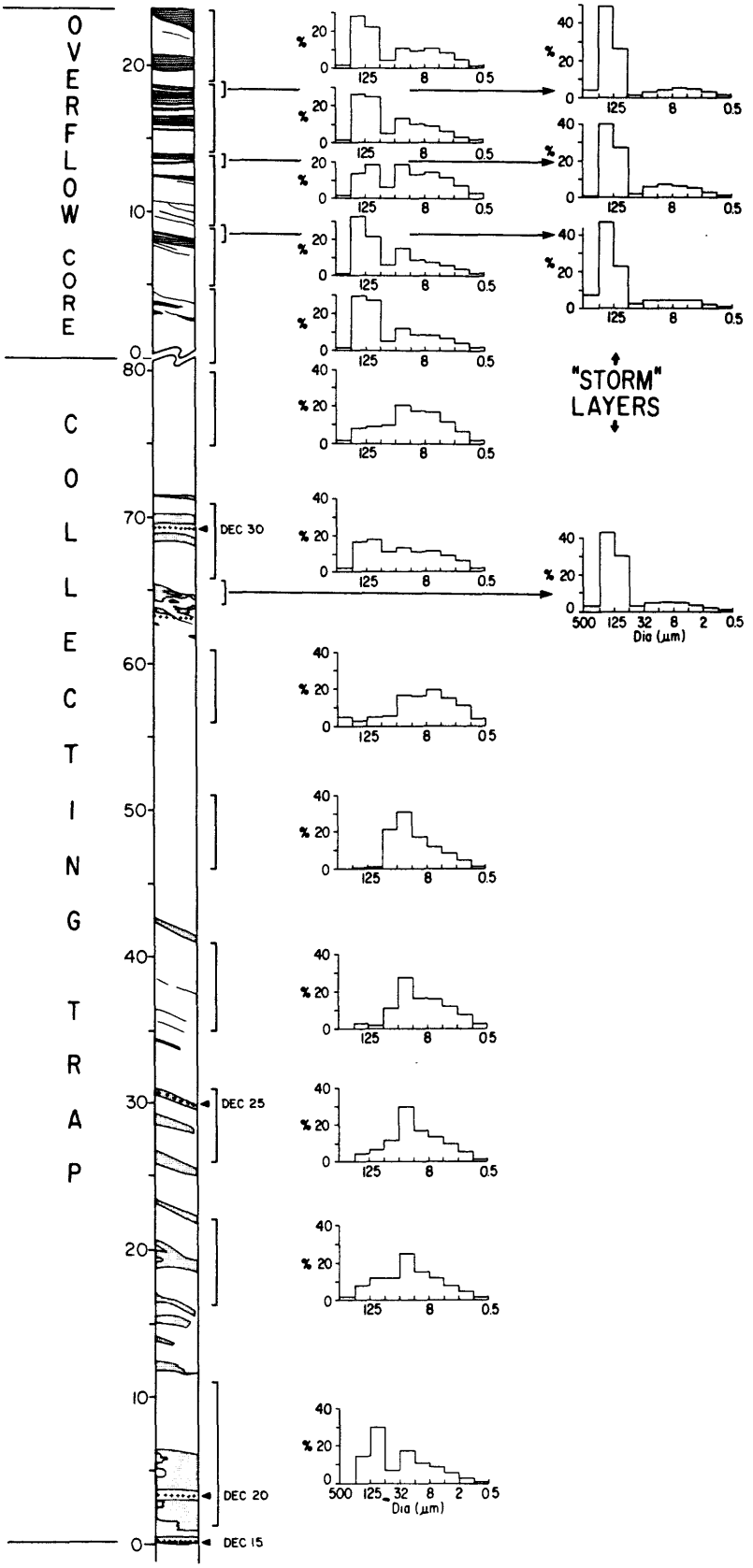
OVERFLOW CORE
COLLECTING TRAP
20
10
0
80
70
60
50
40
30
20
10
0
DEC 30
DEC 25
DEC 20
DEC 15
"STORM" LAYERS
%
125
8
0.5
500 125 32 8 2 0.5
Dia (μm)

Figure A2-7.

weighed. The size distribution of the fine fraction (<64 μm) was measured using a Coulter counter. The samples were not disaggregated with a sonic probe. The mean size of the material in the collecting tube ranged from 17 μm to 46 μm (medium to coarse silt). The material in the overflow core was slightly larger with mean sizes between 38 μm and 63 μm. The variability in size of the trapped material is illustrated by the grain size distribution for each sample (fig. A2-7). The grain size distributions were bimodal in the overflow core, nearly uniform in the top part of the collecting tube (55-81 cm), and mostly unimodal in the lower part of the collecting tube (10-50 cm).

The most striking feature of the X-ray photograph of the trapped material (fig. A2-7) was alternating light and dark layers which correspond to fine and coarse sediments (see also Parmenter and others, 1983). Since the uniformly spaced samples of trapped material often combined light and dark layers, additional samples were taken to determine the size distribution of sediment in the dark layers. The material obtained from the dark layer at 62-64 cm from the bottom of the collecting tube had a mean size of 83 μm and 46 percent of the material was between 125-500 μm. Material from the three dark layers at 8-9, 13-14, and 18-19 cm from the bottom of the overflow core had mean sizes of 90 μm, 74 μm, and 94 μm respectively, and 41-54 percent of the sediment weight was fine sand (125-500 μm). The sediment in the light layer at 54-59 cm had a mean size of 25 μm and 50% of the material was less than 4 μm. The dark layers probably represent the sediment in suspension during storms.

Estimates of $\bar{B}$ and suspended-matter concentration

The calibration slope $\bar{B}$ is not constant but changes with time as the size distribution of suspended matter changes. We wish to use the particle size

distribution of the trap samples to estimate the size distribution of suspended matter in the water column during storm periods and then compute an appropriate calibration slope, $\bar{B}$, for the transmissometer using the laboratory calibration. Estimates of the SMC during storms are equal to the product of $\bar{B}$ and the attenuation coefficient, c_p, for each storm period.

A direct method for estimating $\bar{B}$ is to use actual material from the sediment trap in a labatory calibration. We tested one sample (#7 in table A2-2) and the results agreed well with eq. (9). This laboratory calibration of a fine layer required approximately 30 gram of material (wet weight). Calibration of coarser layers would require 150-300 grams and therefore we were unable to determine $\bar{B}$ using the direct method for each storm layer which contained only 10-15 grams of material.

There are three indirect methods for estimating $\bar{B}$. The preferred method of estimating $\bar{B}$ as a function of time would be to use the size distribution of the sediment layer between successive teflon timing marks which occur at 5-day intervals in the trap, and eq. (9). In cases where the teflon timing marks are not clearly defined, then a possible method is to use the coarse sediment layers as natural timing marks, provided these coarse layers (containing some sediment greater than 125 μm) can be matched one for one with specific storm events in the time series of computed bottom stress. When coarse layers and storm events cannot be matched in time, then a method of last resort is to estimate an "average" storm value of $\bar{B}$ based on the size distribution of sediments found in all coarse layers. This average storm $\bar{B}$ assumes that the size distribution of material placed in suspension by all storms is similar and provides a crude average storm suspended sediment distribution, intended only to illustrate typical particle-size changes.

Estimates of $\bar{B}$ for storm periods at station K (fig. A2-5c) were determined in the following way. A clearly identifiable teflon timing mark was found at the bottom of the collecting tube (0-1 cm) marking December 15 and three other distinct teflon timing marks were found at 2-3 cm, 29-31 cm, and 69-71 cm (from the bottom of the trap) marking December 20th, 25th, and 30th. Not enough material was collected in the trap between December 15-20 for $\bar{B}$ to be determined by any method; thus $\bar{B}$ was unknown during this time. The value of $\bar{B}$ used for the long storm period between December 20-24 was the average $\bar{B}$ (6.4 ± 1.4 mg/l/m^{-1}) for three sediment samples (1-11, 16-22, and 26-31 cm from the bottom of the trap). The value of $\bar{B}$ (4.5 ± 1.1 mg/l/m^{-1}) for storms between December 25-30, was computed from the size distributions of the four trap samples at 36-41 cm, 46-51 cm, 56-61 cm and 66-71 cm representing material collected between December 25-30.

The teflon timing marks in the trap were not clearly defined after December 30 and could not be used to determine the time a sediment sample was collected. It was also not possible to match coarse layers with specific stress or storm events so that an "average" storm value of $\bar{B}$ was computed using the size distribution of sediments found in four coarse layers (see fig. A2-7). This value of $\bar{B}$ (12.2 ± 2.0 mg/l/m^{-1}) was used from January 1 to March 1, 1980 during each storm event. During the period from January 17 to February 8 photographs of the bottom (see fig. A2-4b) showed an extensive layer of clam shells covering approximately 80 percent of the bottom (fig. A2-5b). The armoring of the bottom by shells possibly explains the low light attenuation coefficient (indicating almost no resuspension) during the storm events on January 15-18, January 24-25, and February 7-8 (see fig. A2-5b). During these storms, the maximum bottom stress was nearly twice the maximum bottom stress for the December events, but the light attenuation coefficient

was about 5 times smaller. We don't know what effect the shell layer had on erosion thresholds, and we could not estimate the size distribution of material in suspension from the traps; therefore $\bar{B}$ was unknown during this period.

An estimate of the SMC during six storms at station K (fig. A2-5d) was computed as the product of the light attenuation coefficient at 2 mab (fig. A2-5b) and the calibration slope $\bar{B}$ estimated for six storm periods from material trapped 3 mab (fig. A2-5c). Since we were interested in only the storm periods, the calibration slope $\bar{B}$ was set to zero during the calm periods between storms. Estimates of the maximum SMC were 40 mg/l for storms during December, 22 mg/l during January, and 18 mg/l for a storm between February 8 to 10. The maximum, minimum, and mean concentrations are listed in table A2-3 for six storms.

We also analyzed trapped material from sediment traps deployed during the same winter period at station Q and at station MB (see fig. A2-3) and calculated values of $\bar{B}$ using eq. (9). Three coarse layers at Q were dominated by 62 μm material, in contrast to the coarser 125 μm material (see fig. A2-7) found at station K (see fig. A2-7). As a result, the $\bar{B}$ (10.3 ± 1.4 mg/l/m^{-1}) at station Q was smaller than the $\bar{B}$ at station K. The transmissometer at 2 mab failed at station Q, so no estimates were made of SMC. At station MB the teflon timing marks were not clearly defined, and there were no obvious coarse sediment layers in the 85 cm of trapped material collected. An estimate of the SMC (fig. A2-6d) at 2 mab (during the same storm periods defined for station K) was the product of the calibration slope $\bar{B}$ (5.4 ± 1.3 mg/l/m^{-1}) computed from the size distributions of seven samples from a trap 3 mab and the attenuation coefficient calculated from light measurements 2 mab. The mean SMC at station MB for the same six storms listed

Table A2-3. Estimates of maximum and minimum average suspended-matter concentration during 6 winter storms at station K on Georges Bank from December 19, 1979 to February 10, 1980. (Values in parenthesis are estimates based on assuming 75-90% non-combustible content and the average B listed in Table 4.)

Date	Storm* duration (days)	Concentration (mg/L) Maximum	Minimum	Mean
December 19 - 24	4.2	40 (14)	3 (1)	8 (3)
December 27 - 30	2.1	29 (14)	2 (1)	11 (6)
January 5 - 7	1.9	11	6	8
January 11 - 13	1.3	20	7	12
January 14 - 16	1.7	22	7	10
February 8 - 10	2.1	18	9	12

*See text for definition of storm.

in table A2-3 ranged between 2 and 4 mg/l. It is important to note that although the magnitude of the light attenuation coefficient was similar at stations K (fig. A2-5b) and MB (fig. A2-6b) during storms occurring between January 5-7 and February 8-10, the estimated SMC were 2 to 3 times greater at station K because of the different suspended sediment size distribution.

DISCUSSION

We have used the size distribution of material collected in sediment traps at 3 mab to estimate the calibration slope, $\bar{B}$, which relates the computed light attenuation coefficient at 2 mab to the SMC during storms. The time variation of $\bar{B}$ is modeled as a constant during each storm period. This procedure has several problems which fall into four categories: 1) effect of sediment type on calibration slope, 2) determination of sediment size distribution from sediment traps, 3) criteria for changing $\bar{B}$ based on computed bottom stress, and 4) different time scales of attenuation and particle size observations. Each is discussed below.

The determination of the calibration slope $\bar{B}$ was based on the results of calibration experiments using inorganic material. The value of $\bar{B}$ for organic material such as fecal pellets, zooplankton, phytoplankton or amorphous organic matter is not known. Yet the composition of suspended matter collected by Meade and others (1975) in the Middle Atlantic Bight near the bottom had 40 percent organic material and Bothner and others (1982) have found that approximately 20 percent of the material collected in sediment traps on the Continental Shelf was combustible. An example of changing sediment type may be illustrated by the time series of bottom stress and attenuation coefficient at station K (fig. A2-5). If we assume that the surficial sediment type and availability of erodible sediment remains the same

during the deployment period, then we would expect that as the bottom stress increases the attenuation coefficient would also increase; this did not occur however. During December large fluctuations in the attenuation coefficient were associated with relatively small stresses while between January 5-7 and February 7-10 large stresses were associated with attenuation coefficients approximately one third the December values. One possible explanation for this variability is that during the period December 20-30 (storms 2 and 3 in fig. A2-5a), a large patch of organic material (see fig. A2-4c), surrounded by relatively clear water, was advected past station K by the mean and tidal flows resulting in changes of the attenuation coefficient at the tidal period (see fig. A2-5b). Crude estimates of the size of the patch based on the cross-shelf tidal excursion (~7 km) and the net alongshelf flow (~3 cm/s) suggest a patch of at least 7 km in the cross-shelf direction and approximately 13-15 km in the alongshelf direction. It is possible that no "patch" was present during the December 17-19 storm (storm 1 in fig. A2-5a, where $\bar{B}$ was unknown, see above) nor during later more intense storms (no. 4 and 5, in fig. A2-5a). We cannot conclusively test this "patch" hypothesis without a more closely spaced instrument array and suspended matter samples; however it could explain the observed variability and the large fluctuations in light attenuation during periods of moderate stress.

To obtain a rough estimate of $\bar{B}$ appropriate for periods when the suspended matter may have contained organic material, we used field measurements of light attenuation coefficient and SMC obtained on three cruises (OCEANUS 45, 81, and 91) conducted in the region of Georges Bank and the New England Shelf (table A2-4). The $\bar{B}$ estimates for each cruise were separated into eight groups based on the percent of non-combustible material and then averaged. Assuming that the large fluctuations in light attenuation

Table A2-4. Field measurements of the calibration slope $\bar{B}$ (in mg/l/m^{-1}) from R/V OCEANUS cruises 45, 81, and 91.

Percent non-combustible	OCEANUS 45	OCEANUS 81	OCEANUS 91	Average
5-14	0.1	0.1	0.1	0.1
15-24	0.1	0.2	0.1	0.1
25-34	0.2	0.5	0.2	0.3
35-44	2.4	0.9	0.3	1.2
45-54	2.4	1.0	0.8	1.4
55-64	1.0	1.3	1.3	1.2
65-74	2.8	.6*	1.1	2.0
75-90	2.8	1.5	-	2.2

*only 5 samples and therefore not included in the average

between December 20-30 were associated with organic material, a conservative value of $\bar{B}$ (2.2 mg/l/m,$^{-1}$) was used to estimate SMC from the light attenuation during this period. The final best estimate of SMC for the deployment period (fig. A2-5e) contrasts sharply with the original plot of light attenuation coefficient (fig. A2-5b)--the larger attenuation coefficients in December actually correspond to a smaller SMC (1-14 mg/l) than the SMC estimated for January and February (6-22 mg/l). This final plot of SMC agrees intuitively with the computed bottom stress (fig. A2-5a).

Determination of the size distribution of suspended matter in the water column from the trap sample has many difficulties. First, the transmissometer was located approximately 2 mab, while the sediment trap opening was at 3 mab. The concentration of fine suspended material is more uniform with height above the bottom than coarse material. Consequently the material trapped at 3 mab will probably contain a greater amount of fines than at 2 mab, resulting in an underestimate of $\bar{B}$ and SMC at 2 mab. Second, it is possible that physical compaction, chemical reactions within the trap, or that the size analysis procedures (possibly sonic disaggregation) may alter the size distribution of the suspended matter as it occurred in the water. Third, we have assumed that the particles collected by sediment traps were an unbiased representation of the particles in suspension. Sediment traps have trapping efficiencies proportional to the grain diameter (Butman and others, submitted) and may undertrap fine material-resulting in an overestimate of $\bar{B}$. The trap efficiency may also change with the current strength and it is possible that the coarse layers are a result of undertrapping of fine material during strong flows (i.e. storms). We cannot resolve these problems with the data obtained here; traps must be carefully calibrated in the lab for the range of flow conditions and particle sizes encountered in the field.

The calibration slope $\bar{B}$ was changed as a function of time during storms which we determined by the magnitude and duration of the bottom stress. The bottom stress is a function the physical roughness of the bottom, and under similar wave and current conditions a roughness of 2 cm results in a stress of 29 dynes/cm^2 while a roughness of 10 cm yields a stress of approximately 70 dynes/cm^2 (Lyne and others). In this analysis, we assumed a constant bottom roughness and thus the computed stress does not reflect changes in roughness which did occur. For example, between January 16 and February 7 shells covered at least 80 percent of the bottom (fig. A2-4b) which certainly changed the physical roughness and thus the bottom stress estimates during this period are incorrect. In addition, the shells possibly armored the bottom, reducing the amount of sediment available for resuspension, and probably increased the stress required for erosion of sediments to the point where no motion occurred even though the bottom stress was large. These uncertainities in bottom stress and variation in sediment variability may alter the value of the calibration slope $\bar{B}$ for the light attenuation observations for some time periods.

The transmissometer record (fig. A2-5b) showed large changes in light attenuation over several hours, but the available size distribution data from the sediment traps resolved time changes of at best a few days (see $\bar{B}$ in fig. A2-5c). The poor time resolution of the size distribution of suspended matter allowed only very simple step changes in $\bar{B}$ for each storm period. In reality $\bar{B}$ changes more rapidly with time, and there is an obvious need to improve the time resolution of changes in the size distribution of suspended matter. Water samples collected by instruments moored on the bottom would overcome some of the problems associated with using sediment traps but probably would be limited by the number of samples available unless the size distribution of suspended matter in the water samples could be analyzed <u>in situ</u>.

SUMMARY

The calibration of beam transmissometers depends upon particle diameter and may also depend upon particle shape, roughness, and organic composition. The transmissometer calibration slope, $\bar{B}$, relating SMC and light attenuation coefficient will change temporally and spatially on the continental shelf and slope where there is a wide range of both bottom stress and surficial sediment sizes.

The average SMC during six storms at two locations on the Continental Shelf was estimated at a single point 2 mab from the product of a time varying, particle size, transmissometer calibration slope $\bar{B}$ and the observed light attenuation coefficient. The average SMC due to storms in the Middle Atlantic Bight was 3 mg/l with a maximum of 5 mg/l; the average SMC on the south flank of Georges Bank was 8-12 mg/l with a maximum of 22 mg/l. The magnitude of the light attenuation coefficient was similar at each station in the Middle Atlantic Bight and on Georges Bank but the estimates of SMC were 2 to 3 times greater on Georges Bank because of a different suspended sediment size distribution determined from material collected in sediment traps.

We have labored to interpret the time series of light attenuation recorded at several locations on the continental shelf. The light attenuation is clearly a complex function of many factors: the time variability of particle size and shape partially associated with local resuspension, the possible seasonal changes in organic composition of suspended material, the existence of irregular temporal and spatial "patches" of suspended matter, and the armoring of the bottom by shells. This analysis clearly shows that light attenuation measurements alone are insufficient to estimate SMC on the continental shelf when the size as well as concentration of particles in suspension changes with time. Time series of light attenuation may be very

different from particle concentration. Although we used sediment traps to crudely estimate the size of particles in suspension, uncertainities in trap efficiency as a function of particle size and current speed, flocculation or deflocculation of particles after entering the trap, and the poor time resolution, make traps marginal for determining sediment particle size as a function of time. New methods for obtaining time series measurements of particle size and concentration at a number of heights above the sea floor are needed to further enhance our understanding of particle transport on the shelf.

ACKNOWLEDGEMENTS

Carol M. Parmenter generously made the sediment trap data available and provided helpful suggestions and advice. John Larson assisted in the transmissometer calibration experiment and Larry Poppe performed some of the particle size analysis.

REFERENCES

Anderson, R. V., 1977, Short-term sedimentation response in lakes in the western United States as measured by automated sampling: Limnology and Oceanography, v. 22, p. 423-433.

Baker, E. T., and Lavelle, J. W., 1984, The effect of particle size on the light attenuation coefficient of natural suspensions: Journal of Geophysical Research, v. 89, no. C5, p. 8197-8203.

Bartz, R., Zaneveld, J. R. V., and Pak, H., 1978, A transmissometer for profiling and moored observations in water: SPIE, v. 160, Ocean Optics V, p. 102-108.

Bothner M. H., Parmenter, C. M., and Milliman, J. D., 1981a, Temporal and spatial variations in suspended matter in Continental Shelf and Slope Waters off the North-eastern United States: Estuarine, Coastal and Shelf Science, v. 13, p. 213-213.

Bothner, M. H., Spiker, E. C., Johnson, P. P., Rendigs, R. R., and Aruscavage, P. J., 1981b, Geochemical evidence for modern sediment accumulation on the continental Shelf off southern New England: Journal Sedimentary Petrology, v. 51, p. 281-292.

Bothner, M. H., Parmenter, C. M., Rendigs, R. R., Butman, B., Poppe, L. J., and Milliman, J. D., 1982, Studies of suspended matter along the North and Middle Atlantic Outer Continental Shelf: U.S. Geological Survey Open-file Report 82-938, 38 p.

Butman, B. and Folger, D. W., 1979, An instrument system for long-term sediment transport studies on the Continental Shelf: Journal of Geophysical Research, v. 84, p. 1215-1220.

Butman, C. A., Grant, W. D., and Stolzenbach, K. D., Predictions of sediment trap bases in turbulent flows: a theoretical analysis based on observations from the literature: Journal of Marine Research, (in press).

Drake, D. E., 1977, Suspended particulate matter in the New York Bight Apex, fall 1973: Journal of Sedimentary Petrology, v. 47, p. 209-228.

Drake, D. E. and Cacchione, D. A., 1985, Seasonal variation in sediment transport on the Russian River shelf, California: Continental Shelf Research, v. 4, p. 495-514.

Grant, W. D. and Madsen, O. S., 1979, Combined wave and current interaction with a rough bottom: Journal of Geophysical Research, v. 84, p. 1797-1808.

Grant, W. D. and Madsen, O. S., 1982, Moveable bed roughness in unsteady oscillatory flow: Journal of Geophysical Research, v. 87, p. 469-481.

Lyne, V. D., Butman, B., Grant, W. D., Computations of bottom stress for Georges Bank and the Mid-Atlantic Bight Continental Shelf: Continental Shelf Research. (in preparation).

Manheim, F. T., Meade, R H., and Bond, G. C., 1970, Suspended matter in surface waters of the Atlantic Continental Margin from Cape Cod to the Florida Keys: Science, v. 167, p. 371-376.

Mantz, P. A., 1977, Incipient transport of fine grains and flakes by fluids-extended shields diagram, Proceedings of the American Society of Civil Engineers: Journal of Hydraulics Division, v. 103, p. 601-615.

Meade, R. H., Sachs, P. L., Manheim, F. T., Hathaway, J. C., and Spencer, D. W., 1975, Sources of suspended matter in waters of the Middle Atlantic Bight: Journal of Sedimentary Petrology, v. 45, p. 171-188.

Moody, J. A., Butman, B., Beardsley, R. C., Brown, W. S., Daifuki, P., Irish, J. D., Mayer, D. A., Mofjeld, H. O., Petrie, B., Ramp, S., Smith, P.,and Wright W. R., 1984, Atlas of tidal elevation and current observations on the Northeast American Continental Shelf and Slope: U.S. Geological Survey Bulletin 1611, 122 p.

Parmenter, C. M., Bothner, M. H., and Butman, B., 1983, Characteristics of resuspended sediment from Georges Bank collected with a sediment trap: Estuarine, Coastal and Shelf Science, v. 17, p. 521-533.

Schlee, J., 1966, A modified Woods Hole rapid sediment analyzer: Journal of Sedimentary Petrology, v. 36, p. 403-413.

Spinrad, R. W., Zaneveld, J. R. V., and Kitchen, J. C., 1983, A study of the optical characteristics of the suspended particles in the benthic nepheloid layer of the Scotian Rise: Journal of Geophysical Research, v. 88, p. 7641-7645.

Sternberg, R. W. and Creager, J. S., 1965, An instrument system to measure boundary-layer conditions at the sea floor: Marine Geology, v. 3, p. 475-482.

Sternberg, R. W., Cacchione, D. A., Drake, D. E. and Kranck, K., 1986, Suspended sediment transport in an estuarine tidal channel within San Francisco Bay, California: Marine Geology (in press).

Twichell, D. C., McClennen, C. E., and Butman, B., 1981, Morphology and processes associated with the accumulation of the fine-grained sediment deposit on the southern New England Shelf: Journal of Sedimentary Petrology, v. 51, p 269-280.

Williams, A. J. 1985, BASS, Acoustic current meter array for benthic flowfield measurements, in, Nowell, A. R. M. and Hollister, C. D., (eds.), Deep Ocean Sediment Transport: Elsevier, p. 345-355.

Young, R. A., 1978, Suspended-matter distribution in the New York Bight apex related to Hurricane Belle: Geology, v. 6, p. 301-304.

APPENDIX 3

LYDONIA CANYON EXPERIMENT

MOORING LOCATIONS AND DATA QUALITY

Table A3-1 is a summary of the moored instrumentation deployed as part of the Lydonia Canyon Experiment. The table contains the station designation, the station latitude and longitude, the water and instrument depth, the USGS mooring ID, the instrument type (V is EG&G vector averaging current meter, VTCT is vector averaging current meter modified to record conductivity and transmission, VTr is a vector averaging current meter modified to record transmisssion, VP is a vector averaging current meter modified to measure pressure, and T is a bottom tripod), the deployment start and stop dates, and the number of days of data. For each variable (direction, speed, temperature, conductivity, transmission and pressure) the stop time (if earlier than the recovery date), the percent data return, and the data quality is also tabulated. For data quality Q is questionable, L is lost, F is fouled, NG is no good. If no percent data return is shown, the parameter was not measured at that location.

Table A3.1A. Summary of instrument locations, deployment period, and the current direction and speed data obtained as part of the Lydonia Canyon Experiment. Stop times for the variables are listed only if the data ended prior to recovery of the mooring. The quality codes are: Q (questionable, see table A3.1C), NG (no good), L (lost), F (fouled). See text for inatrument codes.

Station	Latitude	Longitude	Water Depth	Inst. Depth	Dep. #	Mooring ID	Inst. Type	Deploy	Recover	# Days	Direction			Speed		
											Stop	%	Quality	Stop	%	Quality
LCA	40°34.21N	67°44.55W	100	80	1	2071	VTCT	801130	810424	144		100			100	
	40°34.37N	67°44.67W	100	80	2	2251	V	810504	810926	144		100			100	
	40°34.20N	67°44.81W	100	99	1	2041	T	801024	810424	181	810424	63		810424	63	
	40°34.25N	67°44.76W	100	99	2	2231	T	810505	810926	144		100			100	
	40°34.22N	67°44.14W	100	99	3	2291	T	810926	820128	124	811014	14	Q	811014	14	Q
	40°33.78N	67°44.76W	103	102	4	2401	T	820128	820707	160	820217	13	Q	-	0	NG
	40°33.83N	67°44.21W	104	103	5	2571	T	820708	820712	34		100			100	
	40°33.76N	67°44.58W	106	105	5	2641	T	820812	821111	90	-	0	NG		100	
LCB	40°31.55N	67°42.82W	282	92	1	2081	VTCT	801128	810428	150		100			100	
	40°31.56N	67°42.83W	288	108	2	2261	V	810429	810926	150		100			100	
	40°31.50N	67°42.74W	295	125	3	2301	VTCT	810927	820130	124		100			100	
	40°31.52N	67°42.83W	300	108	4	2411	VTCT	820131	820707	156		100			100	
	40°31.49N	67°42.79W	295	104	5	2581	V	820708	821111	125		100			100	
	40°31.55N	67°42.82W	282	227	1	2082	V	801128	810428	150		100			100	
	40°31.56N	67°42.83W	288	238	2	2262	V	810429	810926	150		100	Q		100	Q
	40°31.50N	67°42.74W	295	245	3	2302	V	810927	820130	124		100			100	
	40°31.52N	67°42.83W	300	248	4	2412	V	820131	820707	156		100			100	
	40°31.49N	67°42.79W	295	244	5	2582	VTCT	820708	821111	125		100			100	
	40°31.55N	67°42.82W	282	277	1	2083	VTCT	801128	810428	150		100	Q		100	
	40°31.56N	67°42.83W	288	282	2	2263	V	810429	810926	150		100			100	
	40°31.54N	67°42.79W	290	285	3	2311	VTCT	810927	820128	122		100			100	
	40°31.52N	67°42.83W	300	294	4	2413	VTCT	820131	820707	156		100	Q		100	Q
	40°31.49N	67°42.79W	295	290	5	2583	VTr	820708	821111	125		100			100	
LCC	40°29.43N	67°43.50W	184	134	1	2091	V	801024	810425	182	810325	83		810325	83	
LCD	40°29.25N	67°41.25W	193	143	1	2101	V	801027	810425	179	810310	74		810310	74	
LCE	40°25.38N	67°39.88W	600	116	1	2111	VTr	801201	810501	150		100			100	
	40°25.38N	67°39.88W	600	216	1	2112	VTr	801201	810501	150		100			100	
	40°25.38N	67°39.88W	600	425	1	2113	VP	801201	810501	150	-	0	L	-	0	L
	40°25.61N	67°39.60W	580	475	2	2281	V	810505	810926	144		100			100	
	40°25.40N	67°39.84W	590	493	3	2321	V	810928	820130	123		100			100	

Table A3.1A - Continued

Station	Latitude	Longitude	Water Depth	Inst. Depth	Dep. #	Mooring ID	Inst. Type	Deploy	Recover	# Days	Direction Stop	Direction %	Direction Quality	Speed Stop	Speed %	Speed Quality
LCE	40°25.38N	67°39.88	600	595	1	2114	VTr	801201	810505	150	100			100		
	40°25.40N	67°39.84W	590	584	3	2322	VTr	810928	820130	123	100			100		
LCF	40°21.18N	67°39.01W	505	205	1	2121	VP	801027	810427	181	810416	94		810416	94	
	40°21.18N	67°39.01W	505	405	1	2122	V	801027	810427	181	100			100		
LCG	40°21.44N	67°41.63W	495	195	1	2131	V	801027	810427	181	100			100		
	40°21.44N	67°41.63W	495	395	1	2132	V	801027	810427	181	100			100		
LCH	40°17.59N	67°39.54W	1,554	290	1	2141	VP	801201	810427	146	100			100		
	40°17.59N	67°39.54W	1,554	540	1	2142	V	801201	810427	146	100			100		
	40°17.59N	67°39.54W	1,554	890	1	2143	V	801201	810427	146	100	Q		100	Q	
	40°17.93N	67°39.52W	1,380	1,375	1	2211	VTr	810120	810428	97	100			100		
	40°17.59N	67°39.54W	1,554	1,454	1	2144	V	801201	810427	146	100	Q		100	Q	
LCI	40°22.84N	67°33.14W	250	10	1	2151	V	801127	810430	154	100			100		
	40°22.95N	67°32.73W	250	55	1	2152	VTr	801202	810429	148	100			100		
	40°22.96N	67°33.01W	250	59	2	2271	V	810503	810927	146	100			100		
	40°23.00N	67°32.93W	251	55	3	2331	V	810927	820131	125	100			100		
	40°23.05N	67°32.96W	249	59	4	2421	V	820201	820708	157	100			100		
	40°22.95N	67°32.73W	250	195	1	2153	V	801202	810429	148	100			100		
	40°22.96N	67°33.01W	250	199	2	2272	V	810503	810927	146	100		810514	8		
	40°23.00N	67°32.93W	251	201	3	2332	V	810927	820131	125	811019	18		811029	26	
	40°23.05N	67°32.96W	249	199	4	2422	V	820201	820708	157	100			100		
	40°22.95N	67°32.73W	250	245	1	2154	VTr	801202	810429	148	100			100		
	40°22.96N	67°33.01W	250	245	2	2273	V	810503	810927	146	100			100		
	40°23.11N	67°32.52W	247	242	3	2341	VTr	810927	820131	125	100			100		
	40°23.05N	67°32.96W	249	243	4	2423	VTr	820201	820708	157	100			100		

Table A3.1A - Continued

Station	Latitude	Longitude	Water Depth	Inst. Depth	Dep. #	Mooring ID	Inst. Type	Deploy	Recover	# Days	Direction Stop	Direction %	Direction Quality	Speed Stop	Speed %	Speed Quality
LCJ	40°21.18N	67°31.98W	571	83	1	2161	VP	801127	810429	152	810402	82	Q	810402	82	Q
	40°21.18N	67°31.98W	571	223	1	2162	V	801127	810429	152	100	Q		100	Q	
	40°21.18N	67°31.98W	571	471	1	2163	V	801127	810429	152	100	Q		100	Q	
LCK	40°16.27N	67°46.99W	554	204	1	2171	V	801127	810427	150	100			100		
	40°16.27N	67°46.99W	554	454	1	2172	V	801127	810427	150	100			100		
LCL	40°32.31N	67°36.40W	125	10	1	2181	V	801024	-	-	-	0	L	-	0	L
	40°31.68N	67°36.55W	125	65	1	2182	V	801130	810425	145	100			100		
	40°31.68N	67°36.55W	125	105	1	2183	VTCT	801130	810425	145	100			100		
	40°32.30N	67°36.83W	126	125	1	2051	T	801125	810502	158	-	0	NG	810324	32	Q
	40°32.37N	67°36.26W	125	124	2	2241	T	810426	810926	153	100		-	0	NG	
	40°32.39N	67°36.43W	127	126	4	2511	T	820131	820708	158	820426	53		820426	53	
LCM	40°29.47N	67°48.24W	123	103	1	2191	V	801128	810425	150	100			100		
	40°29.57N	67°48.55W	120	119	1	2031	T	801024	810426	183	100			100		
	40°29.57N	67°48.55W	120	119	1	2032	T	801024	810426	183						
LCN	40°21.32N	67°40.38W	1,041	243	1	2201	VP	801129	810427	148	100			100		
	40°21.32N	67°40.38W	1,041	841	1	2202	V	801129	810427	148	100			100		
LCO	40°26.73N	67°39.73W	555	554	1	2221	P	810120	810427	96						
	40°26.74N	67°39.75W	555	554	3	2351	P	811001	820129	120						
	40°26.77N	67°39.72W	552	551	4	2471	P	820202	820707	154						
LCP	40°31.95N	67°42.07W	132	113	3	2361	V	810928	820128	122	100			100		
	40°32.02N	67°42.07W	131	130	3	2371	T	810926	820128	124	100			100		
LCQ	40°27.25N	67°38.27W	185	180	4	2431	VTCT	820130	810707	157	100			100		
LCR	40°26.62N	67°38.80W	240	183	4	2441	V	820130	820707	157	100			100	Q	
	40°26.62N	67°38.80	240	215	4	2442	V	820130	820707	157	100			100	Q	

Table A3.1A - Continued

Station	Latitude	Longitude	Water Depth	Inst. Depth	Dep. #	Mooring ID	Inst. Type	Deploy	Recover	# Days	Direction Stop	Direction %	Direction Quality	Speed Stop	Speed %	Speed Quality
LCS	40°27.61N	67°40.03W	560	554	4	2451	VTr	820129	820707	158	100	Q		100		
LCT	40°26.62N	67°40.61W	203	178	4	2461	V	820201	820707	156	100	Q		100		
LCU	40°32.37N	67°44.37W	141	134	5	2591	VTCT	820708	821111	125	100			100		

Table A3.1B. Summary of the temperature, conductivity, transmission, and pressure data obtained as part of Lydonia Canyon Experiment (see table A3.1A for explanation).

Station	Dep. #	Mooring ID	Temperature			Conductivity			Transmission			Pressure		
			Stop	%	Quality	Stop	%	Quality	Stop	%	Quality	Stop	%	Quality
LCA	1	2071		100			100	F		100	F			
	2	2251		100										
	1	2041	810424	63					801212	27	F	810424	63	
	2	2231		100					810717	51	F		100	
	3	2291		100					811212	62	F		100	
	4	2401	820217	13	Q				820217	13	Q	820217	13	Q
	5	2571		100						100			100	
	5	2641		100						100			100	
LCB	1	2081		100			100			100	F			
	2	2261		100										
	3	2301		100			100			100	F			
	4	2411		100			100			100	F			
	5	2581		100										
	1	2082		100										
	2	2262		100										
	3	2302		100										
	4	2412		100										
	5	2582		100			100			100	F			
	1	2083		100			100			100				
	2	2263		100										
	3	2311		100			100			100				
	4	2413		100	Q		100	Q		100	Q			
	5	2583		100						100	F			
LCC	1	2091	810325	83										
LCD	1	2101	810310	74										
LCE	1	2111		100					810401	75				
	1	2112		100						100	F			
	1	2113	-	0	L							-	0	L
	2	2281		100										
	3	2321		100										
	1	2114		100						100				
	3	2322		100						100	F			

Table A3.1B - Continued

Station	Dep. #	Mooring ID	Temperature Stop	Temperature %	Temperature Quality	Conductivity Stop	Conductivity %	Conductivity Quality	Transmission Stop	Transmission %	Transmission Quality	Pressure Stop	Pressure %	Pressure Quality
LCF	1	2121	810416	94								810330	85	
	1	2122		100										
LCG	1	2131		100										
	1	2132		100										
LCH	1	2141		100									100	
	1	2142		100										
	1	2143		100	Q									
	1	2211		100						100	F			
	1	2144		100	Q									
LCI	1	2151		100										
	1	2152		100						100	Q			
	2	2271		100										
	3	2331		100										
	4	2421		100										
	1	2153		100										
	2	2272		100										
	3	2332		100										
	4	2422		100										
	1	2154		100					-	0	NG			
	2	2273		100										
	3	2341		100						100	Q			
	4	2423		100					-	0	NG			
LCJ	1	2161	810402	82	Q							810402	82	Q
	1	2162		100	Q									
	1	2163		100	Q									

Table A3.1B - Continued

Station	Dep. #	Mooring ID	Temperature Stop	Temperature %	Temperature Quality	Conductivity Stop	Conductivity %	Conductivity Quality	Transmission Stop	Transmission %	Transmission Quality	Pressure Stop	Pressure %	Pressure Quality
LCK	1	2171		100										
	1	2172		100										
LCL	1	2181	-	0	L									
	1	2182		100										
	1	2183		100			100		810407	88	F			
	1	2051	810502	99					810331	78	F	810502	99	Q
	2	2241		100					810726	59			100	
	4	2511		100					820426	53	Q		100	Q
LCM	1	2191		100										
	1	2031		100					810124	50	F		100	
	1	2032	810218	64					810218	64				
LCN	1	2201		100									100	
	1	2202		100										
LCO	1	2221		100									100	
	3	2351	-	0	NG							-	0	NG
	4	2471		100									100	
LCP	3	2361		100										
	3	2371		100						100			100	
LCQ	4	2431		100			100	NG		100	F			
LCR	4	2441		100										
	4	2442		100										
LCS	4	2451		100					-	0	NG			
LCT	4	2461		100										
LCU	5	2591		100			100			[illegible]				

Table A3.1C Comments on data obtained as part of Lydonia Canyon Experiment

LYDONIA CANYON

Station	Dep. #	Mooring ID	Comments
LCA	1	2071	Salinity too fresh compared to OC95; apparently fouled
	2	2251	
	1	2041	Deck A went bad about half way through
	2	2231	Rotor 2 failed as well
	3	2291	Rotors died; questionable as to when went bad
	4	2401	Failed almost immediately never completely decoded
	5	2571	Recovered early
	5	2641	Vane never went through West; leak in cable
LCB	1	2081	
	2	2261	
	3	2301	Mooring wrapped by long-line at time of recovery
	4	2411	Vane fouled at recovery; data appears OK
	5	2581	
	1	2082	
	2	2262	Vector resolver failed; currents from Bearing and Rotor count
	3	2302	Mooring wrapped by long-line at time of recovery
	4	2412	
	5	2582	
	1	2083	Vane problem; direction probably OK
	2	2263	
	3	2311	
	4	2413	Clock fast by 11.5 minutes at recovery
	5	2583	Transmissometer cable damaged at recovery; data appears OK
LCC	1	2091	Mooring moved during deployment
LCD	1	2101	Mooring moved during deployment
LCE	1	2111	
	1	2112	
	1	2113	
	2	2281	
	3	2321	
	1	2114	
	3	2322	

Table A3.1C - Continued

Station	Dep #	Mooring ID	Comments
LCF	1	2121	
	1	2122	
LCG	1	2131	
	1	2132	
LCH	1	2141	
	1	2142	
	1	2143	Lots of read errors; interpolation up to 3 hours required
	1	2211	
	1	2144	Many gaps in time base; heavy scrubbing, interpolation
LCI	1	2151	
	1	2152	Beam attenuation large compared to OC91 section; fouled near end
	2	2271	Mooring wrapped by long-line; heavy scrubbing on 3 days
	3	2331	
	4	2421	
	1	2153	
	2	2272	
	3	2332	
	4	2422	
	1	2154	
	2	2273	
	3	2341	Large spikes in beam attenuation uncorrelated to currents; low compared to OC104, OC113
	4	2423	
LCJ	1	2161	Mooring hit several times; scrubbed data probably OK
	1	2162	Mooring hit; data probably OK
	1	2163	Mooring hit; data probably OK
LCK	1	2171	
	1	2172	

Table A3.1C - Continued

Station	Dep. #	Mooring ID	Comments
LCL	1	2181	
	1	2182	
	1	2183	
	1	2051	Pressure on Deck B 20mbar higher than Deck A; gap between decks
	2	2241	Slip lines parted during deployment
	4	2511	Mooring moved during deployment; unexplained high starting beam attenuation (transient)
LCM	1	2191	
	1	2031	
	1	2032	Test of Sea Data recorder on same tripod
LCN	1	2201	
	1	2202	
LCO	1	2221	
	3	2351	
	4	2471	
LCP	3	2361	
	3	2371	Speed created from Rotor 2
LCQ	4	2431	
LCR	4	2441	Lower VACM wrapped by lobster pot; questionable if affected data
	4	2442	Mooring wrapped by lobster pot line; appears to have occurred 5/25
LCS	4	2451	Question of compass problem; data seems OK
LCT	4	2461	Question of compass problem; data seems OK
LCU	5	2591	Beam attenuation less than OC122 and OC130

APPENDIX 4

SLOPE EXPERIMENT

MOORING LOCATIONS AND DATA QUALITY

Table A4-1 is a summary of the moored instrumentation deployed as part of the Slope Experiment. The table contains the station designation, the station latitude and longitude, the water and instrument depth, the USGS mooring ID, the instrument type (V is EG&G vector averaging current meter, VTCT is vector averaging current meter modified to record conductivity and transmission, VTr is a vector averaging current meter modified to record transmisssion, VP is a vector averaging current meter modified to measure pressure, and T is a bottom tripod), the deployment start and stop dates, and the number of days of data. For each variable (direction, speed, temperature, conductivity, transmission and pressure) the stop time (if earlier than the recovery date), the percent data return, and the data quality is also tabulated. For data quality Q is questionable, L is lost, F is fouled, NG is no good. If no percent dataa return is shown, the parameter was not measured at that location.

Table A4-1A Summary of instrument locations, deployment period, and the current direction and speed data obtained as part of the Slope Experiment. Stop times are listed only if the data ended prior to recovery of the mooring. The quality codes are: Q (questionable, see Table A4.1C), NG (no good), L (lost), F (fouled). If there is no entry for a variable, it was not measured at that location.

											Direction			Speed		
Ststion	Latitude	Longitude	Water Depth	Inst. Depth	Dep. #	Mooring ID	Inst. Type	Deploy	Recover	# Days	Stop	%	Quality	Stop	%	Quality
SA	40°04.79N	68°33.60W	490	166	1	2711P	TDR	821115	831019	337						
	40°04.60N	68°33.82W	500	133	3	2771P	TDR	840317	841117	244						
	40°04.79N	68°33.60W	490	182	1	2711	VTCT	821115	831019	337		100			100	
	40°04.79N	68°33.48W	485	184	2	2761	V	831020	840317	148		100			100	
	40°04.60N	68°33.82W	500	149	3	2771	V	840317	841117	244		100			100	
	40°04.79N	68°33.60W	490	387	1	2712	V	821115	831019	337		100			100	
	40°04.79N	68°33.48W	485	478	2	2762	V	831020	840317	148		100			100	
	40°04.60N	68°33.82W	500	496	3	2772	V	840317	841117	244	-	0	L	-	0	L
SB	40°01.05N	68°32.42W	1,611	411	1	2671	V	821110	831019	342		100			100	
	40°01.05N	68°32.42W	1,611	711	1	2671P	T/P	821110	831019	342						
	40°01.05N	68°32.42W	1,611	1,011	1	2672	V	821110	831019	342		100			100	
	40°01.05N	68°32.42W	1,611	1,511	1	2673	V	821110	831019	342		100			100	
SC	39°58.48N	68°31.39W	2,132	120	1	2681P	TDR	821110	831021	344						
	39°58.48N	68°31.39W	2,132	130	1	2681	VTCT	821110	831021	344		100			100	
	39°58.48N	68°31.39W	2,132	330	1	2682	VTCT	821110	831021	344		100			100	
	39°58.48N	68°31.39W	2,132	630	1	2682P	T/P	821110	831021	344						
	39°58.48N	68°31.39W	2,132	930	1	2683	V	821110	831021	344	-	0	L	-	0	L
	39°58.48N	68°31.39W	2,132	1,430	1	2684	V	821110	831021	344	-	0	L	-	0	L
	39°58.48N	68°31.39W	2,132	2,030	1	2685	V	821110	831021	344	-	0	L	-	0	L
SD	40°16.78N	67°46.57W	485	385	1	2691	V	821112	831021	342	831019	96		831019	96	
SE	39°53.84N	70°03.71W	491	124	2	2741P	TDR	831023	840313	141						
	39°53.87N	70°03.72W	403	137	3	2781P	TDR	840315	841115	244						
	39°53.84N	70°03.71W	491	140	2	2741	VTCT	831023	840313	141	831216	38	Q	831216	38	Q
	39°53.87N	70°03.72W	504	153	3	2781	V	840315	841115	244		100		-	0	NG

Table A4-1A - Continued

Station	Latitude	Longitude	Water Depth	Inst. Depth	Dep. #	Mooring ID	Inst. Type	Deploy	Recover	# Days	Direction Stop	Direction %	Direction Quality	Speed Stop	Speed %	Speed Quality
SE(cont)	39°53.84N	70°03.71W	491	240	2	2742	VTCT	831023	840313	141	-	0	NG	840313	78	
	39°53.87N	70°03.72W	504	253	3	2782	V	840315	841115	244	100		100			
	39°53.86N	70°03.87W	500	400	1	2701	V	821109	831023	347	100	Q	100	Q		
	39°53.84N	70°03.71W	491	380	2	2743	V	831023	840313	141	100		100			
	39°53.87N	70°03.72W	504	403	3	2783	V	840315	841115	244	100		100			
	39°53.84N	70°03.71W	491	484	2	2744	VTCT	831023	840313	141	100		100			
	39°53.88N	70°03.72W	504	497	3	2784	VTCT	840315	841115	244	100	Q	100	Q		
SF	39°57.65N	70°00.90W	205	10	3	2791	V	840316	841118	246	100	840814	61			
	39°57.67N	70°01.06W	204	53	3	2792	V	840316	841115	243	100		100			
	39°57.66N	70°00.94W	202	126	2	2751	VTCT	831018	840313	147	100		100			
	39°57.67N	70°01.06W	204	128	3	2793	VTCT	840316	841115	243	840724	53		840724	53	
	39°57.66N	70°00.94W	202	195	2	2752	VTCT	831018	840313	147	840125	67		840125	67	
	39°57.67N	70°01.06W	204	197	3	2794	VTCT	840316	841115	243	840807	59		840807	59	
SG	39°48.50N	70°05.00W	1,150	949	3	2811	V	840313	841115	246	100		100			
	39°48.50N	50°05.00W	1,150	1,143	3	2812	VTr	840313	841115	246	100		100			
SH	39°50.55N	70°01.38W	1,220	1,019	3	2821	V	840315	841115	244	8440811	61			100	
	39°50.55N	70°01.38W	1,220	1,213	3	2822	VTr	840315	841115	244	840902	70		840902	70	
ST	40°10.96N	69°58.16W	100	56	3	2831	V	840516	841116	183	100		100			
	40°10.96N	69°58.16W	100	93	3	2832	VTCT	840516	841116	183	100	841110	97	Q		
	40°11.04N	69°58.33W	101	100	2	2731	T	831018	840315	148	831113	18		831113	18	
	40°10.92N	69°58.26W	102	101	3	2801	T	840316	841118	247	841111	97	?	841111	97	?

Table A4-1B. Summary of the temperature, conductivity, light transmission, and pressure data obtained as part of the Slope Experiment (see Table A4.1A for explanation).

Station	Dep. #	Mooring ID	Temperature Stop	Temperature %	Temperature Quality	Conductivity Stop	Conductivity %	Conductivity Quality	Transmission Stop	Transmission %	Transmission Quality	Pressure Stop	Pressure %	Pressure Quality
SA	1	2711P		100									100	
	3	2771P		100									100	
	1	2711		100			100			100	NG			
	2	2761		100										
	3	2771		100										
	1	2712		100										
	2	2762		100										
	3	2772	-	0	L									
SB	1	2671		100										
	1	2671P	821013	99								831013	99	
	1	2672		100										
	1	2673		100										
SC	1	2681P		100									100	
	1	2681		100			100			100	NG			
	1	2682		100			100			100	Q			
	1	2682P	830426	48								830426	48	
	1	2683	-	0	L									
	1	2684	-	0	L									
	1	2685	-	0	L									
SD	1	2691	831019	96										
SE	2	2741P		100									100	
	3	2781P	841115	99								841115	99	
	2	2741	831216	38	Q	831216	38	Q	831216	38	Q			
	3	2781	-	0	NG									

Table A4-1B. - Continued

Station	Dep. #	Mooring ID	Temperature Stop	Temperature %	Temperature Quality	Conductivity Stop	Conductivity %	Conductivity Quality	Transmission Stop	Transmission %	Transmission Quality	Pressure Stop	Pressure %	Pressure Quality
SE(cont)	2	2742		100			100			100				
	3	2782		100										
	1	2701	-	0	NG									
	2	2743		100										
	3	2783		100	Q									
	2	2744		100			100	NG		100				
	3	2784		100	Q	840703	45	Q		100	Q			
SF	3	2791		100										
	3	2792		100										
	2	2751		100			100			100				
	3	2793	840724	53		840724	53		840724	53				
	2	2752		100			100			100	F			
	3	2794	840807	59		-	0	NG	840627	42	F			
SG	3	2811		100										
	3	2812		100						100				
SH	3	2821		100										
	3	2822	840902	70		840902	70		840902	70				
ST	3	2831		100										
	3	2832		100			100			100	F			
	2	2731		100						100	Q		100	
	3	2801	841111	97					-	0	NG	841111	97	

Table A4.1C. Comments on data obtained as part of the Slope Experiment (see Table A4.1A for explanation).

Station	Dep #	Mooring ID	Comments
SA	1	2711P	
	3	2771P	
	1	2711	Transmissometer cable bad; occasional stretches of apparently good data
	2	2761	
	3	2771	
	1	2712	
	2	2762	
	3	2772	
SB	1	2671	
	1	2671P	
	1	2672	
	1	2673	
SC	1	2681P	
	1	2681	Transmissometer cable bad; occasional stretches of apparently good data
	1	2682	Unexplained beam attenuation spikes
	1	2682P	
	1	2683	
	1	2684	
	1	2685	
SD	1	2691	
SE	2	2741P	
	3	2781P	
	2	2741	Lots of read errors; cassette jammed in reader
	3	2781	

Table A4.1C Continued

Station	Dep #	Mooring ID	Comments
SE(cont)	2	2742	Rotor and vane did not work for first month of deployment; compass bad
	3	2782	
	1	2701	Lots of read errors; heavy scrubbing required
	2	2743	
	3	2783	Bad low order temperature bit; averaged data probably OK
	2	2744	FR thermistor flooded within 2 hours; conductivity sensor had bad capacitor
	3	2784	Clock 3 hours fast at recovery
SF	3	2791	Mooring wrapped by long-line at recovery; surface buoy shot
	3	2792	
	2	2751	
	3	2793	Cassette tape broke during reading
	2	2752	
	3	2794	Reader ate cassette tape
SG	3	2811	
	3	2812	
SH	3	2821	
	3	2822	Battery dead at recovery
ST	3	2831	
	3	2832	Rotor count doubled, speed divided by 2; probably OK
	2	2731	Transmissometer cable had leak in splice mold; stretches of apparently good data
	3	2801	Rotor and vane fouled from end; unusual calibration constants used for decode